

Dipl.-Ing. Michael KLANNER BSc

# Wave Based Method for Structural Vibrations of Thick Plates

## DOCTORAL THESIS

to achieve the academic degree of  
Doktor der technischen Wissenschaften

submitted to the Faculty of Mechanical Engineering and Economic  
Sciences at the University of Technology Graz

Supervisor: Univ.-Prof. Dr.-Ing. habil. Katrin Ellermann

Institute of Mechanics  
University of Technology Graz

Graz, August 2018



## **AFFIDAVIT**

I declare that I have authored this thesis independently, that I have not used other than the declared sources/resources, and that I have explicitly indicated all material which has been quoted either literally or by content from the sources used. The text document uploaded to TUGRAZonline is identical to the present doctoral thesis.

.....

Date

.....

Signature



# Abstract

The noise and vibration characteristics of newly developed products become increasingly important due to restrictive governmental regulations and customers' demand for acoustical comfort. A detailed knowledge about the product's structural behaviour is required in the early design phases to allow for an efficient optimization of the sound and vibration properties. Nowadays, virtual simulation tools are applied to get this information in a time- and cost-efficient way.

The flexural vibrations of plates are considered to be one of the most important sources of sound. Therefore, an accurate but simple mathematical model of the plate is required and efficient numerical techniques to solve the resulting governing equations have to be developed. This dissertation addresses the modeling of the structural vibrations of plates and the improvement and extension of an efficient numerical technique called Wave Based Method.

The most common mathematical models of plates are the Kirchhoff plate theory and the Mindlin plate theory. While the simpler Kirchhoff plate theory is generally applicable for thin plates and low frequencies, the more complicated Mindlin plate theory can be used for thick plates and higher frequencies. In this work, both models are analysed and their range of validity concerning the plate thickness and excitation frequency is thoroughly examined.

The Finite Element Method (FEM) is generally applied to predict the harmonic response of a plate in the low frequency range. Since the computational load of the FEM strongly increases with rising frequencies, alternative calculation methods are needed to get accurate results for plate vibration problems in the so-called mid-frequency range. A deterministic method called Wave Based Method (WBM) is able to tackle problems in the mid-frequency range due to an increased computational efficiency. This dissertation considers the development of the WBM for thick plate vibration problems governed by the Mindlin plate theory.

The general methodology of the WBM is specialized for the governing equations of the Mindlin plate theory and a different approach to select the basis functions in the WBM is proposed. Furthermore, new particular solution functions, which are closed-form analytical solutions of an infinite plate under certain excitation types, are presented. The computational performance of the WBM compared to the FEM is investigated through a variety of validation examples and the advantages of the new wave function selection is shown.



# **Acknowledgement**

First of all, I would like to express my deep gratitude to my research supervisor Univ.-Prof. Dr.-Ing. habil. Katrin Ellermann for giving me the great opportunity to conduct research in the very interesting field of structural mechanics. I thank Katrin for her valuable and constructive suggestions and patient guidance during the past years, which made this thesis possible.

I would also like to thank the University of Technology Graz for allowing me to become a researcher at this great institution and getting a deep insight in the scientific world for engineers.

Furthermore, I want to specially thank all my colleagues at the Institute of Mechanics for the great discussions, which gave me new perspectives at my own research, and the awesome time I had and still have working with them.

Especially I want to thank my family for their incredible support during my research and helping me through all steps of my education, which finally made all of this possible.

Finally, I want to thank my dear Liesa for constantly motivating me and the support and patience during the last several years. I am very grateful that you bring out the best of me.



# Table of Contents

<b>Abstract</b>	<b>v</b>
<b>Acknowledgement</b>	<b>vii</b>
<b>Table of Contents</b>	<b>ix</b>
<b>List of Figures</b>	<b>xiii</b>
<b>List of Tables</b>	<b>xxvii</b>
<b>List of Symbols</b>	<b>xxix</b>
<b>I Introduction to the simulation of steady-state structural vibrations</b>	<b>1</b>
<b>1 Introduction</b>	<b>3</b>
1.1 Motivation . . . . .	3
1.2 Scope and objectives of the dissertation . . . . .	5
1.3 Outline of the dissertation . . . . .	7
<b>2 State-of-the-art mathematical models for structural vibrations</b>	<b>9</b>
2.1 Vibrations of linear elastic solids . . . . .	9
2.2 Simplified models for thin structures: Plate theories . . . . .	13
2.2.1 Mindlin plate theory . . . . .	14
2.2.2 Kirchhoff plate theory . . . . .	23
2.2.3 Higher order plate theories . . . . .	27
2.3 Useful ranges of validity for the Kirchhoff and Mindlin plate theory . . . . .	28
2.3.1 Free vibrations of an infinite plate . . . . .	29
2.3.2 Influence of boundary conditions and other effects . . . . .	32
2.3.3 Further error sources and final remarks on the plate model validity	58
<b>3 Numerical techniques for the calculation of steady-state plate vibrations</b>	<b>59</b>
3.1 Element based techniques . . . . .	59
3.1.1 Conventional Finite Element Method . . . . .	59
3.1.2 Advances in the Finite Element Method . . . . .	66
3.2 Statistical methods . . . . .	67
3.2.1 Statistical Energy Analysis . . . . .	68
3.2.2 Improvements and extensions of the SEA . . . . .	70
3.3 Trefftz based approaches . . . . .	70
3.3.1 Source Simulation Techniques . . . . .	71
3.3.2 Indirectly coupled methods . . . . .	72

## Table of Contents

3.3.3	Directly coupled methods	72
<b>4</b>	<b>The Wave Based Method</b>	<b>75</b>
4.1	Methodology for a generalized Helmholtz problem	75
4.1.1	Generalized Helmholtz problem	75
4.1.2	The modeling procedure of the WBM	77
4.2	Properties of a wave based model	81
4.3	State-of-the-art developments	83
4.3.1	Physical problems tackled by the WBM	83
4.3.2	Current improvements and extensions of the WBM	87
4.3.3	Applications of the WBM to engineering problems	91
<b>II</b>	<b>Extensions and improvements of the Wave Based Method for structural vibrations</b>	<b>93</b>
<b>5</b>	<b>Particular solution functions for plate bending vibrations</b>	<b>95</b>
5.1	Basic mathematical principles	95
5.1.1	The Hankel transform	96
5.1.2	The residue theorem and Jordan's lemma	96
5.2	Particular solutions for the Mindlin plate theory	97
5.2.1	Point load excitation	98
5.2.2	Other axisymmetric load cases	103
5.2.3	Non-axisymmetric loading	111
5.3	Particular solutions for the Kirchhoff plate theory	116
<b>6</b>	<b>Extension of the Wave Based Method to thick plate vibrations</b>	<b>119</b>
6.1	Stress singularities in the Mindlin plate theory	119
6.1.1	Vibrations of an infinite wedge domain	120
6.1.2	Static solution for an infinite wedge domain	127
6.1.3	Comparison of the singularities in the static and dynamic solution	131
6.2	Application of the Wave Based Method	132
6.2.1	Field variable expansion	133
6.2.2	Construction of the system matrices	142
6.3	Modified selection of the wave functions	145
6.4	Validation examples	148
6.4.1	Single domain problems	150
6.4.2	Multi domain problem	181
<b>III</b>	<b>Conclusion and final remarks</b>	<b>191</b>
<b>7</b>	<b>Conclusion</b>	<b>193</b>
7.1	Validity ranges of the Kirchhoff and Mindlin plate	193
7.2	Development of the WBM for thick plate vibrations	194
7.3	New particular solution functions for plate vibrations	195
7.4	Improvement of the WBM - A new wave function selection	196

<b>8 Future research topics</b>	<b>197</b>
<b>IV Addenda</b>	<b>199</b>
<b>A The sub-region three-field generalized mixed variational principle for elas-</b>	
<b>todynamics</b>	<b>201</b>
<b>B The sub-region three-field generalized mixed variational principle for thick</b>	
<b>plates</b>	<b>205</b>
<b>C The sub-region three-field generalized mixed variational principle for thin</b>	
<b>plates</b>	<b>211</b>
<b>D Regularity conditions for integer eigenvalues in an infinite wedge domain</b>	<b>215</b>
<b>E Additional results for the validation examples</b>	<b>217</b>
<b>Bibliography</b>	<b>295</b>
<b>Curriculum Vitae</b>	<b>317</b>
<b>List of Publications</b>	<b>319</b>



# List of Figures

2.1	Normal and shear stress on an infinitesimal element . . . . .	10
2.2	Boundary conditions and coordinate systems of a subdivided elastic solid	13
2.3	Kinematic assumptions of the Mindlin plate theory . . . . .	15
2.4	Infinitesimal plate element . . . . .	18
2.5	Boundary conditions and coordinate systems of a subdivided plate . .	19
2.6	Infinitesimal element at a plate boundary . . . . .	22
2.7	Frequency spectrum of an infinite isotropic plate ( $\nu = 0.3$ ) . . . . .	30
2.8	Dimensions and boundary conditions of the rectangular plate configurations . . . . .	34
2.9	Expected and actual total error of a rectangular Mindlin plate ( $a/b = 0.6\dot{6}$ )	36
2.10	Expected and actual total error of a rectangular Mindlin plate ( $a/b = 1$ )	37
2.11	Expected and actual total error of a rectangular Mindlin plate ( $a/b = 1.5$ )	38
2.12	Additional error of a SCSC rectangular Kirchhoff plate ( $a/b = 0.6\dot{6}$ ) . .	40
2.13	Additional error of a SCSF rectangular Kirchhoff plate ( $a/b = 0.6\dot{6}$ ) . .	40
2.14	Additional error of a SFSF rectangular Kirchhoff plate ( $a/b = 0.6\dot{6}$ ) . .	40
2.15	Additional error of a SCSC rectangular Kirchhoff plate ( $a/b = 1$ ) . . . .	41
2.16	Additional error of a SCSF rectangular Kirchhoff plate ( $a/b = 1$ ) . . . .	41
2.17	Additional error of a SFSF rectangular Kirchhoff plate ( $a/b = 1$ ) . . . .	41
2.18	Additional error of a SCSC rectangular Kirchhoff plate ( $a/b = 1.5$ ) . . .	42
2.19	Additional error of a SCSF rectangular Kirchhoff plate ( $a/b = 1.5$ ) . . .	42
2.20	Additional error of a SFSF rectangular Kirchhoff plate ( $a/b = 1.5$ ) . . .	42
2.21	Dimensions and boundary conditions of the circular plate configurations	43
2.22	Expected and actual total error of a circular Mindlin plate . . . . .	45
2.23	Additional error of a clamped circular Kirchhoff plate . . . . .	46
2.24	Additional error of a simply-supported circular Kirchhoff plate . . . . .	46
2.25	Additional error of a free circular Kirchhoff plate . . . . .	46
2.26	Dimensions and boundary conditions of the sector plate configurations .	47
2.27	Expected and actual total error of a sectorial Mindlin plate ( $\alpha = 30^\circ$ ) .	49
2.28	Expected and actual total error of a sectorial Mindlin plate ( $\alpha = 165^\circ$ ) .	50
2.29	Expected and actual total error of a sectorial Mindlin plate ( $\alpha = 195^\circ$ ) .	51
2.30	Expected and actual total error of a sectorial Mindlin plate ( $\alpha = 330^\circ$ ) .	52
2.31	Additional error of a SCS sectorial Kirchhoff plate ( $\alpha = 30^\circ$ ) . . . . .	54
2.32	Additional error of a SSS sectorial Kirchhoff plate ( $\alpha = 30^\circ$ ) . . . . .	54
2.33	Additional error of a SFS sectorial Kirchhoff plate ( $\alpha = 30^\circ$ ) . . . . .	54
2.34	Additional error of a SCS sectorial Kirchhoff plate ( $\alpha = 165^\circ$ ) . . . . .	55
2.35	Additional error of a SSS sectorial Kirchhoff plate ( $\alpha = 165^\circ$ ) . . . . .	55
2.36	Additional error of a SFS sectorial Kirchhoff plate ( $\alpha = 165^\circ$ ) . . . . .	55
2.37	Additional error of a SCS sectorial Kirchhoff plate ( $\alpha = 195^\circ$ ) . . . . .	56
2.38	Additional error of a SSS sectorial Kirchhoff plate ( $\alpha = 195^\circ$ ) . . . . .	56

## List of Figures

2.39	Additional error of a SFS sectorial Kirchhoff plate ( $\alpha = 195^\circ$ ) . . . . .	56
2.40	Additional error of a SCS sectorial Kirchhoff plate ( $\alpha = 330^\circ$ ) . . . . .	57
2.41	Additional error of a SSS sectorial Kirchhoff plate ( $\alpha = 330^\circ$ ) . . . . .	57
2.42	Additional error of a SFS sectorial Kirchhoff plate ( $\alpha = 330^\circ$ ) . . . . .	57
3.1	FE mesh of a 2D domain with ten quadrilateral elements and 45 nodes . . . . .	60
3.2	Typical SEA system with two subsystems . . . . .	68
4.1	General two-dimensional bounded problem with two domains $\Omega^{(\alpha)}$ and $\Omega^{(\beta)}$ , different boundary conditions $\Gamma_j^{(\alpha)}$ and $\Gamma_j^{(\beta)}$ and the common interface $\Gamma^{(\alpha, \beta)}$ . . . . .	76
4.2	Smallest rectangular bounding box, circumscribing a convex 2D sub-domain . . . . .	78
5.1	Out-of-plane displacement $w_{point}$ and rotation about the $\varphi$ -axis $\psi_{r, point}$ of an infinite Mindlin plate excited by a harmonic point load at $r = 0$ . . . . .	101
5.2	Point load at an arbitrary position $(\check{x}, \check{y})$ . . . . .	102
5.3	Other axisymmetric load cases . . . . .	103
5.4	Out-of-plane displacement $w_{ring}$ and rotation about the $\varphi$ -axis $\psi_{r, ring}$ of an infinite Mindlin plate excited by a harmonic ring load with $r_0 = 0.8$ . . . . .	107
5.5	Out-of-plane displacement $w_{circ}$ and rotation about the $\varphi$ -axis $\psi_{r, circ}$ of an infinite Mindlin plate excited by a harmonic circular load with $r_0 = 0.8$ . . . . .	111
5.6	Alternating circular load . . . . .	112
5.7	Out-of-plane displacement $w_{ac}$ and rotations $\psi_{r, ac}$ and $\psi_{\varphi, ac}$ of an infinite Mindlin plate excited by a harmonic alternating circular load with $r_0 = 0.8$ . . . . .	115
6.1	Infinite wedge domain without external loading . . . . .	120
6.2	Static eigenvalues of an infinite wedge domain with various radial boundary conditions . . . . .	130
6.3	WBM sub-domains and domain coordinate systems of a general Mindlin plate . . . . .	132
6.4	Rectangular domains with arbitrary boundary conditions . . . . .	135
6.5	Corner coordinate systems for special purpose functions within a WBM model . . . . .	139
6.6	Boundary coordinate systems for the modified selection of the wave functions . . . . .	145
6.7	Evanescence wave function defined by the smallest rectangular bounding box . . . . .	146
6.8	Evanescence wave function defined through the boundary coordinate system . . . . .	146
6.9	Geometry of the single domain problems . . . . .	150
6.10	Boundary conditions and harmonic loading of the clamped plates . . . . .	153
6.11	Out-of-plane displacement and rotations about the $x$ - and $y$ -axis of a clamped plate ( $h = 0.005$ m) excited by an alternating circular load at 2610 Hz calculated with the original WBM using only the function set 1 and a truncation factor $T = 2$ . . . . .	154

6.12	Out-of-plane displacement and rotations about the $x$ - and $y$ -axis of a clamped plate ( $h = 0.005$ m) excited by an alternating circular load at 2610 Hz calculated with the modified WBM using only the function set 1 and a truncation factor $T = 2$ . . . . .	155
6.13	Picard conditions for the original and modified wave function selection (clamped plate) . . . . .	157
6.14	Frequency response functions of a clamped plate ( $h = 0.025$ m) excited by an alternating circular load calculated with the FEM (reference mesh) and the modified WBM (function set 1 and set 2, $T = 2$ ) . . . . .	158
6.15	Convergence curves of the out-of-plane displacement (clamped plate with $h = 0.01$ m) for the original WBM ( <i>set1</i> (—○—), <i>set1a2</i> (—*—)) and the modified WBM ( <i>set1</i> (—▲—), <i>set1a2</i> (—◆—)) . . . . .	159
6.16	Convergence curves of the rotation about the $x$ -axis (clamped plate with $h = 0.01$ m) for the original WBM ( <i>set1</i> (—○—), <i>set1a2</i> (—*—)) and the modified WBM ( <i>set1</i> (—▲—), <i>set1a2</i> (—◆—)) . . . . .	159
6.17	Convergence curves of the rotation about the $y$ -axis (clamped plate with $h = 0.01$ m) for the original WBM ( <i>set1</i> (—○—), <i>set1a2</i> (—*—)) and the modified WBM ( <i>set1</i> (—▲—), <i>set1a2</i> (—◆—)) . . . . .	159
6.18	Convergence curves (clamped plate with $h = 0.01$ m excited at 8000 Hz) for the original WBM in double precision ( <i>set1</i> (—○—), <i>set1a2</i> (—*—)) and quadruple precision ( <i>set1</i> (—*—), <i>set1a2</i> (—□—)) . . . . .	160
6.19	Convergence curves of the out-of-plane displacement (clamped plate with $h = 0.01$ ) for the FEM (—○—) and the modified WBM ( <i>set1</i> (—▲—), <i>set1a2</i> (—◆—)) . . . . .	161
6.20	Boundary conditions and harmonic loading of the free plates . . . . .	162
6.21	Out-of-plane displacement and rotations about the $x$ - and $y$ -axis of a free plate ( $h = 0.005$ m) excited by a constant ring load at 1310 Hz calculated with the original WBM using only the function set 1 and a truncation factor $T = 2$ . . . . .	163
6.22	Out-of-plane displacement and rotations about the $x$ - and $y$ -axis of a free plate ( $h = 0.005$ m) excited by a constant ring load at 1310 Hz calculated with the modified WBM using only the function set 1 and a truncation factor $T = 2$ . . . . .	164
6.23	Picard conditions for the original and modified wave function selection (free plate) . . . . .	165
6.24	Frequency response functions of a free plate ( $h = 0.025$ m) excited by a constant ring load calculated with the FEM (reference mesh) and the modified WBM (function set 1 and set 2, $T = 2$ ) . . . . .	166
6.25	Convergence curves of the out-of-plane displacement (free plate with $h = 0.01$ m) for the original WBM ( <i>set1</i> (—○—), <i>set1a2</i> (—*—)) and the modified WBM ( <i>set1</i> (—▲—), <i>set1a2</i> (—◆—)) . . . . .	168
6.26	Convergence curves of the rotation about the $x$ -axis (free plate with $h = 0.01$ m) for the original WBM ( <i>set1</i> (—○—), <i>set1a2</i> (—*—)) and the modified WBM ( <i>set1</i> (—▲—), <i>set1a2</i> (—◆—)) . . . . .	168
6.27	Convergence curves of the rotation about the $y$ -axis (free plate with $h = 0.01$ m) for the original WBM ( <i>set1</i> (—○—), <i>set1a2</i> (—*—)) and the modified WBM ( <i>set1</i> (—▲—), <i>set1a2</i> (—◆—)) . . . . .	168

## List of Figures

6.28 Convergence curves of the out-of-plane displacement (free plate with $h = 0.01$ ) for the FEM (—○—) and the modified WBM ( <i>set1</i> (—▲—), <i>set1a2</i> (—◆—)) . . . . .	169
6.29 Boundary conditions and harmonic loading of the cantilever plates . . . . .	169
6.30 Out-of-plane displacement and rotations about the $x$ - and $y$ -axis of a cantilever plate ( $h = 0.005$ m) excited by a constant circular load at 1780 Hz calculated with the modified WBM using only the function set 1 and a truncation factor $T = 2$ . . . . .	170
6.31 Frequency response functions of a cantilever plate ( $h = 0.025$ m) excited by a constant circular load calculated with the FEM (reference mesh) and the modified WBM (function set 1 and set 2, $T = 2$ ) . . . . .	172
6.32 Convergence curves of the out-of-plane displacement (cantilever plate with $h = 0.01$ m) for the modified WBM solved with the LU ( <i>set1</i> (—▲—), <i>set1a2</i> (—◆—)) and the SVD ( <i>set1</i> (—*—), <i>set1a2</i> (—□—)) . . . . .	173
6.33 Convergence curves of the rotation about the $x$ -axis (cantilever plate with $h = 0.01$ m) for the modified WBM solved with the LU ( <i>set1</i> (—▲—), <i>set1a2</i> (—◆—)) and the SVD ( <i>set1</i> (—*—), <i>set1a2</i> (—□—)) . . . . .	173
6.34 Convergence curves of the rotation about the $y$ -axis (cantilever plate with $h = 0.01$ m) for the modified WBM solved with the LU ( <i>set1</i> (—▲—), <i>set1a2</i> (—◆—)) and the SVD ( <i>set1</i> (—*—), <i>set1a2</i> (—□—)) . . . . .	173
6.35 Convergence curves of the out-of-plane displacement (cantilever plate with $h = 0.01$ ) for the FEM (—○—) and the modified WBM ( <i>set1</i> (—▲—), <i>set1a2</i> (—◆—)) . . . . .	174
6.36 Boundary conditions and harmonic loading of the hard SS plates . . . . .	175
6.37 Out-of-plane displacement and rotations about the $x$ - and $y$ -axis of a hard simply-supported plate ( $h = 0.005$ m) excited by a point load at 2300 Hz calculated with the modified WBM using the function set 1, corner functions and a truncation factor $T = 2$ . . . . .	176
6.38 Picard conditions for the modified wave function selection with and without corner functions (hard simply-supported plate) . . . . .	177
6.39 Frequency response functions of a hard simply-supported plate ( $h = 0.025$ m) excited by a point load calculated with the FEM (reference mesh) and the modified WBM (function set 1 and set 2, corner functions, $T = 2$ ) . . . . .	178
6.40 Convergence curves of the out-of-plane displacement (hard SS plate with $h = 0.01$ m) for the modified WBM ( <i>set1</i> (—▲—), <i>set1a2</i> (—◆—), <i>set1CF</i> (—*—), <i>set1a2CF</i> (—□—)) . . . . .	180
6.41 Convergence curves of the rotation about the $x$ -axis (hard SS plate with $h = 0.01$ m) for the modified WBM ( <i>set1</i> (—▲—), <i>set1a2</i> (—◆—), <i>set1CF</i> (—*—), <i>set1a2CF</i> (—□—)) . . . . .	180
6.42 Convergence curves of the rotation about the $y$ -axis (hard SS plate with $h = 0.01$ m) for the modified WBM ( <i>set1</i> (—▲—), <i>set1a2</i> (—◆—), <i>set1CF</i> (—*—), <i>set1a2CF</i> (—□—)) . . . . .	180
6.43 Convergence curves of the out-of-plane displacement (hard SS plate with $h = 0.01$ ) for the FEM (—○—) and the modified WBM ( <i>set1</i> (—▲—), <i>set1a2</i> (—◆—), <i>set1CF</i> (—*—), <i>set1a2CF</i> (—□—)) . . . . .	181
6.44 Geometry and loading of the multi domain clamped plate . . . . .	182

6.45	Out-of-plane displacement and rotations about the $x$ - and $y$ -axis of a multi domain clamped plate ( $h = 0.005$ m) excited by a constant circular load at 1043 Hz calculated with the modified WBM using both function sets, corner functions and a truncation factor $T = 4$ . . . . .	185
6.46	Frequency response functions of a multi domain clamped plate ( $h = 0.025$ m) excited by a constant circular load calculated with the FEM (reference mesh) and the modified WBM (function set 1 and set 2, corner functions, $T = 4$ ) . . . . .	187
6.47	Convergence curves of the out-of-plane displacement (multi domain clamped plate with $h = 0.01$ m) for the modified WBM ( <i>set1</i> (—▲—), <i>set1a2</i> (—●—), <i>set1CF</i> (—★—), <i>set1a2CF</i> (—■—)) . . . . .	188
6.48	Convergence curves of the rotation about the $x$ -axis (multi domain clamped plate with $h = 0.01$ m) for the modified WBM ( <i>set1</i> (—▲—), <i>set1a2</i> (—●—), <i>set1CF</i> (—★—), <i>set1a2CF</i> (—■—)) . . . . .	188
6.49	Convergence curves of the rotation about the $y$ -axis (multi domain clamped plate with $h = 0.01$ m) for the modified WBM ( <i>set1</i> (—▲—), <i>set1a2</i> (—●—), <i>set1CF</i> (—★—), <i>set1a2CF</i> (—■—)) . . . . .	188
6.50	Convergence curves of the out-of-plane displacement (multi domain clamped plate with $h = 0.005$ ) for the FEM (—○—) and the modified WBM ( <i>set1CF</i> (—★—), <i>set1a2CF</i> (—■—)) . . . . .	190
6.51	Convergence curves of the out-of-plane displacement (multi domain clamped plate with $h = 0.01$ ) for the FEM (—○—) and the modified WBM ( <i>set1CF</i> (—★—), <i>set1a2CF</i> (—■—)) . . . . .	190
6.52	Convergence curves of the out-of-plane displacement (multi domain clamped plate with $h = 0.025$ ) for the FEM (—○—) and the modified WBM ( <i>set1CF</i> (—★—), <i>set1a2CF</i> (—■—)) . . . . .	190
E.1	Out-of-plane displacement and rotations about the $x$ - and $y$ -axis of a clamped plate ( $h = 0.005$ m) excited by an alternating circular load at 850 Hz calculated with the original WBM using only the function set 1 and a truncation factor $T = 2$ . . . . .	218
E.2	Out-of-plane displacement and rotations about the $x$ - and $y$ -axis of a clamped plate ( $h = 0.005$ m) excited by an alternating circular load at 4195 Hz calculated with the original WBM using only the function set 1 and a truncation factor $T = 2$ . . . . .	219
E.3	Out-of-plane displacement and rotations about the $x$ - and $y$ -axis of a clamped plate ( $h = 0.005$ m) excited by an alternating circular load at 850 Hz calculated with the modified WBM using only the function set 1 and a truncation factor $T = 2$ . . . . .	220
E.4	Out-of-plane displacement and rotations about the $x$ - and $y$ -axis of a clamped plate ( $h = 0.005$ m) excited by an alternating circular load at 4195 Hz calculated with the modified WBM using only the function set 1 and a truncation factor $T = 2$ . . . . .	221
E.5	Out-of-plane displacement and rotations about the $x$ - and $y$ -axis of a clamped plate ( $h = 0.01$ m) excited by an alternating circular load at 1650 Hz calculated with the original WBM using only the function set 1 and a truncation factor $T = 2$ . . . . .	222

## List of Figures

E.6 Out-of-plane displacement and rotations about the $x$ - and $y$ -axis of a clamped plate ( $h = 0.01$ m) excited by an alternating circular load at 5080 Hz calculated with the original WBM using only the function set 1 and a truncation factor $T = 2$ . . . . .	223
E.7 Out-of-plane displacement and rotations about the $x$ - and $y$ -axis of a clamped plate ( $h = 0.01$ m) excited by an alternating circular load at 8000 Hz calculated with the original WBM using only the function set 1 and a truncation factor $T = 2$ . . . . .	224
E.8 Out-of-plane displacement and rotations about the $x$ - and $y$ -axis of a clamped plate ( $h = 0.01$ m) excited by an alternating circular load at 1650 Hz calculated with the modified WBM using only the function set 1 and a truncation factor $T = 2$ . . . . .	225
E.9 Out-of-plane displacement and rotations about the $x$ - and $y$ -axis of a clamped plate ( $h = 0.01$ m) excited by an alternating circular load at 5080 Hz calculated with the modified WBM using only the function set 1 and a truncation factor $T = 2$ . . . . .	226
E.10 Out-of-plane displacement and rotations about the $x$ - and $y$ -axis of a clamped plate ( $h = 0.01$ m) excited by an alternating circular load at 8000 Hz calculated with the modified WBM using only the function set 1 and a truncation factor $T = 2$ . . . . .	227
E.11 Out-of-plane displacement and rotations about the $x$ - and $y$ -axis of a clamped plate ( $h = 0.025$ m) excited by an alternating circular load at 3850 Hz calculated with the original WBM using only the function set 1 and a truncation factor $T = 2$ . . . . .	228
E.12 Out-of-plane displacement and rotations about the $x$ - and $y$ -axis of a clamped plate ( $h = 0.025$ m) excited by an alternating circular load at 10700 Hz calculated with the original WBM using only the function set 1 and a truncation factor $T = 2$ . . . . .	229
E.13 Out-of-plane displacement and rotations about the $x$ - and $y$ -axis of a clamped plate ( $h = 0.025$ m) excited by an alternating circular load at 15870 Hz calculated with the original WBM using only the function set 1 and a truncation factor $T = 2$ . . . . .	230
E.14 Out-of-plane displacement and rotations about the $x$ - and $y$ -axis of a clamped plate ( $h = 0.025$ m) excited by an alternating circular load at 3850 Hz calculated with the modified WBM using only the function set 1 and a truncation factor $T = 2$ . . . . .	231
E.15 Out-of-plane displacement and rotations about the $x$ - and $y$ -axis of a clamped plate ( $h = 0.025$ m) excited by an alternating circular load at 10700 Hz calculated with the modified WBM using only the function set 1 and a truncation factor $T = 2$ . . . . .	232
E.16 Out-of-plane displacement and rotations about the $x$ - and $y$ -axis of a clamped plate ( $h = 0.025$ m) excited by an alternating circular load at 15870 Hz calculated with the modified WBM using only the function set 1 and a truncation factor $T = 2$ . . . . .	233
E.17 Frequency response functions of a clamped plate ( $h = 0.005$ m) excited by an alternating circular load calculated with the FEM (reference mesh) and the modified WBM (function set 1 and set 2, $T = 2$ ) . . . . .	234

E.18 Frequency response functions of a clamped plate ( $h = 0.01$ m) excited by an alternating circular load calculated with the FEM (reference mesh) and the modified WBM (function set 1 and set 2, $T = 2$ ) . . . . .	235
E.19 Convergence curves of the out-of-plane displacement (clamped plate with $h = 0.005$ m) for the original WBM ( <i>set1</i> (—○—), <i>set1a2</i> (—*—)) and the modified WBM ( <i>set1</i> (—△—), <i>set1a2</i> (—◆—)) . . . . .	236
E.20 Convergence curves of the rotation about the $x$ -axis (clamped plate with $h = 0.005$ m) for the original WBM ( <i>set1</i> (—○—), <i>set1a2</i> (—*—)) and the modified WBM ( <i>set1</i> (—△—), <i>set1a2</i> (—◆—)) . . . . .	236
E.21 Convergence curves of the rotation about the $y$ -axis (clamped plate with $h = 0.005$ m) for the original WBM ( <i>set1</i> (—○—), <i>set1a2</i> (—*—)) and the modified WBM ( <i>set1</i> (—△—), <i>set1a2</i> (—◆—)) . . . . .	236
E.22 Convergence curves of the out-of-plane displacement (clamped plate with $h = 0.025$ m) for the original WBM ( <i>set1</i> (—○—), <i>set1a2</i> (—*—)) and the modified WBM ( <i>set1</i> (—△—), <i>set1a2</i> (—◆—)) . . . . .	237
E.23 Convergence curves of the rotation about the $x$ -axis (clamped plate with $h = 0.025$ m) for the original WBM ( <i>set1</i> (—○—), <i>set1a2</i> (—*—)) and the modified WBM ( <i>set1</i> (—△—), <i>set1a2</i> (—◆—)) . . . . .	237
E.24 Convergence curves of the rotation about the $y$ -axis (clamped plate with $h = 0.025$ m) for the original WBM ( <i>set1</i> (—○—), <i>set1a2</i> (—*—)) and the modified WBM ( <i>set1</i> (—△—), <i>set1a2</i> (—◆—)) . . . . .	237
E.25 Out-of-plane displacement and rotations about the $x$ - and $y$ -axis of a free plate ( $h = 0.005$ m) excited by a constant ring load at 220 Hz calculated with the original WBM using only the function set 1 and a truncation factor $T = 2$ . . . . .	238
E.26 Out-of-plane displacement and rotations about the $x$ - and $y$ -axis of a free plate ( $h = 0.005$ m) excited by a constant ring load at 2550 Hz calculated with the original WBM using only the function set 1 and a truncation factor $T = 2$ . . . . .	239
E.27 Out-of-plane displacement and rotations about the $x$ - and $y$ -axis of a free plate ( $h = 0.005$ m) excited by a constant ring load at 220 Hz calculated with the modified WBM using only the function set 1 and a truncation factor $T = 2$ . . . . .	240
E.28 Out-of-plane displacement and rotations about the $x$ - and $y$ -axis of a free plate ( $h = 0.005$ m) excited by a constant ring load at 2550 Hz calculated with the modified WBM using only the function set 1 and a truncation factor $T = 2$ . . . . .	241
E.29 Out-of-plane displacement and rotations about the $x$ - and $y$ -axis of a free plate ( $h = 0.01$ m) excited by a constant ring load at 440 Hz calculated with the original WBM using only the function set 1 and a truncation factor $T = 2$ . . . . .	242
E.30 Out-of-plane displacement and rotations about the $x$ - and $y$ -axis of a free plate ( $h = 0.01$ m) excited by a constant ring load at 2580 Hz calculated with the original WBM using only the function set 1 and a truncation factor $T = 2$ . . . . .	243

*List of Figures*

E.31 Out-of-plane displacement and rotations about the $x$ - and $y$ -axis of a free plate ( $h = 0.01$ m) excited by a constant ring load at 4970 Hz calculated with the original WBM using only the function set 1 and a truncation factor $T = 2$ . . . . .	244
E.32 Out-of-plane displacement and rotations about the $x$ - and $y$ -axis of a free plate ( $h = 0.01$ m) excited by a constant ring load at 440 Hz calculated with the modified WBM using only the function set 1 and a truncation factor $T = 2$ . . . . .	245
E.33 Out-of-plane displacement and rotations about the $x$ - and $y$ -axis of a free plate ( $h = 0.01$ m) excited by a constant ring load at 2580 Hz calculated with the modified WBM using only the function set 1 and a truncation factor $T = 2$ . . . . .	246
E.34 Out-of-plane displacement and rotations about the $x$ - and $y$ -axis of a free plate ( $h = 0.01$ m) excited by a constant ring load at 4970 Hz calculated with the modified WBM using only the function set 1 and a truncation factor $T = 2$ . . . . .	247
E.35 Out-of-plane displacement and rotations about the $x$ - and $y$ -axis of a free plate ( $h = 0.025$ m) excited by a constant ring load at 1050 Hz calculated with the original WBM using only the function set 1 and a truncation factor $T = 2$ . . . . .	248
E.36 Out-of-plane displacement and rotations about the $x$ - and $y$ -axis of a free plate ( $h = 0.025$ m) excited by a constant ring load at 5900 Hz calculated with the original WBM using only the function set 1 and a truncation factor $T = 2$ . . . . .	249
E.37 Out-of-plane displacement and rotations about the $x$ - and $y$ -axis of a free plate ( $h = 0.025$ m) excited by a constant ring load at 10700 Hz calculated with the original WBM using only the function set 1 and a truncation factor $T = 2$ . . . . .	250
E.38 Out-of-plane displacement and rotations about the $x$ - and $y$ -axis of a free plate ( $h = 0.025$ m) excited by a constant ring load at 1050 Hz calculated with the modified WBM using only the function set 1 and a truncation factor $T = 2$ . . . . .	251
E.39 Out-of-plane displacement and rotations about the $x$ - and $y$ -axis of a free plate ( $h = 0.025$ m) excited by a constant ring load at 5900 Hz calculated with the modified WBM using only the function set 1 and a truncation factor $T = 2$ . . . . .	252
E.40 Out-of-plane displacement and rotations about the $x$ - and $y$ -axis of a free plate ( $h = 0.025$ m) excited by a constant ring load at 10700 Hz calculated with the modified WBM using only the function set 1 and a truncation factor $T = 2$ . . . . .	253
E.41 Frequency response functions of a free plate ( $h = 0.005$ m) excited by a constant ring load calculated with the FEM (reference mesh) and the modified WBM (function set 1 and set 2, $T = 2$ ) . . . . .	254
E.42 Frequency response functions of a free plate ( $h = 0.01$ m) excited by a constant ring load calculated with the FEM (reference mesh) and the modified WBM (function set 1 and set 2, $T = 2$ ) . . . . .	255

E.43 Convergence curves of the out-of-plane displacement (free plate with $h = 0.005$ m) for the original WBM ( <i>set1</i> (—○—), <i>set1a2</i> (—*—)) and the modified WBM ( <i>set1</i> (—▲—), <i>set1a2</i> (—◆—)) . . . . .	256
E.44 Convergence curves of the rotation about the $x$ -axis (free plate with $h = 0.005$ m) for the original WBM ( <i>set1</i> (—○—), <i>set1a2</i> (—*—)) and the modified WBM ( <i>set1</i> (—▲—), <i>set1a2</i> (—◆—)) . . . . .	256
E.45 Convergence curves of the rotation about the $y$ -axis (free plate with $h = 0.005$ m) for the original WBM ( <i>set1</i> (—○—), <i>set1a2</i> (—*—)) and the modified WBM ( <i>set1</i> (—▲—), <i>set1a2</i> (—◆—)) . . . . .	256
E.46 Convergence curves of the out-of-plane displacement (free plate with $h = 0.025$ m) for the original WBM ( <i>set1</i> (—○—), <i>set1a2</i> (—*—)) and the modified WBM ( <i>set1</i> (—▲—), <i>set1a2</i> (—◆—)) . . . . .	257
E.47 Convergence curves of the rotation about the $x$ -axis (free plate with $h = 0.025$ m) for the original WBM ( <i>set1</i> (—○—), <i>set1a2</i> (—*—)) and the modified WBM ( <i>set1</i> (—▲—), <i>set1a2</i> (—◆—)) . . . . .	257
E.48 Convergence curves of the rotation about the $y$ -axis (free plate with $h = 0.025$ m) for the original WBM ( <i>set1</i> (—○—), <i>set1a2</i> (—*—)) and the modified WBM ( <i>set1</i> (—▲—), <i>set1a2</i> (—◆—)) . . . . .	257
E.49 Out-of-plane displacement and rotations about the $x$ - and $y$ -axis of a cantilever plate ( $h = 0.005$ m) excited by a constant circular load at 420 Hz calculated with the modified WBM using only the function set 1 and a truncation factor $T = 2$ . . . . .	258
E.50 Out-of-plane displacement and rotations about the $x$ - and $y$ -axis of a cantilever plate ( $h = 0.005$ m) excited by a constant circular load at 3170 Hz calculated with the modified WBM using only the function set 1 and a truncation factor $T = 2$ . . . . .	259
E.51 Out-of-plane displacement and rotations about the $x$ - and $y$ -axis of a cantilever plate ( $h = 0.01$ m) excited by a constant circular load at 840 Hz calculated with the modified WBM using only the function set 1 and a truncation factor $T = 2$ . . . . .	260
E.52 Out-of-plane displacement and rotations about the $x$ - and $y$ -axis of a cantilever plate ( $h = 0.01$ m) excited by a constant circular load at 3500 Hz calculated with the modified WBM using only the function set 1 and a truncation factor $T = 2$ . . . . .	261
E.53 Out-of-plane displacement and rotations about the $x$ - and $y$ -axis of a cantilever plate ( $h = 0.01$ m) excited by a constant circular load at 6120 Hz calculated with the modified WBM using only the function set 1 and a truncation factor $T = 2$ . . . . .	262
E.54 Out-of-plane displacement and rotations about the $x$ - and $y$ -axis of a cantilever plate ( $h = 0.025$ m) excited by a constant circular load at 2000 Hz calculated with the modified WBM using only the function set 1 and a truncation factor $T = 2$ . . . . .	263
E.55 Out-of-plane displacement and rotations about the $x$ - and $y$ -axis of a cantilever plate ( $h = 0.025$ m) excited by a constant circular load at 7750 Hz calculated with the modified WBM using only the function set 1 and a truncation factor $T = 2$ . . . . .	264

## List of Figures

E.56 Out-of-plane displacement and rotations about the $x$ - and $y$ -axis of a cantilever plate ( $h = 0.025$ m) excited by a constant circular load at 12770 Hz calculated with the modified WBM using only the function set 1 and a truncation factor $T = 2$ . . . . .	265
E.57 Frequency response functions of a cantilever plate ( $h = 0.005$ m) excited by a constant circular load calculated with the FEM (reference mesh) and the modified WBM (function set 1 and set 2, $T = 2$ ) . . . . .	266
E.58 Frequency response functions of a cantilever plate ( $h = 0.01$ m) excited by a constant circular load calculated with the FEM (reference mesh) and the modified WBM (function set 1 and set 2, $T = 2$ ) . . . . .	267
E.59 Convergence curves of the out-of-plane displacement (cantilever plate with $h = 0.005$ m) for the modified WBM solved with the LU ( <i>set1</i> (—▲), <i>set1a2</i> (—◆)) and the SVD ( <i>set1</i> (—*), <i>set1a2</i> (—□)) . . . . .	268
E.60 Convergence curves of the rotation about the $x$ -axis (cantilever plate with $h = 0.005$ m) for the modified WBM solved with the LU ( <i>set1</i> (—▲), <i>set1a2</i> (—◆)) and the SVD ( <i>set1</i> (—*), <i>set1a2</i> (—□)) . . . . .	268
E.61 Convergence curves of the rotation about the $y$ -axis (cantilever plate with $h = 0.005$ m) for the modified WBM solved with the LU ( <i>set1</i> (—▲), <i>set1a2</i> (—◆)) and the SVD ( <i>set1</i> (—*), <i>set1a2</i> (—□)) . . . . .	268
E.62 Convergence curves of the out-of-plane displacement (cantilever plate with $h = 0.025$ m) for the modified WBM solved with the LU ( <i>set1</i> (—▲), <i>set1a2</i> (—◆)) and the SVD ( <i>set1</i> (—*), <i>set1a2</i> (—□)) . . . . .	269
E.63 Convergence curves of the rotation about the $x$ -axis (cantilever plate with $h = 0.025$ m) for the modified WBM solved with the LU ( <i>set1</i> (—▲), <i>set1a2</i> (—◆)) and the SVD ( <i>set1</i> (—*), <i>set1a2</i> (—□)) . . . . .	269
E.64 Convergence curves of the rotation about the $y$ -axis (cantilever plate with $h = 0.025$ m) for the modified WBM solved with the LU ( <i>set1</i> (—▲), <i>set1a2</i> (—◆)) and the SVD ( <i>set1</i> (—*), <i>set1a2</i> (—□)) . . . . .	269
E.65 Out-of-plane displacement and rotations about the $x$ - and $y$ -axis of a hard simply-supported plate ( $h = 0.005$ m) excited by a point load at 670 Hz calculated with the modified WBM using the function set 1, corner functions and a truncation factor $T = 2$ . . . . .	270
E.66 Out-of-plane displacement and rotations about the $x$ - and $y$ -axis of a hard simply-supported plate ( $h = 0.005$ m) excited by a point load at 3800 Hz calculated with the modified WBM using the function set 1, corner functions and a truncation factor $T = 2$ . . . . .	271
E.67 Out-of-plane displacement and rotations about the $x$ - and $y$ -axis of a hard simply-supported plate ( $h = 0.01$ m) excited by a point load at 1300 Hz calculated with the modified WBM using the function set 1, corner functions and a truncation factor $T = 2$ . . . . .	272
E.68 Out-of-plane displacement and rotations about the $x$ - and $y$ -axis of a hard simply-supported plate ( $h = 0.01$ m) excited by a point load at 4600 Hz calculated with the modified WBM using the function set 1, corner functions and a truncation factor $T = 2$ . . . . .	273

E.69 Out-of-plane displacement and rotations about the $x$ - and $y$ -axis of a hard simply-supported plate ( $h = 0.01$ m) excited by a point load at 7310 Hz calculated with the modified WBM using the function set 1, corner functions and a truncation factor $T = 2$ . . . . .	274
E.70 Out-of-plane displacement and rotations about the $x$ - and $y$ -axis of a hard simply-supported plate ( $h = 0.025$ m) excited by a point load at 3150 Hz calculated with the modified WBM using the function set 1, corner functions and a truncation factor $T = 2$ . . . . .	275
E.71 Out-of-plane displacement and rotations about the $x$ - and $y$ -axis of a hard simply-supported plate ( $h = 0.025$ m) excited by a point load at 9800 Hz calculated with the modified WBM using the function set 1, corner functions and a truncation factor $T = 2$ . . . . .	276
E.72 Out-of-plane displacement and rotations about the $x$ - and $y$ -axis of a hard simply-supported plate ( $h = 0.025$ m) excited by a point load at 15060 Hz calculated with the modified WBM using the function set 1, corner functions and a truncation factor $T = 2$ . . . . .	277
E.73 Frequency response functions of a hard simply-supported plate ( $h = 0.005$ m) excited by a point load calculated with the FEM (reference mesh) and the modified WBM (function set 1 and set 2, corner functions, $T = 2$ ) . . . . .	278
E.74 Frequency response functions of a hard simply-supported plate ( $h = 0.01$ m) excited by a point load calculated with the FEM (reference mesh) and the modified WBM (function set 1 and set 2, corner functions, $T = 2$ ) . . . . .	279
E.75 Convergence curves of the out-of-plane displacement (hard SS plate with $h = 0.005$ m) for the modified WBM ( <i>set1</i> (—▲—), <i>set1a2</i> (—◆—), <i>set1CF</i> (—★—), <i>set1a2CF</i> (—■—)) . . . . .	280
E.76 Convergence curves of the rotation about the $x$ -axis (hard SS plate with $h = 0.005$ m) for the modified WBM ( <i>set1</i> (—▲—), <i>set1a2</i> (—◆—), <i>set1CF</i> (—★—), <i>set1a2CF</i> (—■—)) . . . . .	280
E.77 Convergence curves of the rotation about the $y$ -axis (hard SS plate with $h = 0.005$ m) for the modified WBM ( <i>set1</i> (—▲—), <i>set1a2</i> (—◆—), <i>set1CF</i> (—★—), <i>set1a2CF</i> (—■—)) . . . . .	280
E.78 Convergence curves of the out-of-plane displacement (hard SS plate with $h = 0.025$ m) for the modified WBM ( <i>set1</i> (—▲—), <i>set1a2</i> (—◆—), <i>set1CF</i> (—★—), <i>set1a2CF</i> (—■—)) . . . . .	281
E.79 Convergence curves of the rotation about the $x$ -axis (hard SS plate with $h = 0.025$ m) for the modified WBM ( <i>set1</i> (—▲—), <i>set1a2</i> (—◆—), <i>set1CF</i> (—★—), <i>set1a2CF</i> (—■—)) . . . . .	281
E.80 Convergence curves of the rotation about the $y$ -axis (hard SS plate with $h = 0.025$ m) for the modified WBM ( <i>set1</i> (—▲—), <i>set1a2</i> (—◆—), <i>set1CF</i> (—★—), <i>set1a2CF</i> (—■—)) . . . . .	281
E.81 Out-of-plane displacement and rotations about the $x$ - and $y$ -axis of a multi domain clamped plate ( $h = 0.005$ m) excited by a constant circular load at 350 Hz calculated with the modified WBM using both function sets, corner functions and a truncation factor $T = 4$ . . . . .	282

## List of Figures

E.82 Out-of-plane displacement and rotations about the $x$ - and $y$ -axis of a multi domain clamped plate ( $h = 0.005$ m) excited by a constant circular load at 1650 Hz calculated with the modified WBM using both function sets, corner functions and a truncation factor $T = 4$ . . . . .	283
E.83 Out-of-plane displacement and rotations about the $x$ - and $y$ -axis of a multi domain clamped plate ( $h = 0.01$ m) excited by a constant circular load at 680 Hz calculated with the modified WBM using both function sets, corner functions and a truncation factor $T = 4$ . . . . .	284
E.84 Out-of-plane displacement and rotations about the $x$ - and $y$ -axis of a multi domain clamped plate ( $h = 0.01$ m) excited by a constant circular load at 2060 Hz calculated with the modified WBM using both function sets, corner functions and a truncation factor $T = 4$ . . . . .	285
E.85 Out-of-plane displacement and rotations about the $x$ - and $y$ -axis of a multi domain clamped plate ( $h = 0.01$ m) excited by a constant circular load at 3240 Hz calculated with the modified WBM using both function sets, corner functions and a truncation factor $T = 4$ . . . . .	286
E.86 Out-of-plane displacement and rotations about the $x$ - and $y$ -axis of a multi domain clamped plate ( $h = 0.025$ m) excited by a constant circular load at 1650 Hz calculated with the modified WBM using both function sets, corner functions and a truncation factor $T = 4$ . . . . .	287
E.87 Out-of-plane displacement and rotations about the $x$ - and $y$ -axis of a multi domain clamped plate ( $h = 0.025$ m) excited by a constant circular load at 4740 Hz calculated with the modified WBM using both function sets, corner functions and a truncation factor $T = 4$ . . . . .	288
E.88 Out-of-plane displacement and rotations about the $x$ - and $y$ -axis of a multi domain clamped plate ( $h = 0.025$ m) excited by a constant circular load at 7200 Hz calculated with the modified WBM using both function sets, corner functions and a truncation factor $T = 4$ . . . . .	289
E.89 Frequency response functions of a multi domain clamped plate ( $h = 0.005$ m) excited by a constant circular load calculated with the FEM (reference mesh) and the modified WBM (function set 1 and set 2, corner functions, $T = 4$ ) . . . . .	290
E.90 Frequency response functions of a multi domain clamped plate ( $h = 0.01$ m) excited by a constant circular load calculated with the FEM (reference mesh) and the modified WBM (function set 1 and set 2, corner functions, $T = 4$ ) . . . . .	291
E.91 Convergence curves of the out-of-plane displacement (multi domain clamped plate with $h = 0.005$ m) for the modified WBM ( <i>set1</i> (—▲—), <i>set1a2</i> (—◆—), <i>set1CF</i> (—★—), <i>set1a2CF</i> (—■—)) . . . . .	292
E.92 Convergence curves of the rotation about the $x$ -axis (multi domain clamped plate with $h = 0.005$ m) for the modified WBM ( <i>set1</i> (—▲—), <i>set1a2</i> (—◆—), <i>set1CF</i> (—★—), <i>set1a2CF</i> (—■—)) . . . . .	292
E.93 Convergence curves of the rotation about the $y$ -axis (multi domain clamped plate with $h = 0.005$ m) for the modified WBM ( <i>set1</i> (—▲—), <i>set1a2</i> (—◆—), <i>set1CF</i> (—★—), <i>set1a2CF</i> (—■—)) . . . . .	292

E.94 Convergence curves of the out-of-plane displacement (multi domain clamped plate with $h = 0.025$ m) for the modified WBM ( <i>set1</i> (—▲—), <i>set1a2</i> (—○—), <i>set1CF</i> (—★—), <i>set1a2CF</i> (—■—)) . . . . .	293
E.95 Convergence curves of the rotation about the $x$ -axis (multi domain clamped plate with $h = 0.025$ m) for the modified WBM ( <i>set1</i> (—▲—), <i>set1a2</i> (—○—), <i>set1CF</i> (—★—), <i>set1a2CF</i> (—■—)) . . . . .	293
E.96 Convergence curves of the rotation about the $y$ -axis (multi domain clamped plate with $h = 0.025$ m) for the modified WBM ( <i>set1</i> (—▲—), <i>set1a2</i> (—○—), <i>set1CF</i> (—★—), <i>set1a2CF</i> (—■—)) . . . . .	293



# List of Tables

2.1	Relative error $\varepsilon_{f1}$ of the Kirchhoff and Mindlin plate theory ( $\nu = 0.3$ ) . . . . .	31
2.2	3D FEM models for the analysis of the rectangular plate configurations . . . . .	35
2.3	3D FEM models for the analysis of the circular plate configurations . . . . .	43
2.4	3D FEM models for the analysis of the sector plate configurations . . . . .	48
6.1	Characteristic equations for the static eigenvalues of an infinite wedge domain . . . . .	128
6.2	Comparison of the static and dynamic eigenvalues causing singularities . . . . .	131
6.3	Wave function sets for the Mindlin plate problem . . . . .	134
6.4	Thicknesses of the convex plate configurations and Kirchhoff limits . . . . .	151
6.5	Modal analysis of the convex plate configurations . . . . .	151
6.6	FEM reference models for the convergence analysis . . . . .	152
6.7	FEM reference models for the FRF . . . . .	152
6.8	Special purpose functions for the hard simply-supported plate examples . . . . .	175
6.9	Thicknesses of the multi domain clamped plates and Kirchhoff limits . . . . .	182
6.10	Modal analysis of the multi domain clamped plates . . . . .	183
6.11	FEM reference models for the convergence analysis and the FRF . . . . .	183
6.12	Special purpose functions for the multi domain clamped plate examples . . . . .	184



# List of Symbols

## Abbreviations

1D	One-dimensional
2D	Two-dimensional
3D	Three-dimensional
bcd	Boundary condition
BEM	Boundary Element Method
BE-WBM	Hybrid Boundary Element-Wave Based Method
BKM	Boundary Knot Method
C	Clamped
DDM	Domain Decomposition Method
DEM	Discontinues Enrichment Method
DGM	Discontinuous Galerkin Method
dofs	Degrees of freedom
EDA	Energy Distribution Analysis
ESM	Equivalent Source Method
F	Free
FE	Finite Element
FEM	Finite Element Method
FE-WBM	Hybrid Finite Element-Wave Based Method
FFS	Fast Frequency Sweep
FRF	Frequency Response Funtion
GB	Gigabyte
GGLS-FEM	Galerkin Generalized Least Squares FEM
GHz	Gigahertz
GLS-FEM	Galerkin Least-Squares FEM
GVLS-FEM	Galerkin Gradient Least-Squares FEM
HT-FEM	Hybrid-Trefftz Finite Element Method
LU	Lower-upper
MFS	Method of Fundamental Solutions
PUFEM	Partition of Unity Finite Element Method
RAM	Random-Access Memory
S, SS	Simply-supported
SEA	Statistical Energy Analysis
SmEdA	Statistical modal Energy distribution Analysis
SS1	Hard simply-supported
SS2	Soft simply-supported
SVD	Singular value decomposition
TMM	Transfer Matrix Method
UWVF	Ultra Weak Variational Formulation

## List of Symbols

VTCR	Variational Theory of Complex Rays
WBM	Wave Based Method
WBM-SEA	Hybrid Wave Based Method-Statistical Energy Analysis
WBM-TMM	Hybrid Wave Based-Transfer Matrix Model
WIA	Wave Intensity Analysis

## Arabic symbols

$A$	WBM system matrix
$A^\bullet$	System matrix of the sub-domain $\bullet$
$a$	Length of a rectangular plate
$b$	Width of a rectangular plate
$b$	Right-hand side vector of the WBM linear system
$b^\bullet$	Right-hand side vector of the WBM sub-system $\bullet$
$\bar{B}_\bullet$	Externally prescribed boundary field
$C$	Extensional rigidity of a plate
$C^{(\bullet, \star)}$	Coupling matrix between WBM sub-domains $\bullet$ and $\star$
$c_L$	Propagation velocity of dilatational plane waves
$c_S$	Propagation velocity of rotational plane waves
$D$	Flexural rigidity of a plate
$E$	Young's modulus
$\bar{E}_i$	Total dynamical energy of a SEA subsystem $i$
$e$	Potential function to decouple the membrane equations
$f$	Frequency
$\mathbf{f}$	Force vector acting on a 3D infinitesimal element
$\mathbf{f}_\bullet$	Right-hand side vector in a FE model
$f_i$	components of the 3D force vector with $i = \{x, y, z\}$
$f_m$	External source of the $m^{\text{th}}$ Helmholtz equation
$G$	Shear modulus
$H$	Potential function to decouple the Mindlin equations
$H(\bullet)$	Heaviside step function
$H_i$	Potential functions to decouple the Navier-Cauchy equations with $i = \{1, 2, 3\}$
$H_n^{(1)}(\bullet)$	$n^{\text{th}}$ -order Hankel functions of the first kind
$H_n^{(2)}(\bullet)$	$n^{\text{th}}$ -order Hankel functions of the second kind
$H_{pc}$	Mixed energy at an interface
$h$	Plate thickness
$h_{fe}$	Greatest element size in a FE mesh
$h_{ij}$	Power transfer coefficient
$I_n(\bullet)$	$n^{\text{th}}$ -order modified Bessel function of the first kind
$J_n(\bullet)$	$n^{\text{th}}$ -order Bessel function of the first kind
$j$	Imaginary unit $\sqrt{-1}$
$K_\bullet$	Stiffness matrix in a FE model
$K_n(\bullet)$	$n^{\text{th}}$ -order modified Bessel function of the second kind
$k$	Shear correction factor
$k$	or wavenumber
$k$	Wavenumber used in the basis function $\Phi_\bullet$

$k_b$	Plate bending wavenumber	$[\text{m}^{-1}]$
$k_{f1}$	Bending dominant flexural wavenumber	$[\text{m}^{-1}]$
$k_{f2}$	Shear dominant flexural wavenumber	$[\text{m}^{-1}]$
$k_l$	In-plane longitudinal wavenumber	$[\text{m}^{-1}]$
$k_M$	Shear correction factor defined by Mindlin	$[ - ]$
$k_m$	Wavenumber of the $m^{\text{th}}$ Helmholtz equation	$[\text{m}^{-1}]$
$k_r$	Parameter of the Hankel transform	
$k_s$	Out-of-plane shear wavenumber	$[\text{m}^{-1}]$
$k_t$	In-plane shear wavenumber	$[\text{m}^{-1}]$
$k_W$	Shear correction factor defined by Wittrick	$[ - ]$
$L$	Characteristic length of a problem domain or the Lagrangian function	$[\text{m}]$ $[\text{Js}]$
$L_b$	Length of a boundary	$[\text{m}]$
$L_x, L_y$	Dimensions of the smallest rectangular bounding box	$[\text{m}]$
$\mathbf{M}_\bullet$	Mass matrix in a FE model	
$M_i$	Modal overlap	$[ - ]$
$M_n, M_{ns}$	Bending and twisting moments at a plate boundary	$[\text{N}]$
$\overline{M}_n, \overline{M}_{ns}$	Prescribed bending and twisting moments at a boundary	$[\text{N}]$
$M_r, M_\varphi, M_{r\varphi}$	Bending and twisting moments in a plate (polar)	$[\text{N}]$
$M_x, M_y, M_{xy}$	Bending and twisting moments in a plate (Cartesian)	$[\text{N}]$
$\overline{m}_x, \overline{m}_y$	External moments acting on a plate	$[\text{N/m}]$
$N_\bullet^{(e)}$	Polynomial shape function to approximate the quantity $\bullet$	$[ - ]$
$N_i$	Total number of modes in a SEA subsystem $i$	$[ - ]$
$N_n, N_{ns}$	In-plane force at a plate boundary	$[\text{N/m}]$
$\overline{N}_n, \overline{N}_{ns}$	Prescribed in-plane force at a plate boundary	$[\text{N/m}]$
$N_x, N_y$	Normal forces in a plate	$[\text{N/m}]$
$N_{xy}$	In-plane shear force in a plate	$[\text{N/m}]$
$\mathbf{n}^{(\bullet)}$	Normal unit vector of sub-domain $\Omega^{(\bullet)}$	$[ - ]$
$n_\bullet$	Total number of basis functions $\Phi_\bullet$	$[ - ]$
$n_a^{(e)}$	Number of nodes per element	$[ - ]$
$n_\alpha$	Total number of sub-domains in a WBM model	$[ - ]$
$n_e$	Number of elements	$[ - ]$
$n_{fe}$	Total number of nodes in a FE model	$[ - ]$
$n_G$	Number of Gauss points	$[ - ]$
$n_H$	Number of Helmholtz equations	$[ - ]$
$n_i$	Modal density	$[\text{s}]$
$n_m$	Number of WBM basis functions	$[ - ]$
$n_{rp}$	Number of response points for the error calculation	$[ - ]$
$o$	Potential function to decouple the membrane equations	$[ - ]$
$p$	Order of the polynomial shape function	$[ - ]$
$p_k$	Poles on the real axis	
$Q_n$	Shear force at a plate boundary	$[\text{N/m}]$
$\overline{Q}_n$	Prescribed shear force at a plate boundary	$[\text{N/m}]$
$Q_r, Q_\varphi$	Out-of-plane shear forces in a plate (polar)	$[\text{N/m}]$
$Q_x, Q_y$	Out-of-plane shear forces in a plate (Cartesian)	$[\text{N/m}]$
$\overline{q}$	External normal load acting on a plate	$[\text{N/m}^2]$
$\overline{q}_0$	Magnitude of the external normal load acting on a plate	

*List of Symbols*

$R$	Radius	[m]
$R^*$	or rotatory inertia of an infinitesimal plate element	[m <sup>2</sup> ]
$R_\diamond^{(\bullet)}$	Smallest characteristic length of a sector plate	[m]
$R_\diamond^{(\bullet,\star)}$	Boundary residuals of sub-domain $\Omega^{(\bullet)}$ associated with quantity $\diamond$	
$R_\diamond^{(\bullet,\star)}$	Interface residuals of sub-domains $\Omega^{(\bullet)}$ and $\Omega^{(\star)}$ associated with quantity $\diamond$	
$\mathbf{r}$	Spatial coordinate vector	[m]
$r_0$	Radius of a ring or circular load	[m]
$S$	Constant in the Mindlin plate theory associated with shear	[m <sup>2</sup> ]
$S_N^{(e)}$	Set of node numbers associated with the element $e$	[–]
$\mathbf{s}^{(\bullet)}$	Tangential unit vector of sub-domain $\Omega^{(\bullet)}$	[–]
$T$	Truncation factor	[–]
$t$	Kinetic energy density function	[J/m <sup>3</sup> ]
$t$	Time	[s]
$\mathbf{t}^{(\bullet)}$	Tangential unit vector of sub-domain $\Omega^{(\bullet)}$	[–]
$\overline{U}$	Strain energy density function	[N/m <sup>2</sup> ]
$\overline{U}_b$	Bending energy density	[N/m]
$\overline{U}_m$	Membrane energy density	[N/m]
$\overline{U}_s$	Shear strain energy density	[N/m]
$\mathbf{u}$	3D displacement vector in Cartesian coordinates	[m]
$\mathbf{u}$	or in-plane displacement vector in Cartesian coordinates	[m]
$u$	Displacement in $x$ -direction	[m]
$\hat{\mathbf{u}}$	Vector of the unknown contribution factors in the WBM	
$\hat{u}_\bullet$	Weighting factors of the WBM basis functions $\Phi_\bullet$	
$u_0$	Displacement of the plate middle plane in $x$ -direction	[m]
$u_i$	Displacements in Cartesian coordinates with $i = \{x, y, z\}$	[m]
$\overline{u}_i$	Prescribed boundary displacement in $i$ -direction	[m]
$u_m$	Field variable of the $m^{\text{th}}$ Helmholtz equation	
$u_n, u_s, u_t$	Displacements in boundary coordinates	[m]
$\overline{u}_n, \overline{u}_s, \overline{u}_t$	Prescribed boundary displacements	[m]
$u_{p,m}$	Particular solution functions in a WBM model	
$V_n$	Generalized shear force in the Kirchhoff plate theory	[N/m]
$\overline{V}_n$	Prescribed generalized shear force at the boundary	[N/m]
$v$	Displacement in $y$ -direction	[m]
$v_\bullet$	Weighting functions of quantity $\bullet$	
$\hat{v}_\bullet$	Weighting factors of the basis functions approximating $\tilde{v}_m$	
$v_0$	Displacement of the plate middle plane in $y$ -direction	[m]
$\tilde{v}_m$	Components of the weighting function	
$w$	Out-of-plane displacement	[m]
$\overline{w}$	Prescribed out-of-plane displacement at the boundary	[m]
$\hat{w}_\bullet^{(e)}$	Value of the out-of-plane displacement at FE node $\bullet$	[m]
$w_1, w_2$	Potential functions to decouple the Mindlin equations	[m]
$w_{b1}, w_{b2}$	Potential functions to decouple the Kirchhoff equations	[m]
$Y_n(\bullet)$	$n^{\text{th}}$ -order Bessel function of the second kind	
$z_k^+, z_k^-$	Poles in the upper and lower complex half plane	

## Greek symbols

$\alpha$	Angle in a sector plate	[rad]
	Internal angle in an infinite wedge domain	[rad]
$\beta_i$	Coefficients of the SVD	
$\Gamma$	Boundary of the domain $\Omega$	[−]
$\Gamma^{(\bullet)}$	Gamma function	
$\Gamma^{(\bullet)}$	Boundary of the sub-domain $\Omega^{(\bullet)}$	[−]
$\Gamma^{(\bullet,*)}$	Interface between the sub-domains $\Omega^{(\bullet)}$ and $\Omega^{(*)}$	[−]
$\Gamma_{\sigma}^{(\bullet)}$	Boundary of the sub-domain $\Omega^{(\bullet)}$ with prescribed mechanical boundary conditions	[−]
$\Gamma_u^{(\bullet)}$	Boundary of the sub-domain $\Omega^{(\bullet)}$ with prescribed kinematic boundary conditions	[−]
$\Gamma_{u\sigma}^{(\bullet)}, \Gamma_{u\sigma 1}^{(\bullet)}, \Gamma_{u\sigma 2}^{(\bullet)}$	Boundary of the sub-domain $\Omega^{(\bullet)}$ with prescribed mixed boundary conditions	[−]
$\gamma_{xy}^0$	Membrane strain in a plate	[−]
$\gamma_{xz}, \gamma_{yz}$	Shear strains in a plate	[−]
$\Delta\omega$	Angular frequency band in a SEA model	[rad/s]
$\delta\bullet$	Variational operator	
$\delta(\bullet)$	Dirac delta function	
$\delta_{ij}$	Kronecker delta	[−]
$\varepsilon_{ad}$	Additional relative error of the plate theories caused by boundary conditions	[%]
$\varepsilon_{exp}$	Expected relative error of the plate theories from the infinite plate solutions	[%]
$\varepsilon_{f1}$	Relative error of the first bending dominant flexural vibration in an infinite plate domain	[%]
$\varepsilon_{ij}$	Normal strains ( $i = j$ ) and	[−]
	Shear strains ( $i \neq j$ ) with $(i, j) = \{x, y, z\}$	[−]
$\varepsilon_{tot}$	Total relative error of the plate theories	[%]
$\varepsilon_{xx}^0, \varepsilon_{yy}^0$	Membrane strains in a plate	[−]
$\eta$	Material loss factor	[−]
$\eta_i$	Damping loss factor of SEA subsystem $i$	[−]
$\eta_{ij}$	Coupling loss factor between SEA subsystem $i$ and $j$	[−]
$\kappa_x, \kappa_y, \kappa_{xy}$	Flexural strains (curvatures) in a plate	[m <sup>−1</sup> ]
$\lambda$	Wavelength	[m]
	or Lamé's first parameter	[N/m <sup>2</sup> ]
	or eigenvalues in an infinite wedge domain	[−]
$\lambda^s, \lambda^a$	Symmetric and antisymmetric dynamic eigenvalues	[−]
$\bar{\lambda}_M^s, \bar{\lambda}_M^a$	Symmetric and antisymmetric static eigenvalues exhibiting moment singularities	[−]
$\bar{\lambda}_Q^s, \bar{\lambda}_Q^a$	Symmetric and antisymmetric static eigenvalues exhibiting shear force singularities	[−]
$\mu$	Lamé's second parameter	[N/m <sup>2</sup> ]
$\mu_1, \mu_2$	Constants in the Mindlin plate theory	[−]
$\nu$	Poisson's ratio	[−]
$\xi$	Wavenumber along the $x$ -axis in an infinite plate	[m <sup>−1</sup> ]
$\Pi_{\bullet}$	Potential energy	[J]

## List of Symbols

$\bar{\Pi}_{\bullet}$	Averaged power flows in a SEA subsystem	[J/s]
$\rho$	Volumetric mass density	[kg/m <sup>3</sup> ]
$\sigma$	Cauchy stress tensor in Cartesian coordinates	[N/m <sup>2</sup> ]
$\sigma_i$	Singular values of a matrix	
$\sigma_{ij}$	Normal stresses ( $i = j$ ) and	[N/m <sup>2</sup> ]
$\sigma_n, \sigma_s, \sigma_t$	Shear stresses ( $i \neq j$ ) with ( $i, j = \{x, y, z\}$ )	[N/m <sup>2</sup> ]
$\bar{\sigma}_n, \bar{\sigma}_s, \bar{\sigma}_t$	Boundary traction in boundary coordinates	[N/m <sup>2</sup> ]
$\Psi_{\bullet}$	Prescribed boundary traction	[N/m <sup>2</sup> ]
$\Phi$	Special purpose functions in the WBM	[–]
$\Phi_{\bullet}$	Potential function to decouple the Navier-Cauchy equations	[m <sup>2</sup> ]
$\psi$	WBM basis functions for quantity $\bullet$	[–]
$\psi_0(\bullet)$	Rotation vector in Cartesian coordinates	[rad]
$\psi_n, \psi_s$	Digamma function	[–]
$\bar{\psi}_n, \bar{\psi}_s$	Rotation about the positive $s$ -axis and negative $n$ -axis	[rad]
$\psi_r, \psi_{\varphi}$	Prescribed rotations at the boundary	[rad]
$\psi_x, \psi_y$	Rotation about the positive $\varphi$ -axis and negative $r$ -axis	[rad]
$\hat{\psi}_{x\bullet}^{(e)}, \hat{\psi}_{y\bullet}^{(e)}$	Rotation about the positive $y$ -axis and negative $x$ -axis	[rad]
$\Omega$	Value of the rotations at FE node $\bullet$	[rad]
$\Omega^{(\bullet)}$	Problem domain	[–]
$\omega$	Problem sub-domain $\bullet$	[–]
$\omega$	Angular frequency	[rad/s]
$\omega_{3D}, \omega_{3Df1}, \omega_{3Df2}$	Angular frequencies in an infinite plate given by the 3D elasticity theory (asymmetric)	[rad/s]
$\omega_{3Ds}$	Angular frequency of the first asymmetric thickness-shear mode in an infinite plate given by the 3D elasticity theory	[rad/s]
$\omega_c$	Center angular frequency in a SEA model	[rad/s]
$\omega_c$	or cut-off angular frequency	[rad/s]
$\omega_k$	Angular frequency in an infinite plate given by the Kirchhoff plate theory	[rad/s]
$\omega_{mf1}, \omega_{mf2}, \omega_{ms}$	Angular frequencies in an infinite plate given by the Mindlin plate theory	[rad/s]
$\omega_s$	Angular frequency of the lowest, thickness-shear mode	[rad/s]

## Miscellaneous symbols

$\infty$	Infinity
$\mathcal{B}_{\bullet}$	General boundary differential operator
$\nabla$	Del operator
$\nabla^2$	Laplace operator
$\nabla_a^2$	2D Laplace operator for axisymmetric problems (polar)
$\cup$	Union operator
$\cap$	Intersection operator
$\forall \bullet$	For all $\bullet$
$\frac{\partial \bullet}{\partial \star}$	Partial derivative
$\ddot{\bullet}$	Second derivative with respect to time
$\bullet^T$	Transpose of $\bullet$
$\bullet^H$	Complex conjugate transpose of $\bullet$
$\bullet_{,\star}$	Partial derivative in index notation

$\bullet!$	Factorial
$\bullet^{(*)}$	Quantity $\bullet$ associated with sub-domain $\star$
$\#\bullet$	Number of quantity $\bullet$
$\mathcal{H}_0[\bullet], \tilde{\bullet}$	Zero-order Hankel transform of $\bullet$
$\mathcal{H}_0^{-1}[\bullet]$	Inverse zero-order Hankel transform of $\bullet$
$\mathcal{H}_1[\bullet], \tilde{\bullet}$	First-order Hankel transform of $\bullet$
$\mathcal{H}_1^{-1}[\bullet]$	Inverse first-order Hankel transform of $\bullet$
$\text{Re}[\bullet]$	Real part of the complex number $\bullet$
$\text{Im}[\bullet]$	Imaginary part of the complex number $\bullet$
$\text{Abs}[\bullet],  \bullet $	Absolute value of $\bullet$
$\text{arg}[\bullet]$	Argument of the complex number $\bullet$
$\text{avg}( \bullet )$	Averaged absolute value
$\text{cond}(\bullet)$	Conditioning of the matrix $\bullet$
$\text{Res}[\bullet]$	Residue at a pole
$\langle \delta \rangle$	Averaged relative error
$ \varepsilon $	Absolute error compared to the reference
$\emptyset$	Empty set
$\mathbb{N}_0$	Set of positive integers including 0
$\mathbb{Z}$	Set of integers
$\mathcal{T}_\bullet$	Specific Partial differential operator



## **Part I**

# **Introduction to the simulation of steady-state structural vibrations**



# 1 Introduction

This chapter deals with the general context of vibrational analysis. A brief introduction concerning the importance of numerical simulation techniques for structural vibrations of plates is given in Section 1.1. In Section 1.2 the scope and objectives of the dissertation are outlined and finally an overview of the main topics covered by the dissertation is shown in Section 1.3.

## 1.1 Motivation

In the global and dynamic market of today, companies are constantly competing against each other to increase their market share. One important point in winning this competition is the fast development of new products [1]. Therefore, the development cycles and the time-to-market should be as short as possible to respond quickly to the changing customer demands [1]. Other important factors in the product development process, besides the customer demands and time-to-market, are the costs and quality of the product, but also environmental factors like noise, air and water pollution emitted by the products [2]. Due to restrictive government regulations [3] and growing political and public awareness of negative consequences resulting from pollution [2], the environmental factors become increasingly relevant and have to be taken into account in the early design phases of a product.

Especially the noise and vibration characteristics of newly developed products are of high interest, since not only the governing legislation has to be fulfilled, but also the customer's sensitiveness for the acoustical comfort steadily increases [4]. A major source of noise is the vibration of solid structures, which can lead to a radiation of sound in the surrounding fluid. Whether sound radiation occurs, depends on the type of deformation, since only motion perpendicular to a surface can cause radiation [5]. Therefore, having a detailed knowledge of the vibration characteristics of a product in the early design stage is crucial to efficiently optimize the sound properties and to avoid undesired noise.

Virtual simulation tools are a possibility to gain this knowledge in a more time and cost efficient way compared to physical experimentation methods [6]. Furthermore, virtual models allow for a more profound insight into complex processes, which is not readily possible with a physical prototype and parameter variations are easily realized with a minimum of additional costs. In order to get a valid virtual prototype to analyze vibration characteristics, an accurate structural model of the investigated product is required and efficient computational methods are needed to predict the structural vibrations and radiated noise of the structure.

One of the most investigated structure as a sound source is the flat plate [7], since the flexural vibrations of thin structures are strongly related to sound radiation [8] and are by

## 1 Introduction

far the most important deformation type for the radiation of sound [5]. Several different models exist, which describe the structural behaviour of a plate [9]. The accuracy of these models depends on a variety of parameters, especially the plate thickness and the excitation frequency. Two very common theories are applied to investigate the vibration characteristics of plate structures: the Kirchhoff plate theory [10] and the Mindlin plate theory [11]. The main advantage of these two theories is the simplicity compared to more detailed models, e.g. a three-dimensional elasticity model, but certain restrictions have to be fulfilled to get accurate results.

Generally, these models lead to systems of partial differential equations, which have to be solved for certain initial and boundary conditions. An analytical solution of these problems is only feasible for very simple geometries and boundary conditions, which hardly occur in real life applications. Therefore, different numerical methods have been developed to predict approximate solutions of more complicated cases. By far the most used numerical method in structural dynamics is the Finite Element Method (FEM) [12], which enables solutions for nearly every possible problem configuration. The problem domain is decomposed into small elements and simple functions within each element approximate the exact solution. Even though nearly every kind of problem can be solved accurately with the FEM, the computational load increases very fast if, for example, higher frequencies are considered.

The complete frequency range can be divided into three regions, the low-, the mid- and high-frequency range [13, 12]. These three frequency ranges are generally defined by the ratio of the free wavelength  $\lambda$  to a characteristic length  $L$  of the problem domain and not by absolute frequency values. The three frequency ranges are characterized as follows:

- **Low-frequency range**

In the low-frequency range, the response of a component either only depends on the boundary conditions and does not involve wave propagation ( $\lambda/L \gg 1$ ) or only a small number of local modes contribute to the total response ( $\lambda/L \approx 1$ ) [12]. Furthermore, small changes in the model properties or geometry have only a minor influence on the component's response and therefore, a deterministic calculation of the response at certain points or the spatial response field in the domain is usually of interest [13].

- **High-frequency range**

In the high-frequency range, a huge number of local modes contribute to the total response of a component ( $\lambda/L \ll 1$ ) [12]. The response becomes very sensitive to small perturbations in the model properties and geometry and therefore, averaged values like the space and frequency averaged energy values are calculated instead of the deterministic values at certain points [13].

- **Mid-frequency range**

The mid-frequency range is situated between the low- and high-frequency range ( $\lambda/L < 1$ , but  $\lambda/L \not\ll 1$ ), where an intermediate number of local modes contribute to the total response of the component. It is also possible that some components of an assembly are still vibrating in the low-frequency range, while others are already in the high-frequency range. This state of vibration is also called a mid-frequency problem [12].

In the low-frequency range, element-based numerical methods, e.g. the FEM, are very well suited to analyze the vibrations of a structure, while statistical methods like the Statistical Energy Analysis (SEA) are efficiently applicable in the high frequency range. The mid-frequency range leaves a gap regarding the computational methods (the so-called mid-frequency gap), since the element-based methods become too computationally demanding and the requirements for the statistical methods are not yet met [13]. Therefore, it is an important task to develop new computational methods, which can predict sufficiently accurate results for plate vibration problems in the mid-frequency range with an acceptable computational load.

## 1.2 Scope and objectives of the dissertation

In the past two decades, a great effort has been put into the development of new computational methods or improving the established ones to close the mid-frequency gap. While some approaches try to improve the computational efficiency of low-frequency methods to extend their applicability to the mid-frequency range, others aim to relax some of the required assumptions of the statistical methods, which allows for their use at low frequencies.

One of these methods is the Wave Based Method (WBM) [14], which has been developed at the KU Leuven over the past 20 years. The WBM is a deterministic method and is based on the so-called Trefftz principle [15]. Even though it is a deterministic method, an improved computational efficiency is obtained by using a *priori* information of the final solution, which allows for its application in the mid-frequency range. The WBM has already been developed for many different types of problems, e.g. interior and exterior acoustics, poroelastic materials and structural dynamics. Especially in the field of structural dynamics, the investigations have been focused on beam, thin plate, membrane and shell vibration problems. Although this already covers a broad band of problems arising in structural dynamics, there is still room for extensions and improvements of the WBM in the field of structural vibrations.

While the WBM for thin plate vibration problems governed by the Kirchhoff plate theory is well developed, the prediction of thick plate vibrations is not yet feasible with the WBM. Furthermore, the definition of a thin and thick plate is not consistent in the literature, which is crucial for choosing the most appropriate theory. This leads to the following two goals in this dissertation:

### 1.) Analysis of the validity ranges of the Kirchhoff and Mindlin plate theory

Generally, the literature states that the Kirchhoff plate theory is applicable for thin plates and low frequencies, while the more accurate, but also more complicated, Mindlin plate theory can be used for thick plates and higher frequencies. Therefore, two different limits of the theories have to be distinguished, a geometrical limit (thin or thick plate), which can be defined through a ratio of the plate thickness to the smallest lateral dimension, and a frequency limit, which can be specified by the ratio of the bending wavelength to the plate thickness. A review of the literature shows that several definitions of a thin and thick plate exist, which are rather different from each other. Also the frequency limits for the Kirchhoff and Mindlin plate

## 1 Introduction

theory are not consistent within the literature. Therefore, one goal of this dissertation is the review of the stated limits in the literature and the analysis of the underlying assumptions, which have led to the definition of these limits. Furthermore, collecting additional information on the validity of the two plate theories, especially for plate bending vibrations, is an objective of this thesis.

### 2.) Extension of the WBM to thick plate vibration problems

The WBM for harmonic vibrations of thin plates governed by the Kirchhoff plate theory has been well developed by Vanmaele and her co-workers [16, 17, 18]. Since the applicability of the Kirchhoff plate theory is limited to thin plates, the vibrations of thick plates cannot yet be predicted by the WBM. The main goal of this dissertation is to close this gap and extend the WBM to thick plate vibration problems governed by the Mindlin plate theory. Therefore, the universal methodology of the WBM for generalized Helmholtz problems stated in a WBM review article by Deckers and her co-workers [14] has to be specialized for the governing equations of the Mindlin plate theory and specific problems like stress singularities in the response field have to be addressed.

The practical application of the WBM involves several challenges, e.g. the need of analytical particular solution functions to represent external loadings or the ill-conditioning of the WBM system matrix, which has to be considered in the matrix building and solution process. This leads to two additional goals of this dissertation:

### 3.) Development of new particular solution functions for plate vibrations

The application of the WBM and generally most of the other Trefftz methods requires the transformation of a system of inhomogeneous partial differential equations into a homogenous one. This is usually achieved by finding closed-form particular solution functions, which fulfil the inhomogeneous partial differential equations, while neglecting the applied boundary conditions (infinite domain). For plate vibration problems, only the solutions for an infinite plate domain excited by a point load is available in the literature, which limits the efficient use of the WBM for other load cases. Although a technique to find an approximate solution for general load cases has been developed by Jonckheere and his co-workers [19, 20], new particular solution functions are of major interest. Therefore, the development of analytical particular solution functions for plate vibration problems under certain load cases is another goal of this dissertation.

### 4.) Improvement of the stability and conditioning of the WBM

Among all indirect Trefftz methods, the ill-conditioning of the resulting system matrix is a great challenge, since an accurate but efficient construction of the system matrix is required and the solution of the system of linear equations has to be performed with appropriate linear solvers. The conditioning of the system matrix is strongly influenced by the chosen basis functions [21] and therefore, a goal of this dissertation is the analysis of the applied function selection and the identification of possible improvements in the function selection concerning the accuracy and stability of the WBM. Furthermore, investigating the efficiency, stability and accuracy of different solvers for the system of linear equations arising in the WBM is an important point in this work.

## 1.3 Outline of the dissertation

This dissertation is structured into four parts. The first part contains the introduction and theoretical background and in the second part the main research questions are answered. The main conclusions are drawn in the third part and finally several appendices are collected in the fourth part.

### **Part I: Introduction to the simulation of steady-state structural vibrations**

Part I consists of four chapters. Apart from a general introduction and the theoretical background on mathematical models and numerical techniques, the first research goal is addressed.

**Chapter 1** gives a short introduction on the importance of numerical techniques in the product development process and states the main research goals of this dissertation.

**Chapter 2** introduces the most important mathematical models for structural vibrations of plates. Furthermore, the first research goal is addressed by a detailed analysis of the useful ranges of validity of the Kirchhoff and Mindlin plate theory.

**Chapter 3** presents an overview of the most important numerical techniques to solve structural vibration problems. Additionally, improvements and extensions of the common element-based and statistical methods to close the mid-frequency gap as well as Trefftz based approaches are outlined.

**Chapter 4** provides an in-depth discussion of the WBM. The general methodology of the WBM for generalized Helmholtz problems is stated and the required steps to build a WBM model are explained. The properties of the WBM are compared to other methods and a comprehensive literature survey of the WBM is presented, including all fields of application and improvements and extensions of the WBM.

### **Part II: Extensions and improvements of the WBM for structural vibrations**

Part II focuses on the main research goals, the extension of the WBM to the vibrations of thick plates, and is structured into two chapters.

**Chapter 5** discusses the development of new particular solution functions for thin and thick plates. First the mathematical principle used to derive the particular solutions are stated and then the known solutions of the point load excitation are reviewed. The response field of an infinite plate to a constant ring load, a constant circular load and an alternating circular load are developed by either analytically integrating the point force solution or using the Hankel transform.

**Chapter 6** handles the extension of the WBM to plate vibrations governed by the Mindlin plate theory. Stress singularities arising in the Mindlin plate theory are analyzed to formulate so-called special purpose functions, which can improve the computational properties of the WBM. The general methodology of the WBM is specialized for the Mindlin plate theory by transforming the governing equations of the Mindlin plate to Helmholtz equations, defining the basis functions, proving the T-completeness of the function sets and developing the weighted residual formulation, which finally leads to a system of linear equations. A different wave function selection with advanced numerical properties is presented and a variety of validation examples is solved with the WBM.

**Part III: Conclusion and final remarks**

**Chapter 7** summarizes the main developments of the dissertation and concludes with the main achievements yielded by this work.

**Chapter 8** proposes further research topics, which have not been covered in this work.

**Part IV: Addenda**

Part IV collects the derivation of different variational formulations for structural problems, additional results of the validation examples, the bibliography, the author's curriculum vitae and a publication list.

## 2 State-of-the-art mathematical models for structural vibrations

This chapter presents the mathematical modelling techniques for solid structures and especially simplified models for thin structures and their range of validity are reviewed. In Section 2.1, the basic equations of elasticity are stated for linear elastic, isotropic materials and small deformations and displacements. Furthermore, a generalized mixed variational principle is shown, which allows for the representation of the basic equations in a strong and weak integral form. Simplified models for thin structures, e.g. the Kirchhoff plate theory or the Mindlin plate theory, are presented in Section 2.2. Several assumptions are used in the development of these simplified models, which are only fulfilled under certain conditions. Therefore, the range of validity of the different simplified models is investigated in Section 2.3.

### 2.1 Vibrations of linear elastic solids

The basic equations of elasticity are reviewed in this section, which can also be found in many textbooks, e.g. [22] or [23]. The equilibrium approach and the variational approach are used to derive the governing equations. A linear elastic, isotropic material is assumed and the deformation and displacements of the body are considered to be small. Therefore, the linear strain-displacement relations and Hooke's law for isotropic materials are valid. The stresses and the body force vector  $\mathbf{f}$  acting on an infinitesimal element are shown in Figure 2.1. Applying Newton's second law to the infinitesimal element and using the Einstein summation convention, the equations of motion in terms of stresses are given by

$$\sigma_{ij,j} + f_i = \rho \frac{\partial^2 u_i}{\partial t^2} \quad (i, j) = \{x, y, z\}, \quad (2.1)$$

with  $\sigma_{ij}$  ( $i = j$ ) the normal stresses,  $\sigma_{ij} = \sigma_{ji}$  ( $i \neq j$ ) the shear stresses,  $f_i$  the body forces,  $\rho$  the density,  $t$  the time and  $u_i$  the displacements. In Equation (2.1) the index notation  $\bullet, \star$  denotes the partial derivative of  $\bullet$  with respect to  $\star$ . The linear strain-displacement relations are

$$\varepsilon_{ij} = \frac{1}{2}(u_{i,j} + u_{j,i}), \quad (2.2)$$

with  $\varepsilon_{ij}$  ( $i = j$ ) the normal strains and  $\varepsilon_{ij} = \varepsilon_{ji}$  ( $i \neq j$ ) the shear strains. The constitutive relations for an isotropic, linear elastic material (Hooke's law)

$$\sigma_{ij} = \lambda \varepsilon_{kk} \delta_{ij} + 2 \mu \varepsilon_{ij} \quad k = \{x, y, z\}, \quad (2.3)$$

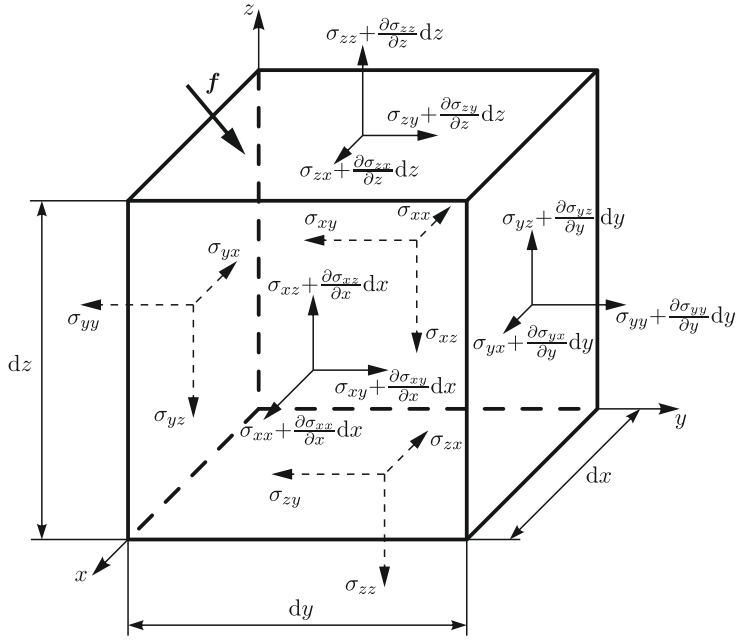


Figure 2.1: Normal and shear stress on an infinitesimal element

with  $\delta_{ij}$  the Kronecker delta and  $\lambda$  and  $\mu$  the Lamé constants, relate the stresses and strains. The Lamé constants are given by

$$\lambda = \frac{E(1 + j\eta)\nu}{(1 + \nu)(1 - 2\nu)}, \quad (2.4)$$

$$\mu = \frac{E(1 + j\eta)}{2(1 + \nu)}, \quad (2.5)$$

with  $E$  the Young's modulus,  $\nu$  the Poisson's ratio,  $\eta \geq 0$  the material loss factor and  $j = \sqrt{-1}$  the imaginary unit. The constitutive relations can also be defined through the strain energy density function for linear, isotropic materials [24]

$$\bar{U} = \frac{\lambda}{2} \varepsilon_{ii} \varepsilon_{jj} + \mu \varepsilon_{ij} \varepsilon_{ij} \quad (2.6)$$

and the relation

$$\sigma_{ij} = \frac{\partial \bar{U}}{\partial \varepsilon_{ij}}. \quad (2.7)$$

The substitution of the linear strain-displacement relations (Equation (2.2)) and the constitutive relations (Equation (2.3)) into the equations of motion in terms of stresses (Equation (2.1)) and the assumption of harmonic vibrations at angular frequency  $\omega$ , lead to the Navier-Cauchy equations [23]

$$\mu u_{i,jj} + (\lambda + \mu) u_{j,ij} + f_i = -\rho \omega^2 u_i, \quad (2.8)$$

where the factor  $e^{j\omega t}$  is omitted.

In the absence of body forces ( $f_i = 0$ ), it is possible to decompose the Navier-Cauchy equations using

$$u_x = \frac{\partial \Phi}{\partial x} + \frac{\partial H_3}{\partial y} - \frac{\partial H_2}{\partial z}, \quad (2.9)$$

$$u_y = \frac{\partial \Phi}{\partial y} + \frac{\partial H_1}{\partial z} - \frac{\partial H_3}{\partial x}, \quad (2.10)$$

$$u_z = \frac{\partial \Phi}{\partial z} + \frac{\partial H_2}{\partial x} - \frac{\partial H_1}{\partial y}, \quad (2.11)$$

where  $\Phi$  is a potential function, which gives rise to dilatation and  $H_1$ ,  $H_2$  and  $H_3$  are potential functions, which give rise to rotation [23, 25]. The Navier-Cauchy equations (Equation (2.8)) are fulfilled if the potential functions satisfy the Helmholtz equations

$$\nabla^2 \Phi + \frac{\omega^2}{c_L^2} \Phi = 0, \quad (2.12)$$

$$\nabla^2 H_i + \frac{\omega^2}{c_S^2} H_i = 0 \quad i = \{1, 2, 3\}, \quad (2.13)$$

with

$$c_L = \sqrt{\frac{\lambda + 2\mu}{\rho}} \quad \text{and} \quad c_S = \sqrt{\frac{\mu}{\rho}}, \quad (2.14)$$

the propagation velocities of dilatational (longitudinal) and rotational (shear) plane waves in an infinite elastic solid [23, 25] and  $\nabla^2 = \partial^2/\partial x^2 + \partial^2/\partial y^2 + \partial^2/\partial z^2$  the three-dimensional Laplace operator in Cartesian coordinates.

In Figure 2.2 an elastic solid  $\Omega$ , which is divided into two sub-domains  $\Omega = \Omega^{(\alpha)} \cup \Omega^{(\beta)}$ , is shown. The Navier-Cauchy equations are three coupled second-order partial differential equations and require three boundary conditions at every point of the problem surface  $\Gamma = \Gamma^{(\alpha)} \cup \Gamma^{(\beta)}$ . The boundary coordinate systems, shown in Figure 2.2, with the normal unit vectors  $\mathbf{n}^{(l)}$  and the tangential unit vectors  $\mathbf{s}^{(l)}$  and  $\mathbf{t}^{(l)}$  ( $l = \{\alpha, \beta\}$ ), which satisfy  $\mathbf{n}^{(l)} \cdot \mathbf{s}^{(l)} = 0$  and  $\mathbf{n}^{(l)} \times \mathbf{s}^{(l)} = \pm \mathbf{t}^{(l)}$  (+ for  $l = \alpha$  and - for  $l = \beta$ ), are used to define the common boundary and interface conditions. Each sub-domain surface is subdivided into three non-overlapping parts  $\Gamma^{(\alpha)} = \Gamma_u^{(\alpha)} \cup \Gamma_\sigma^{(\alpha)} \cup \Gamma^{(\alpha, \beta)}$  and  $\Gamma^{(\beta)} = \Gamma_u^{(\beta)} \cup \Gamma_\sigma^{(\beta)} \cup \Gamma^{(\alpha, \beta)}$ , where  $\Gamma^{(\alpha, \beta)}$  is the interface between the two sub-domains. The common boundary conditions are [20]:

- Dirichlet boundary conditions (kinematic boundary conditions) with prescribed normal displacement  $\bar{u}_n^{(l)}$  and tangential displacements  $\bar{u}_s^{(l)}$  and  $\bar{u}_t^{(l)}$ :

$$\mathbf{r} \in \Gamma_u^{(l)} \begin{cases} R_{u_n}^{(l)} = u_n^{(l)} - \bar{u}_n^{(l)} = 0, \\ R_{u_s}^{(l)} = u_s^{(l)} - \bar{u}_s^{(l)} = 0, \\ R_{u_t}^{(l)} = u_t^{(l)} - \bar{u}_t^{(l)} = 0, \end{cases} \quad (2.15)$$

with  $u_n^{(l)} = \mathbf{n}^{(l)T} \mathbf{u}^{(l)}$ ,  $u_s^{(l)} = \mathbf{s}^{(l)T} \mathbf{u}^{(l)}$  and  $u_t^{(l)} = \mathbf{t}^{(l)T} \mathbf{u}^{(l)}$  and the displacement vector  $\mathbf{u}^{(l)} = [u_x^{(l)}, u_y^{(l)}, u_z^{(l)}]^T$ . The special case of fixed boundaries is given by  $\bar{u}_n^{(l)} = 0$ ,  $\bar{u}_s^{(l)} = 0$  and  $\bar{u}_t^{(l)} = 0$ .

- Neumann boundary conditions (mechanical boundary conditions) with prescribed normal traction  $\bar{\sigma}_n^{(l)}$  and tangential tractions  $\bar{\sigma}_s^{(l)}$  and  $\bar{\sigma}_t^{(l)}$ :

$$\mathbf{r} \in \Gamma_{\sigma}^{(l)} \begin{cases} R_{\sigma_n}^{(l)} = \sigma_n^{(l)} - \bar{\sigma}_n^{(l)} = 0, \\ R_{\sigma_s}^{(l)} = \sigma_s^{(l)} - \bar{\sigma}_s^{(l)} = 0, \\ R_{\sigma_t}^{(l)} = \sigma_t^{(l)} - \bar{\sigma}_t^{(l)} = 0, \end{cases} \quad (2.16)$$

with  $\sigma_n^{(l)} = \mathbf{n}^{(l)T} \boldsymbol{\sigma}^{(l)} \mathbf{n}^{(l)}$ ,  $\sigma_s^{(l)} = \mathbf{s}^{(l)T} \boldsymbol{\sigma}^{(l)} \mathbf{n}^{(l)}$  and  $\sigma_t^{(l)} = \mathbf{t}^{(l)T} \boldsymbol{\sigma}^{(l)} \mathbf{n}^{(l)}$  and the Cauchy stress tensor

$$\boldsymbol{\sigma}^{(l)} = \begin{bmatrix} \sigma_{xx}^{(l)} & \sigma_{yx}^{(l)} & \sigma_{zx}^{(l)} \\ \sigma_{xy}^{(l)} & \sigma_{yy}^{(l)} & \sigma_{zy}^{(l)} \\ \sigma_{xz}^{(l)} & \sigma_{yz}^{(l)} & \sigma_{zz}^{(l)} \end{bmatrix}. \quad (2.17)$$

The special case of a free boundary is given by  $\bar{\sigma}_n^{(l)} = 0$ ,  $\bar{\sigma}_s^{(l)} = 0$  and  $\bar{\sigma}_t^{(l)} = 0$ .

The so-called mixed boundary conditions are a combination of Dirichlet and Neumann boundary conditions in different coordinate directions and are defined by

$$\mathbf{r} \in \Gamma_{u\sigma}^{(l)} \begin{cases} R_{u_n}^{(l)} = u_n^{(l)} - \bar{u}_n^{(l)} = 0 \quad \text{or} \quad R_{\sigma_n}^{(l)} = \sigma_n^{(l)} - \bar{\sigma}_n^{(l)} = 0, \\ R_{u_s}^{(l)} = u_s^{(l)} - \bar{u}_s^{(l)} = 0 \quad \text{or} \quad R_{\sigma_s}^{(l)} = \sigma_s^{(l)} - \bar{\sigma}_s^{(l)} = 0, \\ R_{u_t}^{(l)} = u_t^{(l)} - \bar{u}_t^{(l)} = 0 \quad \text{or} \quad R_{\sigma_t}^{(l)} = \sigma_t^{(l)} - \bar{\sigma}_t^{(l)} = 0 \end{cases} \quad (2.18)$$

and the special case of rolling boundary conditions with zero normal displacement ( $\bar{u}_n^{(l)} = 0$ ) and zero tangential tractions ( $\bar{\sigma}_s^{(l)} = 0$  and  $\bar{\sigma}_t^{(l)} = 0$ ).

At the common interface  $\Gamma^{(\alpha, \beta)}$ , the two sub-domains are forced to move together and the continuity of displacements and the force equilibrium across the interface

$$\mathbf{r} \in \Gamma^{(\alpha, \beta)} \begin{cases} R_{u_n}^{(\alpha, \beta)} = u_n^{(\alpha)} + u_n^{(\beta)} = 0, \\ R_{u_s}^{(\alpha, \beta)} = u_s^{(\alpha)} + u_s^{(\beta)} = 0, \\ R_{u_t}^{(\alpha, \beta)} = u_t^{(\alpha)} + u_t^{(\beta)} = 0, \\ R_{\sigma_n}^{(\alpha, \beta)} = \sigma_n^{(\alpha)} - \sigma_n^{(\beta)} = 0, \\ R_{\sigma_s}^{(\alpha, \beta)} = \sigma_s^{(\alpha)} - \sigma_s^{(\beta)} = 0, \\ R_{\sigma_t}^{(\alpha, \beta)} = \sigma_t^{(\alpha)} - \sigma_t^{(\beta)} = 0, \end{cases} \quad (2.19)$$

have to be fulfilled. At the common interface, the normal and tangential boundary vectors of the two sub-domains are related by  $\mathbf{n}^{(\alpha)} = -\mathbf{n}^{(\beta)}$ ,  $\mathbf{s}^{(\alpha)} = -\mathbf{s}^{(\beta)}$  and  $\mathbf{t}^{(\alpha)} = -\mathbf{t}^{(\beta)}$ .

Together, the basic equations (Equations (2.1)–(2.3)) and the boundary and interface conditions (Equations (2.15), (2.16), (2.18) and (2.19)) describe the problem of elastodynamics in strong form. For certain numerical methods, it is beneficial to describe the problem of elastodynamics in a weak form. The variational approach is a possibility to derive a weak form of the elastodynamic problem.

Compared to the previously shown equilibrium approach, the sub-region three-field generalized mixed variational principle for elasticity, shown in [26] for the static problem, is an

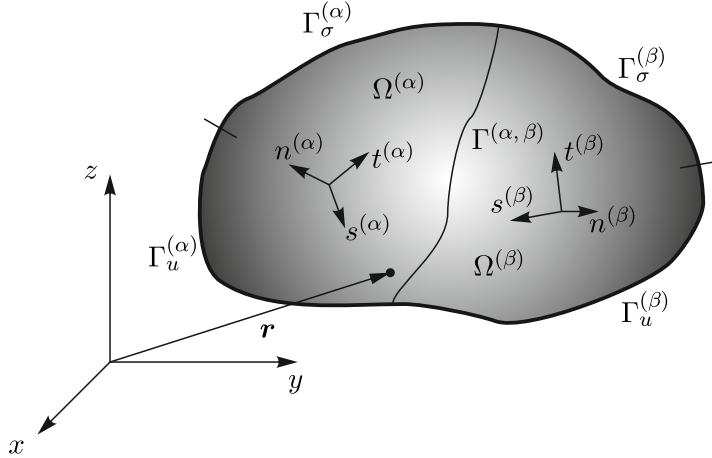


Figure 2.2: Boundary conditions and coordinate systems of a subdivided elastic solid

alternative approach to derive the basic equations and boundary and interface conditions of elasticity. The stationary condition of the functional

$$\begin{aligned}
 \delta L = 0 = \int_{t_0}^{t_1} \left( \sum_l \iiint_{\Omega^{(l)}} \left( \left( \frac{\partial \bar{U}(\varepsilon_{ij}^{(l)})}{\partial \varepsilon_{ij}^{(l)}} - \sigma_{ij}^{(l)} \right) \delta \varepsilon_{ij}^{(l)} - \left( \varepsilon_{ij}^{(l)} - \frac{1}{2} (u_{i,j}^{(l)} + u_{j,i}^{(l)}) \right) \delta \sigma_{ij}^{(l)} \right. \right. \\
 - \left( \sigma_{ij,j}^{(l)} + f_i^{(l)} - \rho \ddot{u}_i^{(l)} \right) \delta u_i^{(l)} \Big) dV + \iint_{\Gamma_{\sigma}^{(l)}} (\sigma_r^{(l)} - \bar{\sigma}_r^{(l)}) \delta u_r^{(l)} dS - \iint_{\Gamma_u^{(l)}} (u_r^{(l)} - \bar{u}_r^{(l)}) \delta \sigma_r^{(l)} dS \\
 \left. \left. + \iint_{\Gamma^{(\alpha, \beta)}} \left( (\sigma_r^{(\alpha)} - \sigma_r^{(\beta)}) \delta u_r^{(\alpha)} - (u_r^{(\alpha)} + u_r^{(\beta)}) \delta \sigma_r^{(\beta)} \right) dS \right) dt, \right) \quad (2.20)
 \end{aligned}$$

with  $\delta \bullet$  the variation operator,  $l = \{\alpha, \beta\}$ ,  $(i, j) = \{x, y, z\}$ ,  $r = \{n, s, t\}$  and  $\bullet$  the second derivative with respect to time is equivalent to the basic equations of elasticity (Equations (2.1)–(2.3)) and the boundary and interface conditions (Equations (2.15), (2.16), (2.18) and (2.19)). The integral form of the elastodynamic problem in Equation (2.20) is derived in Appendix A by extending the approach shown in [26] to dynamic problems. The strong integral form in Equation (2.20) can be transformed into a weak form through integration by parts.

## 2.2 Simplified models for thin structures: Plate theories

If one dimension of an elastic solid is sufficiently small compared to the other two dimensions, it is not always necessary to solve the three-dimensional elasticity equations derived in Section 2.1. Simplified two-dimensional models, the so-called plate models, have been developed to study the deformation and stress fields in thin plane elastic solids.

The plate models introduce additional assumptions of the displacement field, which simplify the governing equations compared to the Navier-Cauchy equations from three-dimens-

ional elasticity. Depending on the kinematic assumptions, several plate theories, the classical plate theory (Kirchhoff plate theory) [10], the first order shear deformation theory (Mindlin plate theory) [11] and higher order shear deformation theories, e.g. the Reddy plate theory [27], have been developed.

In Section 2.2.1 the Mindlin plate theory is reviewed and the underlying assumptions of the theory and the resulting governing equations are stated. The Kirchhoff plate theory is derived in Section 2.2.2 and an overview of higher order plate theories is given in Section 2.2.3. A comparison of the Kirchhoff and Mindlin plate theory and their range of validity are shown in Section 2.3.

### 2.2.1 Mindlin plate theory

The Mindlin plate theory, a first order shear deformation theory developed by Mindlin in 1951 [11], is reviewed in this section. A further description of the theory can be found in many textbooks, e.g. [22, 9]. In the Mindlin plate theory, it is assumed that [22]

- the plate thickness is small compared to the other two dimensions of the plate,
- the out-of-plane displacement of the plate is small compared to the plate thickness,
- straight lines, which are normal to the middle plane in the undeformed plate (transverse normals), remain straight in the deformed state,
- the transverse normals are inextensible and the transverse stress component is negligible

and therefore, the linear strain-displacement relations are valid and the displacements, shown in Figure 2.3, are given by

$$u(x, y, z, t) = u_0(x, y, t) + z \psi_x(x, y, t), \quad (2.21)$$

$$v(x, y, z, t) = v_0(x, y, t) + z \psi_y(x, y, t), \quad (2.22)$$

$$w(x, y, z, t) = w(x, y, t). \quad (2.23)$$

In Equations (2.21)–(2.23),  $u_0(x, y, t)$  and  $v_0(x, y, t)$  are the displacements in  $x$ - and  $y$ -direction of the points on the middle plane ( $z = 0$ ),  $w(x, y, t)$  is the out-of-plane displacement in  $z$ -direction (independent of  $z$ ),  $\psi_x(x, y, t)$  is the positive rotation about the  $y$ -axis and  $\psi_y(x, y, t)$  is the negative rotation about the  $x$ -axis. The plate thickness is denoted by  $h$  and the geometric middle plane, as seen in Figure 2.3, coincides with the  $xy$ -plane.

Substituting Equations (2.21)–(2.23) into the linear strain-displacement relations (Equation (2.2)) leads to

$$\varepsilon_{xx} = \frac{\partial u_0}{\partial x} + z \frac{\partial \psi_x}{\partial x} = \varepsilon_{xx}^0 + z \kappa_x, \quad (2.24)$$

$$\varepsilon_{yy} = \frac{\partial v_0}{\partial y} + z \frac{\partial \psi_y}{\partial y} = \varepsilon_{yy}^0 + z \kappa_y, \quad (2.25)$$

$$\varepsilon_{zz} = 0, \quad (2.26)$$

$$\varepsilon_{xy} = \frac{1}{2} \left( \frac{\partial u_0}{\partial y} + \frac{\partial v_0}{\partial x} + z \left( \frac{\partial \psi_x}{\partial y} + \frac{\partial \psi_y}{\partial x} \right) \right) = \frac{1}{2} \gamma_{xy}^0 + z \kappa_{xy}, \quad (2.27)$$

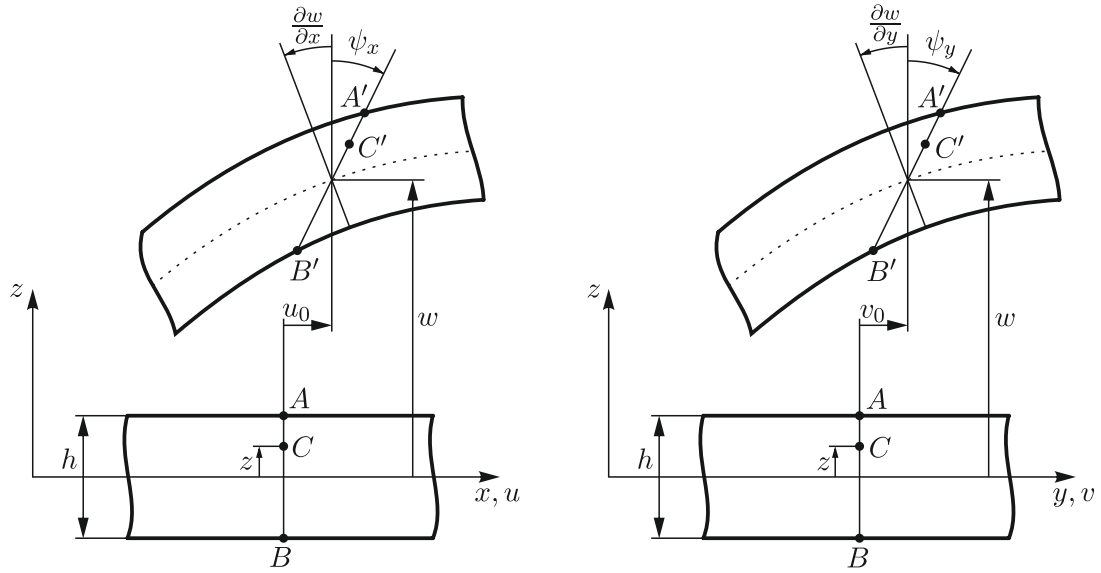


Figure 2.3: Kinematic assumptions of the Mindlin plate theory

$$\varepsilon_{xz} = \frac{1}{2} \left( \psi_x + \frac{\partial w}{\partial x} \right) = \frac{1}{2} \gamma_{xz}, \quad (2.28)$$

$$\varepsilon_{yz} = \frac{1}{2} \left( \psi_y + \frac{\partial w}{\partial y} \right) = \frac{1}{2} \gamma_{yz}, \quad (2.29)$$

with  $\varepsilon_{xx}^0$ ,  $\varepsilon_{yy}^0$  and  $\gamma_{xy}^0$  the strains of the middle surface (membrane strains),  $\kappa_x$ ,  $\kappa_y$  and  $\kappa_{xy}$  the flexural strains (curvatures) and  $\gamma_{xz}$  and  $\gamma_{yz}$  the shear strains [9].

From the linear strain-displacement relations it is apparent, that the strains due to flexure vary linearly in thickness direction, while the membrane and shear strains are constant through the plate thickness. Even though  $\varepsilon_{zz} = 0$ , a state of plane stress ( $\sigma_{zz} = 0$ ) is assumed, since the thickness of the plate is small compared to the other two dimensions. The plane stress-reduced constitutive relations for a linear elastic isotropic material are given by [22]

$$\begin{aligned} \sigma_{xx} &= \frac{E(1+j\eta)}{1-\nu^2} (\varepsilon_{xx} + \nu \varepsilon_{yy}), & \sigma_{xy} &= 2G \varepsilon_{xy}, \\ \sigma_{yy} &= \frac{E(1+j\eta)}{1-\nu^2} (\varepsilon_{yy} + \nu \varepsilon_{xx}), & \sigma_{xz} &= 2G \varepsilon_{xz}, \\ \sigma_{zz} &= 0 \quad (\text{neglected}), & \sigma_{yz} &= 2G \varepsilon_{yz}, \end{aligned} \quad (2.30)$$

with  $G = \mu$  the shear modulus. Substituting Equations (2.24)–(2.29) into Equation (2.30) and integrating over the plate thickness  $h$ , the normal forces

$$N_x = \int_{-\frac{h}{2}}^{\frac{h}{2}} \sigma_{xx} dz = C(\varepsilon_{xx}^0 + \nu \varepsilon_{yy}^0), \quad (2.31)$$

$$N_y = \int_{-\frac{h}{2}}^{\frac{h}{2}} \sigma_{yy} dz = C(\varepsilon_{yy}^0 + \nu \varepsilon_{xx}^0), \quad (2.32)$$

the shear forces

$$N_{xy} = \int_{-\frac{h}{2}}^{-\frac{h}{2}} \sigma_{xy} dz = \frac{C}{2} (1 - \nu) \gamma_{xy}^0, \quad (2.33)$$

$$Q_x = \int_{-\frac{h}{2}}^{-\frac{h}{2}} \sigma_{xz} dz = k^2 G h \gamma_{xz}, \quad (2.34)$$

$$Q_y = \int_{-\frac{h}{2}}^{-\frac{h}{2}} \sigma_{yz} dz = k^2 G h \gamma_{yz} \quad (2.35)$$

and the bending and twisting moments

$$M_x = \int_{-\frac{h}{2}}^{-\frac{h}{2}} \sigma_{xx} z dz = D (\kappa_x + \nu \kappa_y), \quad (2.36)$$

$$M_y = \int_{-\frac{h}{2}}^{-\frac{h}{2}} \sigma_{yy} z dz = D (\kappa_y + \nu \kappa_x), \quad (2.37)$$

$$M_{xy} = \int_{-\frac{h}{2}}^{-\frac{h}{2}} \sigma_{xy} z dz = D (1 - \nu) \kappa_{xy} \quad (2.38)$$

are obtained. In Equations (2.31)–(2.38)

$$C = \frac{E (1 + j \eta) h}{1 - \nu^2} \quad (2.39)$$

is the extensional rigidity of the plate,

$$D = \frac{E (1 + j \eta) h^3}{12 (1 - \nu^2)} \quad (2.40)$$

is the flexural rigidity of the plate and  $k^2$  is the shear correction factor (Reissner 5/6, Mindlin  $\pi^2/12$ ) to account for the actual shear stress distribution in  $z$ -direction.

The normal and shear forces and the bending and twisting moments, given in Equations (2.31)–(2.38), can also be defined through the membrane energy density

$$\bar{U}_m(\varepsilon_{xx}^0, \varepsilon_{yy}^0, \gamma_{xy}^0) = \frac{C}{2} \left( (\varepsilon_{xx}^0)^2 + (\varepsilon_{yy}^0)^2 + 2 \nu \varepsilon_{xx}^0 \varepsilon_{yy}^0 + \frac{1}{2} (1 - \nu) (\gamma_{xy}^0)^2 \right), \quad (2.41)$$

the bending energy density

$$\bar{U}_b(\kappa_x, \kappa_y, \kappa_{xy}) = \frac{D}{2} \left( \kappa_x^2 + \kappa_y^2 + 2 \nu \kappa_x \kappa_y + 2 (1 - \nu) \kappa_{xy}^2 \right) \quad (2.42)$$

and the shear strain energy density

$$\bar{U}_s(\gamma_{xz}, \gamma_{yz}) = \frac{k^2 G h}{2} (\gamma_{xz}^2 + \gamma_{yz}^2) \quad (2.43)$$

and the relations

$$\begin{aligned} N_x &= \frac{\partial \bar{U}_m}{\partial \varepsilon_{xx}^0}, & N_y &= \frac{\partial \bar{U}_m}{\partial \varepsilon_{yy}^0}, & N_{xy} &= \frac{\partial \bar{U}_m}{\partial \gamma_{xy}^0}, \\ M_x &= \frac{\partial \bar{U}_b}{\partial \kappa_x}, & M_y &= \frac{\partial \bar{U}_b}{\partial \kappa_y}, & 2 M_{xy} &= \frac{\partial \bar{U}_b}{\partial \kappa_{xy}}, \\ Q_x &= \frac{\partial \bar{U}_s}{\partial \gamma_{xz}}, & Q_y &= \frac{\partial \bar{U}_s}{\partial \gamma_{yz}}. \end{aligned} \quad (2.44)$$

An infinitesimal plate element is shown in Figure 2.4, with the shear forces  $Q_x$  and  $Q_y$ , the bending moments  $M_x$  and  $M_y$ , the twisting moment  $M_{xy}$ , the external normal load  $\bar{q}$  and the external moments  $\bar{m}_x$  and  $\bar{m}_y$  in Figure 2.4a and the membrane forces  $N_x$ ,  $N_y$  and  $N_{xy}$  in Figure 2.4b (body forces are neglected). The equilibrium of forces in  $x$ -,  $y$ - and  $z$ -direction and the equilibrium of moments about the  $x$ - and  $y$ -axis lead to the governing equations of the Mindlin plate theory

$$\frac{\partial N_x}{\partial x} + \frac{\partial N_{xy}}{\partial y} = \rho h \frac{\partial^2 u_0}{\partial t^2}, \quad (2.45)$$

$$\frac{\partial N_{xy}}{\partial x} + \frac{\partial N_y}{\partial y} = \rho h \frac{\partial^2 v_0}{\partial t^2}, \quad (2.46)$$

$$\frac{\partial Q_x}{\partial x} + \frac{\partial Q_y}{\partial y} + \bar{q} = \rho h \frac{\partial^2 w}{\partial t^2}, \quad (2.47)$$

$$\frac{\partial M_x}{\partial x} + \frac{\partial M_{xy}}{\partial y} - Q_x + \bar{m}_x = \frac{\rho h^3}{12} \frac{\partial^2 \psi_x}{\partial t^2}, \quad (2.48)$$

$$\frac{\partial M_{xy}}{\partial x} + \frac{\partial M_y}{\partial y} - Q_y + \bar{m}_y = \frac{\rho h^3}{12} \frac{\partial^2 \psi_y}{\partial t^2}. \quad (2.49)$$

Substituting Equations (2.31)–(2.38) into the governing equations (Equations (2.45)–(2.49)) leads to the equations of motion in terms of displacements

$$\frac{\partial^2 u_0}{\partial x^2} + \frac{1-\nu}{2} \frac{\partial^2 u_0}{\partial y^2} + \frac{1+\nu}{2} \frac{\partial^2 v_0}{\partial x \partial y} = \frac{\rho h}{C} \frac{\partial^2 u_0}{\partial t^2}, \quad (2.50)$$

$$\frac{\partial^2 v_0}{\partial y^2} + \frac{1-\nu}{2} \frac{\partial^2 v_0}{\partial x^2} + \frac{1+\nu}{2} \frac{\partial^2 u_0}{\partial x \partial y} = \frac{\rho h}{C} \frac{\partial^2 v_0}{\partial t^2}, \quad (2.51)$$

$$k^2 G h \left( \frac{\partial^2 w}{\partial x^2} + \frac{\partial^2 w}{\partial y^2} + \Phi \right) + \bar{q} = \rho h \frac{\partial^2 w}{\partial t^2}, \quad (2.52)$$

$$\frac{D}{2} \left( (1-\nu) \nabla^2 \psi_x + (1+\nu) \frac{\partial \Phi}{\partial x} \right) - k^2 G h \left( \psi_x + \frac{\partial w}{\partial x} \right) + \bar{m}_x = \frac{\rho h^3}{12} \frac{\partial^2 \psi_x}{\partial t^2}, \quad (2.53)$$

$$\frac{D}{2} \left( (1-\nu) \nabla^2 \psi_y + (1+\nu) \frac{\partial \Phi}{\partial y} \right) - k^2 G h \left( \psi_y + \frac{\partial w}{\partial y} \right) + \bar{m}_y = \frac{\rho h^3}{12} \frac{\partial^2 \psi_y}{\partial t^2}, \quad (2.54)$$

where  $\nabla^2 = \partial^2 / \partial x^2 + \partial^2 / \partial y^2$  is the two-dimensional Laplace operator in Cartesian coordinates and  $\Phi = \partial \psi_x / \partial x + \partial \psi_y / \partial y$ . It is apparent that Equations (2.50) and (2.51) are decoupled from the Equations (2.52)–(2.54) and therefore, the in-plane deformation  $u_0$  and  $v_0$  (membrane behaviour) is decoupled from the out-of-plane deformation  $w$ ,  $\psi_x$  and  $\psi_y$  (bending behaviour). The decoupling only occurs if linear strain-displacement relations are assumed and the plate geometry and material properties are symmetric with respect to the middle plane.

In the absence of surface loads ( $\bar{q} = 0$ ,  $\bar{m}_x = 0$ ,  $\bar{m}_y = 0$ ) and the assumption of harmonic vibrations at angular frequency  $\omega$ , it is possible to decompose Equations (2.50) and (2.51) using [17]

$$u_0(x, y) = -\frac{1}{k_t^2} \frac{\partial e(x, y)}{\partial x} + \frac{1}{k_t^2} \frac{\partial o(x, y)}{\partial y}, \quad (2.55)$$

$$v_0(x, y) = -\frac{1}{k_t^2} \frac{\partial e(x, y)}{\partial y} - \frac{1}{k_t^2} \frac{\partial o(x, y)}{\partial x}, \quad (2.56)$$

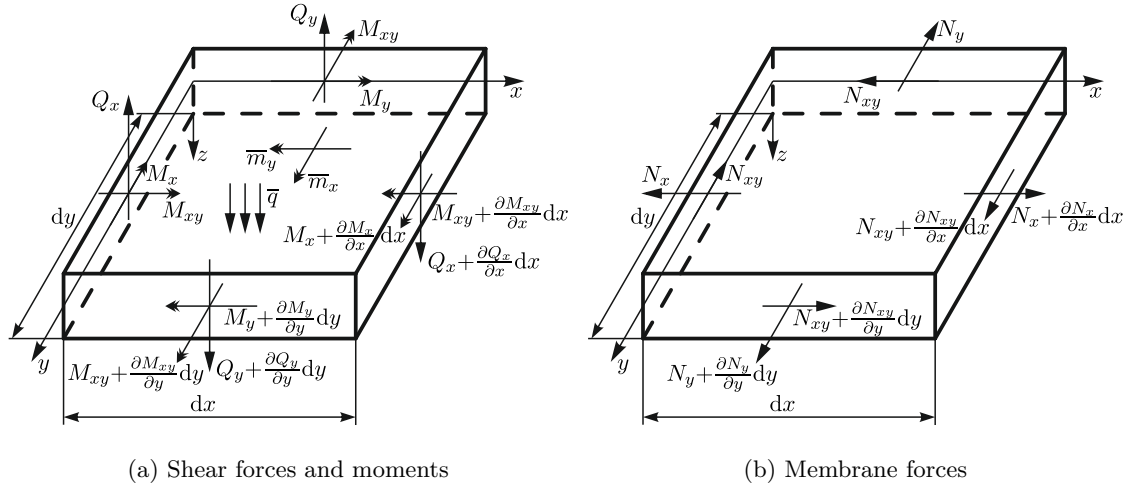


Figure 2.4: Infinitesimal plate element

with  $e(x, y)$  the dilatational strain and  $o(x, y)$  the rotational strain and

$$k_l = \sqrt{\frac{\omega^2 \rho h}{C}} \quad \text{and} \quad k_t = \sqrt{\frac{\omega^2 \rho}{G}} \quad (2.57)$$

the in-plane longitudinal and in-plane shear wavenumber. Substituting Equations (2.55) and (2.56) into Equations (2.50) and (2.51) leads to two uncoupled Helmholtz equations

$$(\nabla^2 + k_l^2)e(x, y) = 0, \quad (2.58)$$

$$(\nabla^2 + k_t^2)o(x, y) = 0. \quad (2.59)$$

Similar, the decomposition of Equations (2.52)–(2.54) is achieved by applying three potential functions  $w_1(x, y)$ ,  $w_2(x, y)$  and  $H(x, y)$  and the relations [11]

$$w(x, y) = w_1(x, y) + w_2(x, y), \quad (2.60)$$

$$\psi_x(x, y) = (\mu_1 - 1) \frac{\partial w_1(x, y)}{\partial x} + (\mu_2 - 1) \frac{\partial w_2(x, y)}{\partial x} + \frac{\partial H(x, y)}{\partial y}, \quad (2.61)$$

$$\psi_y(x, y) = (\mu_1 - 1) \frac{\partial w_1(x, y)}{\partial y} + (\mu_2 - 1) \frac{\partial w_2(x, y)}{\partial y} - \frac{\partial H(x, y)}{\partial x}, \quad (2.62)$$

which transform Equations (2.52)–(2.54) to three uncoupled Helmholtz equations

$$(\nabla^2 + k_{f1}^2)w_1(x, y) = 0, \quad (2.63)$$

$$(\nabla^2 + k_{f2}^2)w_2(x, y) = 0, \quad (2.64)$$

$$(\nabla^2 + k_s^2)H(x, y) = 0, \quad (2.65)$$

with

$$k_{f1}^2 = \frac{1}{2} k_b^4 \left( R + S + \sqrt{(R - S)^2 + \frac{4}{k_b^4}} \right), \quad (2.66)$$

$$k_{f2}^2 = \frac{1}{2} k_b^4 \left( R + S - \sqrt{(R - S)^2 + \frac{4}{k_b^4}} \right), \quad (2.67)$$

$$k_s^2 = \frac{2}{1 - \nu} \left( R k_b^4 - \frac{1}{S} \right), \quad (2.68)$$

the bending dominant and shear dominant flexural wavenumber and the out-of-plane shear wavenumber [28]. The constants in Equations (2.60)–(2.62) and Equations (2.66)–(2.68) are given by

$$\begin{aligned} S &= \frac{D}{k^2 G h}, & k_b^4 &= \frac{\rho h \omega^2}{D}, & R &= \frac{h^2}{12}, \\ \mu_1 &= \frac{k_{f2}^2}{R k_b^4 - 1/S}, & \mu_2 &= \frac{k_{f1}^2}{R k_b^4 - 1/S}. \end{aligned} \quad (2.69)$$

In Figure 2.5 a plate domain  $\Omega$ , which is divided into two sub-domains  $\Omega = \Omega^{(\alpha)} \cup \Omega^{(\beta)}$ , is shown. The in-plane deformation of the plate is defined by two coupled second-order partial differential equations, while the out-of-plane deformation is governed by three coupled second-order partial differential equations. Therefore, two boundary conditions are required for the membrane behaviour and three boundary conditions for the bending behaviour at every point of the plate boundary  $\Gamma = \Gamma^{(\alpha)} \cup \Gamma^{(\beta)}$ .

The boundary coordinate systems, shown in Figure 2.5, with the normal unit vectors  $\mathbf{n}^{(l)} = [n_x^{(l)}, n_y^{(l)}, 0]^T$  and the tangential unit vectors  $\mathbf{s}^{(l)} = [s_x^{(l)}, s_y^{(l)}, 0]^T$  ( $l = \{\alpha, \beta\}$ ), which satisfy  $\mathbf{n}^{(l)} \times \mathbf{s}^{(l)} = \mathbf{e}_z$ , are used to define the common boundary and interface conditions. The boundary of each sub-domain is subdivided into four non-overlapping parts  $\Gamma^{(\alpha)} = \Gamma_u^{(\alpha)} \cup \Gamma_\sigma^{(\alpha)} \cup \Gamma_{u\sigma}^{(\alpha)} \cup \Gamma^{(\alpha, \beta)}$  and  $\Gamma^{(\beta)} = \Gamma_u^{(\beta)} \cup \Gamma_\sigma^{(\beta)} \cup \Gamma_{u\sigma}^{(\beta)} \cup \Gamma^{(\alpha, \beta)}$ , where  $\Gamma^{(\alpha, \beta)}$  is the interface between the two sub-domains.

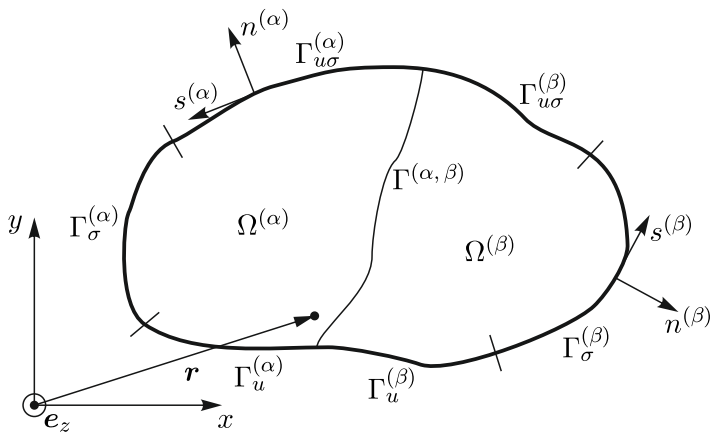


Figure 2.5: Boundary conditions and coordinate systems of a subdivided plate

The common boundary conditions for the in-plane deformation ( $u_0, v_0$ ) are [17]:

- Dirichlet boundary conditions (kinematic boundary conditions) with prescribed normal displacement  $\bar{u}_n^{(l)}$  and tangential displacement  $\bar{u}_s^{(l)}$ :

$$\mathbf{r} \in \Gamma_u^{(l)} \begin{cases} R_{u_n}^{(l)} = u_n^{(l)} - \bar{u}_n^{(l)} = 0, \\ R_{u_s}^{(l)} = u_s^{(l)} - \bar{u}_s^{(l)} = 0, \end{cases} \quad (2.70)$$

with  $u_n^{(l)} = \mathbf{n}^{(l)T} \mathbf{u}^{(l)}$  and  $u_s^{(l)} = \mathbf{s}^{(l)T} \mathbf{u}^{(l)}$  and the in-plane displacement vector  $\mathbf{u}^{(l)} = [u_0^{(l)}, v_0^{(l)}]^T$ . The special case of fixed boundaries is given by  $\bar{u}_n^{(l)} = 0$  and  $\bar{u}_s^{(l)} = 0$ .

- Neumann boundary conditions (mechanical boundary conditions) with prescribed normal force  $\bar{N}_n^{(l)}$  and tangential force  $\bar{N}_{ns}^{(l)}$ :

$$\mathbf{r} \in \Gamma_\sigma^{(l)} \begin{cases} R_{N_n}^{(l)} = N_n^{(l)} - \bar{N}_n^{(l)} = 0, \\ R_{N_{ns}}^{(l)} = N_{ns}^{(l)} - \bar{N}_{ns}^{(l)} = 0, \end{cases} \quad (2.71)$$

where the special case of a free boundary is given by  $\bar{N}_n^{(l)} = 0$  and  $\bar{N}_{ns}^{(l)} = 0$ .

- Mixed boundary conditions are a combination of Dirichlet and Neumann boundary conditions in different coordinate directions. Two different combinations are feasible  $(\Gamma_{u\sigma}^{(l)} = \Gamma_{u\sigma 1}^{(l)} \cup \Gamma_{u\sigma 2}^{(l)})$ :

$$\mathbf{r} \in \Gamma_{u\sigma 1}^{(l)} \begin{cases} R_{u_s}^{(l)} = u_s^{(l)} - \bar{u}_s^{(l)} = 0, \\ R_{N_n}^{(l)} = N_n^{(l)} - \bar{N}_n^{(l)} = 0, \end{cases} \quad (2.72)$$

and

$$\mathbf{r} \in \Gamma_{u\sigma 2}^{(l)} \begin{cases} R_{u_n}^{(l)} = u_n^{(l)} - \bar{u}_n^{(l)} = 0, \\ R_{N_{ns}}^{(l)} = N_{ns}^{(l)} - \bar{N}_{ns}^{(l)} = 0. \end{cases} \quad (2.73)$$

The special case of a simply-supported boundary is given if  $\bar{u}_s^{(l)} = 0$  and  $\bar{N}_n^{(l)} = 0$  for the first combination and  $\bar{u}_n^{(l)} = 0$  and  $\bar{N}_{ns}^{(l)} = 0$  for the second combination.

At the common interface  $\Gamma^{(\alpha, \beta)}$ , the continuity of displacements and the force equilibrium across the interface

$$\mathbf{r} \in \Gamma^{(\alpha, \beta)} \begin{cases} R_{u_n}^{(\alpha, \beta)} = u_n^{(\alpha)} + u_n^{(\beta)} = 0, \\ R_{u_s}^{(\alpha, \beta)} = u_s^{(\alpha)} + u_s^{(\beta)} = 0, \\ R_{N_n}^{(\alpha, \beta)} = N_n^{(\alpha)} - N_n^{(\beta)} = 0, \\ R_{N_{ns}}^{(\alpha, \beta)} = N_{ns}^{(\alpha)} - N_{ns}^{(\beta)} = 0, \end{cases} \quad (2.74)$$

have to be fulfilled.

The common boundary conditions for the out-of-plane deformation ( $w, \psi_x, \psi_y$ ) are [20]:

- Dirichlet boundary conditions (kinematic boundary conditions) with prescribed out-of-plane displacement  $\bar{w}^{(l)}$  and rotations  $\bar{\psi}_n^{(l)}$  and  $\bar{\psi}_s^{(l)}$ :

$$\mathbf{r} \in \Gamma_u^{(l)} \begin{cases} R_w^{(l)} = w^{(l)} - \bar{w}^{(l)} = 0, \\ R_{\psi_n}^{(l)} = \psi_n^{(l)} - \bar{\psi}_n^{(l)} = 0, \\ R_{\psi_s}^{(l)} = \psi_s^{(l)} - \bar{\psi}_s^{(l)} = 0, \end{cases} \quad (2.75)$$

with  $\psi_n^{(l)} = \mathbf{n}^{(l)T} \boldsymbol{\psi}^{(l)}$  and  $\psi_s^{(l)} = \mathbf{s}^{(l)T} \boldsymbol{\psi}^{(l)}$  and the rotation vector  $\boldsymbol{\psi}^{(l)} = [\psi_x^{(l)}, \psi_y^{(l)}]^T$ . The special case of fixed boundaries is given by  $\bar{w}^{(l)} = 0$ ,  $\bar{\psi}_n^{(l)} = 0$  and  $\bar{\psi}_s^{(l)} = 0$ .

- Neumann boundary conditions (mechanical boundary conditions) with prescribed bending moment  $\bar{M}_n^{(l)}$ , twisting moment  $\bar{M}_{ns}^{(l)}$  and shear force  $\bar{Q}_n^{(l)}$ :

$$\mathbf{r} \in \Gamma_{\sigma}^{(l)} \begin{cases} R_{M_n}^{(l)} = M_n^{(l)} - \bar{M}_n^{(l)} = 0, \\ R_{M_{ns}}^{(l)} = M_{ns}^{(l)} - \bar{M}_{ns}^{(l)} = 0, \\ R_{Q_n}^{(l)} = Q_n^{(l)} - \bar{Q}_n^{(l)} = 0, \end{cases} \quad (2.76)$$

where the special case of a free boundary is given by  $\bar{M}_n^{(l)} = 0$ ,  $\bar{M}_{ns}^{(l)} = 0$  and  $\bar{Q}_n^{(l)} = 0$ .

- Mixed boundary conditions are a combination of Dirichlet and Neumann boundary conditions. Two different types are considered ( $\Gamma_{u\sigma}^{(l)} = \Gamma_{u\sigma 1}^{(l)} \cup \Gamma_{u\sigma 2}^{(l)}$ ), the soft support:

$$\mathbf{r} \in \Gamma_{u\sigma 1}^{(l)} \begin{cases} R_w^{(l)} = w^{(l)} - \bar{w}^{(l)} = 0, \\ R_{M_n}^{(l)} = M_n^{(l)} - \bar{M}_n^{(l)} = 0, \\ R_{M_{ns}}^{(l)} = M_{ns}^{(l)} - \bar{M}_{ns}^{(l)} = 0, \end{cases} \quad (2.77)$$

and the hard support:

$$\mathbf{r} \in \Gamma_{u\sigma 2}^{(l)} \begin{cases} R_w^{(l)} = w^{(l)} - \bar{w}^{(l)} = 0, \\ R_{M_n}^{(l)} = M_n^{(l)} - \bar{M}_n^{(l)} = 0, \\ R_{\psi_s}^{(l)} = \psi_s^{(l)} - \bar{\psi}_s^{(l)} = 0. \end{cases} \quad (2.78)$$

The special case of simply-supported boundaries is given if  $\bar{w}^{(l)} = 0$  and  $\bar{M}_n^{(l)} = 0$  and  $\bar{M}_{ns}^{(l)} = 0$  for soft simply-supported and  $\bar{\psi}_s^{(l)} = 0$  for hard simply-supported boundary conditions. In general, the soft simply-supported boundary conditions are used to avoid the plate paradox shown in [29].

At the common interface  $\Gamma^{(\alpha, \beta)}$ , the continuity of the displacement and rotations and the force and moment equilibrium across the interface

$$\mathbf{r} \in \Gamma^{(\alpha, \beta)} \begin{cases} R_w^{(\alpha, \beta)} = w^{(\alpha)} - w^{(\beta)} = 0, \\ R_{\psi_n}^{(\alpha, \beta)} = \psi_n^{(\alpha)} + \psi_n^{(\beta)} = 0, \\ R_{\psi_s}^{(\alpha, \beta)} = \psi_s^{(\alpha)} + \psi_s^{(\beta)} = 0, \\ R_{M_n}^{(\alpha, \beta)} = M_n^{(\alpha)} - M_n^{(\beta)} = 0, \\ R_{M_{ns}}^{(\alpha, \beta)} = M_{ns}^{(\alpha)} - M_{ns}^{(\beta)} = 0, \\ R_{Q_n}^{(\alpha, \beta)} = Q_n^{(\alpha)} + Q_n^{(\beta)} = 0, \end{cases} \quad (2.79)$$

have to be applied to ensure a rigid connection between both sub-domains.

The bending moment  $M_n^{(l)}$ , twisting moment  $M_{ns}^{(l)}$ , shear force  $Q_n^{(l)}$  and rotations  $\psi_n^{(l)}$  and  $\psi_s^{(l)}$  are shown in Figure 2.6a and the normal force  $N_n^{(l)}$  and tangential force  $N_{ns}^{(l)}$  in

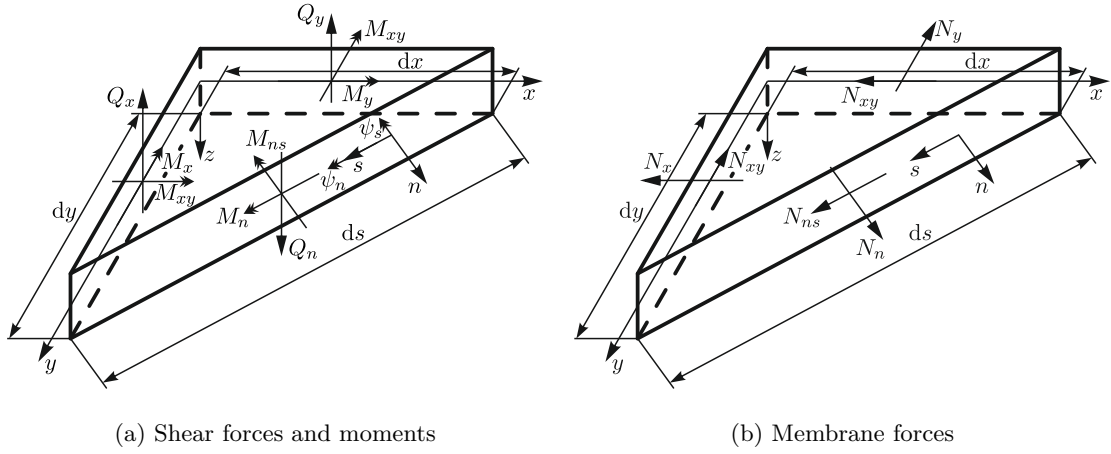


Figure 2.6: Infinitesimal element at a plate boundary

Figure 2.6b ( $\bullet^{(l)}$  is omitted in the figures). The equilibrium of forces and moments for the infinitesimal plate elements in Figure 2.6 lead to

$$N_n^{(l)} = n_x^{(l)2} N_x^{(l)} + n_y^{(l)2} N_y^{(l)} + 2 n_x^{(l)} n_y^{(l)} N_{xy}^{(l)}, \quad (2.80)$$

$$N_{ns}^{(l)} = n_x^{(l)} n_y^{(l)} (N_y^{(l)} - N_x^{(l)}) + (n_x^{(l)2} - n_y^{(l)2}) N_{xy}^{(l)}, \quad (2.81)$$

$$M_n^{(l)} = n_x^{(l)2} M_x^{(l)} + n_y^{(l)2} M_y^{(l)} + 2 n_x^{(l)} n_y^{(l)} M_{xy}^{(l)}, \quad (2.82)$$

$$M_{ns}^{(l)} = n_x^{(l)} n_y^{(l)} (M_y^{(l)} - M_x^{(l)}) + (n_x^{(l)2} - n_y^{(l)2}) M_{xy}^{(l)}, \quad (2.83)$$

$$Q_n^{(l)} = n_x^{(l)} Q_x^{(l)} + n_y^{(l)} Q_y^{(l)}. \quad (2.84)$$

The strong form of the plate membrane problem is finally given by the governing equations in terms of displacements (Equations (2.50) and (2.51)) and the boundary and interface conditions in Equations (2.70)–(2.74). The plate bending problem (Mindlin plate theory) is governed by Equations (2.52)–(2.54) and the boundary and interface conditions (Equations (2.75)–(2.79)).

The plate membrane problem and the plate bending problem is completely decoupled in case of a planar plate if linear strain-displacement relations are assumed and the plate geometry and material properties are symmetric with respect to the middle plane. The assembly of non-coplanar plates leads to a coupling of the in-plane and out-of-plane deformation through the interface conditions [17], while the governing equations are still decoupled. For curved plates, so-called shells, the membrane and bending behaviour is coupled through the governing equations [22].

As in Section 2.1, the sub-region three-field generalized mixed variational principle for thick plates, shown in [26, 30] for the static problem, can be applied to derive the governing equations and boundary and interface conditions of the Mindlin plate theory. Since the scope of this work is on pure bending problems, the integral form of the plate membrane problem is omitted. The extension of the approach shown in [26, 30] to the dynamic

problem leads to the stationary condition of the functional

$$\begin{aligned}
 \delta L = 0 = \int_{t_0}^{t_1} \left( \sum_l \iint_{\Omega^{(l)}} \left( \left( \frac{\partial \bar{U}_b^{(l)}}{\partial \kappa_x^{(l)}} - M_x^{(l)} \right) \delta \kappa_x^{(l)} + \left( \frac{\partial \bar{U}_b^{(l)}}{\partial \kappa_y^{(l)}} - M_y^{(l)} \right) \delta \kappa_y^{(l)} \right. \right. \\
 + \left( \frac{\partial \bar{U}_b^{(l)}}{\partial \kappa_{xy}^{(l)}} - 2 M_{xy}^{(l)} \right) \delta \kappa_{xy}^{(l)} + \left( \frac{\partial \bar{U}_s^{(l)}}{\partial \gamma_{xz}^{(l)}} - Q_x^{(l)} \right) \delta \gamma_{xz}^{(l)} + \left( \frac{\partial \bar{U}_s^{(l)}}{\partial \gamma_{yz}^{(l)}} - Q_y^{(l)} \right) \delta \gamma_{yz}^{(l)} \\
 - \left( \kappa_x^{(l)} - \frac{\partial \psi_x^{(l)}}{\partial x} \right) \delta M_x^{(l)} - \left( \kappa_y^{(l)} - \frac{\partial \psi_y^{(l)}}{\partial y} \right) \delta M_y^{(l)} - \left( 2 \kappa_{xy}^{(l)} - \frac{\partial \psi_x^{(l)}}{\partial y} \right. \\
 \left. \left. - \frac{\partial \psi_y^{(l)}}{\partial x} \right) \delta M_{xy}^{(l)} - \left( \gamma_{xz}^{(l)} - \frac{\partial w^{(l)}}{\partial x} - \psi_x^{(l)} \right) \delta Q_x^{(l)} - \left( \gamma_{yz}^{(l)} - \frac{\partial w^{(l)}}{\partial y} - \psi_y^{(l)} \right) \delta Q_y^{(l)} \right. \\
 - \left( \frac{\partial M_x^{(l)}}{\partial x} + \frac{\partial M_{xy}^{(l)}}{\partial y} - Q_x^{(l)} + \bar{m}_x^{(l)} - \frac{\rho h^3}{12} \ddot{\psi}_x^{(l)} \right) \delta \psi_x^{(l)} - \left( \frac{\partial M_y^{(l)}}{\partial y} + \frac{\partial M_{xy}^{(l)}}{\partial x} - Q_y^{(l)} \right. \\
 \left. + \bar{m}_y^{(l)} - \frac{\rho h^3}{12} \ddot{\psi}_y^{(l)} \right) \delta \psi_y^{(l)} - \left( \frac{\partial Q_x^{(l)}}{\partial x} + \frac{\partial Q_y^{(l)}}{\partial y} + \bar{q}^{(l)} - \rho h \ddot{w}^{(l)} \right) \delta w^{(l)} \right) \mathrm{d}x \mathrm{d}y \\
 - \int_{\Gamma_u^{(l)} \cup \Gamma_{u\sigma_2}^{(l)}} \left( (\psi_s^{(l)} - \bar{\psi}_s^{(l)}) \delta M_{ns}^{(l)} + (w^{(l)} - \bar{w}^{(l)}) \delta Q_n^{(l)} \right) \mathrm{d}s \\
 + \int_{\Gamma_\sigma^{(l)}} \left( (M_{ns}^{(l)} - \bar{M}_{ns}^{(l)}) \delta \psi_s^{(l)} + (Q_n^{(l)} - \bar{Q}_n^{(l)}) \delta w^{(l)} \right) \mathrm{d}s \\
 - \int_{\Gamma_u^{(l)}} (\psi_n^{(l)} - \bar{\psi}_n^{(l)}) \delta M_n^{(l)} \mathrm{d}s + \int_{\Gamma_\sigma^{(l)} \cup \Gamma_{u\sigma_2}^{(l)}} (M_n^{(l)} - \bar{M}_n^{(l)}) \delta \psi_n^{(l)} \mathrm{d}s \\
 + \int_{\Gamma^{(\alpha, \beta)}} \left( (M_n^{(\alpha)} - M_n^{(\beta)}) \delta \psi_n^{(\alpha)} + (M_{ns}^{(\alpha)} - M_{ns}^{(\beta)}) \delta \psi_s^{(\alpha)} + (Q_n^{(\alpha)} + Q_n^{(\beta)}) \delta w^{(\alpha)} \right. \\
 \left. - (\psi_n^{(\alpha)} + \psi_n^{(\beta)}) \delta M_n^{(\beta)} - (\psi_s^{(\alpha)} + \psi_s^{(\beta)}) \delta M_{ns}^{(\beta)} - (w^{(\beta)} - w^{(\alpha)}) \delta Q_n^{(\beta)} \right) \mathrm{d}s \right) \mathrm{d}t, \quad (2.85)
 \end{aligned}$$

which gives the integral form of the Mindlin plate theory and is equivalent to all field equations and boundary and interface conditions of the plate bending problem. In Equation (2.85) only the hard mixed boundary conditions are considered. The soft mixed boundary conditions can be included in a similar way. Equation (2.85) is derived in Appendix B. The transformation of the strong integral form in Equation (2.85) to the weak form can be achieved through integration by parts.

## 2.2.2 Kirchhoff plate theory

The Kirchhoff plate theory, also called the classical plate theory, developed by Kirchhoff in 1850 [10], is the simplest plate model with further assumptions compared to the Mindlin plate theory. It is additionally assumed that [22]

- A straight line, which is normal to the middle plane in the undeformed state, remains not only straight but also normal to the middle surface in the deformed state
- The effects due to rotatory inertia are negligible

and therefore, the influence of transverse shear deformation is neglected. Since the membrane and bending behaviour is decoupled in the Kirchhoff plate theory under the same assumptions as for the Mindlin plate theory, only the out-of-plane deformation is considered in the following derivation ( $u_0 = 0$  and  $v_0 = 0$ ).

The rotations in the Kirchhoff plate theory are given by

$$\psi_x(x, y, t) = -\frac{\partial w(x, y, t)}{\partial x}, \quad (2.86)$$

$$\psi_y(x, y, t) = -\frac{\partial w(x, y, t)}{\partial y}, \quad (2.87)$$

since transverse normals remain straight and normal to the middle plane after deformation. The displacements are therefore defined by

$$u(x, y, z, t) = -z \frac{\partial w(x, y, t)}{\partial x}, \quad (2.88)$$

$$v(x, y, z, t) = -z \frac{\partial w(x, y, t)}{\partial y}, \quad (2.89)$$

$$w(x, y, z, t) = w(x, y, t) \quad (2.90)$$

and the linear strain-displacement relations lead to

$$\varepsilon_{xx} = -z \frac{\partial^2 w}{\partial x^2} = z \kappa_x, \quad \varepsilon_{zz} = 0, \quad (2.91)$$

$$\varepsilon_{yy} = -z \frac{\partial^2 w}{\partial y^2} = z \kappa_y, \quad \varepsilon_{xz} = 0, \quad (2.92)$$

$$\varepsilon_{xy} = -z \frac{\partial^2 w}{\partial x \partial y} = z \kappa_{xy}, \quad \varepsilon_{yz} = 0. \quad (2.93)$$

The equilibrium of forces and moments for an infinitesimal element are the same as for the Mindlin plate theory. Rearranging Equations (2.48) and (2.49) and neglecting the rotatory inertia terms and external moment loading ( $\bar{m}_x = 0$ ,  $\bar{m}_y = 0$ ) give

$$Q_x = \frac{\partial M_x}{\partial x} + \frac{\partial M_{xy}}{\partial y}, \quad (2.94)$$

$$Q_y = \frac{\partial M_{xy}}{\partial x} + \frac{\partial M_y}{\partial y}. \quad (2.95)$$

Substituting Equations (2.94) and (2.95) into Equation (2.47) leads to the governing equation of the Kirchhoff plate

$$\frac{\partial^2 M_x}{\partial x^2} + \frac{\partial^2 M_y}{\partial y^2} + 2 \frac{\partial^2 M_{xy}}{\partial x \partial y} + \bar{q} = \rho h \frac{\partial^2 w}{\partial t^2}, \quad (2.96)$$

with the bending moments  $M_x$  and  $M_y$  and the twisting moment  $M_{xy}$  defined in Equations (2.36)–(2.38). The shear forces cannot be calculated from Equations (2.34) and (2.35), since the plate is assumed to be infinitely stiff in transverse shear ( $\varepsilon_{xz} = 0$ ,  $\varepsilon_{yz} = 0$ ) [25]. Substituting Equations (2.91)–(2.93) and Equations (2.36)–(2.38) into the Equation (2.96) results in the governing equation of the Kirchhoff plate in terms of the out-of-plane displacement

$$\nabla^2 \nabla^2 w + \frac{\rho h}{D} \frac{\partial^2 w}{\partial t^2} = \frac{\bar{q}}{D}. \quad (2.97)$$

If harmonic vibrations at angular frequency  $\omega$  are assumed and the surface load  $\bar{q}$  is absent, Equation (2.97) can be decomposed into two uncoupled Helmholtz equations

$$(\nabla^2 + k_b^2)w_{b1}(x, y) = 0, \quad (2.98)$$

$$(\nabla^2 - k_b^2)w_{b2}(x, y) = 0, \quad (2.99)$$

with

$$k_b^4 = \frac{\rho h \omega^2}{D} \quad (2.100)$$

the plate bending wavenumber.

Equation (2.97) is a fourth-order partial differential equation and therefore the Kirchhoff plate theory requires two boundary conditions at every point of the boundary. As for the Mindlin plate theory a subdivided plate domain  $\Omega = \Omega^{(\alpha)} \cup \Omega^{(\beta)}$  is viewed and the coordinate systems shown in Figure 2.5 and defined in Section 2.2.1 are used to specify the boundary and interface conditions. The common boundary conditions for the Kirchhoff plate theory are [20]:

- Dirichlet boundary conditions (kinematic boundary conditions) with prescribed out-of-plane displacement  $\bar{w}^{(l)}$  and rotation  $\bar{\psi}_n^{(l)}$ :

$$\mathbf{r} \in \Gamma_u^{(l)} \begin{cases} R_w^{(l)} = w^{(l)} - \bar{w}^{(l)} = 0, \\ R_{\psi_n}^{(l)} = \psi_n^{(l)} - \bar{\psi}_n^{(l)} = 0, \end{cases} \quad (2.101)$$

with  $\psi_n^{(l)} = -\left(\frac{\partial w^{(l)}}{\partial x} n_x^{(l)} + \frac{\partial w^{(l)}}{\partial y} n_y^{(l)}\right) = -\frac{\partial w^{(l)}}{\partial n^{(l)}}$ . The special case of fixed boundaries is given by  $\bar{w}^{(l)} = 0$  and  $\bar{\psi}_n^{(l)} = 0$ .

- Neumann boundary conditions (mechanical boundary conditions) with prescribed bending moment  $\bar{M}_n^{(l)}$  and generalized shear force  $\bar{V}_n^{(l)}$ :

$$\mathbf{r} \in \Gamma_\sigma^{(l)} \begin{cases} R_{M_n}^{(l)} = M_n^{(l)} - \bar{M}_n^{(l)} = 0, \\ R_{V_n}^{(l)} = V_n^{(l)} - \bar{V}_n^{(l)} = 0, \end{cases} \quad (2.102)$$

with  $V_n^{(l)} = Q_n^{(l)} + \frac{\partial M_{ns}^{(l)}}{\partial s^{(l)}}$  a combined boundary condition of shear force and twisting moment and  $Q_n$ ,  $M_n$  and  $M_{ns}$  defined in Equations (2.82)–(2.84). The free boundary condition is given by  $\bar{M}_n^{(l)} = 0$  and  $\bar{V}_n^{(l)} = 0$ .

- Mixed boundary conditions are a combination of Dirichlet and Neumann boundary conditions. In the Kirchhoff plate theory only the hard support is applicable:

$$\mathbf{r} \in \Gamma_{u\sigma}^{(l)} \begin{cases} R_w^{(l)} = w^{(l)} - \bar{w}^{(l)} = 0, \\ R_{M_n}^{(l)} = M_n^{(l)} - \bar{M}_n^{(l)} = 0. \end{cases} \quad (2.103)$$

The special case of simply-supported boundaries is given if  $\bar{w}^{(l)} = 0$  and  $\bar{M}_n^{(l)} = 0$ .

In the Kirchhoff plate theory, corner forces can appear at discontinuities of the boundary, e.g. polygonal plates, which need to be considered in the boundary conditions. A detailed description of the corner forces and of more complicated plate loadings, e.g. moment loading, can be found in e.g. [31]. The corner forces and moment loadings are not considered in this work.

At the common interface  $\Gamma^{(\alpha, \beta)}$ , the continuity of the displacement and rotation and the force and moment equilibrium across the interface

$$\mathbf{r} \in \Gamma^{(\alpha, \beta)} \left\{ \begin{array}{l} R_w^{(\alpha, \beta)} = w^{(\alpha)} - w^{(\beta)} = 0, \\ R_{\psi_n}^{(\alpha, \beta)} = \psi_n^{(\alpha)} + \psi_n^{(\beta)} = 0, \\ R_{M_n}^{(\alpha, \beta)} = M_n^{(\alpha)} - M_n^{(\beta)} = 0, \\ R_{V_n}^{(\alpha, \beta)} = V_n^{(\alpha)} + V_n^{(\beta)} = 0, \end{array} \right. \quad (2.104)$$

have to be fulfilled.

An integral form of the Kirchhoff plate problem can be derived by extending the sub-region three-field generalized mixed variational principle for thin plates, shown in [32] and [26] for the static plate deformation, to the dynamic case. The final result is given by

$$\begin{aligned} \delta L = 0 = \int_{t_0}^{t_1} \left( \sum_l \iint_{\Omega^{(l)}} \left( \left( \frac{\partial \bar{U}_b^{(l)}}{\partial \kappa_x^{(l)}} - M_x^{(l)} \right) \delta \kappa_x^{(l)} + \left( \frac{\partial \bar{U}_b^{(l)}}{\partial \kappa_y^{(l)}} - M_y^{(l)} \right) \delta \kappa_y^{(l)} \right. \right. \\ + \left( \frac{\partial \bar{U}_b^{(l)}}{\partial \kappa_{xy}^{(l)}} - 2 M_{xy}^{(l)} \right) \delta \kappa_{xy}^{(l)} - \left( \kappa_x^{(l)} + \frac{\partial^2 w^{(l)}}{\partial x^2} \right) \delta M_x^{(l)} - \left( \kappa_y^{(l)} + \frac{\partial^2 w^{(l)}}{\partial y^2} \right) \delta M_y^{(l)} \\ - 2 \left( \kappa_{xy}^{(l)} + \frac{\partial^2 w^{(l)}}{\partial x \partial y} \right) \delta M_{xy}^{(l)} - \left( \frac{\partial^2 M_x^{(l)}}{\partial x^2} + \frac{\partial^2 M_y^{(l)}}{\partial y^2} + 2 \frac{\partial^2 M_{xy}^{(l)}}{\partial x \partial y} + \bar{q}^{(l)} \right. \\ \left. \left. - \rho h \ddot{w}^{(l)} \right) \delta w^{(l)} \right) dx dy - \int_{\Gamma_u^{(l)} \cup \Gamma_{u\sigma}^{(l)}} (w^{(l)} - \bar{w}^{(l)}) \delta V_n^{(l)} ds + \int_{\Gamma_\sigma^{(l)}} (V_n^{(l)} - \bar{V}_n^{(l)}) \delta w^{(l)} ds \\ + \int_{\Gamma_u^{(l)}} \left( \frac{\partial w^{(l)}}{\partial n^{(l)}} + \bar{\psi}_n^{(l)} \right) \delta M_n^{(l)} ds - \int_{\Gamma_\sigma^{(l)} \cup \Gamma_{u\sigma}^{(l)}} (M_n^{(l)} - \bar{M}_n^{(l)}) \frac{\partial \delta w^{(l)}}{\partial n^{(l)}} ds \\ + \int_{\Gamma^{(\alpha, \beta)}} \left( (M_n^{(\beta)} - M_n^{(\alpha)}) \frac{\partial \delta w^{(\alpha)}}{\partial n^{(\alpha)}} + (V_n^{(\alpha)} + V_n^{(\beta)}) \delta w^{(\alpha)} \right. \\ \left. + \left( \frac{\partial w^{(\alpha)}}{\partial n^{(\alpha)}} + \frac{\partial w^{(\beta)}}{\partial n^{(\beta)}} \right) \delta M_n^{(\beta)} + (w^{(\alpha)} - w^{(\beta)}) \delta V_n^{(\beta)} \right) ds \right) dt, \end{aligned} \quad (2.105)$$

which is equivalent to all field equations and boundary conditions of the Kirchhoff plate theory excluding the effects due to concentrated corner forces. In [26] and [32] corner forces are considered in the variational principle for the static problem and it is straight forward to include them in Equation (2.105). The derivation of Equation (2.105) is shown in Appendix C. Integration by parts of the strong integral form in Equation (2.105) leads to a weak form suitable for certain numerical methods.

### 2.2.3 Higher order plate theories

Mindlin's first order shear deformation theory is in general sufficient to analyze the vibrations of isotropic moderately thick plates if appropriate shear correction factors are applied [33]. The vibration analysis of highly orthotropic or composite plates may require higher order shear deformation theories instead of the Mindlin plate theory to yield accurate results [33]. A great review of higher order plate theories can be found in [33] and [34] and a short overview is given in this section.

The first straight forward extension of the Mindlin plate theory is the second order shear deformation theory, where the displacement field

$$u(x, y, z, t) = u_0(x, y, t) + z \psi_x(x, y, t) + z^2 \varphi_x(x, y, t), \quad (2.106)$$

$$v(x, y, z, t) = v_0(x, y, t) + z \psi_y(x, y, t) + z^2 \varphi_y(x, y, t), \quad (2.107)$$

$$w(x, y, z, t) = w_0(x, y, t) + z \psi_z(x, y, t) + z^2 \varphi_z(x, y, t), \quad (2.108)$$

is assumed [34]. Introducing the rotations  $\psi_z(x, y, t)$  and  $\varphi_z(x, y, t)$  leads to the inclusion of the effect of transverse normal strain, while the case of inextensible transverse normals is given by  $\psi_z(x, y, t) = 0$  and  $\varphi_z(x, y, t) = 0$  [35]. Essenburg showed that the effect of transverse normal strain is especially significant if surface displacements are prescribed [36]. The introduction of second order terms in the displacements leads to additional unknowns, which are difficult to interpret in physical terms [35]. Furthermore, the inclusion of second order terms in the in-plane displacements hardly improves the obtained results [37]. The second order shear deformation theory is used for example, in [38] for the analysis of the static deformation of infinite plates resting on an elastic half space, in [39] to investigate the dynamic response of fiber reinforced composite plates and in [40] to model the static and dynamic behaviour of laminated orthotropic plates.

The general displacement field of a third order shear deformation theory is given by [34]

$$u(x, y, z, t) = u_0(x, y, t) + z \psi_x(x, y, t) + z^2 \varphi_x(x, y, t) + z^3 \zeta_x(x, y, t), \quad (2.109)$$

$$v(x, y, z, t) = v_0(x, y, t) + z \psi_y(x, y, t) + z^2 \varphi_y(x, y, t) + z^3 \zeta_y(x, y, t), \quad (2.110)$$

$$w(x, y, z, t) = w_0(x, y, t) + z \psi_z(x, y, t) + z^2 \varphi_z(x, y, t), \quad (2.111)$$

which allows for the inclusion of cross sectional warping and effects due to transverse normal strain. A third order plate theory using all components given in Equation (2.109) – (2.111) is developed in [41] and validated for an infinite homogenous plate subjected to a static sinusoidal pressure, while in [42] only the out-of-plane effects are considered ( $u_0 = 0$ ,  $v_0 = 0$ ,  $\varphi_x = 0$ ,  $\varphi_y = 0$  and  $\psi_z = 0$ ) to investigate the static deformation of isotropic rectangular plates.

Another class of third order plate theories is build upon the classical plate theory and satisfies the requirement of shear stress free boundary conditions at the top and bottom surface of the plate [34]. Therefore, shear correction factors are avoided, which is the main advantage of these theories. An overview of this class of third order theories is given in [43] and [9]. The most popular third order plate theory, the Reddy plate theory [27],

considers the displacement field

$$u(x, y, z, t) = u_0(x, y, t) + z \psi_x(x, y, t) - \frac{4z^3}{3h^2} \left( \psi_x(x, y, t) + \frac{\partial w_0(x, y, t)}{\partial x} \right), \quad (2.112)$$

$$v(x, y, z, t) = v_0(x, y, t) + z \psi_y(x, y, t) - \frac{4z^3}{3h^2} \left( \psi_y(x, y, t) + \frac{\partial w_0(x, y, t)}{\partial y} \right), \quad (2.113)$$

$$w(x, y, z, t) = w_0(x, y, t), \quad (2.114)$$

which satisfies the stress free boundary conditions at  $z = \pm h/2$  of the plate and neglects the effects due to transverse normal strain. Applications of the Reddy plate theory for isotropic and laminated composite plates can be found in e.g [9] and [44].

In [9] it is stated that the development of even higher order theories has not been attempted due to the growing algebraic complexity and computational effort and since only a marginal gain in accuracy is expected. For an extensive overview of plate theories, especially trigonometric shear deformation theories and stress based plate theories, the reader is referred to [34].

## 2.3 Useful ranges of validity for the Kirchhoff and Mindlin plate theory

The assumptions used in the Kirchhoff and Mindlin plate theory are only valid if certain geometrical and frequency limits are not exceeded. In general, it is stated that the Kirchhoff plate theory is only valid for thin plates and low frequencies, while the Mindlin plate theory is applicable to moderately thick plates and higher frequencies.

There is no precise definition of a thin or a moderately thick plate in the literature. In [22, 45, 46] a plate is considered to be thin if the ratio of the plate thickness  $h$  to the lesser of the other two dimensions is smaller than 1/20, while [47, 48] requires a ratio of less than 1/10 and [9] a ratio of less than 1/30. A moderately thick plate is defined in [46, 48] as a plate with a ratio of thickness to the lateral dimension smaller than 1/5, while [49] considers an upper limit of 3/20.

The frequency limit of both theories is given in the literature either by the ratio of the occurring bending wavelength  $\lambda$  to the plate thickness  $h$  or by the ratio of the angular frequency  $\omega$  to the angular frequency of the lowest, simple thickness-shear mode in a plate  $\omega_s = \frac{\pi}{h} \sqrt{\frac{G}{\rho}}$ . Many different frequency limits for the Kirchhoff plate theory can be found in the literature. In [5] the limit is defined by  $\lambda/h > 6$  ( $\omega/\omega_s < 0.17$ ), while in [23] and [50] the limit  $\lambda/h > 7.85$  ( $\omega/\omega_s < 0.1$ ) is given. A stricter limit is stated in [51] and [52] where the ratio  $\lambda/h > 20$  ( $\omega/\omega_s < 0.015$ ) is considered. Finally, in [11] the range  $\lambda/h > 5...10$  ( $\omega/\omega_s < 0.24...0.06$ ) limits the validity of the Kirchhoff plate theory. The limits for the Mindlin plate theory also differ in the literature. In [50], the limit  $\lambda/h > 2$  ( $\omega/\omega_s < 0.77$ ) is stated, while in [23] a ratio  $\lambda/h > 2.8$  ( $\omega/\omega_s < 0.5$ ) is considered. The very strict limit  $\lambda/h > 10$  ( $\omega/\omega_s < 0.06$ ) is given in [52], while in [51] the looser limit  $\lambda/h > 1$  ( $\omega/\omega_s < 1.76$ ) is defined.

Since the ranges of validity for both plate models are very different in the literature, the stated limits are reviewed in the following sections. Therefore, the free vibrations of an

infinite plate are examined with both plate theories and the analytical results are compared to the exact elasticity solution. This approach is also used in [23] and [50] to define the frequency limits of the plate theories.

To investigate the influence of the plate boundary conditions, the free vibration solutions of simple plate geometries, e.g. rectangular plates, circular plates and sector plates, with different boundary conditions are calculated with the Kirchhoff and Mindlin plate theory and compared to each other. Exact elasticity solutions for free plate vibrations are only available in the literature for the simply-supported rectangular plate [53] and therefore highly accurate finite element models are used to calculate the eigenfrequencies of all other plate configurations.

### 2.3.1 Free vibrations of an infinite plate

Even though an infinite plate is not feasible in a real life application, Mindlin showed in [54] that a simplified plate model only leads to accurate results for finite plates if the plate theory is able to accurately predict the frequency spectrum of an infinite plate.

The exact elasticity solution of the free vibrations of a plate with traction-free surfaces in a state of plane strain is due to Rayleigh [55] and Lamb [56] and leads to an infinite number of frequency branches. The Kirchhoff plate theory can only predict the lowest asymmetric frequency branch, which corresponds to (bending dominant) flexural deformation, while the Mindlin plate theory gives the first three asymmetric frequency branches, which leads to a bending dominant flexural, shear dominant flexural and thickness-twist deformation [28, 57].

The solutions for the free vibration of an infinite plate in a state of plane strain (independency of the  $y$ -coordinate) can be found in several textbooks, e.g. [23] and [50]. The analytical solution for the Kirchhoff plate theory is given in explicit form by

$$\frac{\omega_k}{\omega_s} = \frac{(\xi h)^2}{2\pi} \sqrt{\frac{2}{3(1-\nu)}}, \quad (2.115)$$

with  $\omega_k$  the angular frequency defined by the Kirchhoff plate theory,  $\omega_s = \frac{\pi}{h} \sqrt{\frac{G}{\rho}}$  the angular frequency of the lowest, simple thickness-shear mode in a plate and  $\xi$  the wavenumber along the  $x$ -direction. The explicit solutions for the three frequency branches of the Mindlin plate theory are

$$\frac{\omega_{mf1}}{\omega_s} = \frac{1}{\pi} \sqrt{g - \sqrt{g^2 - \frac{2k^2(\xi h)^4}{1-\nu}}}, \quad (2.116)$$

$$\frac{\omega_{mf2}}{\omega_s} = \frac{1}{\pi} \sqrt{g + \sqrt{g^2 - \frac{2k^2(\xi h)^4}{1-\nu}}}, \quad (2.117)$$

$$\frac{\omega_{ms}}{\omega_s} = \frac{1}{\pi} \sqrt{(\xi h)^2 + 12k^2}, \quad (2.118)$$

with

$$g = 6k^2 + \frac{(\xi h)^2}{2} \left( k^2 + \frac{2}{1-\nu} \right) \quad (2.119)$$

and  $\omega_{mf1}$  the angular frequency of the bending dominant flexural vibration,  $\omega_{mf2}$  the angular frequency of the shear dominant flexural vibration and  $\omega_{ms}$  the angular frequency for the thickness-twist vibration. In general, the solutions for the exact elasticity theory cannot be given in explicit form. The asymmetric frequency branches are defined by the solutions of the transcendental equation

$$4 \sin\left(\frac{\beta}{2}\right) \cos\left(\frac{\alpha}{2}\right) (\xi h)^2 \alpha \beta + \cos\left(\frac{\beta}{2}\right) \sin\left(\frac{\alpha}{2}\right) ((\xi h)^2 - \beta^2)^2 = 0, \quad (2.120)$$

with

$$\alpha = \sqrt{\pi^2 \frac{1-2\nu}{2(1+\nu)} \left(\frac{\omega_{3D}}{\omega_s}\right)^2 - (\xi h)^2}, \quad (2.121)$$

$$\beta = \sqrt{\pi^2 \left(\frac{\omega_{3D}}{\omega_s}\right)^2 - (\xi h)^2} \quad (2.122)$$

and  $\omega_{3D}$  the asymmetric frequency branches of the plate using the three-dimensional elasticity theory. The exact solution corresponding to the thickness-twist vibration of the Mindlin plate theory is given by

$$\frac{\omega_{3Ds}}{\omega_s} = \frac{1}{\pi} \sqrt{\pi^2 + (\xi h)^2}, \quad (2.123)$$

with  $\omega_{3Ds}$  the frequency branch of the first asymmetric thickness-shear vibration calculated with the elasticity theory.

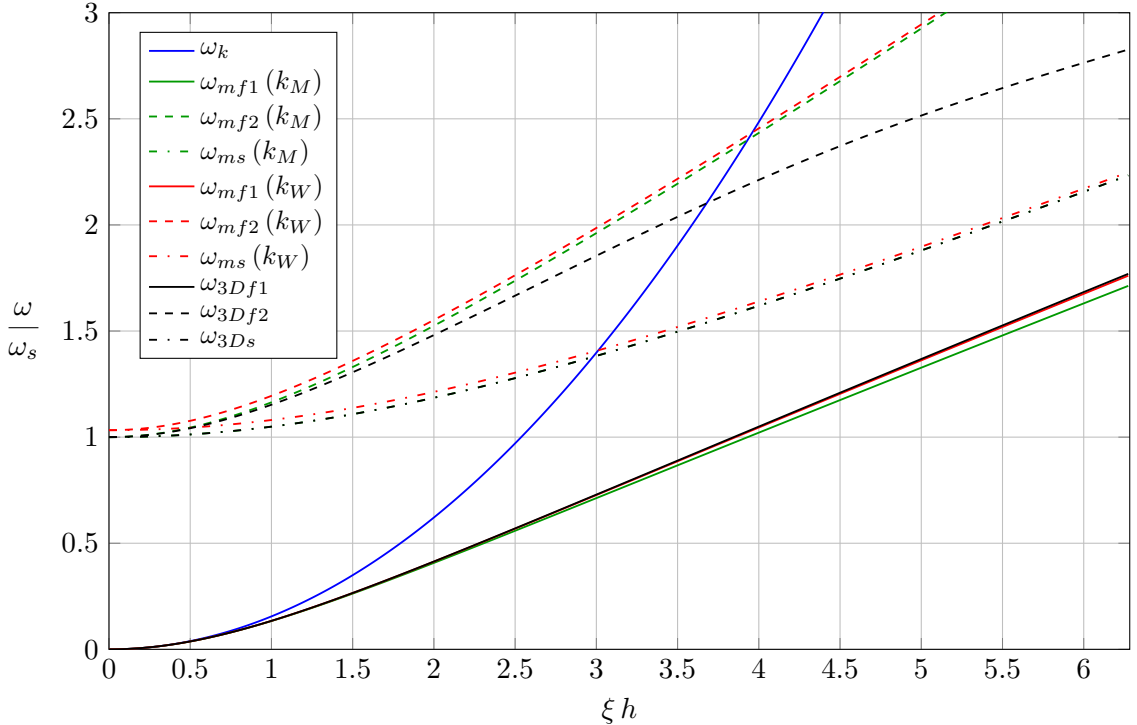


Figure 2.7: Frequency spectrum of an infinite isotropic plate ( $\nu = 0.3$ )

### 2.3 Useful ranges of validity for the Kirchhoff and Mindlin plate theory

The solutions for the Kirchhoff plate theory (Equation (2.115)), the Mindlin plate theory (Equations (2.116) – (2.118)) and the exact three-dimensional model (Equations (2.120) and (2.123)) are illustrated in Figure 2.7 for the Poisson’s ratio  $\nu = 0.3$ . For the Mindlin plate theory the shear correction factors  $k_M^2 = \frac{\pi^2}{12}$  (Mindlin [11]) and  $k_W^2 = \frac{5}{6-\nu}$  (Wittrick [58]) are used.

It is apparent from Figure 2.7 that the Kirchhoff plate theory is only valid for small values of  $\xi h$ , while the Mindlin plate theory agrees very well with the exact elasticity solution for the shown range. The shear correction factor  $k_W$  leads to a better result for the first asymmetric frequency branch (bending dominated flexure), but is less accurate for the shear dominant flexural and thickness-twist vibrations compared to the shear correction factor  $k_M$ . By comparing Equations (2.118) and (2.123) it is apparent that the Mindlin plate theory becomes exact for the thickness-twist vibrations if the shear correction factor  $k_M$  is used. Therefore, the lines of the two frequency branches cannot be distinguished in Figure 2.7.

To assess the validity of the plate theories, the relative error for bending dominant flexural vibrations

$$\varepsilon_{f1} = 100 \cdot \frac{|\{\omega_k, \omega_{mf1}\} - \omega_{3Df1}|}{\omega_{3Df1}} \quad (2.124)$$

is defined. In Table 2.1 the limits for the frequency ratio  $\omega_{mf1}/\omega_s$  and the ratio  $\lambda/h = 2\pi/(\xi h)$  to reach a relative error of 1%, 2%, 5% and 10% are given. The Poisson’s ratio is set to  $\nu = 0.3$  and the shear correction factor  $k_W$  is used to calculate  $\omega_{mf1}$  in Table 2.1. The maximum relative error of the Mindlin plate theory using the shear correction factor  $k_W$  is less than 0.5% for  $\omega/\omega_s < 1$ , whereas the shear correction factor  $k_M$  leads to a maximum relative error of 3.2% for  $\omega/\omega_s < 1$ .

Table 2.1: Relative error  $\varepsilon_{f1}$  of the Kirchhoff and Mindlin plate theory ( $\nu = 0.3$ )

	1%		2%		5%		10%	
	$\frac{\omega_{mf1}}{\omega_s}$	$\frac{\lambda}{h}$	$\frac{\omega_{mf1}}{\omega_s}$	$\frac{\lambda}{h}$	$\frac{\omega_{mf1}}{\omega_s}$	$\frac{\lambda}{h}$	$\frac{\omega_{mf1}}{\omega_s}$	$\frac{\lambda}{h}$
Kirchhoff	0.0087	26.35	0.0175	18.55	0.0435	11.58	0.0865	8.028
Mindlin $k_M$	0.2208	4.693	0.5864	2.458	--	--	--	--
Mindlin $k_W$	--	--	--	--	--	--	--	--

As it is shown in the next section, in general, the shear dominant flexural and thickness-twist vibrations occur at rather high frequencies compared to the bending dominant flexural vibrations. Angular frequencies higher than  $\omega_s$  are not considered in this work and therefore the validity of the Mindlin plate theory is not examined for  $\omega/\omega_s > 1$ .

Comparing the results in Table 2.1 to the limits stated in the literature shows that nearly all recommendations allow for an error greater than 10% in case of the Kirchhoff plate theory. Only the strictest rule defined in [51] and [52] leads to an error between 1% and 2% for an infinite plate. Depending on the used shear correction factor, the rules applied for the Mindlin plate lead to an error of approximately 1.8%–2.4% ( $k_M$ ) and 0.2%–0.3% ( $k_W$ ). The strictest rule for the Mindlin plate theory results in a negligible error. Applying the looser limit from [51] would lead to  $\omega/\omega_s < 1.76$ , where not only

the first asymmetric frequency branch, but also the higher frequency branches need to be accurately represented. According to [50] the Mindlin plate theory is limited to  $\omega/\omega_s < 1.2$ , since the next higher thickness-modes cannot be approximated by the theory.

### 2.3.2 Influence of boundary conditions and other effects

In the previous section, the errors introduced by the approximate plate theories in case of an infinite plate have been shown. If the plate has finite dimensions and the simplified plate models are used to calculate the eigenfrequencies, the applied boundary conditions introduce additional errors. To examine the ability of the plate theories to accurately approximate the exact elasticity solution, several simple plate geometries, e.g. rectangular plates, circular plates and sector plates, with different combinations of classical boundary conditions are investigated.

An exact elasticity solution is only available in the literature for the hard simply-supported rectangular plate [53, 59, 60]. Solutions for rectangular plates with other combinations of boundary conditions are only feasible through approximate numerical methods. Malik and Bert [61] and Liew and Teo [62] used the differential quadrature method to calculate eigenfrequencies of rectangular plates with different boundary conditions, while Liew and his co-workers [63] applied the Ritz method to numerically solve the problem.

Exact solutions for the free vibrations of rectangular Mindlin plates are only available if two opposite sides are simply-supported (Levy-type plates), while the other two sides can have arbitrary combinations of boundary conditions. Mindlin [57] investigated the free vibrations of simply-supported rectangular plates, while Hashemi and Arsanjani [64] developed the analytical solutions for all possible combinations of Levy-type plates. All other combinations of boundary conditions have to be solved with numerical methods, e.g. [65] and [66].

The situation for the results of rectangular Kirchhoff plates is similar to that of rectangular Mindlin plates. Analytical solutions are only available for Levy-type plates, which are presented by Leissa [67]. Leissa [67] also used the Ritz method to calculate the eigenfrequencies for all other possible combinations of classical boundary conditions.

Since no analytical solutions for circular plates using the exact elasticity theory are available, Liew and Yang [68] used the Ritz method with a set of orthogonal polynomials to calculate the eigenfrequencies for all classical boundary conditions, while Zhou and his co-workers [69] applied the Chebyshev-Ritz method to find the eigenfrequencies. The analytical solutions for circular Mindlin plates are given by Irie et al. [70] and for circular Kirchhoff plates by Leissa [71] for all classical boundary conditions.

Even though several numerical solutions for annular sector plates with different combinations of boundary conditions using the exact elasticity theory exist in the literature, e.g. [72] and [73], no solutions can be found for sector plates. Exact analytical solutions for sector plates having simply-supported radial edges and arbitrary boundary conditions at the circular edge are reported by Huang and McGee [74] for the Mindlin plate theory and by Huang et al. [75] for the Kirchhoff plate theory. If other boundary conditions are applied at the radial edges, numerical methods have to be used in order to get the free vibration results for the sector plate. Wang and Wang [76] developed the differential

### 2.3 Useful ranges of validity for the Kirchhoff and Mindlin plate theory

quadrature method for the free vibration analysis of sectorial Kirchhoff plates with various combinations of boundary conditions, while McGee and his co-workers [77] and McGee et al. [78] applied the classical Ritz method to calculate the eigenfrequencies. Numerical results for sectorial Mindlin plates are given by Liu and Liew [79] applying the differential quadrature method and by Huang et al. [80] who employed the classical Ritz method.

To investigate the influence of boundary conditions on the validity of the plate theories, all previously mentioned analytical solutions for the free vibrations of plates are implemented in *MATLAB® R2017b* and eleven rectangular plates, three circular plates and twelve sector plates with different lateral dimensions and boundary conditions are analyzed. The thickness of the Kirchhoff and Mindlin plate configurations is varied from very thin plates to moderately thick plates in 230 steps. The first 100 asymmetric bending dominant flexural modes are calculated and therefore not only the low frequency range but also the so-called mid frequency range is considered in the analysis.

Since an exact elasticity solution is only available for the simply-supported rectangular plate, the commercial Finite Element software *ANSYS® 17.1* is used to build three-dimensional FEM models of all other plate configurations with two different thicknesses. The quadratic 20-node hexahedral element SOLID186 is applied to calculate the eigenfrequencies of the plate configurations and at least six quadric elements in thickness direction are used to avoid shear locking effects [81]. According to [82] at least six linear or three quadric elements per wavelength are required to successfully control the approximation error of the FEM, while for higher frequencies the pollution error becomes significant and a higher number of elements should be applied [83, 84]. To ensure accurate results at least 15 quadric elements per wavelength in lateral direction are used in the FEM simulations.

It is expected that the Mindlin plate theory using the shear correction factor  $k_W$  leads to highly accurate results within the validity region of the Kirchhoff plate theory, since the ratio of  $\omega/\omega_s$  is very small. Therefore, with exception of the simply-supported rectangular plate, the Mindlin plate theory using  $k_W$  serves as reference solution for the Kirchhoff plate theory. For the Mindlin plate theory, the three-dimensional FEM models are used as reference solutions.

To assess the validity of the plate models and the influence of the boundary conditions, the additional error  $\varepsilon_{ad}$ , caused by the boundary conditions, is defined by

$$\varepsilon_{ad} = |\varepsilon_{tot} - \varepsilon_{exp}|, \quad (2.125)$$

with

$$\varepsilon_{tot} = 100 \cdot \frac{\omega_k - \omega_{mf1}}{\omega_{mf1}} \text{ (Kirchhoff)} \quad \text{and} \quad \varepsilon_{tot} = 100 \cdot \frac{\omega_{mf1} - \omega_{3D}}{\omega_{3D}} \text{ (Mindlin)} \quad (2.126)$$

the total relative error compared to the reference solution and

$$\varepsilon_{exp} = 100 \cdot \frac{\omega_k^{inf} - \omega_{mf1}}{\omega_{mf1}} \text{ (Kirchhoff)} \quad \text{and} \quad \varepsilon_{exp} = 100 \cdot \frac{\omega_{mf1}^{inf} - \omega_{3D}}{\omega_{3D}} \text{ (Mindlin)} \quad (2.127)$$

the expected relative error, which results from the infinite plate solution. The angular eigenfrequencies  $\omega_k^{inf}$  (Kirchhoff) and  $\omega_{mf1}^{inf}$  (Mindlin) are calculated using the frequency equations of the infinite plate (Equation (2.115) for Kirchhoff and Equation (2.116) for

Mindlin) and the wavenumber of the reference solution  $\xi_{ref} = \{\xi_{mf1}, \xi_{3D}\}$ , calculated by substituting the reference solution  $\omega_{ref} = \{\omega_{mf1}, \omega_{3D}\}$  into the corresponding frequency equations of the infinite plate (Equation (2.116) for Mindlin as reference and Equation (2.120) for the 3D solution as reference).

### Rectangular plate configurations

The dimensions and boundary conditions of the rectangular plate configurations are shown in Figure 2.8. The lateral dimensions of the plate in  $x$ - and  $y$ -direction are denoted by  $a$  and  $b$ . The boundaries 1 ( $x = 0$ ) and 3 ( $x = a$ ) are simply-supported for all plate configurations, while the boundaries 2 ( $y = 0$ ) and 4 ( $y = b$ ) are either simply-supported (S), clamped (C) or free (F). Four different combinations of boundary conditions, SSSS, SCSC, SCSF and SFSF are examined.

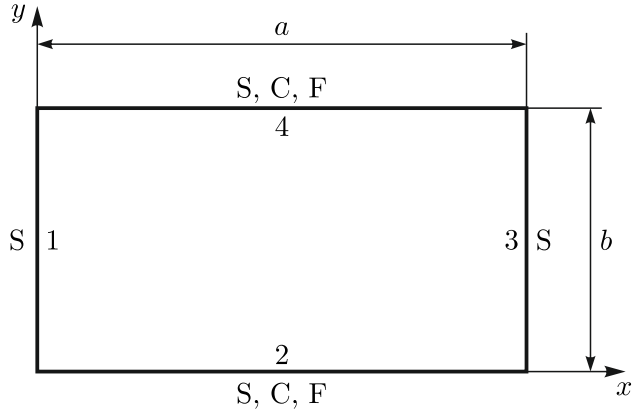


Figure 2.8: Dimensions and boundary conditions of the rectangular plate configurations

The angular frequency ratios  $\{\omega_{3D}, \omega_{mf1}, \omega_k\}/\omega_s$  only depend on the ratios  $a/b$  and  $a/h$  and the Poisson's ratio  $\nu$  of the plate, which is set to  $\nu = 0.3$  for the following analysis. Three different ratios of the lateral dimensions  $a/b = \{0.66, 1, 1.5\}$  are used to investigate the influence of the boundary conditions. The analytical solutions of the Kirchhoff plate [67] and the Mindlin plate [64] are evaluated for 230 different ratios of the smallest lateral dimension of the plate  $a$  or  $b$  to the plate thickness  $h$ , varying from very thin plates ( $\{a, b\}/h = 500$ ) to moderately thick plates ( $\{a, b\}/h = 10$ ).

Since the evaluation of the 3D FEM models is very time consuming, the eigenfrequencies of the plates are only calculated for two different plate thicknesses  $\{a, b\}/h = \{10, 20\}$ . In Table 2.2 the total number of elements, the degrees of freedom, the number of elements in plate thickness direction and the minimum number of elements per wavelength  $\lambda$  in lateral dimension are listed for the different FEM models. The same FEM mesh is applied for all combinations of boundary conditions.

In the case of the simply-supported plate, the numerical results show that no additional error is introduced by the boundary condition for the Kirchhoff and Mindlin plate theory compared to the exact elasticity solution. The total error of the asymmetric bending

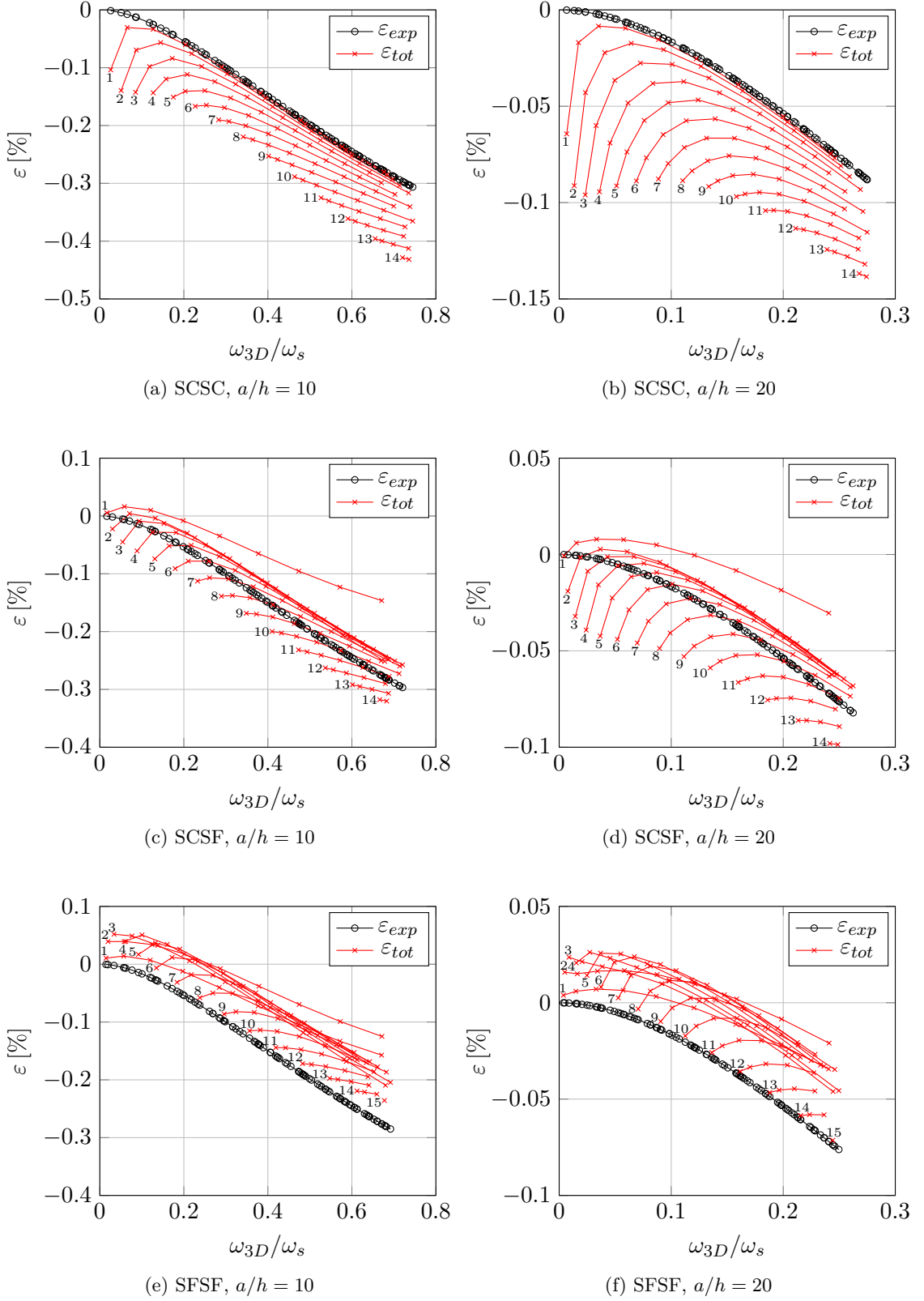
Table 2.2: 3D FEM models for the analysis of the rectangular plate configurations

$a/b$	$a/h (b/h)$	# elements	# FE dofs	# z-divisions	# elements/ $\lambda$
0.66	10	129600	1767639	6	25
	20	518400	7034439	6	49
1	10	86400	1180839	6	20
	20	345600	4694439	6	40
1.5	10	129600	1767639	6	24
	20	518400	7034439	6	49

modes of simply-supported rectangular Kirchhoff and Mindlin plates is equivalent to the error occurring in an infinite plate. Straight simply-supported boundary conditions do not introduce additional errors, since no coupling between the different frequency branches occurs at the boundary [57] and boundary layers are not present [85].

The total and expected errors of the Mindlin plate theory for other combinations of boundary conditions are shown in Figures 2.9–2.11. The shear correction factor  $k_W$  is applied. The total errors of the first 100 asymmetric bending dominant flexural modes are plotted and marked by red crosses. Bending modes with a similar nodal pattern are connected by a solid red line and the assigned values define the number of maxima (minima) of the corresponding mode shapes in  $y$ -direction. The number of maxima (minima) of the mode shapes in  $x$ -direction rises with increasing frequency. The expected error resulting from the infinite plate solution is plotted by a solid black line. Several conclusions are apparent from the given results:

- For all rectangular plate configurations, the angular eigenfrequencies  $\omega$  do not exceed the angular frequency of the lowest, simple thickness-shear mode in the plate  $\omega_s$ . Therefore, only asymmetric bending dominant flexural vibration is expected (pure in-plane modes are not considered in this work) and the ability of the Mindlin plate theory to model the other frequency branches plays only a minor part, if the first 100 bending modes are calculated and the ratio  $\{a, b\}/h > 10$ .
- Free boundary conditions have a stiffening (positive additional error) and clamped boundary conditions a softening (negative additional error) effect compared to the infinite plate solution.
- The additional error introduced by the boundary conditions decreases if the plate becomes thinner and the ratio of the lateral dimensions  $a/b$  has only a minor impact. The mode shape also influences the additional error.
- The maximum additional error occurs for free boundary conditions, but since a stiffening of the plate is introduced, the total error is even lower than the error in the infinite plate for higher frequencies. Clamped boundary conditions lead to the highest total error for rectangular plates.
- The additional error introduced by the boundary conditions is small and does not exceed 0.25% for  $\{a, b\}/h = 10$  and 0.075% for  $\{a, b\}/h = 20$ .
- The Mindlin plate theory leads to excellent results with a maximum total error of less than 0.6% for the first 100 bending modes and a ratio  $\{a, b\}/h = 10$ .


 Figure 2.9: Expected and actual total error of a rectangular Mindlin plate ( $a/b = 0.66\bar{4}$ )

### 2.3 Useful ranges of validity for the Kirchhoff and Mindlin plate theory

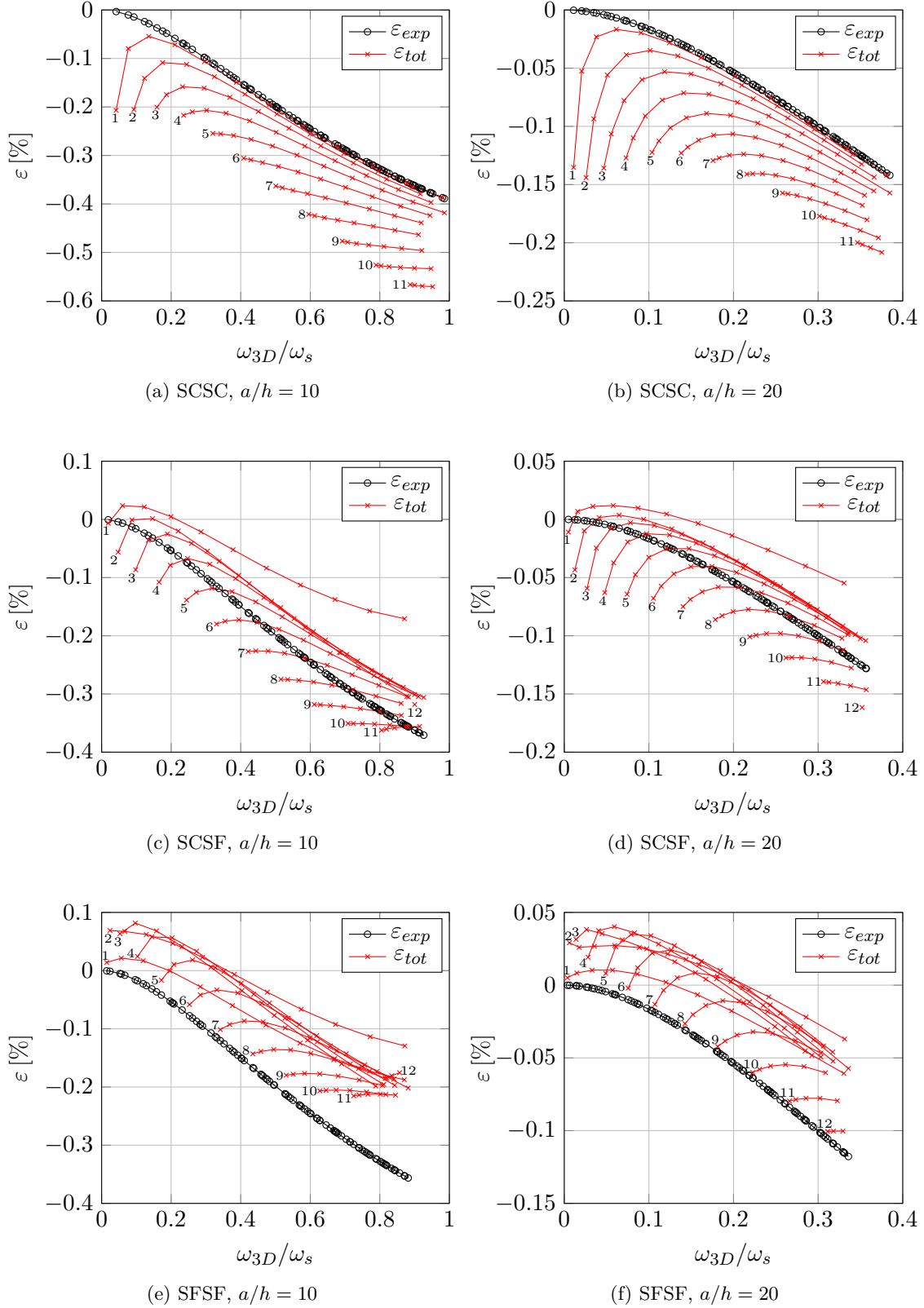
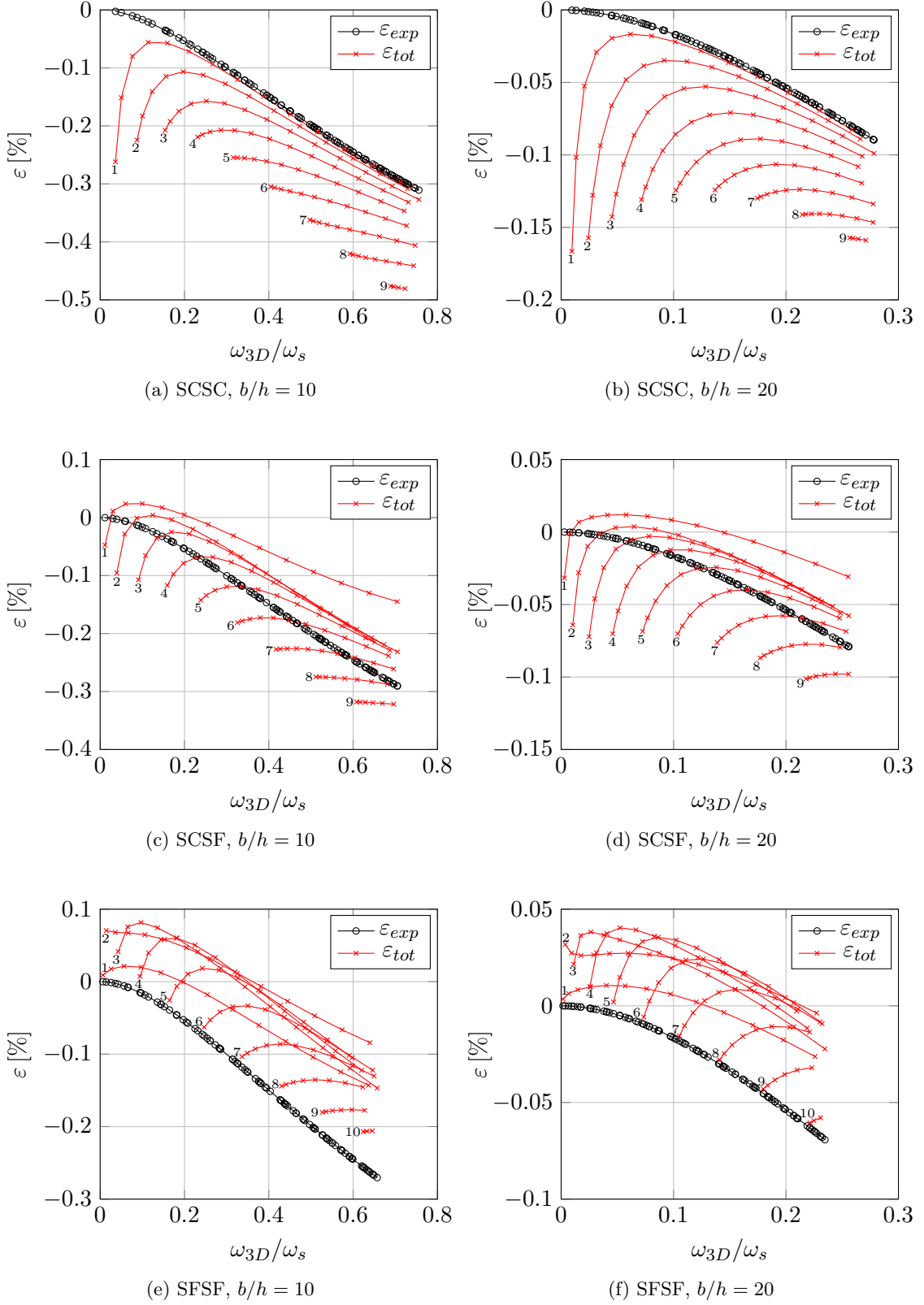


Figure 2.10: Expected and actual total error of a rectangular Mindlin plate ( $a/b = 1$ )


 Figure 2.11: Expected and actual total error of a rectangular Mindlin plate ( $a/b = 1.5$ )

### 2.3 Useful ranges of validity for the Kirchhoff and Mindlin plate theory

The additional error  $\varepsilon_{ad}$  of the Kirchhoff plate theory with SCSC, SCSF and SFSF boundary conditions depending on the angular frequency ratio  $\omega_{mf1}/\omega_s$  ( $x$ -axis) and the ratio of the smallest lateral dimension to the plate thickness  $\{a, b\}/h$  ( $y$ -axis with logarithmic scale) is shown in Figures 2.12 – 2.20. Vertical dashed lines illustrate the 1%, 2% and 5% error limits defined from the infinite plate solution in Table 2.1. The  $x$ -axis is limited by an angular frequency ratio of  $\omega_{mf1}/\omega_s < 0.045$ , since the expected error of the Kirchhoff plate theory already exceeds 5%. The first 100 asymmetric bending dominated flexural modes are shown, which are ordered from top to bottom. The additional error is illustrated by the colorbar.

From Figures 2.12 – 2.20 the following can be concluded:

- The additional error introduced by the boundary conditions rises, if the plate thickness increases or higher frequencies are viewed. The mode shape also influences the additional error.
- The introduction of boundary conditions leads to a further stiffening effect compared to the Mindlin plate theory, since the additional error is always positive. This effect is more pronounced for clamped boundaries compared to the free boundaries.
- The accurate prediction of the fundamental eigenfrequency (first mode) of SCSC rectangular plates requires a ratio of the smallest lateral dimension to the plate thickness of  $\{a, b\}/h > 30$  (1% total error),  $\{a, b\}/h > 20$  (2% total error) or  $\{a, b\}/h > 13$  (5% total error). These limits depend on the stiffness of the boundary conditions and therefore are looser for the SFSF rectangular plate, see Figures 2.12 and 2.14. Comparing the Figures 2.12, 2.15 and 2.18, it is apparent that the ratio of the lateral dimensions  $a/b$  has only a minor effect on the limits.
- Highly accurate results are only guaranteed, if the angular frequency limit defined from the infinite plate solution  $\omega_k/\omega_s < 0.0087$  is fulfilled and a ratio  $\{a, b\}/h > 30$  is given.
- The first 100 bending modes can only be calculated accurately for very thin plates. Depending on the desired accuracy the limit ranges from  $\{a, b\}/h > 160$  (1% total error),  $\{a, b\}/h > 120$  (2% total error) to  $\{a, b\}/h > 70$  (5% total error). These limits are only slightly changing for the different boundary conditions and lateral dimensions of the rectangular plate.
- Since the frequency limit of the Kirchhoff plate theory requires very thin plates to predict the first 100 eigenfrequencies, the additional error, introduced by the boundary conditions, is in general negligible for higher order modes.
- As long as the frequency limit, defined from the infinite plate solution, for the Kirchhoff plate theory is fulfilled and the ratio of the smallest lateral dimension to the plate thickness  $\{a, b\}/h > 30$ , the additional error introduced by the boundary conditions can be neglected for all modes ( $\varepsilon_{ad} < 1\%$  at  $\omega_{mf1}/\omega_s = 0.045$ ).

The Kirchhoff plate theory only models asymmetric bending dominant flexural modes and therefore an additional error is introduced by the boundary conditions if a coupling of different mode types occurs at the boundary [57]. Such a coupling is only absent for straight simply-supported boundaries. Furthermore, the Kirchhoff plate theory is not able to model boundary layers, which are present in the elasticity theory [85].

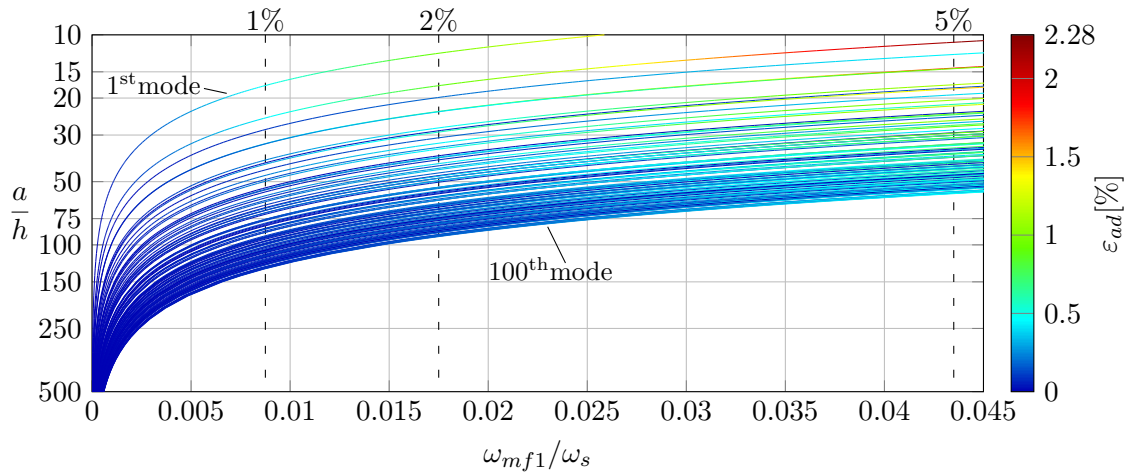


Figure 2.12: Additional error of a SCSC rectangular Kirchhoff plate ( $a/b = 0.66\ddot{\circ}$ )

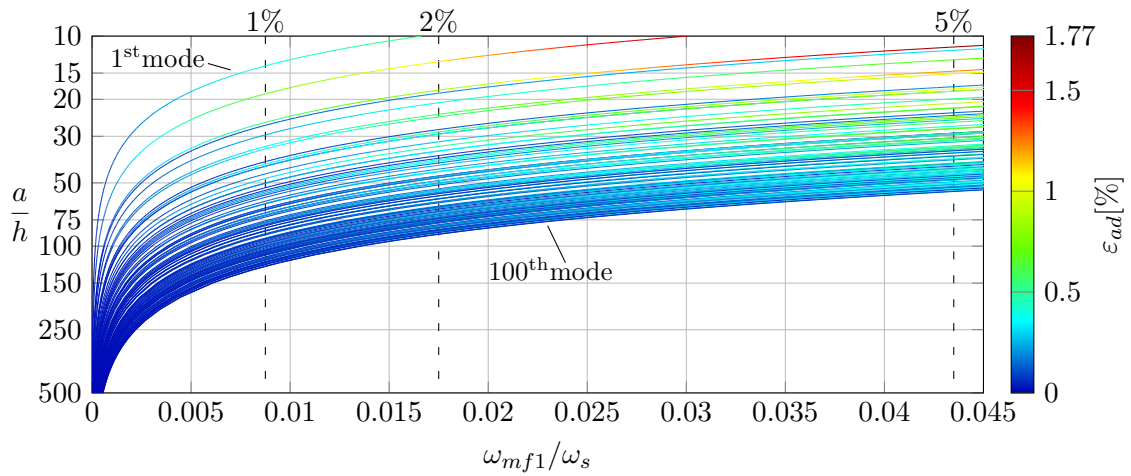


Figure 2.13: Additional error of a SCSF rectangular Kirchhoff plate ( $a/b = 0.66\ddot{\circ}$ )

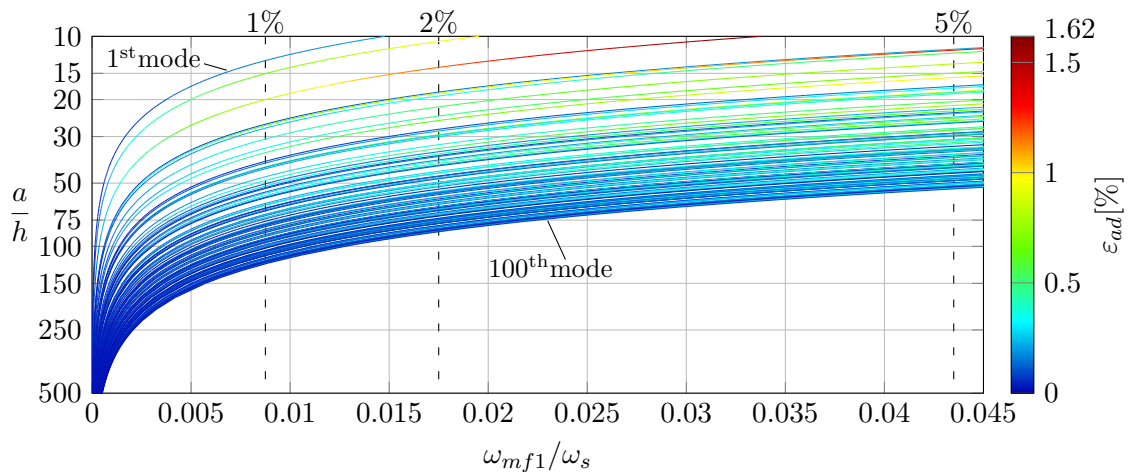


Figure 2.14: Additional error of a SFSC rectangular Kirchhoff plate ( $a/b = 0.66\ddot{\circ}$ )

### 2.3 Useful ranges of validity for the Kirchhoff and Mindlin plate theory

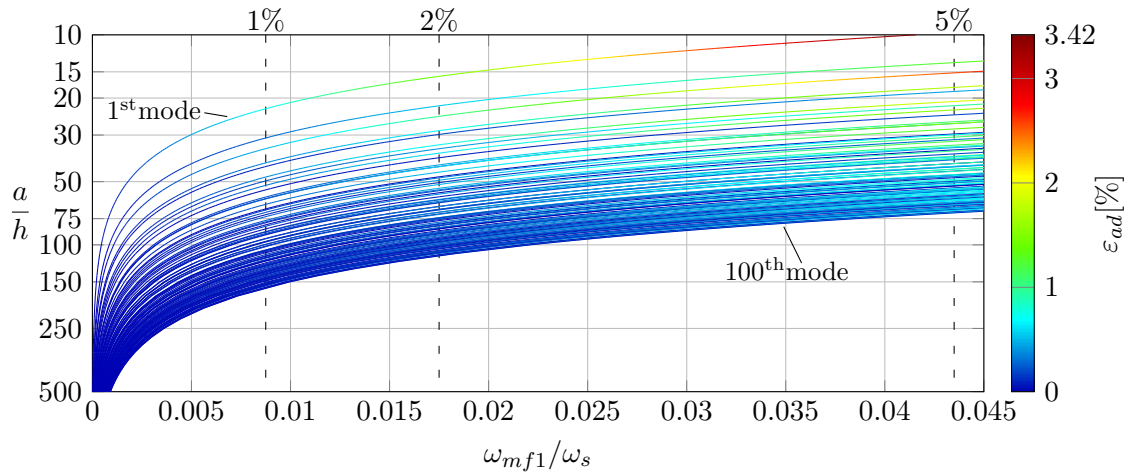


Figure 2.15: Additional error of a SCSC rectangular Kirchhoff plate ( $a/b = 1$ )

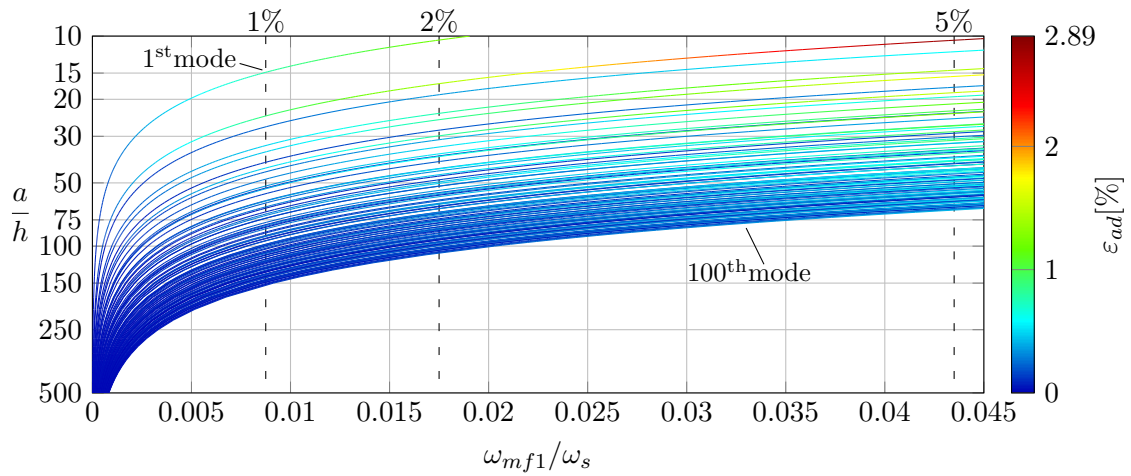


Figure 2.16: Additional error of a SCSF rectangular Kirchhoff plate ( $a/b = 1$ )

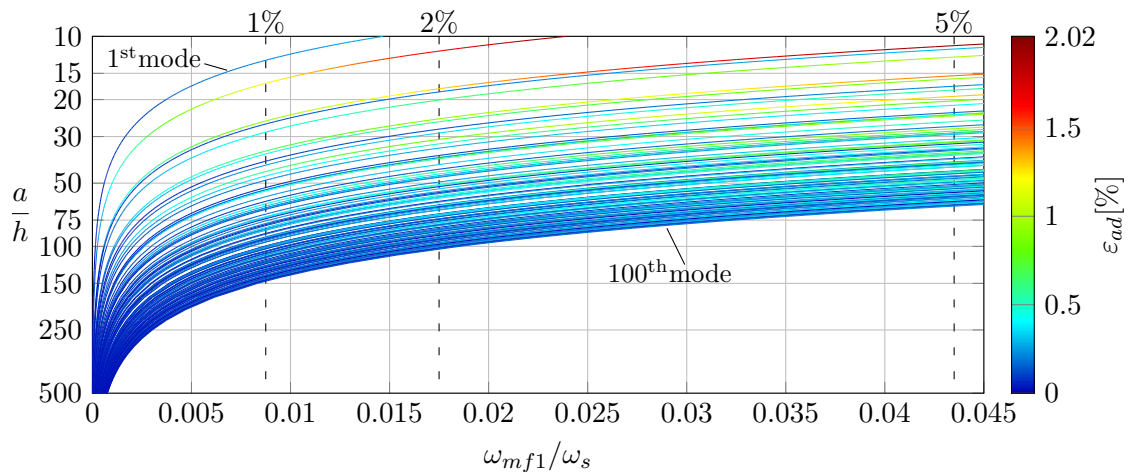


Figure 2.17: Additional error of a SFSF rectangular Kirchhoff plate ( $a/b = 1$ )

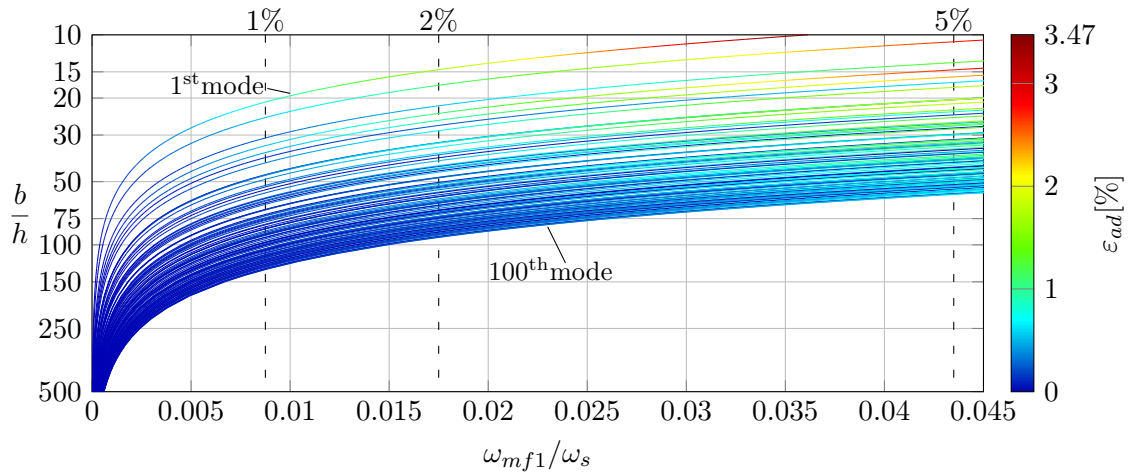


Figure 2.18: Additional error of a SCSC rectangular Kirchhoff plate ( $a/b = 1.5$ )

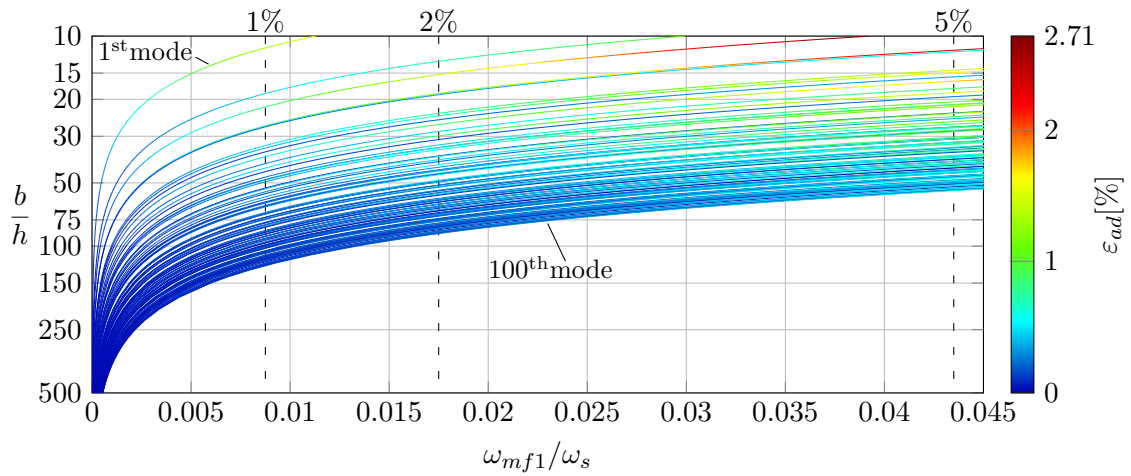


Figure 2.19: Additional error of a SCSF rectangular Kirchhoff plate ( $a/b = 1.5$ )

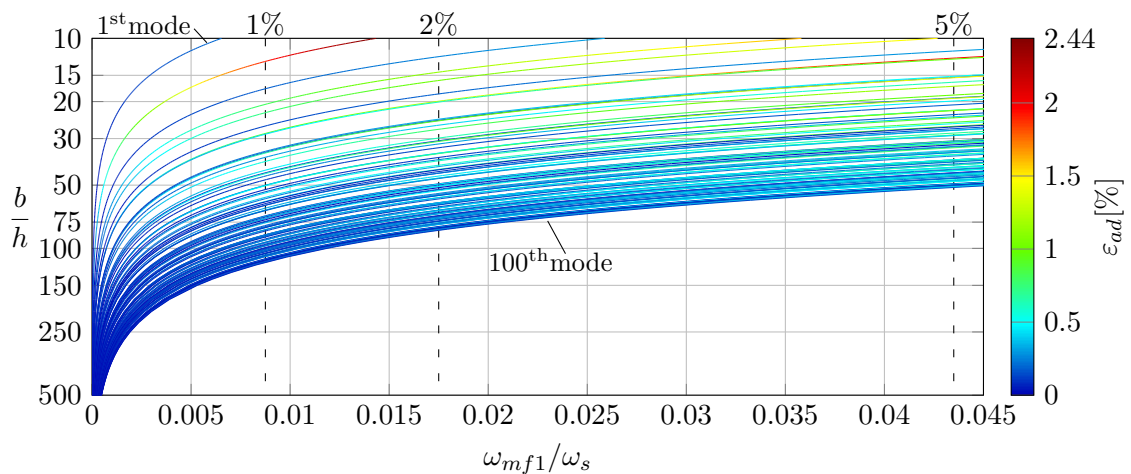


Figure 2.20: Additional error of a SFSF rectangular Kirchhoff plate ( $a/b = 1.5$ )

### Circular plate configurations

The dimensions and boundary conditions of the circular plate configurations are illustrated in Figure 2.21. The radius of the circular plate is denoted by  $R$  and the boundary of the plate is either simply-supported, clamped or free. The angular frequency ratios  $\{\omega_{3D}, \omega_{mf1}, \omega_k\}/\omega_s$  for circular plates only depend on the ratio of the characteristic lateral dimension to the plate thickness ( $2R/h$ ) and the Poisson's ratio  $\nu$ .

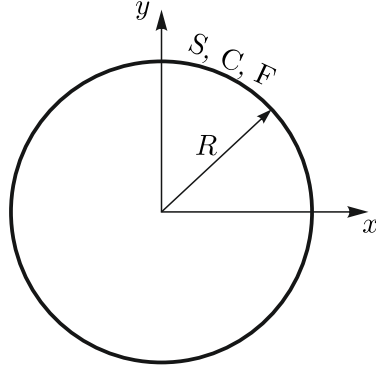


Figure 2.21: Dimensions and boundary conditions of the circular plate configurations

The analytical solutions for circular Kirchhoff [71] and Mindlin plates [70] are used to analyze the eigenfrequencies of the plates for 230 different thicknesses, ranging from  $2R/h = 500$  (thin plate) to  $2R/h = 10$  (moderately thick plate) and the Poisson's ratio  $\nu = 0.3$  is applied.

In total six different 3D FEM models are solved for the analysis of the circular plate configurations with two different ratios  $2R/h = \{10, 20\}$ . The FEM model properties are listed in Table 2.3 and are identical for all three boundary conditions.

Table 2.3: 3D FEM models for the analysis of the circular plate configurations

$2R/h$	# elements	# FE dofs	# z-divisions	# elements/ $\lambda$
10	256000	3372531	8	15
20	256000	3372531	8	15

The total and expected errors of the circular Mindlin plates are shown in Figure 2.22. Similar to the rectangular plate results, the total errors of the asymmetric bending dominant flexural modes are plotted and marked by red crosses and bending modes with a similar nodal pattern are connected by a solid red line. The assigned values define the number of nodal lines (lines of zero displacement) in circumferential direction.

The number of nodal lines in radial direction generally rises with increasing frequency. The only exception is the fundamental mode (mode with the lowest frequency) of the free circular plate, which has two nodal lines in radial direction and zero nodal lines in

circumferential direction. The expected error resulting from the infinite plate solution is plotted by a solid black line.

In case of the moderately thick plates ( $2R/h = 10$ ) with clamped and simply-supported boundary conditions (Figures 2.22a and 2.22c) only the first 82 modes are plotted, since the modes 83 to 100 exceed the angular frequency ratio  $\omega_{3D}/\omega_s = 1$  ( $\omega_{3D}/\omega_s \approx 1.1$  for the 100<sup>th</sup> mode) and therefore shear dominant modes appear. The first 100 asymmetric bending modes are shown for all other circular plate configurations.

The findings for the circular and rectangular plates are similar. A few additional conclusions are:

- For curved boundaries, the simply-supported boundary conditions introduce an additional error, since a coupling between the different mode types occurs at the boundary and a boundary layer is present [85].
- If no circumferential nodal lines are present in the mode shape, the additional error in case of completely free boundary conditions is most pronounced.
- The Mindlin plate theory is able to predict the first 100 eigenfrequencies very accurately independent of the boundary conditions if the ratio of the characteristic length to the plate thickness  $2R/h < 10$ .

The additional error  $\varepsilon_{ad}$  of the Kirchhoff plate theory with clamped, simply-supported and free boundary conditions is illustrated in Figures 2.23 – 2.25. The  $y$ -axis has a logarithmic scale and shows the ratio of the characteristic length to the plate thickness  $2R/h$ . The vertical dashed lines indicate the 1%, 2% and 5% error limits defined from the infinite plate solution. Similar to the rectangular plate, the first 100 asymmetric bending dominated flexural modes are shown, which are ordered from top to bottom. Due to the symmetry of the circular plates several double modes appear in the analysis.

The findings for the circular and rectangular Kirchhoff plate are very similar. The additional error for the simply-supported circular plate, shown in Figure 2.24, is less than 0.25% but not 0% as for the rectangular plate, since simply-supported boundary conditions lead to boundary layers if the boundary is curved.

Since the clamped circular plate is stiffer than the SCSC rectangular plate, the limit for the ratio of the smallest characteristic length  $2R$  to the plate thickness  $h$  to accurately predict the first 100 modes is even stricter. Depending on the desired accuracy a ratio  $2R/h = 185$  (1% total error),  $2R/h = 125$  (2% total error) and  $2R/h = 75$  (5% total error) is required.

A limit for the ratio  $2R/h > 30$  is sufficient to ensure accurate results if the frequency limit defined by the infinite plate solutions is not exceeded. Even though the additional error introduced by the boundary conditions is higher for the clamped circular plate compared to the SCSC rectangular plate, the additional error is still negligible ( $\varepsilon \approx 1\%$  at  $\omega_{mf1}/\omega_s = 0.04$ ).

An accurate prediction of the fundamental mode for the clamped circular plate requires a ratio  $2R/h = 33$  (1% total error),  $2R/h = 23$  (2% total error) and  $2R/h = 15$  (5% total error), which is slightly higher compared to the SCSC rectangular plate.

### 2.3 Useful ranges of validity for the Kirchhoff and Mindlin plate theory

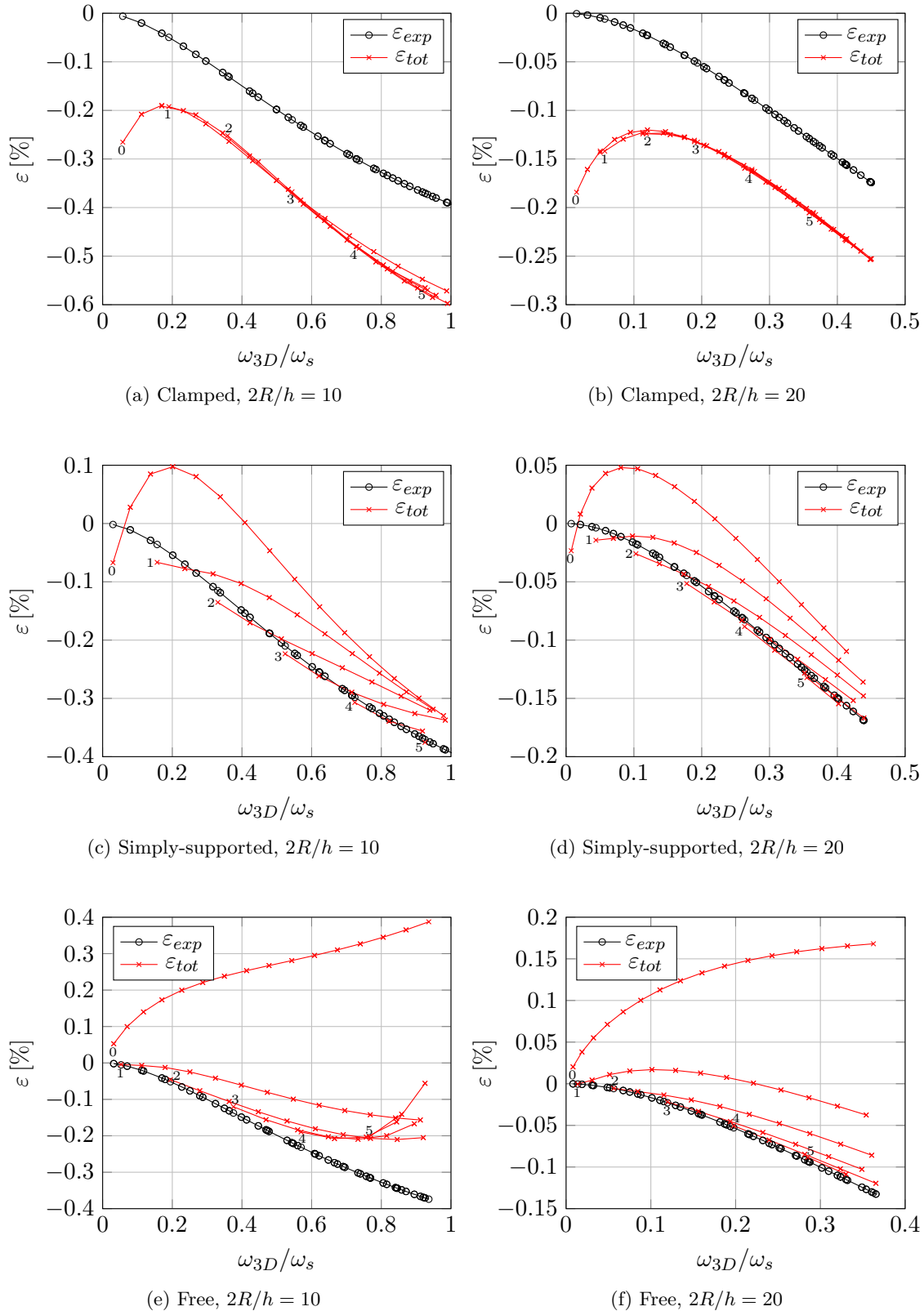


Figure 2.22: Expected and actual total error of a circular Mindlin plate

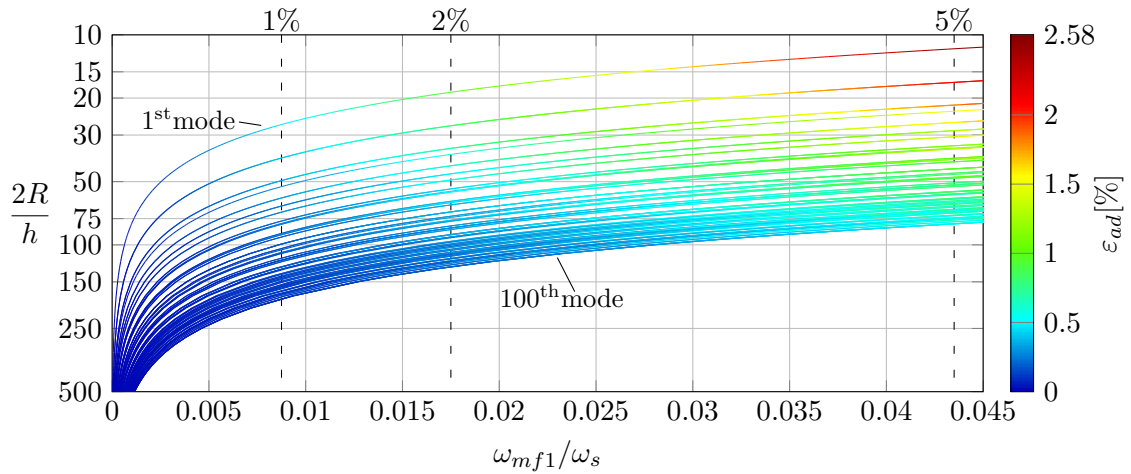


Figure 2.23: Additional error of a clamped circular Kirchhoff plate

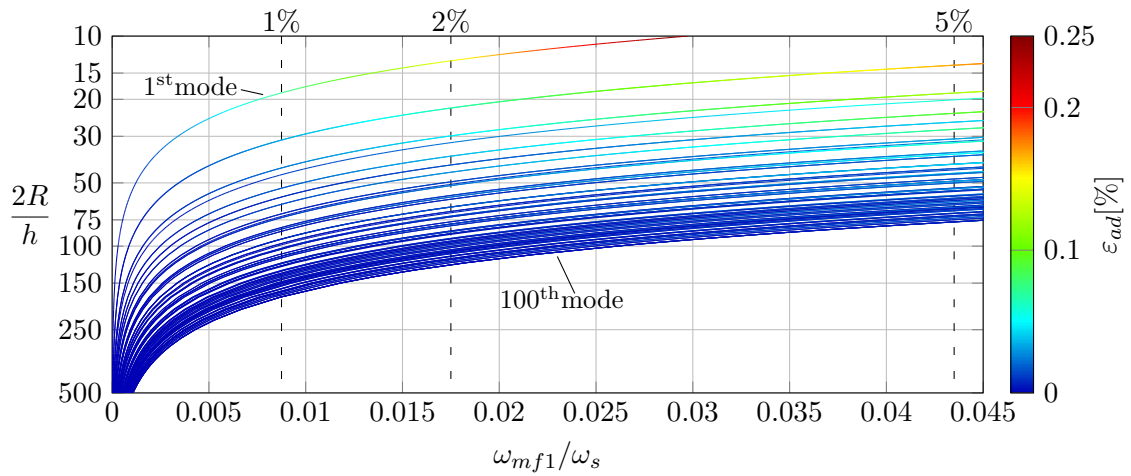


Figure 2.24: Additional error of a simply-supported circular Kirchhoff plate

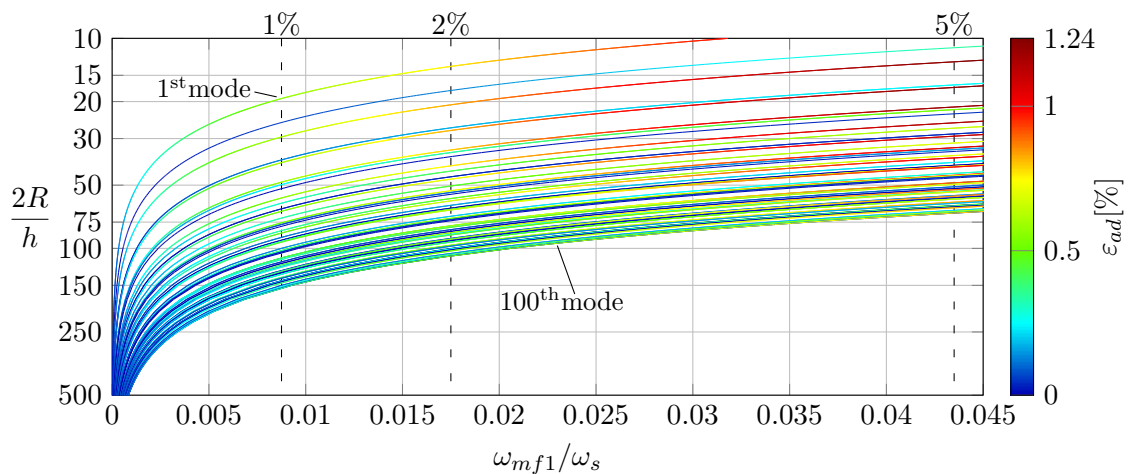


Figure 2.25: Additional error of a free circular Kirchhoff plate

### Sector plate configurations

In Figure 2.26 the dimensions and boundary conditions of the sector plate configurations are illustrated. The radius of the plate is denoted by  $R$  and the sector angle by  $\alpha$ . The radial edges 1 and 3 are always simply-supported, while the circumferential edge 2 is either simply-supported (S), clamped (C) or free (F). The angular frequency ratios  $\{\omega_{3D}, \omega_{mf1}, \omega_k\}/\omega_s$  for sector plates only depend on the sector angle  $\alpha$ , the ratio of the plate radius  $R$  to the plate thickness  $h$  and the Poisson's ratio  $\nu$ , which is set to  $\nu = 0.3$ .

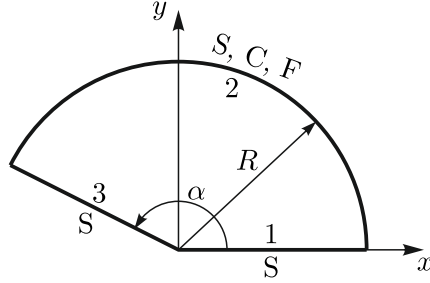


Figure 2.26: Dimensions and boundary conditions of the sector plate configurations

Four different sector angles  $\alpha = \{30^\circ, 165^\circ, 195^\circ, 330^\circ\}$  with three different combinations of boundary conditions SSS, SCS and SFS are investigated. The smallest characteristic lateral dimension of the plate, denoted by  $R^*$ , depends on the chosen sector angle  $\alpha$  and is given by  $R^* = R \sin(\alpha)$  ( $\alpha = 30^\circ$ ),  $R^* = R$  ( $\alpha = 165^\circ$ ),  $R^* = R(1 - \sin(\alpha))$  ( $\alpha = 195^\circ$ ) and  $R^* = 2R$  ( $\alpha = 330^\circ$ ). The analytical solutions for sectorial Kirchhoff [75] and Mindlin plates [74] are evaluated for 230 different thicknesses, ranging from  $R^*/h = 500$  (thin plate) to  $R^*/h = 10$  (moderately thick plate).

The 3D elasticity results are calculated for two different thicknesses  $R^*/h = \{10, 20\}$  using the FEM models listed in Table 2.4. The meshing for the SFS sector plates differs from the FEM meshes of the SSS and SCS sector plates, since a higher number of elements per wavelength in lateral dimension have been required for the SFS sector plates to get accurate results.

If the radial edges are simply-supported and the sector angle  $\alpha$  exceeds  $180^\circ$ , stress singularities can arise at the corner ( $r = 0$ ) [75, 74] and affect the solutions of the Kirchhoff and Mindlin plate theory. The strength of the singularity increases with rising sector angle and therefore weak ( $\alpha = 195^\circ$ ) and strong singularities ( $\alpha = 330^\circ$ ) are expected.

The total and expected errors of the Mindlin plate theory for the three different boundary conditions are shown in Figures 2.27 – 2.30. The total errors of the bending modes are marked by red crosses and bending modes with a similar nodal pattern are connected by a solid red line. The assigned values define the number of nodal lines (lines of zero displacement) in circumferential direction. The number of nodal lines in radial direction rises with increasing frequency. The solid black line illustrates the expected errors.

In case of the moderately thick plates ( $R^*/h = 10$ ) with a sector angle  $\alpha = 330^\circ$  (Figures 2.30a, 2.30c and 2.30e) only the first 73 (clamped), 74 (simply-supported) and 99

Table 2.4: 3D FEM models for the analysis of the sector plate configurations

$\alpha$	$R^*/h$	BC	# elements	# FE dofs	# $z$ -divisions	# elements/ $\lambda$
$30^\circ$	10	SCS, SSS	259200	3520839	6	20
		SFS	236016	3129039	8	28
	20	SCS, SSS	405000	5494539	6	25
		SFS	236016	3129039	8	28
$165^\circ$	10	SCS, SSS	375000	4951176	8	18
		SFS	300396	3863526	12	23
	20	SCS, SSS	375000	4951176	8	17
		SFS	300396	3863526	12	23
$195^\circ$	10	SCS, SSS	257470	3352146	10	26
		SFS	397431	5200764	9	36
	20	SCS, SSS	397736	5252706	8	34
		SFS	393484	5257914	7	41
$330^\circ$	10	SCS, SSS	325704	4195893	12	28
		SFS	424134	5554950	9	41
	20	SCS, SSS	393147	5150553	9	33
		SFS	403137	5391060	7	44

(free) modes are plotted, since the higher order modes exceed the angular frequency ratio  $\omega_{3D}/\omega_s = 1$ . The first 100 bending modes are shown for all other configurations. The sector plate with  $\alpha = 30^\circ$  (Figure 2.27) leads to similar findings as the rectangular and circular plate. Especially the additional error  $\varepsilon_{ad}$  for the SSS plate is close to zero, since two straight boundaries and only one slightly curved boundary are present.

Comparing the results in Figure 2.27 ( $\alpha = 30^\circ$ ) and Figure 2.28 ( $\alpha = 165^\circ$ ), it is apparent that a difference in the additional error only occurs for mode shapes without nodal lines in radial direction. Especially for a free circumferential edge (SFS), the mode with zero radial and circumferential nodal lines leads to a high total error (25% for  $R/h = 10$  and 23% for  $R/h = 20$ ). Similar results are found in [86] for annular Kirchhoff plates with a clamped inner boundary. A further investigation of the higher errors, appearing for mode shapes without nodal lines in radial direction is not carried out in this work.

To investigate the influence of corner stress singularities on the Mindlin plate, the results for the sector plate with  $\alpha = 165^\circ$  (Figure 2.28) and  $\alpha = 195^\circ$  (Figure 2.29) are compared. Stress singularities only occur for mode shapes without nodal lines in radial direction [74]. Even though a higher additional error is apparent in Figure 2.29 for modes with zero nodal lines in radial direction, the error cannot be attributed to the stress singularities, since a similar error is found for the sector plate with  $\alpha = 165^\circ$ . Therefore, the Mindlin plate theory is capable of accurately representing the singularities in the corner.

The additional and total error for the sector plate with  $\alpha = 330^\circ$  (stronger stress singularities) are similar compared to the previous examples. The additional errors for modes with zero or one nodal line(s) in radial direction are higher. The higher error for modes with one radial nodal line is due to the fact that the modes with one radial nodal line are equivalent to the vibrations of a sector plate with  $\alpha = 165^\circ$  and zero radial nodal lines.

### 2.3 Useful ranges of validity for the Kirchhoff and Mindlin plate theory

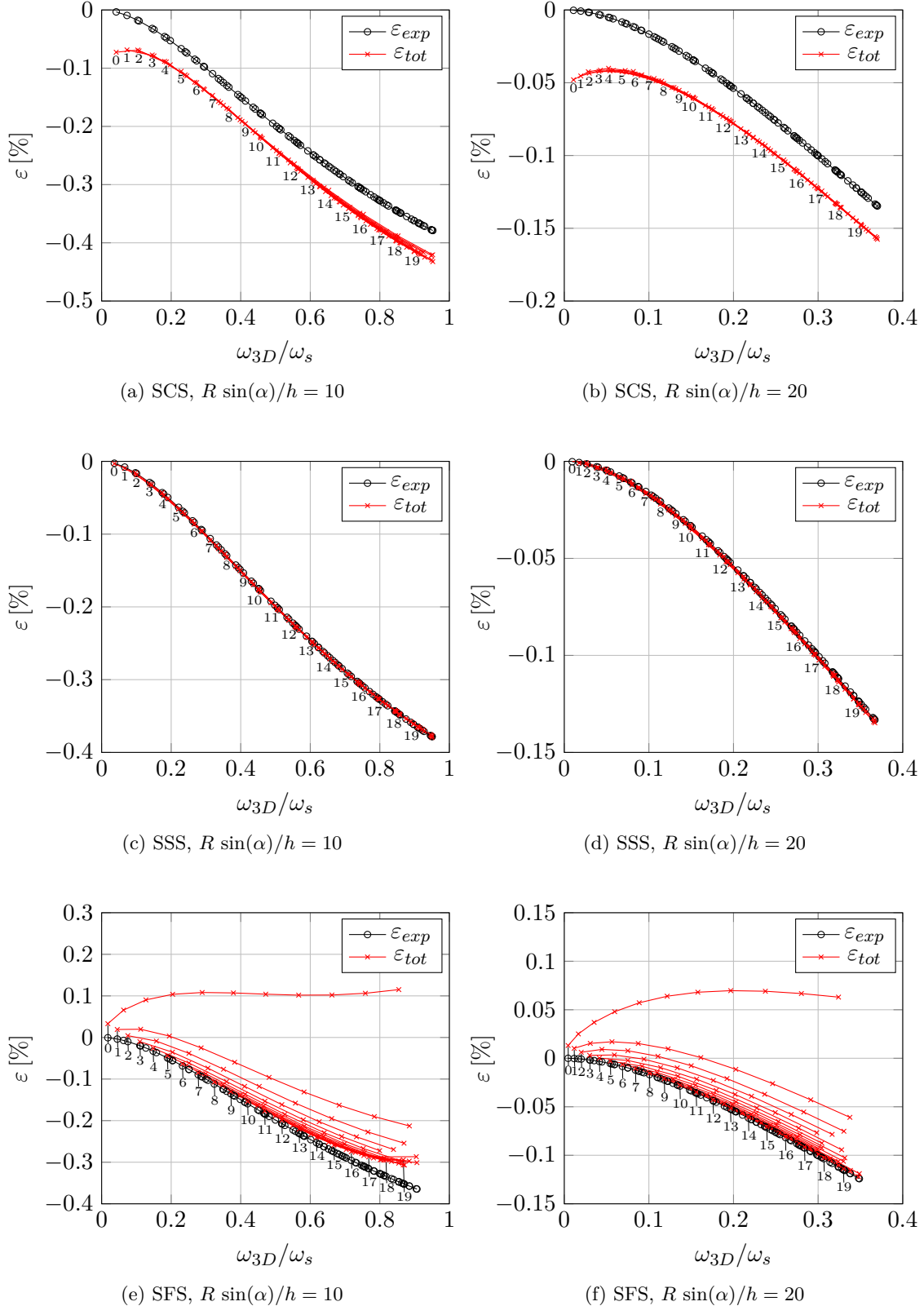
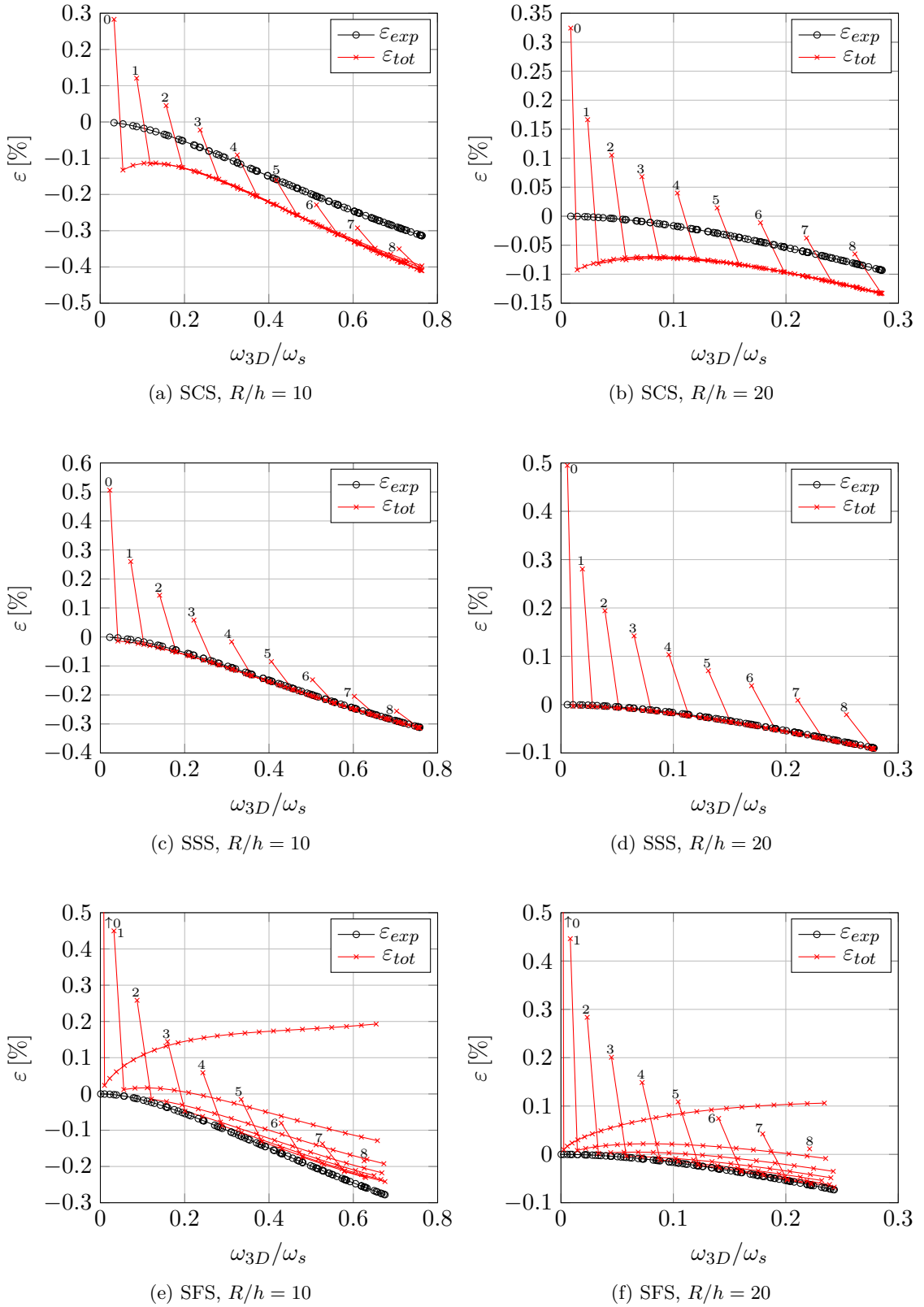


Figure 2.27: Expected and actual total error of a sectorial Mindlin plate ( $\alpha = 30^\circ$ )


 Figure 2.28: Expected and actual total error of a sectorial Mindlin plate ( $\alpha = 165^\circ$ )

### 2.3 Useful ranges of validity for the Kirchhoff and Mindlin plate theory

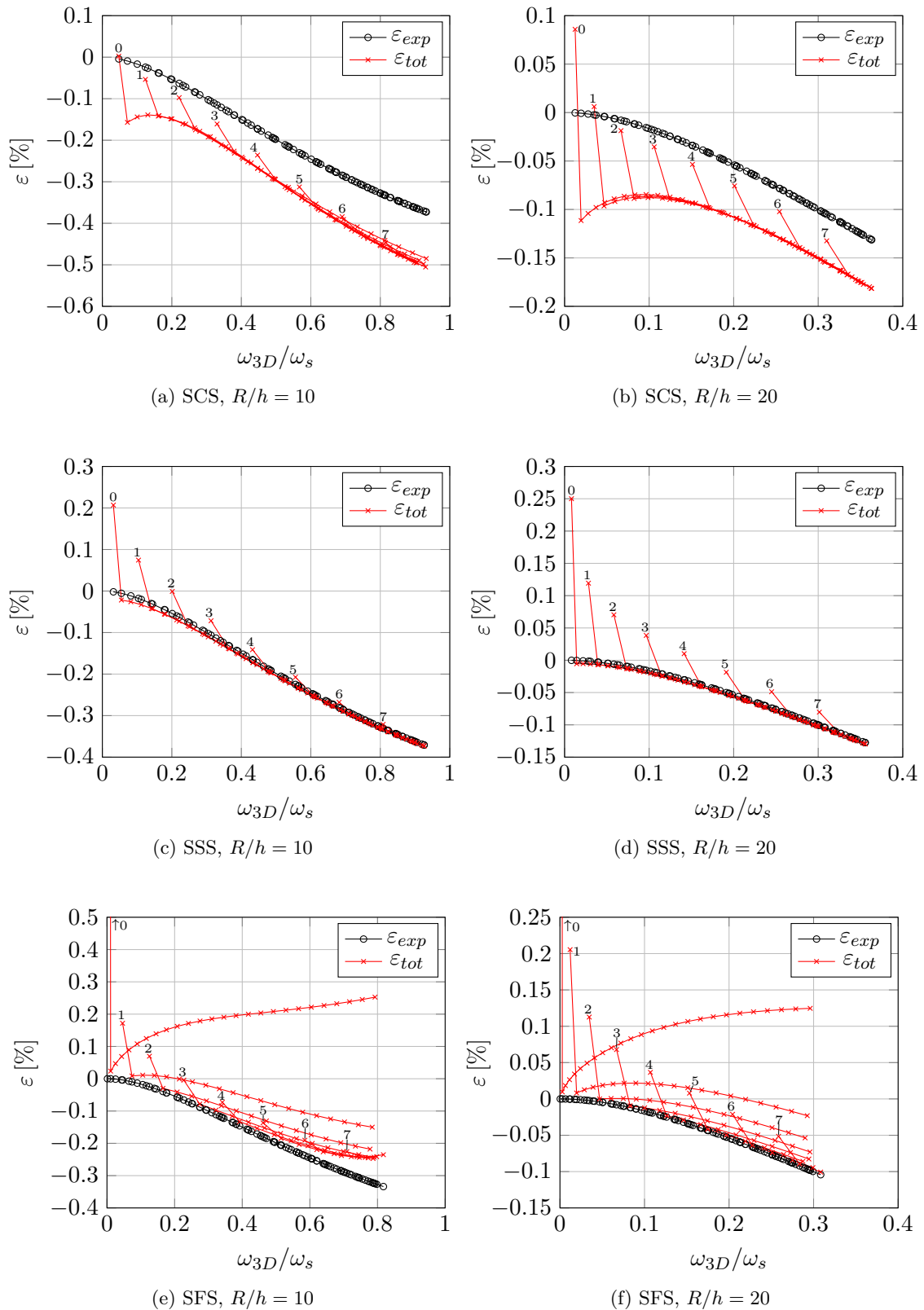
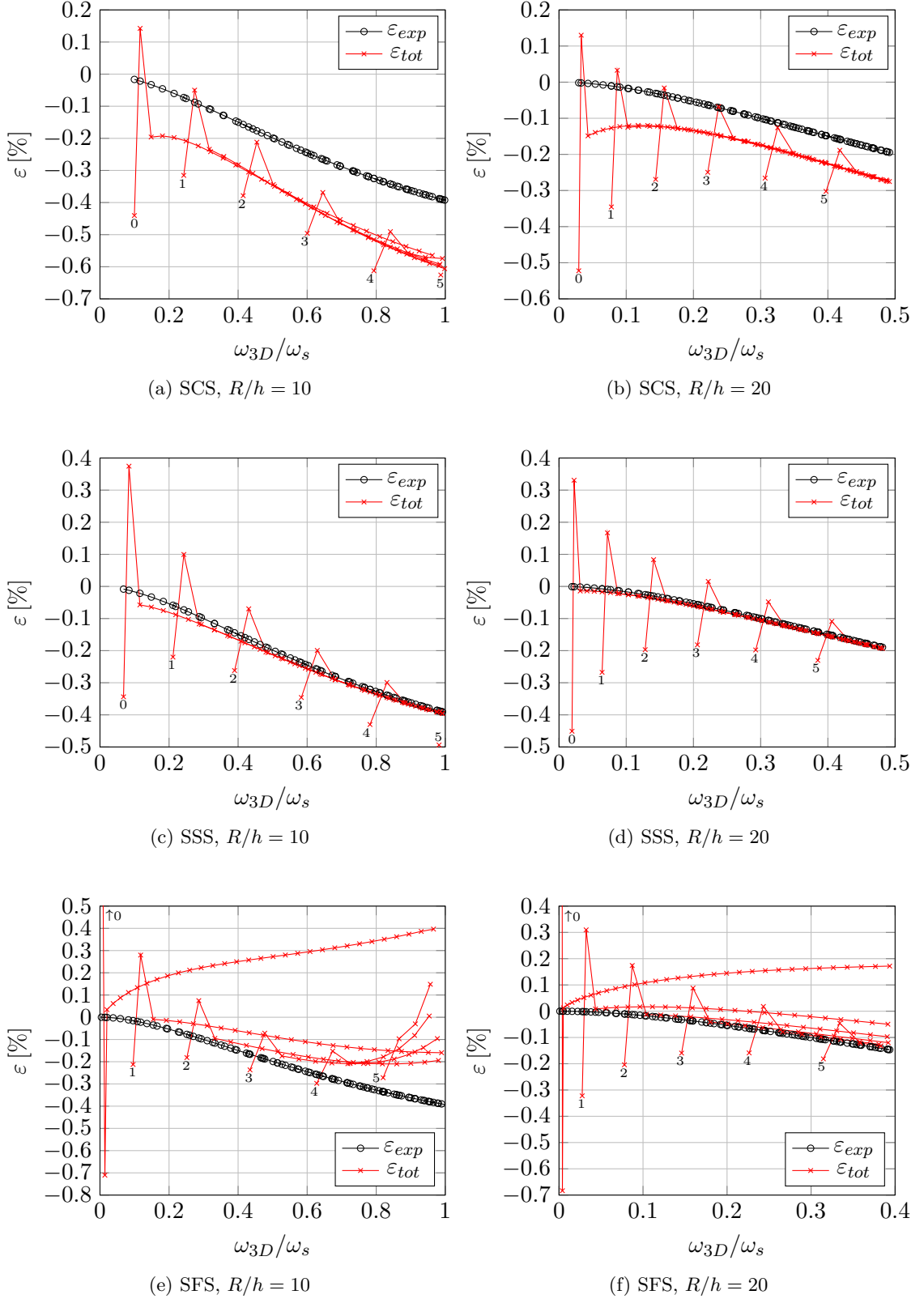


Figure 2.29: Expected and actual total error of a sectorial Mindlin plate ( $\alpha = 195^\circ$ )


 Figure 2.30: Expected and actual total error of a sectorial Mindlin plate ( $\alpha = 330^\circ$ )

### 2.3 Useful ranges of validity for the Kirchhoff and Mindlin plate theory

The additional error  $\varepsilon_{ad}$  of the Kirchhoff plate for the three different combinations of boundary conditions SCS, SSS and SFS are illustrated in Figures 2.31–2.42. The y-axis has a logarithmic scale and shows the ratio of the characteristic length to the plate thickness  $R^*/h$ . The 1%, 2% and 5% error limits defined from the infinite plate solution are plotted with vertical dashed lines. The first 100 asymmetric bending dominated flexural modes are shown, which are ordered from top to bottom.

The results of the sector plates with  $\alpha = 30^\circ$  in Figures 2.31–2.33 and with  $\alpha = 165^\circ$  in Figures 2.34–2.36 lead to similar findings as the results of the rectangular and circular plates, since no stress singularities are present for these plate configurations. The additional errors are low, since the two straight radial boundaries are simply-supported and only the circumferential boundary introduces additional errors.

The colorbars illustrating the additional error in Figures 2.37–2.42 ( $\alpha = \{195^\circ, 330^\circ\}$ ) are limited by 3%, since the additional errors for modes with stress singularities are rather high.

According to [75], the Kirchhoff plate theory only includes moment singularities at the corner  $r = 0$ . The occurring shear force singularities are not modelled by the Kirchhoff plate theory, since the influence of shear deformation is neglected.

Stress singularities only occur, if the mode shape has no radial nodal lines. For  $\alpha = 195^\circ$  eight such modes are present within the first 100 modes, while for  $\alpha = 330^\circ$  only six modes have stress singularities.

It is apparent from Figures 2.37–2.42 that the stress singularities lead to a larger additional error compared to the Mindlin plate theory, while the additional errors for modes without stress singularities are in the expected limits. The additional errors of the first eigenfrequency for very thin plates ( $R^*/h = 100$ ) are  $\varepsilon_{ad} \approx 3.5\%$  ( $\alpha = 195^\circ$ ) and  $\varepsilon_{ad} \approx 4\%$  ( $\alpha = 330^\circ$ ) in case of the SCS sector plate. While the additional error hardly depends on the ratio  $R^*/h$  for sector plates with a sector angle  $\alpha = 195^\circ$  ( $\varepsilon_{ad} \approx 4\%$  at  $R^*/h = 30$ ), a significant increase in the additional error is noted for a sector angle  $\alpha = 330^\circ$  ( $\varepsilon_{ad} \approx 10\%$  at  $R^*/h = 30$ ).

The higher additional error for  $\alpha = 330^\circ$  compared to  $\alpha = 195^\circ$  is expected, since the stress singularity increases with rising  $\alpha$ . The influence of the stress singularity on the additional error slightly decreases with a higher number of nodal lines in circumferential direction. The additional error of the highest mode with stress singularities for a ratio  $R^*/h = 100$  is given by  $\varepsilon_{ad} \approx 1\%$  ( $\alpha = 195^\circ$ ) and  $\varepsilon_{ad} \approx 3\%$  ( $\alpha = 330^\circ$ ) for the SCS plate.

If discontinuities at a plate boundary are present, e.g. corners in polygonal plates, and shear force singularities are expected, the Kirchhoff plate theory is in general not able to predict accurate results for all modes having shear force singularities, even for very thin plates and low frequencies.

Since an analytical solution for free vibrations of sectorial Kirchhoff plates is only available for simply-supported radial edges, the analytical static solution for all different combinations of boundary conditions derived in [87], can be used to estimate if a shear force singularity occurs.

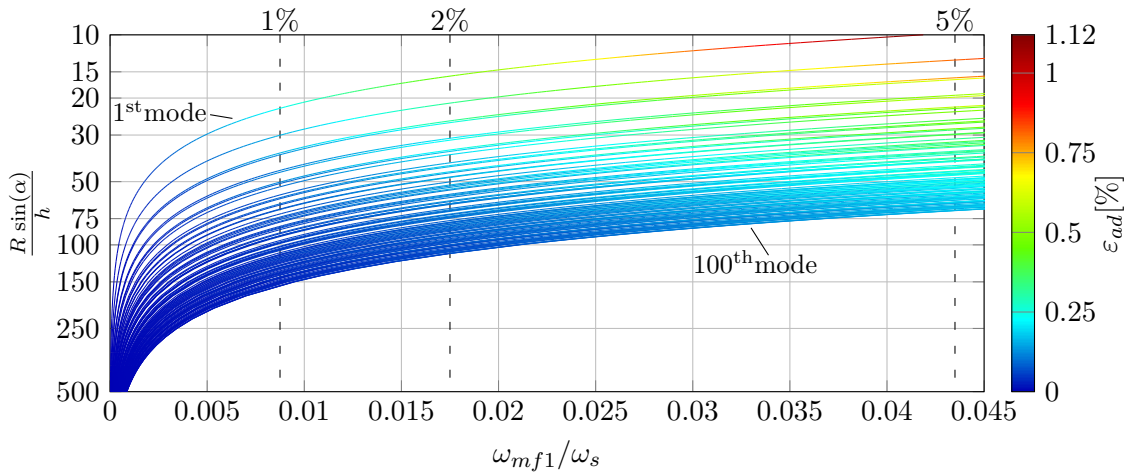


Figure 2.31: Additional error of a SCS sectorial Kirchhoff plate ( $\alpha = 30^\circ$ )

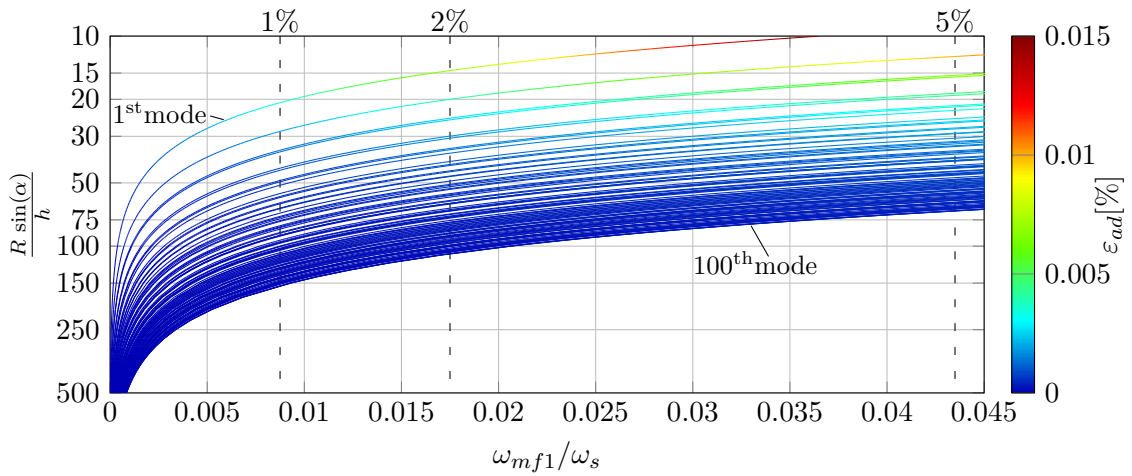


Figure 2.32: Additional error of a SSS sectorial Kirchhoff plate ( $\alpha = 30^\circ$ )

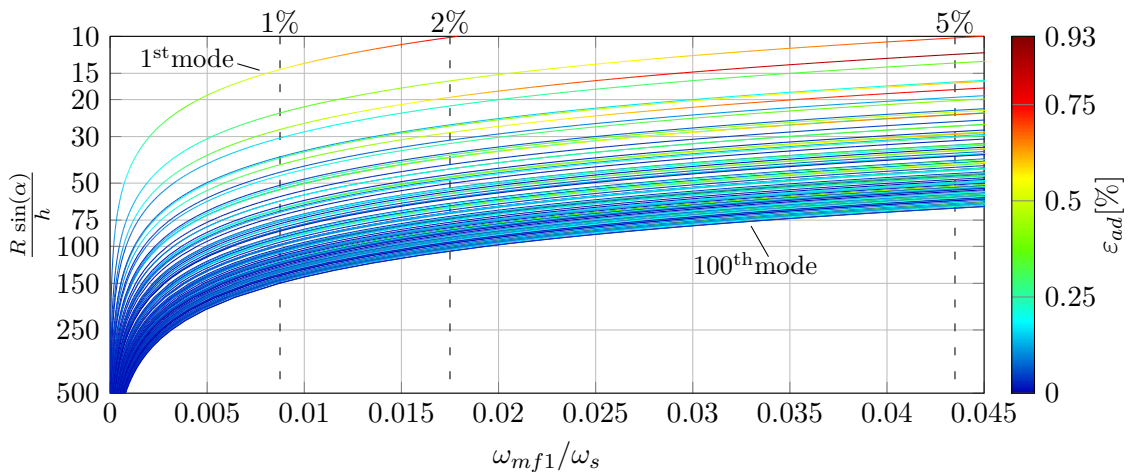


Figure 2.33: Additional error of a SFS sectorial Kirchhoff plate ( $\alpha = 30^\circ$ )

### 2.3 Useful ranges of validity for the Kirchhoff and Mindlin plate theory

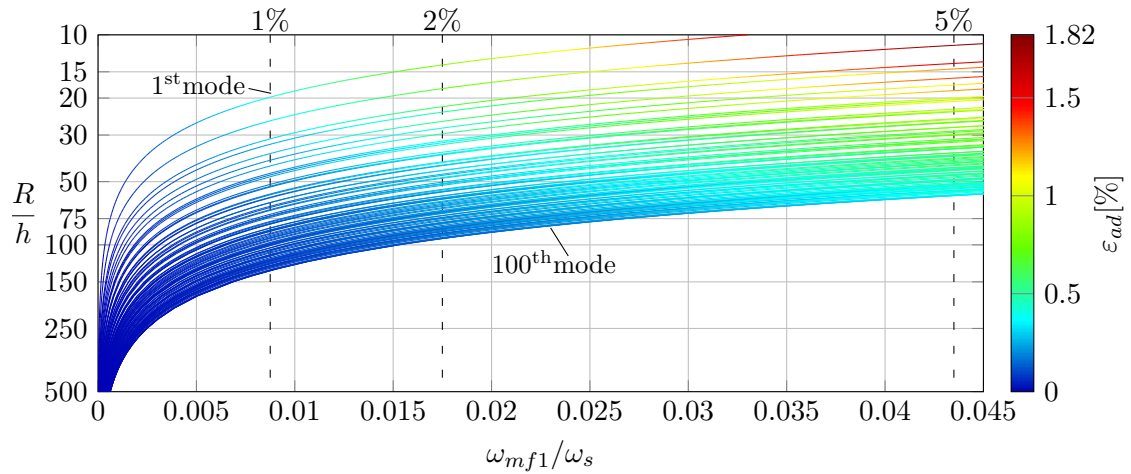


Figure 2.34: Additional error of a SCS sectorial Kirchhoff plate ( $\alpha = 165^\circ$ )

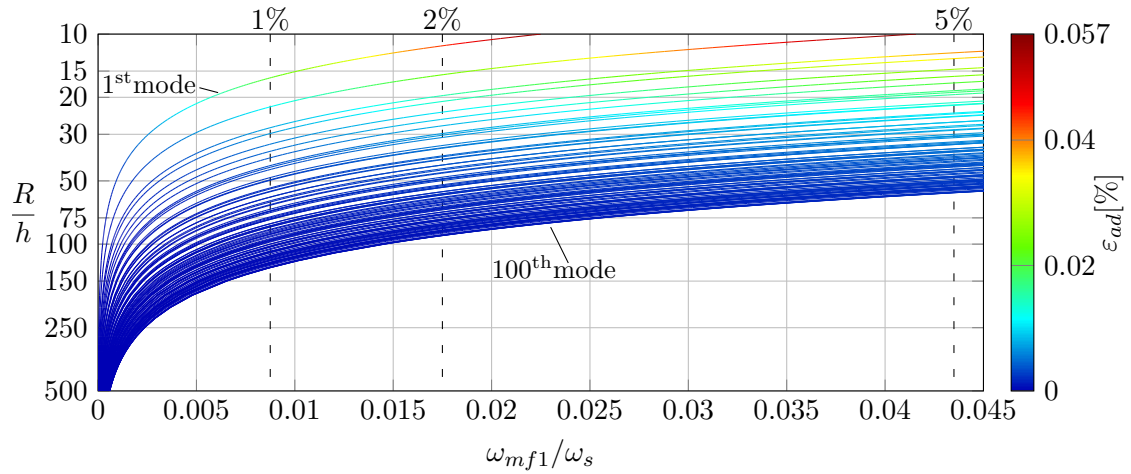


Figure 2.35: Additional error of a SSS sectorial Kirchhoff plate ( $\alpha = 165^\circ$ )

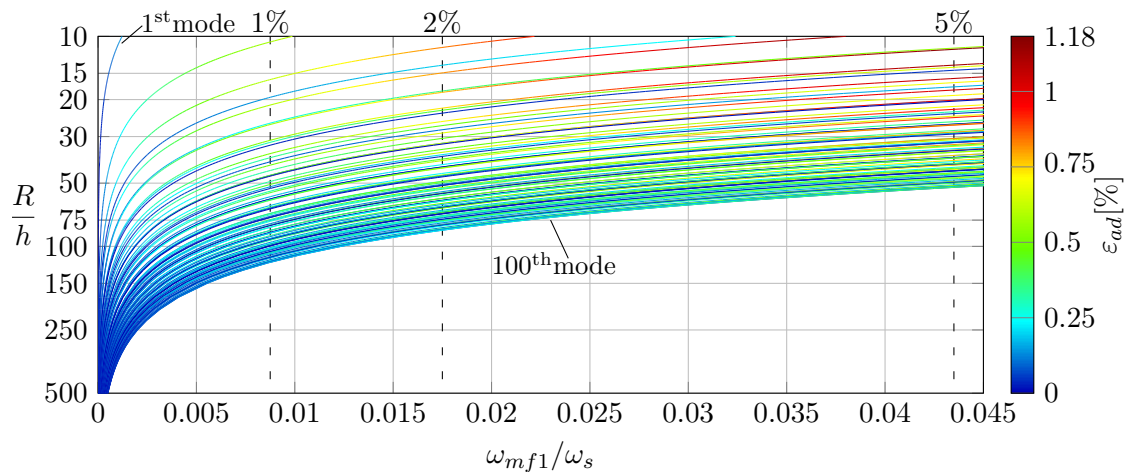


Figure 2.36: Additional error of a SFS sectorial Kirchhoff plate ( $\alpha = 165^\circ$ )

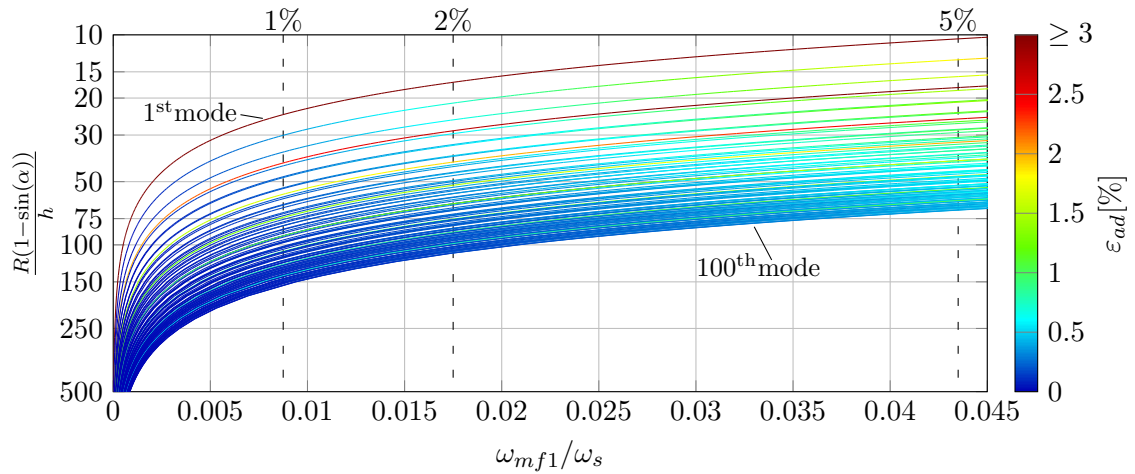


Figure 2.37: Additional error of a SCS sectorial Kirchhoff plate ( $\alpha = 195^\circ$ )

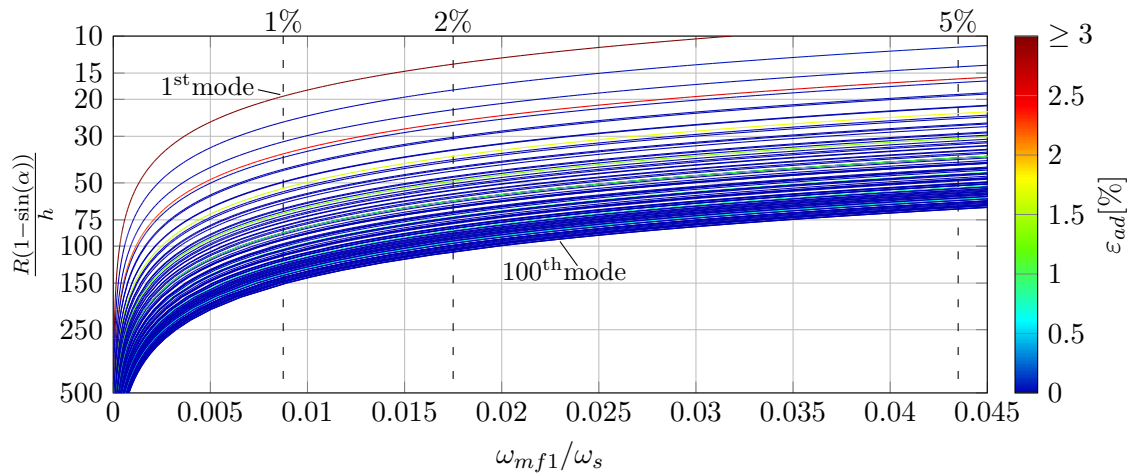


Figure 2.38: Additional error of a SSS sectorial Kirchhoff plate ( $\alpha = 195^\circ$ )

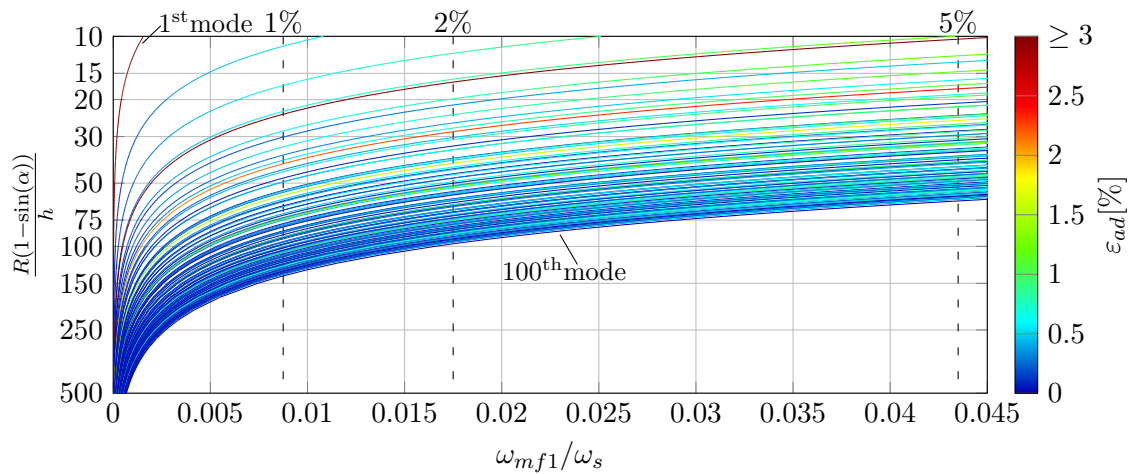


Figure 2.39: Additional error of a SFS sectorial Kirchhoff plate ( $\alpha = 195^\circ$ )

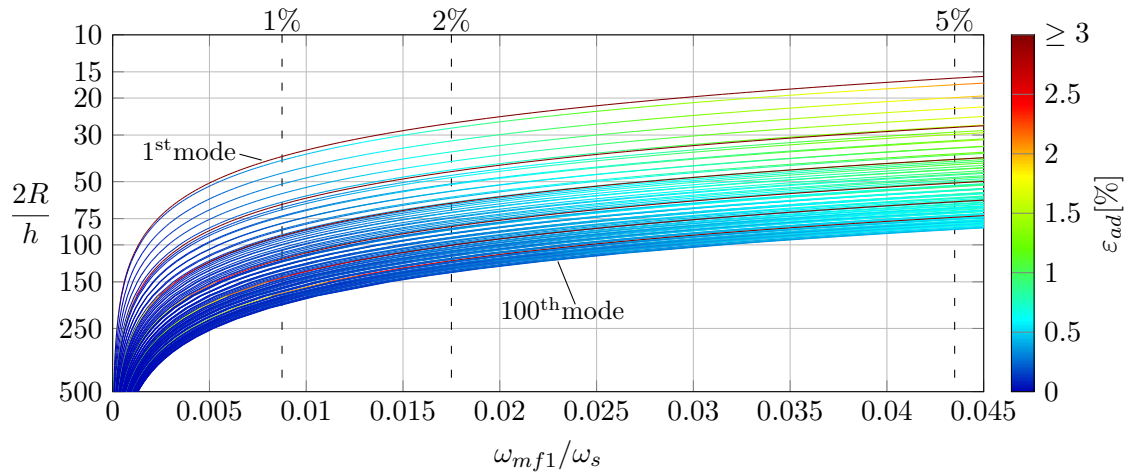


Figure 2.40: Additional error of a SCS sectorial Kirchhoff plate ( $\alpha = 330^\circ$ )

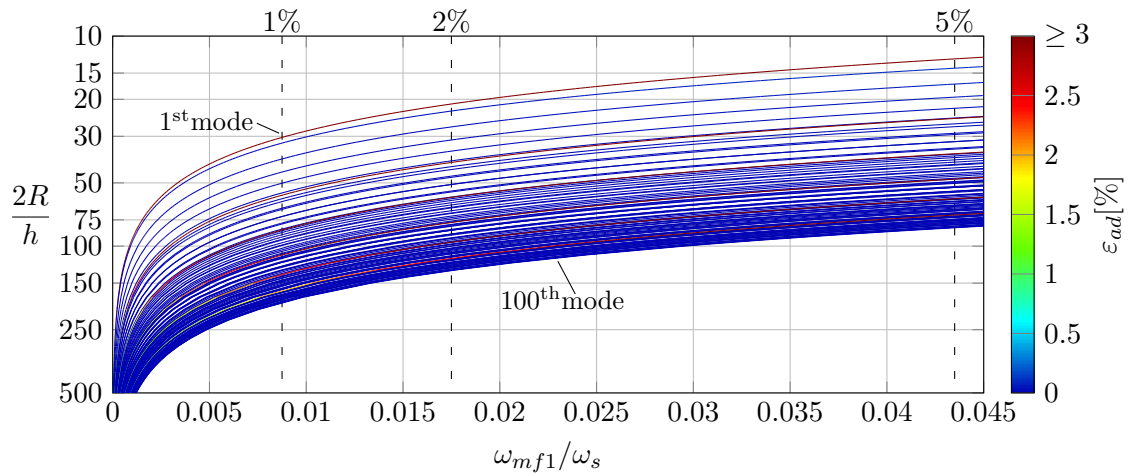


Figure 2.41: Additional error of a SSS sectorial Kirchhoff plate ( $\alpha = 330^\circ$ )

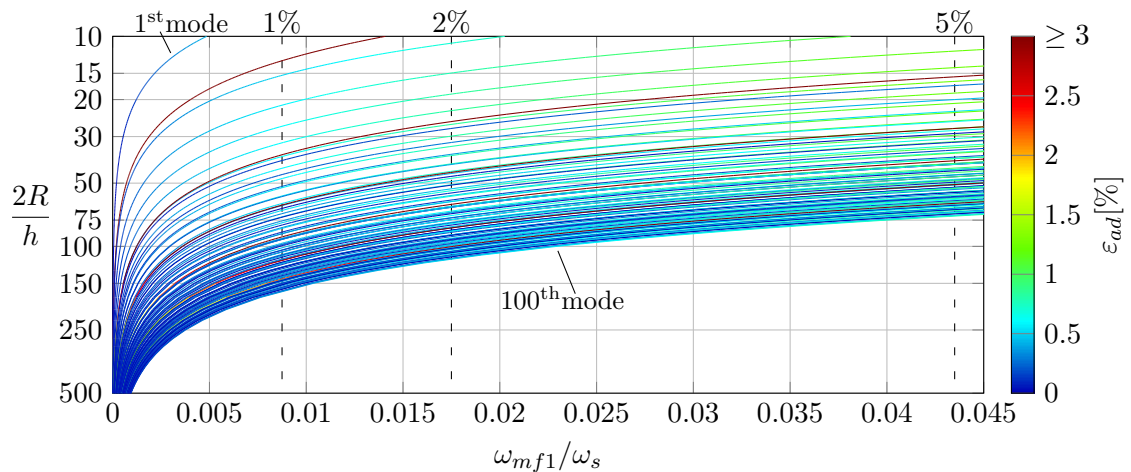


Figure 2.42: Additional error of a SFS sectorial Kirchhoff plate ( $\alpha = 330^\circ$ )

### 2.3.3 Further error sources and final remarks on the plate model validity

In the previous two sections the validity of the Kirchhoff and Mindlin plate theory has been examined by comparing the free vibration solutions for an infinite plate and certain types of bounded plates to the solutions derived by the elasticity theory. For plates without complicated effects, the following limits for the Kirchhoff plate theory are proposed:

- The Kirchhoff plate theory is able to predict the angular eigenfrequencies very accurately ( $\approx 1\%$  error) if the angular frequency ratio  $\omega_k/\omega_s < 0.009$  ( $\lambda/h > 25$ ) and the ratio of the smallest characteristic lateral dimension to the plate thickness is greater than 30.
- The results of the Kirchhoff plate theory are still acceptable ( $\approx 5\%$  error) if  $\omega_k/\omega_s < 0.04$  ( $\lambda/h > 12.5$ ) and the ratio of the smallest characteristic lateral dimension to the plate thickness is greater than 20.

The limit for the ratio of the smallest characteristic lateral dimension to the plate thickness agrees very well with the stated limits in the literature, while the frequency limits in the literature allow for a rather high error of approximately 10%.

The Mindlin plate theory predicts the eigenfrequencies highly accurately for the complete viewed frequency range  $\omega_{mf1}/\omega_s < 1$  ( $\lambda/h > 1.5$ ) if the ratio of the smallest characteristic lateral dimension to the plate thickness is greater than ten. Due to the given results, it is recommended to use the shear correction factor  $k_W$  introduced by Wittrick, if the vibrations of moderately thick plates are analyzed. The accuracy of the Mindlin plate theory for even thicker plates and higher frequencies is not examined in this work. A general limit for the Mindlin plate theory is given by  $\omega_{mf1}/\omega_s = 1.2$ , since, according to [50], the next higher thickness-modes appear, which cannot be approximated by the Mindlin plate theory.

If shear force singularities are present in the plate domain, it is recommended to use the Mindlin rather than the Kirchhoff plate theory, since the singularity strongly affects the global response. The Mindlin plate theory is able to model the shear force singularity, while the Kirchhoff plate theory fails to do so.

For the definition of the validity ranges of the plates theory, only their ability to accurately predict the eigenfrequency is taken into account. Especially the deviations of the corresponding mode shapes to the mode shapes predicted by the elasticity theory will affect the general accuracy of the plate theories. The investigation of this aspect is not in the scope of this work.

The stated limits are only applicable for isotropic plates. Especially highly orthotropic and composite plates require an accurate representation of the shear deformation. Therefore, the Kirchhoff plate theory leads to inaccurate results even for thin plates [88] and appropriate shear correction factors are needed for the Mindlin plate theory [89].

# 3 Numerical techniques for the calculation of steady-state plate vibrations

An analytical solution for the mathematical models described in Section 2.1 and Section 2.2 is only feasible for a very limited number of problems with simple geometries and specific boundary conditions and source terms. Therefore, approximate numerical methods have been developed to solve the partial differential equation(s) with arbitrary boundary conditions and loadings in general problem domains. There are several possibilities to classify the variety of numerical methods [20]. In the following, the numerical methods applied to solve steady-state structural vibration problems are categorized into three groups: element based techniques, statistical methods and Trefftz based approaches.

## 3.1 Element based techniques

In element based techniques, either the whole problem domain (domain methods) or the boundary of the problem domain (boundary methods) is divided into a large number of small elements [90]. Locally defined simple shape functions are used to approximate the field variable(s), e.g. the displacements and rotations. The most popular domain method is the (conventional) Finite Element Method (FEM) [91, 92], while the Boundary Element Method (BEM) [93, 94] is a typical boundary method. In the following sections, the (conventional) FEM for steady-state plate vibrations is reviewed and several extensions and improvements of the FEM are discussed. The BEM is most effective for problem domains with a small boundary to volume ratio and especially for unbounded domains [20] and since only bounded problems are investigated in this work, a review of the BEM is not included.

### 3.1.1 Conventional Finite Element Method

The conventional FEM is at present very widely used in practice to solve engineering problems, especially because the method has been developed extensively over the last 75 years and is able to tackle real-life applications [92]. Furthermore, many commercial software packages are available, which simplifies the use of FEM in engineering and science. It needs to be noted that the term "conventional" refers to the classical FEM, which uses simple polynomial shape functions and an unaltered weak form of the mathematical problem. For steady-state vibration problems, the conventional FEM is practically limited to low frequencies, since the computational time strongly increases with higher frequencies [95]. This limit is further discussed in a subsequent section and extensions and improvements of the FEM to overcome this limit are reviewed in Section 3.1.2.

The procedure to solve a steady-state plate vibration problem with FEM consists in general of five steps [20, 96]:

- The problem domain is discretized into a large number of non-overlapping elements.
- Within each element, the field variables, e.g. the displacements and rotations, are approximated by simple polynomial shape functions. The contribution factors (nodal values) of the polynomial shape functions are the unknowns in the FE model.
- The polynomial shape functions violate the governing equations and certain types of boundary conditions. Minimizing the resulting residuals in an integral sense leads to the FE system matrices. The minimization can be achieved either by a variational principle, a weighted residual approach or a least-square approach.
- The unknown nodal values are obtained by solving a sparse system of linear equations.
- Through a post-processing step, the primary field variables (displacements and rotations) and derived quantities, e.g. stresses, can be calculated for the whole domain.

In the next section, the general modeling steps for steady-state plate vibrations are described for the Kirchhoff and Mindlin plate theory.

### FEM model for steady-state structural plate vibrations

The first modelling step is the discretization of the problem domain  $\Omega$  into  $n_e$  non-overlapping elements ( $\Omega = \cup_{e=1}^{n_e} \Omega^{(e)}$  with  $\Omega^{(i)} \cap \Omega^{(j)} = 0, \forall i \neq j$ ), which are all interconnected by  $n_{fe}$  nodes. The number of nodes per element  $n_a^{(e)}$  generally depends on the dimension of the problem, the order of the used polynomial functions within the element and the applied element type, e.g. triangular or quadrilateral elements. A coarse discretization of a two-dimensional domain, the so-called FE mesh, with ten quadrilateral elements using second order polynomial functions (eight nodes per element) is shown in Figure 3.1. A total number of  $n_{fe} = 45$  nodes connect the  $n_e = 10$  elements. The node numbers associated

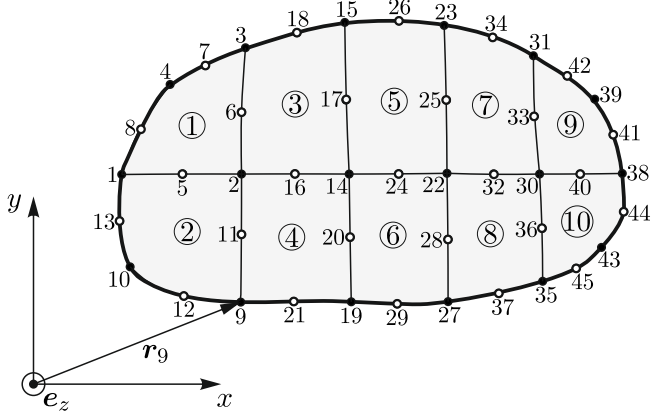


Figure 3.1: FE mesh of a 2D domain with ten quadrilateral elements and 45 nodes

with one element are collected in the set  $S_N^{(e)}$ , e.g.  $S_N^{(5)} = \{14, 15, 17, 22, 23, 24, 25, 26\}$ . Since second order polynomial functions are applied within the elements, also curved boundaries can be approximated rather accurately. It is apparent from Figure 3.1 that a certain node at position  $\mathbf{r} = \mathbf{r}_{fe}$  can be associated with several different elements, e.g. node 9 is related to the elements 2 and 4.

In the following, the sparse system of linear equations, resulting from the FEM approximation, is derived for the Mindlin and Kirchhoff plate theory. Since the bending behaviour of plates is of major interest in this work, the FEM models stated below do not include the membrane behaviour of the plates.

### a.) Mindlin plate FEM model

The primary field variables of the Mindlin plate theory are the out-of-plane displacement  $w(\mathbf{r})$  and the rotations  $\psi_x(\mathbf{r})$  and  $\psi_y(\mathbf{r})$ , which are collected in the vector  $\boldsymbol{\psi}(\mathbf{r}) = [\psi_x, \psi_y]^T$ . Within each element, the primary field variables are approximated by a sum of  $n_a^{(e)}$  polynomial shape functions

$$\begin{aligned} w^{(e)}(\mathbf{r}) &\approx \sum_a N_{wa}^{(e)}(\mathbf{r}) \hat{w}_a^{(e)} = \mathbf{N}_w^{(e)}(\mathbf{r}) \hat{\mathbf{w}}^{(e)}, & a \in S_N^{(e)}, \quad \mathbf{r} \in \Omega^{(e)}, \\ \boldsymbol{\psi}^{(e)}(\mathbf{r}) &\approx \sum_a \begin{bmatrix} N_{\psi_x a}^{(e)}(\mathbf{r}) \hat{\psi}_{xa}^{(e)} \\ N_{\psi_y a}^{(e)}(\mathbf{r}) \hat{\psi}_{ya}^{(e)} \end{bmatrix} = \begin{bmatrix} \mathbf{N}_{\psi_x}^{(e)}(\mathbf{r}) & 0 \\ 0 & \mathbf{N}_{\psi_y}^{(e)}(\mathbf{r}) \end{bmatrix} \begin{bmatrix} \hat{\psi}_x^{(e)} \\ \hat{\psi}_y^{(e)} \end{bmatrix} = \mathbf{N}_{\psi}^{(e)}(\mathbf{r}) \hat{\boldsymbol{\psi}}^{(e)}, \end{aligned} \quad (3.1)$$

where  $N_{wa}^{(e)}$ ,  $N_{\psi_x a}^{(e)}$  and  $N_{\psi_y a}^{(e)}$  are the polynomial shape functions for the displacements and rotations, which are gathered in the row vectors  $\mathbf{N}_w^{(e)}$ ,  $\mathbf{N}_{\psi_x}^{(e)}$  and  $\mathbf{N}_{\psi_y}^{(e)}$ . The contribution factors of the shape functions  $\hat{w}_a^{(e)}$ ,  $\hat{\psi}_{xa}^{(e)}$  and  $\hat{\psi}_{ya}^{(e)}$  are collected in the column vectors  $\hat{\mathbf{w}}^{(e)}$ ,  $\hat{\boldsymbol{\psi}}_x^{(e)}$  and  $\hat{\boldsymbol{\psi}}_y^{(e)}$ .

Since the polynomial shape functions are defined within one element, their values are zero in all other elements. Furthermore, each shape function  $N_{wa}^{(e)}$ ,  $N_{\psi_x a}^{(e)}$  and  $N_{\psi_y a}^{(e)}$  has a value of 1 at the node position  $\mathbf{r} = \mathbf{r}_a$  and a zero value for all other node positions  $\mathbf{r} = \mathbf{r}_{fe}$  ( $fe \neq a$ ). Through these properties of the shape functions, the nodal values are equivalent to the contribution factors and are equal to the value of the field variables at  $\mathbf{r} = \mathbf{r}_a$  in the final solution.

The approximate solutions do not fulfill the governing equations and certain boundary conditions exactly and therefore, a variational principle, a weighted residual approach or a least-square approach is used to minimize the residuals in an integral sense. In the conventional FEM, a weighted residual approach is applied and the weighting functions are expanded in the same locally defined functions as the primary field variables (Galerkin approach). For many problems, the weighted residual approach becomes equivalent to the variational principle, e.g. for structural plate vibrations [91].

In the conventional FEM, the strain and stress fields are derived quantities, which are calculated from the displacement and rotation fields using the Equations (2.24) – (2.29) and Equations (2.34) – (2.38). Therefore, the variational form of the Mindlin plate theory, shown in Equation (2.85), is simplified, since only a variation with respect to the primary field variables is required.

### 3 Numerical techniques for the calculation of steady-state plate vibrations

Assuming harmonic vibrations at angular frequency  $\omega$  and applying integration by parts reduce the general three-field variational form of the Mindlin plate theory in Equation (2.85) to a weak form [91]

$$\begin{aligned} & \iint_{\Omega} \left( (\mathbf{S} \delta \psi)^T \mathbf{D} \mathbf{S} \psi + \delta \psi^T \alpha \psi + \delta \psi^T \alpha \nabla w + (\delta \nabla w)^T \alpha \psi + (\nabla \delta w)^T \alpha \nabla w \right) dx dy \\ & - \iint_{\Omega} \left( \delta \psi^T \frac{\omega^2 \rho h^3}{12} \psi + \delta w \omega^2 \rho h w \right) dx dy - \iint_{\Omega} \left( \delta \psi^T \bar{\mathbf{m}} + \delta w \bar{q} \right) dx dy \\ & - \int_{\Gamma_{\sigma}} \left( \delta \psi^T \mathbf{n} \bar{M}_n + \delta \psi^T \mathbf{s} \bar{M}_s + \delta w \bar{Q}_n \right) ds - \int_{\Gamma_{u\sigma 2}} \delta \psi^T \mathbf{n} \bar{M}_n ds = 0, \end{aligned} \quad (3.2)$$

with  $\alpha = k^2 G h$ ,  $\nabla$  the del operator,  $\bar{\mathbf{m}} = [\bar{m}_x, \bar{m}_y]^T$ ,  $\mathbf{n}$  and  $\mathbf{s}$  the normal and tangential unit vector at the boundary and

$$\mathbf{S} = \begin{bmatrix} \frac{\partial}{\partial x} & 0 \\ 0 & \frac{\partial}{\partial y} \\ \frac{\partial}{\partial y} & \frac{\partial}{\partial x} \end{bmatrix}, \quad \mathbf{D} = D \begin{bmatrix} 1 & \nu & 0 \\ \nu & 1 & 0 \\ 0 & 0 & \frac{1-\nu}{2} \end{bmatrix}. \quad (3.3)$$

Using the approximation functions for the field variables from Equation (3.1) in Equation (3.2) and expanding the variations  $\delta \bullet$  with the same functions (Galerkin approach) finally leads to a system of linear equations

$$\left( -\omega^2 \begin{bmatrix} \mathbf{M}_{ww} & 0 \\ 0 & \mathbf{M}_{\psi\psi} \end{bmatrix} + \begin{bmatrix} \mathbf{K}_{ww} & \mathbf{K}_{w\psi} \\ \mathbf{K}_{\psi w} & \mathbf{K}_{\psi\psi} \end{bmatrix} \right) \begin{bmatrix} \hat{\mathbf{w}} \\ \hat{\psi} \end{bmatrix} = \begin{bmatrix} \mathbf{f}_w \\ \mathbf{f}_{\psi} \end{bmatrix}, \quad (3.4)$$

which has to be solved for the unknown nodal values  $\hat{\mathbf{w}} = [\hat{w}_1, \hat{w}_2, \dots, \hat{w}_{fe}]^T$  and  $\hat{\psi} = [\hat{\psi}_{x1}, \hat{\psi}_{x2}, \dots, \hat{\psi}_{xfe}, \hat{\psi}_{y1}, \hat{\psi}_{y2}, \dots, \hat{\psi}_{yfe}]^T$ .

The global mass matrices  $\mathbf{M}_{ww}$  and  $\mathbf{M}_{\psi\psi}$  and the global stiffness matrices  $\mathbf{K}_{ww}$ ,  $\mathbf{K}_{w\psi} = \mathbf{K}_{\psi w}^T$  and  $\mathbf{K}_{\psi\psi}$  are calculated through an assembly process of the element matrices, which are defined by

$$\begin{aligned} \mathbf{M}_{ww}^{(e)} &= \iint_{\Omega} \mathbf{N}_w^{(e)T} \rho h \mathbf{N}_w^{(e)} dx dy, & \mathbf{M}_{\psi\psi}^{(e)} &= \iint_{\Omega} \mathbf{N}_{\psi}^{(e)T} \frac{\rho h^3}{12} \mathbf{N}_{\psi}^{(e)} dx dy, \\ \mathbf{K}_{ww}^{(e)} &= \iint_{\Omega} (\nabla \mathbf{N}_w^{(e)})^T \alpha \nabla \mathbf{N}_w^{(e)} dx dy, & \mathbf{K}_{w\psi}^{(e)} &= \iint_{\Omega} (\nabla \mathbf{N}_w^{(e)})^T \alpha \mathbf{N}_{\psi}^{(e)} dx dy, \\ \mathbf{K}_{\psi\psi}^{(e)} &= \iint_{\Omega} (\mathbf{S} \mathbf{N}_{\psi}^{(e)})^T \mathbf{D} \mathbf{S} \mathbf{N}_{\psi}^{(e)} dx dy + \iint_{\Omega} \mathbf{N}_{\psi}^{(e)T} \alpha \mathbf{N}_{\psi}^{(e)} dx dy. \end{aligned} \quad (3.5)$$

The forces acting on an element are given by

$$\begin{aligned} \mathbf{f}_w^{(e)} &= \iint_{\Omega} \mathbf{N}_w^{(e)T} \bar{q} dx dy + \int_{\Gamma_{\sigma}} \mathbf{N}_w^{(e)T} \bar{Q}_n ds, \\ \mathbf{f}_{\psi}^{(e)} &= \iint_{\Omega} \mathbf{N}_{\psi}^{(e)T} \bar{\mathbf{m}} dx dy + \int_{\Gamma_{\sigma}} \mathbf{N}_{\psi}^{(e)T} (\mathbf{n} \bar{M}_n + \mathbf{s} \bar{M}_s) ds + \int_{\Gamma_{u\sigma 2}} \mathbf{N}_{\psi}^{(e)T} \mathbf{n} \bar{M}_n ds, \end{aligned} \quad (3.6)$$

### 3.1 Element based techniques

which are assembled to the global forces  $\mathbf{f}_w$  and  $\mathbf{f}_\psi$ . Boundary conditions with prescribed primary variables  $\bar{w}$ ,  $\bar{\psi}_n$  and  $\bar{\psi}_s$  are applied through row and column elimination.

For a detailed description of the assembly process, the evaluation of the integrals and the inclusion of the boundary conditions, the reader is referred to [91] and [92].

#### b.) Kirchhoff plate FEM model

The Kirchhoff plate theory only has the out-of-plane displacement  $w(\mathbf{r})$  as primary field variable, which is approximated by a sum of  $n_a^{(e)}$  polynomial shape functions within the element

$$w^{(e)}(\mathbf{r}) \approx \sum_a N_{wa}^{(e)}(\mathbf{r}) \hat{w}_a^{(e)} = \mathbf{N}_w^{(e)}(\mathbf{r}) \hat{\mathbf{w}}^{(e)}, \quad a \in S_N^{(e)}, \quad \mathbf{r} \in \Omega^{(e)}. \quad (3.7)$$

While the polynomial shape functions used for the Mindlin plate theory only have to be  $C_0$  continuous, the Kirchhoff plate theory requires  $C_1$  continuous shape functions, which leads to difficulties in the implementation [91]. The other properties of the shape functions are similar between both theories.

The general three-field variational form in Equation (2.105) is used to derive a weak integral form of the Kirchhoff plate theory. If only the variation with respect to  $w$  is considered and harmonic vibration at frequency  $\omega$  is assumed, Equation (2.105) simplifies to

$$\begin{aligned} & \iint_{\Omega} (\mathcal{L} \delta w)^T \mathbf{D} \mathcal{L} w \, dx \, dy - \iint_{\Omega} \delta w \omega^2 \rho h w \, dx \, dy - \iint_{\Omega} \delta w \bar{q} \, dx \, dy \\ & - \int_{\Gamma_\sigma} \left[ \delta w \bar{V}_n - \frac{\partial \delta w}{\partial n} \bar{M}_n \right] ds + \int_{\Gamma_{u\sigma}} \frac{\partial \delta w}{\partial n} \bar{M}_n \, ds = 0, \end{aligned} \quad (3.8)$$

where

$$\mathcal{L} = \left[ \frac{\partial^2}{\partial x^2}, \frac{\partial^2}{\partial y^2}, 2 \frac{\partial^2}{\partial x \partial y} \right]^T \quad (3.9)$$

and integration by parts is applied. Inserting the approximation functions from Equation (3.7) into Equation (3.8) leads to a system of linear equations

$$(-\omega^2 \mathbf{M} + \mathbf{K}) \hat{\mathbf{w}} = \mathbf{f}_w, \quad (3.10)$$

where  $\mathbf{M}$  is the global mass matrix,  $\mathbf{K}$  the global stiffness matrix,  $\mathbf{f}_w$  the global force vector and  $\hat{\mathbf{w}} = [\hat{w}_1, \hat{w}_2, \dots, \hat{w}_{fe}]$  the unknown nodal values. The global matrices and force vector are defined through an assembly of the element matrices and force vectors, which are given by

$$\begin{aligned} \mathbf{M}^{(e)} &= \iint_{\Omega} \mathbf{N}_w^{(e)T} \rho h \mathbf{N}_w^{(e)} \, dx \, dy, \\ \mathbf{K}^{(e)} &= \iint_{\Omega} (\mathcal{L} \mathbf{N}_w^{(e)})^T \mathbf{D} \mathcal{L} \mathbf{N}_w^{(e)} \, dx \, dy, \\ \mathbf{f}_w^{(e)} &= \iint_{\Omega} \mathbf{N}_w^{(e)T} \bar{q} \, dx \, dy + \int_{\Gamma_\sigma} \left( \mathbf{N}_w^{(e)T} \bar{V}_n - \frac{\partial \mathbf{N}_w^{(e)T}}{\partial n} \bar{M}_n \right) ds - \int_{\Gamma_{u\sigma}} \frac{\partial \mathbf{N}_w^{(e)T}}{\partial n} \bar{M}_n \, ds. \end{aligned} \quad (3.11)$$

### Mesh requirements for accurate FEM results

The structural models described in the Sections 2.1 and 2.2 can all be decomposed into a set of Helmholtz equations if harmonic vibrations are assumed. The vibrations of the linear elastic solid are governed by four (Equations (2.12) and (2.13)), the plate membrane vibrations by two (Equations (2.58) and (2.59)), the Mindlin plate bending vibrations by three (Equations (2.63)–(2.65)) and the Kirchhoff plate bending vibrations by two Helmholtz equations (Equations (2.98) and (2.99)).

The accuracy of the FEM based on the Galerkin approach is influenced by the interpolation and pollution error if problems described by Helmholtz equations are solved [83, 84, 97, 98]. The interpolation error, also called the approximation error, occurs through the approximation of the dynamic field by simple polynomial shape functions and is dominant at lower frequencies. The pollution error (dispersion error) results from a difference in wavelengths between the physical problem at hand and the FE discretized problem and becomes important at rising frequencies [99].

The *a priori* error estimators developed in [83] and [84] can be used to asses the FE mesh requirements to bound the interpolation and pollution error. The rule to limit the interpolation error is given by [84, 99]

$$\left( \frac{k h_{fe}}{p} \right)^p < C, \quad (3.12)$$

where  $k = 2\pi/\lambda$  is the wavenumber of the viewed Helmholtz equation,  $h_{fe}$  the greatest element size in the FE model,  $p$  the order of the polynomial shape functions and  $C$  a constant. Setting the constant  $C = 1$  leads to the well known rule of thumb that a constant number of six to ten linear elements ( $p = 1$ ) or three to four quadric elements ( $p = 2$ ) per wavelength are required to get accurate results [100].

The relation to bound the pollution error is defined by [84, 96, 99]

$$k L \left( \frac{k h_{fe}}{p} \right)^{2p} < C, \quad (3.13)$$

where  $L$  is a characteristic length of the problem domain and  $C = 1$  is used in this work. It is apparent from Equation (3.13) that a constant number of elements per wavelength is not sufficient to limit the pollution error for rising frequencies ( $k L > 1$ ). A variable number of elements per wavelength is required to control the pollution error

$$\frac{\# \text{elements}}{\lambda} \rightarrow 2\pi \sqrt{2\pi \frac{L}{\lambda}}, \quad p = 1 \text{ (linear)}, \quad (3.14)$$

$$\frac{\# \text{elements}}{\lambda} \rightarrow \pi \sqrt[4]{2\pi \frac{L}{\lambda}}, \quad p = 2 \text{ (quadric)}, \quad (3.15)$$

which depends on the ratio of the characteristic length of the problem domain to the wavelength  $L/\lambda$ .

The *a priori* error estimators used to define the criteria in Equations (3.12) and (3.13) are proven in [83] and [84] only for dispersion-free problems, e.g steady-state acoustics [96]. It is assumed that the relations are also applicable for the dispersive Kirchhoff and Mindlin plate vibration problem, even though there is no formal prove in the literature [96, 101, 13].

### Properties of conventional FEM models

The conventional FEM uses locally defined simple shape functions to approximate the field variables. Applying this approach to the analysis of structural vibration problems leads to the following characteristic features of the FEM [17, 20]:

*a.) Geometric flexibility*

The discretization of the problem domain into a large number of small elements gives the FEM great flexibility to model complex geometries. The necessity of small elements to control the pollution error, as described in the previous section, inherently leads to almost no restrictions concerning the problem domain.

*b.) Properties of the system matrices*

Since the shape functions in the FEM are locally defined within one small element, the system matrices are large and sparsely populated with a banded structure. The system matrices are real-valued for real-valued material parameters and the symmetry of the matrices is guaranteed if a variational approach exists for the investigated problem [91].

*c.) Frequency independent model matrices*

In general, the mass and stiffness matrix are frequency independent, which allows for the reuse of the matrices for different frequencies. It is also possible to apply modal reduction schemes, which improves the computational efficiency. However, in certain cases the material properties of the view problem are frequency dependent and prohibit the reuse of the system matrices and the modal reduction techniques.

*d.) Model size*

The size of the system matrices depends on the total number of nodes  $n_{fe}$  and degrees of freedom per node. To fulfill the mesh requirements described in the previous section, the model size increases rapidly with rising frequencies.

*e.) Model generation process*

The model generation process includes the meshing of the problem domain and the creation of the system matrices. The matrices are generated by the integration of simple polynomial functions, which is not very demanding, since very efficient numerical integration schemes, e.g. Gauss-Legendre quadrature, can be applied. If the same FE mesh is used over a wide frequency range and the matrices are frequency independent, the model generation process hardly contributes to the total computational time. A refinement of the model can be achieved by a reduction of the element size (h-refinement) or an increase in the element order (p-refinement), which requires a (partial) recalculation of the system matrices.

*f.) Accuracy of derived quantities*

The primary field variables are approximated by polynomial shape functions of order  $p$ . Derived quantities, e.g. stresses, have a lower spatial resolution, since these quantities are only approximated by lower order polynomials.

### 3.1.2 Advances in the Finite Element Method

The conventional FEM is limited to the lower frequency range, since a rather fine discretization of the problem domain is required to control the pollution error, which leads to a rapid increase in the computational load for rising frequencies. Therefore, several attempts have been made to either optimize the modelling and solution process of the FEM to decrease the computation time or to modify the FE formalism to reduce the pollution error and hence the model size. An outline of these improvements to the FEM are given in the following sections. The reader is referred to [99] and [96] for a more profound overview.

#### Improvements in the FE modelling and solution process

A commonly used approach to optimize the FE modelling process is an adaptive refinement of the FE mesh. The quality of the mesh is increased in regions with the highest approximation errors. An *a posterior* error estimator is mandatory to identify these regions. Following the rules for adequate meshes in Equations (3.12) and (3.13), either the element size is reduced (h-refinement) [83] or the order of the elements is increased (p-refinement) [102, 103] or both methods are combined (hp-refinement) [104, 84, 105].

In the conventional FEM, the system of linear equations is solved by direct solution methods, e.g. Gaussian elimination or factorization, which require a huge amount of memory and computation time for large systems. The application of iterative solvers in general accelerates the solution process but their stability depends on the conditioning of the linear system [99].

The response of a system over a broad frequency range (frequency response function) is of great interest, but computationally demanding if a fine frequency discretization is required. Instead of solving the large linear system of equations for every frequency step, so-called Fast Frequency Sweep (FFS) methods can be applied. In FFS the solution of the large linear system is only calculated in certain expansion points and the derivatives of the solution are used to predict the response of the system in the neighborhood of the expansion points [106, 107]. A considerable reduction of computation time can be expected if the frequency response function is sufficiently smooth.

Another possibility to reduce the computational load is the subdivision of a large problem into a number of smaller problems, which can be solved independently. Then a distribution of the problem over a large number of parallel computers is possible, which leads to an efficient solution process. Methods using this approach are commonly referred to as Domain Decomposition Methods (DDM), which are described in e.g. [108, 109, 110].

#### Modifications in the FE formalism

Compared to the previous enhancements of the FEM, which try to optimize the modelling and solution process and therefore allow for the use of more accurate meshes, other approaches attempt to reduce the pollution error through a modification of the underlying system of equations. These techniques either try to stabilize the FEM by adding terms

to the weak integral formulation used by the FEM (Stabilized FEM), to generalize the FEM by introducing a *priori* information of the solution in the approximation functions (Generalized FEM) or to interfere in the numerical integration scheme applied in the FEM.

The Galerkin Least-Squares FEM (GLS-FEM), presented in [111] for 1D and in [112] for 2D Helmholtz equations, adds a least-square operator based on a dispersion analysis to the standard FEM weak formulation to reduce the pollution error. While in the 1D case the pollution error can be eliminated completely, only an improvement over the classical FEM is achieved in the 2D case, since the dispersion is direction dependent. The reduction of the pollution error through the GLS-FEM is less pronounced for elastic wave propagation [113]. A similar approach is the Galerkin Gradient Least-Squares FEM (G $\nabla$ LS-FEM), which includes a least-square term containing residuals of the gradient of the governing differential equation to the weak formulation of the FEM [114, 115]. The method reduces the pollution error also for elastic waves and is therefore superior for the analysis of plate vibrations compared to the classical and GLS-FEM [113]. The combination of both methods is called Galerkin Generalized Least Squares FEM (GGLS-FEM) [116].

The Partition of Unity Finite Element Method (PUFEM) uses a multiplication of the classical polynomial basis functions with functions containing a *priori* information of the local behaviour of the solution to improve the classical FEM [117]. The PUFEM applies generalized harmonic polynomials or a system of plane waves to avoid the pollution error in the numerical simulation of plate vibrations [118]. The Discontinues Enrichment Method (DEM) adds free-space solutions of the homogenous differential equations to the classical polynomial shape functions, to incorporate a *priori* knowledge of the solution. A Lagrange multiplier technique is used to enforce the continuity at the element interfaces [119]. The DEM is applied in [120] to investigate the vibrations of Kirchhoff plates in the medium-frequency range and the advantages of the DEM compared to the classical FEM are shown.

Instead of using the classical Gauss-Legendre or Gauss-Lobatto rule to integrate the polynomial shape functions, a generalized integration rule is proposed in [121] to reduce the dispersion error in the FEM solution of the Helmholtz equation. Through a dispersion analysis, the optimal location of the integration points is defined, which increases the obtained accuracy from second-order (classical FEM) to fourth-order. In [122] the modified integration rule is extended to 1D, 2D and 3D linear elastodynamic problems.

## 3.2 Statistical methods

In contrast to the element based techniques, statistical methods do not calculate the distribution of the field variables in the problem domain, but determine space and frequency averaged energy quantities for a statistical ensemble [13]. The most popular method and basis for several other approaches is the Statistical Energy Analysis (SEA) [123, 124]. An overview of the SEA is given in Section 3.2.1. Since the conventional SEA is in general limited to high frequency vibrations [125], several improvements have been made to extend its applicability to lower frequencies, which are outlined in Section 3.2.2.

### 3.2.1 Statistical Energy Analysis

In the SEA, the considered system is divided into a (small) number of subsystems, which are groups of similar modes within a physical component of a system. Modes are considered to be similar if they all have a resonance frequency in a given frequency band and similar mode shapes, which results in similar values of the damping, excitation and coupling parameters. These subsystems act as energy storage elements, which can dissipate energy through system damping, transfer energy to other elements and receive energy through external sources [123]. Further assumptions in the SEA are [126, 127]:

- The coupling between the subsystems is conservative.
- The excitation forces are uncorrelated white noise.
- Only a direct weak coupling between the subsystems exists (see [128] for a discussion).
- The energy is equally partitioned between the modes in the subsystems (equipartition of energy) or a diffuse wave field is given in the subsystems.
- The damping loss factor is equal for all modes in a subsystem and the damping is light.
- The number of modes in a subsystem is large and the resonance frequencies are uniformly distributed in the viewed frequency band.

In general, these assumptions are only fulfilled in the high frequency region. Several extensions to the classical SEA to relax the given assumptions are outlined in Section 3.2.2.

A typical SEA model, consisting of two subsystems, is shown in Figure 3.2.

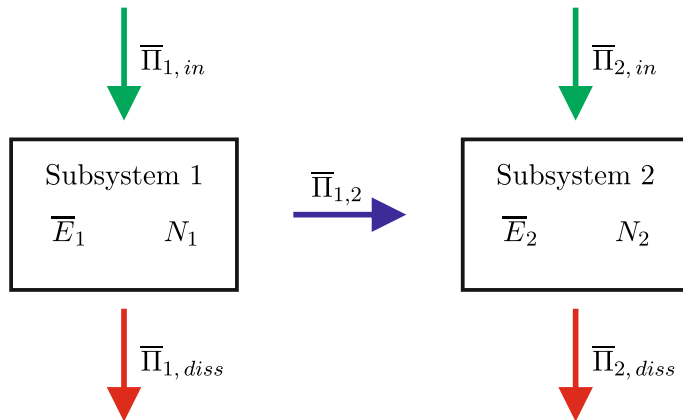


Figure 3.2: Typical SEA system with two subsystems

There is only one primary variable for each subsystem  $i$ , which is the total dynamical energy of the subsystem modes  $\bar{E}_i$ . The bar over  $E_i$  indicates an average over a frequency band  $\Delta\omega$ , centered at angular frequency  $\omega_c$ . Another characteristic parameter is the total

number of modes  $N_i$  in the subsystem  $i$  for the chosen frequency band. For steady-state conditions, the power balance equation for each subsystem  $i$  is given by

$$\bar{\Pi}_{i,in} = \bar{\Pi}_{i,diss} + \sum_{\substack{j=1 \\ j \neq i}}^n \bar{\Pi}_{ij}, \quad i = 1, 2, \dots, n \quad (3.16)$$

where  $\bar{\Pi}_{i,in}$  is the averaged power input to subsystem  $i$  from external sources,  $\bar{\Pi}_{i,diss}$  the averaged dissipated power in the subsystem  $i$ ,  $\bar{\Pi}_{ij}$  the averaged power flow from subsystem  $i$  to subsystem  $j$  and  $n$  the total number of subsystems. The averaged dissipated power in subsystem  $i$  is defined by

$$\bar{\Pi}_{i,diss} = \omega_c \eta_i \bar{E}_i, \quad (3.17)$$

where  $\eta_i$  is the damping loss factor. If the assumptions for the SEA stated above are fulfilled, the averaged power flow between two subsystems is proportional to the difference in averaged total energy in the subsystems

$$\bar{\Pi}_{ij} = \omega_c (\eta_{ij} \bar{E}_i - \eta_{ji} \bar{E}_j), \quad (3.18)$$

where  $\eta_{ji} = (N_i/N_j) \eta_{ij}$  are the coupling loss factors.

Using Equations (3.17) and (3.18) in the power balance equations (Equation (3.16)) leads to a system of linear equations [125]

$$\begin{bmatrix} M_1 + \sum_{j \neq 1}^n h_{1j} & -h_{21} & \cdots & -h_{n1} \\ -h_{12} & M_2 + \sum_{j \neq 2}^n h_{2j} & \cdots & -h_{n2} \\ \vdots & \vdots & \ddots & \vdots \\ -h_{1n} & -h_{2n} & \cdots & M_n + \sum_{j \neq n}^n h_{nj} \end{bmatrix} \begin{bmatrix} \frac{\bar{E}_1}{n_1} \\ \frac{\bar{E}_2}{n_2} \\ \vdots \\ \frac{\bar{E}_n}{n_n} \end{bmatrix} = \begin{bmatrix} \bar{\Pi}_{1,in} \\ \bar{\Pi}_{2,in} \\ \vdots \\ \bar{\Pi}_{n,in} \end{bmatrix}, \quad (3.19)$$

where  $n_i = N_i/\Delta\omega$  is the modal density,  $M_i = \omega_c \eta_i n_i$  the modal overlap and  $h_{ij} = \omega_c \eta_{ij} n_i$  the power transfer coefficient. Due to the reciprocity relation  $h_{ij} = h_{ji}$ , the system matrix of the SEA is symmetric. Furthermore, the system matrix is small and sparsely populated, since the number of subsystems is in general low and because a certain subsystem is only coupled with directly connected subsystems (no indirect coupling). The solution of Equation (3.19) leads to the averaged total energies in the subsystems, which can be used to calculate other parameters, e.g. the average vibration levels.

The SEA modelling process leads to several advantages [125]:

- Through the low number of degrees of freedom, the SEA matrix system can be solved very efficiently. Therefore, numerical experiments can be performed in a very efficient way.
- The model of a subsystem only requires relatively few gross parameters, e.g. modal density, coupling loss factor, damping loss factor and power input.

- Since it is a statistical approach, it is well suited for high frequency problems, because the vibration characteristics of a system, e.g. eigenfrequencies and mode shapes, are very sensitive to uncertainties in geometry and material parameters.

Nevertheless, the application of the SEA is limited through the assumptions stated above, which in general are only fulfilled in the high frequency range. Furthermore, the definition of the subsystem requires a lot of user experience to fulfill the similarity requirement between the modes and all the other assumptions. The SEA also only predicts spatial and frequency averaged energy levels and local information, e.g. displacements or stresses, is not available [13].

### 3.2.2 Improvements and extensions of the SEA

Several extensions and improvements to the SEA have been developed to relax the required assumptions and to simplify the use of the SEA in practice, which are outlined in this section.

The assumption that a diffuse wave field is required within each of the subsystem is relaxed by the Wave Intensity Analysis (WIA) [129, 130]. A Fourier series is used to model the direction dependency of the vibrational wavefields in each component, which leads to a conventional SEA model with additional indirect coupling loss factors.

The Statistical modal Energy distribution Analysis (SmEdA) does not assume equipartition of modal energies within one subsystem, therefore the coupling between pairs of modes of different subsystems are examined instead of the coupling between the whole subsystems [131]. This improves the results compared to SEA especially if the modal overlap in subsystems is low and localized excitation is present in the model [131].

In the Energy Distribution Analysis (EDA) a post-processing procedure is applied to FEM models to calculate frequency averaged subsystem energies [132, 133]. Since the EDA is based on a deterministic technique, correlated and localized excitations as well as strongly coupled subsystems can be examined [134].

There are several other extensions and generalizations of the SEA, which are outlined for instance in [134].

## 3.3 Trefftz based approaches

In 1926, Trefftz [15] proposed a deterministic numerical method as an alternative to the Rayleigh-Ritz method, which incorporates *a priori* information of the problem solution in the definition of the approximation functions. If the problem is governed by linear partial differential equations, the solution can be found by a boundary discretization alone. According to [135], the Trefftz formulations can be classified into the indirect and direct Trefftz method. The indirect methods use solutions of the homogenous partial differential equations as basis functions and the unknown contribution factors are determined by a minimization of the boundary residuals. In the direct methods, a weighted residual approach is applied and the weighting functions are expanded in terms of solutions of the homogenous partial differential equations. A boundary discretization is used to solve the

resulting boundary integral equation. While the unknowns in the direct Trefftz method are physical quantities (e.g. displacements or rotations), the contribution factors in the indirect Trefftz method have no direct physical meaning [135].

The basis functions in the indirect Trefftz method (or the weighting functions in the direct Trefftz method) have to form a so-called T-complete set. A basis function set is T-complete if it is able to represent any possible solution field in the problem domain and fulfills the homogenous partial differential equations [20]. Since the T-complete set is globally defined and non-orthogonal, all Trefftz methods lead to an ill-conditioned system of linear equations [136].

Since the direct Trefftz method is a rather new method, it is rarely applied to dynamic problems [137]. In [138] and [139] the direct method is used to solve the Helmholtz equation (acoustics and membrane vibrations). Apart from that, the direct Trefftz method has been applied to the static in-plane elasticity problem [140], the static thin plate bending problem [141] and the static moderately thick plate bending problem [142].

The indirect Trefftz method is widely used to solve elastostatic and steady-state acoustic models and some of the applied methods have been extended to steady-state elastodynamic problems, e.g. plate vibrations. A different choice of the basis function sets and procedure to fit the boundary and interface conditions lead to a variety of indirect Trefftz methods. A broad overview of the indirect Trefftz methods applied to the Helmholtz equation is given in [137] and [143]. In the subsequent sections, several indirect Trefftz methods, which have been applied or can be extended to analyze plate vibrations, are reviewed. The source simulation techniques, appearing with different names in the literature, are meshless methods and are outlined in Section 3.3.1. An overview of indirect Trefftz methods using a domain decomposition and an indirect coupling approach is given in Section 3.3.2. The methods applying a domain decomposition and a direct coupling are stated in Section 3.3.3.

The main focus of this work is an indirect Trefftz method using a domain decomposition and a direct coupling called Wave Based Method (WBM), which is fully described in Chapter 4.

### 3.3.1 Source Simulation Techniques

These kinds of methods apply distributed source terms, which lie outside the viewed problem domain, as basis function set. Depending on the choice of source terms and their locations and the way of imposing the boundary conditions, the methods appear with different names, e.g. Source Simulation Technique [144], Method of Fundamental Solutions (MFS) [145, 146], Equivalent Source Method (ESM) [147], Wave Superposition Method [148], Boundary Knot Method (BKM) [149, 150], etc.. In [151] a review of the different forms of the Source Simulation Techniques is given. A main advantage of these methods is that no meshing of the domain is required.

Apart from the application of these methods to acoustics and static structural problems, several extensions to plate vibration problems can be found in the literature. In [152] the scattering of flexural waves in heterogeneous thin plates is analyzed using a collocation method to fit the boundary conditions and the response of the plate to a point force is

applied as source terms. The MFS has been used to determine the eigenfrequencies of thin plates [153, 154] and the frequency response function of a vibroacoustic problem [155]. The BKM is used in [156] to predict the eigenfrequencies of arbitrary shaped thin plates.

The main drawback of these methods, apart from the ill-conditioned system matrices, is that no rule exists to find the optimal number and position of the source points [151]. Since the BKM applies non-singular general solutions instead of singular fundamental solutions as basis function set, the source points can be placed on the boundary, which mitigates this drawback.

### 3.3.2 Indirectly coupled methods

These types of methods decompose the problem domain into several sub-domains and apply the T-complete set as basis functions within every sub-domain. Since the inter-element continuity is in general not fulfilled *a priori*, a coupling scheme between the elements is required. In the indirect coupling approaches, auxiliaries like an auxiliary frame containing standard polynomial shape functions or Lagrange multipliers are applied.

Depending on the indirect coupling technique, the used T-complete set and the approach used to minimize the boundary and interface residuals, several methods have been developed.

The hybrid-Trefftz Finite Element method (HT-FEM) [157] applies an auxiliary inter-element displacement or traction frame to couple adjacent elements. A modified variational principle is used to enforce the continuity of the field variables. In [158] the HT-FEM is applied to linear elastodynamics, in [159] to the analysis of forced Kirchhoff plate vibrations and in [160] to transient plate bending problems.

The Discontinuous Galerkin Method (DGM) with Lagrange multipliers [161, 162, 163] can be considered as a special case of the DEM by dropping the standard polynomial field from the approximation functions. Therefore, only the free-space solutions are used to approximate the field variables, and Lagrange multipliers are applied to enforce the inter-element continuity in a weak form.

### 3.3.3 Directly coupled methods

The last group of Trefftz methods also applies a domain decomposition, but enforces the inter-element continuity of the field variables in a direct way. The Trefftz collocation method [164] uses simple point collocation to impose the boundary and interface conditions, while the least-square method, proposed in [165], enforces the continuity between the elements through a least-square approach.

The Ultra Weak Variational Formulation (UWVF) [166, 167] uses the adjoint partial differential equation to derive a different variational formulation of the problem at hand. Through the variational formulation of the UWVF, the interface conditions are inherently satisfied [20]. In [168] the UWVF has been extended to elastic wave propagation problems and in [169] to the analysis of thin clamped plate vibration problems.

### 3.3 Trefftz based approaches

The Variational Theory of Complex Rays (VTCR) [170, 171] applies a variational formulation, which enables a *priori* independent approximations within the sub-domains. Complex rays termed interior rays, edge rays and corner rays, which satisfy the partial differential equations of the viewed problem, are used as basis functions. The amplitudes of the complex rays are discretized by piecewise polynomials.

The Wave Based Method (WBM) [21], which also corresponds to this category of Trefftz methods, is described in detail in the next chapter.



# 4 The Wave Based Method

In this chapter, the Wave Based Method (WBM), developed by Desmet [21] in 1998, is reviewed in detail. The WBM is a deterministic approach and belongs to the category of indirect Trefftz methods with a direct coupling between the sub-domains. It can be applied to solve any steady-state dynamic problem, which is governed by a set of Helmholtz equations. For two-dimensional bounded problems, the basis function set consists of travelling and evanescent waves, which may be enriched by special purpose functions to treat certain effects, e.g. singularities in the solution. The direct coupling of sub-domains and the enforcement of boundary conditions are performed with a weighted residual formulation [14], although in earlier works a least-square approach has been tested [21, 96].

In Section 4.1, the methodology of the WBM to solve problems governed by Helmholtz equations is outlined. The properties of the WBM are discussed in Section 4.2 and a broad review of the state-of-the-art developments of the WBM are given in Section 4.3. The following sections are mainly based on the comprehensive review papers of Deckers and her co-workers [14] and Pluymers et al. [137] with additional information on recent developments.

## 4.1 Methodology for a generalized Helmholtz problem

In this section the WBM modelling steps for a two-dimensional bounded problem governed by a set of Helmholtz equations are outlined. The reader is referred to, e.g. [99] and [172] for unbounded and three-dimensional problems. In Section 4.1.1 the generalized bounded Helmholtz problem, which can be solved by the WBM, is described. The modeling steps of the WBM to solve the outlined problem are given in Section 4.1.2.

### 4.1.1 Generalized Helmholtz problem

The general bounded two-dimensional problem domain  $\Omega$ , shown in Figure 4.1, is decomposed into two sub-domains  $\Omega = \Omega^{(\alpha)} \cup \Omega^{(\beta)}$  (the generalization to an arbitrary number of sub-domains is straightforward). Such a decomposition might be necessary because the parameters of the sub-domains are different or the geometry of the problem domain is concave (more details on this restriction of the WBM are given in the subsequent sections). It is assumed that the mathematical model of the physical problem at hand gives rise to a number of  $n_H$  Helmholtz equations with a total number of  $n_H$  field variables

$$\nabla^2 u_m^{(l)} + k_m^{(l)2} u_m^{(l)} = f_m^{(l)}, \quad m = 1, \dots, n_H, \quad \mathbf{r} \in \Omega^{(l)}, \quad l = \{\alpha, \beta\}, \quad (4.1)$$

where  $\mathbf{r}$  is the spatial coordinate,  $u_m^{(l)}(\mathbf{r})$  the field variable of the  $m^{\text{th}}$  Helmholtz equation in the sub-domain  $l$ ,  $k_m^{(l)}$  the associated physical wavenumber and  $f_m^{(l)}$  an external source

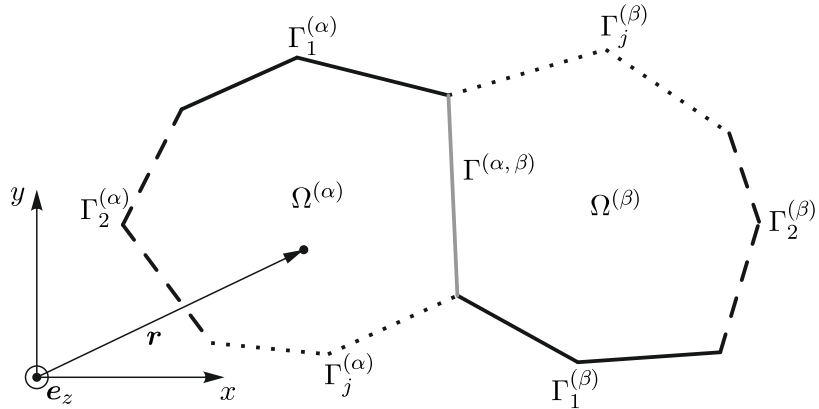


Figure 4.1: General two-dimensional bounded problem with two domains  $\Omega^{(\alpha)}$  and  $\Omega^{(\beta)}$ , different boundary conditions  $\Gamma_j^{(\alpha)}$  and  $\Gamma_j^{(\beta)}$  and the common interface  $\Gamma^{(\alpha, \beta)}$

term. The field variables  $u_m^{(l)}(\mathbf{r})$  of the sub-domain  $l$  are gathered in the column vector  $\mathbf{u}^{(l)}(\mathbf{r}) = [u_1^{(l)}, u_2^{(l)}, \dots, u_{n_H}^{(l)}]^T$ .

In order to obtain a well-posed problem,  $n_H$  boundary conditions need to be imposed on every point of the domain boundary  $\Gamma = \partial\Omega$ . Since the problem domain in Figure 4.1 is decomposed into two sub-domains, the domain boundary is partitioned into two external sub-domain boundaries  $\Gamma = \Gamma^{(\alpha)} \cup \Gamma^{(\beta)}$  and both sub-domains share a common interface  $\Gamma^{(\alpha, \beta)}$ . The external sub-domain boundaries can be divided into non-overlapping parts  $\Gamma^{(l)} = \bigcup_j \Gamma_j^{(l)}$ , which allows for the definition of different types of boundary conditions at each boundary part  $\Gamma_j^{(l)}$ . The set of boundary conditions at a boundary part  $\Gamma_j^{(l)}$  can be given in a general form

$$\mathcal{B}_{j,k}^{(l)} \mathbf{u}^{(l)} = \bar{B}_{j,k}^{(l)}, \quad k = 1, \dots, n_H, \quad \mathbf{r} \in \Gamma_j^{(l)}, \quad (4.2)$$

where  $\mathcal{B}_{j,k}^{(l)}$  is a general boundary differential operator and  $\bar{B}_{j,k}^{(l)}(\mathbf{r})$  an externally prescribed boundary field. Furthermore, continuity conditions at the common interface have to be fulfilled, which can be given by

$$\mathcal{B}_k^{(\alpha)} \mathbf{u}^{(\alpha)} + \mathcal{B}_k^{(\beta)} \mathbf{u}^{(\beta)} = 0, \quad k = 1, \dots, 2n_H, \quad \mathbf{r} \in \Gamma^{(\alpha, \beta)}, \quad (4.3)$$

with  $\mathcal{B}_k^{(\alpha)}$  and  $\mathcal{B}_k^{(\beta)}$  general boundary differential operators, which ensure the continuity between the field variables  $\mathbf{u}^{(\alpha)}$  and  $\mathbf{u}^{(\beta)}$ . The well-posedness of the problem is only retained if one continuity condition is imposed for each of the  $n_H$  field variables on each sub-domain. It is apparent that in general the field variables within one sub-domain are coupled through the boundary conditions and a coupling of the field variables of different sub-domains occurs by imposing the continuity conditions.

The generalized Helmholtz problem is solved when the field variables  $u_m^{(l)}$  fulfilling the governing equations (Equation (4.1)), the boundary conditions in Equation (4.2) and the interface conditions in Equation (4.3) are determined. In the next section, the WBM is used to find an approximate solution for the field variables  $u_m^{(l)}$ , since analytical solutions are rarely feasible.

### 4.1.2 The modeling procedure of the WBM

In general, the WBM requires four to five modelling steps in order to solve a generalized Helmholtz problem:

- In case of a concave problem domain, a partitioning into convex sub-domains is needed.
- For each sub-domain a suitable set of wave functions has to be selected. If source terms are present in the sub-domain, a specific particular solution of the Helmholtz equation is required. Special purpose functions can be added if certain effects have to be treated, e.g. singularities in the solution field.
- The system of linear equations is constructed through the fitting of the boundary and interface conditions via a weighted residual approach.
- The solution of the system of linear equations leads to the contribution factors of the selected wave functions.
- A postprocessing step is needed to calculate the dynamic variables and derived quantities.

A detailed description of each modelling step is given in the subsequent sections.

#### Partitioning of the problem domain

As previously mentioned, the WBM is restricted to convex problem (sub)-domains. If the general problem domain is non-convex, a partitioning into convex sub-domains is required. This limitation is due to the selected basis function set applied in the WBM, which is only a T-complete set, if it is used in a convex domain [21]. Through the partitioning into convex sub-domains, the applied function set becomes T-complete, but the additional interface conditions, given in Equation (4.3), have to be fulfilled.

In general, many different configurations of convex sub-domains are possible for the partitioning of a concave problem domain. In [96] it is proposed that the total number of sub-domains and the number of small sub-domains should be minimized, while highly irregular sub-domains and large area ratios between the sub-domains are avoided.

#### Selection of the basis function sets

The WBM is an indirect Trefftz approach and therefore analytical solutions of the homogenous partial differential equations are used as basis function set. If the problem domain is decomposed into  $n_\alpha$  non-overlapping sub-domains, each field variable  $u_m^{(\alpha)}$  in each sub-domain is approximated by a solution expansion

$$u_m^{(\alpha)} \approx \hat{u}_m^{(\alpha)} = \sum_{w_m=1}^{n_m^{(\alpha)}} \left( \hat{u}_{w_m}^{(\alpha)} \Phi_{w_m}^{(\alpha)} \right) + u_{p,m}^{(\alpha)} = \Phi_m^{(\alpha)} \hat{\mathbf{u}}_m^{(\alpha)} + u_{p,m}^{(\alpha)}, \quad \alpha = 1, \dots, n_\alpha, \quad (4.4)$$

#### 4 The Wave Based Method

where  $\Phi_{w_m}^{(\alpha)}$  are the wave functions defined in the sub-domain  $\Omega^{(\alpha)}$ ,  $\hat{u}_{w_m}^{(\alpha)}$  the wave contribution factors,  $n_m^{(\alpha)}$  the number of used wave functions and  $u_{p,m}^{(\alpha)}$  the particular solution functions. The  $n_m^{(\alpha)}$  wave functions and contribution factors are gathered in the row vector  $\Phi_m^{(\alpha)}$  and the column vector  $\hat{u}_m^{(\alpha)}$ .

The particular solution function  $u_{p,m}^{(\alpha)}$  has to fulfill the inhomogeneous Helmholtz equation

$$\nabla^2 u_{p,m}^{(\alpha)} + k_m^{(\alpha)2} u_{p,m}^{(\alpha)} = f_m^{(\alpha)} \quad (4.5)$$

without the necessity of satisfying any boundary or interface conditions. In general, the particular solution functions are found by solving the Helmholtz equation in an infinitely extended medium.

The applied wave functions  $\Phi_{w_m}^{(\alpha)}$  in Equation (4.4) are solutions of the homogeneous Helmholtz equation

$$\nabla^2 \Phi_{w_m}^{(\alpha)} + k_m^{(\alpha)2} \Phi_{w_m}^{(\alpha)} = 0, \quad (4.6)$$

while the contribution factors  $\hat{u}_{w_m}^{(\alpha)}$  are freely chosen constants. Several different possibilities exist to define T-complete wave function sets  $\Phi_{w_m}^{(\alpha)}$ , e.g. plane waves or Bessel type functions [173].

The WBM applies plane waves as function set. The characteristic lengths  $L_x^{(\alpha)}$  and  $L_y^{(\alpha)}$  of the smallest rectangle (see Figure 4.2), circumscribing the convex sub-domain, and a local sub-domain coordinate system  $\{x_D, y_D\}$  are used to select the wavenumbers for the plane wave functions [21]. The plane wave functions are a combination of cosine and/or sine functions in one direction (either in  $x_D$ - or  $y_D$ -direction) and exponential functions in the second direction. The wavenumber component associated with the sine or cosine functions is chosen as such that an integer number of half wavelengths fits into the corresponding bounding box dimension [20]. The dispersion relation determines the second wavenumber component corresponding to the exponential functions. Depending on the second wavenumber component, either a propagating wave (real wavenumber), an evanescent wave (imaginary wavenumber) or a harmonic decaying wave (complex wavenumber) occurs [100]. This selection of wavenumbers leads to a T-complete function set in convex domains, as it is shown in [21] for steady-state acoustic problems and in [17] for thin

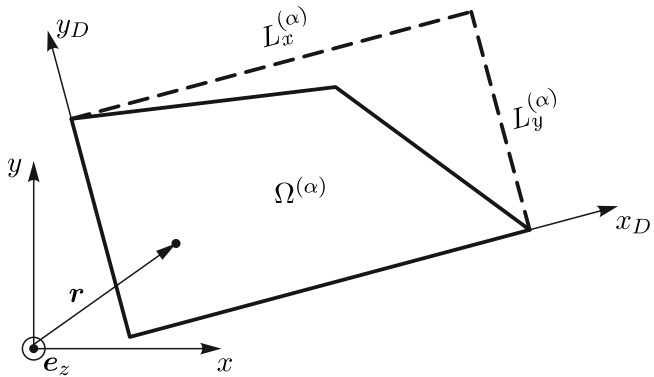


Figure 4.2: Smallest rectangular bounding box, circumscribing a convex 2D sub-domain

plate bending vibrations. The advantage of the inclusion of evanescent waves in the basis function set is the possibility to capture near field effects, e.g. edge effects at boundaries.

### Construction of the system of linear equations

The solution expansions given in Equation (4.4) fulfill the Helmholtz equations (Equation (4.1)) independently of the contribution factors. However, the boundary conditions in Equation (4.2) and the interface conditions in Equation (4.3) are in general violated by the proposed basis functions. The approximation of the boundary and interface conditions can be achieved by different approaches [135]. The simplest approach is the collocation method, where the boundary and interface residuals are forced to vanish at certain collocation points. Even though this approach is the simplest and computationally most efficient, the errors between the collocation points may be rather high [135]. Using specific locations of the collocation points, e.g. the evaluation points of the Gauss-Legendre quadrature, can remove this drawback [136]. In the WBM however, a least-square approach or a weighted residual formulation is applied. In the least-square approach a functional defined by the sum of the squares of the boundary and interface residuals is minimized. Weighting factors, which preserve the numerical equivalence between the different residuals, are required. In the weighted residual formulation, the boundary and interface residuals are orthogonalised with respect to some weighting functions and integrated over the problem boundary and interfaces. The sum of these integrals is forced to vanish for any combination of weighting functions.

In [21] and [96] both methods have been compared and it is argued that in the WBM, the weighted residual formulation is superior to the least-square approach, since numerical tests have shown a higher convergence rate for the weighted residual formulation. Furthermore, it is not straightforward to assess *a priori* the required weighting factors in the least-square approach, which have great influence on the convergence rate. Therefore, the weighted residual formulation is used in this work to fit the boundary and interface conditions.

The weighting functions  $v_{\bullet}^{(\alpha)}(\mathbf{r})$  are used to orthogonalize the boundary and interface residuals of the sub-domains  $\Omega^{(\alpha)}$  ( $\alpha = 1, \dots, n_{\alpha}$ ) and an integration over the boundaries and interfaces leads to

$$\begin{aligned} & \sum_{\beta=1, \beta \neq \alpha}^{n_{\alpha}} \sum_{k=1}^{n_H} \int_{\Gamma^{(\alpha, \beta)}} v_k^{(\alpha)} \left( \mathcal{B}_k^{(\alpha)} \mathbf{u}^{(\alpha)} + \mathcal{B}_k^{(\beta)} \mathbf{u}^{(\beta)} \right) ds \\ & + \sum_j \sum_{k=1}^{n_H} \int_{\Gamma_j^{(\alpha)}} v_{j,k}^{(\alpha)} \left( \mathcal{B}_{j,k}^{(\alpha)} \mathbf{u}^{(\alpha)} - \bar{B}_{j,k}^{(\alpha)} \right) ds = 0. \end{aligned} \quad (4.7)$$

The first term enforces the interface conditions between the sub-domains  $\Omega^{(\alpha)}$  and  $\Omega^{(\beta)}$  and the second term the boundary conditions imposed on the sub-domain  $\Omega^{(\alpha)}$ . The boundary and interface specific weighting functions  $v_{\bullet}^{(\alpha)}$  can be computed by

$$v_{\bullet}^{(\alpha)} = \mathcal{T}_{\bullet}^{(\alpha)} \tilde{\mathbf{v}}^{(\alpha)}, \quad (4.8)$$

where  $\mathcal{T}_{\bullet}^{(\alpha)}$  is a specific partial differential operator and  $\tilde{\mathbf{v}}^{(\alpha)} = [\tilde{v}_1^{(\alpha)}, \tilde{v}_2^{(\alpha)}, \dots, \tilde{v}_{n_H}^{(\alpha)}]^T$  a column vector containing the different weighting function components  $\tilde{v}_m^{(\alpha)}$ . A commonly

## 4 The Wave Based Method

applied approach to find the problem dependent partial differential operator  $\mathcal{T}_\bullet^{(\alpha)}$  is a variational analysis of the problem at hand [96]. In the WBM, the Galerkin approach is applied and the weighting function components  $\tilde{v}_m^{(\alpha)}$  are expand in the same wave functions as the field variables  $u_m^{(\alpha)}$  leading to

$$\tilde{v}_m^{(\alpha)} = \sum_{w_m=1}^{n_m^{(\alpha)}} \hat{v}_{w_m}^{(\alpha)} \Phi_{w_m}^{(\alpha)} = \mathbf{\Phi}_m^{(\alpha)} \hat{\mathbf{v}}_m^{(\alpha)}, \quad (4.9)$$

where  $\hat{v}_{w_m}^{(\alpha)}$  are the weighing factors of the weighting functions, which are gathered in the column vector  $\hat{\mathbf{v}}_m^{(\alpha)}$ .

Using the approximate expansion of the field variables (Equation (4.4)) and the weighting function expansion (Equation (4.9)) in the weighted residual approach, given in Equation (4.7), results in

$$\hat{\mathbf{v}}^{(\alpha)T} \left( \left[ \mathbf{C}^{(\alpha,1)}, \dots, \mathbf{C}^{(\alpha,\alpha-1)}, \mathbf{A}^{(\alpha)}, \mathbf{C}^{(\alpha,\alpha+1)}, \dots, \mathbf{C}^{(\alpha,n_\alpha)} \right] \begin{bmatrix} \hat{\mathbf{u}}^{(1)} \\ \vdots \\ \hat{\mathbf{u}}^{(\alpha-1)} \\ \hat{\mathbf{u}}^{(\alpha)} \\ \hat{\mathbf{u}}^{(\alpha+1)} \\ \vdots \\ \hat{\mathbf{u}}^{(n_\alpha)} \end{bmatrix} - \mathbf{b}^{(\alpha)} \right) = 0, \quad (4.10)$$

where  $\hat{\mathbf{v}}^{(\alpha)} = [\hat{\mathbf{v}}_1^{(\alpha)T}, \hat{\mathbf{v}}_2^{(\alpha)T}, \dots, \hat{\mathbf{v}}_{n_H}^{(\alpha)T}]^T$  and  $\hat{\mathbf{u}}^{(\alpha)} = [\hat{\mathbf{u}}_1^{(\alpha)T}, \hat{\mathbf{u}}_2^{(\alpha)T}, \dots, \hat{\mathbf{u}}_{n_H}^{(\alpha)T}]^T$  are column vectors containing the weighting functions factors  $\hat{v}_m^{(\alpha)}$  and the wave function contribution factors  $\hat{\mathbf{u}}_m^{(\alpha)}$ . The coupling matrices  $\mathbf{C}^{(\alpha,\beta)}$  result from the interface conditions between the adjacent sub-domains  $\Omega^{(\alpha)}$  and  $\Omega^{(\beta)}$ , while the sub-domain matrix  $\mathbf{A}^{(\alpha)}$  originates from the minimization of the boundary residuals and a back coupling at the interfaces. Non-zero boundary conditions  $\bar{B}_{j,k}^{(\alpha)} \neq 0$  and source terms  $f_m^{(\alpha)}$  lead to the load vector  $\mathbf{b}^{(\alpha)}$ . Applying this procedure to all sub-domains ( $\alpha = 1, \dots, n_\alpha$ ) and enforcing that Equation (4.10) vanishes for any combination of weighing functions lead to the linear system

$$\mathbf{A} \hat{\mathbf{u}} = \mathbf{b}, \quad (4.11)$$

where the square system matrix  $\mathbf{A}$  is an assembly of all sub-domain matrices  $\mathbf{A}^{(\alpha)}$  and coupling matrices  $\mathbf{C}^{(\alpha,\beta)}$ , the column vector  $\hat{\mathbf{u}} = [\hat{\mathbf{u}}^{(1)T}, \hat{\mathbf{u}}^{(2)T}, \dots, \hat{\mathbf{u}}^{(n_\alpha)T}]^T$  contains all unknown wave contribution factors and the column vector  $\mathbf{b} = [\mathbf{b}^{(1)T}, \mathbf{b}^{(2)T}, \dots, \mathbf{b}^{(n_\alpha)T}]^T$  gathers all load vectors.

### Solution of the linear system and postprocessing steps

The linear system in Equation (4.11) has to be solved for the unknown wave contribution factors. Since the linear system of equations is in general ill-conditioned [21], direct solvers are preferred for the solution, e.g. LU factorization (Gaussian elimination) or singular value

decomposition (SVD). Substituting the resulting contribution factors into the solution expansion given in Equation (4.4) leads to an analytical approximation of the field variables. Derived quantities, e.g. stresses, can be computed with the same spatial resolution as the primary field variables by applying the associated differential operators.

## 4.2 Properties of a wave based model

In this section, the properties of the WBM are stated and the advantages and disadvantages compared to the FEM are described. Even though both methods are deterministic methods, the fundamental difference in the choice of approximation functions leads to different features concerning the model discretization, the degrees of freedom, the geometric flexibility, the construction and properties of the system matrices and the problem dependent computational load.

### Problem subdivision and degrees of freedom

Compared to the FEM, which requires a discretization of the problem domain into a large number of small elements, the WBM applies a domain decomposition into a small number of large convex sub-domains, which is mandatory for the T-completeness of the applied function set [21]. In addition to the decomposition rules stated in [96] (see Section 4.1.2), steep changes of the boundary conditions within one sub-domain should be avoided [14].

An increase in the accuracy in the conventional FEM is achieved by either a finer discretization of the problem domain (h-refinement) or an increase of the polynomial order (p-refinement). In general, a local refinement requires a (partial) remeshing of the domain. Furthermore, a remeshing of the whole problem domain might be necessary due to the mesh requirements at higher frequencies. The WBM applies a higher number of wave function within one sub-domain to increase the accuracy and therefore a remeshing of the problem is not required, even at high frequencies.

The degrees of freedom in the FEM represent the value of the field variable at the nodal positions (nodal values) and therefore have direct physical meaning. In general, the number of degrees of freedom are rather high in the FEM, especially for high frequencies. The unknowns in the WBM are the contribution factors of the applied wave functions, which have no direct physical meaning. A postprocessing step is needed in order to get the values of the field variables at certain positions. The application of analytical solutions of the governing equations in the WBM introduces *a priori* information of the solution and therefore the number of degrees of freedom is in general considerably lower compared to the FEM.

### Complexity of the model geometry

The fine discretization in the FEM leads to a high flexibility concerning the geometric complexity of the model, which allows for the application of the FEM to almost any problem domain. Since the WBM is most effective for a small number of large convex sub-domains, highly complex domains, which have to be partitioned into a larger number

of sub-domains to fulfill the convexity requirement, lead to a decrease in the computation efficiency of the WBM. This is due to the increase of interfaces between the sub-domains, which require the integration of highly oscillating functions [14]. This drawback is relaxed by improvements of the WBM like the Multi-Level WBM [174, 175] and the hybrid Finite Element-Wave Based Method [96], which are outlined in Section 4.3.

### Construction of the system matrices

While the construction of the system matrices in the FEM requires the integration of lower order polynomial functions, in the WBM integrals of highly oscillating functions have to be evaluated. Therefore, the computational load to build the system matrices is higher for the WBM compared to the FEM and furthermore, due to the frequency dependency of the WBM matrices, the system matrix has to be computed for each considered frequency. Although, an analytical integration of the integrals appearing in the WBM is possible for straight boundaries [96], in general, a numerical integration technique is applied. Using numerical integration gives a higher flexibility concerning the boundary shape of the sub-domains and also allows for the evaluation of integrals, which cannot be solved analytically, e.g. integrals resulting from source terms. The Gauss-Legendre quadrature appears to be the most effective numerical integration technique for the occurring integrands [96] and the matrix multiplication technique shown in [176] can be applied to evaluate the integrals very efficiently. Since the resulting system matrix is ill-conditioned, the numerical integration has to be performed very carefully to ensure sufficiently accurate matrix coefficients. In [17] a rule is derived for the optimal number of Gauss points, which leads to accurate results (relative error of  $10^{-10}$  compared to the analytical solution) with a minimum of computational costs.

### Properties of the system matrices

The FEM leads to system matrices, which are in general large, symmetric, real-valued, frequency independent and sparsely populated with a banded structure (see Section 3.1.1). In contrast, the system matrices resulting from the WBM are always complex, frequency dependent and fully populated [20]. The system matrix has a considerable lower size compared to the FEM and is symmetric or non-symmetric, depending on the analyzed physical problem. As pointed out in [136], Trefftz methods lead to an ill-conditioned system of linear equations, which is also true for the WBM. In [21] it is shown that accurate results can be obtained, even though the system matrix is ill-conditioned, if direct solution methods are applied and the WBM matrices fulfill both Picard conditions [177, 178].

### Accuracy of derived quantities

Since the FEM uses polynomial shape functions for the approximation of the primary field variables, the solutions of the derived quantities, which are calculated by applying partial differential operators to the primary field variables, have a lower spatial resolution and accuracy. The WBM however uses wave functions for the approximation of the primary

field variables and since the derivations of the wave functions are again wave functions, the derived quantities are predicted with the same spatial resolution as the primary variables [14].

### System matrix solution and computational load

The system matrix of the FEM allows for the use of efficient sparse direct or iterative solvers, but due to the large size of the matrices, the system solution process is still the most demanding step in FEM, while the computational load for the construction of the system matrices is usually negligible. Even though the construction of the WBM matrices is more demanding than the calculation of the FEM system matrices, the considerably smaller size of the fully populated WBM matrices allows for a more sufficient solution process compared to the FEM. Furthermore, due to the application of analytical solutions of the homogenous governing equations, the convergence rate of the WBM is superior [20]. This holds true for moderately complex geometries, since the computational load of the WBM rises with the required number of convex sub-domains.

## 4.3 State-of-the-art developments

In this section, the state-of-the-art developments of the WBM are presented. In Section 4.3.1 an overview of the physical problems, which are currently analyzed with the WBM, is given. Further improvements and extensions of the WBM are outlined in Section 4.3.2, especially the treatment of singularities and methods to relax the geometrical limitations of the WBM. Finally, some applications of the WBM to engineering problems are stated in Section 4.3.3. Several review papers of the WBM exist in the literature, e.g. [179, 137, 180] for two-dimensional bounded and unbounded acoustic problems including the coupling of the WBM to FEM, [181] for steady-state structural problems, [182] for the WBM applied to poroelastic materials and [95, 14] for general reviews.

### 4.3.1 Physical problems tackled by the WBM

Since the WBM can be applied to any problem, which is governed by a (set of) Helmholtz equation(s), a great variety of physical problems can be tackled by the WBM. In the following sections, the problems analyzed with the WBM so far, are stated.

#### Steady-state acoustic problems

The steady-state acoustic problem is governed by one Helmholtz equation [99] and therefore can be solved by the WBM. Depending on the problem domain, interior acoustic problems (bounded domain) and exterior acoustic problems (unbounded domain) are distinguished.

### a.) *Interior acoustic problem*

The first developments of the WBM for steady-state acoustics in bounded two-dimensional and three-dimensional domains have been carried out by Desmet [21]. The weighted residual formulation as well as a least-square approach are used to fit the boundary conditions and general information on the practical implementation of the WBM, e.g. the wave function scaling, the numerical integration of the wave functions, the wave function truncation and the linear dependency of the wave functions, is given.

In [183] a high performance implementation of the WBM for uncoupled two-dimensional acoustic problems in convex and non-convex domains is compared to a commercial FEM code and the high computational efficiency of the WBM is shown. An object-oriented implementation scheme for the WBM is developed in [184] and applied to the steady-state acoustics of a two-dimensional L-shaped problem domain. Several other examples of two-dimensional interior acoustic problems solved by the WBM can be found in [99] and [96].

Applications of the WBM in three-dimensional interior acoustics are given in [185] and [186] for convex domains and in [187] and [188] for non-convex domains. In [99] an impedance coupling between sub-domains is developed for two- and three-dimensional problems and compared to the originally proposed direct coupling of the velocity and pressure fields. It is shown that the impedance coupling exhibits better convergence characteristics than the pressure and velocity coupling. The three-dimensional axisymmetric acoustic problem in bounded domains is tackled in [189] by introducing a specific wave function set.

### b.) *Exterior acoustic problem*

While in interior acoustic problems the field variables have to satisfy the governing equations and the boundary conditions, exterior acoustic problems also require the fulfillment of the so-called Sommerfeld radiation condition. In [99] the WBM is developed for two-dimensional exterior acoustic problems. A truncation surface is introduced, which divides the problem domain into a bounded and an unbounded part. In the bounded part, the classical wave functions are applied and in the unbounded part new wave functions are presented, which also satisfy the Sommerfeld radiation conditions. In [190] the steady-state acoustics of a two-dimensional car-like cavity with an open boundary are analyzed with the WBM and in [172] several other two-dimensional examples are presented.

The extension to three-dimensional exterior acoustic problems is mainly performed in [191], [172] and [192] and applications of the method are shown in [193] for simple three-dimensional geometries and in [194] for a truck engine geometry. Investigations concerning the required number of wave functions and optimal decomposition strategies for three-dimensional exterior acoustic problems are presented in [195].

A modification of the wave function set used in unbounded acoustic domains is applied in [196] to analyze two-dimensional semi-infinite radiation and scattering problems and transmission or diffraction problems. Similar approaches are also used for the three-dimensional case [197, 172].

### Steady-state structural dynamics

The steady-state vibrations of linear elastic solid structures are governed by a set of four Helmholtz equations (Equations (2.12) and (2.13)). Even though, the WBM could be used to solve the three-dimensional elasticity equations, only simplified models, e.g. plate membrane and bending problems and shell vibrations, are solved by the WBM so far.

#### a.) Plate membrane problems

The WBM for steady-state vibrations of the in-plane behaviour of two-dimensional structural solids is developed by Vanmaele and her co-workers [198, 181, 17]. Therefore, the coupled dynamic Navier equations are decomposed into two uncoupled Helmholtz equations, which simplifies the definition of the T-complete function set. Two different types of decompositions are analyzed and a direct coupling approach between sub-domains is used.

#### b.) Plate bending problems

In [21], Desmet already considered the uncoupled plate bending problem and derived the wave function sets for steady-state Kirchhoff plate vibrations. The WBM is also applied in [199] and [200] to investigate the vibrations of thin convex plates and the weighted residual approach is used to fit the boundary conditions, while in [201] a least-square approach is implemented. Further developments of the WBM for steady-state Kirchhoff plate vibrations are shown in [17], [16] and [181], analysing an additional function set, the importance of corner residuals in the Kirchhoff plate theory and non-convex problem domains. Applications of the WBM to orthotropic Kirchhoff plates are given in [202] and [203]. The treatment of point connections, e.g. point connected masses, springs or dampers, are shown in [13].

#### c.) Three-dimensional flat plate assemblies

If flat plates are assembled at an arbitrary angle, a coupling between the membrane and bending vibrations occurs through the common interface of the flat plates. Therefore, a combination of the WBM for plate membrane and plate bending problems is proposed [204, 205, 17, 181], where a full coupling and a reduced coupling (in-plane displacements are neglected) are analyzed. While the full coupling leads to accurate predictions of the out-of-plane displacements, the neglecting of the in-plane displacements results in a large error.

#### d.) Shell vibrations

The first attempts to use the WBM for cylindrical shell vibrations are reported in [206] and [21], where a two-dimensional acoustic cavity is coupled with a force-excited shell structure. The analysis of free vibrations of ring stiffened cylindrical shells with intermediate large frame ribs is performed in [207]. Therefore, the WBM is applied to the Donnell-Mushtari shell theory and coupled with circular and annular circular thin plates. A similar approach is used in [208] for the free vibration analysis of cylindrical shells with a nonuniform and eccentric stiffeners distribution. The WBM is further extended to the free and forced vibrations of cylindrical shells with discontinuities in thickness [209], elastically

coupled annular plates and cylindrical shell structures [210] and non-uniformly supported cylindrical shells [211]. All these extensions apply the Flügge shell theory and external loading is introduced through the boundary conditions.

### Coupled vibro-acoustic problems

In the coupled vibro-acoustic problem, a vibrating structure is in contact with a fluid and a mutual coupling interaction between the structural vibrations and the acoustic pressure field occurs. While the pressure field acts as external loading on the structure, the surface vibrations are treated as boundary conditions in the acoustic problem.

The WBM for a coupled vibro-acoustic problem of a plate interacting with a bounded two- or three-dimensional acoustic domain is developed in [21]. The acoustic pressure exciting the plate is included by a particular solution function fulfilling the inhomogeneous terms in the partial differential equation of the Kirchhoff plate theory. The plate vibrations are treated as velocity boundary conditions in the acoustic problem. Further applications of the WBM to bounded vibro-acoustic problems are given in [212] and [96] for two-dimensional domains and in [213] and [214] for three-dimensional domains.

The extension of the WBM to coupled vibro-acoustic problems with a two-dimensional unbounded acoustic domain is shown in [215] using a least-square fit of the boundary conditions, while in [216] a weighted residual approach and an impedance coupling between sub-domains is applied. In [217] and [192] the WBM is applied to coupled vibro-acoustic problems with a three-dimensional unbounded acoustic domain.

### Poroelastic material modelling

Poroelastic materials comprise two constituents, the frame (an elastic solid) and the fluid filling. The vibrations of both constituents can be strongly coupled, depending on the frequency range. Different mathematical models have been proposed for poroelastic materials, e.g. the equivalent fluid model, the Biot model and the equivalent solid model, which result in partial differential equations [182].

The WBM is applied in [218] to analyze two-dimensional problems including poroelastic materials, which are modelled as an equivalent fluid. The same approach is used in [219] to investigate the acoustic performance of sound absorbing materials.

The development of the WBM for poroelastic materials modelled by the more accurate Biot theory is shown in [220]. The partial differential equations resulting from the Biot model are decomposed into three Helmholtz equations, which allows for a straightforward definition of the T-complete function sets. Applications of the WBM to two-dimensional poroelastic material problems using the Biot model can be found in [221] and in [222] the WBM for a poroelastic material coupled with an acoustic domain is presented. The three-dimensional axisymmetric Biot model is investigated in [189] by modifying the original wave function set of the WBM.

### 4.3.2 Current improvements and extensions of the WBM

The main drawback of the WBM is given by the geometrical limitation due to the need for convex sub-domains. Several improvements and extensions have been made to enhance the geometrical flexibility of the WBM. First of all, the convergence of the WBM in certain non-convex domains with smooth concave parts is shown in [223], which allows for the application of the WBM without subdividing the domain. In case of other types of non-convex domains, which would require a partitioning into a large number of convex sub-domains, the Multi-Level WBM and the Hybrid Finite Element-Wave Based Method or the Hybrid Boundary Element-Wave Based Method have been developed. These extensions, as well as the treatment of singularities in the solution field and other hybrid methods, are outlined in the subsequent sections.

#### Treatment of singularities in the solution field

Singularities in the solution field may occur due to discontinuities in the material parameters, boundary conditions or boundary shape (e.g. corner points in polygonal domains). If such singularities are present in the solution, the WBM suffers from convergence problems, since the representation of a singularity is difficult with the classical wave function set. Therefore, so-called special purpose functions are added to the classical wave function set, which are able to capture the singular behaviour [198].

The special purpose functions, developed for the WBM, have to satisfy the partial differential equations and can be found in the literature for corner singularities, which occur especially in polygonal shaped domains. The first special purpose functions have been developed for the two-dimensional plate bending problem using the Kirchhoff plate theory [224, 18]. An infinite wedge domain is examined and an exact analytical solution for specific boundary conditions is defined, which represents the singularity in the corner and can be added to the original wave function set. Since such a solution only exists for a specific type of boundary condition, the solution of the static problem is examined to define special purpose functions for arbitrary boundary conditions. This concept has been extended to treat singularities in two-dimensional acoustic problems [225, 220] and plate membrane problems [198], although it is shown that in certain configurations, logarithmic singularities are present, which cannot be handled by the proposed approach. Special purpose functions for the two-dimensional Biot model are only available for the so-called sliding edge boundary conditions [226, 222, 220], due to a lack of analytical solutions of the static problem for other combinations of boundary conditions. Therefore, another approach is shown in [227], where a coupling of the FEM and the WBM is proposed. The FEM is used to model the areas in the vicinity of the singularities, while the WBM is applied to the rest of the problem domain.

#### Multi-Level WBM

The requirement of the WBM that the domain has to be decomposed into convex sub-domains especially limits the method if a bounded domain contains several inclusions or multiple scatterers are present in an unbounded domain. To overcome these limitations,

## 4 The Wave Based Method

a multi-level approach has been proposed, where every inclusion (scatterer) is treated as a separate level and the superposition principle is applied to link all levels through the weighted residual method [14]. The problem geometries, which appear at the different levels, are very well suited for the application of the WBM, since in general only a low number of convex sub-domains is required for moderately complex inclusions (scatterers).

The Multi-Level WBM is first applied in [228] and [174] for two-dimensional acoustic problems with multiple scatterers in unbounded domains. The extension to three-dimensional unbounded acoustic problems is shown in [172] and in [229] symmetric boundary conditions for the Multi-Level WBM are derived to improve the computational efficiency for symmetric two- and three-dimensional acoustic problems. The application of the multi-level approach to bounded problems with multiple inclusions is shown in [175, 230] for the two-dimensional acoustic and membrane problem, in [13] for the two-dimensional plate bending problem (Kirchhoff plate theory) and in [231] for the two-dimensional Biot equations (poroelastic material).

A very similar approach is shown in [232] for certain concave problem domains without inclusions. A complement-graph conception is applied, which enables the analysis of concave geometries without a partitioning into convex sub-domains. Therefore, the concave problem domain is supplemented by artificial convex sub-domains to finally yield a convex geometry. The proposed method is used to analyze two-dimensional plate bending problems.

### Hybrid WB methods

Another possibility to enhance the WBM is the combination of the WBM with another numerical method, e.g. FEM, BEM, SEA or the Transfer Matrix Method. If each method is applied according to its own strengths, powerful hybrid methodologies can be obtained, which combine the advantages of both approaches.

#### a.) Hybrid Finite Element-Wave Based Method (FE-WBM)

The hybrid FE-WBM uses the geometric flexibility of the FEM to model the complex parts of the problem domain, while the WBM is applied in the remaining moderately complex areas to retain the computational efficiency. Several different coupling approaches are proposed to ensure the continuity between the FEM and the WBM domains.

The first hybrid FE-WBM approach is presented in [96] for two-dimensional acoustic problems in bounded domains. Three different types of auxiliary frames (Lagrange multiplier technique) are proposed to indirectly couple the FEM to the WBM, a pressure frame, a velocity frame and an equivalent velocity frame. Several applications of the hybrid FE-WBM applying a velocity frame are shown in [233] and [234] for two-dimensional bounded acoustic problems. A direct coupling approach is investigated in [235] and it is stated that the convergence rate of the direct and indirect coupling methods is very similar. A two-dimensional vibro-acoustic problem is examined in [236], where the structural domain and the adjacent acoustic domains are discretized with the FEM and the remaining acoustic areas are modeled with the WBM.

The extension to three-dimensional acoustic problems in bounded domains is presented in [237] and three different direct coupling approaches between FEM and WBM, the pressure-velocity coupling, the impedance coupling and a mixed impedance-pressure coupling, are proposed. A comparison of direct and indirect coupling approaches for three-dimensional acoustic problems in bounded domains can be found in [99] and [238]. In [239] a three-dimensional vibro-acoustic problem is analyzed with the hybrid FE-WBM, where the structural components are modelled with the FEM and the WBM is used in the acoustic domain. A direct coupling between the structural and acoustic domain is implemented. The same approach is used in [240] to study the sound transmission through a panel.

A further increase in the computational efficiency can be gained if a model reduction technique is applied to the FEM part of the hybrid FE-WBM. In [241, 101] a modally reduced structural FEM model, where the uncoupled structural modes are used to reduce the degrees of freedom, is directly coupled to an acoustic WBM model to solve three-dimensional vibro-acoustic problems. The analysis of three-dimensional interior acoustic problems is shown in [242, 243], where a direct coupling approach is applied to link a modally reduced acoustic FEM model to an acoustic WBM model. The Craig-Bampton approach is used to reduce the FEM model and a further optimization of the method is achieved, by applying a projection approach to the static constraint modes. A summary of these enhancements can be found in [230] and an application to a large-sized vehicle model in [244].

The hybrid FE-WBM for two-dimensional acoustic problems in unbounded domains has been developed in [172]. The FEM is used inside the truncation surface to model the complex geometry, while the WBM is applied in the exterior domain. The methodology is similar to the so-called DtN map, but is numerically more efficient [245].

The application of the hybrid FE-WBM to structural vibrations is shown in [246] for the plate membrane problem and in [17] for combined plate-beam problems, where the beams are modelled with the FEM and a direct coupling to a WBM plate model is implemented.

Finally the extension of the hybrid FE-WBM to the Biot model is carried out in [247] and [227]. The hybrid FE-WBM is especially used to treat corner singularities as mentioned in a previous section. In [248] and [20] a three-dimensional bounded acoustic problem coupled with a trim layer (poroelastic material) is analyzed with the hybrid FE-WBM. The acoustic domain is modeled with the WBM and the poroelastic material with FEM, which allows for a detailed description of the trim layer.

#### *b.) Hybrid Boundary Element-Wave Based Method (BE-WBM)*

Even though, the Multi-Level WBM leads to a significant improvement of the applicability of the WBM in case of several inclusions (scatterers) in the problem domain, only moderately complex inclusions (scatterers) can be handled due to the convexity requirement of the WBM. To overcome this limitation, the hybrid BE-WBM has been developed. The geometrical flexibility of the BEM is used to model the complex inclusions (scatterers), while the WBM is applied for the moderately ones to improve the computational efficiency.

In [249, 229] the hybrid BE-WBM is developed for two- and three-dimensional acoustic problems in unbounded domains. Similar to the Multi-Level WBM, simple scatterers are described in separate levels by the WBM, while the complex scatters are modeled with the

## 4 The Wave Based Method

BEM in one single level. The superposition principle and a weighted residual approach is applied to combine all levels in one system of linear equations.

The extension of the hybrid FE-WBM to two- and three-dimensional acoustic problems in bounded domains is shown in [250] and [251]. The complex inclusions are modelled by the BEM, while the moderately complex bounded domain and simple inclusions are described by the WBM. A significant increase in computational efficiency is reported compared to the FEM.

### *c.) Hybrid Wave Based Method-Statistical Energy Analysis (WBM-SEA)*

Depending on the frequency, each subsystem of a structure may have a different vibrational behaviour. While in the low frequency range, all subsystems can be accurately described by deterministic methods, statistical approaches have to be applied in the high frequency range due to the high dependency of the system response to uncertainties. In the so-called mid-frequency range, some of the subsystems still have a deterministic behaviour, while others have to be described in a statistical way. Therefore, the hybrid WBM-SEA has been developed, where the deterministic subsystems are modeled with the WBM, while the statistical subsystems are described by the SEA.

In [252] the hybrid WBM-SEA is developed for three-dimensional vibro-acoustic problems in bounded domains, following an approach shown in [253] for the hybrid FE-SEA. A deterministic acoustic WBM model is coupled to a SEA plate model. An interface grid is applied to couple the indirect deterministic WBM to the SEA. Further applications of the hybrid WBM-SEA can be found in [13].

### *d.) Hybrid Wave Based-Transfer Matrix Model (WBM-TMM)*

Another hybrid method, the hybrid Wave Based-Transfer Matrix Model (WBM-TMM), is developed in [254] to predict the transmission loss through a multilayered thin structure by analysing two acoustic chambers separated by the investigated panel. The WBM is used to model the acoustic chambers, while the multilayered panel is modelled with the TMM. In [255] this approach is extended to multilayered structures with air cavities. A slightly different approach is used in [20] and [256] to couple the WBM and the TMM. The method is applied to vibro-acoustic simulations, especially to investigate the absorption and transmission characteristics of multilayered materials.

## **Other improvements and extensions**

Several other improvements and extensions of the WBM have been made, which do not belong to the categories listed above. In [176] B-splines are used to model the problem geometry to improve the geometric flexibility of the WBM and different integration schemes are investigated and applied to two-dimensional acoustic problems. Different types of wave function selections are proposed in [257] and the effects on the convergence rates of the WBM are investigated. Attempts to increase the accuracy of the WBM are shown in [258], where the so-called V-Cycling method is applied and three different strategies, the Matrix Subdivision approach, the Optimization approach and orthonormal wave functions, are

implemented. An enrichment of the classical wave function set to incorporate a *priori* information of discontinuities in the boundary conditions is developed in [259].

A boundary and interface error indicator-controlled adaptive local refinement strategy for the WBM is proposed in [260] and [261] for three dimensional acoustic problems in unbounded domains. A low number of wave functions is used in an initial step and depending on the boundary and interface residuals, the number of wave functions is increased until a certain residual goal is reached.

In the WBM an analytical particular solution is required to transform the inhomogeneous partial differential equation(s) to homogeneous one(s) (see Section 4.1). In general, such analytical solutions are only available for simple source terms, e.g. a point source. Therefore, two different approaches are proposed in [19] and [20] based on the numerical integration of the point source solution and the decomposition of the applied source into the wave number domain. The methods are tested for two-dimensional plate vibration problems under distributed deterministic and random excitation.

In [262, 13] a very efficient way to perform a Monte Carlo simulation with the WBM is shown, where randomly distributed point masses are added to a plate. Another approach to include non-deterministic input parameters is developed in [263] by introducing the interval perturbation WBM and the hybrid perturbation WBM.

Several potential application areas of the WBM are reviewed in [264], [265] and [266].

### 4.3.3 Applications of the WBM to engineering problems

The sound transmission loss of finite lightweight multilayered structures is examined with the WBM in [267] and a comparison to measurements and the TMM shows very good results. The absorption, reflection and transmission coefficients of two-dimensional rigid frame porous structures with periodic inclusions are investigated in [268] using a unit cell model and the Bloch-Floquet boundary conditions. Therefore, the wave functions for periodic semi-infinite two-dimensional acoustics problems are derived and applied in the WBM. The acoustic performance of sound absorbing materials has been investigated in [219] using an equivalent fluid model for the porous material.

The sensitivity of a vibro-acoustic model to changes in the design parameters has been investigated in [269] by applying the WBM and the direct differentiation method, while in [270, 271] the WBM and the adjoint variable method are applied to investigate the sensitivity of a two-dimensional acoustic problem. In [272] the hybrid FE-WBM has been applied for a topology optimization of bounded acoustic problems, where the non-design domains are modeled by the WBM, while the design domains are described by a FEM model. A great increase in computational efficiency compared to a pure FEM model is reported. The optimization of an acoustic lens design has been carried out in [273] by applying the multi-level WBM and a genetic algorithm.

In [274] the WBM is used for the calculation of the structural intensity in a plates, while the frequency averaged input power into plates is evaluated in [275] by applying the Lorentzian function as weighting function.

#### *4 The Wave Based Method*

An efficient optimisation of local vibration control treatments for structural components is presented in [276] using the WBM and multilayered damping models are investigated in [277].

## **Part II**

# **Extensions and improvements of the Wave Based Method for structural vibrations**



# 5 Particular solution functions for plate bending vibrations

As outlined in Section 4.1.2, a particular solution function is required if the WBM is used to solve inhomogeneous partial differential equations. Especially for plate bending problems, an analytical closed-form solution is only available in the literature for an undamped isotropic plate under point force excitation. To extend the applicability of the WBM to other excitations, Jonckheere et al. [19] developed two methods, which allow for the introduction of distributed excitations in the WBM for plate vibrations. The first method uses a numerical integration of the point force solution (Hankel-based approach), while in the second approach the Fourier transform is applied to decompose the distributed load in the wavenumber domain (Fourier-based approach). The Hankel-based approach requires the numerical integration of highly oscillating functions for each response point and is therefore computationally demanding, especially for large excitation areas. The Fourier-based approach performs very well if the forward and inverse Fourier transform can be calculated analytically. For localized discontinuous loads, the Fourier-based approach leads to inaccurate results, since the so-called Gibbs phenomenon appears [20].

In this chapter, the point force excitation of Kirchhoff and Mindlin plates is reviewed and damping through a complex Young's modulus is introduced. To extend the applicability of the WBM, the closed-form solutions for harmonic vibrations of Kirchhoff and Mindlin plates subjected to a constant harmonic ring load, a constant harmonic circular load and an alternating harmonic circular load are derived. Two different approaches are applied to define closed-form analytical solutions. The first approach uses the analytical integration of the harmonic point force solution, while the second approach applies the Hankel transform to solve the inhomogeneous partial differential equations.

In Section 5.1, the Hankel transform, the residue theorem and Jordan's lemma, which are required to derive the new particular solutions, are stated. The solutions for the Mindlin theory are developed in Section 5.2 and the solutions for the Kirchhoff theory are derived as special case of the Mindlin solutions in Section 5.3.

## 5.1 Basic mathematical principles

The Hankel transform is a powerful integral transformation technique for axisymmetric problems, e.g. the plate bending problem under point force excitation. Its definition and properties, which are used to solve the subsequent problems, are stated in Section 5.1.1. Especially the inverse Hankel transform requires the integration of complicated integrands over infinite limits. Therefore, in Section 5.1.2 the basics of the residue theorem

and Jordan's lemma, which are very useful tools to evaluate these kinds of integrals, are shown.

### 5.1.1 The Hankel transform

The Hankel transform is an integral transformation technique, which is used in the following sections to solve the axisymmetric plate vibration problems. The forward and inverse Hankel transform of order zero and one are defined by [278]

$$\mathcal{H}_0[f(r)] = \tilde{f}(k_r) = \int_{r=0}^{\infty} f(r) r J_0(k_r r) dr, \quad (5.1)$$

$$\mathcal{H}_0^{-1}[\tilde{f}(k_r)] = f(r) = \int_{k_r=0}^{\infty} \tilde{f}(k_r) k_r J_0(k_r r) dk_r, \quad (5.2)$$

$$\mathcal{H}_1[f(r)] = \tilde{\tilde{f}}(k_r) = \int_{r=0}^{\infty} f(r) r J_1(k_r r) dr, \quad (5.3)$$

$$\mathcal{H}_1^{-1}[\tilde{\tilde{f}}(k_r)] = f(r) = \int_{k_r=0}^{\infty} \tilde{\tilde{f}}(k_r) k_r J_1(k_r r) dk_r, \quad (5.4)$$

with  $\tilde{f}(k_r)$  the zero-order and  $\tilde{\tilde{f}}(k_r)$  the first-order Hankel transform of the function  $f(r)$  and  $J_n(\bullet)$  the  $n^{\text{th}}$ -order Bessel function of the first kind. The operational properties of the Hankel transform [278]

$$\mathcal{H}_0\left[\left(\frac{d^2}{dr^2} + \frac{1}{r} \frac{d}{dr}\right)f(r)\right] = -k_r^2 \tilde{f}(k_r), \quad (5.5)$$

$$\mathcal{H}_1\left[\frac{df(r)}{dr}\right] = -k_r \tilde{\tilde{f}}(k_r), \quad (5.6)$$

are used in the subsequent derivations, to transform partial differential equations into algebraic ones.

### 5.1.2 The residue theorem and Jordan's lemma

The residue theorem is a method in complex analysis, which allows for the evaluation of line integrals over closed curves in the complex plane. Even though, the residue theorem is defined for integrals over closed curves in the complex plane, the evaluation of integrals on the real axis ranging from  $-\infty$  to  $\infty$  is possible. If Jordan's lemma is applicable, the residue theorem results in the integral formulas [279]

$$\int_{-\infty}^{\infty} f(x) e^{j a x} dx = \begin{cases} 2\pi j \sum_{k=1}^{s^+} \text{Res}_{z=z_k^+} [f(z) e^{j a z}] + \pi j \sum_{k=1}^m \text{Res}_{z=p_k} [f(z) e^{j a z}] & a > 0, \\ -2\pi j \sum_{k=1}^{s^-} \text{Res}_{z=z_k^-} [f(z) e^{j a z}] - \pi j \sum_{k=1}^m \text{Res}_{z=p_k} [f(z) e^{j a z}] & a < 0, \end{cases} \quad (5.7)$$

where  $z_k^+$  are poles in the upper half plane,  $z_k^-$  poles in the lower half plane,  $p_k$  poles on the real axis and  $\text{Res}[\bullet]$  is the residue at the pole. Equation (5.7) is only valid if the condition

$$\lim_{|z| \rightarrow +\infty} f(z) = 0 \quad (5.8)$$

is satisfied [279]. There are several methods for the evaluation of residues. Since only simple poles appear in the subsequent calculations, the formula [279]

$$\text{Res}_{z=z_k} \left[ f(z) e^{j a z} \right] = \lim_{z \rightarrow z_k} (z - z_k) f(z) e^{j a z} \quad (5.9)$$

can be applied, which is valid for simple poles  $z_k \neq \infty$ .

## 5.2 Particular solutions for the Mindlin plate theory

In this section, the particular solution function for a Mindlin plate under harmonic point load excitation is reviewed and a comparison with existing solutions is carried out. New solutions for a harmonic constant ring load, a harmonic constant circular load and a harmonic alternating circular load are derived with two different approaches, the analytical integration of the point force solution and the direct use of the Hankel transform.

An infinitely extended Mindlin plate is considered in the following and therefore no boundary conditions have to be fulfilled. The governing equations in terms of displacements for the out-of-plane deformation, given in Equations (2.52)–(2.54) for Cartesian coordinates, can be transformed into a polar coordinate system  $\{r, \varphi, z\}$  using  $x = r \cos(\varphi)$  and  $y = r \sin(\varphi)$ . For axisymmetric problems, the deformation is independent of  $\varphi$  and the governing equations for harmonic vibrations are simplified to [280]

$$\left( \nabla_a^2 - \frac{1}{r^2} + \frac{\rho h^3 \omega^2}{12 D} \right) \psi_r - \frac{k^2 G h}{D} \left( \psi_r + \frac{dw}{dr} \right) = 0, \quad (5.10)$$

$$\left( \frac{d}{dr} + \frac{1}{r} \right) \psi_r + \left( \nabla_a^2 + \frac{\rho \omega^2}{k^2 G} \right) w + \frac{1}{k^2 G h} \bar{q} = 0, \quad (5.11)$$

where  $\nabla_a^2 = \frac{d^2}{dr^2} + \frac{1}{r} \frac{d}{dr}$  is the two-dimensional Laplace operator in polar coordinates for axisymmetric problems,  $\psi_r = \psi_x \cos(\varphi) + \psi_y \sin(\varphi)$  is the positive rotation about the  $\varphi$ -axis and the moment loadings are set to  $\bar{m}_x = 0$  and  $\bar{m}_y = 0$ . Since the problem is axisymmetric, the negative rotation about the  $r$ -axis  $\psi_\varphi = -\psi_x \sin(\varphi) + \psi_y \cos(\varphi) = 0$ . Rewriting Equations (5.10) and (5.11) leads to a decoupled differential equation for the out-of-plane displacement

$$\left( \nabla_a^2 + k_{f1}^2 \right) \left( \nabla_a^2 + k_{f2}^2 \right) w = -\frac{S}{D} \left( \nabla_a^2 + R k_b^4 - S^{-1} \right) \bar{q} \quad (5.12)$$

and the rotation is given by

$$\psi_r = \left( R k_b^4 - S^{-1} \right)^{-1} \frac{d}{dr} \left( \left( \nabla_a^2 + S k_b^4 + S^{-1} \right) w + \frac{S}{D} \bar{q} \right). \quad (5.13)$$

In Equations (5.12) and (5.13), the flexural wavenumbers, defined in Equations (2.66) and (2.67), and the constants given in Equation (2.69) are used.

Instead of solving Equation (5.12) directly, the zero-order Hankel transform can be applied, which leads to

$$\tilde{w} = \frac{S(k_r^2 - R k_b^4 + S^{-1})}{D(k_r^2 - k_{f1}^2)(k_r^2 - k_{f2}^2)} \tilde{q}, \quad (5.14)$$

where the operational property of the Hankel transform, shown in Equation (5.5), is used. Similarly, the solution of Equation (5.13) can be determined from the first-order Hankel transform

$$\begin{aligned}\tilde{\psi}_r &= \left( R k_b^4 - S^{-1} \right)^{-1} k_r \left( \left( k_r^2 - S k_b^4 - S^{-1} \right) \tilde{w} - \frac{S}{D} \tilde{\bar{q}} \right) \\ &= \frac{k_r}{D \left( k_r^2 - k_{f1}^2 \right) \left( k_r^2 - k_{f2}^2 \right)} \tilde{\bar{q}},\end{aligned}\quad (5.15)$$

where Equations (5.6) and (5.14) are applied. If the zero-order Hankel transform of the external normal load  $\tilde{\bar{q}}$  is known, the inverse Hankel transforms of Equations (5.14) and (5.15) lead to the solution of the out-of-plane displacement  $w(r)$  and the rotation  $\psi_r(r)$  in the spatial domain.

### 5.2.1 Point load excitation

An external normal point load at the origin of the coordinate system ( $x = 0$  and  $y = 0$  or  $r = 0$ ) is defined by

$$\bar{q}_{point}(x, y) = \bar{q}_0 \delta(x) \delta(y) \quad \text{or} \quad \bar{q}_{point}(r) = \frac{\bar{q}_0 \delta(r)}{2\pi r}, \quad (5.16)$$

where  $\bar{q}_0$  is the amplitude of the harmonic point load and  $\delta(\bullet)$  the Dirac delta function. The corresponding zero-order Hankel transform is given by [278]

$$\tilde{\bar{q}}_{point}(k_r) = \frac{\bar{q}_0}{2\pi}. \quad (5.17)$$

Using Equation (5.17) in Equations (5.14) and (5.15) and applying the inverse Hankel transform leads to the solution of the out-of-plane displacement and rotation in an integral form

$$w_{point}(r) = \frac{S \bar{q}_0}{2\pi D} \int_{k_r=0}^{\infty} \frac{k_r^2 - R k_b^4 + S^{-1}}{\left( k_r^2 - k_{f1}^2 \right) \left( k_r^2 - k_{f2}^2 \right)} k_r J_0(k_r r) dk_r, \quad (5.18)$$

$$\psi_{r, point}(r) = \frac{\bar{q}_0}{2\pi D} \int_{k_r=0}^{\infty} \frac{k_r^2}{\left( k_r^2 - k_{f1}^2 \right) \left( k_r^2 - k_{f2}^2 \right)} J_1(k_r r) dk_r. \quad (5.19)$$

A closed-form solution of these integrals can be obtained, using the integral representations of the Bessel function of the first kind [281]

$$J_0(k_r r) = \frac{2}{\pi} \int_{u=0}^{\infty} \sin(k_r r \cosh(u)) du, \quad (5.20)$$

$$J_1(k_r r) = -\frac{2}{\pi} \int_{u=0}^{\infty} \cos(k_r r \cosh(u)) \cosh(u) du, \quad (5.21)$$

and interchanging the order of integration

$$w_{point}(r) = \frac{S \bar{q}_0}{\pi^2 D} \int_{u=0}^{\infty} \int_{k_r=0}^{\infty} \frac{k_r^2 - R k_b^4 + S^{-1}}{\left( k_r^2 - k_{f1}^2 \right) \left( k_r^2 - k_{f2}^2 \right)} k_r \sin(k_r r \cosh(u)) dk_r du, \quad (5.22)$$

$$\psi_{r, point}(r) = -\frac{\bar{q}_0}{\pi^2 D} \int_{u=0}^{\infty} \int_{k_r=0}^{\infty} \frac{k_r^2 \cosh(u)}{\left( k_r^2 - k_{f1}^2 \right) \left( k_r^2 - k_{f2}^2 \right)} \cos(k_r r \cosh(u)) dk_r du. \quad (5.23)$$

## 5.2 Particular solutions for the Mindlin plate theory

Both integrals are symmetric with respect to  $k_r$  and therefore can be written as

$$w_{point}(r) = \frac{S \bar{q}_0 j}{2 \pi^2 D} \int_{u=0}^{\infty} \int_{k_r=-\infty}^{\infty} \frac{k_r^2 - R k_b^4 + S^{-1}}{(k_r^2 - k_{f1}^2)(k_r^2 - k_{f2}^2)} k_r e^{-j k_r r \cosh(u)} dk_r du, \quad (5.24)$$

$$\psi_{r, point}(r) = -\frac{\bar{q}_0}{2 \pi^2 D} \int_{u=0}^{\infty} \int_{k_r=-\infty}^{\infty} \frac{k_r^2 \cosh(u)}{(k_r^2 - k_{f1}^2)(k_r^2 - k_{f2}^2)} e^{-j k_r r \cosh(u)} dk_r du, \quad (5.25)$$

since an integral of an odd function vanishes for a symmetric integration interval. The residue theorem and Jordan's lemma can be applied to perform the integration with respect to  $k_r$ .

In the following calculations, it is assumed that the material loss factor  $\eta > 0$ . The special case of an undamped plate is considered at the end of this section using the limit absorption principle stated in [282]. The integrands in Equations (5.24) and (5.25) have the same first-order poles, which are given by

$$k_{r1} = k_{f1} \quad \text{with } \text{Im}[k_{r1}] < 0 \text{ independent of } \omega, \quad (5.26)$$

$$k_{r2} = -k_{f1} \quad \text{with } \text{Im}[k_{r2}] > 0 \text{ independent of } \omega, \quad (5.27)$$

$$k_{r3} = k_{f2} \quad \text{with } \text{Im}[k_{r3}] > 0 \text{ for } \omega < \omega_c \text{ and } \text{Im}[k_{r3}] < 0 \text{ for } \omega > \omega_c, \quad (5.28)$$

$$k_{r4} = -k_{f2} \quad \text{with } \text{Im}[k_{r4}] < 0 \text{ for } \omega < \omega_c \text{ and } \text{Im}[k_{r4}] > 0 \text{ for } \omega > \omega_c, \quad (5.29)$$

with  $k_{f1} = \sqrt{k_{f1}^2}$  and  $k_{f2} = \sqrt{k_{f2}^2}$  (principal square roots),  $\omega_c$  the so-called cut-off frequency and  $\text{Im}[\bullet]$  the imaginary part of a complex number. While for the undamped case ( $\eta = 0$ ) the cut-off frequency is given by  $\omega_c = \sqrt{\frac{k^2 G}{\rho R}}$  [51], an explicit formula for  $\omega_c$  is not available in the general damped case ( $\eta > 0$ ). The implicit function  $g_{\omega_c}(\omega) = \text{Im}[k_{f2}^2]$  can be used to numerically calculate  $\omega_c$ , by evaluating the condition  $g_{\omega_c}(\omega = \omega_c) = 0$ .

Comparing the general integral formulas in Equation (5.7) with the integrals in Equations (5.24) and (5.25), it is apparent that the parameter  $a = -r \cosh(u) < 0$  and therefore, only simple poles in the lower half-plane contribute to the final results. Using Equation (5.9) and defining

$$g_w(k_r) = \frac{k_r^2 - R k_b^4 + S^{-1}}{(k_r^2 - k_{f1}^2)(k_r^2 - k_{f2}^2)} k_r e^{-j k_r r \cosh(u)}, \quad (5.30)$$

$$g_{\psi_r}(k_r) = \frac{k_r^2 \cosh(u)}{(k_r^2 - k_{f1}^2)(k_r^2 - k_{f2}^2)} e^{-j k_r r \cosh(u)}, \quad (5.31)$$

results in the residues at the simple poles

$$\text{Res}_{k_r=k_{f1}} [g_w(k_r)] = \frac{k_{f1}^2 - R k_b^4 + S^{-1}}{2(k_{f1}^2 - k_{f2}^2)} e^{-j k_{f1} r \cosh(u)}, \quad (5.32)$$

$$\text{Res}_{k_r=\mp k_{f2}} [g_w(k_r)] = -\frac{k_{f2}^2 - R k_b^4 + S^{-1}}{2(k_{f1}^2 - k_{f2}^2)} e^{\pm j k_{f2} r \cosh(u)}, \quad (5.33)$$

## 5 Particular solution functions for plate bending vibrations

$$\text{Res}_{k_r=k_{f1}} [g_{\psi_r}(k_r)] = \frac{k_{f1} \cosh(u)}{2(k_{f1}^2 - k_{f2}^2)} e^{-j k_{f1} r \cosh(u)}, \quad (5.34)$$

$$\text{Res}_{k_r=\mp k_{f2}} [g_{\psi_r}(k_r)] = \pm \frac{k_{f2} \cosh(u)}{2(k_{f1}^2 - k_{f2}^2)} e^{\pm j k_{f2} r \cosh(u)}. \quad (5.35)$$

The Heine's formulas for the integral representation of the Hankel functions [283]

$$H_0^{(1)}(z) = -\frac{2j}{\pi} \int_{u=0}^{\infty} e^{jz \cosh(u)} du, \quad 0 < \arg[z] < \pi, \quad (5.36)$$

$$H_0^{(2)}(z) = \frac{2j}{\pi} \int_{u=0}^{\infty} e^{-jz \cosh(u)} du, \quad -\pi < \arg[z] < 0, \quad (5.37)$$

$$H_1^{(1)}(z) = -\frac{2}{\pi} \int_{u=0}^{\infty} e^{jz \cosh(u)} \cosh(u) du, \quad 0 < \arg[z] < \pi, \quad (5.38)$$

$$H_1^{(2)}(z) = -\frac{2}{\pi} \int_{u=0}^{\infty} e^{-jz \cosh(u)} \cosh(u) du, \quad -\pi < \arg[z] < 0, \quad (5.39)$$

with  $H_n^{(1)}(\bullet)$  and  $H_n^{(2)}(\bullet)$  the  $n^{\text{th}}$ -order Hankel functions of the first and second kind, can be applied to perform the integration with respect to  $u$ . The final results are given by

$$w_{\text{point}}(r) = \frac{j \bar{q}_0}{4D(k_{f1}^2 - k_{f2}^2)} \left( \frac{1}{\mu_1 - 1} H_0^{(2)}(k_{f1} r) - \frac{1}{\mu_2 - 1} H_0^{(2)}(\mp k_{f2} r) \right), \quad (5.40)$$

$$\psi_{r,\text{point}}(r) = -\frac{j \bar{q}_0}{4D(k_{f1}^2 - k_{f2}^2)} \left( k_{f1} H_1^{(2)}(k_{f1} r) \pm k_{f2} H_1^{(2)}(\mp k_{f2} r) \right), \quad (5.41)$$

where the upper signs have to be applied for  $\omega < \omega_c$  and the lower signs for  $\omega > \omega_c$ . In the derivation of Equations (5.40) and (5.41), the relations between the Hankel functions [284]

$$H_0^{(1)}(jz) = -H_0^{(2)}(-jz), \quad H_1^{(1)}(jz) = H_1^{(2)}(-jz), \quad -\frac{1}{2}\pi < \arg[z] \leq \frac{1}{2}\pi, \quad (5.42)$$

are used. The final results in Equations (5.40) and (5.41) can be presented in a different form

$$w_{\text{point}}(r) = -\frac{j \bar{q}_0}{4D(k_{f1}^2 - k_{f2}^2)} \left( \frac{1}{\mu_1 - 1} H_0^{(1)}(-k_{f1} r) - \frac{1}{\mu_2 - 1} H_0^{(1)}(\pm k_{f2} r) \right), \quad (5.43)$$

$$= -\frac{\bar{q}_0}{2\pi D(k_{f1}^2 - k_{f2}^2)} \left( \frac{1}{\mu_1 - 1} K_0(j k_{f1} r) - \frac{1}{\mu_2 - 1} K_0(\mp j k_{f2} r) \right),$$

$$\psi_{r,\text{point}}(r) = -\frac{j \bar{q}_0}{4D(k_{f1}^2 - k_{f2}^2)} \left( k_{f1} H_1^{(2)}(-k_{f1} r) \pm k_{f2} H_1^{(2)}(\pm k_{f2} r) \right), \quad (5.44)$$

$$= \frac{j \bar{q}_0}{2\pi D(k_{f1}^2 - k_{f2}^2)} (k_{f1} K_1(j k_{f1} r) \pm k_{f2} K_1(\mp j k_{f2} r)),$$

applying Equation (5.42) or the relations [284]

$$K_0(z) = -\frac{1}{2}\pi j H_0^{(2)}(-jz), \quad K_1(z) = -\frac{1}{2}\pi H_1^{(2)}(-jz), \quad -\frac{1}{2}\pi < \arg[z] \leq \pi, \quad (5.45)$$

with  $K_n(\bullet)$  the  $n^{\text{th}}$ -order modified Bessel function of the second kind.

The out-of-plane displacement  $w_{point}(r)$  and the rotation  $\psi_{r,point}(r)$  of a steel plate ( $E = 2.1 \times 10^{11} \text{ N/m}^2$ ,  $\rho = 7850 \text{ kg/m}^3$ ,  $\nu = 0.3$ ,  $h = 2 \text{ mm}$ ) excited by a point load  $\bar{q}_0 = 1 \text{ N}$  at angular frequency  $\omega = 1200 \text{ rad/s}$  are shown in Figure 5.1. The shear correction factor  $k_W$  is applied and the material loss factor  $\eta$  is varied from 0 (undamped plate) to 0.5 (highly damped plate). It is apparent from Figure 5.1 that the displacement and rotation decay with rising distance from the source point. As expected, the decay is more pronounced for higher damping values.

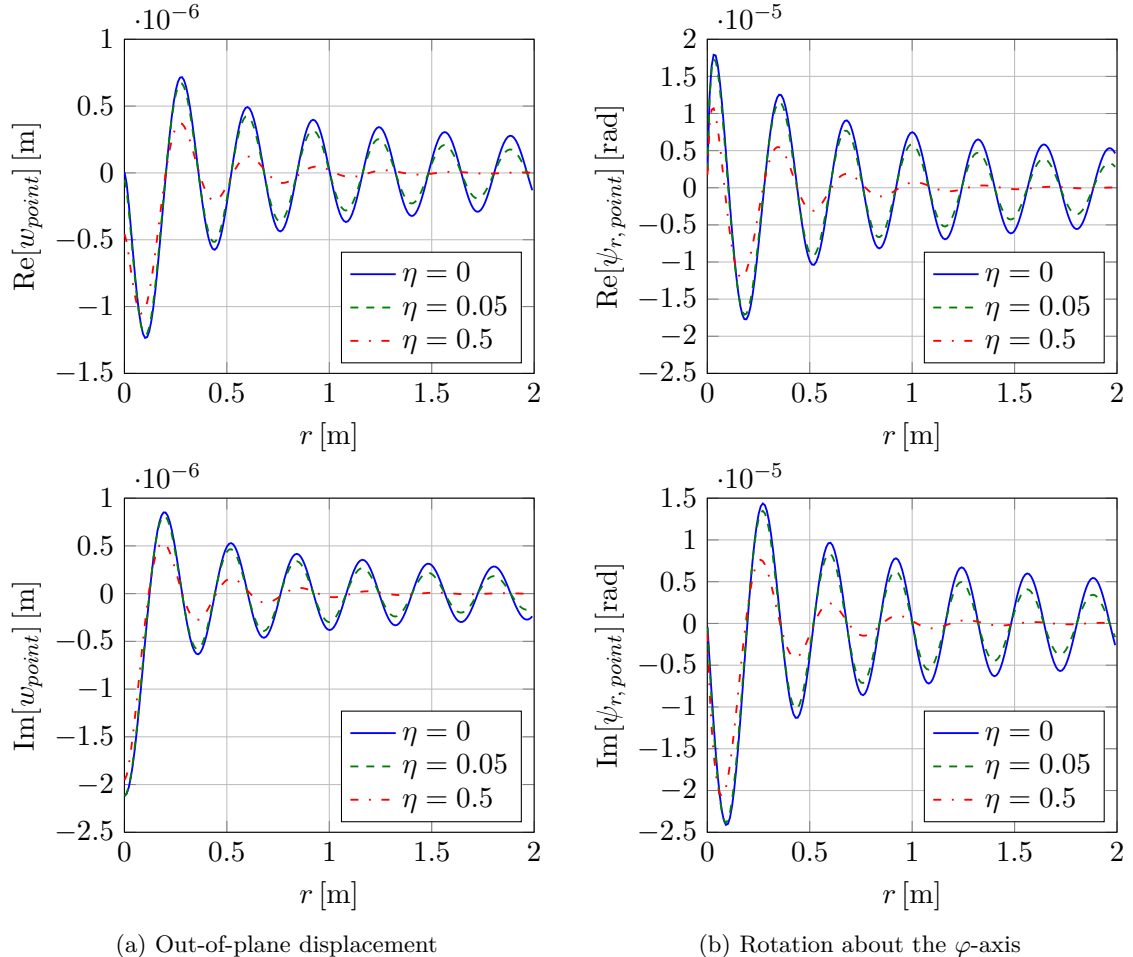


Figure 5.1: Out-of-plane displacement  $w_{point}$  and rotation about the  $\varphi$ -axis  $\psi_{r,point}$  of an infinite Mindlin plate excited by a harmonic point load at  $r = 0$

### Limit absorption principle - the undamped plate

According to the limit absorption principle, which is stated in [282], a purely elastic solid is an idealization of a weakly absorbing material and therefore the solution of the undamped plate can be found by the limiting case  $\eta \rightarrow 0$ . Since  $k_{f1}^2$  is always real positive for  $\eta \rightarrow 0$ , the principle square root  $k_{f1} = \sqrt{k_{f1}^2}$  is also real positive. Depending on the frequency,

$k_{f2}^2$  is either real negative ( $\omega < \omega_c$ ) or real positive ( $\omega > \omega_c$ ). The principle square roots are therefore given by  $k_{f2} = j \sqrt{|k_{f2}^2|}$  ( $\omega < \omega_c$ ) and  $k_{f2} = \sqrt{k_{f2}^2}$  ( $\omega > \omega_c$ ).

The results for an undamped plate excited by a harmonic point load, given by Rose and Wang [51], lead to the same amplitude as the results given in Equation (5.43), but are complex conjugated. A numerical integration of Equations (5.18) and (5.19) for an arbitrary parameter set agrees with the results shown in Equations (5.43) and (5.44) and therefore it is assumed that the presented derivations are mathematically correct.

### Point load at an arbitrary point of the coordinate system

If the point of excitation is not located at the origin of the coordinate system, but at an arbitrary position  $(\check{r}, \check{\varphi})$ , see Figure 5.2, a shift of the coordinate system can be performed to calculate the out-of-plane displacement  $w_{point}(r, \varphi)$  and the rotations  $\psi_{r, point}(r, \varphi)$  and  $\psi_{\varphi, point}(r, \varphi)$ . Transforming the solutions  $w_{point}(r_1)$  and  $\psi_{r_1, point}(r_1)$  to the coordinate system  $(r, \varphi)$  leads to

$$w_{point}(r, \varphi) = \frac{j \bar{q}_0}{4 D (k_{f1}^2 - k_{f2}^2)} \left( \frac{1}{\mu_1 - 1} H_0^{(2)}(k_{f1} d) - \frac{1}{\mu_2 - 1} H_0^{(2)}(\mp k_{f2} d) \right), \quad (5.46)$$

$$\psi_{r, point}(r, \varphi) = -\frac{j \bar{q}_0 (r - \check{r} \cos(\varphi - \check{\varphi}))}{4 d D (k_{f1}^2 - k_{f2}^2)} \left( k_{f1} H_1^{(2)}(k_{f1} d) \pm k_{f2} H_1^{(2)}(\mp k_{f2} d) \right), \quad (5.47)$$

$$\psi_{\varphi, point}(r, \varphi) = -\frac{j \bar{q}_0 \check{r} \sin(\varphi - \check{\varphi})}{4 d D (k_{f1}^2 - k_{f2}^2)} \left( k_{f1} H_1^{(2)}(k_{f1} d) \pm k_{f2} H_1^{(2)}(\mp k_{f2} d) \right), \quad (5.48)$$

with the distance of the response point  $P$  to the point of excitation

$$d = \sqrt{r^2 + \check{r}^2 - 2 r \check{r} \cos(\varphi - \check{\varphi})}. \quad (5.49)$$

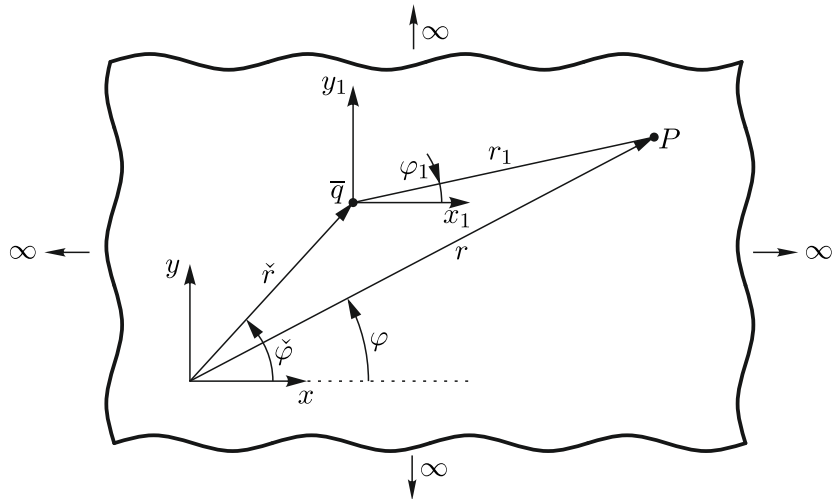


Figure 5.2: Point load at an arbitrary position  $(\check{r}, \check{\varphi})$

### 5.2.2 Other axisymmetric load cases

In this section, the solutions for a Mindlin plate excited by a constant harmonic ring load and a constant harmonic circular load, shown in Figures 5.3a and 5.3b, are derived. Since the problems are axisymmetric, two different approaches can be used to find the solutions. In the first approach, an analytical integration of the point force solution, given in Equations (5.46) – (5.48), is performed, using the addition theorems for Bessel functions. A similar technique has been applied in [285] for the analysis of pavement structures. The second technique is based on the Hankel transform and a direct evaluation of the resulting integrals.

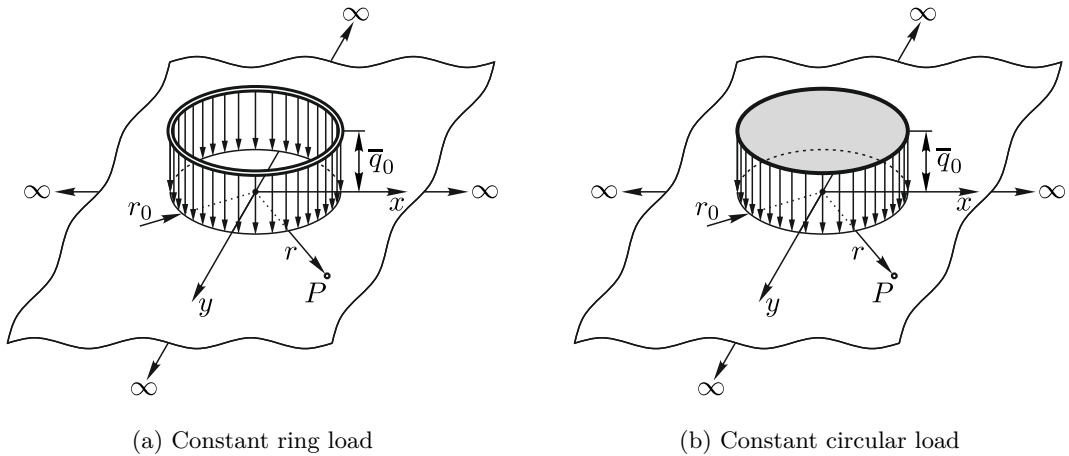


Figure 5.3: Other axisymmetric load cases

#### Constant ring load

The constant ring load, illustrated in Figure 5.3a, is given by

$$\bar{q}_{ring}(\check{r}) = \bar{q}_0 \delta(\check{r} - r_0), \quad (5.50)$$

where  $\bar{q}_0$  is the load per unit length and  $r_0$  the radius of the constant ring load. Since the governing equations of the Mindlin plate theory are linear partial differential equations, the solution for an arbitrary distributed load can be found by an integration of the unit point force solution multiplied by the load distribution. This results in

$$w_{ring}(r, \varphi) = \int_{\check{r}=0}^{\infty} \int_{\check{\varphi}=0}^{2\pi} \bar{q}_{ring}(\check{r}) w_{point}(r, \varphi, \check{r}, \check{\varphi}) \check{r} d\check{\varphi} d\check{r}, \quad (5.51)$$

$$\psi_{r, ring}(r, \varphi) = \int_{\check{r}=0}^{\infty} \int_{\check{\varphi}=0}^{2\pi} \bar{q}_{ring}(\check{r}) \psi_{r, point}(r, \varphi, \check{r}, \check{\varphi}) \check{r} d\check{\varphi} d\check{r}, \quad (5.52)$$

$$\psi_{\varphi, ring}(r, \varphi) = \int_{\check{r}=0}^{\infty} \int_{\check{\varphi}=0}^{2\pi} \bar{q}_{ring}(\check{r}) \psi_{\varphi, point}(r, \varphi, \check{r}, \check{\varphi}) \check{r} d\check{\varphi} d\check{r}, \quad (5.53)$$

where Equations (5.46) – (5.48) are applied.

## 5 Particular solution functions for plate bending vibrations

The integrals with respect to  $\check{\varphi}$  can be evaluated using the addition theorems for Bessel functions [281, 283]

$$H_0^{(2)}(\gamma z) = J_0(\gamma a) H_0^{(2)}(\gamma b) + 2 \sum_{m=1}^{\infty} J_m(\gamma a) H_m^{(2)}(\gamma b) \cos(m\beta), \quad (5.54)$$

$$z^{-1} H_1^{(2)}(\gamma z) = \frac{2}{\gamma a b} \sum_{m=0}^{\infty} (m+1) J_{m+1}(\gamma a) H_{m+1}^{(2)}(\gamma b) \frac{\sin((m+1)\beta)}{\sin(\beta)}, \quad (5.55)$$

$$\frac{b - a e^{-j\beta}}{z} H_1^{(2)}(\gamma z) = \sum_{m=-\infty}^{\infty} J_m(\gamma a) H_{m+1}^{(2)}(\gamma b) e^{j m \beta}, \quad (5.56)$$

with  $z = \sqrt{a^2 + b^2 - 2 a b \cos(\beta)}$  and the restriction  $b > a > 0$ . Applying the integral formulas for trigonometric functions

$$\int_{\check{\varphi}=0}^{2\pi} e^{j m (\varphi - \check{\varphi})} d\check{\varphi} = \begin{cases} 2\pi, & m = 0 \\ 0, & m \in \mathbb{Z} \setminus \{0\} \end{cases}, \quad (5.57)$$

$$\int_{\check{\varphi}=0}^{2\pi} \cos(m(\varphi - \check{\varphi})) d\check{\varphi} = \begin{cases} 2\pi, & m = 0 \\ 0, & m \in \mathbb{Z} \setminus \{0\} \end{cases}, \quad (5.58)$$

$$\int_{\check{\varphi}=0}^{2\pi} \sin(m(\varphi - \check{\varphi})) d\check{\varphi} = 0, \quad m \in \mathbb{Z}, \quad (5.59)$$

leads to

$$w_{ring}(r) = \frac{j\pi}{2D(k_{f1}^2 - k_{f2}^2)} \begin{cases} \int_{\check{r}=0}^{\infty} \bar{q}_{ring}(\check{r}) \left( \frac{J_0(k_{f1}\check{r}) H_0^{(2)}(k_{f1}r)}{\mu_1 - 1} - \frac{J_0(\mp k_{f2}\check{r}) H_0^{(2)}(\mp k_{f2}r)}{\mu_2 - 1} \right) \check{r} d\check{r}, & r > \check{r}, \\ \int_{\check{r}=0}^{\infty} \bar{q}_{ring}(\check{r}) \left( \frac{J_0(k_{f1}r) H_0^{(2)}(k_{f1}\check{r})}{\mu_1 - 1} - \frac{J_0(\mp k_{f2}r) H_0^{(2)}(\mp k_{f2}\check{r})}{\mu_2 - 1} \right) \check{r} d\check{r}, & r < \check{r}, \end{cases} \quad (5.60)$$

$$\psi_{r,ring}(r) = \frac{-j\pi}{2D(k_{f1}^2 - k_{f2}^2)} \begin{cases} \int_{\check{r}=0}^{\infty} \bar{q}_{ring}(\check{r}) \left( k_{f1} J_0(k_{f1}\check{r}) H_1^{(2)}(k_{f1}r) \pm k_{f2} J_0(\mp k_{f2}\check{r}) H_1^{(2)}(\mp k_{f2}r) \right) \check{r} d\check{r}, & r > \check{r}, \\ \int_{\check{r}=0}^{\infty} \bar{q}_{ring}(\check{r}) \left( k_{f1} J_1(k_{f1}r) H_0^{(2)}(k_{f1}\check{r}) \pm k_{f2} J_1(\mp k_{f2}r) H_0^{(2)}(\mp k_{f2}\check{r}) \right) \check{r} d\check{r}, & r < \check{r}, \end{cases} \quad (5.61)$$

$$\psi_{\varphi,ring}(r) = 0, \quad (5.62)$$

where the cases  $r > \check{r}$  and  $r < \check{r}$  have to be distinguished. Since the problem is axisymmetric for the chosen coordinate system, the results are independent of  $\varphi$  and the rotation  $\psi_{\varphi,ring}(r)$  is equal to zero.

## 5.2 Particular solutions for the Mindlin plate theory

The integration with respect to  $\check{r}$  leads to the final results

$$w_{ring}(r) = \frac{j \bar{q}_0 \pi r_0}{2 D (k_{f1}^2 - k_{f2}^2)} \begin{cases} \left( \frac{J_0(k_{f1} r_0) H_0^{(2)}(k_{f1} r)}{\mu_1 - 1} - \frac{J_0(\mp k_{f2} r_0) H_0^{(2)}(\mp k_{f2} r)}{\mu_2 - 1} \right), & r > r_0, \\ \left( \frac{J_0(k_{f1} r) H_0^{(2)}(k_{f1} r_0)}{\mu_1 - 1} - \frac{J_0(\mp k_{f2} r) H_0^{(2)}(\mp k_{f2} r_0)}{\mu_2 - 1} \right), & r < r_0, \end{cases} \quad (5.63)$$

$$\psi_{r,ring}(r) = \frac{-j \bar{q}_0 \pi r_0}{2 D (k_{f1}^2 - k_{f2}^2)} \begin{cases} \left( k_{f1} J_0(k_{f1} r_0) H_1^{(2)}(k_{f1} r) \pm k_{f2} J_0(\mp k_{f2} r_0) H_1^{(2)}(\mp k_{f2} r) \right), & r > r_0, \\ \left( k_{f1} J_1(k_{f1} r) H_0^{(2)}(k_{f1} r_0) \pm k_{f2} J_1(\mp k_{f2} r) H_0^{(2)}(\mp k_{f2} r_0) \right), & r < r_0, \end{cases} \quad (5.64)$$

where the integration property of the Dirac delta function is used. From Equation (5.63) it is apparent that the out-of-plane displacement is finite at  $r = 0$  and continuous at  $r = r_0$ . The formula for the Wronskian determinant of Bessel functions [284]

$$J_1(x) H_0^{(2)}(x) - J_0(x) H_1^{(2)}(x) = -\frac{2i}{\pi x} \quad (5.65)$$

can be applied to show the continuity of the rotation  $\psi_{r,ring}$  at  $r = r_0$ .

In the second solution technique, the zero-order Hankel transform of the constant ring load

$$\tilde{\bar{q}}_{ring}(k_r) = \bar{q}_0 r_0 J_0(k_r r_0) \quad (5.66)$$

is combined with the transformed solutions of the Mindlin plate given in Equations (5.14) and (5.15) and the inverse Hankel transform is applied

$$w_{ring}(r) = \frac{S \bar{q}_0 r_0}{D} \int_{k_r=0}^{\infty} \frac{k_r^2 - R k_b^4 + S^{-1}}{(k_r^2 - k_{f1}^2)(k_r^2 - k_{f2}^2)} k_r J_0(k_r r) J_0(k_r r_0) dk_r, \quad (5.67)$$

$$\psi_{r,ring}(r) = \frac{\bar{q}_0 r_0}{D} \int_{k_r=0}^{\infty} \frac{k_r^2}{(k_r^2 - k_{f1}^2)(k_r^2 - k_{f2}^2)} J_1(k_r r) J_0(k_r r_0) dk_r. \quad (5.68)$$

The evaluation of these integrals can be done by the general formula for integrals involving products of two Bessel functions [286]

$$\int_{x=0}^{\infty} \frac{x^{\mu-\nu+2\ell+1}}{x^2 + a^2} J_{\mu}(p x) J_{\nu}(q x) dx = (-1)^{\ell} a^{\mu-\nu+2\ell} K_{\mu}(p a) I_{\nu}(q a) \quad \ell \in \mathbb{N}_0, \quad (5.69)$$

## 5 Particular solution functions for plate bending vibrations

with the restrictions

$$-(\ell + 1) < \operatorname{Re}[\mu] < \operatorname{Re}[\nu] - 2\ell + 2 \quad \text{and} \quad p > q \quad \text{and} \quad -\frac{\pi}{2} < \arg[a] < \frac{\pi}{2} \quad (5.70)$$

and  $I_n(\bullet)$  the  $n^{\text{th}}$ -order modified Bessel function of the first kind. Using the partial fraction decompositions

$$\frac{S(k_r^2 - R k_b^4 + S^{-1})}{(k_r^2 - k_{f1}^2)(k_r^2 - k_{f2}^2)} = \frac{1}{k_{f1}^2 - k_{f2}^2} \left( \frac{-1}{(\mu_1 - 1)(k_r^2 - k_{f1}^2)} + \frac{1}{(\mu_2 - 1)(k_r^2 - k_{f2}^2)} \right), \quad (5.71)$$

$$\begin{aligned} \frac{k_r}{(k_r^2 - k_{f1}^2)(k_r^2 - k_{f2}^2)} &= \frac{1}{k_{f1}^2 - k_{f2}^2} \left( \frac{k_r}{k_r^2 - k_{f1}^2} - \frac{k_r}{k_r^2 - k_{f2}^2} \right) \\ &= \frac{1}{k_r(k_{f1}^2 - k_{f2}^2)} \left( \frac{k_{f1}^2}{k_r^2 - k_{f1}^2} - \frac{k_{f2}^2}{k_r^2 - k_{f2}^2} \right), \end{aligned} \quad (5.72)$$

and the parameters  $\mu = 0$ ,  $\nu = 0$  and  $l = 0$  to evaluate the integral in Equation (5.67) and the parameters  $\mu = 1$ ,  $\nu = 0$ ,  $l = 0$  for  $r > r_0$  and  $\mu = 0$ ,  $\nu = 1$ ,  $l = 0$  for  $r < r_0$  to integrate Equation (5.68) result in

$$w_{ring}(r) = \frac{-\bar{q}_0 r_0}{D(k_{f1}^2 - k_{f2}^2)} \begin{cases} \left( \frac{I_0(j k_{f1} r_0) K_0(j k_{f1} r)}{\mu_1 - 1} - \frac{I_0(\mp j k_{f2} r_0) K_0(\mp j k_{f2} r)}{\mu_2 - 1} \right), & r > r_0, \\ \left( \frac{I_0(j k_{f1} r) K_0(j k_{f1} r_0)}{\mu_1 - 1} - \frac{I_0(\mp j k_{f2} r) K_0(\mp j k_{f2} r_0)}{\mu_2 - 1} \right), & r < r_0, \end{cases} \quad (5.73)$$

$$\psi_{r,ring}(r) = \frac{j \bar{q}_0 r_0}{D(k_{f1}^2 - k_{f2}^2)} \begin{cases} (k_{f1} I_0(j k_{f1} r_0) K_1(j k_{f1} r) \pm k_{f2} I_0(\mp j k_{f2} r_0) K_1(\mp j k_{f2} r)), & r > r_0, \\ (-k_{f1} I_1(j k_{f1} r) K_0(j k_{f1} r_0) \mp k_{f2} I_1(\mp j k_{f2} r) K_0(\mp j k_{f2} r_0)), & r < r_0, \end{cases} \quad (5.74)$$

which become equivalent to Equations (5.63) and (5.64) if the relations between the Bessel functions

$$I_0(z) = J_0(-j z), \quad I_1(z) = j J_1(-j z), \quad -\pi < \arg[z] \leq \frac{1}{2}\pi, \quad (5.75)$$

and the relations shown in Equation (5.45) are applied.

If the radius of the ring load approaches zero and the load per unit length is set to  $\bar{q}_0 \mapsto \frac{\bar{q}_0}{2\pi r_0}$ , the ring load becomes equivalent to a point load. Using  $J_0(0) = 1$  or  $I_0(0) = 1$ , it follows from Equations (5.63) and (5.64) or Equations (5.73) and (5.74) that  $w_{ring}(r) = w_{point}(r)$  and  $\psi_{r,ring}(r) = \psi_{r,point}(r)$  for  $r_0 \rightarrow 0$ .

The out-of-plane displacement  $w_{ring}(r)$  and the rotation  $\psi_{r,ring}(r)$  of a steel plate (parameters as in the previous section) excited by a constant ring load ( $\bar{q}_0 = \frac{1}{2\pi r_0} \text{ N/m}$ ,

$r_0 = 0.8$  m) at angular frequency  $\omega = 1200$  rad/s are illustrated in Figure 5.4. The shear correction factor  $k_W$  is applied. The out-of-plane displacement and the rotation are continuous at  $r = r_0$  and are decaying with rising  $r$  (more pronounced for higher  $\eta$ ). The maximum displacement and rotation are approximately five times lower compared to the point force excitation, even though the total load is equivalent in both cases.

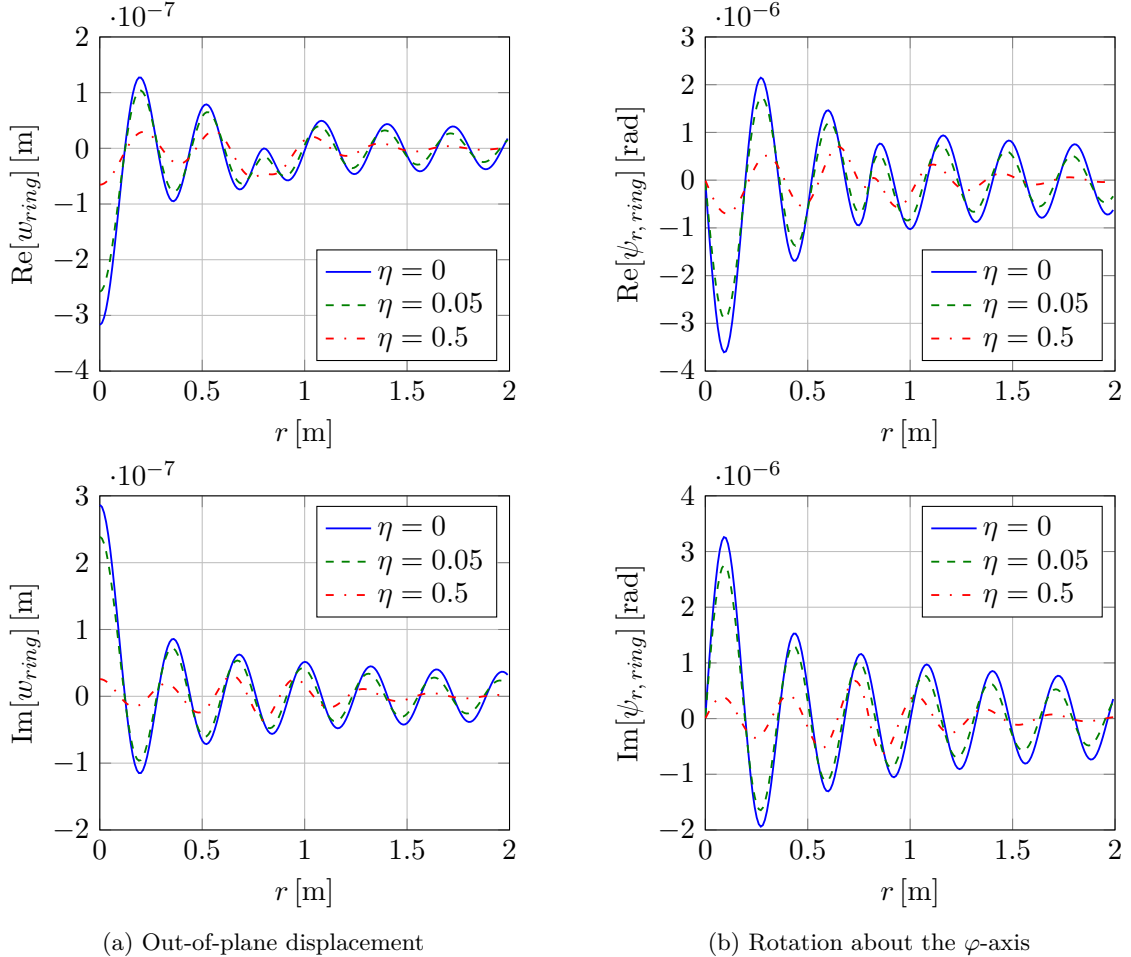


Figure 5.4: Out-of-plane displacement  $w_{ring}$  and rotation about the  $\varphi$ -axis  $\psi_{r,ring}$  of an infinite Mindlin plate excited by a harmonic ring load with  $r_0 = 0.8$

### Constant circular load

The constant circular load, shown in Figure 5.3b, is defined by

$$\bar{q}_{circ}(\check{r}) = \bar{q}_0 H(r_0 - \check{r}), \quad (5.76)$$

where  $\bar{q}_0$  is the amplitude of the surface pressure,  $H(\bullet)$  the Heaviside step function and  $r_0$  the radius of the constant circular load. Similar to the solution of the constant ring load,

an integration of the unit point force solution multiplied by the circular load distribution can be applied to find the out-of-plane displacement and the rotations

$$w_{circ}(r, \varphi) = \int_{\check{r}=0}^{\infty} \int_{\check{\varphi}=0}^{2\pi} \bar{q}_{circ}(\check{r}) w_{point}(r, \varphi, \check{r}, \check{\varphi}) \check{r} d\check{\varphi} d\check{r}, \quad (5.77)$$

$$\psi_{r, circ}(r, \varphi) = \int_{\check{r}=0}^{\infty} \int_{\check{\varphi}=0}^{2\pi} \bar{q}_{circ}(\check{r}) \psi_{r, point}(r, \varphi, \check{r}, \check{\varphi}) \check{r} d\check{\varphi} d\check{r}, \quad (5.78)$$

$$\psi_{\varphi, circ}(r, \varphi) = \int_{\check{r}=0}^{\infty} \int_{\check{\varphi}=0}^{2\pi} \bar{q}_{circ}(\check{r}) \psi_{\varphi, point}(r, \varphi, \check{r}, \check{\varphi}) \check{r} d\check{\varphi} d\check{r}. \quad (5.79)$$

The integration with respect to  $\check{\varphi}$  is equivalent to the integrations from Equations (5.51)–(5.53) to Equations (5.60)–(5.62). Applying the property of the Heaviside step function leads to

$$w_{circ}(r) = \frac{j \bar{q}_0 \pi}{2 D (k_{f1}^2 - k_{f2}^2)} \begin{cases} \int_{\check{r}=0}^{r_0} \left( \frac{J_0(k_{f1} \check{r}) H_0^{(2)}(k_{f1} r)}{\mu_1 - 1} - \frac{J_0(\mp k_{f2} \check{r}) H_0^{(2)}(\mp k_{f2} r)}{\mu_2 - 1} \right) \check{r} d\check{r}, & r > r_0, \\ \left( \int_{\check{r}=0}^r \left( \frac{J_0(k_{f1} \check{r}) H_0^{(2)}(k_{f1} r)}{\mu_1 - 1} - \frac{J_0(\mp k_{f2} \check{r}) H_0^{(2)}(\mp k_{f2} r)}{\mu_2 - 1} \right) \check{r} d\check{r} \right. \\ \left. + \int_{\check{r}=r}^{r_0} \left( \frac{J_0(k_{f1} r) H_0^{(2)}(k_{f1} \check{r})}{\mu_1 - 1} - \frac{J_0(\mp k_{f2} r) H_0^{(2)}(\mp k_{f2} \check{r})}{\mu_2 - 1} \right) \check{r} d\check{r} \right), & r < r_0, \end{cases} \quad (5.80)$$

$$\psi_{r, circ}(r) = \frac{-j \bar{q}_0 \pi}{2 D (k_{f1}^2 - k_{f2}^2)} \begin{cases} \int_{\check{r}=0}^{r_0} \left( k_{f1} J_0(k_{f1} \check{r}) H_1^{(2)}(k_{f1} r) \right. \\ \left. \pm k_{f2} J_0(\mp k_{f2} \check{r}) H_1^{(2)}(\mp k_{f2} r) \right) \check{r} d\check{r}, & r > r_0, \\ \left( \int_{\check{r}=0}^r \left( k_{f1} J_0(k_{f1} \check{r}) H_1^{(2)}(k_{f1} r) \right. \\ \left. \pm k_{f2} J_0(\mp k_{f2} \check{r}) H_1^{(2)}(\mp k_{f2} r) \right) \check{r} d\check{r} \right. \\ \left. + \int_{\check{r}=r}^{r_0} \left( k_{f1} J_1(k_{f1} r) H_0^{(2)}(k_{f1} \check{r}) \right. \\ \left. \pm k_{f2} J_1(\mp k_{f2} r) H_0^{(2)}(\mp k_{f2} \check{r}) \right) \check{r} d\check{r} \right), & r < r_0, \end{cases} \quad (5.81)$$

$$\psi_{\varphi, circ}(r) = 0, \quad (5.82)$$

where the cases  $r > r_0$  and  $r < r_0$  have to be distinguished.

## 5.2 Particular solutions for the Mindlin plate theory

To evaluate the integrals in Equations (5.80) and (5.81), the recurrence formulas for Bessel and Hankel functions [281]

$$\frac{d}{dz}(z J_1(z)) = z J_0(z) \quad \rightarrow \quad z J_1(z) = \int z J_0(z) dz, \quad (5.83)$$

$$\frac{d}{dz}(z H_1^{(2)}(z)) = z H_0^{(2)}(z) \quad \rightarrow \quad z H_1^{(2)}(z) = \int z H_0^{(2)}(z) dz, \quad (5.84)$$

and the formula for the Wronskian determinant of Bessel functions, given in Equation (5.65), can be applied. The integration with respect to  $r$  leads to the final results

$$w_{circ}(r) = \frac{j \bar{q}_0 \pi r_0}{2 D (k_{f1}^2 - k_{f2}^2)} \begin{cases} \left( \frac{J_1(k_{f1} r_0) H_0^{(2)}(k_{f1} r)}{(\mu_1 - 1) k_{f1}} \right. \\ \left. \pm \frac{J_1(\mp k_{f2} r_0) H_0^{(2)}(\mp k_{f2} r)}{(\mu_2 - 1) k_{f2}} \right), & r > r_0, \\ \left( \frac{J_0(k_{f1} r) H_1^{(2)}(k_{f1} r_0) - \frac{2j}{\pi k_{f1} r_0}}{(\mu_1 - 1) k_{f1}} \right. \\ \left. \pm \frac{J_0(\mp k_{f2} r) H_1^{(2)}(\mp k_{f2} r_0) \pm \frac{2j}{\pi k_{f2} r_0}}{(\mu_2 - 1) k_{f2}} \right), & r < r_0, \end{cases} \quad (5.85)$$

$$\psi_{r,circ}(r) = \frac{-j \bar{q}_0 \pi r_0}{2 D (k_{f1}^2 - k_{f2}^2)} \begin{cases} \left( J_1(k_{f1} r_0) H_1^{(2)}(k_{f1} r) \right. \\ \left. - J_1(\mp k_{f2} r_0) H_1^{(2)}(\mp k_{f2} r) \right), & r > r_0, \\ \left( J_1(k_{f1} r) H_1^{(2)}(k_{f1} r_0) \right. \\ \left. - J_1(\mp k_{f2} r) H_1^{(2)}(\mp k_{f2} r_0) \right), & r < r_0, \end{cases} \quad (5.86)$$

where the continuity of the rotation  $\psi_{r,circ}$  at  $r = r_0$  is apparent from Equation (5.86) and can be shown for the out-of-plane displacement  $w_{circ}$  by using Equation (5.65).

The results in Equations (5.85) and (5.86) can also be derived by the Hankel transform of the constant circular load, which is given by

$$\tilde{q}_{circ}(k_r) = \frac{\bar{q}_0 r_0}{k_r} J_1(k_r r_0). \quad (5.87)$$

Using the transformed solutions of the Mindlin plate (Equations (5.14) and (5.15)) and the inverse Hankel transform leads to

$$w_{circ}(r) = \frac{S \bar{q}_0 r_0}{D} \int_{k_r=0}^{\infty} \frac{k_r^2 - R k_b^4 + S^{-1}}{(k_r^2 - k_{f1}^2)(k_r^2 - k_{f2}^2)} J_0(k_r r) J_1(k_r r_0) dk_r, \quad (5.88)$$

$$\psi_{r,circ}(r) = \frac{\bar{q}_0 r_0}{D} \int_{k_r=0}^{\infty} \frac{k_r}{(k_r^2 - k_{f1}^2)(k_r^2 - k_{f2}^2)} J_1(k_r r) J_1(k_r r_0) dk_r. \quad (5.89)$$

The integrals in Equations (5.88) and (5.89) can be evaluated by the general formula given in Equation (5.69) and the partial fraction decompositions, shown in Equations (5.71) and (5.72). The parameters  $\mu = 0$ ,  $\nu = 1$  and  $l = 0$  have to be applied to solve Equation (5.88) for  $r > r_0$ , while an expanding of the fractions in Equation (5.71) to

$$\frac{1}{k_r^2 - k_{f1}^2} = \frac{1}{k_{f1}^2} \left( \frac{k_r^2}{k_r^2 - k_{f1}^2} - 1 \right), \quad (5.90)$$

$$\frac{1}{k_r^2 - k_{f2}^2} = \frac{1}{k_{f2}^2} \left( \frac{k_r^2}{k_r^2 - k_{f2}^2} - 1 \right) \quad (5.91)$$

is necessary to find the solution of Equation (5.88) for  $r < r_0$ . After the expansion, the parameters  $\mu = 1$ ,  $\nu = 0$  and  $l = 0$  can be used to evaluate the integrals involving the rational terms while the integrals with the constant factors are forms of discontinuous Weber-Schafheitlin integrals [281]

$$\int_{x=0}^{\infty} J_0(qx) J_1(px) dx = \begin{cases} 0, & p < q \\ \frac{1}{p}, & p > q \end{cases}. \quad (5.92)$$

Finally, the parameters  $\mu = 1$ ,  $\nu = 1$  and  $l = 0$  are used to evaluate the integrals in Equation (5.89), leading to

$$w_{circ}(r) = \frac{j \bar{q}_0 r_0}{D (k_{f1}^2 - k_{f2}^2)} \begin{cases} \left( \frac{I_1(j k_{f1} r_0) K_0(j k_{f1} r)}{(\mu_1 - 1) k_{f1}} \right. \\ \left. \pm \frac{I_1(\mp j k_{f2} r_0) K_0(\mp j k_{f2} r)}{(\mu_2 - 1) k_{f2}} \right), & r > r_0, \\ \left( - \frac{I_0(j k_{f1} r) K_1(j k_{f1} r_0) + \frac{j}{k_{f1} r_0}}{(\mu_1 - 1) k_{f1}} \right. \\ \left. \mp \frac{I_0(\mp j k_{f2} r) K_1(\mp j k_{f2} r_0) \mp \frac{j}{k_{f2} r_0}}{(\mu_2 - 1) k_{f2}} \right), & r < r_0, \end{cases} \quad (5.93)$$

$$\psi_{r, circ}(r) = \frac{\bar{q}_0 r_0}{D (k_{f1}^2 - k_{f2}^2)} \begin{cases} (I_1(j k_{f1} r_0) K_1(j k_{f1} r) \\ - I_1(\mp j k_{f2} r_0) K_1(\mp j k_{f2} r)), & r > r_0, \\ (I_1(j k_{f1} r) K_1(j k_{f1} r_0) \\ - I_1(\mp j k_{f2} r) K_1(\mp j k_{f2} r_0)), & r < r_0, \end{cases} \quad (5.94)$$

which become equivalent to Equations (5.85) and (5.86) if the relations between the Bessel function in Equations (5.45) and (5.75) are applied. The point force solution can be found as a limiting case of Equations (5.85) and (5.86) or Equations (5.93) and (5.94) by setting  $\bar{q}_0 \mapsto \frac{\bar{q}_0}{\pi r_0^2}$  and using the limits

$$\lim_{r_0 \rightarrow 0} \frac{J_1(z r_0)}{r_0} = \frac{z}{2}, \quad (5.95)$$

$$\lim_{r_0 \rightarrow 0} \frac{I_1(z r_0)}{r_0} = \frac{z}{2}. \quad (5.96)$$

In Figure 5.5, the out-of-plane displacement  $w_{circ}(r)$  and the rotation  $\psi_{r,circ}(r)$  of a steel plate (same parameters as in Figure 5.1) excited by a constant circular load ( $\bar{q}_0 = \frac{1}{\pi r_0^2} \text{ N/m}^2$ ,  $r_0 = 0.8 \text{ m}$ ) at angular frequency  $\omega = 1200 \text{ rad/s}$  are shown. The shear correction factor  $k_W$  is used. Similar to the constant ring load excitation, the out-of-plane displacement and the rotation are continuous at  $r = r_0$  and are decaying with rising  $r$ . The maximum displacement and rotation are even lower compared to the ring load excitation, which is expected since the load is spread over a larger area.

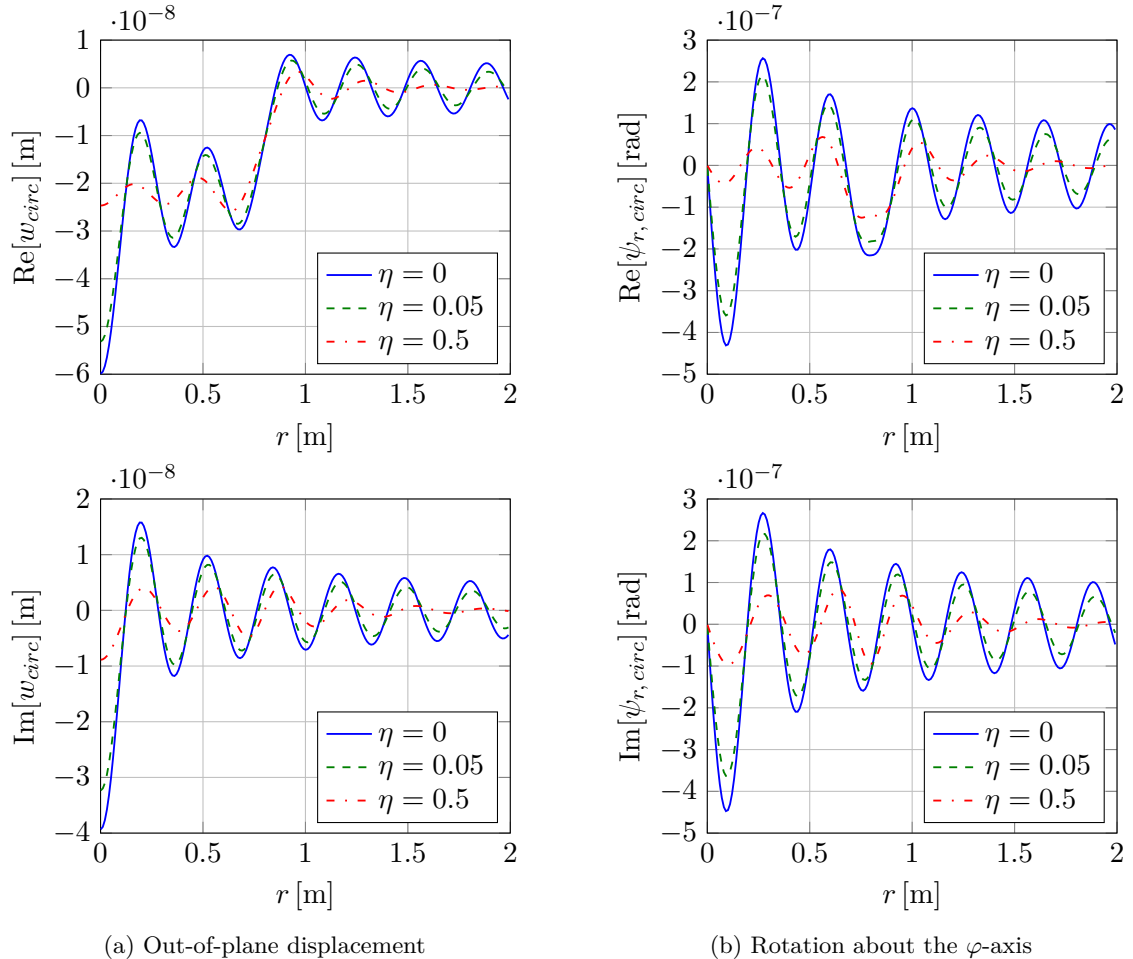


Figure 5.5: Out-of-plane displacement  $w_{circ}$  and rotation about the  $\varphi$ -axis  $\psi_{r,circ}$  of an infinite Mindlin plate excited by a harmonic circular load with  $r_0 = 0.8$

### 5.2.3 Non-axisymmetric loading

For certain types of non-axisymmetric loadings, a closed-form solution for the out-of-plane displacement and the rotations can be found by the analytical integration of the point force solution. A practically important non-axisymmetric loading, which occurs when a circular cylinder is mounted to a plate and excited by a harmonic horizontal force [287], is shown in Figure 5.6.

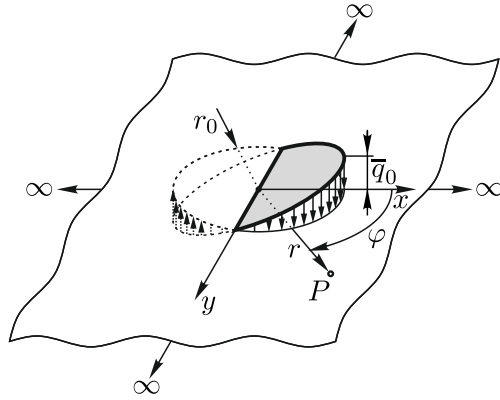


Figure 5.6: Alternating circular load

The alternating circular load is given in polar coordinates by

$$\bar{q}_{ac}(\check{r}, \check{\varphi}) = \frac{\bar{q}_0 \check{r}}{r_0} H(r_0 - \check{r}) \cos(\check{\varphi}), \quad (5.97)$$

where  $\bar{q}_0$  is the maximum amplitude and  $r_0$  the radius of the alternating circular load. The integration of the point force solution multiplied with the given loading leads to the out-of-plane displacement and rotations

$$w_{ac}(r, \varphi) = \int_{\check{r}=0}^{\infty} \int_{\check{\varphi}=0}^{2\pi} \bar{q}_{ac}(\check{r}) w_{point}(r, \varphi, \check{r}, \check{\varphi}) \check{r} d\check{\varphi} d\check{r}, \quad (5.98)$$

$$\psi_{r,ac}(r, \varphi) = \int_{\check{r}=0}^{\infty} \int_{\check{\varphi}=0}^{2\pi} \bar{q}_{ac}(\check{r}) \psi_{r,point}(r, \varphi, \check{r}, \check{\varphi}) \check{r} d\check{\varphi} d\check{r}, \quad (5.99)$$

$$\psi_{\varphi,ac}(r, \varphi) = \int_{\check{r}=0}^{\infty} \int_{\check{\varphi}=0}^{2\pi} \bar{q}_{ac}(\check{r}) \psi_{\varphi,point}(r, \varphi, \check{r}, \check{\varphi}) d\check{\varphi} \check{r} d\check{r}. \quad (5.100)$$

The evaluation of these integrals with respect to  $\check{\varphi}$  results in

$$w_{ac}(r, \varphi) = \frac{j \bar{q}_0 \pi \cos(\varphi)}{2 D (k_{f1}^2 - k_{f2}^2) r_0} \begin{cases} \int_{\check{r}=0}^{r_0} \left( \frac{J_1(k_{f1} \check{r}) H_1^{(2)}(k_{f1} r)}{\mu_1 - 1} - \frac{J_1(\mp k_{f2} \check{r}) H_1^{(2)}(\mp k_{f2} r)}{\mu_2 - 1} \right) \check{r}^2 d\check{r}, & r > r_0, \\ \left( \int_{\check{r}=0}^r \left( \frac{J_1(k_{f1} \check{r}) H_1^{(2)}(k_{f1} r)}{\mu_1 - 1} - \frac{J_1(\mp k_{f2} \check{r}) H_1^{(2)}(\mp k_{f2} r)}{\mu_2 - 1} \right) \check{r}^2 d\check{r} \right. \\ \left. + \int_{\check{r}=r}^{r_0} \left( \frac{J_1(k_{f1} r) H_1^{(2)}(k_{f1} \check{r})}{\mu_1 - 1} - \frac{J_1(\mp k_{f2} r) H_1^{(2)}(\mp k_{f2} \check{r})}{\mu_2 - 1} \right) \check{r}^2 d\check{r} \right), & r < r_0, \end{cases} \quad (5.101)$$

## 5.2 Particular solutions for the Mindlin plate theory

$$\psi_{r,ac}(r, \varphi) = \frac{j \bar{q}_0 \pi \cos(\varphi)}{4 D (k_{f1}^2 - k_{f2}^2) r_0} \begin{cases} \int_{\check{r}=0}^{r_0} \left( \frac{H_0^{(2)}(k_{f1} r) - H_2^{(2)}(k_{f1} r)}{(k_{f1} J_1(k_{f1} \check{r}))^{-1}} \right. \\ \left. \pm \frac{H_0^{(2)}(\mp k_{f2} r) - H_2^{(2)}(\mp k_{f2} r)}{(k_{f2} J_1(\mp k_{f2} \check{r}))^{-1}} \right) \check{r}^2 d\check{r}, & r > r_0, \\ \left( \int_{\check{r}=0}^r \left( \frac{H_0^{(2)}(k_{f1} r) - H_2^{(2)}(k_{f1} r)}{(k_{f1} J_1(k_{f1} \check{r}))^{-1}} \right. \right. \\ \left. \left. \pm \frac{H_0^{(2)}(\mp k_{f2} r) - H_2^{(2)}(\mp k_{f2} r)}{(k_{f2} J_1(\mp k_{f2} \check{r}))^{-1}} \right) \check{r}^2 d\check{r} \right. \\ \left. + \int_{\check{r}=r}^{r_0} \left( \frac{J_0(k_{f1} r) - J_2(k_{f1} r)}{(k_{f1} H_1^{(2)}(k_{f1} \check{r}))^{-1}} \right. \right. \\ \left. \left. \pm \frac{J_0(\mp k_{f2} r) - J_2(\mp k_{f2} r)}{(k_{f2} H_1^{(2)}(\mp k_{f2} \check{r}))^{-1}} \right) \check{r}^2 d\check{r} \right), & r < r_0, \end{cases} \quad (5.102)$$

$$\psi_{\varphi,ac}(r, \varphi) = \frac{-j \bar{q}_0 \pi \sin(\varphi)}{2 D (k_{f1}^2 - k_{f2}^2) r_0 r} \begin{cases} \int_{\check{r}=0}^{r_0} \left( J_1(k_{f1} \check{r}) H_1^{(2)}(k_{f1} r) \right. \\ \left. - J_1(\mp k_{f2} \check{r}) H_1^{(2)}(\mp k_{f2} r) \right) \check{r}^2 d\check{r}, & r > r_0, \\ \left( \int_{\check{r}=0}^r \left( J_1(k_{f1} \check{r}) H_1^{(2)}(k_{f1} r) \right. \right. \\ \left. \left. - J_1(\mp k_{f2} \check{r}) H_1^{(2)}(\mp k_{f2} r) \right) \check{r}^2 d\check{r} \right. \\ \left. + \int_{\check{r}=r}^{r_0} \left( J_1(k_{f1} r) H_1^{(2)}(k_{f1} \check{r}) \right. \right. \\ \left. \left. - J_1(\mp k_{f2} r) H_1^{(2)}(\mp k_{f2} \check{r}) \right) \check{r}^2 d\check{r} \right), & r < r_0, \end{cases} \quad (5.103)$$

where the addition theorems for Bessel functions (Equations (5.54)–(5.56)) and the integral formulas for trigonometric functions

$$\int_{\check{\varphi}=0}^{2\pi} \cos(\check{\varphi}) e^{jm(\varphi-\check{\varphi})} d\check{\varphi} = \begin{cases} \pi e^{\pm j\varphi}, & m = \pm 1 \\ 0, & m \in \mathbb{Z} \setminus \{ \pm 1 \} \end{cases}, \quad (5.104)$$

$$\int_{\check{\varphi}=0}^{2\pi} \cos(\check{\varphi}) \cos(m(\varphi-\check{\varphi})) d\check{\varphi} = \begin{cases} \pi \cos(\varphi), & m = 1 \\ 0, & m \in \mathbb{N}_0 \setminus \{ 1 \} \end{cases}, \quad (5.105)$$

$$\int_{\check{\varphi}=0}^{2\pi} \cos(\check{\varphi}) \sin(m(\varphi-\check{\varphi})) d\check{\varphi} = \begin{cases} \pi \sin(\varphi), & m = 1 \\ 0, & m \in \mathbb{N}_0 \setminus \{ 1 \} \end{cases}, \quad (5.106)$$

are applied. The recurrence formulas for Bessel and Hankel functions [281]

$$\frac{d}{dz} (z^2 J_2(z)) = z^2 J_1(z) \rightarrow z^2 J_2(z) = \int z^2 J_1(z) dz, \quad (5.107)$$

$$\frac{d}{dz} (z^2 H_2^{(2)}(z)) = z^2 H_1^{(2)}(z) \rightarrow z^2 H_2^{(2)}(z) = \int z^2 H_1^{(2)}(z) dz, \quad (5.108)$$

and the Wronskian determinants of Bessel functions [284]

$$J_1(x) H_2^{(2)}(x) - J_2(x) H_1^{(2)}(x) = \frac{2i}{\pi x} \quad (5.109)$$

$$J_2(x) H_0^{(2)}(x) - J_0(x) H_2^{(2)}(x) = -\frac{4i}{\pi x^2} \quad (5.110)$$

allow for the integration with respect to  $\check{r}$ , which leads to the final results

$$w_{ac}(r, \varphi) = \frac{j \bar{q}_0 \pi r_0 \cos(\varphi)}{2 D (k_{f1}^2 - k_{f2}^2)} \begin{cases} \left( \frac{J_2(k_{f1} r_0) H_1^{(2)}(k_{f1} r)}{k_{f1} (\mu_1 - 1)} \right. \\ \left. \pm \frac{J_2(\mp k_{f2} r_0) H_1^{(2)}(\mp k_{f2} r)}{k_{f2} (\mu_2 - 1)} \right), & r > r_0, \\ \left( \frac{J_1(k_{f1} r) H_2^{(2)}(k_{f1} r_0) - \frac{2j r}{\pi k_{f1} r_0^2}}{k_{f1} (\mu_1 - 1)} \right. \\ \left. \pm \frac{J_1(\mp k_{f2} r) H_2^{(2)}(\mp k_{f2} r_0) \pm \frac{2j r}{\pi k_{f2} r_0^2}}{k_{f2} (\mu_2 - 1)} \right), & r < r_0, \end{cases} \quad (5.111)$$

$$\psi_{r, ac}(r, \varphi) = \frac{j \bar{q}_0 \pi r_0 \cos(\varphi)}{4 D (k_{f1}^2 - k_{f2}^2)} \begin{cases} \left( \frac{H_0^{(2)}(k_{f1} r) - H_2^{(2)}(k_{f1} r)}{J_2(k_{f1} r_0)^{-1}} \right. \\ \left. - \frac{H_0^{(2)}(\mp k_{f2} r) - H_2^{(2)}(\mp k_{f2} r)}{J_2(\mp k_{f2} r_0)^{-1}} \right), & r > r_0, \\ \left( \frac{J_0(k_{f1} r) - J_2(k_{f1} r)}{H_2^{(2)}(k_{f1} r_0)^{-1}} - \frac{4j}{\pi k_{f1}^2 r_0^2} \right. \\ \left. - \frac{J_0(\mp k_{f2} r) - J_2(\mp k_{f2} r)}{H_2^{(2)}(\mp k_{f2} r_0)^{-1}} + \frac{4j}{\pi k_{f2}^2 r_0^2} \right), & r < r_0, \end{cases} \quad (5.112)$$

$$\psi_{\varphi, ac}(r, \varphi) = \frac{-j \bar{q}_0 \pi r_0 \sin(\varphi)}{2 D (k_{f1}^2 - k_{f2}^2) r} \begin{cases} \left( \frac{J_2(k_{f1} r_0) H_1^{(2)}(k_{f1} r)}{k_{f1}} \right. \\ \left. \pm \frac{J_2(\mp k_{f2} r_0) H_1^{(2)}(\mp k_{f2} r)}{k_{f2}} \right), & r > r_0, \\ \left( \frac{J_1(k_{f1} r) H_2^{(2)}(k_{f1} r_0) - \frac{2j r}{\pi k_{f1} r_0^2}}{k_{f1}} \right. \\ \left. \pm \frac{J_1(\mp k_{f2} r) H_2^{(2)}(\mp k_{f2} r_0) \pm \frac{2j r}{\pi k_{f2} r_0^2}}{k_{f2}} \right), & r < r_0, \end{cases} \quad (5.113)$$

where the cases  $r > r_0$  and  $r < r_0$  have to be distinguished.

Since the loading is not axisymmetric, the out-of-plane displacement and the rotations depend on  $r$  and  $\varphi$ . The continuity of the field variables  $w_{ac}$ ,  $\psi_{r,ac}$  and  $\psi_{\varphi,ac}$  at  $r = r_0$  is apparent if the Wronskian determinants given in Equations (5.109) and (5.110) are applied. The out-of-plane displacement  $w_{ac}(r, \varphi)$  and the rotations  $\psi_{r,ac}(r, \varphi)$  and  $\psi_{\varphi,ac}(r, \varphi)$  of a damped steel plate ( $\eta = 0.05$ ) excited by an alternating circular load ( $\bar{q}_0 = 1 \text{ N/m}^2$ ,  $r_0 = 0.8 \text{ m}$ ) at angular frequency  $\omega = 1200 \text{ rad/s}$  are illustrated in Figure 5.7.

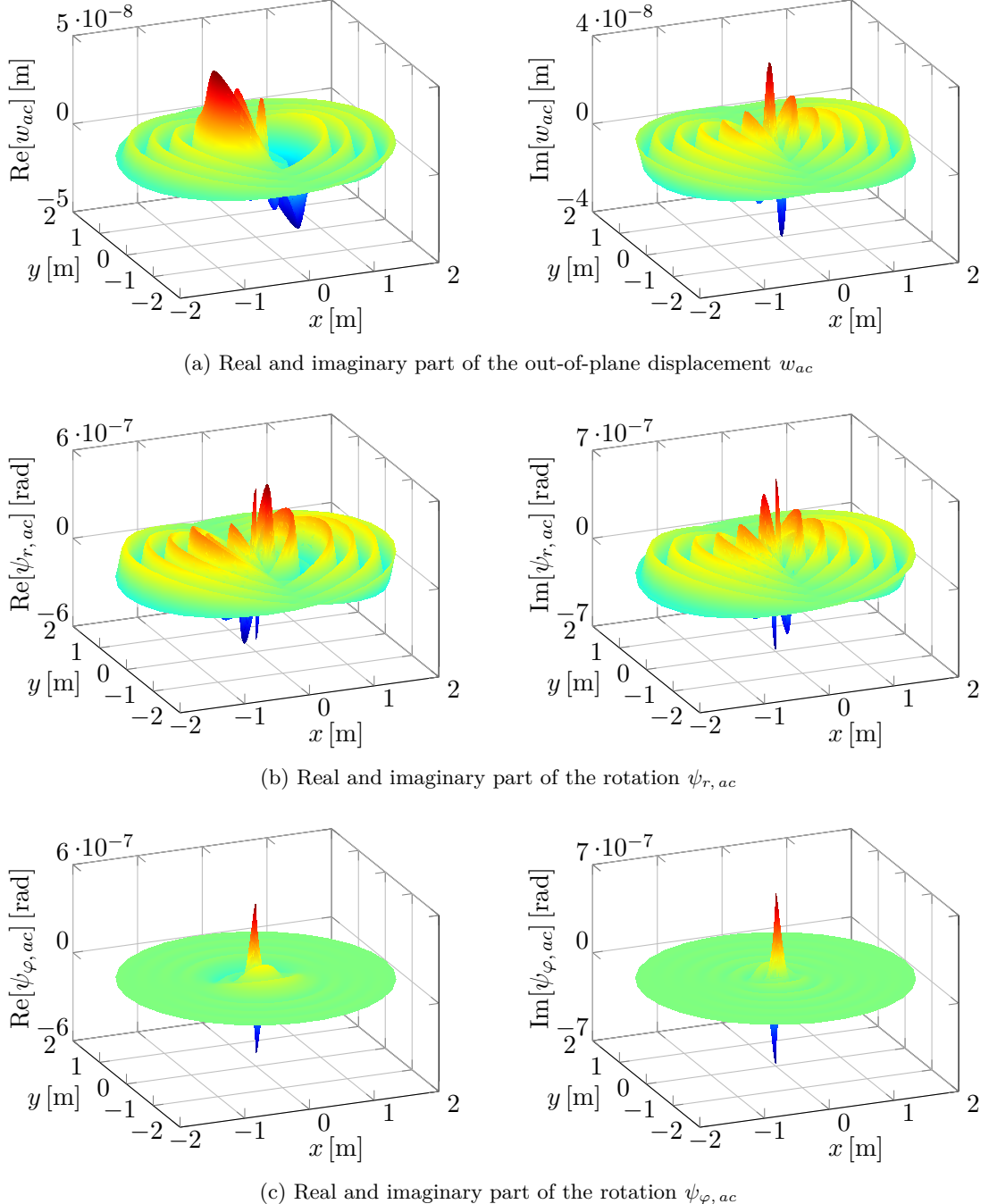


Figure 5.7: Out-of-plane displacement  $w_{ac}$  and rotations  $\psi_{r,ac}$  and  $\psi_{\varphi,ac}$  of an infinite Mindlin plate excited by a harmonic alternating circular load with  $r_0 = 0.8$

### 5.3 Particular solutions for the Kirchhoff plate theory

The particular solution functions for the Kirchhoff plate theory can be obtained as a special case of the Mindlin plate solutions. If the rotatory inertia is neglected and the shear modulus is set to infinity (neglecting the shear deformation), the Mindlin plate theory reduces to the Kirchhoff plate theory [11]. In this case, the constants in Equation (2.69) are given by  $R = 0$ ,  $S = 0$ ,  $\mu_1 = 0$  and  $\mu_2 = 0$  and the wavenumbers, defined in Equations (2.66) and (2.67), become  $k_{f1} = k_b$  and  $k_{f2} = j k_b$  with  $k_b = \sqrt[4]{k_b^4}$ . Furthermore, the cut-off frequency  $\omega_c$  rises to infinity and therefore  $\omega$  is always less than  $\omega_c$ . Using these simplifications in the solutions of the Mindlin plate (Equations (5.40), (5.41), (5.63), (5.64), (5.85), (5.86), (5.111)–(5.113)) leads to the following results for the Kirchhoff plate:

a.) *Point force*

$$w_{point}(r) = \frac{j \bar{q}_0}{8 D k_b^2} \left( -H_0^{(2)}(k_b r) + H_0^{(2)}(-j k_b r) \right), \quad (5.114)$$

$$\psi_{r, point}(r) = -\frac{j \bar{q}_0}{8 D k_b} \left( H_1^{(2)}(k_b r) + j H_1^{(2)}(-j k_b r) \right). \quad (5.115)$$

b.) *Constant ring load*

$$w_{ring}(r) = \frac{j \bar{q}_0 \pi r_0}{4 D k_b^2} \begin{cases} \left( -J_0(k_b r_0) H_0^{(2)}(k_b r) \right. \\ \left. + J_0(-j k_b r_0) H_0^{(2)}(-j k_b r) \right), & r > r_0, \\ \left( -J_0(k_b r) H_0^{(2)}(k_b r_0) \right. \\ \left. + J_0(-j k_b r) H_0^{(2)}(-j k_b r_0) \right), & r < r_0, \end{cases} \quad (5.116)$$

$$\psi_{r, ring}(r) = \frac{-j \bar{q}_0 \pi r_0}{4 D k_b} \begin{cases} \left( J_0(k_b r_0) H_1^{(2)}(k_b r) \right. \\ \left. + j J_0(-j k_b r_0) H_1^{(2)}(-j k_b r) \right), & r > r_0, \\ \left( J_1(k_b r) H_0^{(2)}(k_b r_0) \right. \\ \left. + j J_1(-j k_b r) H_0^{(2)}(-j k_b r_0) \right), & r < r_0. \end{cases} \quad (5.117)$$

c.) *Constant circular load*

$$w_{circ}(r) = \frac{j \bar{q}_0 \pi r_0}{4 D k_b^3} \begin{cases} \left( -J_1(k_b r_0) H_0^{(2)}(k_b r) \right. \\ \left. + j J_1(-j k_b r_0) H_0^{(2)}(-j k_b r) \right), & r > r_0, \\ \left( \frac{4 j}{\pi k_b r_0} - J_0(k_b r) H_1^{(2)}(k_b r_0) \right. \\ \left. + j J_0(-j k_b r) H_1^{(2)}(-j k_b r_0) \right), & r < r_0, \end{cases} \quad (5.118)$$

$$\psi_{r, circ}(r) = \frac{-j \bar{q}_0 \pi r_0}{4 D k_b^2} \begin{cases} \left( J_1(k_b r_0) H_1^{(2)}(k_b r) \right. \\ \left. - J_1(-j k_b r_0) H_1^{(2)}(-j k_b r) \right), & r > r_0, \\ \left( J_1(k_b r) H_1^{(2)}(k_b r_0) \right. \\ \left. - J_1(-j k_b r) H_1^{(2)}(-j k_b r_0) \right), & r < r_0. \end{cases} \quad (5.119)$$

d.) Alternating circular load

$$w_{ac}(r, \varphi) = \frac{j \bar{q}_0 \pi r_0 \cos(\varphi)}{4 D k_b^3} \begin{cases} \left( -J_2(k_b r_0) H_1^{(2)}(k_b r) + j J_2(-j k_b r_0) H_1^{(2)}(-j k_b r) \right), & r > r_0, \\ \left( \frac{4 j r}{\pi k_b r_0^2} - J_1(k_b r) H_2^{(2)}(k_b r_0) + j J_1(-j k_b r) H_2^{(2)}(-j k_b r_0) \right), & r < r_0, \end{cases} \quad (5.120)$$

$$\psi_{r, ac}(r, \varphi) = \frac{j \bar{q}_0 \pi r_0 \cos(\varphi)}{8 D k_b^2} \begin{cases} \left( \frac{H_0^{(2)}(k_b r) - H_2^{(2)}(k_b r)}{J_2(k_b r_0)^{-1}} - \frac{H_0^{(2)}(-j k_b r) - H_2^{(2)}(-j k_b r)}{J_2(-j k_b r_0)^{-1}} \right), & r > r_0, \\ \left( \frac{-8 j}{\pi k_b^2 r_0^2} + \frac{J_0(k_b r) - J_2(k_b r)}{H_2^{(2)}(k_b r_0)^{-1}} - \frac{J_0(-j k_b r) - J_2(-j k_b r)}{H_2^{(2)}(-j k_b r_0)^{-1}} \right), & r < r_0, \end{cases} \quad (5.121)$$

$$\psi_{\varphi, ac}(r, \varphi) = \frac{-j \bar{q}_0 \pi r_0 \sin(\varphi)}{4 D k_b^3 r} \begin{cases} \left( J_2(k_b r_0) H_1^{(2)}(k_b r) - j J_2(-j k_b r_0) H_1^{(2)}(-j k_b r) \right), & r > r_0, \\ \left( \frac{-4 j r}{\pi k_b r_0^2} + J_1(k_b r) H_2^{(2)}(k_b r_0) - j J_1(-j k_b r) H_2^{(2)}(-j k_b r_0) \right), & r < r_0. \end{cases} \quad (5.122)$$

In the Kirchhoff plate theory, the rotations are not independent from the out-of-plane displacement and can be computed by

$$\psi_r(r, \varphi) = -\frac{\partial w(r, \varphi)}{\partial r} \quad \text{and} \quad \psi_{\varphi}(r, \varphi) = -\frac{1}{r} \frac{\partial w(r, \varphi)}{\partial \varphi}. \quad (5.123)$$

These relations are fulfilled by the results in Equations (5.114) – (5.122). The particular solutions for the Kirchhoff plate theory can also be found in a paper from the present author [288], which are identical to the present results.



# 6 Extension of the Wave Based Method to thick plate vibrations

The WBM for thin plate vibration problems (Kirchhoff plate theory) has been extensively developed by Vanmaele and her co-workers [17, 16] including the definition of different function sets and the treatment of corner stress singularities. Since the Kirchhoff plate theory is limited to thin plates and low frequencies, see Section 2.3, an extension of the WBM to thick plate vibrations using the Mindlin plate theory is shown in this chapter.

If stress singularities are present in the problem domain, the WBM suffers from convergence problems [18] and therefore so-called special purpose functions have to be defined to resolve this issue. In Section 6.1 stress singularities occurring within the Mindlin plate theory are examined for static and dynamic deformations, which allows for the definition of special purpose functions in a subsequent section. The application of the WBM to the Mindlin plate theory is shown in Section 6.2, where the general description of the WBM from Section 4.1 is specialized for vibrations of Mindlin plates. In Section 6.3, a modified selection of the wave functions is presented, which leads to a higher accuracy and stability of the WBM. Several validation examples with convex and non-convex domains having different boundary conditions are investigated in Section 6.4. A comparison of the WBM and the classical FEM over a wide frequency range is presented and the effect of different function sets and special purpose functions on the convergence rate of the WBM is shown.

## 6.1 Stress singularities in the Mindlin plate theory

Singularities in the bending or shear stress field are of course physically impossible, but they are a result of the modeling process and the linear theory of elasticity [289]. Such singularities may occur if plates are loaded with concentrated forces or moments, since finite stress resultants are applied over regions with vanishingly small areas [289]. Furthermore, singularities can appear if discontinuities in the plate domain or at the plate boundary are present, e.g. rapid changes of the plate thickness, the material parameters or the boundary conditions. A particular case of stress singularities in the Mindlin plate theory arises in the vicinity of an angular corner if a certain critical angle is reached [74, 290].

The singularities due to concentrated loads do not affect the convergence rate of the WBM, since the included particular solution functions exactly represent the singular behaviour. However, corner stress singularities have a strong influence on the stability and convergence rate of the WBM, because the singularity in the stress field has to be constructed with plane wave functions [18].

Therefore, the corner bending and shear force singularities appearing in Mindlin plates are analyzed in the subsequent sections. The following assumptions, which have also been used in [17] for Kirchhoff plates, are made for the analytical study of the corner stress singularities:

- An external loading has no effect on the stress singularities in the corner point provided that the loading is integrable [291].
- The boundary conditions applied at edges away from the corner point hardly affect the stresses in the vicinity of the corner [291].
- The plate consists of a single linear elastic material (an extension to multiple materials is possible).

Through these assumptions, a study of an unloaded infinite wedge domain with an internal angle  $\alpha$ , see Figure 6.1, can be performed to investigate the stress singularities at the corner point ( $r = 0$ ).

In Section 6.1.1 the vibrations of the infinite wedge domain are analyzed and the behaviour of the bending moments and shear forces in the vicinity of the corner is investigated. Since an exact dynamic solution can only be defined for hard simply-supported radial edges, the static solution of the infinite wedge domain is stated in Section 6.1.2 for arbitrary boundary conditions. A comparison of the singular stress behaviour in the static and dynamic case is presented in Section 6.1.3.

### 6.1.1 Vibrations of an infinite wedge domain

The exact solutions for the free vibrations of thick sectorial plates with simply-supported radial edges have been presented by Huang et al. [74] and are the basis for the following derivations. Compared to [74], the boundary conditions at the circumferential edge are not included and a differentiation between symmetric and antisymmetric bending deformation is made. In general, the material loss factor  $\eta$  is unequal to zero and therefore, the differentiation between the cases  $\omega > \omega_c$  and  $\omega < \omega_c$ , which has been performed by Huang and his co-workers [74], is omitted.

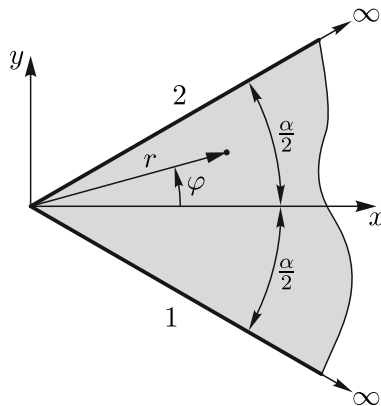


Figure 6.1: Infinite wedge domain without external loading

### General analytical solution for an infinite wedge

In the absence of external loadings ( $\bar{q} = 0$ ,  $\bar{m}_x = 0$ ,  $\bar{m}_y = 0$ ), the governing equations of the Mindlin plate theory are given in polar coordinates by [292]

$$\left(\nabla^2 + k_{f1}^2\right)w_1(r, \varphi) = 0, \quad (6.1)$$

$$\left(\nabla^2 + k_{f2}^2\right)w_2(r, \varphi) = 0, \quad (6.2)$$

$$\left(\nabla^2 + k_s^2\right)H(r, \varphi) = 0, \quad (6.3)$$

where  $\nabla^2 = \frac{\partial^2}{\partial r^2} + \frac{1}{r} \frac{\partial}{\partial r} + \frac{1}{r^2} \frac{\partial^2}{\partial \varphi^2}$  is the two-dimensional Laplace operator in polar coordinates. The out-of-plane displacement  $w(r, \varphi)$  and the rotations  $\psi_r(r, \varphi)$  and  $\psi_\varphi(r, \varphi)$  are defined by [292]

$$w(r, \varphi) = w_1(r, \varphi) + w_2(r, \varphi), \quad (6.4)$$

$$\psi_r(r, \varphi) = (\mu_1 - 1) \frac{\partial w_1(r, \varphi)}{\partial r} + (\mu_2 - 1) \frac{\partial w_2(r, \varphi)}{\partial r} + \frac{1}{r} \frac{\partial H(r, \varphi)}{\partial \varphi}, \quad (6.5)$$

$$\psi_\varphi(r, \varphi) = (\mu_1 - 1) \frac{1}{r} \frac{\partial w_1(r, \varphi)}{\partial \varphi} + (\mu_2 - 1) \frac{1}{r} \frac{\partial w_2(r, \varphi)}{\partial \varphi} - \frac{\partial H(r, \varphi)}{\partial r}, \quad (6.6)$$

where the constants from Equation (2.69) are used.

The general analytical solutions of Equations (6.1)–(6.3) proposed in [74] do not distinguish between symmetric and antisymmetric bending. Therefore, the modified general solutions

$$w_1(r, \varphi) = \sum_{k=1}^{\infty} \cos(\lambda_k^s \varphi) R_{1\lambda_k^s}(k_{f1} r) + \sin(\lambda_k^a \varphi) R_{1\lambda_k^a}(k_{f1} r), \quad (6.7)$$

$$w_2(r, \varphi) = \sum_{k=1}^{\infty} \cos(\lambda_k^s \varphi) R_{2\lambda_k^s}(k_{f2} r) + \sin(\lambda_k^a \varphi) R_{2\lambda_k^a}(k_{f2} r), \quad (6.8)$$

$$H(r, \varphi) = \sum_{k=1}^{\infty} -\sin(\lambda_k^s \varphi) R_{3\lambda_k^s}(k_s r) + \cos(\lambda_k^a \varphi) R_{3\lambda_k^a}(k_s r), \quad (6.9)$$

with

$$\begin{aligned} R_{1\lambda}(k_{f1} r) &= A_{1\lambda} J_\lambda(k_{f1} r) + B_{1\lambda} Y_\lambda(k_{f1} r), \\ R_{2\lambda}(k_{f2} r) &= A_{2\lambda} J_\lambda(k_{f2} r) + B_{2\lambda} Y_\lambda(k_{f2} r), \quad \lambda = \lambda_k^s \text{ or } \lambda_k^a, \\ R_{3\lambda}(k_s r) &= A_{3\lambda} J_\lambda(k_s r) + B_{3\lambda} Y_\lambda(k_s r), \end{aligned} \quad (6.10)$$

are used, where the eigenvalues  $\lambda$  depend on the prescribed boundary conditions at  $\varphi = \pm\alpha/2$  and symmetric bending modes are associated with  $\lambda_k^s$ , while  $\lambda_k^a$  lead to antisymmetric bending modes. In Equation (6.10),  $A_{i\lambda}$  and  $B_{i\lambda}$  ( $i = \{1, 2, 3\}$ ) are arbitrary constants, which are determined by imposing three regularity conditions at  $r = 0$  and three boundary conditions at the circumferential edge. Since an infinite wedge domain is considered, only the regularity conditions at  $r = 0$  [74]

$$w(0, \varphi) = \text{finite}, \quad (6.11)$$

$$\psi_r(0, \varphi) = \text{finite}, \quad (6.12)$$

$$\psi_\varphi(0, \varphi) = \text{finite}, \quad (6.13)$$

are taken into account.

Following the procedure shown in [74], first the regularity condition for the out-of-plane displacement is imposed. Since the results for negative and positive values of  $\lambda$  lead to identical admissible solution functions, only the case  $\lambda \geq 0$  is considered. Using the limit

$$\lim_{z \rightarrow 0} J_\nu(z) = \text{finite}, \quad \nu \geq 0, \quad (6.14)$$

in Equation (6.4) leads to

$$\lim_{r \rightarrow 0} w(r, \varphi) = \lim_{r \rightarrow 0} (B_{1\lambda} Y_\lambda(k_{f1} r) + B_{2\lambda} Y_\lambda(k_{f2} r)) = \text{finite}, \quad (6.15)$$

where the multiplications with  $\cos(\lambda_k^s \varphi)$  or  $\sin(\lambda_k^a \varphi)$  can be omitted. Applying the relation [281]

$$Y_\nu(z) = \frac{J_\nu(z) \cos(\nu \pi) - J_{-\nu}(z)}{\sin(\nu \pi)}, \quad \nu \notin \mathbb{Z} \quad (6.16)$$

and Equation (6.14) simplify Equation (6.15) to

$$\lim_{r \rightarrow 0} \left( -B_{1\lambda} \frac{J_{-\lambda}(k_{f1} r)}{\sin(\lambda \pi)} - B_{2\lambda} \frac{J_{-\lambda}(k_{f2} r)}{\sin(\lambda \pi)} \right) = \text{finite}. \quad (6.17)$$

The series representation of the Bessel function of the first kind [284]

$$J_\nu(z) = \sum_{k=0}^{\infty} \frac{(-1)^k z^{2k+\nu}}{k! 2^{2k+\nu} \Gamma(k+\nu+1)}, \quad (6.18)$$

with  $\Gamma(\bullet)$  the gamma function and  $\bullet!$  the factorial shows that the out-of-plane displacement is only limited if all coefficients of  $r^{2k-\lambda}$  with  $2k-\lambda < 0$  vanish. This leads to

$$B_{1\lambda} k_{f1}^{-\lambda} + B_{2\lambda} k_{f2}^{-\lambda} = 0, \quad 0 \leq \lambda \leq 2, \quad (6.19)$$

$$B_{1\lambda} = B_{2\lambda} = 0, \quad \lambda > 2, \quad (6.20)$$

since for  $\lambda > 2$  more than one linearly independent equation has to be fulfilled and for  $0 \leq \lambda \leq 2$  only  $k = 0$  has to be considered [74]. If  $\lambda$  is an integer value, a different representation for the Bessel function of the second kind has to be applied, since the relation in Equation (6.16) is only valid for non-integer values. The procedure is outlined in Appendix D and leads to Equation (6.19) for  $\lambda = \{0, 1, 2\}$  and to Equation (6.20) for  $\lambda = \{3, 4, \dots\}$ .

The second regularity condition for the rotation,  $\lim_{r \rightarrow 0} \psi_r(r, \varphi) = \text{finite}$ , can be simplified to

$$\begin{aligned} \lim_{r \rightarrow 0} & \left( \frac{(\mu_1 - 1) k_{f1}}{2} \left( C_{1\lambda} J_{\lambda-1}(k_{f1} r) + B_{1\lambda} \frac{J_{-\lambda+1}(k_{f1} r) - J_{-\lambda-1}(k_{f1} r)}{\sin(\lambda \pi)} \right) \right. \\ & + \frac{(\mu_2 - 1) k_{f2}}{2} \left( C_{2\lambda} J_{\lambda-1}(k_{f2} r) + B_{2\lambda} \frac{J_{-\lambda+1}(k_{f2} r) - J_{-\lambda-1}(k_{f2} r)}{\sin(\lambda \pi)} \right) \\ & \left. - \frac{\lambda}{r} \left( C_{3\lambda} J_\lambda(k_s r) - B_{3\lambda} \frac{J_{-\lambda}(k_s r)}{\sin(\lambda \pi)} \right) \right) = \text{finite}, \end{aligned} \quad (6.21)$$

where Equations (6.14) and (6.16), the recurrence formula for Bessel functions of the first kind

$$\frac{dJ_\nu(z)}{dz} = \frac{1}{2} (J_{\nu-1}(z) - J_{\nu+1}(z)) \quad (6.22)$$

### 6.1 Stress singularities in the Mindlin plate theory

and the identities  $\sin((\lambda \pm 1)\pi) = -\sin(\lambda\pi)$  and  $\tan((\lambda - 1)\pi) = \tan(\lambda\pi)$  are used in Equation (6.5). The multiplications with  $\cos(\lambda_k^s \varphi)$  or  $\sin(\lambda_k^a \varphi)$  can be omitted in Equation (6.21) and  $C_{i\lambda} = A_{i\lambda} + B_{i\lambda} \cot(\lambda\pi)$  ( $i = \{1, 2, 3\}$ ). Substituting the series representation of the Bessel function (Equation (6.18)) into Equation (6.21) and gathering terms with the same exponents for the variable  $r$  lead to

$$\begin{aligned} \lim_{r \rightarrow 0} \left( \sum_{k=0}^{\infty} (-1)^k \left( \frac{(\mu_1 - 1) k_{f1}^{2k-\lambda+2} B_{1\lambda} + (\mu_2 - 1) k_{f2}^{2k-\lambda+2} B_{2\lambda}}{k! 2^{2k-\lambda+2} \sin(\lambda\pi) \Gamma(k - \lambda + 2)} r^{2k-\lambda+1} \right. \right. \\ \left. \left. + \frac{(\mu_1 - 1) k_{f1}^{2k+\lambda} C_{1\lambda} + (\mu_2 - 1) k_{f2}^{2k+\lambda} C_{2\lambda} - \frac{\lambda}{k+\lambda} k_s^{2k+\lambda} C_{3\lambda}}{k! 2^{2k+\lambda} \Gamma(k + \lambda)} r^{2k+\lambda-1} \right. \right. \\ \left. \left. - \frac{(\mu_1 - 1) k_{f1}^{2k-\lambda} B_{1\lambda} + (\mu_2 - 1) k_{f2}^{2k-\lambda} B_{2\lambda} - \frac{\lambda}{k-\lambda} k_s^{2k-\lambda} B_{3\lambda}}{k! 2^{2k-\lambda} \sin(\lambda\pi) \Gamma(k - \lambda)} r^{2k-\lambda-1} \right) \right) = \text{finite}, \end{aligned} \quad (6.23)$$

where the relation  $\Gamma(k \pm \lambda + 1) = (k \pm \lambda) \Gamma(k \pm \lambda)$  is applied.

Using a similar procedure for the third regularity condition,  $\lim_{r \rightarrow 0} \psi_\varphi(r, \varphi) = \text{finite}$ , gives

$$\begin{aligned} \lim_{r \rightarrow 0} \left( \sum_{k=0}^{\infty} (-1)^k \left( \frac{k_s^{2k-\lambda+2} B_{3\lambda}}{k! 2^{2k-\lambda+2} \sin(\lambda\pi) \Gamma(k - \lambda + 2)} r^{2k-\lambda+1} \right. \right. \\ \left. \left. - \frac{(\mu_1 - 1) k_{f1}^{2k+\lambda} C_{1\lambda} + (\mu_2 - 1) k_{f2}^{2k+\lambda} C_{2\lambda} - \frac{\lambda}{k+\lambda} k_s^{2k+\lambda} C_{3\lambda}}{k! 2^{2k+\lambda} \Gamma(k + \lambda + 1) \lambda^{-1}} r^{2k+\lambda-1} \right. \right. \\ \left. \left. + \frac{(\mu_1 - 1) k_{f1}^{2k-\lambda} B_{1\lambda} + (\mu_2 - 1) k_{f2}^{2k-\lambda} B_{2\lambda} - \frac{\lambda}{k-\lambda} k_s^{2k-\lambda} B_{3\lambda}}{k! 2^{2k-\lambda} \sin(\lambda\pi) \Gamma(k - \lambda + 1) \lambda^{-1}} r^{2k-\lambda-1} \right) \right) = \text{finite}, \end{aligned} \quad (6.24)$$

where the multiplications with  $\sin(\lambda_k^s \varphi)$  or  $-\cos(\lambda_k^a \varphi)$  are omitted. As pointed out in [74], different cases have to be distinguished to define the relations between the constants  $A_{i\lambda}$  and  $B_{i\lambda}$  ( $i = \{1, 2, 3\}$ ).

**Case I:**  $\lambda \in \mathbb{N}_0$

For integer values of  $\lambda$ , a different representation of the Bessel function of the second kind has to be applied. It is shown in Appendix D that the constants  $B_{1\lambda}$ ,  $B_{2\lambda}$  and  $B_{3\lambda}$  have to be equal to zero and  $A_{i\lambda}$  ( $i = \{1, 2, 3\}$ ) can be chosen arbitrary.

**Case II:**  $0 < \lambda < 1$

In this range, Equations (6.23) and (6.24) are only fulfilled if the coefficients of  $r^{\lambda-1}$  and  $r^{-\lambda-1}$  ( $k = 0$ ) are equal to zero, since all other terms vanish in the limit  $r \rightarrow 0$ . Therefore, the two relations

$$(\mu_1 - 1) k_{f1}^{-\lambda} B_{1\lambda} + (\mu_2 - 1) k_{f2}^{-\lambda} B_{2\lambda} + k_s^{-\lambda} B_{3\lambda} = 0, \quad (r^{-\lambda-1}) \quad (6.25)$$

$$(\mu_1 - 1) k_{f1}^{\lambda} C_{1\lambda} + (\mu_2 - 1) k_{f2}^{\lambda} C_{2\lambda} - k_s^{\lambda} C_{3\lambda} = 0, \quad (r^{\lambda-1}) \quad (6.26)$$

have to be satisfied. It follows from Equation (6.19) that

$$B_{1\lambda} = - \left( \frac{k_{f1}}{k_{f2}} \right)^\lambda B_{2\lambda}, \quad (6.27)$$

which can be used in Equation (6.25) to get

$$B_{3\lambda} = \left( \frac{k_s}{k_{f2}} \right)^\lambda (\mu_1 - \mu_2) B_{2\lambda}. \quad (6.28)$$

Rearranging Equation (6.26) finally leads to

$$B_{2\lambda} = \frac{(\mu_1 - 1) k_{f1}^\lambda A_{1\lambda} + (\mu_2 - 1) k_{f2}^\lambda A_{2\lambda} - k_s^\lambda A_{3\lambda}}{\cot(\lambda \pi) k_{f2}^{-\lambda} ((\mu_1 - 1) k_{f1}^{2\lambda} - (\mu_2 - 1) k_{f2}^{2\lambda} + (\mu_1 - \mu_2) k_s^{2\lambda})}, \quad (6.29)$$

while the constants  $A_{i\lambda}$  ( $i = \{1, 2, 3\}$ ) can be chosen arbitrary.

**Case III:**  $1 < \lambda < 2$

In this case, the coefficients of  $r^{2k-\lambda+1}$  ( $k = 0$ ) and  $r^{2k-\lambda-1}$  ( $k = \{0, 1\}$ ) have to be zero to fulfill the Equations (6.23) and (6.24), which leads to the conditions

$$(\mu_1 - 1) k_{f1}^{-\lambda} B_{1\lambda} + (\mu_2 - 1) k_{f2}^{-\lambda} B_{2\lambda} + k_s^{-\lambda} B_{3\lambda} = 0, \quad (r^{-\lambda-1}), \quad (6.30)$$

$$(\mu_1 - 1) k_{f1}^{2-\lambda} B_{1\lambda} + (\mu_2 - 1) k_{f2}^{2-\lambda} B_{2\lambda} - k_s^{2-\lambda} f(\lambda) B_{3\lambda} = 0, \quad (r^{-\lambda+1}), \quad (6.31)$$

where  $f(\lambda) = (\lambda/(2-\lambda))^{\pm 1}$  (+ for  $\psi_r$  and - for  $\psi_\varphi$ ). Combining these conditions with the relation in Equation (6.19) gives only the trivial solution  $B_{1\lambda} = B_{2\lambda} = B_{3\lambda} = 0$ , since the determinate of the coefficient matrix is unequal to zero for any parameter set. The constants  $A_{i\lambda}$  ( $i = \{1, 2, 3\}$ ) can be chosen arbitrary.

**Case IV:**  $\lambda > 2$

For  $\lambda > 2$ , Equation (6.20) shows that  $B_{1\lambda} = B_{2\lambda} = 0$  (regularity condition of the out-of-plane displacement) and therefore, the terms in Equation (6.23) related to  $r^{2k-\lambda+1}$  vanish. Furthermore, it follows from Equations (6.23) that the constant  $B_{3\lambda} = 0$  (coefficients of  $r^{2k-\lambda-1}$ ) and the constants  $A_{i\lambda}$  ( $i = \{1, 2, 3\}$ ) can be chosen arbitrary (coefficients of  $r^{2k+\lambda-1}$ ). The same results can be found from Equation (6.24).

The general analytical solution for the infinite wedge domain is therefore defined by Equations (6.7) – (6.9) and

$$0 < \lambda < 1 \quad \left\{ \begin{array}{l} R_{1\lambda} = A_{1\lambda} \left( J_\lambda(k_{f1} r) - C k_{f1}^{2\lambda} (\mu_1 - 1) Y_\lambda(k_{f1} r) \right) \\ \quad - A_{2\lambda} C (k_{f1} k_{f2})^\lambda (\mu_2 - 1) Y_\lambda(k_{f1} r) \\ \quad + A_{3\lambda} C (k_{f1} k_s)^\lambda Y_\lambda(k_{f1} r), \\ R_{2\lambda} = A_{1\lambda} C (k_{f1} k_{f2})^\lambda (\mu_1 - 1) Y_\lambda(k_{f2} r) \\ \quad + A_{2\lambda} \left( J_\lambda(k_{f2} r) + C k_{f2}^{2\lambda} (\mu_2 - 1) Y_\lambda(k_{f2} r) \right) \\ \quad - A_{3\lambda} C (k_{f2} k_s)^\lambda Y_\lambda(k_{f2} r), \\ R_{3\lambda} = A_{1\lambda} C (k_{f1} k_s)^\lambda (\mu_1 - \mu_2) (\mu_1 - 1) Y_\lambda(k_s r) \\ \quad + A_{2\lambda} C (k_{f2} k_s)^\lambda (\mu_1 - \mu_2) (\mu_2 - 1) Y_\lambda(k_s r) \\ \quad + A_{3\lambda} \left( J_\lambda(k_s r) - C k_s^{2\lambda} (\mu_1 - \mu_2) Y_\lambda(k_s r) \right), \end{array} \right. \quad (6.32)$$

with

$$C = \frac{1}{\cot(\lambda \pi) ((\mu_1 - 1) k_{f1}^{2\lambda} - (\mu_2 - 1) k_{f2}^{2\lambda} + (\mu_1 - \mu_2) k_s^{2\lambda})} \quad (6.33)$$

and

$$\begin{aligned} \lambda \geq 1 & \quad \begin{cases} R_{1\lambda} = A_{1\lambda} J_\lambda(k_{f1} r), \\ R_{2\lambda} = A_{2\lambda} J_\lambda(k_{f2} r), \\ R_{3\lambda} = A_{3\lambda} J_\lambda(k_s r). \end{cases} \\ \lambda = 0 & \end{aligned} \quad (6.34)$$

### Bending moments and shear force singularities

The general analytical solutions from the previous section can be used to identify singularities of the bending moments and shear forces in the vicinity of the corner point  $r = 0$ . The bending moments ( $M_r, M_\varphi, M_{r\varphi}$ ) and shear forces ( $Q_r, Q_\varphi$ ) in polar coordinates are given by [292]

$$M_r(r, \varphi) = D \left( \frac{\partial \psi_r}{\partial r} + \frac{\nu}{r} \left( \psi_r + \frac{\partial \psi_\varphi}{\partial \varphi} \right) \right), \quad (6.35)$$

$$M_\varphi(r, \varphi) = D \left( \frac{1}{r} \left( \psi_r + \frac{\partial \psi_\varphi}{\partial \varphi} \right) + \nu \frac{\partial \psi_r}{\partial r} \right), \quad (6.36)$$

$$M_{r\varphi}(r, \varphi) = \frac{D}{2} (1 - \nu) \left( \frac{1}{r} \left( \frac{\partial \psi_r}{\partial \varphi} - \psi_\varphi \right) + \frac{\partial \psi_\varphi}{\partial r} \right), \quad (6.37)$$

$$Q_r(r, \varphi) = k^2 G h \left( \psi_r + \frac{\partial w}{\partial r} \right), \quad (6.38)$$

$$Q_\varphi(r, \varphi) = k^2 G h \left( \psi_\varphi + \frac{1}{r} \frac{\partial w}{\partial \varphi} \right). \quad (6.39)$$

Depending on the value of  $\lambda$ , either the analytical solutions from Equation (6.34) or Equation (6.32) have to be used in Equations (6.35)–(6.39) to analyze the behaviour of the bending moments and shear forces in the vicinity of the corner point.

The asymptotic forms of the bending moments in case of  $\lambda \geq 1$  or  $\lambda = 0$  are given by

$$M_r|_{r \rightarrow 0} = \frac{D (1 - \nu) \left( (\mu_1 - 1) k_{f1}^\lambda A_{1\lambda} + (\mu_2 - 1) k_{f2}^\lambda A_{2\lambda} - k_s^\lambda A_{3\lambda} \right) f_1(\varphi)}{\Gamma(\lambda - 1) 2^\lambda} r^{\lambda - 2}, \quad (6.40)$$

$$M_\varphi|_{r \rightarrow 0} = \frac{D (\nu - 1) \left( (\mu_1 - 1) k_{f1}^\lambda A_{1\lambda} + (\mu_2 - 1) k_{f2}^\lambda A_{2\lambda} - k_s^\lambda A_{3\lambda} \right) f_1(\varphi)}{\Gamma(\lambda - 1) 2^\lambda} r^{\lambda - 2}, \quad (6.41)$$

$$M_{r\varphi}|_{r \rightarrow 0} = \frac{D (1 - \nu) \left( (\mu_1 - 1) k_{f1}^\lambda A_{1\lambda} + (\mu_2 - 1) k_{f2}^\lambda A_{2\lambda} - k_s^\lambda A_{3\lambda} \right) f_2(\varphi)}{\Gamma(\lambda - 1) 2^\lambda} r^{\lambda - 2}, \quad (6.42)$$

where the recurrence formula (Equation (6.22)) and the series representation of the Bessel function (Equation (6.18)) are applied. Depending on whether symmetric or antisymmetric bending is considered, the function  $f_1(\varphi) = \{\cos(\lambda_k^s \varphi), \sin(\lambda_k^s \varphi)\}$  and the function  $f_2(\varphi) = \{-\sin(\lambda_k^s \varphi), \cos(\lambda_k^s \varphi)\}$ . It is apparent from Equations (6.40)–(6.42) that the bending moments become singular at  $r = 0$  if  $\lambda < 2$  [74]. For the integer values  $\lambda = 0$  and  $\lambda = 1$ , the bending moments at  $r = 0$  approach a finite value, since  $\Gamma(-1) \rightarrow j\infty$  and  $\Gamma(0) \rightarrow j\infty$ .

If  $0 < \lambda < 1$ , the asymptotic forms of the bending moments can be expressed as

$$M_r|_{r \rightarrow 0} = -\frac{D(1-\nu)\left((\mu_1-1)k_{f1}^\lambda A_{1\lambda} + (\mu_2-1)k_{f2}^\lambda A_{2\lambda} - k_s^\lambda A_{3\lambda}\right)}{\sin(\lambda\pi) 2^{2-\lambda} \Gamma(1-\lambda) C} \\ \left((\mu_1-1)C_{\nu1}k_{f1}^2 - (\mu_2-1)C_{\nu1}k_{f2}^2 + (\mu_1-\mu_2)\lambda k_s^2\right) f_1(\varphi) r^{-\lambda}, \quad (6.43)$$

$$M_\varphi|_{r \rightarrow 0} = -\frac{D(1-\nu)\left((\mu_1-1)k_{f1}^\lambda A_{1\lambda} + (\mu_2-1)k_{f2}^\lambda A_{2\lambda} - k_s^\lambda A_{3\lambda}\right)}{\sin(\lambda\pi) 2^{2-\lambda} \Gamma(1-\lambda) C} \\ \left((\mu_1-1)C_{\nu2}k_{f1}^2 - (\mu_2-1)C_{\nu2}k_{f2}^2 - (\mu_1-\mu_2)\lambda k_s^2\right) f_1(\varphi) r^{-\lambda}, \quad (6.44)$$

$$M_{r\varphi}|_{r \rightarrow 0} = \frac{D(1-\nu)\left((\mu_1-1)k_{f1}^\lambda A_{1\lambda} + (\mu_2-1)k_{f2}^\lambda A_{2\lambda} - k_s^\lambda A_{3\lambda}\right)}{\sin(\lambda\pi) 2^{2-\lambda} \Gamma(-\lambda) C} \\ \left((\mu_1-1)k_{f1}^2 - (\mu_2-1)k_{f2}^2 - (\mu_1-\mu_2)k_s^2\right) f_2(\varphi) r^{-\lambda}, \quad (6.45)$$

where  $C_{\nu1} = \left(\frac{2(1+\nu)}{1-\nu} - \lambda\right)$  and  $C_{\nu2} = \left(\frac{2(1+\nu)}{1-\nu} + \lambda\right)$  and Equations (6.16), (6.18) and (6.22) are applied. In this case, the bending moments exhibit a singularity at the corner point for the whole range  $0 < \lambda < 1$  [74].

The asymptotic forms of the shear forces in case of  $\lambda \geq 1$  or  $\lambda = 0$  are given by

$$Q_r|_{r \rightarrow 0} = \frac{k^2 G h \left(\mu_1 k_{f1}^\lambda A_{1\lambda} + \mu_2 k_{f2}^\lambda A_{2\lambda} - k_s^\lambda A_{3\lambda}\right)}{2^\lambda \Gamma(\lambda)} f_1(\varphi) r^{\lambda-1}, \quad (6.46)$$

$$Q_\varphi|_{r \rightarrow 0} = \frac{k^2 G h \left(\mu_1 k_{f1}^\lambda A_{1\lambda} + \mu_2 k_{f2}^\lambda A_{2\lambda} - k_s^\lambda A_{3\lambda}\right)}{2^\lambda \Gamma(\lambda)} f_2(\varphi) r^{\lambda-1}, \quad (6.47)$$

and therefore, no shear force singularities occur for  $\lambda \geq 1$  or  $\lambda = 0$ , since Equations (6.46) and (6.47) approach a finite value for  $r \rightarrow 0$  [74]. For  $0 < \lambda < 1$ , the asymptotic forms of the shear forces are

$$Q_r|_{r \rightarrow 0} = \frac{k^2 G h \cot(\lambda\pi) C f_1(\varphi)}{2^\lambda \Gamma(\lambda)} \left(k_{f1}^\lambda \left((\mu_1-1) \left(k_{f2}^{2\lambda} - k_{f1}^{2\lambda}\right) + \frac{1}{\cot(\lambda\pi) C}\right) A_{1\lambda} + k_{f2}^\lambda \left((\mu_2-1) \left(k_{f2}^{2\lambda} - k_{f1}^{2\lambda}\right) + \frac{1}{\cot(\lambda\pi) C}\right) A_{2\lambda} - k_s^\lambda \left(k_{f2}^{2\lambda} - k_{f1}^{2\lambda}\right) A_{3\lambda}\right) r^{\lambda-1}, \quad (6.48)$$

$$Q_\varphi|_{r \rightarrow 0} = \frac{k^2 G h \cot(\lambda\pi) C f_2(\varphi)}{2^\lambda \Gamma(\lambda)} \left(k_{f1}^\lambda \left((\mu_1-1) \left(k_{f2}^{2\lambda} - k_{f1}^{2\lambda}\right) + \frac{1}{\cot(\lambda\pi) C}\right) A_{1\lambda} + k_{f2}^\lambda \left((\mu_2-1) \left(k_{f2}^{2\lambda} - k_{f1}^{2\lambda}\right) + \frac{1}{\cot(\lambda\pi) C}\right) A_{2\lambda} - k_s^\lambda \left(k_{f2}^{2\lambda} - k_{f1}^{2\lambda}\right) A_{3\lambda}\right) r^{\lambda-1}, \quad (6.49)$$

which show that the shear forces vary as  $r^{\lambda-1}$  and become singular as  $r \rightarrow 0$  [74].

From Equations (6.40)–(6.42) and (6.43)–(6.45) it is apparent that the additional restriction

$$(\mu_1-1)k_{f1}^\lambda A_{1\lambda} + (\mu_2-1)k_{f2}^\lambda A_{2\lambda} - k_s^\lambda A_{3\lambda} = 0 \quad (6.50)$$

for the integration constants  $A_{i\lambda}$  ( $i = \{1, 2, 3\}$ ) removes the singularities of the bending moments, while the singularities in the shear forces remain. Furthermore, this restriction simplifies the solution functions for  $0 < \lambda < 1$  (Equation (6.32)) to Equation (6.34).

### Hard simply-supported infinite wedge

The eigenvalues  $\lambda_k^s$  and  $\lambda_k^a$  are determined through the boundary conditions applied at the radial edges 1 and 2 (see Figure 6.1). However, an analytical solution for the dynamic problem is only available if both radial edges are hard simply-supported

$$w(r, \pm\alpha/2) = 0, \quad (6.51)$$

$$\psi_r(r, \pm\alpha/2) = 0, \quad (6.52)$$

$$M_\varphi(r, \pm\alpha/2) = 0. \quad (6.53)$$

According to [74], the symmetric and antisymmetric eigenvalues for the hard simply-supported infinite wedge are given by

$$\begin{aligned} \lambda_k^s &= (2k - 1) \frac{\pi}{\alpha}, \\ \lambda_k^a &= 2k \frac{\pi}{\alpha}. \end{aligned} \quad k = 1, 2, \dots \quad (6.54)$$

Using these eigenvalues in the general analytical solutions from the previous section and assuming  $\alpha < 2\pi$ , bending moment singularities in the vicinity of the corner are expected for internal angles  $\alpha > \pi/2$ , having the asymptotic behaviour

$$M|_{r \rightarrow 0} \sim r^{\frac{\pi}{\alpha} - 2}, \quad \frac{\pi}{2} < \alpha \leq \pi, \quad (6.55)$$

$$M|_{r \rightarrow 0} \sim r^{-\frac{\pi}{\alpha}} + r^{\frac{2\pi}{\alpha} - 2}, \quad \pi < \alpha \leq \frac{3\pi}{2}, \quad (6.56)$$

$$M|_{r \rightarrow 0} \sim r^{-\frac{\pi}{\alpha}} + r^{\frac{2\pi}{\alpha} - 2} + r^{\frac{3\pi}{\alpha} - 2}, \quad \frac{3\pi}{2} < \alpha \leq 2\pi. \quad (6.57)$$

Shear force singularities only arise for symmetric modes and an internal angle  $\alpha > \pi$ . The asymptotic behaviour of the shear forces in the vicinity of the corner is given by

$$Q|_{r \rightarrow 0} \sim r^{\frac{\pi}{\alpha} - 1}, \quad \pi < \alpha \leq 2\pi. \quad (6.58)$$

Since an analytical solution for the dynamic case is only available for the hard simply-supported boundary conditions, the solutions for the static problem are examined in the subsequent section.

#### 6.1.2 Static solution for an infinite wedge domain

While the literature on analytical solutions for bending vibrations of wedge domains is rather limited, several authors have investigated the static bending deformation of Reissner-Mindlin plates ( $\omega = 0$ ) and examined the stress singularities in the vicinity of the corner point. In [293] a series approach is applied and moment singularities for homogenous boundary conditions (clamped, free, hard simply-supported) are identified. An additional result for hard simply-supported boundary conditions, which has been missed in [293], is reported in [294]. Huang [290] used the Frobenius method to analyze the behaviour of the bending moments and shear forces in the vicinity of a corner point within the first-order shear deformation theory. Ten different combinations of homogenous boundary conditions (clamped, free, hard simply-supported, soft simply-supported) are considered

Table 6.1: Characteristic equations for the static eigenvalues of an infinite wedge domain

Boundary conditions	Characteristic equation	
	Moments	Shear forces
Clamped-clamped	$\sin(\bar{\lambda}_M^s \alpha) = \frac{\bar{\lambda}_M^s (1 + \nu)}{3 - \nu} \sin(\alpha)$	$\cos\left(\bar{\lambda}_Q^s \frac{\alpha}{2}\right) = 0$
	$\sin(\bar{\lambda}_M^a \alpha) = -\frac{\bar{\lambda}_M^a (1 + \nu)}{3 - \nu} \sin(\alpha)$	$\sin\left(\bar{\lambda}_Q^a \frac{\alpha}{2}\right) = 0$
Free-free	$\sin(\bar{\lambda}_M^s \alpha) = -\bar{\lambda}_M^s \sin(\alpha)$	$\sin\left(\bar{\lambda}_Q^s \frac{\alpha}{2}\right) = 0$
	$\sin(\bar{\lambda}_M^a \alpha) = \bar{\lambda}_M^a \sin(\alpha)$	$\cos\left(\bar{\lambda}_Q^a \frac{\alpha}{2}\right) = 0$
Hard SS-hard SS	$\cos\left(\left(\bar{\lambda}_M^s - 1\right) \frac{\alpha}{2}\right) \cos\left(\left(\bar{\lambda}_M^s + 1\right) \frac{\alpha}{2}\right) = 0$	$\cos\left(\bar{\lambda}_Q^s \frac{\alpha}{2}\right) = 0$
	$\sin\left(\left(\bar{\lambda}_M^a - 1\right) \frac{\alpha}{2}\right) \sin\left(\left(\bar{\lambda}_M^a + 1\right) \frac{\alpha}{2}\right) = 0$	$\sin\left(\bar{\lambda}_Q^a \frac{\alpha}{2}\right) = 0$
Soft SS-soft SS	$\sin(\bar{\lambda}_M^s \alpha) = -\bar{\lambda}_M^s \sin(\alpha)$	$\cos\left(\bar{\lambda}_Q^s \frac{\alpha}{2}\right) = 0$
	$\sin(\bar{\lambda}_M^a \alpha) = \bar{\lambda}_M^a \sin(\alpha)$	$\sin\left(\bar{\lambda}_Q^a \frac{\alpha}{2}\right) = 0$
Clamped-free	$\sin^2(\bar{\lambda}_M \alpha) = \frac{4 - \bar{\lambda}_M^2 (1 + \nu)^2 \sin^2(\alpha)}{(3 - \nu)(1 + \nu)}$	$\cos(\bar{\lambda}_Q \alpha) = 0$
Clamped-hard SS	$\sin(2\bar{\lambda}_M \alpha) = -\frac{\bar{\lambda}_M (1 + \nu)}{(3 - \nu)} \sin(2\alpha)$	$\sin(\bar{\lambda}_Q \alpha) = 0$
Clamped-soft SS	$\sin^2(\bar{\lambda}_M \alpha) = \frac{4 - \bar{\lambda}_M^2 (1 + \nu)^2}{(3 - \nu)(1 + \nu)} \sin^2(\alpha)$	$\sin(\bar{\lambda}_Q \alpha) = 0$
Hard SS-free	$\sin(2\bar{\lambda}_M \alpha) = \bar{\lambda}_M \sin(2\alpha)$	$\cos(\bar{\lambda}_Q \alpha) = 0$
Hard SS-soft SS	$\sin(2\bar{\lambda}_M \alpha) = \bar{\lambda}_M \sin(2\alpha)$	$\sin(\bar{\lambda}_Q \alpha) = 0$
Soft SS-free	$\sin(\bar{\lambda}_M \alpha) = \pm \bar{\lambda}_M \sin(\alpha)$	$\cos(\bar{\lambda}_Q \alpha) = 0$

and compared to [293] and [294], also shear force singularities are reported. Functional analytical methods are applied in [295] to study corner stress singularities and the results from Huang [290] are confirmed, while additional homogenous boundary conditions (soft clamped, two different frictional conditions, sliding edge), which are less common, are included. The effect of logarithmic stress singularities and logarithmic intensification of power stress singularities are mentioned in [293], [294], [291], [295] and [296], but only pure power stress singularities have been examined. In [297], several plate configurations with homogenous boundary conditions, which lead to logarithmic corner stress singularities, are reported, while in [291] the possibility of logarithmic corner stress singularities induced by inhomogeneous boundary conditions is stated. In [296], a complex potential method is applied to study corner stress singularities in isotropic homogeneous and bi-material wedges having homogenous boundary conditions, while Huang [298] uses an eigenfunction

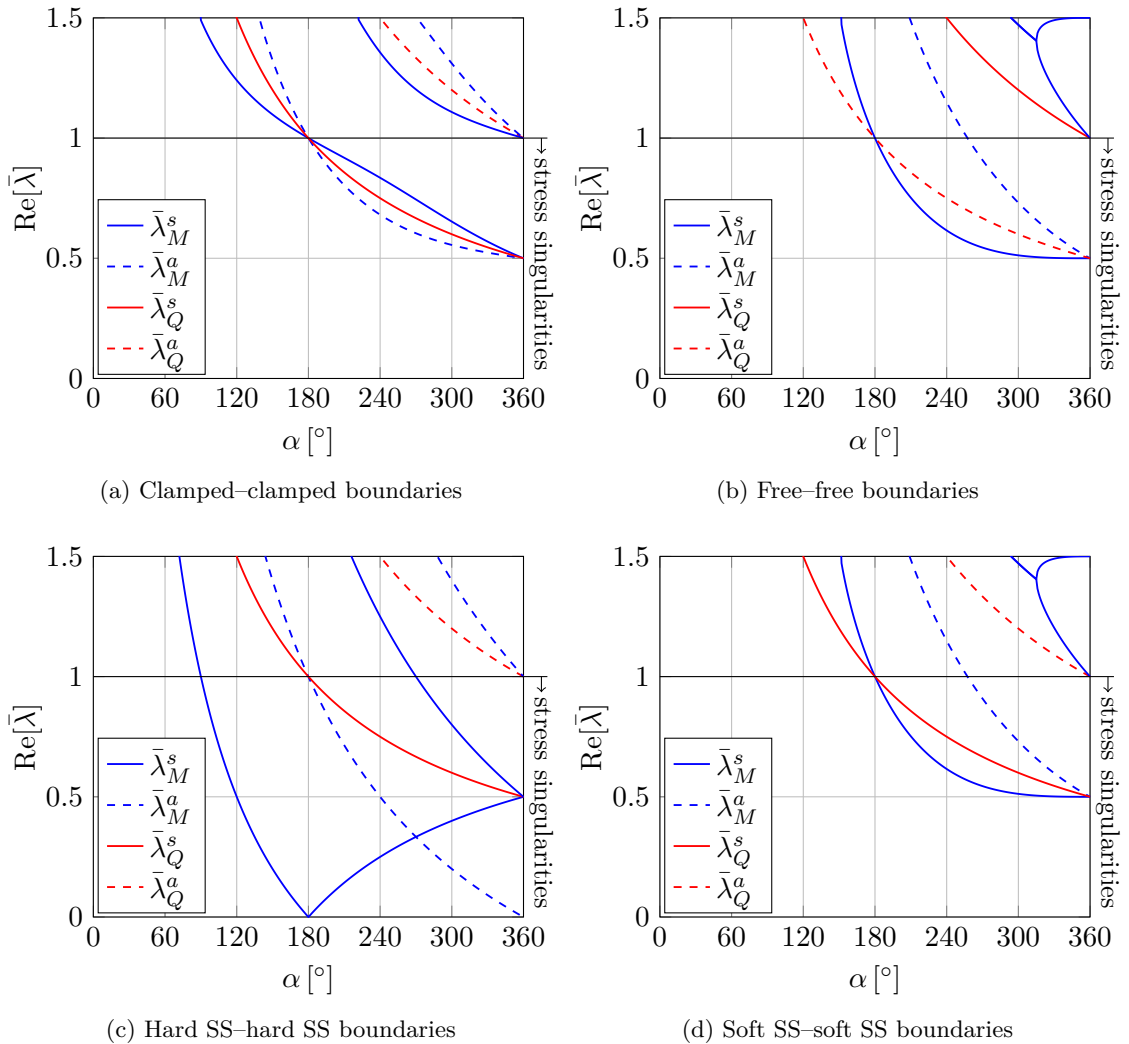
### 6.1 Stress singularities in the Mindlin plate theory

expansion solution to study corner stress singularities in bi-material Mindlin plates.

In this work, plates consisting of a single linear elastic material with homogenous boundary conditions are considered. The effect of logarithmic stress singularities only appears for a few specific internal angles  $\alpha$  and are not taken into account. According to Huang [290], the bending moments and shear forces in the vicinity of the corner have the asymptotic behaviour

$$M|_{r \rightarrow 0} \sim r^{\bar{\lambda}_M - 1} \quad \text{and} \quad Q|_{r \rightarrow 0} \sim r^{\bar{\lambda}_Q - 1} \quad (6.59)$$

where  $\bar{\lambda}_M > 0$  and  $\bar{\lambda}_Q > 0$  are the static eigenvalues for moments and shear force singularities. The characteristic equations to determine the static eigenvalues are derived in [290] and are stated in Table 6.1 for completeness. If the boundary conditions are symmetric, it is possible to distinguish between eigenvalues for symmetric ( $\bar{\lambda}_M^s, \bar{\lambda}_Q^s$ ) and antisymmetric deformations ( $\bar{\lambda}_M^a, \bar{\lambda}_Q^a$ ). The characteristic equations in Table 6.1 are solved with the routine *fsolve* (trust-region dogleg algorithm) from the commercial software package *MATLAB<sup>®</sup> R2016b* and the resulting static eigenvalues are plotted in Figure 6.2.



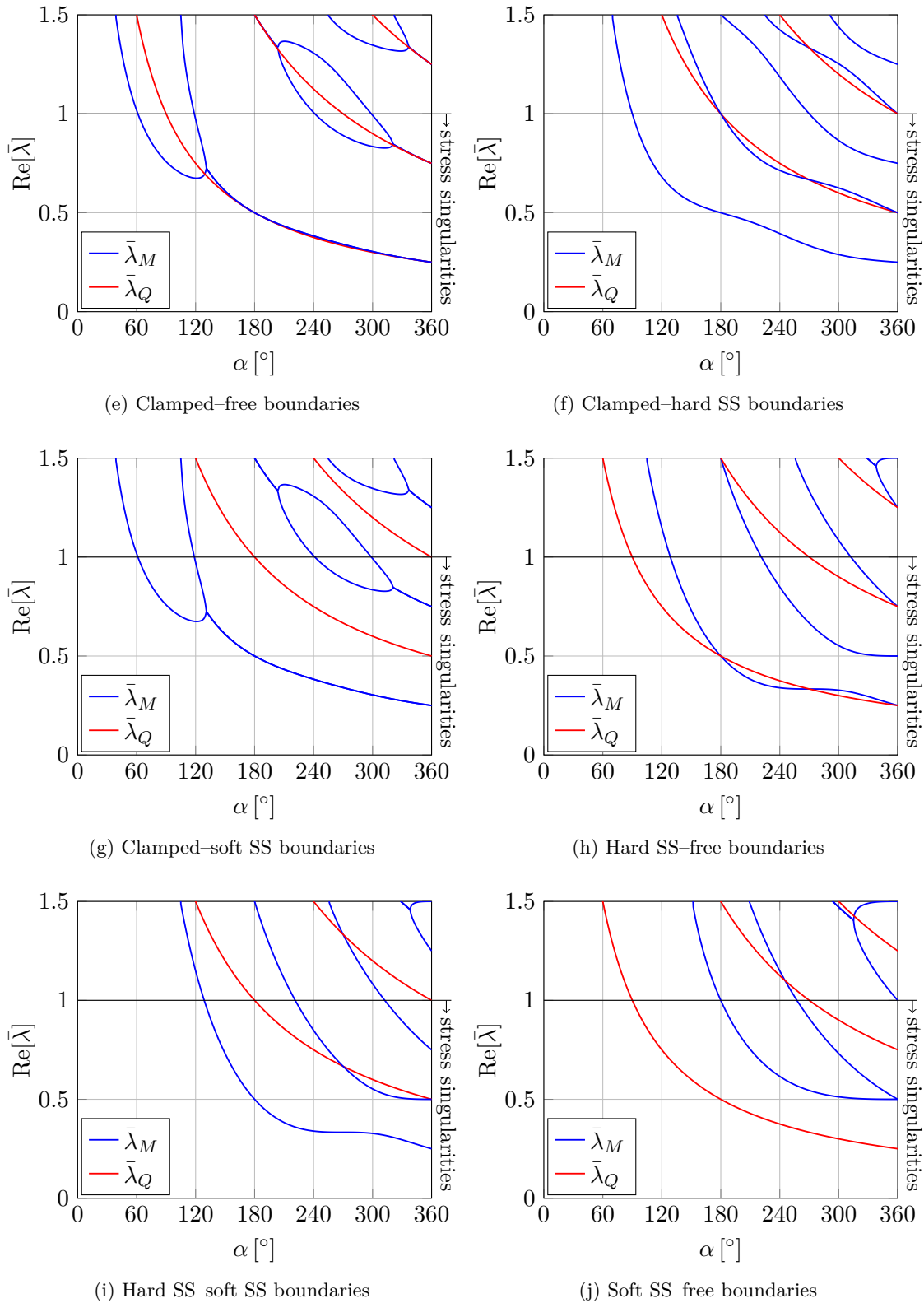


Figure 6.2: Static eigenvalues of an infinite wedge domain with various radial boundary conditions

### 6.1.3 Comparison of the singularities in the static and dynamic solution

The analytical solutions of the static and dynamic hard simply-supported infinite wedge can be used to compare the singular behaviour of the moment and shear forces in the vicinity of the corner point. In case of hard simply-supported radial boundaries, the static eigenvalues can be computed in closed-form and from Equation (6.59) it is apparent that stress singularities only occur for static eigenvalues smaller than 1. The comparison of the static and dynamic eigenvalues listed in Table 6.2 shows that the asymptotic behaviour of the bending moments and shear forces is identical for both cases.

Table 6.2: Comparison of the static and dynamic eigenvalues causing singularities

	Moments		Shear forces	
	static	dynamic	static	dynamic
$\frac{\pi}{2} \wedge \alpha \wedge \pi$	$M \sim r^{\bar{\lambda}_{M1}^s - 1}$ , $\bar{\lambda}_{M1}^s = \frac{\pi}{\alpha} - 1$ ,	$M \sim r^{\lambda_1^s - 2}$ , $\lambda_1^s = \frac{\pi}{\alpha}$ ,	—	—
$\pi \wedge \alpha \wedge \frac{3\pi}{2}$	$M \sim r^{\bar{\lambda}_{M2}^s - 1} + r^{\bar{\lambda}_{M1}^a - 1}$ , $\bar{\lambda}_{M2}^s = -\frac{\pi}{\alpha} + 1$ , $\bar{\lambda}_{M1}^a = \frac{2\pi}{\alpha} - 1$ ,	$M \sim r^{-\lambda_1^s} + r^{\lambda_1^a - 2}$ , $\lambda_1^s = \frac{\pi}{\alpha}$ , $\lambda_1^a = \frac{2\pi}{\alpha}$ ,	$Q \sim r^{\bar{\lambda}_{Q1}^s - 1}$ , $\bar{\lambda}_{Q1}^s = \frac{\pi}{\alpha}$ ,	$Q \sim r^{\lambda_1^s - 1}$ , $\lambda_1^s = \frac{\pi}{\alpha}$ ,
$\frac{3\pi}{2} \wedge \alpha \wedge 2\pi$	$M \sim r^{\bar{\lambda}_{M2}^s - 1} + r^{\bar{\lambda}_{M1}^a - 1} + r^{\bar{\lambda}_{M3}^s - 1}$ , $\bar{\lambda}_{M3}^s = \frac{3\pi}{\alpha} - 1$ ,	$M \sim r^{-\lambda_1^s} + r^{\lambda_1^a - 2} + r^{\lambda_2^s - 2}$ , $\lambda_2^s = \frac{3\pi}{\alpha}$ ,	$Q \sim r^{\bar{\lambda}_{Q1}^s - 1}$ , $\bar{\lambda}_{Q1}^s = \frac{\pi}{\alpha}$ ,	$Q \sim r^{\lambda_1^s - 1}$ , $\lambda_1^s = \frac{\pi}{\alpha}$ ,

The eigenvalues from the static and dynamic case are related by  $\bar{\lambda}_M = \lambda - 1$  ( $\lambda > 1$ ) and  $\bar{\lambda}_M = 1 - \lambda$  ( $\lambda < 1$ ) for moment singularities and  $\bar{\lambda}_Q = \lambda$  ( $\lambda < 1$ ) for shear force singularities.

Since in the static case, two different analytical solutions are used to find the eigenvalues for moment and shear force singularities, both eigenvalues are determined independently from each other. In the dynamic case however, eigenvalues smaller than 1 always induce singularities in both fields if the analytical solutions from Equation (6.32) are applied, while eigenvalues greater than 1 and smaller than 2 only exhibit moment singularities (solutions from Equation (6.34)). For  $0 < \lambda < 1$ , the order of the moment and shear force singularities ( $M \sim r^{-\lambda_M}$ ,  $Q \sim r^{-\lambda_Q}$ ) are therefore related by  $\lambda_Q = 1 - \lambda_M$ . This relation is generally not fulfilled for the eigenvalues of the static solution, with the exception of hard simply-supported radial edges.

By adding the restriction given in Equation (6.50) to the general dynamic solutions in Equation (6.32), the moment singularity for  $0 < \lambda < 1$  vanishes and only the shear force singularities remain. This allows for the independent definition of analytical solutions having either moment singularities ( $1 < \lambda < 2$ ) or shear force singularities ( $0 < \lambda < 1$ ) for the dynamic problem.

## 6.2 Application of the Wave Based Method

In this section, the general methodology of the WBM for generalized Helmholtz problems, shown in Section 4.1, is applied to the Mindlin plate vibration problem. The field variable expansion is presented in Section 6.2.1, including the development of the T-complete function sets and the definition of special purpose functions to treat corner stress singularities. The construction of the system matrices and the derivation of the weighted residual formulation from the sub-region three-field generalized mixed variational form of the Mindlin plate are outlined in Section 6.2.2.

In Figure 6.3, a general Mindlin WBM model with  $n_\alpha$  convex sub-domains is illustrated. Each sub-domain  $\alpha$  has a local domain coordinate system  $(x_D^{(\alpha)}, y_D^{(\alpha)})$ , which is aligned with the smallest rectangular bounding box having the dimensions  $L_x^{(\alpha)}$  and  $L_y^{(\alpha)}$ . Depending on the applied boundary conditions and the interfaces to adjacent sub-domains, the boundary of each sub-domain  $\alpha$  is divided into non-overlapping parts  $\Gamma^{(\alpha)} = \Gamma_u^{(\alpha)} \cup \Gamma_\sigma^{(\alpha)} \cup \Gamma_{u\sigma 1}^{(\alpha)} \cup \Gamma_{u\sigma 2}^{(\alpha)} \cup \Gamma^{(\alpha, \beta)}$ . If a certain type of the four common boundary conditions is not present at the sub-domain  $\alpha$ , the associated boundary part becomes  $\Gamma_\bullet^{(\alpha)} = \emptyset$ . Similar, the part of the interface becomes  $\Gamma^{(\alpha, \beta)} = \emptyset$  if the sub-domains  $\alpha$  and  $\beta$  do not share a common boundary.

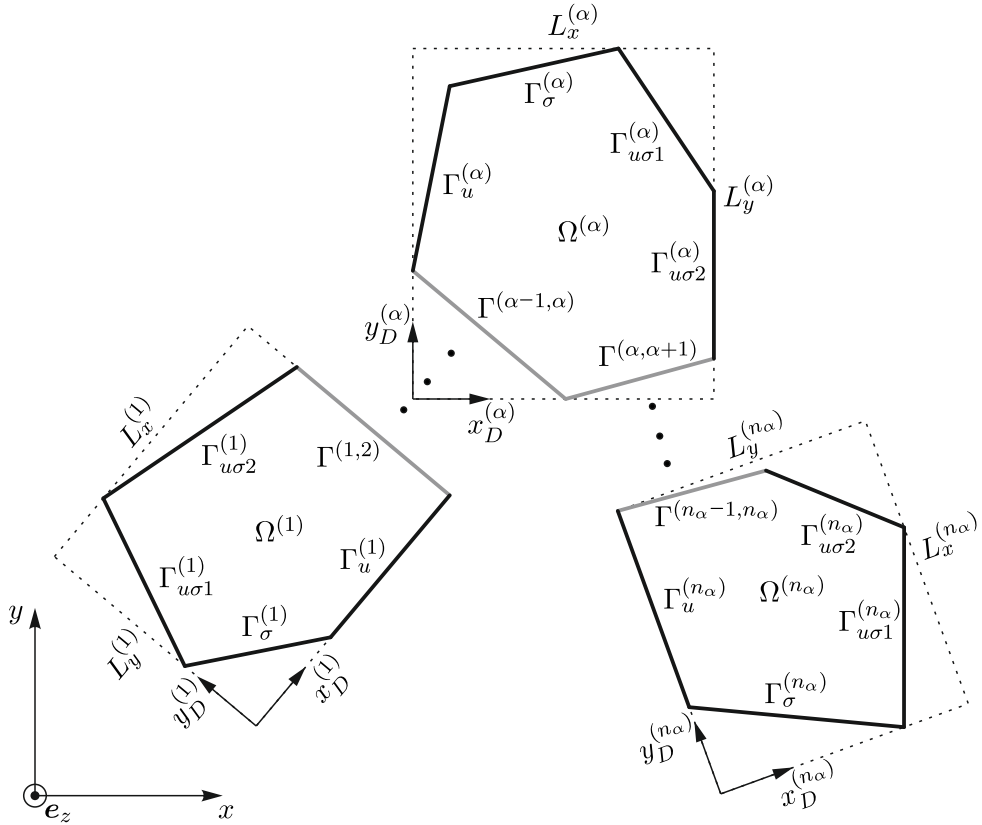


Figure 6.3: WBM sub-domains and domain coordinate systems of a general Mindlin plate

### 6.2.1 Field variable expansion

As pointed out in Section 2.2.1, the governing equations of the Mindlin plate theory can be decomposed into three Helmholtz equations ( $n_H = 3$ ) with the field variables  $w_1^{(\alpha)}(\mathbf{r})$ ,  $w_2^{(\alpha)}(\mathbf{r})$  and  $H^{(\alpha)}(\mathbf{r})$  within each sub-domain  $\alpha$ . The three field variables are approximated by the field variable expansions

$$w_1^{(\alpha)} \approx \hat{w}_1^{(\alpha)} = \sum_{k_{w1}=0}^{n_{w1}^{(\alpha)}} \hat{u}_{k_{w1}}^{(\alpha)} \Phi_{k_{w1}}^{(\alpha)} + \sum_{c_i} \hat{w}_{1C}^{(c_i)} + \hat{w}_{1p}^{(\alpha)}, \quad (6.60)$$

$$w_2^{(\alpha)} \approx \hat{w}_2^{(\alpha)} = \sum_{k_{w2}=0}^{n_{w2}^{(\alpha)}} \hat{u}_{k_{w2}}^{(\alpha)} \Phi_{k_{w2}}^{(\alpha)} + \sum_{c_i} \hat{w}_{2C}^{(c_i)} + \hat{w}_{2p}^{(\alpha)}, \quad (6.61)$$

$$H^{(\alpha)} \approx \hat{H}^{(\alpha)} = \sum_{k_H=0}^{n_H^{(\alpha)}} \hat{u}_{k_H}^{(\alpha)} \Phi_{k_H}^{(\alpha)} + \sum_{c_i} \hat{H}_C^{(c_i)} + \hat{H}_p^{(\alpha)}, \quad (6.62)$$

where  $\Phi_{\bullet}^{(\alpha)}$  are the wave functions, which form a T-complete set,  $\hat{u}_{\bullet}^{(\alpha)}$  the wave contribution factors,  $\hat{w}_{1C}^{(c_i)}$ ,  $\hat{w}_{2C}^{(c_i)}$  and  $\hat{H}_C^{(c_i)}$  the special purpose functions to treat corner stress singularities at the corner  $c_i$  and  $\hat{w}_{1p}^{(\alpha)}$ ,  $\hat{w}_{2p}^{(\alpha)}$  and  $\hat{H}_p^{(\alpha)}$  the particular solution functions.

Since the particular solution functions shown in Chapter 5 are given in terms of the out-of-plane displacement  $w$  and the rotations  $\psi_x$  and  $\psi_y$ , a splitting of the results into the components  $\hat{w}_{1p}^{(\alpha)}$ ,  $\hat{w}_{2p}^{(\alpha)}$  and  $\hat{H}_p^{(\alpha)}$  has to be performed. The terms in the solutions of Chapter 5 associated with the wavenumber  $k_{f1}$  lead to  $\hat{w}_{1p}^{(\alpha)}$ , while the terms associated with  $k_{f2}$  result in  $\hat{w}_{2p}^{(\alpha)}$ . The component  $\hat{H}_p^{(\alpha)}$  is equal to zero for the considered load cases.

#### T-complete sets of wave functions

The wave functions  $\Phi_{\bullet}^{(\alpha)}$  have to form a T-complete set, to ensure the convergence of the WBM to the exact solution. The applied basis functions  $\Phi_{\bullet}^{(\alpha)}$ , which are very similar to the basis functions used in [17] for the Kirchhoff plate theory, are listed in Table 6.3. The wave functions are defined in the local domain coordinate system and two different function sets are considered. In [21], it is shown that using the smallest rectangular bounding box to define the wavenumbers in Table 6.3, results in the highest convergence rate of the WBM. The first wavenumbers are chosen as such that an integer number of half wavelenghts equals the dimension of the bounding box, which leads to

$$k_{i_{w1},x}^{(\alpha)} = \frac{i_{w1} \pi}{L_x^{(\alpha)}} \quad \text{and} \quad k_{j_{w1},y}^{(\alpha)} = \frac{j_{w1} \pi}{L_y^{(\alpha)}}, \quad (6.63)$$

$$k_{i_{w2},x}^{(\alpha)} = \frac{i_{w2} \pi}{L_x^{(\alpha)}} \quad \text{and} \quad k_{j_{w2},y}^{(\alpha)} = \frac{j_{w2} \pi}{L_y^{(\alpha)}}, \quad (6.64)$$

$$k_{i_H,x}^{(\alpha)} = \frac{i_H \pi}{L_x^{(\alpha)}} \quad \text{and} \quad k_{j_H,y}^{(\alpha)} = \frac{j_H \pi}{L_y^{(\alpha)}}. \quad (6.65)$$

Table 6.3: Wave function sets for the Mindlin plate problem

Wave function sets for $w_1$		
Set 1	$\Phi_{i_{w1}}^{(\alpha)} = \cos(k_{i_{w1},x}^{(\alpha)} x_D^{(\alpha)}) \exp(-j k_{i_{w1},y}^{(\alpha)} y_D^{(\alpha)})$	$i_{w1} = 0, 1, \dots n_{w1i}^{(\alpha)}$
	$\Phi_{j_{w1}}^{(\alpha)} = \exp(-j k_{j_{w1},x}^{(\alpha)} x_D^{(\alpha)}) \cos(k_{j_{w1},y}^{(\alpha)} y_D^{(\alpha)})$	$j_{w1} = 0, 1, \dots n_{w1j}^{(\alpha)}$
Set 2	$\Phi'_{i_{w1}}^{(\alpha)} = \sin(k_{i_{w1},x}^{(\alpha)} x_D^{(\alpha)}) \exp(-j k_{i_{w1},y}^{(\alpha)} y_D^{(\alpha)})$	$i_{w1} = 1, 2, \dots n'_{w1i}^{(\alpha)}$
	$\Phi'_{j_{w1}}^{(\alpha)} = \exp(-j k_{j_{w1},x}^{(\alpha)} x_D^{(\alpha)}) \sin(k_{j_{w1},y}^{(\alpha)} y_D^{(\alpha)})$	$j_{w1} = 1, 2, \dots n'_{w1j}^{(\alpha)}$
Wave function sets for $w_2$		
Set 1	$\Phi_{i_{w2}}^{(\alpha)} = \cos(k_{i_{w2},x}^{(\alpha)} x_D^{(\alpha)}) \exp(-j k_{i_{w2},y}^{(\alpha)} y_D^{(\alpha)})$	$i_{w2} = 0, 1, \dots n_{w2i}^{(\alpha)}$
	$\Phi_{j_{w2}}^{(\alpha)} = \exp(-j k_{j_{w2},x}^{(\alpha)} x_D^{(\alpha)}) \cos(k_{j_{w2},y}^{(\alpha)} y_D^{(\alpha)})$	$j_{w2} = 0, 1, \dots n_{w2j}^{(\alpha)}$
Set 2	$\Phi'_{i_{w2}}^{(\alpha)} = \sin(k_{i_{w2},x}^{(\alpha)} x_D^{(\alpha)}) \exp(-j k_{i_{w2},y}^{(\alpha)} y_D^{(\alpha)})$	$i_{w2} = 1, 2, \dots n'_{w2i}^{(\alpha)}$
	$\Phi'_{j_{w2}}^{(\alpha)} = \exp(-j k_{j_{w2},x}^{(\alpha)} x_D^{(\alpha)}) \sin(k_{j_{w2},y}^{(\alpha)} y_D^{(\alpha)})$	$j_{w2} = 1, 2, \dots n'_{w2j}^{(\alpha)}$
Wave function sets for $H$		
Set 1	$\Phi_{i_H}^{(\alpha)} = \sin(k_{i_H,x}^{(\alpha)} x_D^{(\alpha)}) \exp(-j k_{i_H,y}^{(\alpha)} y_D^{(\alpha)})$	$i_H = 1, 2, \dots n_{Hi}^{(\alpha)}$
	$\Phi_{j_H}^{(\alpha)} = \exp(-j k_{j_H,x}^{(\alpha)} x_D^{(\alpha)}) \sin(k_{j_H,y}^{(\alpha)} y_D^{(\alpha)})$	$j_H = 1, 2, \dots n_{Hj}^{(\alpha)}$
Set 2	$\Phi'_{i_H}^{(\alpha)} = \cos(k_{i_H,x}^{(\alpha)} x_D^{(\alpha)}) \exp(-j k_{i_H,y}^{(\alpha)} y_D^{(\alpha)})$	$i_H = 0, 1, \dots n'_{Hi}^{(\alpha)}$
	$\Phi'_{j_H}^{(\alpha)} = \exp(-j k_{j_H,x}^{(\alpha)} x_D^{(\alpha)}) \cos(k_{j_H,y}^{(\alpha)} y_D^{(\alpha)})$	$j_H = 0, 1, \dots n'_{Hj}^{(\alpha)}$

The Helmholtz equations (Equations (2.63)–(2.65)) are only fulfilled if the corresponding wavenumbers are defined by

$$k_{i_{w1},y}^{(\alpha)} = \pm \sqrt{(k_{f1}^{(\alpha)})^2 - (k_{i_{w1},x}^{(\alpha)})^2} \quad \text{and} \quad k_{j_{w1},x}^{(\alpha)} = \pm \sqrt{(k_{f1}^{(\alpha)})^2 - (k_{j_{w1},y}^{(\alpha)})^2}, \quad (6.66)$$

$$k_{i_{w2},y}^{(\alpha)} = \pm \sqrt{(k_{f2}^{(\alpha)})^2 - (k_{i_{w2},x}^{(\alpha)})^2} \quad \text{and} \quad k_{j_{w2},x}^{(\alpha)} = \pm \sqrt{(k_{f2}^{(\alpha)})^2 - (k_{j_{w2},y}^{(\alpha)})^2}, \quad (6.67)$$

$$k_{i_H,y}^{(\alpha)} = \pm \sqrt{(k_s^{(\alpha)})^2 - (k_{i_H,x}^{(\alpha)})^2} \quad \text{and} \quad k_{j_H,x}^{(\alpha)} = \pm \sqrt{(k_s^{(\alpha)})^2 - (k_{j_H,y}^{(\alpha)})^2}. \quad (6.68)$$

It is apparent from Table 6.3 that four different types of wave functions are defined for each field variable ( $\Phi_{k_{w1}}^{(\alpha)} \rightarrow \{\Phi_{i_{w1}}^{(\alpha)}, \Phi_{j_{w1}}^{(\alpha)}, \Phi'_{i_{w1}}^{(\alpha)}, \Phi'_{j_{w1}}^{(\alpha)}\}$ ,  $\Phi_{k_{w2}}^{(\alpha)} \rightarrow \{\Phi_{i_{w2}}^{(\alpha)}, \Phi_{j_{w2}}^{(\alpha)}, \Phi'_{i_{w2}}^{(\alpha)}, \Phi'_{j_{w2}}^{(\alpha)}\}$ ,  $\Phi_{k_H}^{(\alpha)} \rightarrow \{\Phi_{i_H}^{(\alpha)}, \Phi_{j_H}^{(\alpha)}, \Phi'_{i_H}^{(\alpha)}, \Phi'_{j_H}^{(\alpha)}\}$ ) and therefore, the total number of wave functions in

## 6.2 Application of the Wave Based Method

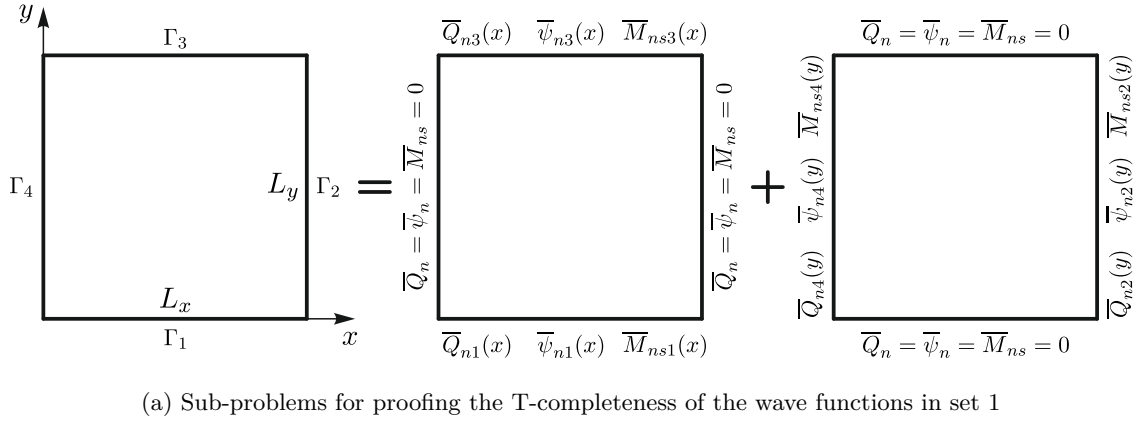
each sub-domain  $\alpha$  is given by

$$n_{w1}^{(\alpha)} = 2 \left( n_{w1i}^{(\alpha)} + n_{w1j}^{(\alpha)} + n_{w1i}'^{(\alpha)} + n_{w1j}'^{(\alpha)} + 2 \right), \quad (6.69)$$

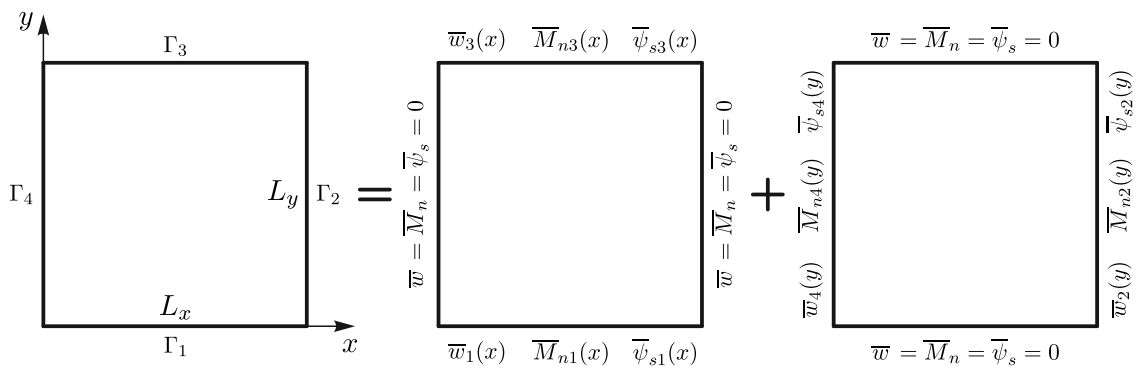
$$n_{w2}^{(\alpha)} = 2 \left( n_{w2i}^{(\alpha)} + n_{w2j}^{(\alpha)} + n_{w2i}'^{(\alpha)} + n_{w2j}'^{(\alpha)} + 2 \right), \quad (6.70)$$

$$n_H^{(\alpha)} = 2 \left( n_{Hi}^{(\alpha)} + n_{Hj}^{(\alpha)} + n_{Hi}'^{(\alpha)} + n_{Hj}'^{(\alpha)} + 2 \right). \quad (6.71)$$

In [21], it is shown that the T-completeness of a function set for convex domains is ensured if the function set is able to represent arbitrary boundary conditions at the edges of a rectangular domain, which encloses the convex domain. Since the Mindlin plate vibration problem is governed by three Helmholtz equations, three arbitrary boundary conditions have to be fulfilled at the edges of the problem domain. To show the T-completeness of the two different function sets given in Table 6.3, two rectangular domains with arbitrary boundary conditions are investigated. In Figure 6.4a a rectangular domain with prescribed boundary conditions  $\bar{Q}_n$ ,  $\bar{\psi}_n$  and  $\bar{M}_{ns}$  at the edges  $\Gamma_1$ – $\Gamma_4$  is shown. Similar to the approach used in [17], the problem is split into two sub-problems to proof the T-completeness of the first function set in Table 6.3. The rectangular domain, illustrated in Figure 6.4b, is used to show the capability of the second function set to represent arbitrary boundary conditions.



(a) Sub-problems for proving the T-completeness of the wave functions in set 1



(b) Sub-problems for proving the T-completeness of the wave functions in set 2

Figure 6.4: Rectangular domains with arbitrary boundary conditions

For the first sub-problems in Figures 6.4a and 6.4b (zero boundary conditions at  $x = 0$  and  $x = L_x$ ), the first wave functions of set 1 ( $\Phi_{i_{w1}}, \Phi_{i_{w2}}, \Phi_{i_H}$ ) and set 2 ( $\Phi'_{i_{w1}}, \Phi'_{i_{w2}}, \Phi'_{i_H}$ ) are applied. Evaluating the displacements, rotations, bending moments and shear forces using the formulas from Section 2.2.1 shows that the boundary conditions at the edges  $\Gamma_2$  and  $\Gamma_4$  are only fulfilled if

$$\sin(k_{i_{w1},x} L_x) = 0, \quad (6.72)$$

$$\sin(k_{i_{w2},x} L_x) = 0, \quad (6.73)$$

$$\sin(k_{i_H,x} L_x) = 0. \quad (6.74)$$

The choice of  $k_{i_{w1},x}$ ,  $k_{i_{w2},x}$  and  $k_{i_H,x}$  given in Equations (6.63)–(6.65) satisfies these conditions and therefore the zero boundary conditions of the first sub-problems are fulfilled. Similar, applying the second wave functions of set 1 ( $\Phi_{j_{w1}}, \Phi_{j_{w2}}, \Phi_{j_H}$ ) and set 2 ( $\Phi'_{j_{w1}}, \Phi'_{j_{w2}}, \Phi'_{j_H}$ ) to the second sub-problems in Figures 6.4a and 6.4b (zero boundary conditions at  $y = 0$  and  $y = L_y$ ) leads to

$$\sin(k_{j_{w1},y} L_y) = 0, \quad (6.75)$$

$$\sin(k_{j_{w2},y} L_y) = 0, \quad (6.76)$$

$$\sin(k_{j_H,y} L_y) = 0, \quad (6.77)$$

for the boundary conditions at  $\Gamma_1$  and  $\Gamma_3$ . These conditions are also fulfilled by the wavenumbers given in Equations (6.63)–(6.65).

For the first sub-problem in Figure 6.4a, the boundary conditions at the edges  $\Gamma_1$  and  $\Gamma_3$  have to be satisfied by the function series

$$w_1(x, y) = \sum_{i_{w1}=0}^{\infty} \cos(k_{i_{w1},x} x) \left( \hat{u}_{i_{w1}} e^{-j \sqrt{k_{f1}^2 - k_{i_{w1},x}^2} y} + \hat{u}_{i_{w1}}^* e^{j \sqrt{k_{f1}^2 - k_{i_{w1},x}^2} y} \right), \quad (6.78)$$

$$w_2(x, y) = \sum_{i_{w2}=0}^{\infty} \cos(k_{i_{w2},x} x) \left( \hat{u}_{i_{w2}} e^{-j \sqrt{k_{f2}^2 - k_{i_{w2},x}^2} y} + \hat{u}_{i_{w2}}^* e^{j \sqrt{k_{f2}^2 - k_{i_{w2},x}^2} y} \right), \quad (6.79)$$

$$H(x, y) = \sum_{i_H=1}^{\infty} \sin(k_{i_H,x} x) \left( \hat{u}_{i_H} e^{-j \sqrt{k_s^2 - k_{i_H,x}^2} y} + \hat{u}_{i_H}^* e^{j \sqrt{k_s^2 - k_{i_H,x}^2} y} \right), \quad (6.80)$$

while the boundary conditions at the edges  $\Gamma_2$  and  $\Gamma_4$  in the second sub-problem have to be fulfilled by the function series

$$w_1(x, y) = \sum_{j_{w1}=0}^{\infty} \cos(k_{j_{w1},y} y) \left( \hat{u}_{j_{w1}} e^{-j \sqrt{k_{f1}^2 - k_{j_{w1},y}^2} x} + \hat{u}_{j_{w1}}^* e^{j \sqrt{k_{f1}^2 - k_{j_{w1},y}^2} x} \right), \quad (6.81)$$

$$w_2(x, y) = \sum_{j_{w2}=0}^{\infty} \cos(k_{j_{w2},y} y) \left( \hat{u}_{j_{w2}} e^{-j \sqrt{k_{f2}^2 - k_{j_{w2},y}^2} x} + \hat{u}_{j_{w2}}^* e^{j \sqrt{k_{f2}^2 - k_{j_{w2},y}^2} x} \right), \quad (6.82)$$

$$H(x, y) = \sum_{j_H=1}^{\infty} \sin(k_{j_H,y} y) \left( \hat{u}_{j_H} e^{-j \sqrt{k_s^2 - k_{j_H,y}^2} x} + \hat{u}_{j_H}^* e^{j \sqrt{k_s^2 - k_{j_H,y}^2} x} \right). \quad (6.83)$$

In Equations (6.78)–(6.83),  $\hat{u}_{i_{w1}}, \hat{u}_{i_{w1}}^*, \hat{u}_{i_{w2}}, \hat{u}_{i_{w2}}^*, \hat{u}_{i_H}, \hat{u}_{i_H}^*, \hat{u}_{j_{w1}}, \hat{u}_{j_{w1}}^*, \hat{u}_{j_{w2}}, \hat{u}_{j_{w2}}^*, \hat{u}_{j_H}$  and  $\hat{u}_{j_H}^*$  are arbitrary constants.

## 6.2 Application of the Wave Based Method

Evaluating  $Q_n(x, y)$ ,  $\psi_n(x, y)$  and  $M_{ns}(x, y)$  at the boundary  $\Gamma_1$  ( $y = 0$ ) using the function series in Equations (6.78)–(6.80) and the relations stated in Section 2.2.1 leads to the conditions

$$Q_n(x, 0) = k^2 G h \left( \sum_{i_{w1}=0}^{\infty} \mu_1 \hat{a}_{i_{w1}} \cos(k_{i_{w1},x} x) + \sum_{i_{w2}=0}^{\infty} \mu_2 \hat{b}_{i_{w2}} \cos(k_{i_{w2},x} x) + \sum_{i_H=1}^{\infty} k_{i_H,x} \hat{c}_{i_H} \cos(k_{i_H,x} x) \right) = \bar{Q}_{n1}(x), \quad (6.84)$$

$$\psi_n(x, 0) = \sum_{i_{w1}=0}^{\infty} (\mu_1 - 1) \hat{a}_{i_{w1}} \cos(k_{i_{w1},x} x) + \sum_{i_{w2}=0}^{\infty} (\mu_2 - 1) \hat{b}_{i_{w2}} \cos(k_{i_{w2},x} x) + \sum_{i_H=1}^{\infty} k_{i_H,x} \hat{c}_{i_H} \cos(k_{i_H,x} x) = \bar{\psi}_{n1}(x), \quad (6.85)$$

$$M_{ns}(x, 0) = D(1 - \nu) \left( \sum_{i_{w1}=0}^{\infty} -(\mu_1 - 1) k_{i_{w1},x} \hat{a}_{i_{w1}} \sin(k_{i_{w1},x} x) - \sum_{i_{w2}=0}^{\infty} (\mu_2 - 1) k_{i_{w2},x} \hat{b}_{i_{w2}} \sin(k_{i_{w2},x} x) - \sum_{i_H=1}^{\infty} \left( k_{i_H,x}^2 - \frac{k_s^2}{2} \right) \hat{c}_{i_H} \sin(k_{i_H,x} x) \right) = \bar{M}_{ns1}(x), \quad (6.86)$$

and the results for the second boundary  $\Gamma_3$  ( $y = L_y$ ) are given by

$$Q_n(x, L_y) = k^2 G h \left( \sum_{i_{w1}=0}^{\infty} \mu_1 \hat{a}_{i_{w1}}^* \cos(k_{i_{w1},x} x) + \sum_{i_{w2}=0}^{\infty} \mu_2 \hat{b}_{i_{w2}}^* \cos(k_{i_{w2},x} x) + \sum_{i_H=1}^{\infty} k_{i_H,x} \hat{c}_{i_H}^* \cos(k_{i_H,x} x) \right) = \bar{Q}_{n3}(x), \quad (6.87)$$

$$\psi_n(x, L_y) = \sum_{i_{w1}=0}^{\infty} (\mu_1 - 1) \hat{a}_{i_{w1}}^* \cos(k_{i_{w1},x} x) + \sum_{i_{w2}=0}^{\infty} (\mu_2 - 1) \hat{b}_{i_{w2}}^* \cos(k_{i_{w2},x} x) + \sum_{i_H=1}^{\infty} k_{i_H,x} \hat{c}_{i_H}^* \cos(k_{i_H,x} x) = \bar{\psi}_{n3}(x), \quad (6.88)$$

$$M_{ns}(x, L_y) = D(1 - \nu) \left( \sum_{i_{w1}=0}^{\infty} (\mu_1 - 1) k_{i_{w1},x} \hat{a}_{i_{w1}}^* \sin(k_{i_{w1},x} x) + \sum_{i_{w2}=0}^{\infty} (\mu_2 - 1) k_{i_{w2},x} \hat{b}_{i_{w2}}^* \sin(k_{i_{w2},x} x) + \sum_{i_H=1}^{\infty} \left( k_{i_H,x}^2 - \frac{k_s^2}{2} \right) \hat{c}_{i_H}^* \sin(k_{i_H,x} x) \right) = \bar{M}_{ns3}(x), \quad (6.89)$$

which have to be fulfilled for any point  $x \in [0, L_x]$  at the boundaries  $\Gamma_1$  and  $\Gamma_3$ . The

arbitrary constants in Equations (6.84) – (6.89) are defined by

$$\hat{a}_{i_w1} = j \sqrt{k_{f1}^2 - k_{i_{w1},x}^2} (\hat{u}_{i_w1} - \hat{u}_{i_{w1}}^*), \quad (6.90)$$

$$\hat{b}_{i_w1} = j \sqrt{k_{f2}^2 - k_{i_{w2},x}^2} (\hat{u}_{i_w2} - \hat{u}_{i_{w2}}^*), \quad (6.91)$$

$$\hat{c}_{i_w1} = \hat{u}_{i_H} + \hat{u}_{i_H}^*, \quad (6.92)$$

$$\hat{a}_{i_w1}^* = -j \sqrt{k_{f1}^2 - k_{i_{w1},x}^2} \left( \hat{u}_{i_w1} e^{-j \sqrt{k_{f1}^2 - k_{i_{w1},x}^2} L_y} - \hat{u}_{i_{w1}}^* e^{j \sqrt{k_{f1}^2 - k_{i_{w1},x}^2} L_y} \right), \quad (6.93)$$

$$\hat{b}_{i_w2}^* = -j \sqrt{k_{f2}^2 - k_{i_{w2},x}^2} \left( \hat{u}_{i_w2} e^{-j \sqrt{k_{f2}^2 - k_{i_{w2},x}^2} L_y} - \hat{u}_{i_{w2}}^* e^{j \sqrt{k_{f2}^2 - k_{i_{w2},x}^2} L_y} \right), \quad (6.94)$$

$$\hat{c}_{i_H}^* = -j \left( \hat{u}_{i_H} e^{-j \sqrt{k_s^2 - k_{i_H,x}^2} L_y} - \hat{u}_{i_H}^* e^{j \sqrt{k_s^2 - k_{i_H,x}^2} L_y} \right). \quad (6.95)$$

The results in Equations (6.84), (6.85), (6.87) and (6.88) can be considered as half-range cosine Fourier series representations of the prescribed shear forces  $\bar{Q}_{n1}$  and  $\bar{Q}_{n3}$  and prescribed rotations  $\bar{\psi}_{n1}$  and  $\bar{\psi}_{n3}$ , while Equations (6.86) and (6.89) are half-range sine Fourier series representations of the prescribed bending moments  $\bar{M}_{ns1}$  and  $\bar{M}_{ns3}$ . As long as the distributions of the prescribed boundary conditions are piecewise continuous and bounded, the Fourier cosine and sine series converge uniformly to the prescribed distributions and the unknown coefficients in Equations (6.90) – (6.95) can be computed by the Euler formulas for Fourier coefficients [299]. Discontinuities in the prescribed distributions reduce the convergence rate of the Fourier cosine and sine series and may lead to the so-called Gibbs phenomenon (over- and undershoots close to the discontinuity) [299]. While for the Fourier cosine series this problem only arises if the prescribed distribution itself has a discontinuity, the Fourier sine series also suffers from this effect if the prescribed values at the end points ( $x = 0$  and  $x = L_x$ ) are unequal to zero. This is due to the required assumption of a periodic extension of the prescribed distribution outside the interval  $x \in [0, L_x]$ .

The results for the second sub-problem in Figure 6.4a can be found by interchanging  $x$  and  $y$  in Equations (6.84) – (6.89) and replacing the indices  $i_{\bullet}$  with  $j_{\bullet}$  and the applied boundary conditions from  $\Gamma_1$  and  $\Gamma_3$  to  $\Gamma_2$  and  $\Gamma_4$ . Therefore, the function set 1 in Table 6.3 is able to represent arbitrary boundary conditions for a rectangular domain and forms a T-complete function set for convex Mindlin plate domains.

The derivation for the function set 2 (rectangular plate in Figure 6.4b) leads to similar results, where the prescribed displacements  $\bar{w}_{\bullet}$  and bending moments  $M_{n\bullet}$  are represented by Fourier sine series and the rotation  $\psi_{s\bullet}$  by Fourier cosine series. Hence, also the function set 2 is a T-complete function set.

### Special purpose functions

According to [17], the WBM suffers from convergency problems if singularities are present in the field variables and therefore, so-called special purpose functions are included in the field variable expansion to avoid this issue. The special purpose functions have to satisfy the governing equations of the Mindlin plate and represent the singular behaviour of the

field variables. The analytical solutions of the infinite wedge domain, given in Section 6.1, can be used to treat corner stress singularities in the Mindlin plate theory. While for hard simply-supported boundary conditions, the exact solutions are available (fulfilling the governing equations and the boundary conditions), the solutions of the static problem are used to define the special purpose functions for all other combinations of boundary conditions. Three different types of corner functions have to be considered, which either exhibit moment singularities, shear force singularities or both at the corner point. If singularities are present at the corner point  $c_i$ , the special purpose functions

$$\begin{aligned} \hat{w}_{1C}^{(c_i)}(r_{c_i}, \varphi_{c_i}) &= \sum_{b=1}^{n_M^{(c_i)}} \hat{u}_{Mw1b}^{(c_i)} \Upsilon_{Mw1b}^{(c_i)} + \sum_{b=1}^{n_Q^{(c_i)}} \hat{u}_{Qw1b}^{(c_i)} \Upsilon_{Qw1b}^{(c_i)} \\ &+ \sum_{b=1}^{n_{MQ}^{(c_i)}} \hat{u}_{MQw1b}^{(c_i)} \Upsilon_{MQw1b}^{(c_i)} + \hat{u}_{MQw2b}^{(c_i)} \bar{\Upsilon}_{MQw1b}^{(c_i)} + \hat{u}_{MQHb}^{(c_i)} \tilde{\Upsilon}_{MQw1b}^{(c_i)}, \end{aligned} \quad (6.96)$$

$$\begin{aligned} \hat{w}_{2C}^{(c_i)}(r_{c_i}, \varphi_{c_i}) &= \sum_{b=1}^{n_M^{(c_i)}} \hat{u}_{Mw2b}^{(c_i)} \Upsilon_{Mw2b}^{(c_i)} + \sum_{b=1}^{n_Q^{(c_i)}} \hat{u}_{Qw1b}^{(c_i)} \Upsilon_{Qw2b}^{(c_i)} + \hat{u}_{QHb}^{(c_i)} \bar{\Upsilon}_{Qw2b}^{(c_i)} \\ &+ \sum_{b=1}^{n_{MQ}^{(c_i)}} \hat{u}_{MQw1b}^{(c_i)} \Upsilon_{MQw2b}^{(c_i)} + \hat{u}_{MQw2b}^{(c_i)} \bar{\Upsilon}_{MQw2b}^{(c_i)} + \hat{u}_{MQHb}^{(c_i)} \tilde{\Upsilon}_{MQw2b}^{(c_i)}, \end{aligned} \quad (6.97)$$

$$\begin{aligned} \hat{H}_C^{(c_i)}(r_{c_i}, \varphi_{c_i}) &= \sum_{b=1}^{n_M^{(c_i)}} \hat{u}_{MHb}^{(c_i)} \Upsilon_{MHb}^{(c_i)} + \sum_{b=1}^{n_Q^{(c_i)}} \hat{u}_{QHb}^{(c_i)} \Upsilon_{QHb}^{(c_i)} \\ &+ \sum_{b=1}^{n_{MQ}^{(c_i)}} \hat{u}_{MQw1b}^{(c_i)} \Upsilon_{MQHb}^{(c_i)} + \hat{u}_{MQw2b}^{(c_i)} \bar{\Upsilon}_{MQHb}^{(c_i)} + \hat{u}_{MQHb}^{(c_i)} \tilde{\Upsilon}_{MQHb}^{(c_i)}, \end{aligned} \quad (6.98)$$

are included in the field variable expansion. These corner functions are defined in a local corner coordinate system  $(r_{c_i}, \varphi_{c_i})$ , which is given by the coordinates of the corner point  $c_i$  and the associated bisecting line. As illustrated in Figure 6.5 the corner functions are not necessarily restricted to one sub-domain  $\alpha$ . While the corner functions defined at the

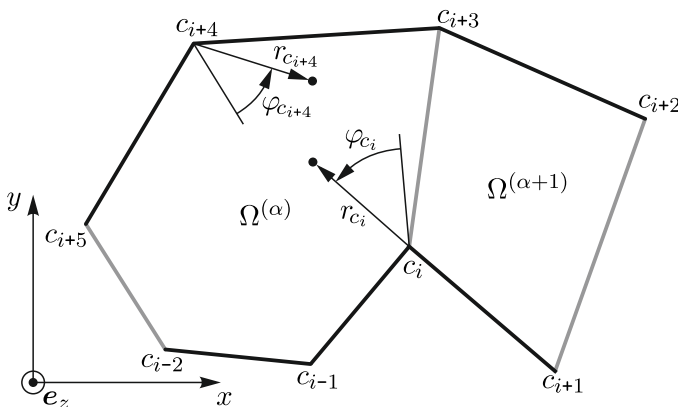


Figure 6.5: Corner coordinate systems for special purpose functions within a WBM model

corner  $c_{i+4}$  only contribute to the field in the sub-domain  $\alpha$ , the corner functions required at the corner  $c_i$  have to be included in the sub-domains  $\alpha$  and  $\alpha + 1$ .

The first kind of corner functions exhibiting moment stress singularities are given by

$$\Upsilon_{Mw1b}^{(c_i)} = \begin{cases} \cos(\lambda_{Mb}^s \varphi_{c_i}) J_{\lambda_{Mb}^s}(k_{f1} r_{c_i}), \\ \sin(\lambda_{Mb}^a \varphi_{c_i}) J_{\lambda_{Mb}^a}(k_{f1} r_{c_i}), \end{cases} \quad (6.99a)$$

$$\Upsilon_{Mw2b}^{(c_i)} = \begin{cases} \cos(\lambda_{Mb}^s \varphi_{c_i}) J_{\lambda_{Mb}^s}(k_{f2} r_{c_i}), \\ \sin(\lambda_{Mb}^a \varphi_{c_i}) J_{\lambda_{Mb}^a}(k_{f2} r_{c_i}), \end{cases} \quad (6.100a)$$

$$\Upsilon_{Mh1b}^{(c_i)} = \begin{cases} -\sin(\lambda_{Mb}^s \varphi_{c_i}) J_{\lambda_{Mb}^s}(k_s r_{c_i}), \\ \cos(\lambda_{Mb}^a \varphi_{c_i}) J_{\lambda_{Mb}^a}(k_s r_{c_i}), \end{cases} \quad (6.101a)$$

$$\Upsilon_{Mh2b}^{(c_i)} = \begin{cases} -\sin(\lambda_{Mb}^s \varphi_{c_i}) J_{\lambda_{Mb}^s}(k_s r_{c_i}), \\ \cos(\lambda_{Mb}^a \varphi_{c_i}) J_{\lambda_{Mb}^a}(k_s r_{c_i}), \end{cases} \quad (6.101b)$$

with  $1 < \lambda_{Mb}^s < 2$  the symmetric and  $1 < \lambda_{Mb}^a < 2$  the anti-symmetric eigenvalues for moment singularities. If both boundaries at the corner  $c_i$  are hard simply-supported, the eigenvalues from the analytical solutions  $\lambda_{Mb}^s = \lambda_k^s$  and  $\lambda_{Mb}^a = \lambda_k^a$  (Equation (6.54)) can be applied. For other boundary conditions the eigenvalues from the static solutions (Table 6.1) are used to define the corner functions. The comparison of the static and dynamic solutions in Section 6.1.3 shows that the same order of singularity in the moments is induced if the eigenvalues are set to  $\lambda_{Mb}^s = \bar{\lambda}_M^s + 1$  and  $\lambda_{Mb}^a = \bar{\lambda}_M^a + 1$  for symmetric boundary conditions and  $\lambda_{Mb}^s = \lambda_{Mb}^a = \bar{\lambda}_M + 1$  for non-symmetric boundary conditions. Since the arbitrary contribution factors  $\hat{u}_{Mw1b}^{(c_i)}$ ,  $\hat{u}_{Mw2b}^{(c_i)}$  and  $\hat{u}_{Mh1b}^{(c_i)}$  of the corner functions representing moment singularities are independent from each other, the total number of included functions at the corner  $c_i$  is given by  $3 n_M^{(c_i)}$ .

If the boundaries at the corner  $c_i$  are not hard simply-supported, the eigenvalues exhibiting moment or shear force singularities are not related. Therefore, corner functions are required, which only lead to shear force singularities, while the moments remain bounded. Using the analytical solutions from Equation (6.32) and applying the additional restriction from Equation (6.50) lead to the corner functions for shear force singularities

$$\Upsilon_{Qw1b}^{(c_i)} = \begin{cases} \cos(\lambda_{Qb}^s \varphi_{c_i}) J_{\lambda_{Qb}^s}(k_{f1} r_{c_i}), \\ \sin(\lambda_{Qb}^a \varphi_{c_i}) J_{\lambda_{Qb}^a}(k_{f1} r_{c_i}), \end{cases} \quad (6.102a)$$

$$\Upsilon_{Qw2b}^{(c_i)} = \begin{cases} -\cos(\lambda_{Qb}^s \varphi_{c_i}) J_{\lambda_{Qb}^s}(k_{f2} r_{c_i}) \frac{\mu_1 - 1}{\mu_2 - 1} \left( \frac{k_{f1}}{k_{f2}} \right)^{\lambda_{Qb}^s}, \\ -\sin(\lambda_{Qb}^a \varphi_{c_i}) J_{\lambda_{Qb}^a}(k_{f2} r_{c_i}) \frac{\mu_1 - 1}{\mu_2 - 1} \left( \frac{k_{f1}}{k_{f2}} \right)^{\lambda_{Qb}^a}, \end{cases} \quad (6.103a)$$

$$\bar{\Upsilon}_{Qw2b}^{(c_i)} = \begin{cases} \cos(\lambda_{Qb}^s \varphi_{c_i}) J_{\lambda_{Qb}^s}(k_{f2} r_{c_i}) \frac{1}{\mu_2 - 1} \left( \frac{k_s}{k_{f2}} \right)^{\lambda_{Qb}^s}, \\ \sin(\lambda_{Qb}^a \varphi_{c_i}) J_{\lambda_{Qb}^a}(k_{f2} r_{c_i}) \frac{1}{\mu_2 - 1} \left( \frac{k_s}{k_{f2}} \right)^{\lambda_{Qb}^a}, \end{cases} \quad (6.104a)$$

$$\Upsilon_{Qh1b}^{(c_i)} = \begin{cases} -\sin(\lambda_{Qb}^s \varphi_{c_i}) J_{\lambda_{Qb}^s}(k_s r_{c_i}), \\ \cos(\lambda_{Qb}^a \varphi_{c_i}) J_{\lambda_{Qb}^a}(k_s r_{c_i}), \end{cases} \quad (6.105a)$$

$$\Upsilon_{Qh2b}^{(c_i)} = \begin{cases} -\sin(\lambda_{Qb}^s \varphi_{c_i}) J_{\lambda_{Qb}^s}(k_s r_{c_i}), \\ \cos(\lambda_{Qb}^a \varphi_{c_i}) J_{\lambda_{Qb}^a}(k_s r_{c_i}), \end{cases} \quad (6.105b)$$

where  $0 < \lambda_{Qb}^s < 1$  are the symmetric and  $0 < \lambda_{Qb}^a < 1$  the anti-symmetric eigenvalues for shear force singularities. The eigenvalues  $\lambda_{Qb}^s$  and  $\lambda_{Qb}^a$  are defined through the static

## 6.2 Application of the Wave Based Method

solutions given in Table 6.1 with the relations  $\lambda_{Qb}^s = \bar{\lambda}_Q^s$  and  $\lambda_{Qb}^a = \bar{\lambda}_Q^a$  for symmetric boundary conditions and  $\lambda_{Qb}^s = \lambda_{Qb}^a = \bar{\lambda}_Q$  for non-symmetric boundary conditions. Since an additional restriction is necessary to define the corner functions for shear force singularities, only two independent functions for each eigenvalue can be included. The corner functions  $\Upsilon_{Qw1b}^{(c_i)}$  and  $\Upsilon_{Qw2b}^{(c_i)}$  have the same contribution factor  $\hat{u}_{Qw1b}^{(c_i)}$  and  $\Upsilon_{QHb}^{(c_i)}$  and  $\bar{\Upsilon}_{Qw2b}^{(c_i)}$  share the contribution factor  $\hat{u}_{QHb}^{(c_i)}$ . This leads to a total number of  $2n_Q^{(c_i)}$  corner functions for shear force singularities at the corner  $c_i$ .

For hard simply-supported boundary conditions a third type of corner functions, which leads to moment and shear force singularities at the corner point  $c_i$ , is defined. The analytical solutions given in Equation (6.32) can be used directly to define these corner functions

$$\Upsilon_{MQw1b}^{(c_i)} = \begin{cases} \cos(\lambda_{MQb}^s \varphi_{c_i}) (J_{\lambda_{MQb}^s}(k_{f1} r_{c_i}) - C k_{f1}^{2\lambda_{MQb}^s} (\mu_1 - 1) Y_{\lambda_{MQb}^s}(k_{f1} r_{c_i})), \\ \sin(\lambda_{MQb}^a \varphi_{c_i}) (J_{\lambda_{MQb}^a}(k_{f1} r_{c_i}) - C k_{f1}^{2\lambda_{MQb}^a} (\mu_1 - 1) Y_{\lambda_{MQb}^a}(k_{f1} r_{c_i})), \end{cases} \quad (6.106a)$$

$$\bar{\Upsilon}_{MQw1b}^{(c_i)} = \begin{cases} -\cos(\lambda_{MQb}^s \varphi_{c_i}) C (k_{f1} k_{f2})^{\lambda_{MQb}^s} (\mu_2 - 1) Y_{\lambda_{MQb}^s}(k_{f1} r_{c_i}), \\ -\sin(\lambda_{MQb}^a \varphi_{c_i}) C (k_{f1} k_{f2})^{\lambda_{MQb}^a} (\mu_2 - 1) Y_{\lambda_{MQb}^a}(k_{f1} r_{c_i}), \end{cases} \quad (6.107a)$$

$$\bar{\Upsilon}_{MQw1b}^{(c_i)} = \begin{cases} \cos(\lambda_{MQb}^s \varphi_{c_i}) C (k_{f1} k_s)^{\lambda_{MQb}^s} Y_{\lambda_{MQb}^s}(k_{f1} r_{c_i}), \\ \sin(\lambda_{MQb}^a \varphi_{c_i}) C (k_{f1} k_s)^{\lambda_{MQb}^a} Y_{\lambda_{MQb}^a}(k_{f1} r_{c_i}), \end{cases} \quad (6.108a)$$

$$\bar{\Upsilon}_{MQw2b}^{(c_i)} = \begin{cases} \cos(\lambda_{MQb}^s \varphi_{c_i}) C (k_{f1} k_{f2})^{\lambda_{MQb}^s} (\mu_1 - 1) Y_{\lambda_{MQb}^s}(k_{f2} r_{c_i}), \\ \sin(\lambda_{MQb}^a \varphi_{c_i}) C (k_{f1} k_{f2})^{\lambda_{MQb}^a} (\mu_1 - 1) Y_{\lambda_{MQb}^a}(k_{f2} r_{c_i}), \end{cases} \quad (6.109a)$$

$$\bar{\Upsilon}_{MQw2b}^{(c_i)} = \begin{cases} \cos(\lambda_{MQb}^s \varphi_{c_i}) (J_{\lambda_{MQb}^s}(k_{f2} r_{c_i}) + C k_{f2}^{2\lambda_{MQb}^s} (\mu_2 - 1) Y_{\lambda_{MQb}^s}(k_{f2} r_{c_i})), \\ \sin(\lambda_{MQb}^a \varphi_{c_i}) (J_{\lambda_{MQb}^a}(k_{f2} r_{c_i}) + C k_{f2}^{2\lambda_{MQb}^a} (\mu_2 - 1) Y_{\lambda_{MQb}^a}(k_{f2} r_{c_i})), \end{cases} \quad (6.110a)$$

$$\bar{\Upsilon}_{MQw2b}^{(c_i)} = \begin{cases} -\cos(\lambda_{MQb}^s \varphi_{c_i}) C (k_{f2} k_s)^{\lambda_{MQb}^s} Y_{\lambda_{MQb}^s}(k_{f2} r_{c_i}), \\ -\sin(\lambda_{MQb}^a \varphi_{c_i}) C (k_{f2} k_s)^{\lambda_{MQb}^a} Y_{\lambda_{MQb}^a}(k_{f2} r_{c_i}), \end{cases} \quad (6.111a)$$

$$\bar{\Upsilon}_{MQHb}^{(c_i)} = \begin{cases} -\sin(\lambda_{MQb}^s \varphi_{c_i}) C (k_{f1} k_s)^{\lambda_{MQb}^s} (\mu_1 - \mu_2) (\mu_1 - 1) Y_{\lambda_{MQb}^s}(k_s r_{c_i}), \\ \cos(\lambda_{MQb}^a \varphi_{c_i}) C (k_{f1} k_s)^{\lambda_{MQb}^a} (\mu_1 - \mu_2) (\mu_1 - 1) Y_{\lambda_{MQb}^a}(k_s r_{c_i}), \end{cases} \quad (6.112a)$$

$$\bar{\Upsilon}_{MQHb}^{(c_i)} = \begin{cases} -\sin(\lambda_{MQb}^s \varphi_{c_i}) C (k_{f2} k_s)^{\lambda_{MQb}^s} (\mu_1 - \mu_2) (\mu_2 - 1) Y_{\lambda_{MQb}^s}(k_s r_{c_i}), \\ \cos(\lambda_{MQb}^a \varphi_{c_i}) C (k_{f2} k_s)^{\lambda_{MQb}^a} (\mu_1 - \mu_2) (\mu_2 - 1) Y_{\lambda_{MQb}^a}(k_s r_{c_i}), \end{cases} \quad (6.113a)$$

$$\bar{\Upsilon}_{MQHb}^{(c_i)} = \begin{cases} -\sin(\lambda_{MQb}^s \varphi_{c_i}) (J_{\lambda_{MQb}^s}(k_s r_{c_i}) - C k_s^{2\lambda_{MQb}^s} (\mu_1 - \mu_2) Y_{\lambda_{MQb}^s}(k_s r_{c_i})), \\ \cos(\lambda_{MQb}^a \varphi_{c_i}) (J_{\lambda_{MQb}^a}(k_s r_{c_i}) - C k_s^{2\lambda_{MQb}^a} (\mu_1 - \mu_2) Y_{\lambda_{MQb}^a}(k_s r_{c_i})), \end{cases} \quad (6.114a)$$

with the constant  $C$  defined in Equation (6.33) and  $0 < \lambda_{MQb}^s = \lambda_k^s < 1$  the symmetric and  $0 < \lambda_{MQb}^a = \lambda_k^a < 1$  the anti-symmetric eigenvalues given in Equation (6.54). The different corner functions are related by their contribution factors  $\hat{u}_{MQw1b}^{(c_i)} (\Upsilon_{\bullet}^{(c_i)})$ ,  $\hat{u}_{MQw2b}^{(c_i)}$

$(\bar{\Upsilon}_{\bullet}^{(c_i)})$  and  $\hat{u}_{MQ_Hb}^{(c_i)} (\tilde{\Upsilon}_{\bullet}^{(c_i)})$ . The total number of independent corner functions exhibiting moment and shear force singularities at the corner  $c_i$  is therefore given by  $3 n_{MQ}^{(c_i)}$ .

The corner functions do not form a T-complete set and are only included to represent the singularities in field variables.

### Notes on the implementation of the function sets

As mentioned in e.g. [21] or [99], the following steps have to be considered in the practical implementation of the function sets to yield proper results with the WBM:

#### a.) Function scaling

The numerical condition of the WBM model is strongly influenced by the amplitudes of the included wave functions and special purpose functions and therefore a scaling of the functions to a maximum amplitude of 1 is necessary [21]. While for the wave functions in Table 6.3 a scaling factor in the exponent of the exponential functions is included [99], it is advantageous to use an implementation of exponentially scaled Bessel functions ( $J_{\nu}(\bullet) \exp(-|\text{Im}(\bullet)|)$ ) to scale the corner functions.

#### b.) Linear dependency of wave functions

At specific frequencies, the selection of the wave numbers given in Equations (6.63) – (6.65) leads to linearly dependent functions, which results in a singular system of linear equations [99]. Removing the dependent wave functions from the field variable expansion resolves this issue.

#### c.) Wave function truncation

To define the total numbers of included wave functions  $n_{w1}^{(\alpha)}$ ,  $n_{w2}^{(\alpha)}$  and  $n_H^{(\alpha)}$  in Equations (6.60) – (6.62), the frequency dependent truncation rule

$$\{k_{i_{w1},x}^{(\alpha)}, k_{i_{w2},x}^{(\alpha)}, k_{i_H,x}^{(\alpha)}, k_{j_{w1},y}^{(\alpha)}, k_{j_{w2},y}^{(\alpha)}, k_{j_H,y}^{(\alpha)}\} \geq T \max(k_{f1}^{(1)}, k_{f1}^{(2)}, \dots, k_{f1}^{(n_{\alpha})}), \quad (6.115)$$

with  $T$  the user-specified truncation factor, is applied. This truncation rule ensures that the highest wavenumber in the field variable expansion exceeds the highest physical oscillatory wavenumber ( $k_{f1}$ ) by a factor of  $T$  [17]. The wavenumber  $k_{f1}$  is used, since it is the only physical wavenumber which corresponds to travelling waves.

### 6.2.2 Construction of the system matrices

The field variable expansions in Equations (6.60) – (6.62) satisfy the governing equations of the Mindlin plate theory exactly and therefore, only a fitting of the prescribed boundary and interface conditions is required. The boundary and interface residuals are minimized by the weighted residual approach outlined in Section 4.1.2, which leads to a system of linear equations with the unknown contribution factors  $\hat{u}_{\bullet}^{(*)}$ . The differential operators for the boundary and interface conditions are defined in the following section and the

## 6.2 Application of the Wave Based Method

differential operators ( $\mathcal{B}_\bullet$ ) used on the weighting functions are derived from the sub-region three-field generalized mixed variational form of the Mindlin plate theory.

### Boundary and interface conditions

The four different kinds of common boundary conditions in the Mindlin plate theory, given in Equations (2.75)–(2.78), can be rewritten in terms of the three field variables  $w_1$ ,  $w_2$  and  $H$  by

$$\mathcal{B}_u^{(\alpha)} \mathbf{u}^{(\alpha)} - \bar{\mathbf{B}}_u^{(\alpha)} = 0, \quad \mathbf{r} \in \Gamma_u^{(\alpha)} \quad (6.116)$$

$$\mathcal{B}_\sigma^{(\alpha)} \mathbf{u}^{(\alpha)} - \bar{\mathbf{B}}_\sigma^{(\alpha)} = 0, \quad \mathbf{r} \in \Gamma_\sigma^{(\alpha)} \quad (6.117)$$

$$\mathcal{B}_{u\sigma 1}^{(\alpha)} \mathbf{u}^{(\alpha)} - \bar{\mathbf{B}}_{u\sigma 1}^{(\alpha)} = 0, \quad \mathbf{r} \in \Gamma_{u\sigma 1}^{(\alpha)} \quad (6.118)$$

$$\mathcal{B}_{u\sigma 2}^{(\alpha)} \mathbf{u}^{(\alpha)} - \bar{\mathbf{B}}_{u\sigma 2}^{(\alpha)} = 0, \quad \mathbf{r} \in \Gamma_{u\sigma 2}^{(\alpha)} \quad (6.119)$$

with the column vector  $\mathbf{u}^{(\alpha)} = [w_1^{(\alpha)}, w_2^{(\alpha)}, H^{(\alpha)}]^T$  gathering the field variables in the sub-domain  $\alpha$  and the column vectors

$$\bar{\mathbf{B}}_u^{(\alpha)} = \begin{bmatrix} \bar{w}^{(\alpha)} \\ \bar{\psi}_n^{(\alpha)} \\ \bar{\psi}_s^{(\alpha)} \end{bmatrix}, \quad \bar{\mathbf{B}}_\sigma^{(\alpha)} = \begin{bmatrix} \bar{Q}_n^{(\alpha)} \\ \bar{M}_n^{(\alpha)} \\ \bar{M}_{ns}^{(\alpha)} \end{bmatrix}, \quad \bar{\mathbf{B}}_{u\sigma 1}^{(\alpha)} = \begin{bmatrix} \bar{w}^{(\alpha)} \\ \bar{M}_n^{(\alpha)} \\ \bar{M}_{ns}^{(\alpha)} \end{bmatrix}, \quad \bar{\mathbf{B}}_{u\sigma 2}^{(\alpha)} = \begin{bmatrix} \bar{w}^{(\alpha)} \\ \bar{M}_n^{(\alpha)} \\ \bar{\psi}_s^{(\alpha)} \end{bmatrix}, \quad (6.120)$$

gathering the prescribed boundary conditions. The boundary operators

$$\begin{aligned} \mathcal{B}_w^{(\alpha)} &= \begin{bmatrix} 1 \\ 1 \\ 0 \end{bmatrix}^T, & \mathcal{B}_{Q_n}^{(\alpha)} &= k^2 G h \begin{bmatrix} \mu_1 \frac{\partial}{\partial n^{(\alpha)}} \\ \mu_2 \frac{\partial}{\partial n^{(\alpha)}} \\ \frac{\partial}{\partial s^{(\alpha)}} \end{bmatrix}^T, \\ \mathcal{B}_{\psi_n}^{(\alpha)} &= \begin{bmatrix} (\mu_1 - 1) \frac{\partial}{\partial n^{(\alpha)}} \\ (\mu_2 - 1) \frac{\partial}{\partial n^{(\alpha)}} \\ \frac{\partial}{\partial s^{(\alpha)}} \end{bmatrix}^T, & \mathcal{B}_{M_n}^{(\alpha)} &= D \begin{bmatrix} (\mu_1 - 1) \left( \frac{\partial^2}{\partial n^{(\alpha)2}} + \nu \frac{\partial^2}{\partial s^{(\alpha)2}} \right) \\ (\mu_2 - 1) \left( \frac{\partial^2}{\partial n^{(\alpha)2}} + \nu \frac{\partial^2}{\partial s^{(\alpha)2}} \right) \\ (1 - \nu) \frac{\partial^2}{\partial n^{(\alpha)} \partial s^{(\alpha)}} \end{bmatrix}^T, \\ \mathcal{B}_{\psi_s}^{(\alpha)} &= \begin{bmatrix} (\mu_1 - 1) \frac{\partial}{\partial s^{(\alpha)}} \\ (\mu_2 - 1) \frac{\partial}{\partial s^{(\alpha)}} \\ -\frac{\partial}{\partial n^{(\alpha)}} \end{bmatrix}^T, & \mathcal{B}_{M_{ns}}^{(\alpha)} &= D (1 - \nu) \begin{bmatrix} (\mu_1 - 1) \frac{\partial^2}{\partial n^{(\alpha)} \partial s^{(\alpha)}} \\ (\mu_2 - 1) \frac{\partial^2}{\partial n^{(\alpha)} \partial s^{(\alpha)}} \\ \frac{1}{2} \left( \frac{\partial^2}{\partial s^{(\alpha)2}} - \frac{\partial^2}{\partial n^{(\alpha)2}} \right) \end{bmatrix}^T, \end{aligned} \quad (6.121)$$

are collected in the matrices

$$\mathcal{B}_u^{(\alpha)} = \begin{bmatrix} \mathcal{B}_w^{(\alpha)} \\ \mathcal{B}_{\psi_n}^{(\alpha)} \\ \mathcal{B}_{\psi_s}^{(\alpha)} \end{bmatrix}, \quad \mathcal{B}_\sigma^{(\alpha)} = \begin{bmatrix} \mathcal{B}_{Q_n}^{(\alpha)} \\ \mathcal{B}_{M_n}^{(\alpha)} \\ \mathcal{B}_{M_{ns}}^{(\alpha)} \end{bmatrix}, \quad \mathcal{B}_{u\sigma 1}^{(\alpha)} = \begin{bmatrix} \mathcal{B}_w^{(\alpha)} \\ \mathcal{B}_{M_n}^{(\alpha)} \\ \mathcal{B}_{M_{ns}}^{(\alpha)} \end{bmatrix}, \quad \mathcal{B}_{u\sigma 2}^{(\alpha)} = \begin{bmatrix} \mathcal{B}_w^{(\alpha)} \\ \mathcal{B}_{M_n}^{(\alpha)} \\ \mathcal{B}_{\psi_s}^{(\alpha)} \end{bmatrix}, \quad (6.122)$$

where  $\frac{\partial}{\partial n^{(\alpha)}}$  and  $\frac{\partial}{\partial s^{(\alpha)}}$  are the normal and tangential derivatives at the boundaries of the sub-domain  $\alpha$ .

The interface conditions between two sub-domains  $\alpha$  and  $\beta$  (Equation (2.79)) can be given in terms of the field variables  $\mathbf{u}^{(\alpha)}$  and  $\mathbf{u}^{(\beta)}$  by

$$\mathcal{B}_u^{(\alpha)} \mathbf{u}^{(\alpha)} - \mathcal{B}_{u^*}^{(\beta)} \mathbf{u}^{(\beta)} = 0, \quad \mathbf{r} \in \Gamma_u^{(\alpha, \beta)} \quad (6.123)$$

$$\mathcal{B}_\sigma^{(\alpha)} \mathbf{u}^{(\alpha)} - \mathcal{B}_{\sigma^*}^{(\beta)} \mathbf{u}^{(\beta)} = 0, \quad \mathbf{r} \in \Gamma_\sigma^{(\alpha, \beta)} \quad (6.124)$$

with the modified boundary operator matrices

$$\mathcal{B}_{u^*}^{(\beta)} = \begin{bmatrix} \mathcal{B}_w^{(\beta)} \\ -\mathcal{B}_{\psi_n}^{(\beta)} \\ -\mathcal{B}_{\psi_s}^{(\beta)} \end{bmatrix}, \quad \mathcal{B}_{\sigma^*}^{(\beta)} = \begin{bmatrix} -\mathcal{B}_{Q_n}^{(\beta)} \\ \mathcal{B}_{M_n}^{(\beta)} \\ \mathcal{B}_{M_{ns}}^{(\beta)} \end{bmatrix}. \quad (6.125)$$

To ensure the well-posedness of the problem, either only the continuity of displacements  $(\Gamma_u^{(\alpha, \beta)} = \Gamma^{(\alpha, \beta)}, \Gamma_\sigma^{(\alpha, \beta)} = \emptyset)$  or the equilibrium of forces and moments  $(\Gamma_\sigma^{(\alpha, \beta)} = \Gamma^{(\alpha, \beta)}, \Gamma_u^{(\alpha, \beta)} = \emptyset)$  is imposed as a boundary condition on the sub-domain  $\alpha$ , while the remaining interface conditions are imposed on the sub-domain  $\beta$ .

### Weighted residual formulation

Applying the weighted residual formulation for the generalized Helmholtz problem (Equation (4.7)) to the Mindlin plate theory requires the definition of the partial differential operators  $\mathcal{T}_\bullet^{(\alpha)}$  for the weighting functions  $\tilde{\mathbf{v}}^{(\alpha)}$ . A general approach to find these partial differential operators is a variational analysis of the problem at hand. Therefore, the variational form of the Mindlin plate, given in Equation (2.85), is investigated and four different partial differential operators

$$\mathcal{T}_u^{(\alpha)} = -\mathcal{B}_\sigma^{(\alpha)}, \quad \mathcal{T}_\sigma^{(\alpha)} = \mathcal{B}_u^{(\alpha)}, \quad \mathcal{T}_{u\sigma 1}^{(\alpha)} = \begin{bmatrix} -\mathcal{B}_{Q_n}^{(\alpha)} \\ \mathcal{B}_{\psi_n}^{(\alpha)} \\ \mathcal{B}_{\psi_s}^{(\alpha)} \end{bmatrix}, \quad \mathcal{T}_{u\sigma 2}^{(\alpha)} = \begin{bmatrix} -\mathcal{B}_{Q_n}^{(\alpha)} \\ \mathcal{B}_{\psi_n}^{(\alpha)} \\ -\mathcal{B}_{M_{ns}}^{(\alpha)} \end{bmatrix}, \quad (6.126)$$

are identified. Finally, the weighted residual formulation for the Mindlin plate theory, used within the framework of the WBM, is given by

$$\begin{aligned} & \sum_{\alpha=1}^{n_\alpha} \left( \int_{\Gamma_u^{(\alpha)}} \left( (\mathcal{T}_u^{(\alpha)} \tilde{\mathbf{v}}^{(\alpha)})^T \mathcal{B}_u^{(\alpha)} \mathbf{u}^{(\alpha)} - \bar{\mathbf{B}}_u^{(\alpha)} \right) ds \right. \\ & \quad + \int_{\Gamma_\sigma^{(\alpha)}} \left( (\mathcal{T}_\sigma^{(\alpha)} \tilde{\mathbf{v}}^{(\alpha)})^T \mathcal{B}_\sigma^{(\alpha)} \mathbf{u}^{(\alpha)} - \bar{\mathbf{B}}_\sigma^{(\alpha)} \right) ds \\ & \quad + \int_{\Gamma_{u\sigma 1}^{(\alpha)}} \left( (\mathcal{T}_{u\sigma 1}^{(\alpha)} \tilde{\mathbf{v}}^{(\alpha)})^T \mathcal{B}_{u\sigma 1}^{(\alpha)} \mathbf{u}^{(\alpha)} - \bar{\mathbf{B}}_{u\sigma 1}^{(\alpha)} \right) ds \\ & \quad \left. + \int_{\Gamma_{u\sigma 2}^{(\alpha)}} \left( (\mathcal{T}_{u\sigma 2}^{(\alpha)} \tilde{\mathbf{v}}^{(\alpha)})^T \mathcal{B}_{u\sigma 2}^{(\alpha)} \mathbf{u}^{(\alpha)} - \bar{\mathbf{B}}_{u\sigma 2}^{(\alpha)} \right) ds \right) \\ & + \sum_{\beta=1, \beta \neq \alpha}^{n_\alpha} \left( \int_{\Gamma_u^{(\alpha, \beta)}} \left( (\mathcal{T}_u^{(\alpha)} \tilde{\mathbf{v}}^{(\alpha)})^T (\mathcal{B}_u^{(\alpha)} \mathbf{u}^{(\alpha)} - \mathcal{B}_{u^*}^{(\beta)} \mathbf{u}^{(\beta)}) \right) ds \right. \\ & \quad \left. + \int_{\Gamma_\sigma^{(\alpha, \beta)}} \left( (\mathcal{T}_\sigma^{(\alpha)} \tilde{\mathbf{v}}^{(\alpha)})^T (\mathcal{B}_\sigma^{(\alpha)} \mathbf{u}^{(\alpha)} - \mathcal{B}_{\sigma^*}^{(\beta)} \mathbf{u}^{(\beta)}) \right) ds \right) = 0, \end{aligned} \quad (6.127)$$

where the first four integrals enforce the boundary conditions at the sub-domain  $\alpha$  and the last two integrals ensure the continuity of displacements and rotations and the equilibrium of forces and moments at the interface between the sub-domains  $\alpha$  and  $\beta$ .

### 6.3 Modified selection of the wave functions

In this section, a modified selection of the wave functions is introduced, which is not based on the smallest rectangular bounding boxes circumscribing the viewed sub-domains. In the classical WBM the traveling and evanescent wave functions, included in the field variable expansion of the sub-domain  $\alpha$ , are defined within a sub-domain coordinate system  $(x_D^{(\alpha)}, y_D^{(\alpha)})$ , which results from the rectangular bounding box circumscribing the sub-domain  $\alpha$ . The modified wave function selection uses the sub-domain coordinate system  $(x_D^{(\alpha)}, y_D^{(\alpha)})$  to specify the travelling wave functions in the sub-domain  $\alpha$ , while a local boundary coordinate system  $(x_{b_k}^{(\alpha)}, y_{b_k}^{(\alpha)})$  is applied to define the evanescent wave functions at the boundary  $\Gamma_k^{(\alpha)}$ . The boundary coordinate systems for two connected sub-domains  $\alpha$  and  $\beta$  are shown in Figure 6.6. The  $x_{b_k}^{(\alpha)}$ -axis always points inward the sub-domain  $\alpha$  and the associated  $y_{b_k}^{(\alpha)}$ -axis originates from a rotation about the  $z$ -axis. At an interface  $\Gamma^{(\alpha, \beta)}$ , two different boundary coordinate systems, one for the sub-domain  $\alpha$  and one for the sub-domain  $\beta$ , is defined.

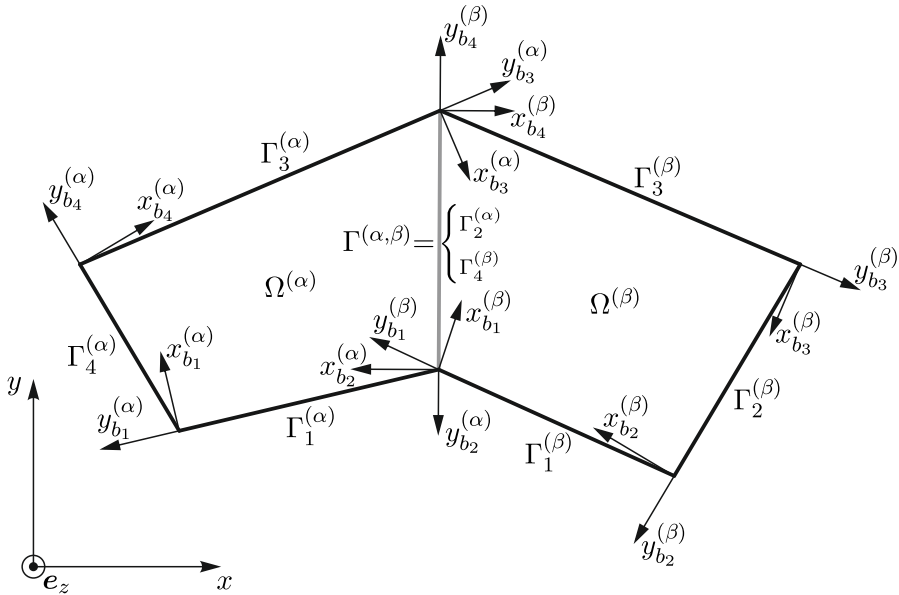


Figure 6.6: Boundary coordinate systems for the modified selection of the wave functions

The modified selection of the wave functions is mainly motivated by the results given in [257], where the convergence rate of the WBM for a rectangular domain and a nearly rectangular domain with a slightly rotated boundary are compared. Van Hal and his co-workers [257] have shown that the convergency rate of the WBM for the rectangular

domain is much higher compared to the slightly modified problem and introduced a modification of the field variable expansion by including more travelling waves. A minimal improvement of the convergence rate has been reported [257].

The modification of the wave function selection in this work follows a different approach. Due to the exponential decay, the evanescent waves in the field variable expansions hardly contribute to the total value of the field variables inside the domain. The main purpose of the evanescent waves is to capture near field effects close to the boundaries. For the rectangular domain, the evanescent waves are perfectly aligned with the boundaries, since the bounding box is identical to the problem domain. For non-rectangular domains, this alignment is not retained and the amplitudes of the evanescent waves become rather localized at the boundaries as illustrated in Figure 6.7.

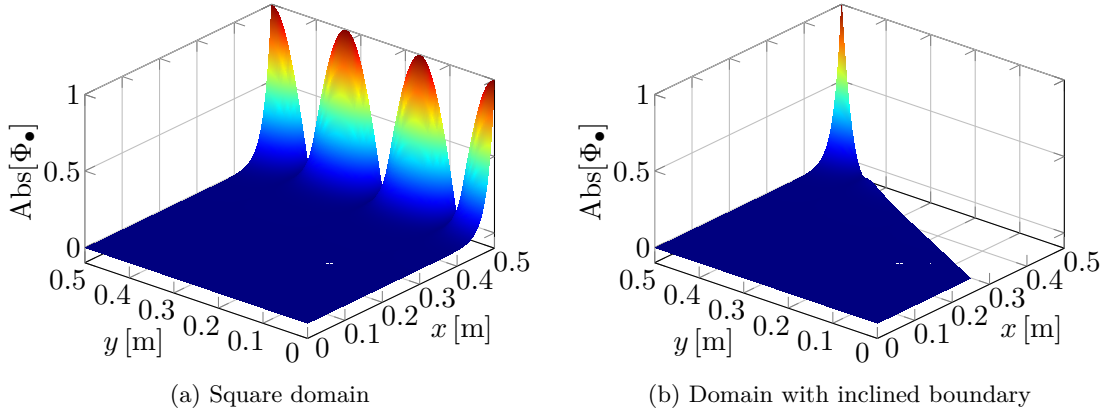


Figure 6.7: Evanescent wave function defined by the smallest rectangular bounding box

The modified wave function selection can be considered as a rotation of the evanescent waves to restore the alignment with the boundaries. An evanescent wave defined through the boundary coordinate system is shown in Figure 6.8 and it is apparent that the rotated wave becomes much more similar to the wave defined at the rectangular domain (Figure 6.7a) compared to the original wave (Figure 6.7b). A drawback of the modification is that the T-completeness of the modified wave function sets cannot be proven as in Section 6.2.1.

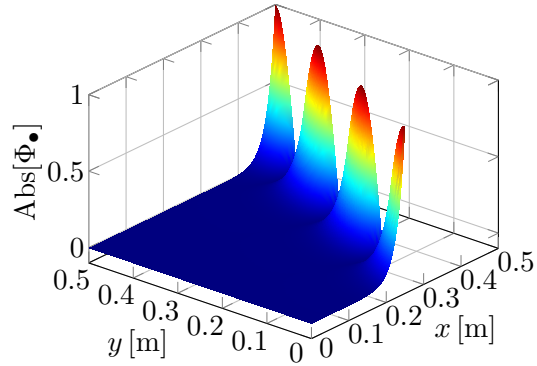


Figure 6.8: Evanescent wave function defined through the boundary coordinate system

### 6.3 Modified selection of the wave functions

The numerical results shown in Section 6.4 indicate though that the modified function sets are still T-complete for convex sub-domains.

As long as the frequency is lower than the cut-off frequency  $\omega_c = \sqrt{\frac{k^2 G}{\rho R}}$ , the physical wavenumber  $k_{f1}$  is a real number and the physical wavenumbers  $k_{f2}$  and  $k_s$  are imaginary numbers. Therefore, the wave functions included in the expansions of the field variables  $w_2^{(\alpha)}$  and  $H^{(\alpha)}$  are always evanescent waves, independent of the chosen wavenumbers in Equations (6.64) and (6.65). The wave functions included for the field variable  $w_1^{(\alpha)}$  are either travelling waves (the wavenumber in Equation (6.63) is low) or evanescent waves (the wavenumber in Equation (6.63) is high).

The modified wave function selection results in the following basis functions for  $w_1^{(\alpha)}$ ,  $w_2^{(\alpha)}$  and  $H^{(\alpha)}$ :

Wave functions for  $w_1^{(\alpha)}$  (travelling waves):

$$\text{Set 1} \begin{cases} \Phi_{i_{w1}}^{(\alpha)} = \cos(k_{i_{w1},x}^{(\alpha)} x_D^{(\alpha)}) \exp(-j k_{i_{w1},y}^{(\alpha)} y_D^{(\alpha)}), \\ \Phi_{j_{w1}}^{(\alpha)} = \exp(-j k_{j_{w1},x}^{(\alpha)} x_D^{(\alpha)}) \cos(k_{j_{w1},y}^{(\alpha)} y_D^{(\alpha)}), \end{cases} \quad (6.128)$$

$$\text{Set 2} \begin{cases} \Phi'_{i_{w1}}^{(\alpha)} = \sin(k_{i_{w1},x}^{(\alpha)} x_D^{(\alpha)}) \exp(-j k_{i_{w1},y}^{(\alpha)} y_D^{(\alpha)}), \\ \Phi'_{j_{w1}}^{(\alpha)} = \exp(-j k_{j_{w1},x}^{(\alpha)} x_D^{(\alpha)}) \sin(k_{j_{w1},y}^{(\alpha)} y_D^{(\alpha)}), \end{cases} \quad (6.129)$$

with the wavenumbers

$$k_{i_{w1},x}^{(\alpha)} = \frac{i_{w1} \pi}{L_x^{(\alpha)}} \quad \text{and} \quad k_{i_{w1},y}^{(\alpha)} = \pm \sqrt{(k_{f1}^{(\alpha)})^2 - (k_{i_{w1},x}^{(\alpha)})^2}, \quad (6.130)$$

$$k_{j_{w1},y}^{(\alpha)} = \frac{j_{w1} \pi}{L_y^{(\alpha)}}, \quad \text{and} \quad k_{j_{w1},x}^{(\alpha)} = \pm \sqrt{(k_{f1}^{(\alpha)})^2 - (k_{j_{w1},y}^{(\alpha)})^2}. \quad (6.131)$$

The travelling waves for the expansion of the field variable  $w_1^{(\alpha)}$  are identical to the original wave function selection and are defined within the local domain coordinate system  $(x_D^{(\alpha)}, y_D^{(\alpha)})$ . The integer indices  $i_{w1}$  and  $j_{w1}$  start from 0 for the function set 1 and from 1 for set 2. As long as  $k_{i_{w1},y}^{(\alpha)}$  and  $k_{j_{w1},x}^{(\alpha)}$  are real valued, the wave functions  $\Phi_{i_{w1}}^{(\alpha)}$ ,  $\Phi_{j_{w1}}^{(\alpha)}$ ,  $\Phi'_{i_{w1}}^{(\alpha)}$  and  $\Phi'_{j_{w1}}^{(\alpha)}$  are travelling waves. Starting from  $i_{w1} > (k_{f1}^{(\alpha)} L_x^{(\alpha)})/\pi$  and  $j_{w1} > (k_{f1}^{(\alpha)} L_y^{(\alpha)})/\pi$ , the wave functions become evanescent and the following different definition of the wave functions is applied.

Wave functions for  $w_1^{(\alpha)}$  (evanescent waves):

$$\text{Set 1: } \Phi_{l_{w1}}^{(\alpha)} = \cos(k_{l_{w1},y}^{(\alpha)} y_{b_k}^{(\alpha)}) \exp(j k_{l_{w1},x}^{(\alpha)} x_{b_k}^{(\alpha)}), \quad (6.132)$$

$$\text{Set 2: } \Phi'_{l_{w1}}^{(\alpha)} = \sin(k_{l_{w1},y}^{(\alpha)} y_{b_k}^{(\alpha)}) \exp(j k_{l_{w1},x}^{(\alpha)} x_{b_k}^{(\alpha)}), \quad (6.133)$$

with the wavenumbers

$$k_{l_{w1},y}^{(\alpha)} = \frac{l_{w1} \pi}{L_{b_k}^{(\alpha)}} \quad \text{and} \quad k_{l_{w1},x}^{(\alpha)} = \sqrt{(k_{f1}^{(\alpha)})^2 - (k_{l_{w1},y}^{(\alpha)})^2}. \quad (6.134)$$

The integer index  $k$  represents the considered boundary  $\Gamma_k^{(\alpha)}$  and  $L_{b_k}^{(\alpha)}$  is the length of the boundary. The wave functions in Equations (6.132) and (6.133) are defined in the local boundary coordinate system  $(x_{b_k}^{(\alpha)}, y_{b_k}^{(\alpha)})$  and the integer index  $l_{w1}$  starts from  $l_{w1} > (k_{f1}^{(\alpha)} L_{b_k}^{(\alpha)})/\pi$ .

Since the wave functions for the field variables  $w_2^{(\alpha)}$  and  $H^{(\alpha)}$  are always evanescent, only one definition of the wave functions is required.

Wave functions for  $w_2^{(\alpha)}$  (evanescent waves):

$$\text{Set 1: } \Phi_{i_{w2}}^{(\alpha)} = \cos(k_{i_{w2},y}^{(\alpha)} y_{b_k}^{(\alpha)}) \exp(j k_{i_{w2},x}^{(\alpha)} x_{b_k}^{(\alpha)}) \quad (6.135)$$

$$\text{Set 2: } \Phi'_{i_{w2}}^{(\alpha)} = \sin(k_{i_{w2},y}^{(\alpha)} y_{b_k}^{(\alpha)}) \exp(j k_{i_{w2},x}^{(\alpha)} x_{b_k}^{(\alpha)}) \quad (6.136)$$

with the wavenumbers

$$k_{i_{w2},y}^{(\alpha)} = \frac{i_{w2} \pi}{L_{b_k}^{(\alpha)}} \quad \text{and} \quad k_{i_{w2},x}^{(\alpha)} = \sqrt{(k_{f2}^{(\alpha)})^2 - (k_{i_{w2},y}^{(\alpha)})^2}. \quad (6.137)$$

The integer index  $i_{w2}$  starts from 0 for the first function set and from 1 for the second function set.

Wave functions for  $H^{(\alpha)}$  (evanescent waves):

$$\text{Set 1: } \Phi_{i_H}^{(\alpha)} = \sin(k_{i_H,y}^{(\alpha)} y_{b_k}^{(\alpha)}) \exp(j k_{i_H,x}^{(\alpha)} x_{b_k}^{(\alpha)}) \quad (6.138)$$

$$\text{Set 2: } \Phi'_{i_H}^{(\alpha)} = \cos(k_{i_H,y}^{(\alpha)} y_{b_k}^{(\alpha)}) \exp(j k_{i_H,x}^{(\alpha)} x_{b_k}^{(\alpha)}) \quad (6.139)$$

with the wavenumbers

$$k_{i_H,y}^{(\alpha)} = \frac{i_H \pi}{L_{b_k}^{(\alpha)}} \quad \text{and} \quad k_{i_H,x}^{(\alpha)} = \sqrt{(k_s^{(\alpha)})^2 - (k_{i_H,y}^{(\alpha)})^2}. \quad (6.140)$$

The integer index  $i_H$  starts from 1 for the first function set and from 0 for the second function set.

Since the amplitudes of the wave functions defined above are always smaller than 1, a wave function scaling is not necessary for the modified wave function selection. For a rectangular problem domain, the wave functions from the modified selection become identical to the originally proposed wave function selection. The truncation rule given in Equation (6.115) can also be applied for the modified wave function selection.

## 6.4 Validation examples

In this section, the WBM is applied to different steady-state harmonic plate bending problems to investigate the computational efficiency and accuracy of the method. A convex plate geometry with various types of boundary conditions and harmonic loadings is examined in Section 6.4.1. In these kinds of problems the WBM models consist of

only one domain and the decomposition into several sub-domains is avoided. In Section 6.4.2 non-convex plate domains are analyzed and the influence of the decomposition of the problem domain on the computational properties of the WBM is shown.

The main objectives of the validation examples are:

- Verifying the capability of the WBM to solve plate vibration problems governed by the Mindlin plate theory
- Comparing the original and modified wave function selection regarding their computational accuracy and efficiency
- Studying the properties of the different wave function sets and the effects of special purpose functions for corner stress singularities
- Investigating the influence of the direct solvers used to calculate the contribution factors in the WBM
- Analysing the computational efficiency of the WBM compared to the classical FEM

The WBM models are built and solved with *MATLAB® R2017b* and an *Intel® Core™ i7* system ( $4 \times 3.4$  GHz, 16 GB RAM), running a Windows 10 operating system, is used to perform the calculations. In [176] it is shown that a numerical evaluation of the integrals arising in the weighted residual formulation of the WBM can be performed in a highly efficient way. As in [17], the Gauss-Legende quadrature rule is applied to numerically evaluate the integrals, while the rule to chose the optimal number of Gauss points, given in [17], is slightly modified to

$$\frac{n_G}{L_b} = \max(0.54 T k_{f1} + 60, 90), \quad (6.141)$$

with  $n_G$  the number of Gauss points and  $L_b$  the length of the viewed boundary. Compared to the rule given in [17], twice as many Gauss points are used to ensure an accurate evaluation of the integrals especially if special purpose functions are included. To solve the system of linear equations resulting from the weighted residual formulation either the *LU*-factorization with partial pivoting, which is implemented in the Matlab function *linsolve*, or the singular value decomposition (SVD) is applied.

In lack of analytical solutions for the considered plate vibration problems, the reference solutions to compare the results of the WBM are calculated with the FEM. The commercial software *ANSYS® 17.1* is used to build the FEM models and the quadratic 8-noded quadrilateral Shell281 element, which has the Mindlin theory implemented, is applied. To get highly accurate reference solutions, very fine FEM meshes are required and therefore, the calculations are performed on an *Intel® Xeon™* server ( $8 \times 2.9$  GHz, 192 GB RAM) running a Windows server 2012 operating system.

To assess the accuracy and efficiency of the WBM, contour plots of the primary field variables ( $w, \psi_x, \psi_y$ ) and the absolute error compared to the reference solution

$$|\varepsilon| = |\bullet_{WBM} - \bullet_{Ref}|, \quad (6.142)$$

with  $\bullet_{WBM}$  the value of the field variable ( $w, \psi_x, \psi_y$ ) calculated with the WBM and  $\bullet_{Ref}$  the value of the reference solution, are shown. Furthermore, frequency response functions

(FRF) over a wide frequency range are calculated with the WBM and the averaged absolute values of the field variables

$$\text{avg}(|\bullet|) = \frac{1}{n_{rp}} \sum_{i=1}^{n_{rp}} |\bullet(x_i, y_i)|, \quad (6.143)$$

are compared to the reference solutions. In Equation (6.143)  $n_{rp}$  denotes the total number of response points,  $(x_i, y_i)$  the coordinates of the response points and  $\bullet = \{w, \psi_x, \psi_y\}$ . The influence of the different wave function selections and the included wave function sets is investigated through convergence curves, where the averaged relative error

$$\langle \delta \rangle = \frac{1}{n_{rp}} \sum_{i=1}^{n_{rp}} \frac{|\bullet_{WBM}(x_i, y_i) - \bullet_{Ref}(x_i, y_i)|}{|\bullet_{Ref}(x_i, y_i)|}, \quad (6.144)$$

is plotted against the total number of included wave functions (# dofs).

To illustrate the computational efficiency of the WBM, several WBM and FEM models are built and the averaged relative error of the models compared to the reference solution is plotted against the computation time. Since the system matrices of the FEM are generally frequency independent, only the direct solution time of the system of linear equations is taken into account, while the time to build the linear system is not considered. In the WBM the system matrix has to be computed for every frequency and therefore, the time to build and solve the linear system is included. All computations for the comparison are performed on an Intel® Core™ i7 system (4×3.4 GHz, 16 GB RAM) and no parallelization of the computations is applied to ensure a proper comparison.

#### 6.4.1 Single domain problems

The geometry of the single domain problems is shown in Figure 6.9. The polygonal plate has the dimensions  $L_x^{(1)} = 1$  m and  $L_y^{(1)} = 0.5$  m and is bounded by four edges  $\Gamma_1^{(1)} - \Gamma_4^{(1)}$ . The material properties of the steel plate are  $E = 2.1 \times 10^{11}$  N/m<sup>2</sup>,  $\rho = 7850$  kg/m<sup>3</sup>,  $\nu = 0.3$  and  $\eta = 0$  and three different thicknesses, see Table 6.4, are considered. The shear cor-

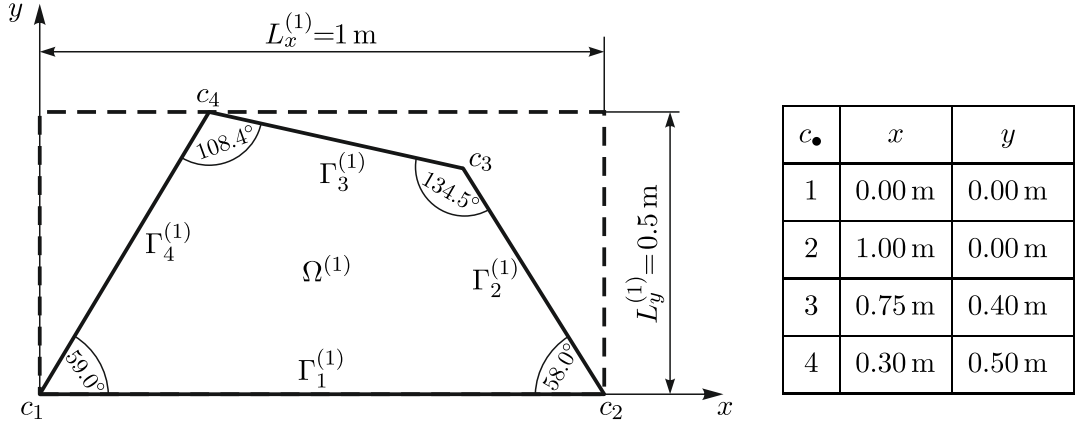


Figure 6.9: Geometry of the single domain problems

reaction factor  $k_W$  is used in the Mindlin plate theory. In Table 6.4 the ratio of the smallest lateral dimension to the plate thickness, the frequency of the lowest, simple thickness-shear mode and the frequency limits for the Kirchhoff plate theory are listed. While the plates with thickness  $h_1$  and  $h_2$  are generally considered as thin plates, the plate with thickness  $h_3$  is moderately thick.

Table 6.4: Thicknesses of the convex plate configurations and Kirchhoff limits

example	$h$ [m]	$L_y^{(1)}/h$	$f_s$ [Hz]	$f_{Gk1\%}$ [Hz]	$f_{Gk2\%}$ [Hz]
$h_1$	0.005	100	320766	2791	5613
$h_2$	0.010	50	160383	1395	2807
$h_3$	0.025	20	64153	558	1123

Four different types of boundary conditions are considered in the following sections. For the clamped and free plates, the boundary conditions at all four edges are identical, while the cantilever plate has one clamped boundary and three free boundaries. For these three types of boundary conditions no stress singularities are present at the four corner points. In the last configurations, all boundaries are hard simply-supported and stress singularities arise in the corners  $c_3$  and  $c_4$ .

A FEM model with a maximum element size of 0.001 m (at least  $\approx 90$  quadric elements per wavelength) is used to calculate the first 100 eigenfrequencies (bending) of the different plate configurations to assess the relevant frequency ranges. Three different frequencies are examined for each thickness and boundary condition, which are located after the

Table 6.5: Modal analysis of the convex plate configurations

bcd	$h$	> 10 modes		> 40 modes		> 70 modes		100 modes	
		$f$ [Hz]	$\lambda$ [m]	$f$ [Hz]	$\lambda$ [m]	$f$ [Hz]	$\lambda$ [m]	$f$ [Hz]	$\lambda$ [m]
clamped	$h_1$	850	0.2402	2610	0.1366	4195	0.1075	5772	0.0914
	$h_2$	1650	0.2427	5080	0.1367	8000	0.1078	10850	0.0917
	$h_3$	3850	0.2444	10700	0.1386	15870	0.1094	20501	0.0931
free	$h_1$	220	0.4726	1310	0.1933	2550	0.1382	3769	0.1135
	$h_2$	440	0.4723	2580	0.1935	4970	0.1382	7246	0.1136
	$h_3$	1050	0.4794	5900	0.1941	10700	0.1386	14885	0.1138
cantilever	$h_1$	420	0.3419	1780	0.1657	3170	0.1239	4506	0.1036
	$h_2$	840	0.3411	3500	0.1656	6120	0.1241	8590	0.1038
	$h_3$	2000	0.3445	7750	0.1668	12770	0.1249	17061	0.1046
hard SS	$h_1$	670	0.2706	2300	0.1456	3800	0.1130	5291	0.0955
	$h_2$	1300	0.2738	4600	0.1439	7310	0.1131	10054	0.0955
	$h_3$	3150	0.2718	9800	0.1459	15060	0.1130	19704	0.0955

10<sup>th</sup>-bending mode, the 40<sup>th</sup>-bending mode and the 70<sup>th</sup>-bending mode. An overview of these frequencies  $f$  and the bending wavelengths  $\lambda$  is given in Table 6.5. Comparing the frequency limits of the Kirchhoff plate theory given in Table 6.4 with the frequencies listed in Table 6.5, it is apparent that accurate results over the complete frequency range can only be expected from the Kirchhoff plate theory for the plates with the thickness  $h_1$ .

The details of the FEM models used to calculate the reference solutions for the error plots and convergence curves are given in Table 6.6. The same FEM mesh is applied for one type of boundary condition independent of the plate thickness or viewed frequency. Even though the geometry of all validation examples is the same, the FEM meshes differ between the applied boundary conditions, since the plate loadings are not identical. An accurate representation of the loadings in the FEM models is necessary to get accurate results, which leads to a different number of nodes (# nodes) and elements (# elements) among the four boundary conditions. Especially for the hard simply-supported plates, a mesh refinement at the corner points  $c_3$  and  $c_4$  is necessary to capture the corner stress singularities. Since very fine FEM meshes are applied (more than 200 quadric elements per wavelength), highly accurate reference solutions can be expected.

Table 6.6: FEM reference models for the convergence analysis

bcd	max(el. size) [m]	# nodes	# elements	min(# el./ $\lambda$ )
clamped	0.00050	7408526	2467599	215
free	0.00055	7077725	2357474	251
cantilever	0.00055	5693529	1896066	225
hard SS	0.00055	7532205	2508486	205

Since the FEM models listed in Table 6.6 are too computationally demanding to calculate frequency response functions over a wide frequency range ( $\approx$  the first 100 bending modes), models with less degrees of freedom are used to get a reference solution. Again, the same FEM mesh is applied for one type of boundary condition independent of the plate thickness or viewed frequency step. According to Equation (3.15), ten quadric elements per wavelength are required to control the pollution error for the highest frequencies in the frequency response functions. Although, the element size is increased compared to

Table 6.7: FEM reference models for the FRF

bcd	max(el. size) [m]	# nodes	# elements	min(# el./ $\lambda$ )
clamped	0.005	74580	24669	20
free	0.005	86215	28544	24
cantilever	0.005	69473	22962	22
hard SS	0.005	69473	22962	20

the models in Table 6.6, at least 20 elements per wavelength are used, which exceeds the requirement of Equation (3.15) by a factor of two.

The convergence curves of the FEM are determined by decreasing the mesh size of the FEM models from 0.05 m (at least  $\approx 2$  elements per wavelength) to 0.001 m (at least  $\approx 90$  elements per wavelength) in 13 steps.

To enable a detailed analysis of the properties of the WBM, each validation example is calculated with various WBM models. Either the original or modified wave function selection is used and models applying only the first wave function sets (*set1*) or both sets (*set1a2*) are built. The resulting systems of linear equations are solved with the LU-factorization or the SVD and the truncation factor is varied from  $T = 0.5$  to  $T = 8$  in steps of 0.25. If corner stress singularities are present, additional models including special purpose functions (*set1CF*, *set1a2CF*) are built.

A regular grid of approximately 10000 response points inside the problem domain is used to calculate the errors and averaged values of the field variables. To avoid high relative errors close to nodal lines (zero values of the field variables), only response points having an amplitude greater than 5% of the maximum value are included in the prediction of the averaged relative error  $\langle \delta \rangle$ .

### Clamped plate

In Figure 6.10, the boundary conditions and loading of the clamped plate configurations are illustrated. The out-of-plane displacement and rotations are set to zero at all four edges and an alternating circular load with an amplitude of  $\bar{q}_0 = 10$  N and a radius of  $r_0 = 0.07$  m harmonically excites the plate. The smallest rectangular bounding box used to define the wave functions in the WBM is indicated by the dashed lines. At corner points with two clamped boundaries, stress singularities are only exhibit if the internal angle exceeds  $180^\circ$ , which is not the case for the given examples. Therefore, no special purpose functions are included in the WBM models. The particular solution functions given in Equations (5.111)–(5.113) are used to represent the harmonic loading.

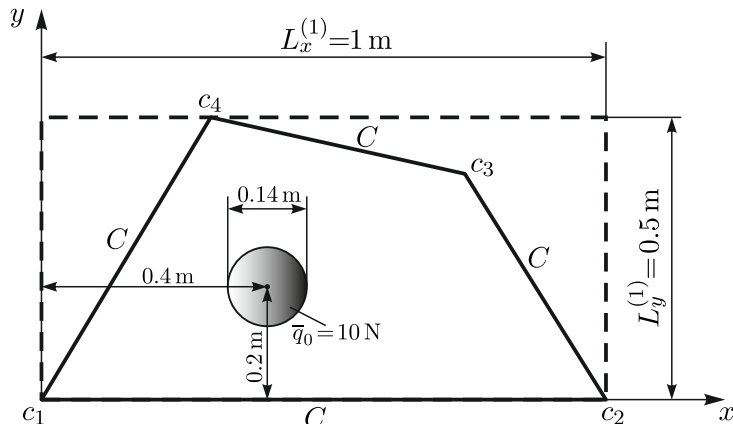


Figure 6.10: Boundary conditions and harmonic loading of the clamped plates

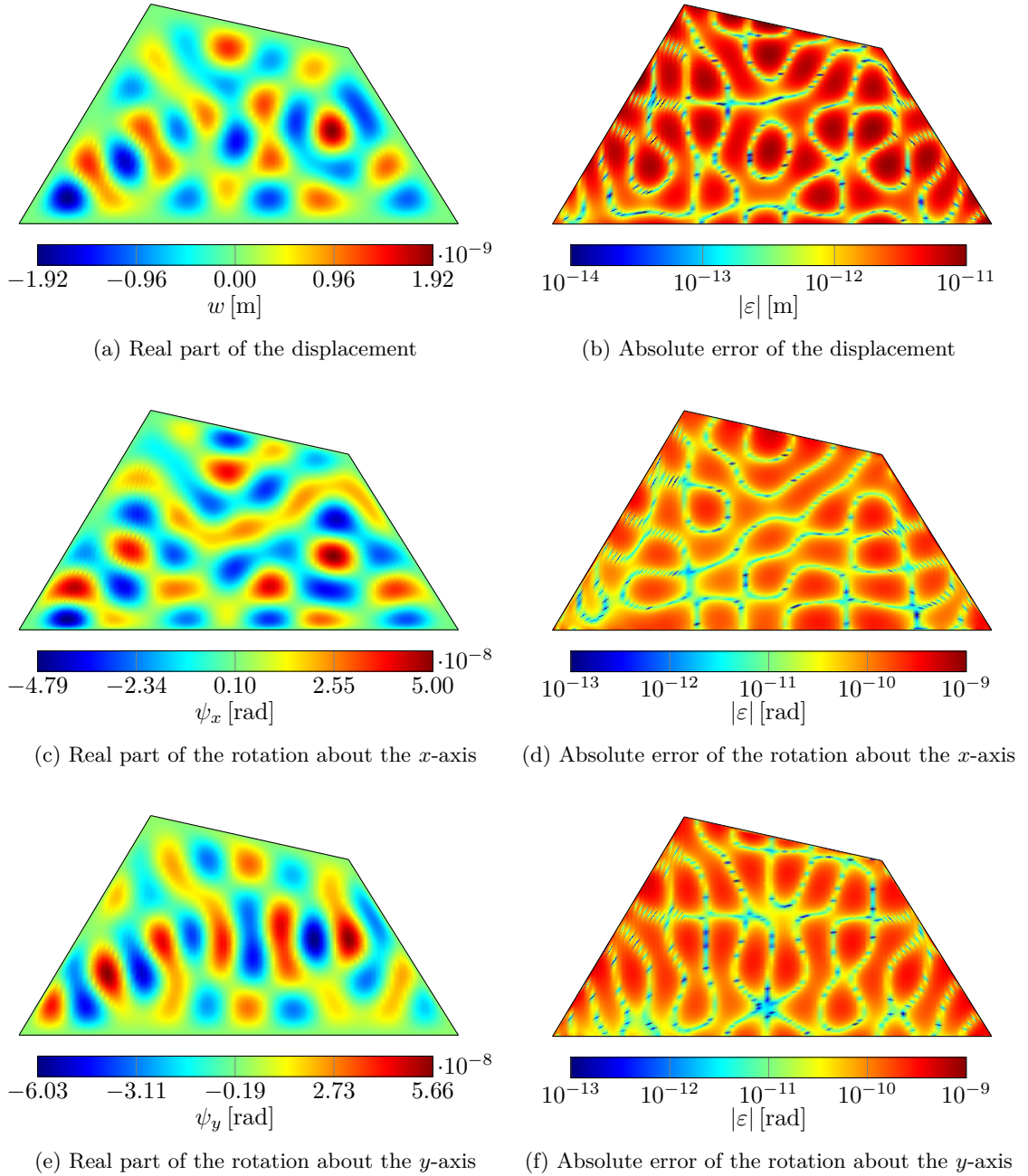


Figure 6.11: Out-of-plane displacement and rotations about the  $x$ - and  $y$ -axis of a clamped plate ( $h = 0.005$  m) excited by an alternating circular load at 2610 Hz calculated with the original WBM using only the function set 1 and a truncation factor  $T = 2$

The contour plots of the field variables ( $w, \psi_x, \psi_y$ ) and absolute errors compared to the reference solution for the clamped plate with a thickness  $h = 0.005$  m excited at 2610 Hz are shown in Figures 6.11 and 6.12. The results in Figure 6.11 are calculated with the original wave function selection, while the modified wave function selection is used in

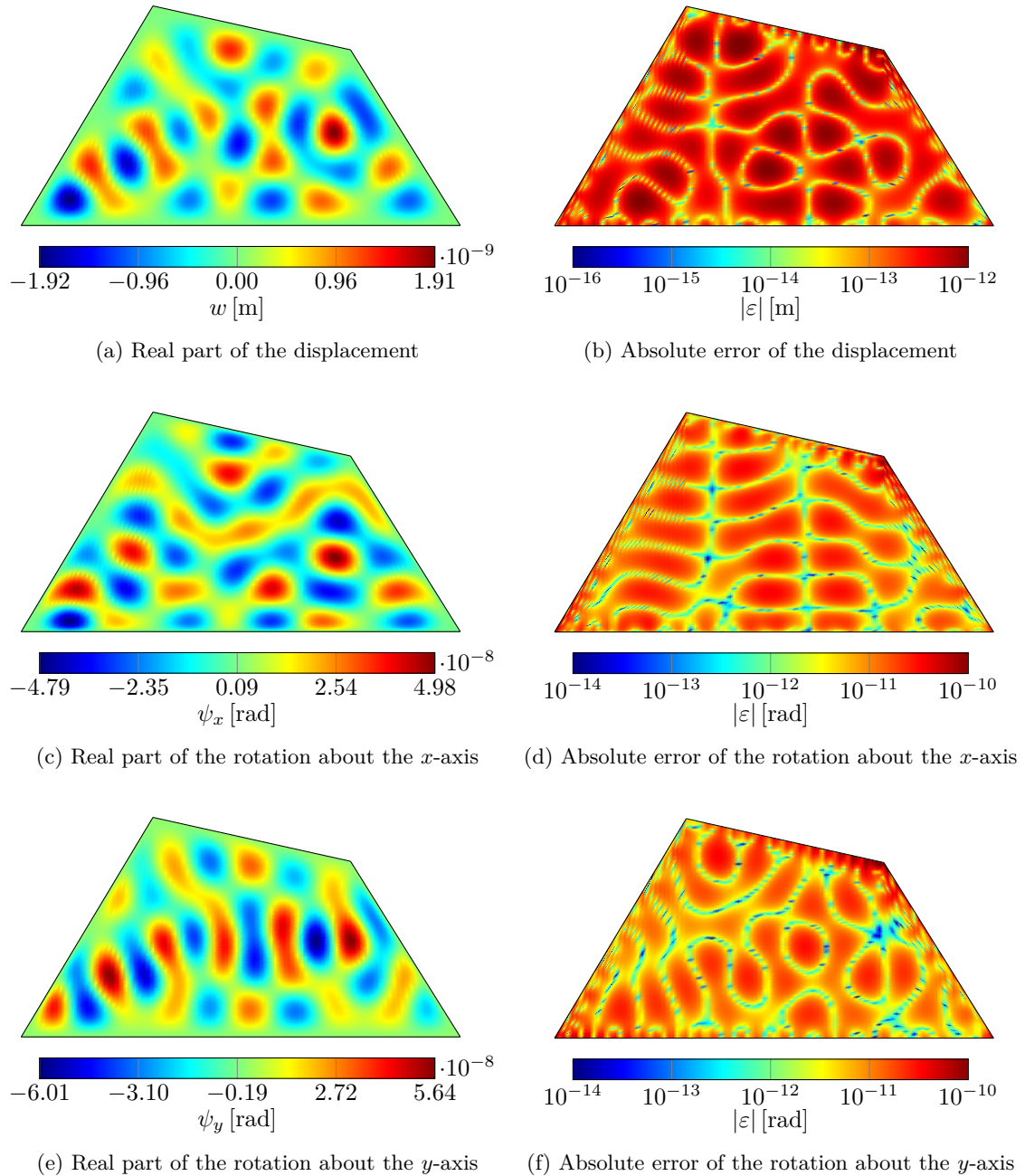


Figure 6.12: Out-of-plane displacement and rotations about the  $x$ - and  $y$ -axis of a clamped plate ( $h = 0.005$  m) excited by an alternating circular load at 2610 Hz calculated with the modified WBM using only the function set 1 and a truncation factor  $T = 2$

Figure 6.12. In both computations only the first wave function sets are included and a truncation factor of  $T = 2$  is applied, which leads to 278 wave functions for the original and 244 wave functions for the modified wave function selection. The system of linear equations is solved with the LU-factorization. The contour plots show that the clamped

boundary conditions are accurately represented by both WBM models and therefore, the prediction errors  $|\varepsilon|$  are rather low. Although, the original wave function selection leads to an accurate result, the error of the modified wave function selection is even about one order of magnitude lower, while using less degrees of freedom. This shows the advanced convergence properties of the modified wave function selection.

The contour and error plots for all other thicknesses and frequencies can be found in Appendix E in Figures E.1–E.16. Since the viewed frequencies are situated directly after the 10<sup>th</sup>-bending mode, the 40<sup>th</sup>-bending mode and the 70<sup>th</sup>-bending mode, the plate deformations are very similar among all plate thicknesses. The WBM models, which apply the modified wave function selection, have a similar accuracy for all other clamped plate examples, independent of the plate thickness or viewed frequency. The contour plots calculated with the original wave function selection show that the clamped boundary conditions are not always accurately fulfilled, especially for higher frequencies and plate thicknesses, see e.g. Figures E.7a, E.7c and E.7e. Therefore, the results calculated with the original selection are less accurate and contrary to the modified wave function selection, the error  $|\varepsilon|$  depends on the viewed frequency and plate thickness. An analysis of the system matrices is carried out to investigate the different computational properties of the two wave function selections.

The system matrices of the WBM are generally ill-conditioned and therefore, accurate solutions can only be obtained if the Picard conditions stated in [177, 178] are satisfied. To verify the Picard conditions, a singular value decomposition [300] of the WBM system matrix

$$\mathbf{A} = \mathbf{U} \Sigma \mathbf{V}^H, \quad (6.145)$$

where  $\mathbf{A}$  is the WBM system matrix,  $\Sigma$  a diagonal matrix containing the singular values  $\sigma_i$ ,  $\mathbf{U}$  and  $\mathbf{V}$  two orthonormal matrices and  $\bullet^H$  the complex conjugate transpose, has to be performed. Furthermore, the coefficients  $\beta_i = \mathbf{U}_i^H \mathbf{b}$ , with  $\mathbf{U}_i$  the  $i^{\text{th}}$ -column of the matrix  $\mathbf{U}$  and  $\mathbf{b}$  the right hand side vector of the WBM linear system, have to be calculated. The Picard conditions are fulfilled if [21]

- the singular values  $\sigma_i$  are ordered in a descending sequence and the difference of two consecutive singular values is only large at the lower end of the sequence and
- the absolute values of the coefficients  $\beta_i$  are smaller or of the same order of magnitude as their associated singular value  $\sigma_i$ .

The singular values  $\sigma_i$  and absolute values  $|\beta_i|$  of the two WBM models applied to calculate the results in Figures 6.11 and 6.12 are plotted in Figure 6.13. It is apparent that the condition number of the original wave function selection ( $\approx 4 \times 10^{21}$  (double precision),  $\approx 9 \times 10^{38}$  (quadruple precision)) is significantly worse compared to the modified selection ( $\approx 5 \times 10^{12}$  (independent of precision)).

For the original wave function selection, the standard double precision floating point arithmetic is not accurate enough to calculate the actual singular values of the system matrix, which leads to several similar numerical values for small  $\sigma_i$  (horizontal line at the lower end of the plot). Therefore, a multiprecision toolbox for *MATLAB® R2017b* [301] is used to compute the singular values with quadruple precision (approximately 34 decimal digits). At the beginning of the sequence, the singular values are identical between the double and quadruple precision computations, but starting from approximately the 220<sup>th</sup> singular

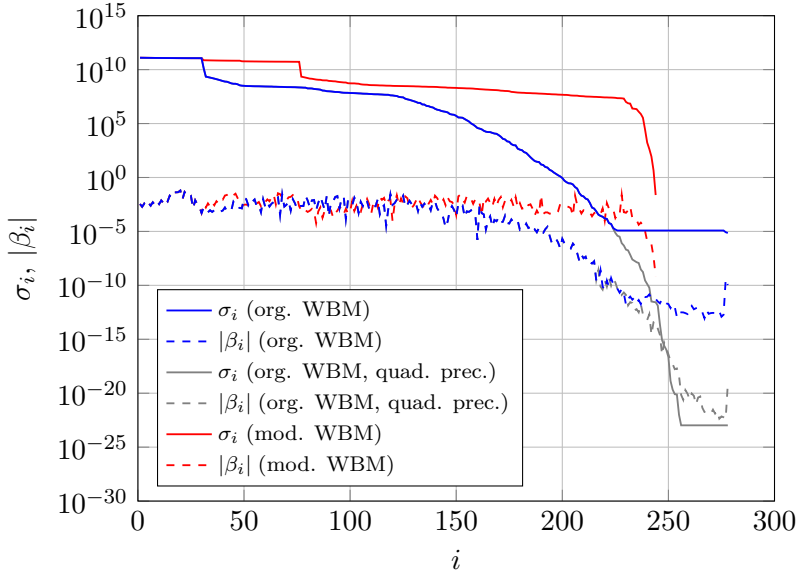


Figure 6.13: Picard conditions for the original and modified wave function selection (clamped plate)

value a huge difference appears. Furthermore, not even quadruple precision is sufficient to calculate all singular values correctly, which is apparent by the horizontal line at the end of the plot in Figure 6.13.

Although, the Picard conditions are still roughly fulfilled by the original wave function selection, the system matrix of the modified selection has considerably better properties. Hence, the accuracy of the WBM using the original wave function selection is generally limited due to the bad conditioning of the system matrix and the inevitable round-off errors in double precision. This effect is more pronounced at high frequencies, since a constant truncation factor  $T$  leads to an increasing number of wave functions in the WBM model for rising frequencies and the conditioning of the WBM system matrix becomes worse.

In Figure 6.14, the frequency response functions for the clamped plate with thickness  $h = 0.025$  m calculated with the WBM and the FEM are compared. The WBM models are built with the modified wave function selection and both function sets are applied. The truncation factor is set to  $T = 2$  and the system of linear equations is solved with the LU-factorization. The frequency starts at 50 Hz and is increased to 20050 Hz in 2000 steps. Therefore, approximately the first 100 bending modes are included in the response function. The WBM results are in excellent agreement with the reference solution over the complete frequency range, even at high frequencies and close to eigenfrequencies. The averaged values of the field variables are plotted to capture the accuracy of the WBM in the whole plate domain. The results for the plates with the thicknesses  $h = 0.005$  m and  $h = 0.01$  m are similar, which can be seen in the Appendix E in Figures E.17 and E.18. Due to the numerical instabilities of the original wave function selection caused by the ill-conditioning of the system matrix and round-off errors, see above, the FRF is not calculated with the WBM using the original selection.

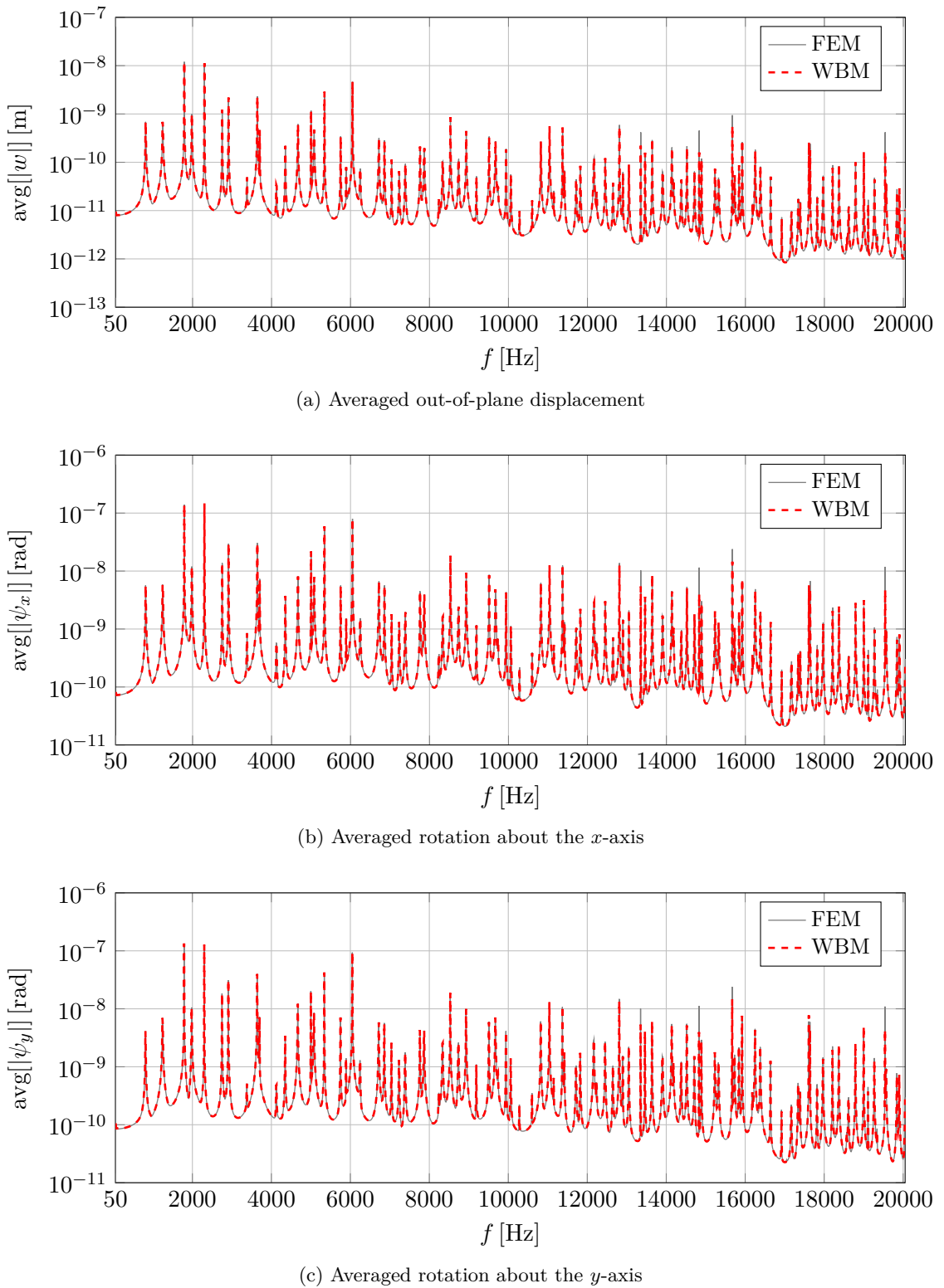


Figure 6.14: Frequency response functions of a clamped plate ( $h = 0.025$  m) excited by an alternating circular load calculated with the FEM (reference mesh) and the modified WBM (function set 1 and set 2,  $T = 2$ )

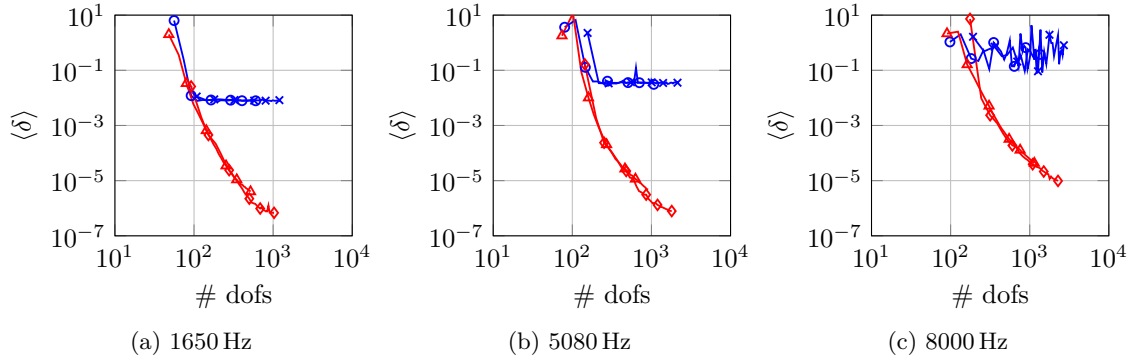


Figure 6.15: Convergence curves of the out-of-plane displacement (clamped plate with  $h = 0.01$  m) for the original WBM ( $set1$  (—○—),  $set1a2$  (—\*—)) and the modified WBM ( $set1$  (—△—),  $set1a2$  (—◇—))

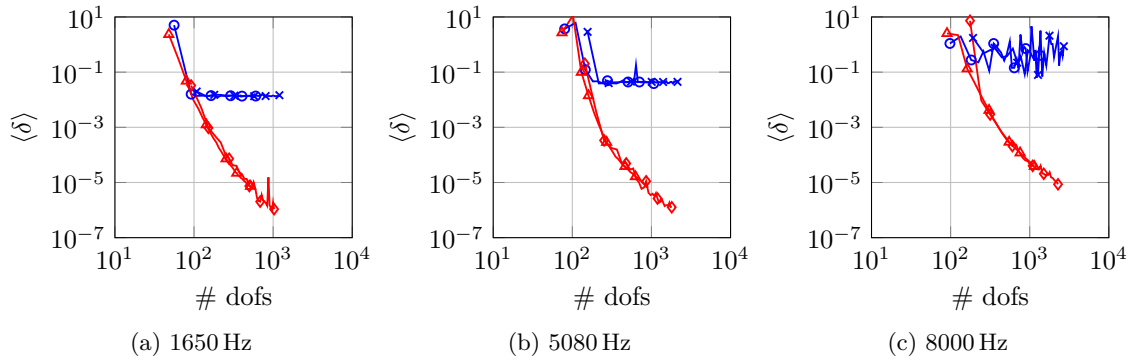


Figure 6.16: Convergence curves of the rotation about the  $x$ -axis (clamped plate with  $h = 0.01$  m) for the original WBM ( $set1$  (—○—),  $set1a2$  (—\*—)) and the modified WBM ( $set1$  (—△—),  $set1a2$  (—◇—))

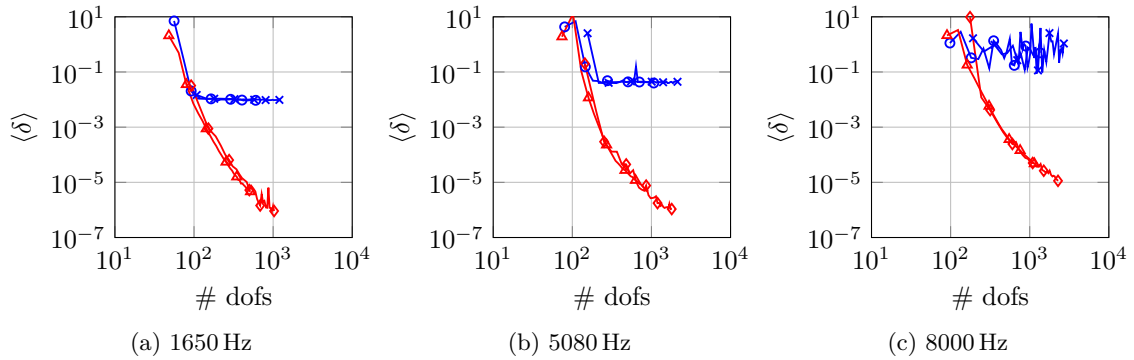


Figure 6.17: Convergence curves of the rotation about the  $y$ -axis (clamped plate with  $h = 0.01$  m) for the original WBM ( $set1$  (—○—),  $set1a2$  (—\*—)) and the modified WBM ( $set1$  (—△—),  $set1a2$  (—◇—))

The convergence rates of different WBM models (solved with LU-factorization) for the clamped plate with thickness  $h = 0.01$  m and all three frequencies are illustrated in Figures 6.15–6.17. The models using the modified wave function selection nearly uniformly converge to highly accurate results for each frequency (less than 0.001% error), while the

original wave function selection stagnates at a certain error level for the first two frequencies (1% for  $f = 1650$  Hz and 3.5% for  $f = 5080$  Hz) and does not converge for the highest frequency. Apparently, including the second wave function sets (*set1a2*) hardly influences the convergence rate of the WBM for the given examples. At the lowest excitation frequency  $f = 1650$  Hz both wave function selections only require approximately 100 wave functions to calculate the amplitudes of the field variables with an error less than 1%. Even for the second frequency  $f = 5080$  Hz and third frequency  $f = 8000$  Hz, only 160 and 260 wave functions have to be included in the WBM models using the modified selection.

According to Section 6.2.1, the WBM using the original wave function selection should converge to the analytical solution of the plate vibration problem. The bad conditioning of the WBM system matrix and the inevitable round-off errors in the numerical implementation cause instabilities in the calculations and prevent the convergence of the results. In Figure 6.18 the convergence curves of the original WBM for the clamped plate ( $h = 0.001$  m) excited at 8000 Hz computed with double and quadruple precision are compared. While the relative error fluctuates between 8% and 400% for the computations in double precision, the quadruple precision arithmetic leads to a stable relative error of approximately 8%. These results clearly show the influence of the conditioning and round-off errors on the accuracy of the original WBM.

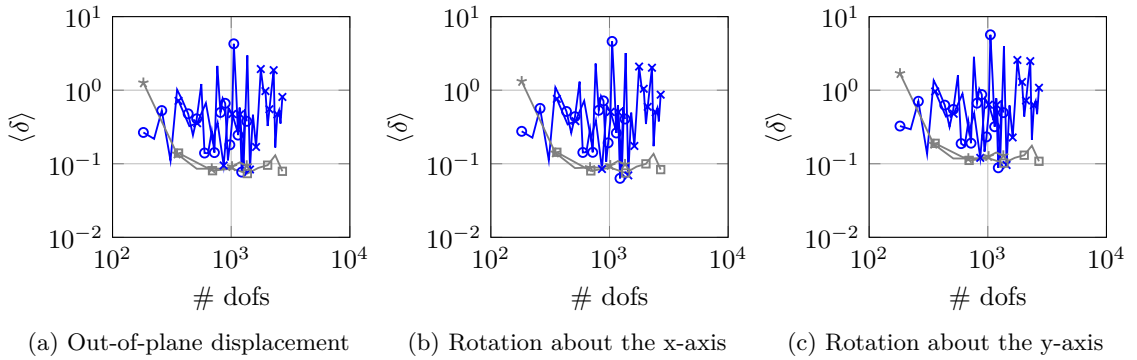


Figure 6.18: Convergence curves (clamped plate with  $h = 0.01$  m excited at 8000 Hz) for the original WBM in double precision (*set1* (—○—), *set1a2* (—\*—)) and quadruple precision (*set1* (—\*—), *set1a2* (—□—))

The convergence curves for the clamped plates with thickness  $h = 0.005$  m and  $h = 0.025$  m are given in Appendix E in Figures E.19–E.24. For the thin plate with thickness  $h = 0.005$  m, the WBM using the original wave function selection stagnates at a relative error of approximately 0.8% to 2%, while for the thick plate ( $h = 0.025$  m) a fluctuation of the relative error between 2% and 20% occurs. As expected, the accuracy of the WBM models applying the modified wave function selection are hardly influenced by the thickness or excitation frequency and the results uniformly converge to a relative error of less than 0.001%.

To show the computational efficiency of the WBM, the convergence curves of the out-of-plane displacement for the clamped plate with thickness  $h = 0.01$  m with respect to the computation time are illustrated in Figure 6.19. The WBM models apply the modified

wave function selection and the LU-factorization is used to solve the linear system of equations. Even though, quadric elements are used in the FEM, the convergence rate of the WBM is considerably higher. Depending on the viewed frequency, the computation time of the FEM to reach a relative error of 1% is approximately 12 times ( $f = 1650$  Hz), 40 times ( $f = 5080$  Hz) and 90 times ( $f = 8000$  Hz) higher compared to the WBM. The results for the rotation about the  $x$ - and  $y$ -axis and the other two thicknesses are practically identical and therefore not shown.

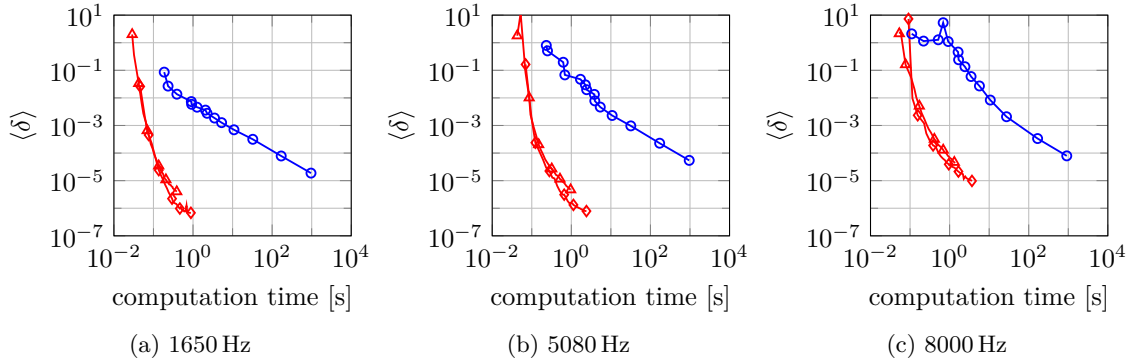


Figure 6.19: Convergence curves of the out-of-plane displacement (clamped plate with  $h = 0.01$ ) for the FEM (—○—) and the modified WBM (*set1* (—▲—), *set1a2* (—◆—))

According to the rule given in Equation (3.15), the FEM with quadric elements ( $p = 2$ ) requires 7.08 (1650 Hz), 8.18 (5080 Hz) and 8.68 (8000 Hz) elements per wavelength to control the pollution error. While this rule leads to an error of 1.9% for  $f = 1650$  Hz and 3.6% for  $f = 5080$  Hz in the given example, the error increases to 15.7% for  $f = 8000$  Hz. The growing error indicates that the constant  $C$  in the rule to control the pollution error (Equation (3.13)) is actually frequency dependent for plate bending problems. Changing the constant  $C$  in Equation (3.13) from 1 to 0.1, reduces the error for the clamped plate examples to less than 2% in the complete frequency range. As stated in [96], an *a priori* error estimator would be required to define a more appropriate rule, which is not yet available in the literature for plate bending vibration problems.

### Free plate

The boundary conditions and loading of the free plate configurations are shown in Figure 6.20. All four edges can move freely and therefore, the normal bending moments, the twisting moments and shear forces are equal to zero at the boundaries. The free plates are excited by a harmonic ring load with a constant amplitude of  $\bar{q}_0 = 10$  N/m and a radius of  $r_0 = 0.09$  m. The smallest rectangular bounding box is identical to the one of the clamped plate and indicated by the dashed lines. If free boundary conditions are imposed on the edges at a corner point, stress singularities only occur for internal angles greater than  $180^\circ$  (see Section 6.1.2). Since all internal angles in the plate domain are smaller than  $180^\circ$ , no stress singularities are exhibit and special purpose functions are not included in the

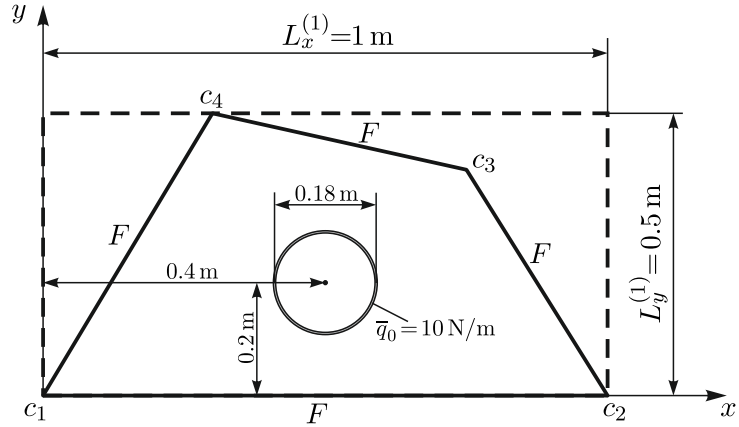


Figure 6.20: Boundary conditions and harmonic loading of the free plates

following WBM models. The constant ring load is represented by the particular solution functions given in Equations (5.63) and (5.64).

The contour and error plots of the out-of-plane displacement and the rotations about the  $x$ - and  $y$ -axis for the free plate with a thickness  $h = 0.005$  m excited at 1310 Hz are shown in Figures 6.21 and 6.22. A WBM model using the original wave function selection is used to calculate the results in Figure 6.21, while the modified selection is applied in Figure 6.22. The truncation factor is set to  $T = 2$  and only the first wave function sets are included, which leads to a total number of 200 wave functions for the original selection and 176 wave functions for the modified selection. The resulting linear systems are solved with the LU-factorization.

The contour plots of the field variables calculated with the original and modified wave function selection are similar, but the error plots in Figures 6.21 and 6.22 show that the accuracy of the WBM model using the original wave function is approximately two orders lower compared to the modified wave function selection. Furthermore, the absolute errors of the original wave function selection in Figure 6.21 are of the same order as the amplitudes of the field variables and therefore, a sufficient accuracy is not yet reached.

Since the accurate representation of the boundary conditions cannot be recognised from the contour plots, the averaged boundary residuals

$$\text{avg}(|R_{M_n}|) = \frac{1}{L_{bnd}} \int_{\Gamma} |M_n^{(WBM)} - \bar{M}_n| \, ds, \quad (6.146)$$

$$\text{avg}(|R_{M_{ns}}|) = \frac{1}{L_{bnd}} \int_{\Gamma} |M_{ns}^{(WBM)} - \bar{M}_{ns}| \, ds, \quad (6.147)$$

$$\text{avg}(|R_{Q_n}|) = \frac{1}{L_{bnd}} \int_{\Gamma} |Q_n^{(WBM)} - \bar{Q}_n| \, ds, \quad (6.148)$$

with  $L_{bnd}$  the total length of the boundary,  $\bar{M}_n = 0$ ,  $\bar{M}_{ns} = 0$  and  $\bar{Q}_n = 0$  the prescribed boundary conditions and  $M_n^{(WBM)}$ ,  $M_{ns}^{(WBM)}$  and  $Q_n^{(WBM)}$  the moments and shear force calculated with the WBM models, are computed. The integrals in Equations (6.146) – (6.148) are evaluated numerically with the trapezoidal rule, which is implemented in the

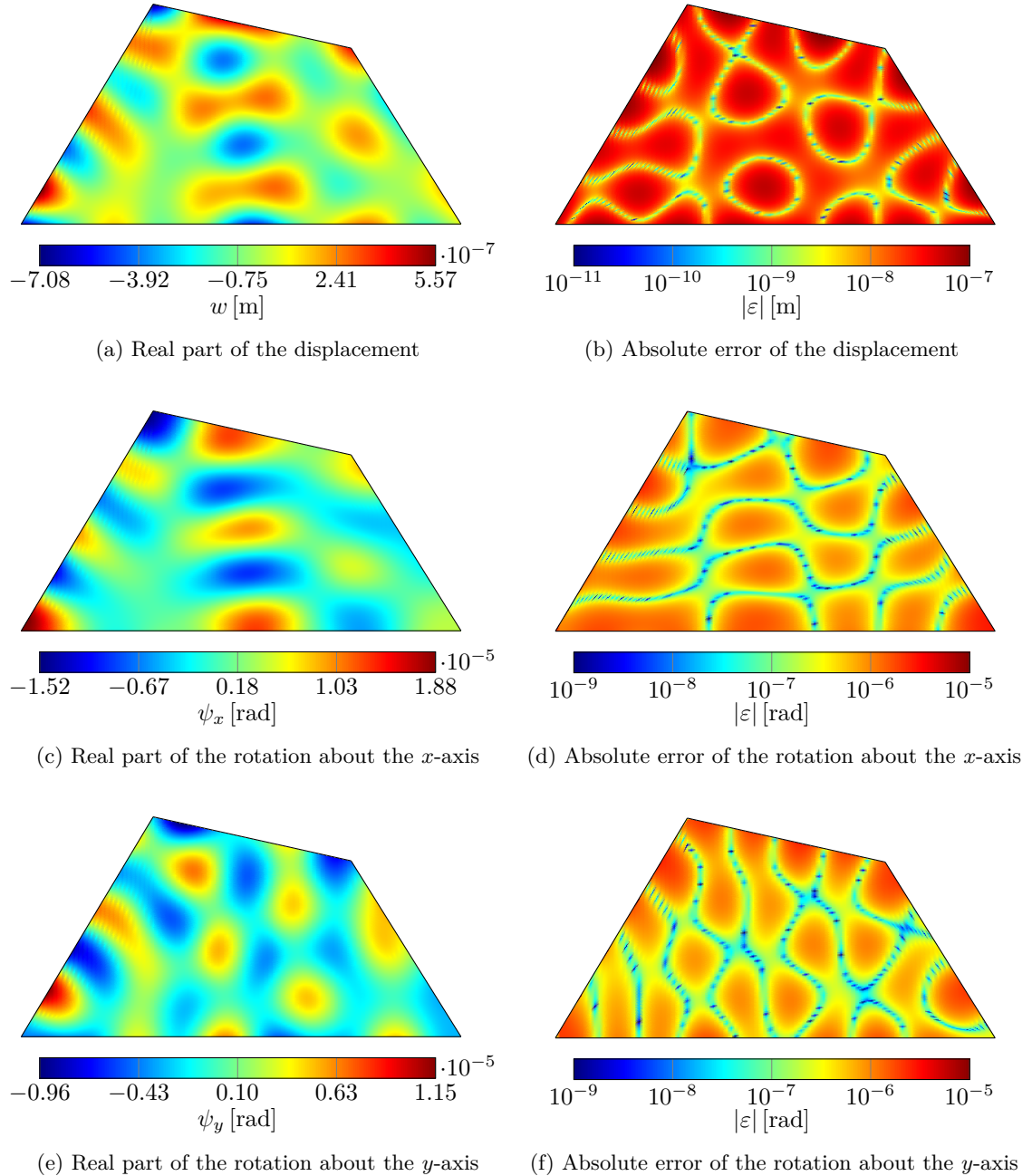


Figure 6.21: Out-of-plane displacement and rotations about the  $x$ - and  $y$ -axis of a free plate ( $h = 0.005$  m) excited by a constant ring load at 1310 Hz calculated with the original WBM using only the function set 1 and a truncation factor  $T = 2$

Matlab function *trapz*. Additionally, the averaged amplitudes of the moments ( $\text{avg}(|M_x|)$ ,  $\text{avg}(|M_y|)$ ,  $\text{avg}(|M_{xy}|)$ ) and shear forces ( $\text{avg}(|Q_x|)$ ,  $\text{avg}(|Q_y|)$ ) in the whole plate domain are calculated for the reference solution, to be able to quantify the boundary residuals. The averaged boundary residuals for the WBM using the original wave function selection

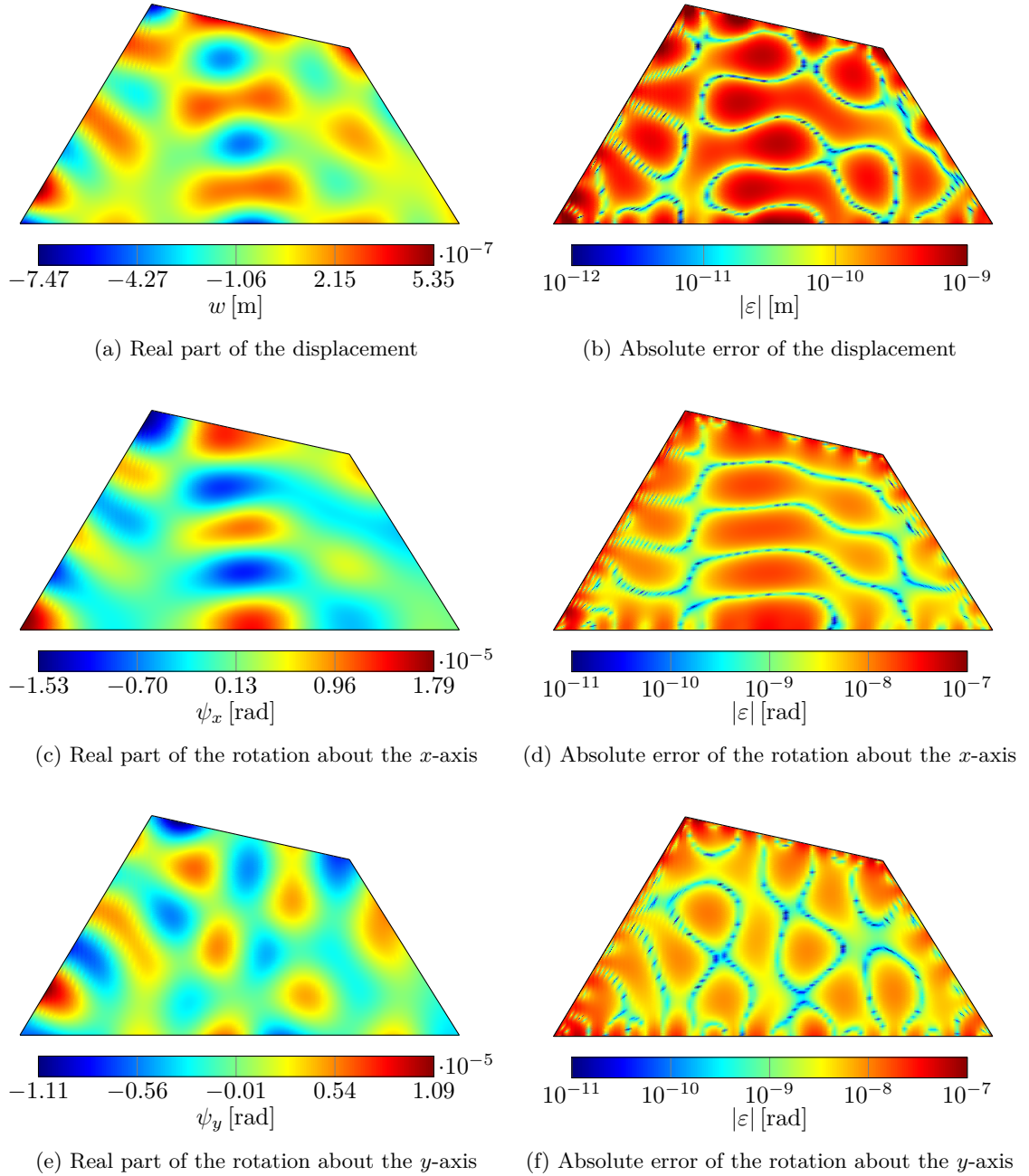


Figure 6.22: Out-of-plane displacement and rotations about the  $x$ - and  $y$ -axis of a free plate ( $h = 0.005$  m) excited by a constant ring load at 1310 Hz calculated with the modified WBM using only the function set 1 and a truncation factor  $T = 2$

are given by  $\text{avg}(|R_{M_n}|) = 0.0026$  N,  $\text{avg}(|R_{M_{ns}}|) = 0.062$  N and  $\text{avg}(|R_{Q_n}|) = 1.659$  N/m, while the modified selection leads to the residuals  $\text{avg}(|R_{M_n}|) = 0.0022$  N,  $\text{avg}(|R_{M_{ns}}|) = 0.0016$  N and  $\text{avg}(|R_{Q_n}|) = 0.291$  N/m. Comparing the residuals with the averaged moments  $\text{avg}(|M_x|) = 0.138$  N,  $\text{avg}(|M_y|) = 0.191$  N and  $\text{avg}(|M_{xy}|) = 0.084$  N and shear

forces  $\text{avg}(|Q_x|) = 6.154 \text{ N/m}$  and  $\text{avg}(|Q_y|) = 7.061 \text{ N/m}$ , shows that the original wave function selection is not able to accurately represent the boundary conditions, especially the twisting moment  $M_{ns}$  (residual  $\approx 50\%$  of the averaged moment) and normal shear force  $Q_n$  (residual  $\approx 25\%$  of the averaged shear force). The residuals of the WBM model using the modified selection are significantly lower ( $\approx 1\%$  to  $5\%$  of the averaged values), which leads to the large difference in accuracy between the two models.

To verify the Picard conditions for the WBM models used to calculate the plate deformations shown in Figures 6.21 and 6.22, a SVD of the system matrices is performed and the singular values  $\sigma_i$  and coefficients  $|\beta_i|$  are plotted in Figure 6.23. Similar to the clamped plate examples, the original wave function selection leads to a system matrix having a rather poor conditioning number ( $\text{cond}(\mathbf{A}) \approx 3 \times 10^{21}$  (double precision),  $\text{cond}(\mathbf{A}) \approx 2 \times 10^{39}$  (quadruple precision)) compared to the modified wave function selection ( $\text{cond}(\mathbf{A}) \approx 1 \times 10^{10}$  (independent of precision)). The system matrix of the modified WBM fulfills both Picard conditions, while for the original WBM model, the ratio of the coefficients  $|\beta_i|$  to the singular values  $\sigma_i$  becomes rather high at the end of the sequence, which violates the second Picard condition. This violation is only evident if quadruple precision is used to build the WBM model, since in double precision the singular values become constant at the end of the sequence and remain well above the constants  $|\beta_i|$ .

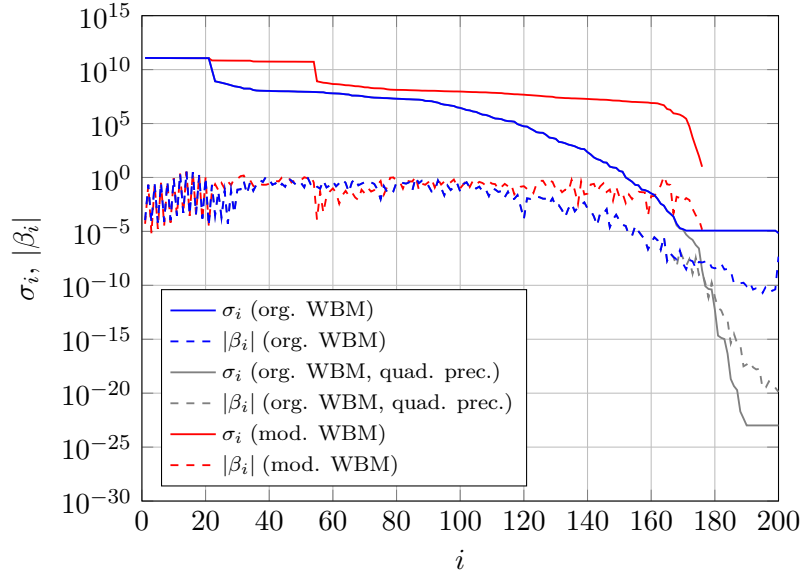


Figure 6.23: Picard conditions for the original and modified wave function selection (free plate)

The contour and error plots for all other thicknesses and frequencies are shown in Appendix E in Figures E.25–E.40. Similar to the findings for the clamped plate configurations, the modified wave function selection leads to highly accurate results independent of the plate thickness or excitation frequency, while the performance of the original wave function selection strongly depends on the thickness and frequency. The plate deformations are very similar among the plate thicknesses, since the viewed frequencies are situated between the same eigenmodes of the plates.

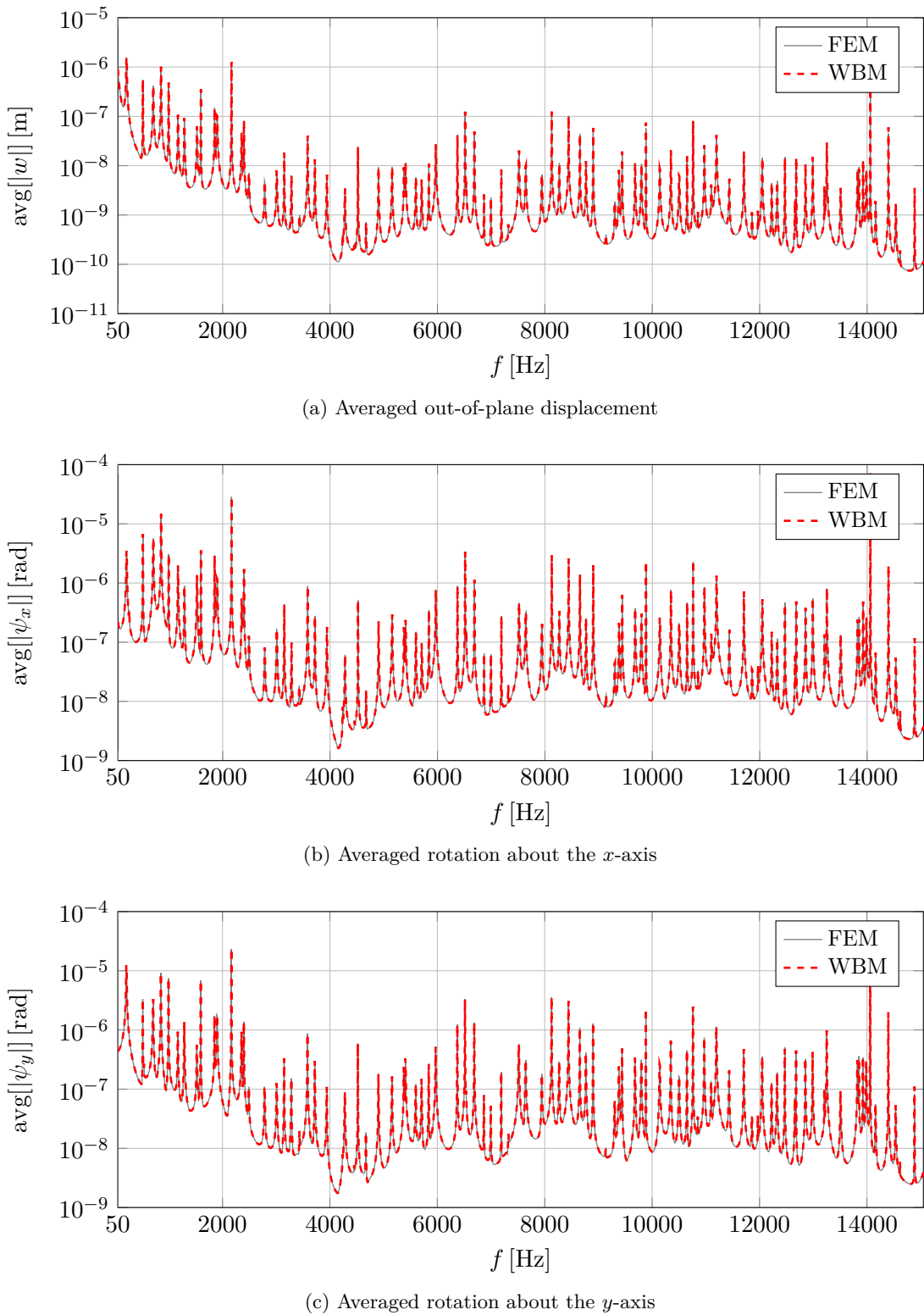


Figure 6.24: Frequency response functions of a free plate ( $h = 0.025$  m) excited by a constant ring load calculated with the FEM (reference mesh) and the modified WBM (function set 1 and set 2,  $T = 2$ )

The frequency response functions of the free plate with a thickness  $h = 0.025$  m calculated with the WBM and FEM are compared in Figure 6.24. The modified wave function selection is used to build the WBM model and both wave function sets are included. The truncation factor is set to  $T = 2$  and the LU-factorization is applied to solve the system of linear equations. To include approximately the first 100 bending modes, the excitation frequency starts at 50 Hz and is increased to 15050 Hz in 2000 steps. Since the truncation factor is constant, the total number of wave functions in the WBM model rises from 44 to 568. Similar to the results of the clamped plate configurations, the WBM solutions are in excellent agreement with the reference model over the whole frequency range, even close to eigenfrequencies. The results for the free plates with the thicknesses  $h = 0.005$  m and  $h = 0.01$  m are given in Appendix E in Figures E.41 and E.42. Independent of the plate thickness, the WBM applying the modified wave function selection leads to highly accurate results for the three field variables over the complete frequency range. Since the contour plots in Figure 6.21 already show that the WBM models using the original wave function selection lead to relatively high errors, the computation of the frequency response functions is omitted.

In Figures 6.25–6.27, the convergency curves of different WBM models (solved with LU-factorization) for the free plate with thickness  $h = 0.01$  m and all frequencies are shown. The WBM models applying the modified wave function selection converge to highly accurate results ( $\approx 0.001\%$  error) for all frequencies, while the original wave function selection stagnates at an averaged relative error of approximately 7% for the first frequency (440 Hz), 30% for the second frequency (2580 Hz) and 75% for the third frequency (4970 Hz). Including the second wave function sets (*set1a2*) leads to a minor improvement of the convergence rate compared to WBM models, which only use the first wave function sets (*set1*). This effect is more pronounced for lower frequencies and only appears for the modified wave function selection.

If the modified wave function selection and the first wave function sets (*set1*) are used in the WBM model, only 59 wave functions (440 Hz), 135 wave functions (2580 Hz) and 199 wave functions (4970 Hz) are required to reach an averaged relative error of 1%. Adding the second wave function sets (*set1a2*) reduces the required degrees of freedom to 52 (440 Hz), 134 (2580 Hz) and 182 (4970 Hz).

Due to the bad conditioning of the system matrix and the violation of the Picard conditions, the WBM models using the original wave function selection have a limited accuracy. If the WBM models are built and solved with quadruple precision, the error decreases to approximately 6% for the first frequency (440 Hz), 10% for the second frequency (2580 Hz) and 40% for the third frequency (4970 Hz).

The convergence curves for the free plates with thickness  $h = 0.005$  m and  $h = 0.025$  m are shown in Appendix E in Figures E.43–E.48. As expected, the convergence rate of the WBM models applying the modified wave function selection is hardly influenced by the plate thickness, since the viewed frequencies are situated between the same eigenmodes and therefore the plate deformations are very similar. On the contrary, the accuracy of the solutions calculated with the original wave function selection strongly depends on the plate thickness and the viewed frequency. While for the lowest frequency, the reached accuracy is still acceptable, the errors at higher frequencies, especially for thicker plates, become too high.

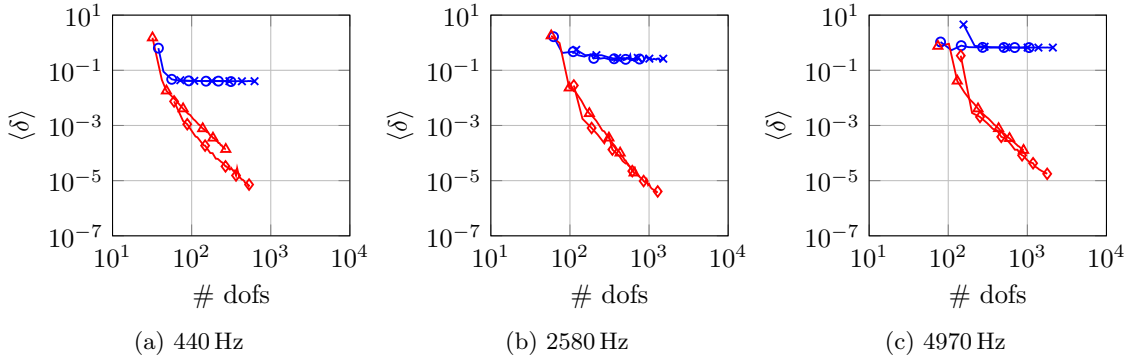


Figure 6.25: Convergence curves of the out-of-plane displacement (free plate with  $h = 0.01$  m) for the original WBM ( $set1$  (—○—),  $set1a2$  (—\*—)) and the modified WBM ( $set1$  (—△—),  $set1a2$  (—◊—))

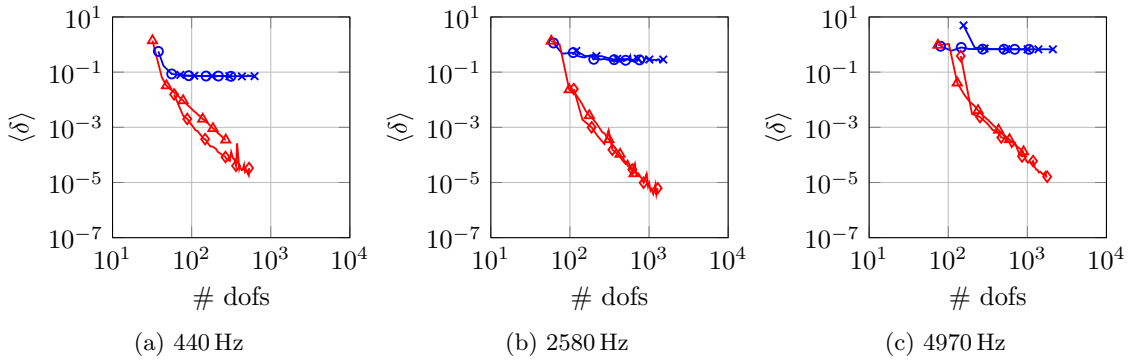


Figure 6.26: Convergence curves of the rotation about the  $x$ -axis (free plate with  $h = 0.01$  m) for the original WBM ( $set1$  (—○—),  $set1a2$  (—\*—)) and the modified WBM ( $set1$  (—△—),  $set1a2$  (—◊—))

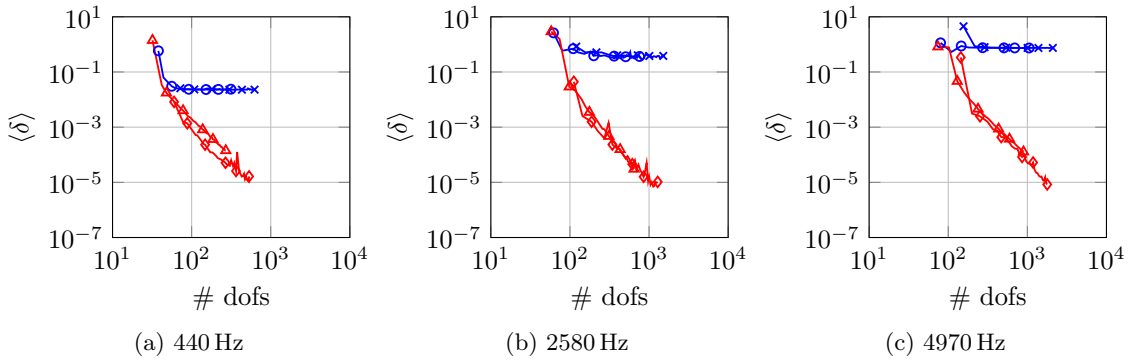


Figure 6.27: Convergence curves of the rotation about the  $y$ -axis (free plate with  $h = 0.01$  m) for the original WBM ( $set1$  (—○—),  $set1a2$  (—\*—)) and the modified WBM ( $set1$  (—△—),  $set1a2$  (—◊—))

A comparison of the computational efficiency between the WBM and the FEM for the free plate with the thickness  $h = 0.01$  is illustrated in Figure 6.28. Since the convergence curves of the three field variables are very similar, only the results for the out-of-plane displacement are shown. The WBM models use the modified wave function selection and

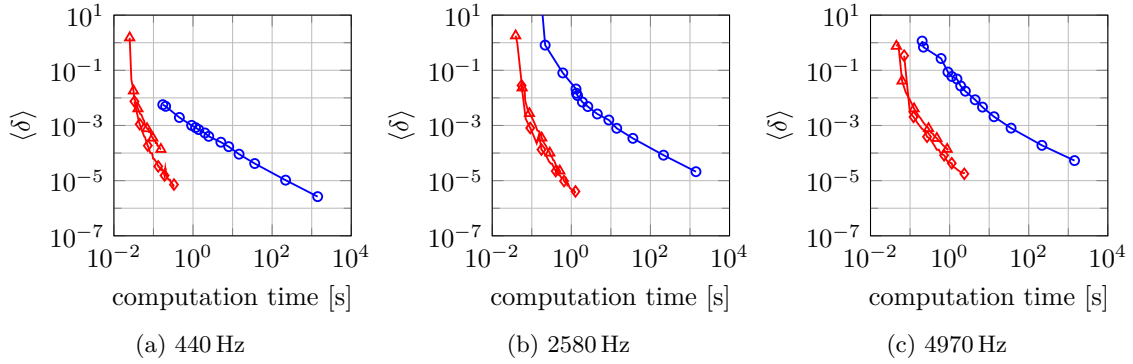


Figure 6.28: Convergence curves of the out-of-plane displacement (free plate with  $h = 0.01$ ) for the FEM (—○—) and the modified WBM (*set1* (—△—), *set1a2* (—◆—))

the LU-factorization is applied to solve the system of linear equations. It is apparent that the WBM outperforms the FEM for the given example and that the difference in computational time increases with rising frequency. The computational time of the FEM to reach an averaged relative error of 1% is 3.5 (440 Hz), 25 (2580 Hz) and 44 times (4970 Hz) higher compared to the WBM. The WBM models including only the first function sets (*set1*) and both function sets (*set1a2*) perform nearly equally for the free plate vibration examples.

### Cantilever plate

In Figure 6.29, the boundary conditions and loading of the cantilever plate configurations are illustrated. The edge, which coincides with the  $x$ -axis is clamped (zero displacement and rotations), while the other edges can move freely (zero normal and twisting moments and normal shear forces). The cantilever plates are harmonically excited by a constant circular load with the amplitude  $\bar{q}_0 = 10 \text{ N/m}^2$  and the radius  $r_0 = 0.05 \text{ m}$ . At the corner points of the cantilever plate, stress singularities are not exhibit, since the critical angles

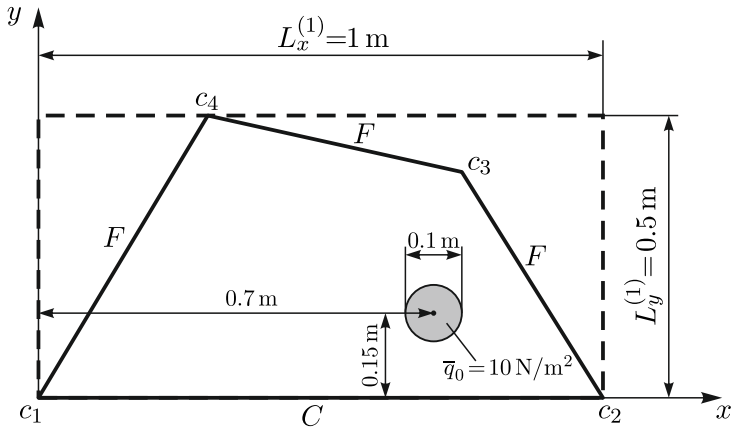


Figure 6.29: Boundary conditions and harmonic loading of the cantilever plates

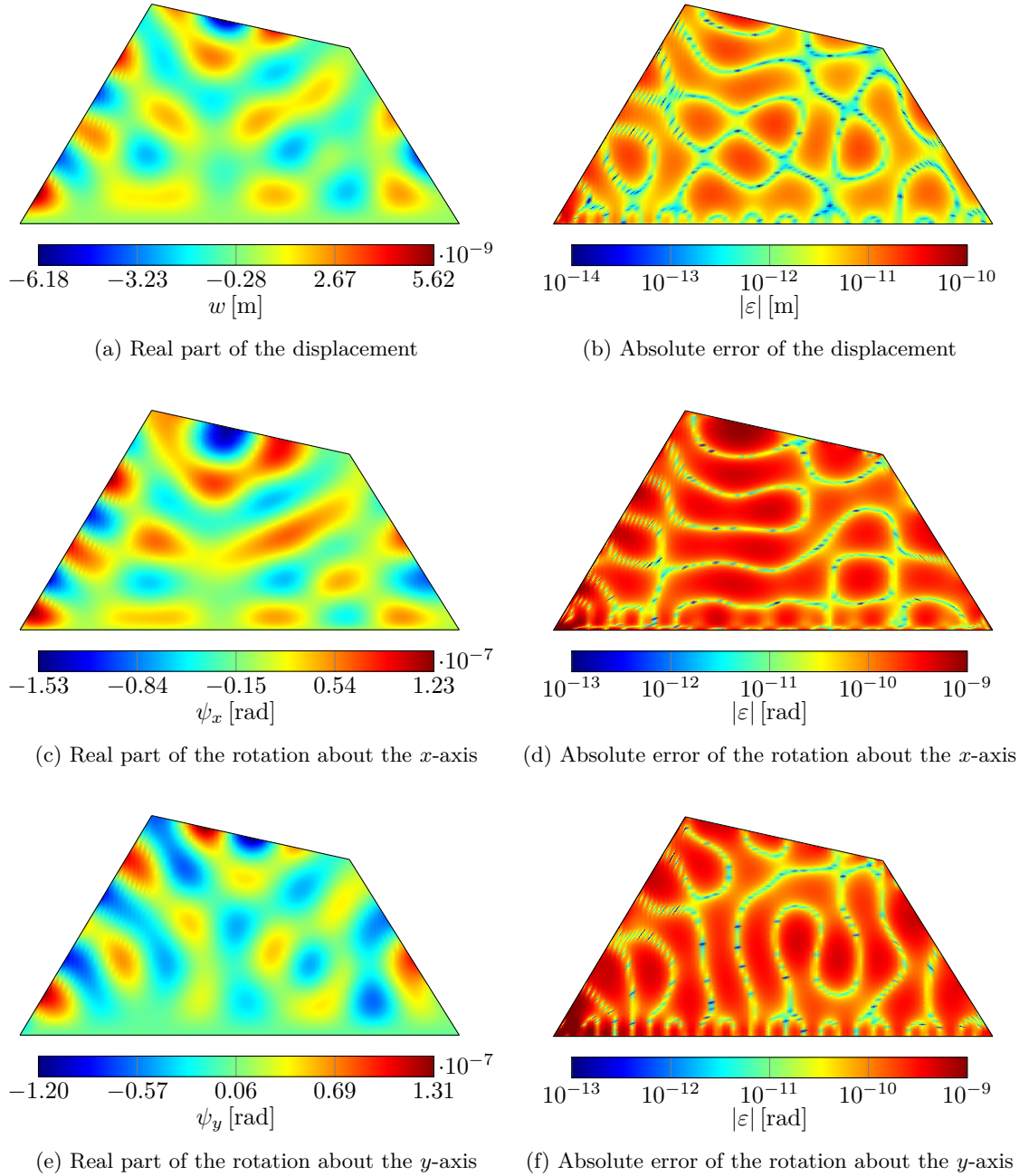


Figure 6.30: Out-of-plane displacement and rotations about the  $x$ - and  $y$ -axis of a cantilever plate ( $h = 0.005$  m) excited by a constant circular load at 1780 Hz calculated with the modified WBM using only the function set 1 and a truncation factor  $T = 2$

shown in Figures 6.2b and 6.2e (180° for the corner points  $c_3$  and  $c_4$  and 61.3° for  $c_1$  and  $c_2$ ) are not exceeded. Therefore, no special purpose functions are included in the following WBM models and the particular solution functions given in Equations (5.85) and (5.86) are used to represent the harmonic loading.

In Figure 6.30, the out-of-plane displacement and rotations about the  $x$ - and  $y$ -axis of the cantilever plate with a thickness of  $h = 0.005$  m excited at 1780 Hz are illustrated. A WBM model applying the modified wave function selection and including only the first wave function sets is used to calculate the response of the plate. The system of linear equations is solved with the LU-factorization and the truncation factor is set to  $T = 2$ , which leads to a total number of 207 wave functions. Due to the findings in the previous two validation examples, WBM models using the original wave function selection are not further considered in the following investigations.

The absolute error of the WBM shown in Figure 6.30 is rather low compared to the amplitudes of the field variables and it is apparent that the clamped boundary conditions are accurately fulfilled. To verify the accurate representation of the free boundary conditions, the averaged boundary residuals defined in Equations (6.146)–(6.148) are computed and compared to the averaged moment and shear force amplitudes. The averaged boundary residuals  $\text{avg}(|R_{M_n}|) = 5.93 \times 10^{-5}$  N,  $\text{avg}(|R_{M_{ns}}|) = 3.15 \times 10^{-5}$  N and  $\text{avg}(|R_{Q_n}|) = 0.0026$  N/m are approximately two orders lower compared to the averaged moments  $\text{avg}(|M_x|) = 0.0018$  N,  $\text{avg}(|M_y|) = 0.0025$  N and  $\text{avg}(|M_{xy}|) = 0.0010$  N and shear forces  $\text{avg}(|Q_x|) = 0.0972$  N/m and  $\text{avg}(|Q_y|) = 0.1300$  N/m, and therefore, all boundary conditions are accurately fulfilled by the WBM model. The WBM system matrices show the same numerical properties as for the clamped and free plate examples.

In Appendix E, the contour and error plots for all other plate thicknesses and frequencies are shown in Figures E.49–E.56. In general, the absolute error is several orders of magnitude lower compared to the amplitude of the field variables except for certain regions close to the corner points. This effect can be explained by the Gibbs phenomenon, which appears if only sine functions are used to approximate the boundary conditions and the sudden change of the enforced boundary conditions at the corners  $c_1$  and  $c_2$ . The following convergence results show that this issue can be resolved by adding the second wave function sets.

The frequency response functions of the cantilever plate with a thickness of  $h = 0.025$  m calculated with the WBM and FEM are compared in Figure 6.31. The frequency is increased from 50 Hz up to 16050 Hz in 2000 steps and therefore, approximately the first 100 bending modes are included in the response function. The modified wave function selection and both wave function sets are used to build the WBM model and the resulting system of linear equations is solved with the LU-factorization. The truncation factor is set to  $T = 2$ , which leads to 44 wave functions for the lowest frequency and 592 wave function for the highest frequency. It is apparent from Figure 6.31 that the results of the WBM are in excellent agreement with the reference solutions for all three field variables. The WBM is able to predict accurate results with a low number of degrees of freedom, even close to the eigenfrequencies.

In Appendix E, the frequency response functions for the cantilever plates with the thicknesses  $h = 0.005$  m and  $h = 0.01$  m are shown in Figures E.57 and E.58. For each thickness, the frequency is increased in 2000 steps and approximately the first 100 bending modes are included in the frequency ranges. It is apparent from Figures E.57 and E.58 that the results of the WBM models and the reference solution coincide over the complete frequency range. Therefore, the accuracy of the WBM applying the modified wave function selection is not influenced by the plate thickness.

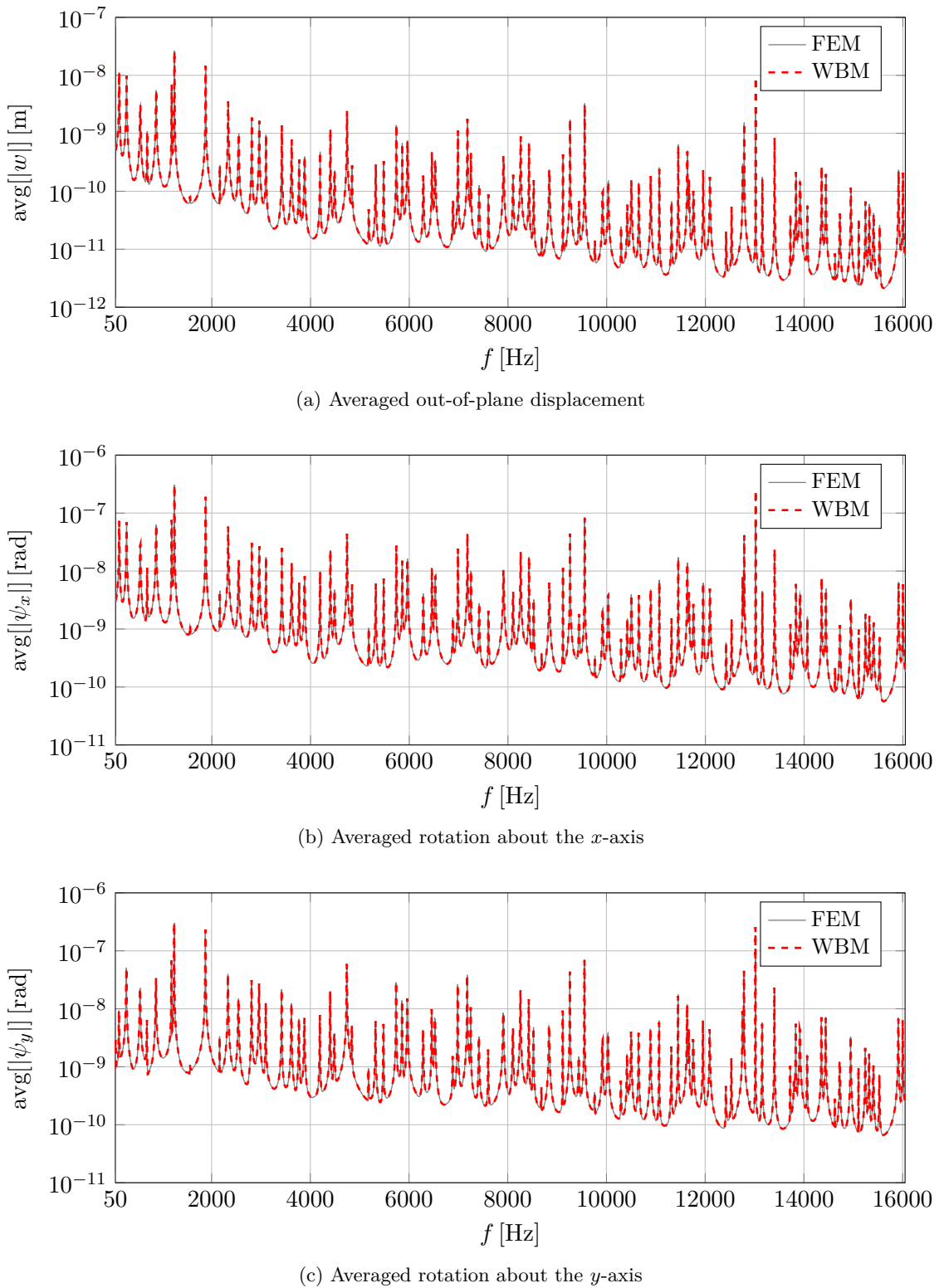


Figure 6.31: Frequency response functions of a cantilever plate ( $h = 0.025$  m) excited by a constant circular load calculated with the FEM (reference mesh) and the modified WBM (function set 1 and set 2,  $T = 2$ )

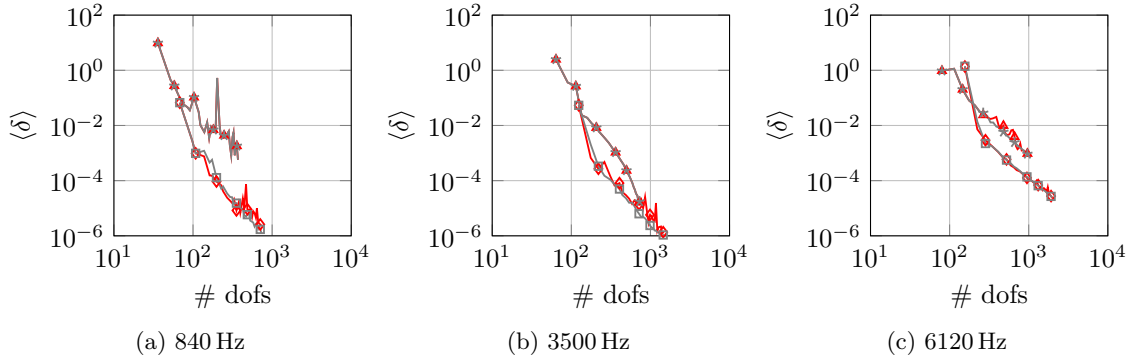


Figure 6.32: Convergence curves of the out-of-plane displacement (cantilever plate with  $h = 0.01$  m) for the modified WBM solved with the LU (set1 (red triangle), set1a2 (red diamond)) and the SVD (set1 (black asterisk), set1a2 (black square)).

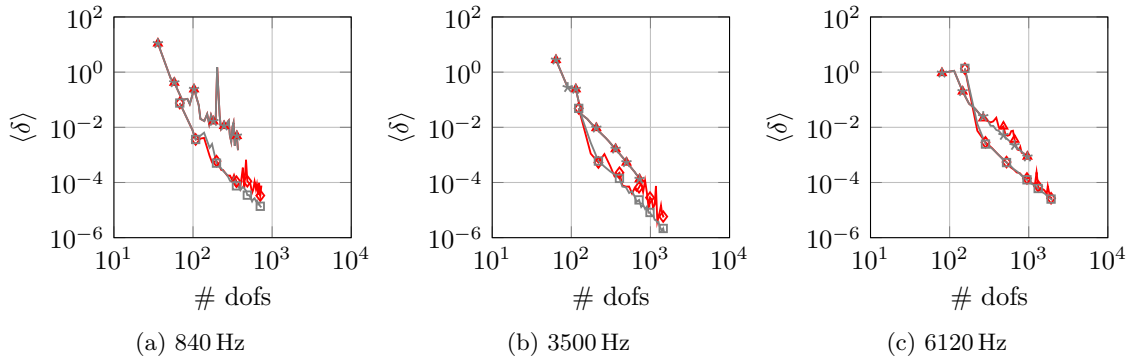


Figure 6.33: Convergence curves of the rotation about the  $x$ -axis (cantilever plate with  $h = 0.01$  m) for the modified WBM solved with the LU (set1 (red triangle), set1a2 (red diamond)) and the SVD (set1 (black asterisk), set1a2 (black square)).

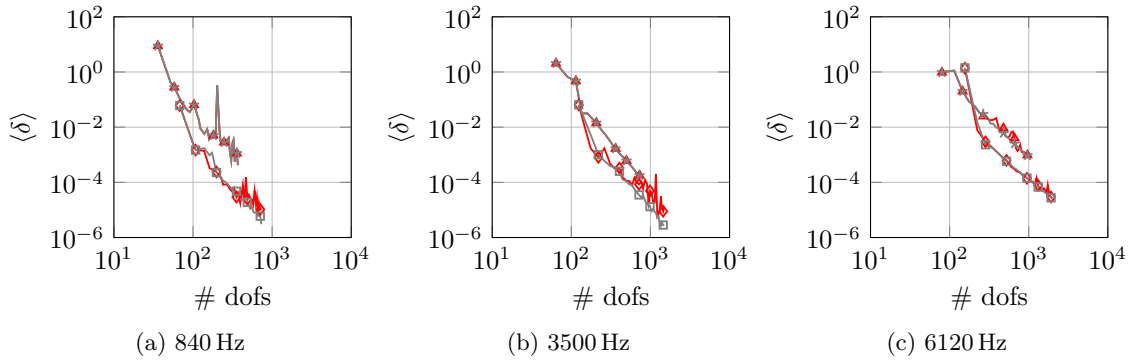


Figure 6.34: Convergence curves of the rotation about the  $y$ -axis (cantilever plate with  $h = 0.01$  m) for the modified WBM solved with the LU (set1 (red triangle), set1a2 (red diamond)) and the SVD (set1 (black asterisk), set1a2 (black square)).

The convergence curves for the cantilever plate with the thickness  $h = 0.01$  m calculated with different WBM models are illustrated in Figures 6.32–6.34. Only the modified wave function selection is considered and the WBM models using either the first wave function sets (set1) or both wave function sets (set1a2) are solved with the LU-factorization or the

singular value decomposition (SVD). Even though the WBM models using the first function sets converge to accurate results, including the second wave function sets considerably improves the convergence rate, especially for the lowest frequency. While this effect cannot be seen for the clamped and free plate configurations, the accurate representation of the sudden change of the boundary conditions at the corners  $c_1$  and  $c_2$  in the cantilever plate requires a high number of wave functions if only the first wave function sets are included. If both wave function sets are used, the WBM nearly uniformly converges to an averaged relative error of less than 0.001% independent of the frequency and a total number of 97 (840 Hz), 166 (3500 Hz) and 223 (6120 Hz) wave functions is required to reach an averaged relative error of 1%.

The convergence rate of the WBM is hardly influenced by the direct solver used to calculate the wave contribution factors, which is apparent from Figures 6.32 – 6.34. Although, the final results are very similar, the computed contribution factors are rather different between the LU-factorization and the SVD. The SVD seems more stable for high numbers of degrees of freedom and gives slightly more accurate results for large WBM models. However, the SVD is computationally more demanding compared to the LU-factorization and therefore, the LU-factorization is recommended to solve the system of linear equations if the WBM model is not too large.

In Appendix E, the convergence curves for the cantilever plates with the thickness  $h = 0.005$  m and  $h = 0.025$  m are shown in Figures E.59 – E.64. The plate thickness has hardly any influence on the convergence properties of the WBM models, since the plate deformations at the chosen frequencies are very similar among the different plate thicknesses.

To assess the computation efficiency of the WBM compared to the FEM, their convergence curves for the out-of-plane displacement of the cantilever plate with a thickness of  $h = 0.01$  m are given in Figure 6.35. The computation time required by the WBM using the modified wave function selection and both wave function sets to reach an averaged relative error of 1% is approximately 5 (840 Hz), 15 (3500 Hz) and 70 (6120 Hz) times lower compared to the FEM, which shows the advanced computational properties of the WBM. The findings for the other plate thicknesses and field variables are very similar and therefore not presented here.

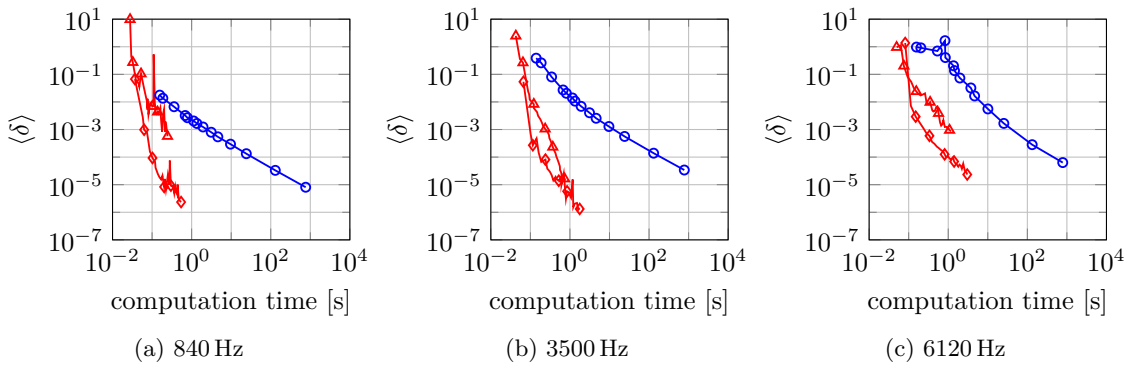


Figure 6.35: Convergence curves of the out-of-plane displacement (cantilever plate with  $h = 0.01$ ) for the FEM (—○—) and the modified WBM (*set1* (—▲—), *set1a2* (—◆—))

### Hard simply-supported plate

In the last single domain example, the hard simply-supported plate shown in Figure 6.36 is analyzed. All four edges are hard simply-supported and the plate is harmonically excited by a point load having an amplitude of  $\bar{q}_0 = 10 \text{ N}$ . If both edges at a corner point are hard simply-supported, moment stress singularities arise for internal angles greater than  $90^\circ$ , while shear force singularities are exhibited for angles greater than  $180^\circ$ . Therefore, moment singularities occur at the corner points  $c_3$  ( $\alpha = 134.5^\circ$ ) and  $c_4$  ( $\alpha = 108.4^\circ$ ).

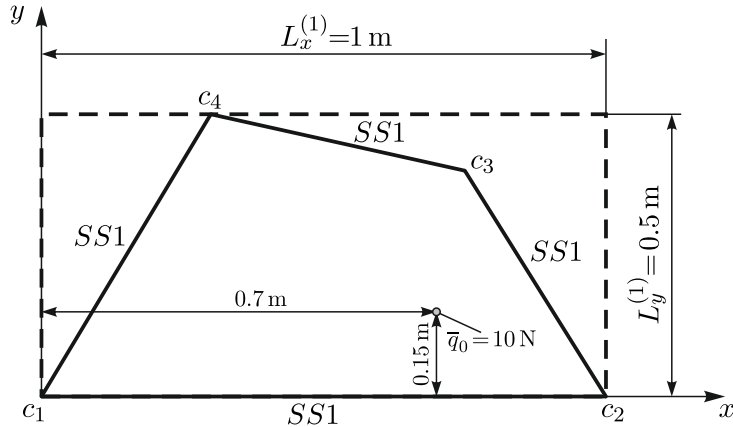


Figure 6.36: Boundary conditions and harmonic loading of the hard SS plates

While in the previous validation examples only the first wave function sets (*set1*) or both sets (*set1a2*) are used to build the WBM models, additional models including special purpose functions (*set1CF*, *set1a2CF*), which represent the corner stress singularities in the corners  $c_3$  and  $c_4$ , are analyzed in the following. From Figure 6.2c it is apparent that only one symmetric eigenvalue leads to moment singularities in the corners  $c_3$  and  $c_4$ . Therefore, three special purpose functions are included for each of the two corners, which are listed in Table 6.8. The particular solution functions given in Equations (5.40) and (5.41) are used to represent the harmonic point loading.

Table 6.8: Special purpose functions for the hard simply-supported plate examples

corner	$\alpha$	corner functions	eigenvalue
$c_3$	$134.5^\circ$	$\Upsilon_{M_{w1}1}^{(c_3)} = \cos(\lambda_{M1}^s \varphi_{c_3}) J_{\lambda_{M1}^s}(k_{f1} r_{c_3})$	$\lambda_{M1}^s = 1.338$
		$\Upsilon_{M_{w2}1}^{(c_3)} = \cos(\lambda_{M1}^s \varphi_{c_3}) J_{\lambda_{M1}^s}(k_{f2} r_{c_3})$	
		$\Upsilon_{M_H1}^{(c_3)} = -\sin(\lambda_{M1}^s \varphi_{c_3}) J_{\lambda_{M1}^s}(k_s r_{c_3})$	
$c_4$	$108.4^\circ$	$\Upsilon_{M_{w1}1}^{(c_4)} = \cos(\lambda_{M1}^s \varphi_{c_4}) J_{\lambda_{M1}^s}(k_{f1} r_{c_4})$	$\lambda_{M1}^s = 1.660$
		$\Upsilon_{M_{w2}1}^{(c_4)} = \cos(\lambda_{M1}^s \varphi_{c_4}) J_{\lambda_{M1}^s}(k_{f2} r_{c_4})$	
		$\Upsilon_{M_H1}^{(c_4)} = -\sin(\lambda_{M1}^s \varphi_{c_4}) J_{\lambda_{M1}^s}(k_s r_{c_4})$	

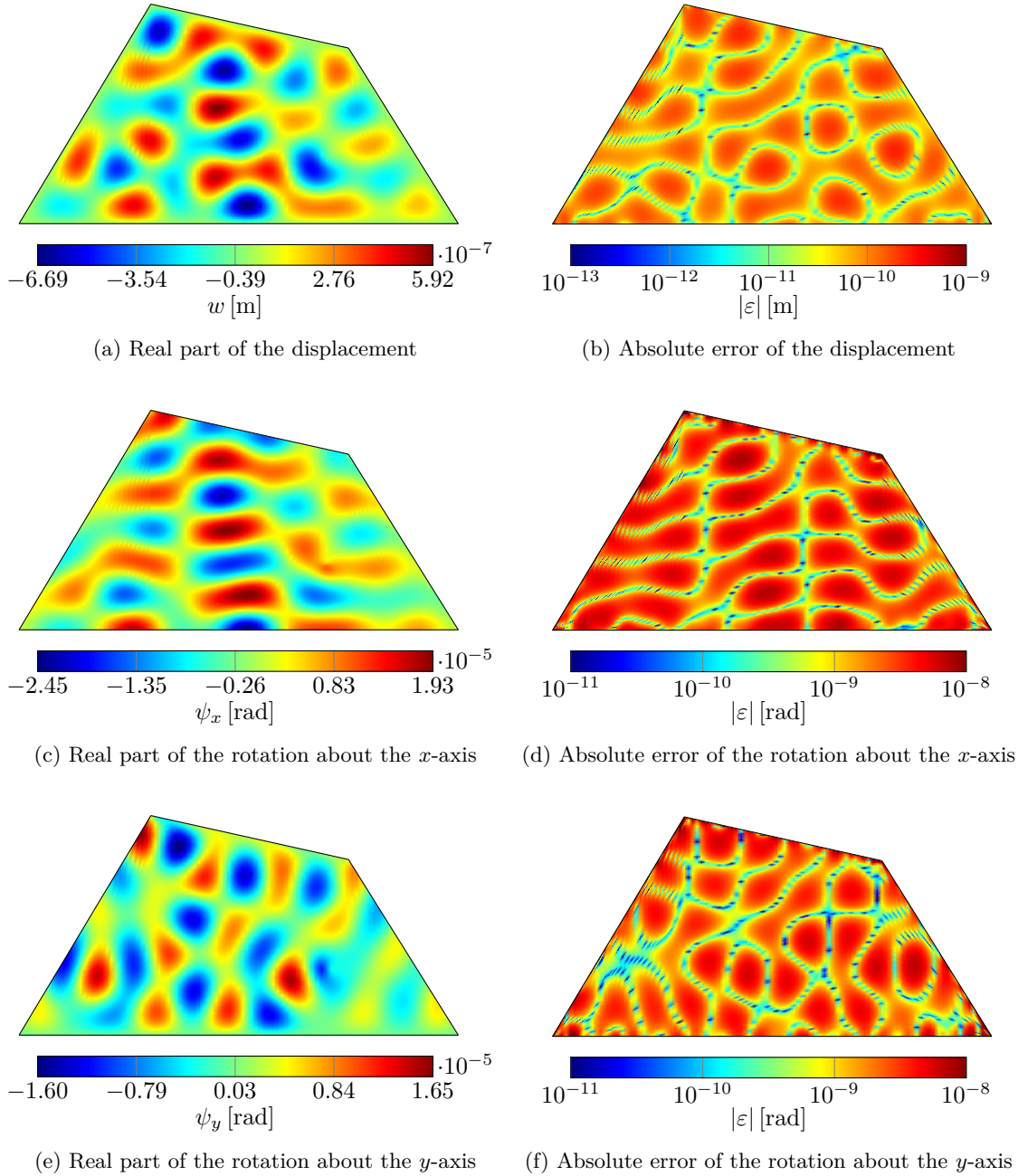


Figure 6.37: Out-of-plane displacement and rotations about the  $x$ - and  $y$ -axis of a hard simply-supported plate ( $h = 0.005$  m) excited by a point load at 2300 Hz calculated with the modified WBM using the function set 1, corner functions and a truncation factor  $T = 2$

The contour and error plots of the hard simply-supported plate with a thickness  $h = 0.005$  m excited at 2300 Hz are shown in Figure 6.37. A WBM model applying the modified wave function selection and including the first wave function sets and the special purpose functions given in Table 6.8 is used to calculate the results in Figure 6.37. The truncation

factor is set to  $T = 2$ , which results in 232 degrees of freedom, and the system of linear equations is solved with the LU-factorization. It is apparent from Figure 6.37a that the out-of-plane displacement boundary conditions are well fulfilled for all four edges. Since the representation of the other two boundary conditions cannot be assessed by Figure 6.37, the averaged boundary residuals  $\text{avg}(|R_{\psi_n}|) = 3.3 \times 10^{-9} \text{ rad}$  and  $\text{avg}(|R_{M_n}|) = 8.4 \times 10^{-4} \text{ N}$  are compared with the averaged rotations  $\text{avg}(|\psi_x|) = 4.9 \times 10^{-6} \text{ rad}$  and  $\text{avg}(|\psi_y|) = 3.7 \times 10^{-6} \text{ rad}$  and averaged moments  $\text{avg}(|M_x|) = 0.365 \text{ N}$ ,  $\text{avg}(|M_y|) = 0.496 \text{ N}$  and  $\text{avg}(|M_{xy}|) = 0.153 \text{ N}$ . Both residuals are at least two orders of magnitude lower compared to the averaged values of the rotations and moments and therefore all boundary conditions are accurately represented by the WBM model. As a result, the absolute errors of the predicted field variables are several orders of magnitude lower compared to the amplitudes of the field variables, which shows the high accuracy of the WBM.

In Figure 6.38, the singular values  $\sigma_i$  and the coefficients  $|\beta_i|$  of the WBM system matrix used to calculate the results in Figure 6.37 are illustrated. Additionally, the values for the same WBM model without special purpose functions are plotted to show the influence of the corner functions on the properties of the WBM system matrix. From Figure 6.38 it is evident that both Picard conditions are fulfilled by the WBM models and including the special purpose functions hardly influences the numerical properties and conditioning of the system matrix ( $\text{cond}(\mathbf{A}) = 1.91 \times 10^{10}$  (*set1*) and  $\text{cond}(\mathbf{A}) = 1.21 \times 10^{11}$  (*set1CF*)).

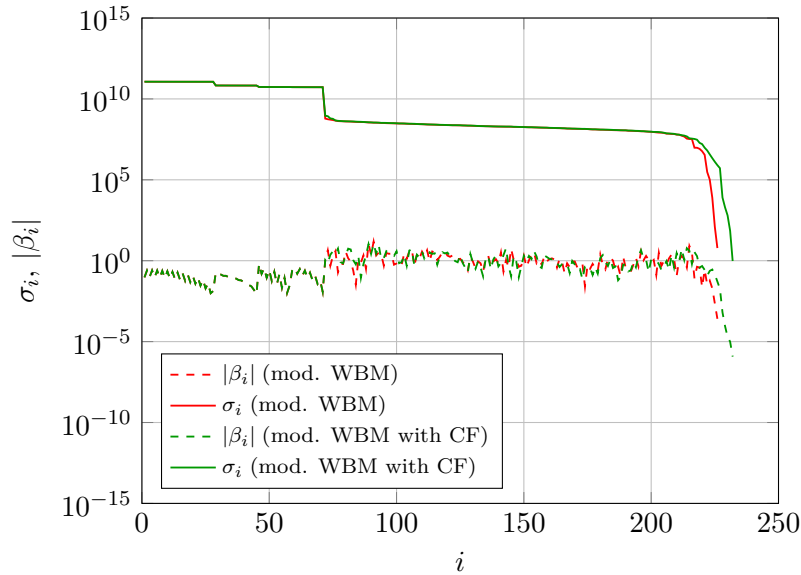


Figure 6.38: Picard conditions for the modified wave function selection with and without corner functions (hard simply-supported plate)

The contour and error plots for all other frequencies and plate thicknesses are given in Appendix E in Figures E.65–E.72. Independent of the plate thickness or frequency, the WBM models using the modified wave function selection and the special purpose functions lead to accurate results for all three field variables. The properties and performance of the original wave function selection is not investigated for the hard simply-supported plate configurations.

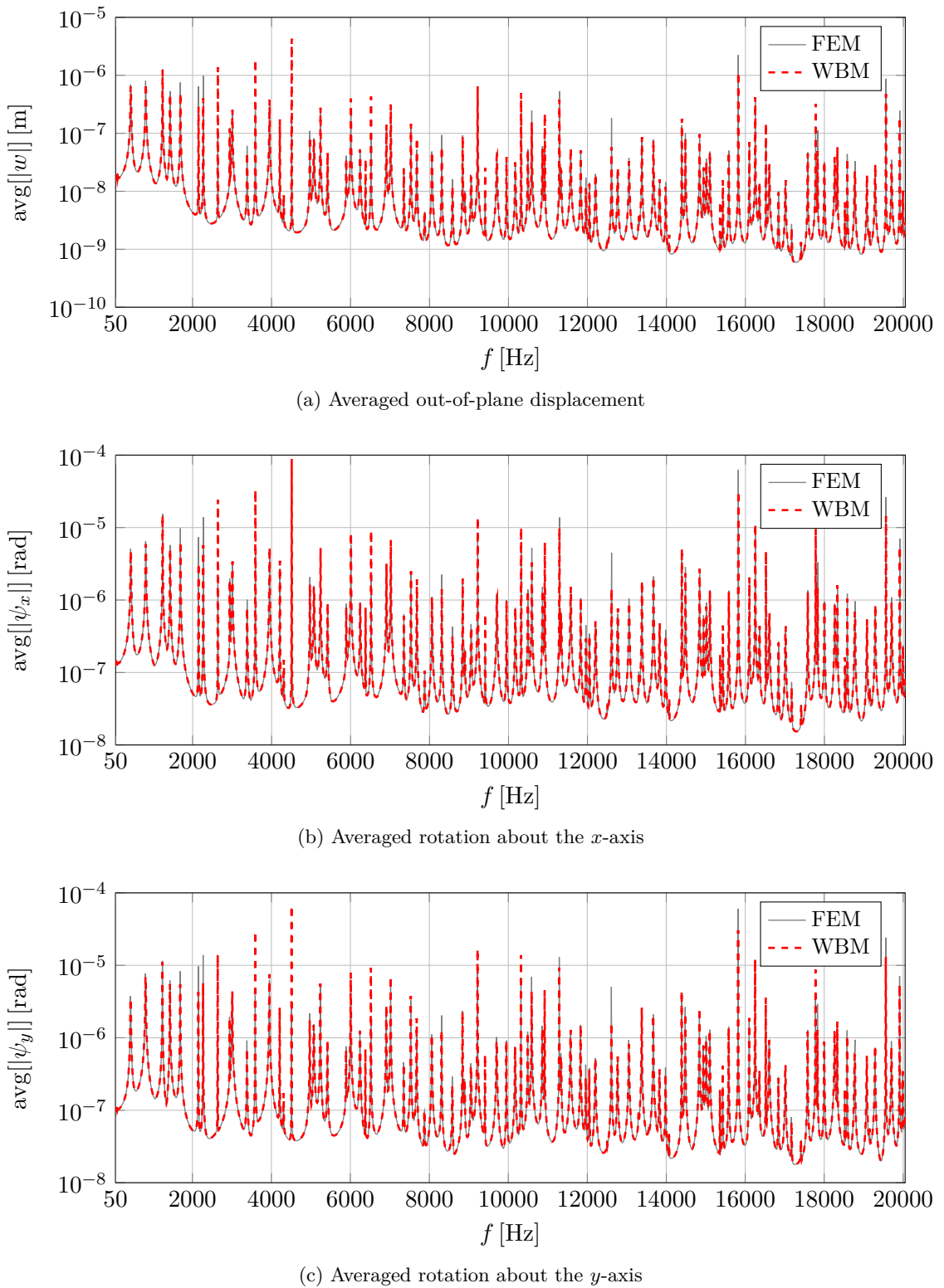


Figure 6.39: Frequency response functions of a hard simply-supported plate ( $h = 0.025$  m) excited by a point load calculated with the FEM (reference mesh) and the modified WBM (function set 1 and set 2, corner functions,  $T = 2$ )

The frequency response functions of the hard simply-supported plate with a thickness  $h = 0.025$  m calculated with the WBM and the FEM are compared in Figure 6.39. Starting from 50 Hz, the frequency is increased to 20050 Hz in 2000 steps and therefore, approximately the first 100 bending modes are covered in the response function. The WBM model uses the modified wave function selection and both wave function sets and the corner functions given in Table 6.8 are included. The truncation factor is set to  $T = 2$ , which leads to 50 degrees of freedom for the lowest frequency and 684 for the highest frequency and the LU-factorization is used to solve the system of linear equations. It is apparent from Figure 6.39 that the results of the WBM model are in excellent agreement with the reference solution over the whole frequency range. The results for the hard simply-supported plates with thickness  $h = 0.005$  m and  $h = 0.01$  m illustrated in Appendix E in Figures E.73 and E.74 show a similar accuracy of the WBM.

To analyze the effect of the special purpose functions on the convergence rate of the WBM, models with and without corner functions are built and the convergence curves for the hard simply-supported plate with a thickness  $h = 0.01$  m are plotted in Figures 6.40–6.42. All WBM models use the modified wave function selection and either only the first wave function sets (*set1*), both wave function sets (*set1a2*) or additionally the corner functions in Table 6.8 (*set1CF*, *set1a2CF*) are included. The convergence curves for the lowest frequency (1300 Hz) in Figures 6.40a, 6.41a and 6.42a show that all WBM models converge to accurate results, but the WBM models including the special purpose functions have an advanced convergence rate compared to the models without corner functions. While the WBM model including corner functions requires 80 wave functions to reach an averaged relative error of 1%, the model without corner functions needs 250 wave functions. Including the second wave function sets leads to a slightly reduced convergence of the WBM for this thickness and frequency.

The effect of the moment singularities on the convergence rate of the WBM is less pronounced for the second frequency (4600 Hz), see Figures 6.40b, 6.41b and 6.42b. If only the first wave function sets are included in the WBM models, a model with 150 degrees of freedom leads to an averaged relative error of 1%, while a model with corner functions only needs 130. Hence, the corner functions only slightly increase the convergence rate for this thickness and frequency. Furthermore, including both wave function sets results in a lower convergence rate for models without corner functions, whereas it hardly effects the convergence for models with corner functions.

For the highest frequency (7310 Hz), the effect of the corner functions on the convergence rate is very similar to the lowest frequency. In contrary to all previous examples, the WBM using the modified wave function selection starts to stagnate at an averaged relative error of approximately 0.1% and including more than approximately 230 wave functions does not further increase the accuracy. This indicates that the reference solutions calculated with the FEM is not accurate enough. Since a FEM model with even more degrees of freedom is not feasible with the available hardware, the averaged boundary residuals of the WBM models are compared to analyze the accuracy of the WBM. While the WBM model having 230 degrees of freedom leads to the averaged boundary residuals  $\text{avg}(|R_w|) = 2.44 \times 10^{-11}$  m,  $\text{avg}(|R_{\psi_n}|) = 2.19 \times 10^{-9}$  rad and  $\text{avg}(|R_{M_n}|) = 5.8 \times 10^{-3}$  N, the model with 1095 degrees of freedom has the averaged boundary residuals  $\text{avg}(|R_w|) = 2.44 \times 10^{-13}$  m,  $\text{avg}(|R_{\psi_n}|) = 2.06 \times 10^{-11}$  rad and  $\text{avg}(|R_{M_n}|) = 1.41 \times 10^{-4}$  N. The averaged boundary residuals of the WBM model with 1095 degrees of freedom are several orders

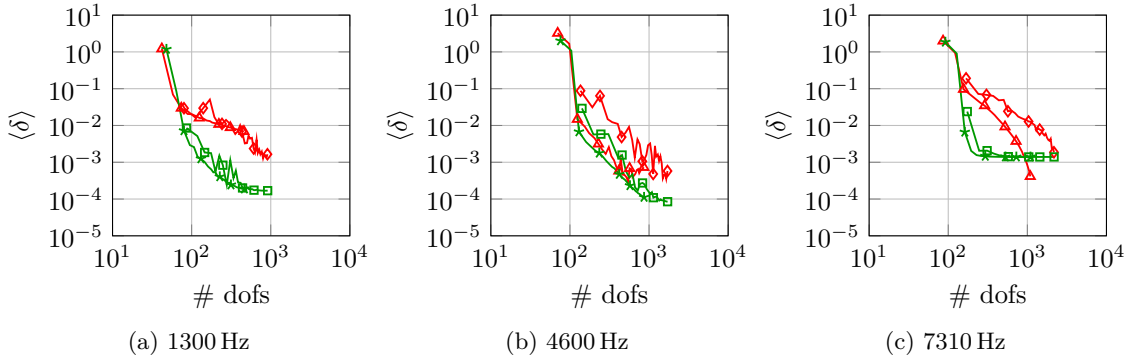


Figure 6.40: Convergence curves of the out-of-plane displacement (hard SS plate with  $h = 0.01$  m) for the modified WBM ( $set1$  (—▲—),  $set1a2$  (—◆—),  $set1CF$  (—★—),  $set1a2CF$  (—■—))

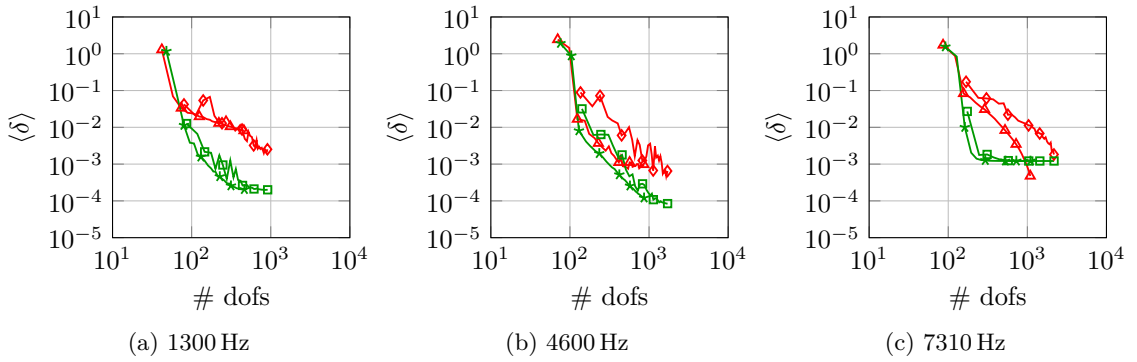


Figure 6.41: Convergence curves of the rotation about the  $x$ -axis (hard SS plate with  $h = 0.01$  m) for the modified WBM ( $set1$  (—▲—),  $set1a2$  (—◆—),  $set1CF$  (—★—),  $set1a2CF$  (—■—))

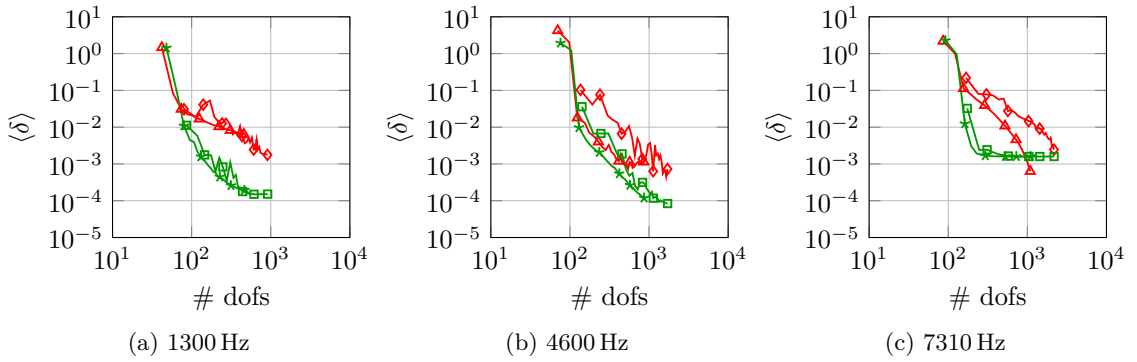


Figure 6.42: Convergence curves of the rotation about the  $y$ -axis (hard SS plate with  $h = 0.01$  m) for the modified WBM ( $set1$  (—▲—),  $set1a2$  (—◆—),  $set1CF$  (—★—),  $set1a2CF$  (—■—))

lower compared to the model with 230 degrees of freedom and therefore, the bigger model should be far more accurate since in the WBM only the boundary conditions have to be fulfilled as accurate as possible and no additional errors are introduced inside the problem domain. This proves that the accuracy of the FEM reference model is not high enough,

which leads to the constant error of the WBM models at the end of Figures 6.40c, 6.41c and 6.42c.

The results for the hard simply-supported plates with thickness  $h = 0.005\text{ m}$  and  $h = 0.025\text{ m}$  are shown in Appendix E in Figures E.75–E.80. The convergence properties of the WBM models including corner functions are independent of the plate thickness, while the stability of the models without corner functions are thickness and frequency dependent, due to the moment singularities in the corner points.

In Figure 6.43, the convergence rate of the WBM models is compared to the FEM for the hard simply-supported plate with the thickness  $h = 0.01\text{ m}$ . Since the convergence rate for all three field variables is rather similar, only the averaged relative error of the out-of-plane displacement is plotted. Although, the evaluation of the integrals involving the special purpose functions given in Table 6.8 is computationally demanding, the numerical efficiency of the WBM models including the corner functions is the highest. Even the WBM models without corner functions outperform the FEM for the given example. The computational time required by the FEM to reach an averaged relative error of 1% is approximately 6 (1300 Hz), 27 (4600 Hz) and 79 (7310 Hz) times higher compared to the WBM including corner functions. Therefore, corner stress singularities do not alter the computational efficiency of the WBM if special purpose functions are included in the model.

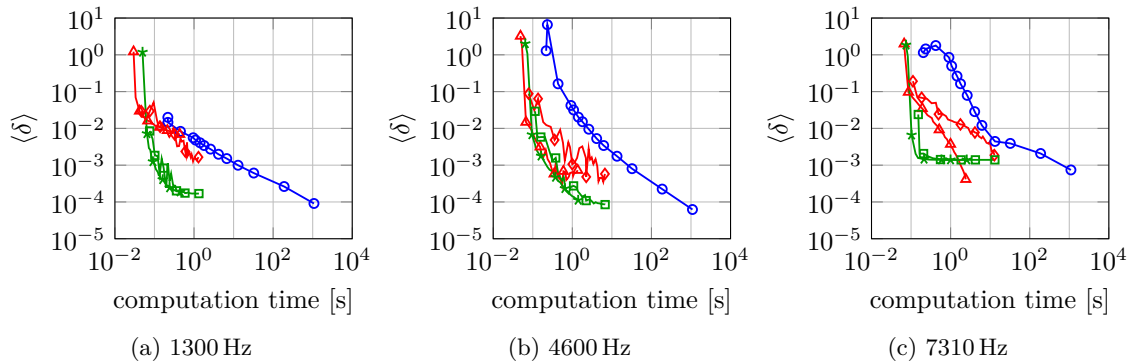


Figure 6.43: Convergence curves of the out-of-plane displacement (hard SS plate with  $h = 0.01$ ) for the FEM (—○—) and the modified WBM (*set1* (—▲—), *set1a2* (—◆—), *set1CF* (—★—), *set1a2CF* (—■—))

## 6.4.2 Multi domain problem

In this section, the computational properties of the WBM for non-convex plate domains are analyzed. In case of non-convex plate domains, a decomposition into convex sub-domains is necessary and interface conditions have to be fulfilled. The polygonal steel plate, shown in Figure 6.44, has the dimensions  $L_x = 1.4\text{ m}$  and  $L_y = 1.2\text{ m}$  and the material parameters  $E = 2.1 \times 10^{11}\text{ N/m}^2$ ,  $\rho = 7850\text{ kg/m}^3$ ,  $\nu = 0.3$  and  $\eta = 0$ . The plate is decomposed into two convex sub-domains  $\Omega^{(1)}$  and  $\Omega^{(2)}$  with the boundaries  $\Gamma_1^{(1)}$ ,  $\Gamma_2^{(1)}$ ,  $\Gamma_3^{(1)}$ ,  $\Gamma_1^{(2)}$ ,  $\Gamma_2^{(2)}$  and  $\Gamma_3^{(2)}$  and the common interface  $\Gamma^{(1,2)}$ , which is given by a straight

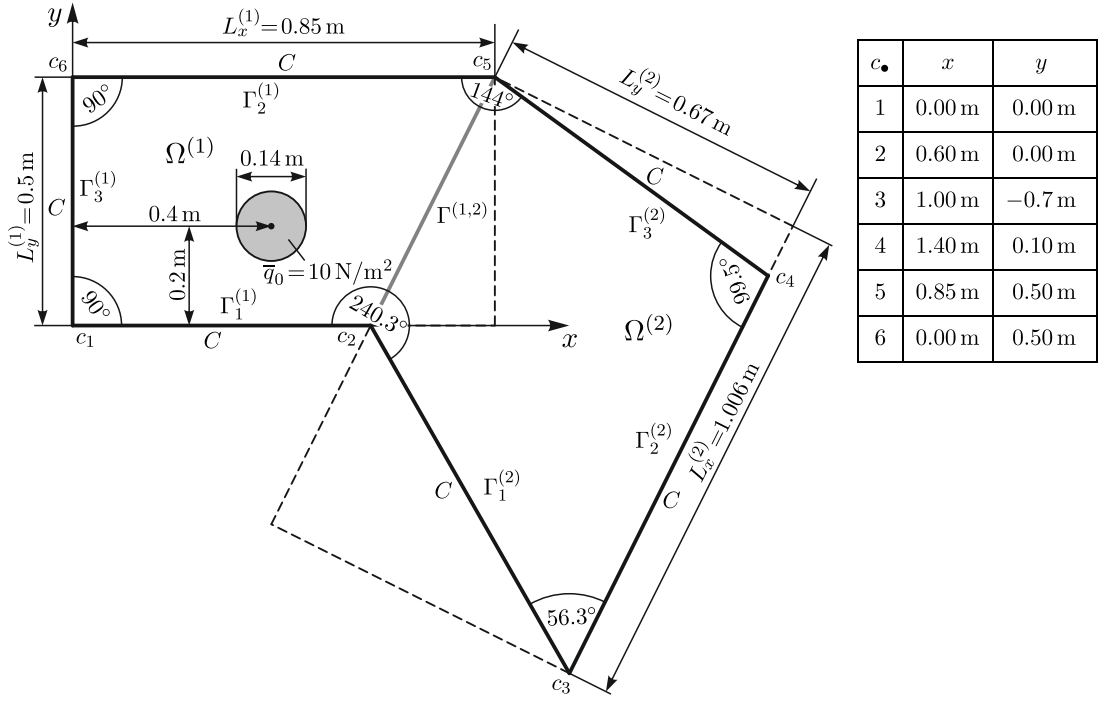


Figure 6.44: Geometry and loading of the multi domain clamped plate

line between the corner points  $c_2$  and  $c_5$ . Three different plate thicknesses are considered, see Table 6.9, and the shear correction factor  $k_W$  (Wittrick) is used in the Mindlin plate theory. The ratio of the smallest lateral dimension to the plate thickness, the frequency of the lowest, simple thickness-shear mode and the frequency limits for the Kirchhoff plate theory are listed in Table 6.9. All three plate configurations are generally considered as thin plates and therefore, the applicability of the Kirchhoff plate theory is only limited by the excitation frequency.

Table 6.9: Thicknesses of the multi domain clamped plates and Kirchhoff limits

example	$h$ [m]	$L_y/h$	$f_s$ [Hz]	$f_{Gk1\%}$ [Hz]	$f_{Gk2\%}$ [Hz]
$h_1$	0.005	240	320766	2791	5613
$h_2$	0.010	120	160383	1395	2807
$h_3$	0.025	48	64153	558	1123

All six boundaries of the plate are clamped (zero out-of-plane displacement and zero rotations about the  $x$ - and  $y$ -axis) and a constant circular load, which is located in the sub-domain  $\Omega^{(1)}$  and has an amplitude of  $\bar{q}_0 = 10 \text{ N/m}^2$  and a radius  $r_0 = 0.07 \text{ m}$ , harmonically excites the plate. The smallest rectangular bounding boxes of the two sub-domains used to define the travelling wave functions in the WBM have the dimensions  $L_x^{(1)} = 0.85 \text{ m}$ ,  $L_y^{(1)} = 0.5 \text{ m}$ ,  $L_x^{(2)} = 1.006 \text{ m}$  and  $L_y^{(2)} = 0.67 \text{ m}$  and are indicated by the dashed lines in Figure 6.44.

Table 6.10: Modal analysis of the multi domain clamped plates

$h$	> 10 modes		> 40 modes		> 70 modes		100 modes	
	$f$ [Hz]	$\lambda$ [m]	$f$ [Hz]	$\lambda$ [m]	$f$ [Hz]	$\lambda$ [m]	$f$ [Hz]	$\lambda$ [m]
$h_1$	350	0.3746	1043	0.2167	1650	0.1721	2255	0.1471
$h_2$	680	0.3794	2060	0.2169	3240	0.1722	4394	0.1473
$h_3$	1650	0.3804	4740	0.2186	7200	0.1738	9493	0.1486

To assess the relevant frequency ranges for the three plate configurations, a modal analysis of the plates with a FEM model having at least 147 quadric elements per wavelength (maximum element size 0.001 m) is performed to calculate the first 100 bending eigenfrequencies. Similar to the single domain problems, three different frequencies are examined, which are located after the the 10<sup>th</sup>-bending mode, the 40<sup>th</sup>-bending mode and the 70<sup>th</sup>-bending mode. In Table 6.10, these frequencies are listed and the corresponding bending wavelengths  $\lambda$  are shown. A comparison of the frequencies given in Table 6.10 and the Kirchhoff frequency limits stated in Table 6.9 shows that the Kirchhoff plate theory is only applicable over the complete frequency range for the thinnest plate with the thickness  $h_1$ .

Since no analytical solutions for the given plate bending problems exist, highly accurate FEM models are used to calculate the reference solutions for the error plots, convergence curves and frequency response functions. In Table 6.11, the details of two different FEM models are listed. The FEM model for the convergence and error plots uses at least 290 quadric elements per wavelength, which ensures highly accurate results, since according to the rule in Equation (3.15) only 9 quadric elements would be sufficient. The same model is used for all three thicknesses and examined frequencies. Due to the high computational load, the reference solutions for the frequency response functions are calculated with a smaller FEM model with only 28 quadric elements per wavelength (three times more than required according to Equation (3.15)).

Table 6.11: FEM reference models for the convergence analysis and the FRF

	max(el. size) [m]	# nodes	# elements	min(# el./ $\lambda$ )
conv.	0.0006	7621372	2538165	290
FRF	0.0050	110855	36676	28

If the boundaries of a plate are clamped, stress singularities in the vicinity of a corner arise for internal corner angles  $\alpha$  greater than 180°, see Figure 6.2a. Therefore, moment and shear force singularities can be expected in the corner  $c_2$  ( $\alpha = 240.3^\circ$ ). To ensure accurate reference solutions, the FEM meshes of the models listed in Table 6.11 are locally refined close to the corner point  $c_2$  to capture the stress singularities.

The convergence curves of the FEM are constructed by decreasing the mesh size of the FEM model from 0.2 m (at least  $\approx 1$  elements per wavelength) to 0.002 m (at least  $\approx 86$  elements per wavelength) in 11 steps.

To analyze the computational properties of the WBM and the influence of the different function sets, several different WBM models are applied to predict the plate responses. Due to the findings in the single domain problems, only the modified wave function selection is considered. The WBM models either include only the first wave function sets (*set1*) or both function sets (*set1a2*) and since corner singularities are exhibit in the problem domain, additional models with special purpose functions (*set1CF*, *set1a2CF*) are built. The truncation factor is varied from  $T = 0.5$  to  $T = 8$  in steps of 0.5 and the particular solution functions given in Equations (5.85) and (5.86) are used to represent the constant circular loading.

In lack of analytical solutions for the dynamic plate bending problem of an infinite wedge with clamped boundary conditions, the eigenvalues from the static problem are used to define the special purpose functions. The static eigenvalues, which exhibit moment or shear force singularities in the corner point  $c_2$ , are calculated through the characteristic equations given in Table 6.1. Moment singularities result from the symmetric eigenvalue  $\bar{\lambda}_M^s = 0.834$  and the antisymmetric eigenvalue  $\bar{\lambda}_M^a = 0.680$ , while shear force singularities arise from the symmetric eigenvalue  $\bar{\lambda}_Q^s = 0.749$ . Using the relations between the static and dynamic eigenvalues stated in Section 6.2.1 leads to the special purpose functions shown in Table 6.12. In total, 8 independent special purpose functions are included, since the corner functions for the shear force singularity are related in pairs through their weighting factors.

To predict the errors and averaged values of the field variables, a regular grid of approximately 10000 response points inside each WBM sub-domain is used. Only response points having an amplitude of the field variable greater than 5 % of the maximum value are considered in the relative error prediction to avoid misleading results due to high relative errors close to nodal lines (zero values of the field variables).

Table 6.12: Special purpose functions for the multi domain clamped plate examples

corner	$\alpha$	corner functions	eigenvalue
$c_2$	$240.3^\circ$	$\Upsilon_{M_{w1}1}^{(c_2)} = \cos(\lambda_{M1}^s \varphi_{c_2}) J_{\lambda_{M1}^s}(k_{f1} r_{c_2})$	$\lambda_{M1}^s = 1.834$
		$\Upsilon_{M_{w2}1}^{(c_2)} = \cos(\lambda_{M1}^s \varphi_{c_2}) J_{\lambda_{M1}^s}(k_{f2} r_{c_2})$	
		$\Upsilon_{M_H1}^{(c_2)} = -\sin(\lambda_{M1}^s \varphi_{c_2}) J_{\lambda_{M1}^s}(k_s r_{c_2})$	
		$\Upsilon_{M_{w1}2}^{(c_2)} = \sin(\lambda_{M2}^a \varphi_{c_2}) J_{\lambda_{M2}^a}(k_{f1} r_{c_2})$	$\lambda_{M2}^a = 1.680$
		$\Upsilon_{M_{w2}2}^{(c_2)} = \sin(\lambda_{M2}^a \varphi_{c_2}) J_{\lambda_{M2}^a}(k_{f2} r_{c_2})$	
		$\Upsilon_{M_H2}^{(c_2)} = \cos(\lambda_{M2}^a \varphi_{c_2}) J_{\lambda_{M2}^a}(k_s r_{c_2})$	
		$\Upsilon_{Q_{w1}1}^{(c_2)} = \cos(\lambda_{Q1}^s \varphi_{c_2}) J_{\lambda_{Q1}^s}(k_{f1} r_{c_2})$	$\lambda_{Q1}^s = 0.749$
		$\Upsilon_{Q_{w2}1}^{(c_2)} = -\cos(\lambda_{Q1}^s \varphi_{c_2}) J_{\lambda_{Q1}^s}(k_{f2} r_{c_2}) \frac{\mu_1-1}{\mu_2-1} \left(\frac{k_{f1}}{k_{f2}}\right)^{\lambda_{Q1}^s}$	
		$\Upsilon_{Q_{w2}1}^{(c_2)} = \cos(\lambda_{Q1}^s \varphi_{c_2}) J_{\lambda_{Q1}^s}(k_{f2} r_{c_2}) \frac{1}{\mu_2-1} \left(\frac{k_s}{k_{f2}}\right)^{\lambda_{Q1}^s}$	
		$\Upsilon_{Q_H1}^{(c_2)} = -\sin(\lambda_{Q1}^s \varphi_{c_2}) J_{\lambda_{Q1}^s}(k_s r_{c_2})$	

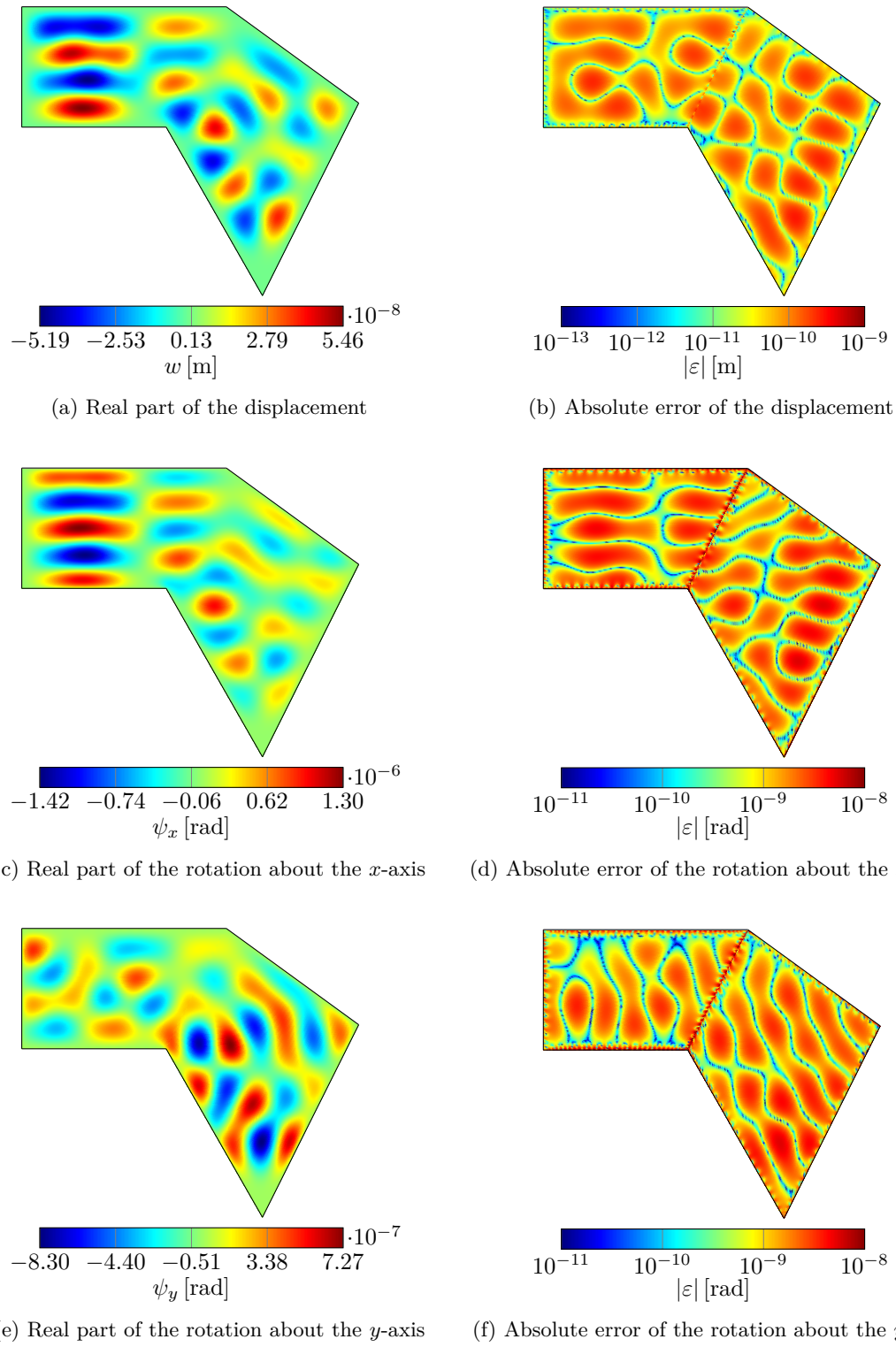


Figure 6.45: Out-of-plane displacement and rotations about the  $x$ - and  $y$ -axis of a multi domain clamped plate ( $h = 0.005 \text{ m}$ ) excited by a constant circular load at 1043 Hz calculated with the modified WBM using both function sets, corner functions and a truncation factor  $T = 4$

The contour plots of the field variables and the error plots compared to the reference solution for the plate with the thickness  $h = 0.005\text{ m}$  excited at  $1043\text{ Hz}$  are illustrated in Figure 6.45. A WBM model using both function sets and the special purpose functions stated in Table 6.12 is applied to calculate the results in Figure 6.45. The truncation factor is set to  $T = 4$ , which leads to a total number of 1270 wave functions, and the system of linear equations is solved with the LU-factorization. It is apparent from Figure 6.45 that the clamped boundary conditions as well as the interface conditions between the sub-domains are well fulfilled. Since in the WBM errors are only introduced through non-zero boundary and interface residuals, the absolute errors within the problem domain are approximately two orders of magnitude lower compared to the amplitudes of the field variables, which shows the high accuracy of the modified WBM also for non-convex plate domains.

The contour and error plots for all other plate thicknesses and frequencies are shown in Appendix E in Figures E.81–E.88. The characteristics of the results for the frequencies  $f_2$  and  $f_3$  are very similar to the results in Figure 6.45 and no dependency on the plate thickness is observed. For the frequency  $f_1$ , the absolute error in the sub-domain  $\Omega^{(2)}$  is an order of magnitude higher compared to sub-domain  $\Omega^{(1)}$  for the thicknesses  $h = 0.01\text{ m}$  and  $h = 0.025\text{ m}$  (but still low), which is not the case for the plate with thickness  $h = 0.005\text{ m}$ . This higher inaccuracy might result from the different sub-domain shapes, since a rectangular sub-domain (or close to rectangular) is beneficial for the accuracy and stability of the WBM. Additionally, the response of the sub-domain  $\Omega^{(1)}$  is mainly influenced by the constant circular load, while the sub-domain  $\Omega^{(2)}$  is only excited through the interface  $\Gamma^{(1,2)}$ . Therefore, small errors at the interface conditions might lead to high errors within the sub-domain  $\Omega^{(2)}$ . Further investigations are necessary to clarify the actual source of this increased error in the sub-domain  $\Omega^{(2)}$ .

The frequency response functions of the multi domain clamped plate with the thickness  $h = 0.025\text{ m}$  calculated with the FEM and the WBM are shown in Figure 6.46. The frequency starts at  $50\text{ Hz}$  and is increased to  $9050\text{ Hz}$  in 2000 steps and therefore, approximately the first 100 bending modes are included in the response. A WBM model using both function sets and the special purpose functions stated in Table 6.12 is applied to predict the averaged amplitudes of the field variables. The truncation factor is set to  $T = 4$ , which leads to 174 wave functions for the lowest and 1782 wave functions for the highest frequency and the SVD is used to solve the system of linear equations. The results of the WBM are in excellent agreement with the reference solution over the whole frequency range, even close to the eigenfrequencies. This clearly shows the applicability of modified WBM in the low- and mid-frequency range for non-convex plates having moment and shear force singularities.

In Appendix E, the frequency response functions for the multi domain clamped plate with the thicknesses  $h = 0.005\text{ m}$  and  $h = 0.01\text{ m}$  are shown in Figures E.89 and E.90. The frequency is increased in 2000 steps to include approximately the first 100 bending modes in the viewed frequency range. Also for these two thicknesses, the results predicted by the WBM models are in excellent agreement with the reference solutions over the complete frequency range and close to the eigenfrequencies. The overall accuracy of the modified WBM is therefore hardly influenced by the plate thickness or excitation frequency, even though local differences of the accuracy are observed.

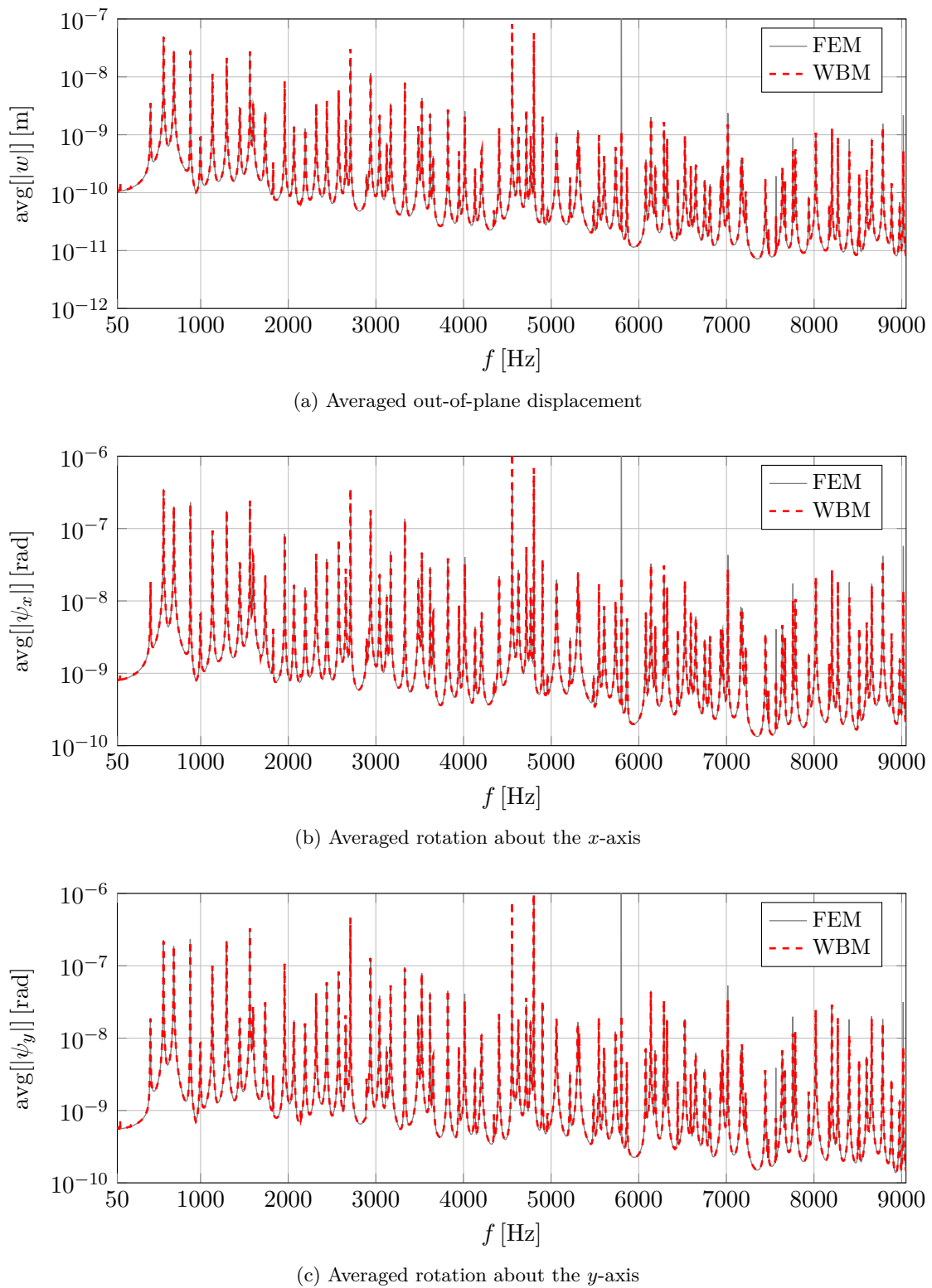


Figure 6.46: Frequency response functions of a multi domain clamped plate ( $h = 0.025$  m) excited by a constant circular load calculated with the FEM (reference mesh) and the modified WBM (function set 1 and set 2, corner functions,  $T = 4$ )

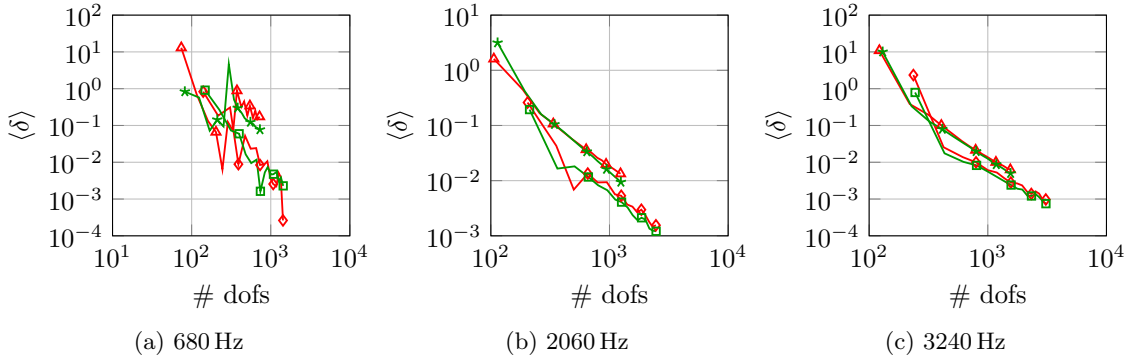


Figure 6.47: Convergence curves of the out-of-plane displacement (multi domain clamped plate with  $h = 0.01$  m) for the modified WBM (*set1* (—▲—), *set1a2* (—◆—), *set1CF* (—★—), *set1a2CF* (—■—))

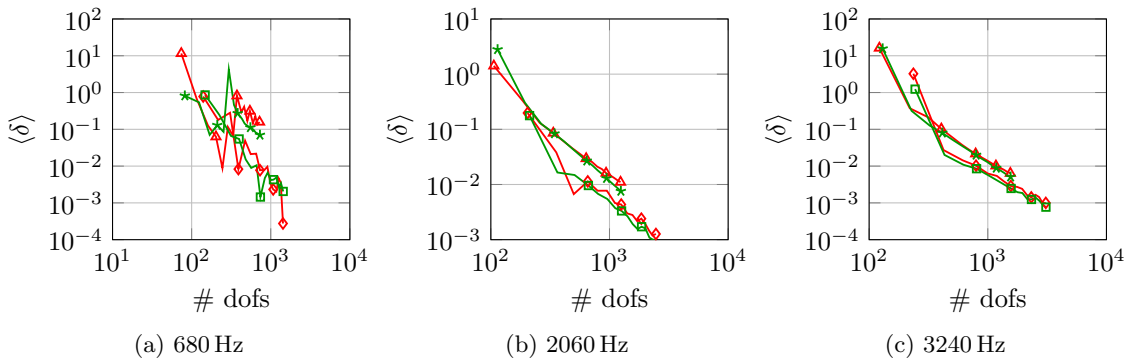


Figure 6.48: Convergence curves of the rotation about the  $x$ -axis (multi domain clamped plate with  $h = 0.01$  m) for the modified WBM (*set1* (—▲—), *set1a2* (—◆—), *set1CF* (—★—), *set1a2CF* (—■—))

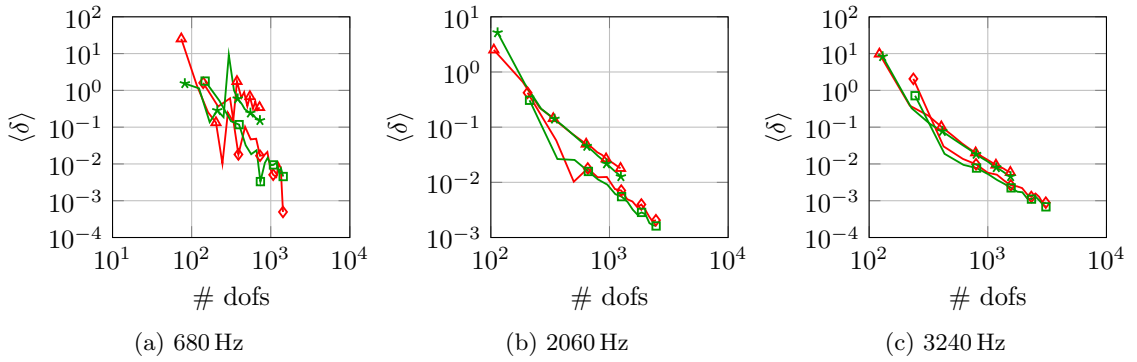


Figure 6.49: Convergence curves of the rotation about the  $y$ -axis (multi domain clamped plate with  $h = 0.01$  m) for the modified WBM (*set1* (—▲—), *set1a2* (—◆—), *set1CF* (—★—), *set1a2CF* (—■—))

A comparison of the convergence rates of different WBM models for the multi domain clamped plate with the thickness  $h = 0.01$  m is illustrated in Figures 6.47–6.49. The WBM models either use only the first function sets (*set1*), both function sets (*set1a2*) or additionally include the special purpose functions (*set1CF*, *set1a2CF*) listed in Table

6.12. The systems of linear equations are solved with the SVD to increase the stability of the computations, although the computational load is higher compared to the LU-factorization. It needs to be noted that both direct solution techniques finally have a comparable accuracy, but the convergence curves of the WBM results calculated with the LU-factorization are less smooth.

Although the WBM is able to reach an averaged relative error of less than 1% for all frequencies, the convergence curves are not perfectly uniform especially for the lowest frequency. Furthermore, it is apparent that including the special purpose functions only slightly increases the convergence of the WBM for the given examples and that using both function sets is more efficient compared to applying only the first function sets. The amplitudes of the shear force corner functions  $(\Upsilon_{Q_{w21}}^{(c_2)}, \bar{\Upsilon}_{Q_{w21}}^{(c_2)}, \Upsilon_{Q_{H1}}^{(c_2)})$  increase very fast with the distance to the corner point  $c_2$ , since the wavenumbers  $k_{f2}$  and  $k_s$  are imaginary numbers. Therefore, the functions are very localized at the points with the highest distances, while the function values are close to zero everywhere else in the plate domain. This property has a negative effect on the conditioning of the system matrix and additionally the numerical integration of these functions is strongly influenced by round of errors, which might explain the minor influence of the special purpose functions on the convergence rate for this example. Compared to the simply-supported plate example, the special purpose functions do not fulfill the clamped boundary conditions along the adjacent edges of the corner point  $c_2$ , which might also reduce their beneficial effect on the convergence rate.

The WBM model including both function sets and the special purpose functions requires approximately 715 (680 Hz), 890 (2060 Hz) and 750 (3240 Hz) wave functions to reach an averaged relative error of less than 1%. In contrary to the previous examples, the required number of wave functions is not steadily increasing with the excitation frequency, but remains nearly at the same level. This also indicates that the corner stress singularities still have a major influence on the convergence rate even though special purpose functions, which represent the singular behaviour, are included in the model.

The convergence curves for the multi domain clamped plates with the thicknesses  $h = 0.005$  m and  $h = 0.025$  m are plotted in Appendix E in Figures E.91–E.96. The findings for these thicknesses are nearly equivalent to the plate with the thickness  $h = 0.01$  m, with the exception that the WBM converges more uniformly for the thinnest plate excited at frequency  $f_1$ . This different behaviour has already been observed in the contour and error plots.

In Figures 6.50–6.52, the computational efficiency of the WBM is compared to the FEM. Only the convergence curves for the out-of-plane displacement are plotted, since the convergence properties for the rotations about the  $x$ - and  $y$ -axis are very similar. It is apparent that the WBM generally outperforms or is at least as efficient as the FEM for all frequencies and thicknesses. The computational time of the FEM to reach an averaged relative error of 1% is approximately 1 to 5 time(s) (frequency  $f_1$ ), 8 to 15 times (frequency  $f_2$ ) and 10 to 13 times (frequency  $f_3$ ) higher compared to the WBM model including both function sets and special purpose functions. The decrease of the computational time is not as pronounced as for the previous examples, which results from the required decomposition of the problem domain into two sub-domains and the difficulties of representing the corner stress singularities even though special purpose functions are available.

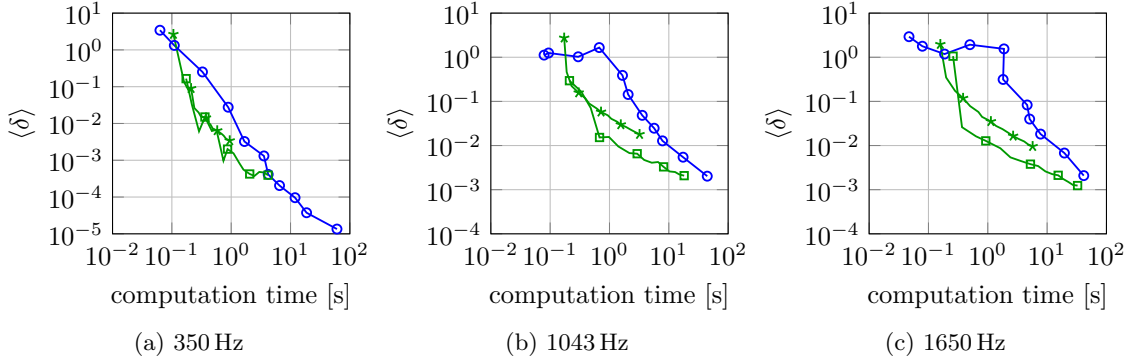


Figure 6.50: Convergence curves of the out-of-plane displacement (multi domain clamped plate with  $h = 0.005$ ) for the FEM (—○—) and the modified WBM (set1CF (—\*—), set1a2CF (—□—))

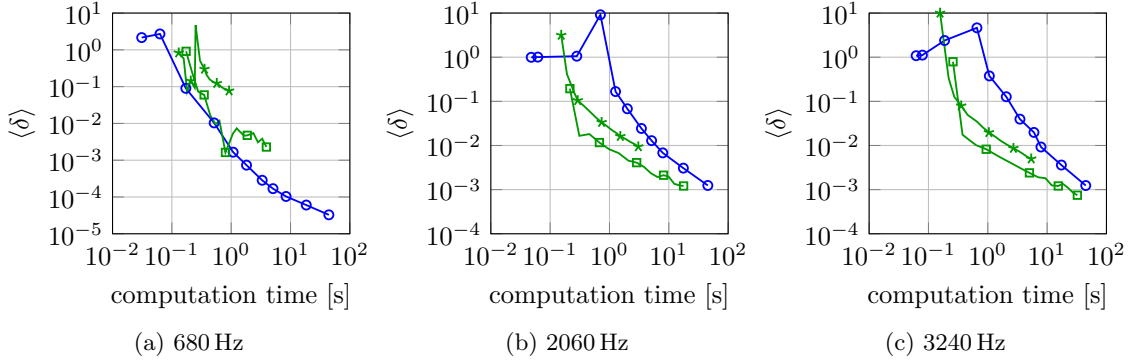


Figure 6.51: Convergence curves of the out-of-plane displacement (multi domain clamped plate with  $h = 0.01$ ) for the FEM (—○—) and the modified WBM (set1CF (—\*—), set1a2CF (—□—))

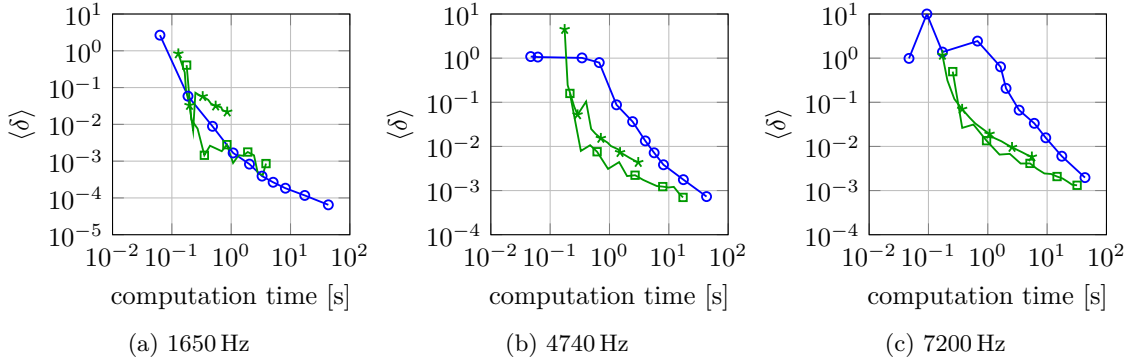


Figure 6.52: Convergence curves of the out-of-plane displacement (multi domain clamped plate with  $h = 0.025$ ) for the FEM (—○—) and the modified WBM (set1CF (—\*—), set1a2CF (—□—))

## **Part III**

### **Conclusion and final remarks**



# 7 Conclusion

This dissertation focuses on the prediction of steady-state harmonic vibrations of plates, especially on the extension and improvement of an efficient numerical method called Wave Based Method (WBM). During the past 15 years, great advances have been made in the development of the WBM, which is a deterministic method based on the Trefftz-principle. The method has been extended to a wide range of problems and the performance, stability and applicability of the WBM have been continuously improved. While the WBM is very well developed for the vibrations of thin plates governed by the Kirchhoff plate theory, the prediction of the vibrations of thick plates is not yet feasible. Furthermore, the definition of a thin and thick plate and therefore the validity ranges of the commonly used plate theories, is not consistent in the literature, which leads to difficulties in the choice of the most appropriate plate theory for a specific problem. To resolve these issues, the following two objectives are formulated:

- The first objective is the definition of the validity ranges of the most common plate theories, the Kirchhoff and Mindlin plate theory, for plate vibration problems depending on the required accuracy.
- The second objective is the extension of the WBM to structural vibrations of thick plates governed by the Mindlin plate theory.

Additional objectives of the dissertation concern the improvement of the WBM and are related to the implementation of the WBM:

- The third objective is the development of particular solution functions, which are analytical solutions of the partial differential equations arising in the plate theories under certain external loadings. These functions are mandatory for the application of the WBM.
- The fourth objective refers to the improvement of the numerical properties of the WBM system matrix and the increase of the stability and accuracy of the method.

The main achievements of this dissertation and the applied approaches to fulfill the stated objectives are summarized in the following sections.

## 7.1 Validity ranges of the Kirchhoff and Mindlin plate

An extensive literature survey on the validity ranges of the Kirchhoff and Mindlin plate theory shows that two different limits, a geometrical limit and a frequency limit, have to be considered in the application of the plate theories. The geometrical limit is generally defined through a ratio of the plate thickness to the smallest lateral dimension of the plate domain and leads to the categorization into thin and thick plates. The frequency limit

## 7 Conclusion

is given by the ratio of the bending wavelength to the plate thickness. Both limits are not consistently defined in the literature and generally the basis for the definitions is not clearly stated.

A common approach to define the frequency limits of the plate theories is the investigation of free vibrations in an infinite plate domain, since analytical solutions of the three-dimensional elasticity model are available. A review of the solutions is carried out and the results for the first bending dominant flexural vibrations of the Kirchhoff and Mindlin plate theory are compared to the solutions given by the three-dimensional elasticity theory. The frequency limits of the two plate models leading to an error of 1%, 2%, 5% and 10% are defined and two different shear correction factors for the Mindlin plate theory are examined, which enables the choice of the most appropriate plate theory depending on the required accuracy. While the limits stated in the literature allow for an error between approximately 1% and more than 10% for the Kirchhoff plate theory, the limits for the Mindlin plate theory lead to an error of approximately 0%–2%.

In real-life applications, plates have finite dimensions and certain boundary conditions are applied at their edges. To investigate the influence of the boundaries, the free vibration characteristics of simple plate geometries are analyzed, since analytical solutions for these geometries are generally available in the literature for the Kirchhoff and Mindlin plate theory. In lack of analytical solutions for the three-dimensional elasticity theory, FEM models are used to calculate the reference solutions. A comparison of the results shows that the influence of the boundaries on the accuracy of the plate theories strongly depends on the applied boundary condition and the mode number. The ratio of the smallest lateral dimension to the plate thickness (geometrical limit) has to be greater than 30 (1% error) or 20 (5% error) for the Kirchhoff plate theory. This limit also draws the line between a thin and a (moderately) thick plate, at least in the context of vibration problems. The Mindlin plate theory predicts highly accurate results for plates with a ratio of the smallest lateral dimension to the plate thickness greater than ten. However, even thicker plates are not examined in this work and therefore, the Mindlin plate theory might be applicable also for plates with higher thicknesses.

The stated limits enable a proper choice of the structural model (Kirchhoff, Mindlin, three-dimensional elasticity) for plate vibration problems depending on the required accuracy. However, special effects, like stress singularities in corners, have to be taken into account prior to the selection of the model, since additional errors can be introduced through these effects.

## 7.2 Development of the WBM for thick plate vibrations

The extension of the WBM to thick plate vibrations is the main objective of this dissertation. The general framework of the WBM is applied to the governing equations of the Mindlin plate theory. The first step is the decomposition of the coupled system of partial differential equations resulting from the Mindlin plate theory into three uncoupled Helmholtz equations, which is achieved through three potential functions.

Since the WBM is an indirect Trefftz method, a T-complete set of basis functions is required, which is formulated in a Cartesian coordinate system. In the WBM, the basis functions are traveling and evanescent waves, depending on the chosen wavenumbers, which are defined in the smallest rectangular bounding box circumscribing the plate domain. The T-completeness of the chosen basis function sets is proven through a rectangular plate domain with arbitrary boundary conditions. Two different basis function sets are defined, which are both T-complete for convex domains.

In the Mindlin plate theory, stress singularities can arise in the vicinity of a corner if certain internal angles are exceeded. These stress singularities can have a major influence on the convergence rate of the WBM. Therefore, the literature on corner stress singularities arising in Mindlin plates is reviewed and a static and dynamic analysis of an infinite wedge plate domain is carried out to get the critical angles and the order of the singularity for various types of boundary conditions. This allows for the identification of corner stress singularities in a specific plate domain and so-called special purpose functions are defined, which accurately represent the singular behaviour near the corner point.

The system of linear equations in the WBM results from a fitting of the boundary and interface conditions, since the governing equations in the problem domain are exactly fulfilled. A weighted residual formulation is used in the WBM to fit the boundary and interface conditions in an integral sense. To get a proper weighted residual formulation for the Mindlin plate problem, the sub-region three-field generalized mixed variational principle for thick plates is extended from the static to the dynamic case.

To verify the capability of the WBM to tackle thick plate vibration problems, several validation examples are considered. In lack of analytical solutions, highly accurate FEM models are used to calculate the reference solutions. Even though, the WBM should theoretically converge to the exact solution, it is shown that the accuracy of the original WBM is limited through the bad conditioning of the system matrix and numerical inaccuracies. A great improvement of the accuracy and stability is achieved by a modified wave function selection, which is summarized in Section 7.4.

### 7.3 New particular solution functions for plate vibrations

In general, the application of the Trefftz principle requires a transformation of inhomogeneous partial differential equations to homogeneous ones, since the applied basis functions only satisfy the homogenous partial differential equations. If particular solution functions, which satisfy the inhomogeneous partial differential equations, while neglecting the boundary conditions, are available, the transformation can be performed in a straightforward and efficient way.

In the WBM such particular solution functions are required, but for plate bending vibrations only solutions for point load excitations are available in the literature. To extend the applicability of the WBM, new particular solution functions are developed and the solutions for the point load are reexamined.

The Hankel transform and the residue theorem are applied to solve the problem of an infinite plate (Mindlin plate theory) excited by a point load. The amplitude of the final

result is identical with the solution stated in the literature, but complex conjugated. To prove the correctness of the presented results, the solutions for the Kirchhoff plate theory are obtained as a special case of the Mindlin plate theory and compared to the solutions in the literature.

Two different approaches, the analytical integration of the point force solution and the Hankel transform, are used to derive closed-form particular solution functions for axisymmetric load cases. The harmonic response of an infinite plate domain to a constant ring load and to a constant circular load are presented. Additionally, the results for an alternating circular load, which are derived through an analytical integration of the point force solution, are shown.

Due to the development of these new particular solution functions, an efficient application of the WBM for the stated load cases is enabled. All presented loadings are considered in the validation examples and excellent results are obtained, which proves the correct derivation of the particular solution functions.

### 7.4 Improvement of the WBM - A new wave function selection

The convergence rate of the WBM and the conditioning of the WBM system matrix are optimal for a rectangular problem domain. As soon as minimal changes are made to the plate geometry, the conditioning of the linear system gets worse and the convergence rate is reduced. Therefore, an alternative wave function selection is proposed to mitigate this effect. While in the original WBM, all basis functions are defined in the smallest rectangular bounding box circumscribing the plate domain, the new selection distinguishes between traveling and evanescent waves.

The traveling waves are still defined in a domain coordinate system, which is given by the smallest rectangular bounding box, while a boundary coordinate system is applied to specify the evanescent wave functions. The goal of this approach is the alignment of the evanescent waves with the boundary lines, which is the situation for the original wave function selection and a rectangular domain. The new wave function selection becomes identical to the original one for a rectangular domain.

The validation examples clearly show the advanced properties of the modified wave function selection compared to the original one. The conditioning of the WBM system matrix is significantly improved and the WBM models using the modified wave function selection reach highly accuracy results. A reduction of the convergence rate through moment singularities is avoided by introducing special purpose functions, which represent the singular behaviour in the vicinity of corner points. This positive effect of the special purpose functions is less pronounced for shear force singularities, since the developed functions are very localized, which introduces numerical problems.

A comparison of the computational time between the modified WBM and the classical FEM shows the high computation efficiency of the WBM. The WBM outperforms the FEM for all validation examples. Therefore, the WBM is able to predict the vibrations of thick plates in the mid-frequency range with high accuracy and reasonable computational load.

## 8 Future research topics

Although, the WBM is already well developed for certain problems, there is still room for further improvements and extensions, which did not fit into the scope of this dissertation. The following future research topics are proposed to further develop the WBM:

- The new wave function selection is also applicable for other physical problems tackled by the WBM. The effects on the convergence rate and stability of the WBM for these problems should be investigated.
- A formal mathematical prove of the T-completeness of the proposed wave function selection is essential to ensure at least the theoretical convergence of the WBM for any type of problem. Since this is a major task, it did not fit into the time frame of this work.
- The alignment of the evanescent wave functions with the boundary is only possible for straight edges. In case of curved boundaries, different approaches have to be developed to allow for a general application of the modified WBM. A possible solution might be a close-fitting polygonal frame.
- Additional closed-form particular solution functions would improve the applicability of the WBM. Especially a constant rectangular load is of major interest, since a piecewise constant interpolation of arbitrary loads would be possible.
- The definition of alternative special purpose functions for shear force singularities, which are not exponentially growing and therefore introduce numerical problems, might increase the convergence rate of the WBM for thick plate vibrations.
- General improvements of the WBM, like the hybrid FE-WBM and the multi level WBM, have to be extended to thick plate vibration problems, to remove the geometrical limitations of the WBM.



## **Part IV**

# **Addenda**



# A The sub-region three-field generalized mixed variational principle for elastodynamics

The sub-region three-field generalized mixed variational principle is proposed in [26] to derive all basic equations of elastostatic problems through a functional stationary condition. To extend the proposed method to the elastodynamic problem, either the d'Alembert's principle can be applied by including inertial forces as externally applied forces [302] or by introducing a kinetic energy density in terms of velocity components and integrating over time between fixed limits at which the displacement variations disappear [303].

The functional used in [26] for the static problem is given by

$$\Pi = \Pi_p^{(\alpha)} - \Pi_c^{(\beta)} + H_{pc}^{(\alpha, \beta)}, \quad (\text{A.1})$$

with

$$\begin{aligned} \Pi_p^{(\alpha)} = & \iiint_{\Omega^{(\alpha)}} \left( \bar{U}(\varepsilon_{ij}^{(\alpha)}) - \sigma_{ij}^{(\alpha)} \left( \varepsilon_{ij}^{(\alpha)} - \frac{1}{2} (u_{i,j}^{(\alpha)} + u_{j,i}^{(\alpha)}) \right) - f_i^{(\alpha)} u_i^{(\alpha)} \right) dV \\ & - \iint_{\Gamma_{\sigma}^{(\alpha)}} \bar{\sigma}_i^{(\alpha)} u_i^{(\alpha)} dS - \iint_{\Gamma_u^{(\alpha)}} \sigma_i^{(\alpha)} (u_i^{(\alpha)} - \bar{u}_i^{(\alpha)}) dS \end{aligned} \quad (\text{A.2})$$

the three-field generalized potential energy of the sub-region  $\Omega^{(\alpha)}$ ,

$$\begin{aligned} \Pi_c^{(\beta)} = & \iiint_{\Omega^{(\beta)}} \left( \sigma_{ij}^{(\beta)} \varepsilon_{ij}^{(\beta)} - \bar{U}(\varepsilon_{ij}^{(\beta)}) + (\sigma_{ij,j}^{(\beta)} + f_i^{(\beta)}) u_i^{(\beta)} \right) dV \\ & - \iint_{\Gamma_{\sigma}^{(\beta)}} (\sigma_i^{(\beta)} - \bar{\sigma}_i^{(\beta)}) u_i^{(\beta)} dS - \iint_{\Gamma_u^{(\beta)}} \sigma_i^{(\beta)} \bar{u}_i^{(\beta)} dS \end{aligned} \quad (\text{A.3})$$

the three-field generalized complementary energy of the sub-region  $\Omega^{(\beta)}$  and

$$H_{pc}^{(\alpha, \beta)} = \iint_{\Gamma^{(\alpha, \beta)}} \sigma_i^{(\beta)} u_i^{(\alpha)} dS \quad (\text{A.4})$$

the mixed energy at the interface  $\Gamma^{(\alpha, \beta)}$ . The traction  $\sigma_i^{(l)} = \sigma_{ij}^{(l)} n_j^{(l)}$  with  $n_j^{(l)}$  the components of the normal unit vector, the prescribed traction  $\bar{\sigma}_i^{(l)}$  and the prescribed displacement  $\bar{u}_i$  are given in Cartesian coordinates.

The variation of Equations (A.2)–(A.4) with respect to  $u_i^{(l)}$ ,  $\sigma_{ij}^{(l)}$  and  $\varepsilon_{ij}^{(l)}$  leads to [26]

$$\begin{aligned} \delta\Pi_p^{(\alpha)} = & \iiint_{\Omega^{(\alpha)}} \left( \left( \frac{\partial \bar{U}(\varepsilon_{ij}^{(\alpha)})}{\partial \varepsilon_{ij}^{(\alpha)}} - \sigma_{ij}^{(\alpha)} \right) \delta\varepsilon_{ij}^{(\alpha)} - \left( \varepsilon_{ij}^{(\alpha)} - \frac{1}{2} (u_{i,j}^{(\alpha)} + u_{j,i}^{(\alpha)}) \right) \delta\sigma_{ij}^{(\alpha)} \right. \\ & \left. - (\sigma_{ij,j}^{(\alpha)} + f_i^{(\alpha)}) \delta u_i^{(\alpha)} \right) dV + \iint_{\Gamma_{\sigma}^{(\alpha)}} (\sigma_i^{(\alpha)} - \bar{\sigma}_i^{(\alpha)}) \delta u_i^{(\alpha)} dS \\ & - \iint_{\Gamma_u^{(\alpha)}} (u_i^{(\alpha)} - \bar{u}_i^{(\alpha)}) \delta\sigma_i^{(\alpha)} dS + \iint_{\Gamma^{(\alpha, \beta)}} \sigma_i^{(\alpha)} \delta u_i^{(\alpha)} dS \end{aligned} \quad (\text{A.5})$$

using the partial integration

$$\iiint_{\Omega^{(\alpha)}} \sigma_{ij}^{(\alpha)} \delta u_{i,j}^{(\alpha)} dV = \iint_{\Gamma^{(\alpha)}} \sigma_i^{(\alpha)} \delta u_i^{(\alpha)} dS - \iiint_{\Omega^{(\alpha)}} \sigma_{ij,j}^{(\alpha)} \delta u_i^{(\alpha)} dV \quad (\text{A.6})$$

with  $\Gamma^{(\alpha)} = \Gamma_{\sigma}^{(\alpha)} \cup \Gamma_u^{(\alpha)} \cup \Gamma^{(\alpha, \beta)}$ ,

$$\begin{aligned} \delta\Pi_c^{(\beta)} = & \iiint_{\Omega^{(\beta)}} \left( \left( \sigma_{ij}^{(\beta)} - \frac{\partial \bar{U}(\varepsilon_{ij}^{(\beta)})}{\partial \varepsilon_{ij}^{(\beta)}} \right) \delta\varepsilon_{ij}^{(\beta)} + \left( \varepsilon_{ij}^{(\beta)} - \frac{1}{2} (u_{i,j}^{(\beta)} + u_{j,i}^{(\beta)}) \right) \delta\sigma_{ij}^{(\beta)} \right. \\ & \left. + (\sigma_{ij,j}^{(\beta)} + f_i^{(\beta)}) \delta u_i^{(\beta)} \right) dV - \iint_{\Gamma_{\sigma}^{(\beta)}} (\sigma_i^{(\beta)} - \bar{\sigma}_i^{(\beta)}) \delta u_i^{(\beta)} dS \\ & + \iint_{\Gamma_u^{(\beta)}} (u_i^{(\beta)} - \bar{u}_i^{(\beta)}) \delta\sigma_i^{(\beta)} dS + \iint_{\Gamma^{(\alpha, \beta)}} \sigma_i^{(\beta)} \delta u_i^{(\beta)} dS \end{aligned} \quad (\text{A.7})$$

using the partial integration

$$\iiint_{\Omega^{(\beta)}} u_i^{(\beta)} \delta\sigma_{ij,j}^{(\beta)} dV = \iint_{\Gamma^{(\beta)}} u_i^{(\beta)} \delta\sigma_i^{(\beta)} dS - \iiint_{\Omega^{(\beta)}} \frac{1}{2} (u_{i,j}^{(\beta)} + u_{j,i}^{(\beta)}) \delta\sigma_{ij}^{(\beta)} dV \quad (\text{A.8})$$

with  $\Gamma^{(\beta)} = \Gamma_{\sigma}^{(\beta)} \cup \Gamma_u^{(\beta)} \cup \Gamma^{(\alpha, \beta)}$  and

$$\delta H_{pc}^{(\alpha, \beta)} = \iint_{\Gamma^{(\alpha, \beta)}} (\sigma_i^{(\beta)} \delta u_i^{(\alpha)} + u_i^{(\alpha)} \delta\sigma_i^{(\beta)}) dS. \quad (\text{A.9})$$

The extension to elastodynamics is ether accomplished by including inertial forces as external body forces by modifying the external body forces  $f_i^{(l)} \mapsto f_i^{(l)} - \rho \ddot{u}_i^{(l)}$  [302] or by introducing a kinetic energy density function  $T = \frac{1}{2} \rho \dot{u}_i^{(l)} \dot{u}_i^{(l)}$  and defining the functional

$$L = \int_{t_0}^{t_1} \left( \iiint_{\Omega} T dV - \Pi \right) dt \quad (\text{A.10})$$

through integration over time between fixed limits ( $t_0, t_1$ ) at which  $\delta u_i^{(l)} = 0$  and setting the first variation  $\delta L = 0$  [303]. The variation of the kinetic energy function is integrated by parts

$$\delta \int_{t_0}^{t_1} \iiint_{\Omega^{(l)}} T \, dV \, dt = \int_{t_0}^{t_1} \iiint_{\Omega^{(l)}} \rho \dot{u}_i^{(l)} \delta \dot{u}_i^{(l)} \, dV \, dt = - \int_{t_0}^{t_1} \iiint_{\Omega^{(l)}} \rho \ddot{u}_i^{(l)} \delta u_i^{(l)} \, dV \, dt \quad (\text{A.11})$$

using

$$\iiint_{\Omega^{(l)}} \rho \dot{u}_i^{(l)} \delta u_i^{(l)} \, dV \Big|_{t_0}^{t_1} = 0. \quad (\text{A.12})$$

Combining the Equations (A.5), (A.7), (A.9) and (A.11) leads to the final result

$$\begin{aligned} \delta L = 0 = & \int_{t_0}^{t_1} \left( \sum_l \iiint_{\Omega^{(l)}} \left( \left( \frac{\partial \bar{U}(\varepsilon_{ij}^{(l)})}{\partial \varepsilon_{ij}^{(l)}} - \sigma_{ij}^{(l)} \right) \delta \varepsilon_{ij}^{(l)} - \left( \varepsilon_{ij}^{(l)} - \frac{1}{2} (u_{i,j}^{(l)} + u_{j,i}^{(l)}) \right) \delta \sigma_{ij}^{(l)} \right. \right. \\ & - \left. \left. \left( \sigma_{ij,j}^{(l)} + f_i^{(l)} - \rho \ddot{u}_i^{(l)} \right) \delta u_i^{(l)} \right) \, dV + \iint_{\Gamma_{\sigma}^{(l)}} (\sigma_i^{(l)} - \bar{\sigma}_i^{(l)}) \delta u_i^{(l)} \, dS - \iint_{\Gamma_u^{(l)}} (u_i^{(l)} - \bar{u}_i^{(l)}) \delta \sigma_i^{(l)} \, dS \right. \\ & \left. + \iint_{\Gamma^{(\alpha, \beta)}} \left( (\sigma_i^{(\alpha)} + \sigma_i^{(\beta)}) \delta u_i^{(\alpha)} + (u_i^{(\alpha)} - u_i^{(\beta)}) \delta \sigma_i^{(\beta)} \right) \, dS \right) \, dt, \end{aligned} \quad (\text{A.13})$$

which is equivalent to the result obtained with  $\delta \Pi = 0$  in [26] and introducing the modified external body forces using d'Alembert's principle. The transformation of the surface integrals in Equation (A.13) to the boundary coordinate systems shown in Figure 2.2

$$\iint_{\Gamma_{\sigma}^{(l)}} (\sigma_i^{(l)} - \bar{\sigma}_i^{(l)}) \delta u_i^{(l)} \, dS = \iint_{\Gamma_{\sigma}^{(l)}} (\sigma_r^{(l)} - \bar{\sigma}_r^{(l)}) \delta u_r^{(l)} \, dS, \quad (\text{A.14})$$

$$\iint_{\Gamma_u^{(l)}} (u_i^{(l)} - \bar{u}_i^{(l)}) \delta \sigma_i^{(l)} \, dS = \iint_{\Gamma_u^{(l)}} (u_r^{(l)} - \bar{u}_r^{(l)}) \delta \sigma_r^{(l)} \, dS, \quad (\text{A.15})$$

$$\iint_{\Gamma^{(\alpha, \beta)}} (\sigma_i^{(\alpha)} + \sigma_i^{(\beta)}) \delta u_i^{(\alpha)} \, dS = \iint_{\Gamma^{(\alpha, \beta)}} (\sigma_r^{(\alpha)} - \sigma_r^{(\beta)}) \delta u_r^{(\alpha)} \, dS, \quad (\text{A.16})$$

$$\iint_{\Gamma^{(\alpha, \beta)}} (u_i^{(\alpha)} - u_i^{(\beta)}) \delta \sigma_i^{(\beta)} \, dS = - \iint_{\Gamma^{(\alpha, \beta)}} (u_r^{(\alpha)} + u_r^{(\beta)}) \delta \sigma_r^{(\beta)} \, dS, \quad (\text{A.17})$$

with  $r = \{n, s, t\}$ , leads to the boundary and interface conditions given in Equation (2.15), (2.16) and (2.19). The mixed boundary conditions can be derived from the Dirichlet and Neumann boundary conditions.



## B The sub-region three-field generalized mixed variational principle for thick plates

The sub-region three-field generalized mixed variational principle is derived in [26] and [30] for the static deformation of elastic thick plates and is extended to the dynamic problem in this chapter. Similar to the previous chapter, either the d'Alembert's principle can be used by applying inertial forces (moments) as externally applied forces (moments) [302] or by introducing a kinetic energy density [303], which includes translational and rotational kinetic energy. The stationary condition  $\delta\Pi = 0$  of the functional [26, 30]

$$\Pi = \Pi_p^{(\alpha)} - \Pi_c^{(\beta)} + H_{pc}^{(\alpha, \beta)}, \quad (\text{B.1})$$

with the three-field generalized potential energy of the plate sub-region  $\Omega^{(\alpha)}$

$$\begin{aligned} \Pi_p^{(\alpha)} = & \iint_{\Omega^{(\alpha)}} \left( \bar{U}_b(\kappa_x^{(\alpha)}, \kappa_y^{(\alpha)}, \kappa_{xy}^{(\alpha)}) + \bar{U}_s(\gamma_{xz}^{(\alpha)}, \gamma_{yz}^{(\alpha)}) - M_x^{(\alpha)} \left( \kappa_x^{(\alpha)} - \frac{\partial \psi_x^{(\alpha)}}{\partial x} \right) \right. \\ & - M_y^{(\alpha)} \left( \kappa_y^{(\alpha)} - \frac{\partial \psi_y^{(\alpha)}}{\partial y} \right) - M_{xy}^{(\alpha)} \left( 2\kappa_{xy}^{(\alpha)} - \frac{\partial \psi_x^{(\alpha)}}{\partial y} - \frac{\partial \psi_y^{(\alpha)}}{\partial x} \right) \\ & - Q_x^{(\alpha)} \left( \gamma_{xz}^{(\alpha)} - \frac{\partial w^{(\alpha)}}{\partial x} - \psi_x^{(\alpha)} \right) - Q_y^{(\alpha)} \left( \gamma_{yz}^{(\alpha)} - \frac{\partial w^{(\alpha)}}{\partial y} - \psi_y^{(\alpha)} \right) \\ & \left. - \bar{m}_x^{(\alpha)} \psi_x^{(\alpha)} - \bar{m}_y^{(\alpha)} \psi_y^{(\alpha)} - \bar{q}^{(\alpha)} w^{(\alpha)} \right) dx dy - \int_{\Gamma_u^{(\alpha)} \cup \Gamma_{u\sigma 2}^{(\alpha)}} \left( M_{ns}^{(\alpha)} (\psi_s^{(\alpha)} - \bar{\psi}_s^{(\alpha)}) \right. \\ & \left. + Q_n^{(\alpha)} (w^{(\alpha)} - \bar{w}^{(\alpha)}) \right) ds - \int_{\Gamma_\sigma^{(\alpha)}} \left( \bar{M}_{ns}^{(\alpha)} \psi_s^{(\alpha)} + \bar{Q}_n^{(\alpha)} w^{(\alpha)} \right) ds \\ & - \int_{\Gamma_u^{(\alpha)}} M_n^{(\alpha)} (\psi_n^{(\alpha)} - \bar{\psi}_n^{(\alpha)}) ds - \int_{\Gamma_\sigma^{(\alpha)} \cup \Gamma_{u\sigma 2}^{(\alpha)}} \bar{M}_n^{(\alpha)} \psi_n^{(\alpha)} ds, \end{aligned} \quad (\text{B.2})$$

the three-field generalized complementary energy of the plate sub-region  $\Omega^{(\beta)}$

$$\begin{aligned} \Pi_c^{(\beta)} = & \iint_{\Omega^{(\beta)}} \left( -\bar{U}_b(\kappa_x^{(\beta)}, \kappa_y^{(\beta)}, \kappa_{xy}^{(\beta)}) - \bar{U}_s(\gamma_{xz}^{(\beta)}, \gamma_{yz}^{(\beta)}) + M_x^{(\beta)} \kappa_x^{(\beta)} + M_y^{(\beta)} \kappa_y^{(\beta)} \right. \\ & + 2M_{xy}^{(\beta)} \kappa_{xy}^{(\beta)} + Q_x^{(\beta)} \gamma_{xz}^{(\beta)} + Q_y^{(\beta)} \gamma_{yz}^{(\beta)} + \left( \frac{\partial M_x^{(\beta)}}{\partial x} + \frac{\partial M_{xy}^{(\beta)}}{\partial y} - Q_x^{(\beta)} + \bar{m}_x^{(\beta)} \right) \psi_x^{(\beta)} \\ & + \left( \frac{\partial M_y^{(\beta)}}{\partial y} + \frac{\partial M_{xy}^{(\beta)}}{\partial x} - Q_y^{(\beta)} + \bar{m}_y^{(\beta)} \right) \psi_y^{(\beta)} + \left( \frac{\partial Q_x^{(\beta)}}{\partial x} + \frac{\partial Q_y^{(\beta)}}{\partial y} + \bar{q}^{(\beta)} \right) w^{(\beta)} \left. \right) dx dy \\ & - \int_{\Gamma_u^{(\beta)} \cup \Gamma_{u\sigma 2}^{(\beta)}} \left( \bar{\psi}_s^{(\beta)} M_{ns}^{(\beta)} + \bar{w}^{(\beta)} Q_n^{(\beta)} \right) ds - \int_{\Gamma_\sigma^{(\beta)} \cup \Gamma_{u\sigma 2}^{(\beta)}} \left( M_n^{(\beta)} - \bar{M}_n^{(\beta)} \right) \psi_n^{(\beta)} ds \\ & - \int_{\Gamma_\sigma^{(\beta)}} \left( (M_{ns}^{(\beta)} - \bar{M}_{ns}^{(\beta)}) \psi_s^{(\beta)} + (Q_n^{(\beta)} - \bar{Q}_n^{(\beta)}) w^{(\beta)} \right) ds - \int_{\Gamma_u^{(\beta)}} M_n^{(\beta)} \bar{\psi}_n^{(\beta)} ds, \end{aligned} \quad (\text{B.3})$$

and the additional energy term of the interface  $\Gamma^{(\alpha, \beta)}$

$$H_{pc}^{(\alpha, \beta)} = \int_{\Gamma^{(\alpha, \beta)}} \left( -M_n^{(\beta)} \psi_n^{(\alpha)} - M_{ns}^{(\beta)} \psi_s^{(\alpha)} + Q_n^{(\beta)} w^{(\alpha)} \right) ds, \quad (B.4)$$

is equivalent to all field equations and boundary and interface conditions for the static deformation of elastic thick plates.

The variation of the potential energy of the plate sub-region  $\Omega^{(\alpha)}$  (Equation (B.2)) is given by

$$\begin{aligned} \delta \Pi_p^{(\alpha)} = & \iint_{\Omega^{(\alpha)}} \left( \left( \frac{\partial \bar{U}_b^{(\alpha)}}{\partial \kappa_x^{(\alpha)}} - M_x^{(\alpha)} \right) \delta \kappa_x^{(\alpha)} + \left( \frac{\partial \bar{U}_b^{(\alpha)}}{\partial \kappa_y^{(\alpha)}} - M_y^{(\alpha)} \right) \delta \kappa_y^{(\alpha)} \right. \\ & + \left( \frac{\partial \bar{U}_b^{(\alpha)}}{\partial \kappa_{xy}^{(\alpha)}} - 2 M_{xy}^{(\alpha)} \right) \delta \kappa_{xy}^{(\alpha)} + \left( \frac{\partial \bar{U}_s^{(\alpha)}}{\partial \gamma_{xz}^{(\alpha)}} - Q_x^{(\alpha)} \right) \delta \gamma_{xz}^{(\alpha)} + \left( \frac{\partial \bar{U}_s^{(\alpha)}}{\partial \gamma_{yz}^{(\alpha)}} - Q_y^{(\alpha)} \right) \delta \gamma_{yz}^{(\alpha)} \\ & - \left( \kappa_x^{(\alpha)} - \frac{\partial \psi_x^{(\alpha)}}{\partial x} \right) \delta M_x^{(\alpha)} - \left( \kappa_y^{(\alpha)} - \frac{\partial \psi_y^{(\alpha)}}{\partial y} \right) \delta M_y^{(\alpha)} - \left( 2 \kappa_{xy}^{(\alpha)} - \frac{\partial \psi_x^{(\alpha)}}{\partial y} \right. \\ & \left. - \frac{\partial \psi_y^{(\alpha)}}{\partial x} \right) \delta M_{xy}^{(\alpha)} - \left( \gamma_{xz}^{(\alpha)} - \frac{\partial w^{(\alpha)}}{\partial x} - \psi_x^{(\alpha)} \right) \delta Q_x^{(\alpha)} - \left( \gamma_{yz}^{(\alpha)} - \frac{\partial w^{(\alpha)}}{\partial y} - \psi_y^{(\alpha)} \right) \delta Q_y^{(\alpha)} \\ & - \left( \frac{\partial M_x^{(\alpha)}}{\partial x} + \frac{\partial M_{xy}^{(\alpha)}}{\partial y} - Q_x^{(\alpha)} + \bar{m}_x^{(\alpha)} \right) \delta \psi_x^{(\alpha)} - \left( \frac{\partial M_y^{(\alpha)}}{\partial y} + \frac{\partial M_{xy}^{(\alpha)}}{\partial x} - Q_y^{(\alpha)} \right. \\ & \left. + \bar{m}_y^{(\alpha)} \right) \delta \psi_y^{(\alpha)} - \left( \frac{\partial Q_x^{(\alpha)}}{\partial x} + \frac{\partial Q_y^{(\alpha)}}{\partial y} + \bar{q}^{(\alpha)} \right) \delta w^{(\alpha)} \Big) dx dy \\ & - \int_{\Gamma_u^{(\alpha)} \cup \Gamma_{u\sigma 2}^{(\alpha)}} \left( (\psi_s^{(\alpha)} - \bar{\psi}_s^{(\alpha)}) \delta M_{ns}^{(\alpha)} + (w^{(\alpha)} - \bar{w}^{(\alpha)}) \delta Q_n^{(\alpha)} \right) ds \\ & + \int_{\Gamma_\sigma^{(\alpha)}} \left( (M_{ns}^{(\alpha)} - \bar{M}_{ns}^{(\alpha)}) \delta \psi_s^{(\alpha)} + (Q_n^{(\alpha)} - \bar{Q}_n^{(\alpha)}) \delta w^{(\alpha)} \right) ds \\ & - \int_{\Gamma_u^{(\alpha)}} (\psi_n^{(\alpha)} - \bar{\psi}_n^{(\alpha)}) \delta M_n^{(\alpha)} ds + \int_{\Gamma_\sigma^{(\alpha)} \cup \Gamma_{u\sigma 2}^{(\alpha)}} (M_n^{(\alpha)} - \bar{M}_n^{(\alpha)}) \delta \psi_n^{(\alpha)} ds \\ & + \int_{\Gamma^{(\alpha, \beta)}} (M_n^{(\alpha)} \delta \psi_n^{(\alpha)} + M_{ns}^{(\alpha)} \delta \psi_s^{(\alpha)} + Q_n^{(\alpha)} \delta w^{(\alpha)}) ds, \end{aligned} \quad (B.5)$$

where the integration by parts in two variables [304]

$$\iint_{\Omega^{(\alpha)}} M_x^{(\alpha)} \frac{\partial \delta \psi_x^{(\alpha)}}{\partial x} dx dy = \int_{\Gamma^{(\alpha)}} M_x^{(\alpha)} \delta \psi_x^{(\alpha)} dy - \iint_{\Omega^{(\alpha)}} \frac{\partial M_x^{(\alpha)}}{\partial x} \delta \psi_x^{(\alpha)} dx dy, \quad (B.6)$$

$$\iint_{\Omega^{(\alpha)}} M_y^{(\alpha)} \frac{\partial \delta \psi_y^{(\alpha)}}{\partial y} dx dy = - \int_{\Gamma^{(\alpha)}} M_y^{(\alpha)} \delta \psi_y^{(\alpha)} dx - \iint_{\Omega^{(\alpha)}} \frac{\partial M_y^{(\alpha)}}{\partial y} \delta \psi_y^{(\alpha)} dx dy, \quad (B.7)$$

$$\iint_{\Omega^{(\alpha)}} M_{xy}^{(\alpha)} \frac{\partial \delta \psi_x^{(\alpha)}}{\partial y} dx dy = - \int_{\Gamma^{(\alpha)}} M_{xy}^{(\alpha)} \delta \psi_x^{(\alpha)} dx - \iint_{\Omega^{(\alpha)}} \frac{\partial M_{xy}^{(\alpha)}}{\partial y} \delta \psi_x^{(\alpha)} dx dy, \quad (B.8)$$

$$\iint_{\Omega^{(\alpha)}} M_{xy}^{(\alpha)} \frac{\partial \delta \psi_y^{(\alpha)}}{\partial x} dx dy = - \int_{\Gamma^{(\alpha)}} M_{xy}^{(\alpha)} \delta \psi_y^{(\alpha)} dy - \iint_{\Omega^{(\alpha)}} \frac{\partial M_{xy}^{(\alpha)}}{\partial x} \delta \psi_y^{(\alpha)} dx dy, \quad (B.9)$$

$$\iint_{\Omega^{(\alpha)}} Q_x^{(\alpha)} \frac{\partial \delta w^{(\alpha)}}{\partial x} dx dy = \int_{\Gamma^{(\alpha)}} Q_x^{(\alpha)} \delta w^{(\alpha)} dy - \iint_{\Omega^{(\alpha)}} \frac{\partial Q_x^{(\alpha)}}{\partial x} \delta w^{(\alpha)} dx dy, \quad (\text{B.10})$$

$$\iint_{\Omega^{(\alpha)}} Q_y^{(\alpha)} \frac{\partial \delta w^{(\alpha)}}{\partial y} dx dy = - \int_{\Gamma^{(\alpha)}} Q_y^{(\alpha)} \delta w^{(\alpha)} dx - \iint_{\Omega^{(\alpha)}} \frac{\partial Q_y^{(\alpha)}}{\partial y} \delta w^{(\alpha)} dx dy, \quad (\text{B.11})$$

the transformation of the bending moments  $M_x^{(\alpha)}$  and  $M_y^{(\alpha)}$  and twisting moment  $M_{xy}^{(\alpha)}$  and rotations  $\psi_x^{(\alpha)}$  and  $\psi_y^{(\alpha)}$  to the boundary coordinates  $(n^{(\alpha)}, s^{(\alpha)})$

$$\begin{aligned} (M_x^{(\alpha)} dy - M_{xy}^{(\alpha)} dx) \delta \psi_x^{(\alpha)} - (M_y^{(\alpha)} dx - M_{xy}^{(\alpha)} dy) \delta \psi_y^{(\alpha)} = \\ (M_n^{(\alpha)} \delta \psi_n^{(\alpha)} + M_{ns}^{(\alpha)} \delta \psi_s^{(\alpha)}) ds \end{aligned} \quad (\text{B.12})$$

and the transformation of the shear forces  $Q_x^{(\alpha)}$  and  $Q_y^{(\alpha)}$  to the boundary coordinates  $(n^{(\alpha)}, s^{(\alpha)})$

$$(Q_x^{(\alpha)} dy - Q_y^{(\alpha)} dx) \delta w^{(\alpha)} = Q_n^{(\alpha)} \delta w^{(\alpha)} ds \quad (\text{B.13})$$

are used.

The variation of the complementary energy of the plate sub-region  $\Omega^{(\beta)}$  (Equation (B.3)) leads to

$$\begin{aligned} \delta \Pi_c^{(\beta)} = & \iint_{\Omega^{(\beta)}} \left( - \left( \frac{\partial \bar{U}_b^{(\beta)}}{\partial \kappa_x^{(\beta)}} - M_x^{(\beta)} \right) \delta \kappa_x^{(\beta)} - \left( \frac{\partial \bar{U}_b^{(\beta)}}{\partial \kappa_y^{(\beta)}} - M_y^{(\beta)} \right) \delta \kappa_y^{(\beta)} \right. \\ & - \left( \frac{\partial \bar{U}_b^{(\beta)}}{\partial \kappa_{xy}^{(\beta)}} - 2 M_{xy}^{(\beta)} \right) \delta \kappa_{xy}^{(\beta)} - \left( \frac{\partial \bar{U}_s^{(\beta)}}{\partial \gamma_{xz}^{(\beta)}} - Q_x^{(\beta)} \right) \delta \gamma_{xz}^{(\beta)} - \left( \frac{\partial \bar{U}_s^{(\beta)}}{\partial \gamma_{yz}^{(\beta)}} - Q_y^{(\beta)} \right) \delta \gamma_{yz}^{(\beta)} \\ & + \left( \kappa_x^{(\beta)} - \frac{\partial \psi_x^{(\beta)}}{\partial x} \right) \delta M_x^{(\beta)} + \left( \kappa_y^{(\beta)} - \frac{\partial \psi_y^{(\beta)}}{\partial y} \right) \delta M_y^{(\beta)} + \left( 2 \kappa_{xy}^{(\beta)} - \frac{\partial \psi_x^{(\beta)}}{\partial y} \right. \\ & \left. - \frac{\partial \psi_y^{(\beta)}}{\partial x} \right) \delta M_{xy}^{(\beta)} + \left( \gamma_{xz}^{(\beta)} - \frac{\partial w^{(\beta)}}{\partial x} - \psi_x^{(\beta)} \right) \delta Q_x^{(\beta)} + \left( \gamma_{yz}^{(\beta)} - \frac{\partial w^{(\beta)}}{\partial y} - \psi_y^{(\beta)} \right) \delta Q_y^{(\beta)} \\ & + \left( \frac{\partial M_x^{(\beta)}}{\partial x} + \frac{\partial M_{xy}^{(\beta)}}{\partial y} - Q_x^{(\beta)} + \bar{m}_x^{(\beta)} \right) \delta \psi_x^{(\beta)} + \left( \frac{\partial M_y^{(\beta)}}{\partial y} + \frac{\partial M_{xy}^{(\beta)}}{\partial x} - Q_y^{(\beta)} \right. \\ & \left. + \bar{m}_y^{(\beta)} \right) \delta \psi_y^{(\beta)} + \left( \frac{\partial Q_x^{(\beta)}}{\partial x} + \frac{\partial Q_y^{(\beta)}}{\partial y} + \bar{q}^{(\beta)} \right) \delta w^{(\beta)} \Big) dx dy \\ & + \int_{\Gamma_u^{(\beta)} \cup \Gamma_{u\sigma 2}^{(\beta)}} \left( (\psi_s^{(\beta)} - \bar{\psi}_s^{(\beta)}) \delta M_{ns}^{(\beta)} + (w^{(\beta)} - \bar{w}^{(\beta)}) \delta Q_n^{(\beta)} \right) ds \\ & - \int_{\Gamma_\sigma^{(\beta)}} \left( (M_{ns}^{(\beta)} - \bar{M}_{ns}^{(\beta)}) \delta \psi_s^{(\beta)} + (Q_n^{(\beta)} - \bar{Q}_n^{(\beta)}) \delta w^{(\beta)} \right) ds \\ & + \int_{\Gamma_u^{(\beta)}} \left( \psi_n^{(\beta)} - \bar{\psi}_n^{(\beta)} \right) \delta M_n^{(\beta)} ds - \int_{\Gamma_\sigma^{(\beta)} \cup \Gamma_{u\sigma 2}^{(\beta)}} \left( M_n^{(\beta)} - \bar{M}_n^{(\beta)} \right) \delta \psi_n^{(\beta)} ds \\ & + \int_{\Gamma^{(\alpha, \beta)}} \left( \psi_n^{(\beta)} \delta M_n^{(\beta)} + \psi_s^{(\beta)} \delta M_{ns}^{(\beta)} + w^{(\beta)} \delta Q_n^{(\beta)} \right) ds, \end{aligned} \quad (\text{B.14})$$

where the integration by parts in two variables [304]

$$\iint_{\Omega^{(\beta)}} \psi_x^{(\beta)} \frac{\partial \delta M_x^{(\beta)}}{\partial x} dx dy = \int_{\Gamma^{(\beta)}} \psi_x^{(\beta)} \delta M_x^{(\beta)} dy - \iint_{\Omega^{(\beta)}} \frac{\partial \psi_x^{(\beta)}}{\partial x} \delta M_x^{(\beta)} dx dy, \quad (\text{B.15})$$

$$\iint_{\Omega^{(\beta)}} \psi_y^{(\beta)} \frac{\partial \delta M_y^{(\beta)}}{\partial y} dx dy = - \int_{\Gamma^{(\beta)}} \psi_y^{(\beta)} \delta M_y^{(\beta)} dx - \iint_{\Omega^{(\beta)}} \frac{\partial \psi_y^{(\beta)}}{\partial y} \delta M_y^{(\beta)} dx dy, \quad (\text{B.16})$$

$$\iint_{\Omega^{(\beta)}} \psi_x^{(\beta)} \frac{\partial \delta M_{xy}^{(\beta)}}{\partial y} dx dy = - \int_{\Gamma^{(\beta)}} \psi_x^{(\beta)} \delta M_{xy}^{(\beta)} dx - \iint_{\Omega^{(\beta)}} \frac{\partial \psi_x^{(\beta)}}{\partial y} \delta M_{xy}^{(\beta)} dx dy, \quad (\text{B.17})$$

$$\iint_{\Omega^{(\beta)}} \psi_y^{(\beta)} \frac{\partial \delta M_{xy}^{(\beta)}}{\partial x} dx dy = \int_{\Gamma^{(\beta)}} \psi_y^{(\beta)} \delta M_{xy}^{(\beta)} dy - \iint_{\Omega^{(\beta)}} \frac{\partial \psi_y^{(\beta)}}{\partial x} \delta M_{xy}^{(\beta)} dx dy, \quad (\text{B.18})$$

$$\iint_{\Omega^{(\beta)}} w^{(\beta)} \frac{\partial \delta Q_x^{(\beta)}}{\partial x} dx dy = \int_{\Gamma^{(\beta)}} w^{(\beta)} \delta Q_x^{(\beta)} dy - \iint_{\Omega^{(\beta)}} \frac{\partial w^{(\beta)}}{\partial x} \delta Q_x^{(\beta)} dx dy, \quad (\text{B.19})$$

$$\iint_{\Omega^{(\beta)}} w^{(\beta)} \frac{\partial \delta Q_y^{(\beta)}}{\partial y} dx dy = - \int_{\Gamma^{(\beta)}} w^{(\beta)} \delta Q_y^{(\beta)} dx - \iint_{\Omega^{(\beta)}} \frac{\partial w^{(\beta)}}{\partial y} \delta Q_y^{(\beta)} dx dy, \quad (\text{B.20})$$

the transformation of the bending moments  $M_x^{(\beta)}$  and  $M_y^{(\beta)}$  and twisting moment  $M_{xy}^{(\beta)}$  and rotations  $\psi_x^{(\beta)}$  and  $\psi_y^{(\beta)}$  to the boundary coordinates  $(n^{(\beta)}, s^{(\beta)})$

$$\begin{aligned} \left( \delta M_x^{(\beta)} dy - \delta M_{xy}^{(\beta)} dx \right) \psi_x^{(\beta)} - \left( \delta M_y^{(\beta)} dx - \delta M_{xy}^{(\beta)} dy \right) \psi_y^{(\beta)} = \\ \left( \psi_n^{(\beta)} \delta M_n^{(\beta)} + \psi_s^{(\beta)} \delta M_{ns}^{(\beta)} \right) ds \end{aligned} \quad (\text{B.21})$$

and the transformation of the shear forces  $Q_x^{(\beta)}$  and  $Q_y^{(\beta)}$  to the boundary coordinates  $(n^{(\beta)}, s^{(\beta)})$

$$\left( \delta Q_x^{(\beta)} dy - \delta Q_y^{(\beta)} dx \right) w^{(\beta)} = w^{(\beta)} \delta Q_n^{(\beta)} ds \quad (\text{B.22})$$

are used.

The variation of the additional energy term of the interface  $\Gamma^{(\alpha, \beta)}$  (Equation (B.4)) results in

$$\begin{aligned} \delta H_{pc}^{(\alpha, \beta)} = \int_{\Gamma^{(\alpha, \beta)}} \left( -M_n^{(\beta)} \delta \psi_n^{(\alpha)} - \psi_n^{(\alpha)} \delta M_n^{(\beta)} - \psi_s^{(\alpha)} \delta M_{ns}^{(\beta)} \right. \\ \left. - M_{ns}^{(\beta)} \delta \psi_s^{(\alpha)} + w^{(\alpha)} \delta Q_n^{(\beta)} + Q_n^{(\beta)} \delta w^{(\alpha)} \right) ds. \end{aligned} \quad (\text{B.23})$$

The extension to the dynamic problem of thick plates is achieved either by modifying the external normal load  $\bar{q}^{(l)} \mapsto \bar{q}^{(l)} - \rho h \ddot{w}^{(l)}$  and the external moments  $\bar{m}_x^{(l)} \mapsto \bar{m}_x^{(l)} - \frac{\rho h^3}{12} \ddot{\psi}_x^{(l)}$  and  $\bar{m}_y^{(l)} \mapsto \bar{m}_y^{(l)} - \frac{\rho h^3}{12} \ddot{\psi}_y^{(l)}$  (d'Alembert's principle) or by introducing the kinetic energy density of a thick plate [22]

$$T = \frac{\rho h}{2} \left( \dot{w}^{(l)2} + \frac{h^2}{12} (\dot{\psi}_x^{(l)2} + \dot{\psi}_y^{(l)2}) \right) \quad (\text{B.24})$$

and defining the functional

$$L = \int_{t_0}^{t_1} \left( \iint_{\Omega} T \, dx \, dy - \Pi \right) dt \quad (\text{B.25})$$

through integration over time between fixed limits  $(t_0, t_1)$  at which  $\delta w^{(l)} = 0$ ,  $\delta \psi_x^{(l)} = 0$  and  $\delta \psi_y^{(l)} = 0$  and setting the first variation  $\delta L = 0$  [303]. Integrating the variation of the kinetic energy by parts leads to

$$\begin{aligned} \delta \int_{t_0}^{t_1} \iint_{\Omega^{(l)}} T \, dx \, dy \, dt &= \int_{t_0}^{t_1} \iint_{\Omega^{(l)}} \rho h \left( \dot{w}^{(l)} \delta \dot{w}^{(l)} + \frac{h^2}{12} \left( \dot{\psi}_x^{(l)} \delta \dot{\psi}_x^{(l)} + \dot{\psi}_y^{(l)} \delta \dot{\psi}_y^{(l)} \right) \right) dx \, dy \, dt \\ &= - \int_{t_0}^{t_1} \iint_{\Omega^{(l)}} \rho h \left( \ddot{w}^{(l)} \delta w^{(l)} + \frac{h^2}{12} \left( \ddot{\psi}_x^{(l)} \delta \psi_x^{(l)} + \ddot{\psi}_y^{(l)} \delta \psi_y^{(l)} \right) \right) dx \, dy \, dt, \end{aligned} \quad (\text{B.26})$$

where

$$\iint_{\Omega^{(l)}} \rho h \left( \dot{w}^{(l)} \delta w^{(l)} + \frac{h^2}{12} \left( \dot{\psi}_x^{(l)} \delta \psi_x^{(l)} + \dot{\psi}_y^{(l)} \delta \psi_y^{(l)} \right) \right) dx \, dy \Big|_{t_0}^{t_1} = 0 \quad (\text{B.27})$$

is used. Combining Equations (B.5), (B.14), (B.23) and (B.26) leads to the final result

$$\begin{aligned} \delta L = 0 &= \int_{t_0}^{t_1} \left( \sum_l \iint_{\Omega^{(l)}} \left( \left( \frac{\partial \bar{U}_b^{(l)}}{\partial \kappa_x^{(l)}} - M_x^{(l)} \right) \delta \kappa_x^{(l)} + \left( \frac{\partial \bar{U}_b^{(l)}}{\partial \kappa_y^{(l)}} - M_y^{(l)} \right) \delta \kappa_y^{(l)} \right. \right. \\ &\quad + \left( \frac{\partial \bar{U}_b^{(l)}}{\partial \kappa_{xy}^{(l)}} - 2 M_{xy}^{(l)} \right) \delta \kappa_{xy}^{(l)} + \left( \frac{\partial \bar{U}_s^{(l)}}{\partial \gamma_{xz}^{(l)}} - Q_x^{(l)} \right) \delta \gamma_{xz}^{(l)} + \left( \frac{\partial \bar{U}_s^{(l)}}{\partial \gamma_{yz}^{(l)}} - Q_y^{(l)} \right) \delta \gamma_{yz}^{(l)} \\ &\quad - \left( \kappa_x^{(l)} - \frac{\partial \psi_x^{(l)}}{\partial x} \right) \delta M_x^{(l)} - \left( \kappa_y^{(l)} - \frac{\partial \psi_y^{(l)}}{\partial y} \right) \delta M_y^{(l)} - \left( 2 \kappa_{xy}^{(l)} - \frac{\partial \psi_x^{(l)}}{\partial y} \right. \\ &\quad \left. \left. - \frac{\partial \psi_y^{(l)}}{\partial x} \right) \delta M_{xy}^{(l)} - \left( \gamma_{xz}^{(l)} - \frac{\partial w^{(l)}}{\partial x} - \psi_x^{(l)} \right) \delta Q_x^{(l)} - \left( \gamma_{yz}^{(l)} - \frac{\partial w^{(l)}}{\partial y} - \psi_y^{(l)} \right) \delta Q_y^{(l)} \right. \\ &\quad - \left( \frac{\partial M_x^{(l)}}{\partial x} + \frac{\partial M_{xy}^{(l)}}{\partial y} - Q_x^{(l)} + \bar{m}_x^{(l)} - \frac{\rho h^3}{12} \ddot{\psi}_x^{(l)} \right) \delta \psi_x^{(l)} - \left( \frac{\partial M_y^{(l)}}{\partial y} + \frac{\partial M_{xy}^{(l)}}{\partial x} - Q_y^{(l)} \right. \\ &\quad \left. + \bar{m}_y^{(l)} - \frac{\rho h^3}{12} \ddot{\psi}_y^{(l)} \right) \delta \psi_y^{(l)} - \left( \frac{\partial Q_x^{(l)}}{\partial x} + \frac{\partial Q_y^{(l)}}{\partial y} + \bar{q}^{(l)} - \rho h \ddot{w}^{(l)} \right) \delta w^{(l)} \right) dx \, dy \\ &\quad - \int_{\Gamma_u^{(l)} \cup \Gamma_{u\sigma^2}^{(l)}} \left( (\psi_s^{(l)} - \bar{\psi}_s^{(l)}) \delta M_{ns}^{(l)} + (w^{(l)} - \bar{w}^{(l)}) \delta Q_n^{(l)} \right) ds \\ &\quad + \int_{\Gamma_\sigma^{(l)}} \left( (M_{ns}^{(l)} - \bar{M}_{ns}^{(l)}) \delta \psi_s^{(l)} + (Q_n^{(l)} - \bar{Q}_n^{(l)}) \delta w^{(l)} \right) ds \\ &\quad - \int_{\Gamma_u^{(l)}} (\psi_n^{(l)} - \bar{\psi}_n^{(l)}) \delta M_n^{(l)} ds + \int_{\Gamma_\sigma^{(l)} \cup \Gamma_{u\sigma^2}^{(l)}} (M_n^{(l)} - \bar{M}_n^{(l)}) \delta \psi_n^{(l)} ds \\ &\quad + \int_{\Gamma^{(\alpha, \beta)}} \left( (M_n^{(\alpha)} - M_n^{(\beta)}) \delta \psi_n^{(\alpha)} + (M_{ns}^{(\alpha)} - M_{ns}^{(\beta)}) \delta \psi_s^{(\alpha)} + (Q_n^{(\alpha)} + Q_n^{(\beta)}) \delta w^{(\alpha)} \right. \\ &\quad \left. - (\psi_n^{(\alpha)} + \psi_n^{(\beta)}) \delta M_n^{(\beta)} - (\psi_s^{(\alpha)} + \psi_s^{(\beta)}) \delta M_{ns}^{(\beta)} - (w^{(\beta)} - w^{(\alpha)}) \delta Q_n^{(\beta)} \right) ds \Big) dt. \end{aligned} \quad (\text{B.28})$$



## C The sub-region three-field generalized mixed variational principle for thin plates

In [26] and [32] the sub-region three-field generalized mixed variational principle for the static deformation of elastic thin plates is derived. In this chapter the method is extended to the dynamic problem using either the d'Alembert's principle [302] or the introduction of a kinetic energy density [303]. The stationary condition  $\delta\Pi = 0$  of the functional [26, 32]

$$\Pi = \Pi_p^{(\alpha)} - \Pi_c^{(\beta)} + H_{pc}^{(\alpha, \beta)}, \quad (\text{C.1})$$

with the three-field generalized potential energy of the plate sub-region  $\Omega^{(\alpha)}$

$$\begin{aligned} \Pi_p^{(\alpha)} = & \iint_{\Omega^{(\alpha)}} \left( \bar{U}_b(\kappa_x^{(\alpha)}, \kappa_y^{(\alpha)}, \kappa_{xy}^{(\alpha)}) - \bar{q}^{(\alpha)} w^{(\alpha)} - M_x^{(\alpha)} \left( \kappa_x^{(\alpha)} + \frac{\partial^2 w^{(\alpha)}}{\partial x^2} \right) \right. \\ & \left. - M_y^{(\alpha)} \left( \kappa_y^{(\alpha)} + \frac{\partial^2 w^{(\alpha)}}{\partial y^2} \right) - 2 M_{xy}^{(\alpha)} \left( \kappa_{xy}^{(\alpha)} + \frac{\partial^2 w^{(\alpha)}}{\partial x \partial y} \right) \right) dx dy \\ & - \int_{\Gamma_u^{(\alpha)} \cup \Gamma_{u\sigma}^{(\alpha)}} \left( Q_n^{(\alpha)} + \frac{\partial M_{ns}^{(\alpha)}}{\partial s^{(\alpha)}} \right) (w^{(\alpha)} - \bar{w}^{(\alpha)}) ds - \int_{\Gamma_\sigma^{(\alpha)}} \bar{V}_n^{(\alpha)} w^{(\alpha)} ds \\ & + \int_{\Gamma_u^{(\alpha)}} M_n^{(\alpha)} \left( \frac{\partial w^{(\alpha)}}{\partial n^{(\alpha)}} + \bar{\psi}_n^{(\alpha)} \right) ds + \int_{\Gamma_\sigma^{(\alpha)} \cup \Gamma_{u\sigma}^{(\alpha)}} \bar{M}_n^{(\alpha)} \frac{\partial w^{(\alpha)}}{\partial n^{(\alpha)}} ds, \end{aligned} \quad (\text{C.2})$$

the three-field generalized complementary energy of the plate sub-region  $\Omega^{(\beta)}$

$$\begin{aligned} \Pi_c^{(\beta)} = & \iint_{\Omega^{(\beta)}} \left( - \bar{U}_b(\kappa_x^{(\beta)}, \kappa_y^{(\beta)}, \kappa_{xy}^{(\beta)}) + M_x^{(\beta)} \kappa_x^{(\beta)} + M_y^{(\beta)} \kappa_y^{(\beta)} + 2 M_{xy}^{(\beta)} \kappa_{xy}^{(\beta)} \right. \\ & \left. + \left( \frac{\partial^2 M_x^{(\beta)}}{\partial x^2} + \frac{\partial^2 M_y^{(\beta)}}{\partial y^2} + 2 \frac{\partial^2 M_{xy}^{(\beta)}}{\partial x \partial y} + \bar{q}^{(\beta)} \right) w^{(\beta)} \right) dx dy - \int_{\Gamma_u^{(\beta)}} M_n^{(\beta)} \bar{\psi}_n^{(\beta)} ds \\ & - \int_{\Gamma_u^{(\beta)} \cup \Gamma_{u\sigma}^{(\beta)}} \left( Q_n^{(\beta)} + \frac{\partial M_{ns}^{(\beta)}}{\partial s^{(\beta)}} \right) \bar{w}^{(\beta)} ds + \int_{\Gamma_\sigma^{(\beta)} \cup \Gamma_{u\sigma}^{(\beta)}} \left( M_n^{(\beta)} - \bar{M}_n^{(\beta)} \right) \frac{\partial w^{(\beta)}}{\partial n^{(\beta)}} ds \\ & - \int_{\Gamma_\sigma^{(\beta)}} \left( Q_n^{(\beta)} + \frac{\partial M_{ns}^{(\beta)}}{\partial s^{(\beta)}} - \bar{V}_n^{(\beta)} \right) w^{(\beta)} ds, \end{aligned} \quad (\text{C.3})$$

and the additional energy term of the interface  $\Gamma^{(\alpha, \beta)}$

$$H_{pc}^{(\alpha, \beta)} = \int_{\Gamma^{(\alpha, \beta)}} \left( M_n^{(\beta)} \frac{\partial w^{(\alpha)}}{\partial n^{(\alpha)}} + \left( Q_n^{(\beta)} + \frac{\partial M_{ns}^{(\beta)}}{\partial s^{(\beta)}} \right) w^{(\alpha)} \right) ds, \quad (\text{C.4})$$

is equivalent to all field equations and boundary and interface conditions for the static deformation of elastic thin plates (excluding the effects due to corner forces).

The variation of the potential energy of the plate sub-region  $\Omega^{(\alpha)}$  (Equation (C.2)) gives

$$\begin{aligned} \delta\Pi_p^{(\alpha)} = & \iint_{\Omega^{(\alpha)}} \left( \left( \frac{\partial \bar{U}_b^{(\alpha)}}{\partial \kappa_x^{(\alpha)}} - M_x^{(\alpha)} \right) \delta \kappa_x^{(\alpha)} + \left( \frac{\partial \bar{U}_b^{(\alpha)}}{\partial \kappa_y^{(\alpha)}} - M_y^{(\alpha)} \right) \delta \kappa_y^{(\alpha)} \right. \\ & + \left( \frac{\partial \bar{U}_b^{(\alpha)}}{\partial \kappa_{xy}^{(\alpha)}} - 2 M_{xy}^{(\alpha)} \right) \delta \kappa_{xy}^{(\alpha)} - \left( \kappa_x^{(\alpha)} + \frac{\partial^2 w^{(\alpha)}}{\partial x^2} \right) \delta M_x^{(\alpha)} - \left( \kappa_y^{(\alpha)} + \frac{\partial^2 w^{(\alpha)}}{\partial y^2} \right) \delta M_y^{(\alpha)} \\ & - 2 \left( \kappa_{xy}^{(\alpha)} + \frac{\partial^2 w^{(\alpha)}}{\partial x \partial y} \right) \delta M_{xy}^{(\alpha)} - \left( \frac{\partial^2 M_x^{(\alpha)}}{\partial x^2} + \frac{\partial^2 M_y^{(\alpha)}}{\partial y^2} + 2 \frac{\partial^2 M_{xy}^{(\alpha)}}{\partial x \partial y} + \bar{q}^{(\alpha)} \right) \delta w^{(\alpha)} \Big) dx dy \\ & - \int_{\Gamma_u^{(\alpha)} \cup \Gamma_{u\sigma}^{(\alpha)}} (w^{(\alpha)} - \bar{w}^{(\alpha)}) \delta V_n^{(\alpha)} ds + \int_{\Gamma_\sigma^{(\alpha)}} (V_n^{(\alpha)} - \bar{V}_n^{(\alpha)}) \delta w^{(\alpha)} ds \\ & + \int_{\Gamma_u^{(\alpha)}} \left( \frac{\partial w^{(\alpha)}}{\partial n^{(\alpha)}} + \bar{\psi}_n^{(\alpha)} \right) \delta M_n^{(\alpha)} ds - \int_{\Gamma_\sigma^{(\alpha)} \cup \Gamma_{u\sigma}^{(\alpha)}} (M_n^{(\alpha)} - \bar{M}_n^{(\alpha)}) \frac{\partial \delta w^{(\alpha)}}{\partial n^{(\alpha)}} ds \\ & \left. - \int_{\Gamma^{(\alpha, \beta)}} \left( M_n^{(\alpha)} \frac{\partial \delta w^{(\alpha)}}{\partial n^{(\alpha)}} - V_n^{(\alpha)} \delta w^{(\alpha)} \right) ds, \right) \end{aligned} \quad (C.5)$$

where the integration by parts in two variables [304]

$$\begin{aligned} & \iint_{\Omega^{(\alpha)}} \left( M_x^{(\alpha)} \frac{\partial^2 \delta w^{(\alpha)}}{\partial x^2} + M_y^{(\alpha)} \frac{\partial^2 \delta w^{(\alpha)}}{\partial y^2} + 2 M_{xy}^{(\alpha)} \frac{\partial^2 \delta w^{(\alpha)}}{\partial x \partial y} \right) dx dy = \\ & \int_{\Gamma^{(\alpha)}} \left( M_n^{(\alpha)} \frac{\partial \delta w^{(\alpha)}}{\partial n^{(\alpha)}} - V_n^{(\alpha)} \delta w^{(\alpha)} \right) ds + \iint_{\Omega^{(\alpha)}} \left( \frac{\partial^2 M_x^{(\alpha)}}{\partial x^2} + \frac{\partial^2 M_y^{(\alpha)}}{\partial y^2} + 2 \frac{\partial^2 M_{xy}^{(\alpha)}}{\partial x \partial y} \right) \delta w^{(\alpha)} dx dy \end{aligned} \quad (C.6)$$

is used.

The variation of the complementary energy of the plate sub-region  $\Omega^{(\beta)}$  (Equation (C.2)) leads to

$$\begin{aligned} \delta\Pi_c^{(\beta)} = & \iint_{\Omega^{(\beta)}} \left( - \left( \frac{\partial \bar{U}_b^{(\beta)}}{\partial \kappa_x^{(\beta)}} - M_x^{(\beta)} \right) \delta \kappa_x^{(\beta)} - \left( \frac{\partial \bar{U}_b^{(\beta)}}{\partial \kappa_y^{(\beta)}} - M_y^{(\beta)} \right) \delta \kappa_y^{(\beta)} \right. \\ & - \left( \frac{\partial \bar{U}_b^{(\beta)}}{\partial \kappa_{xy}^{(\beta)}} - 2 M_{xy}^{(\beta)} \right) \delta \kappa_{xy}^{(\beta)} + \left( \kappa_x^{(\beta)} + \frac{\partial^2 w^{(\beta)}}{\partial x^2} \right) \delta M_x^{(\beta)} + \left( \kappa_y^{(\beta)} + \frac{\partial^2 w^{(\beta)}}{\partial y^2} \right) \delta M_y^{(\beta)} \\ & + 2 \left( \kappa_{xy}^{(\beta)} + \frac{\partial^2 w^{(\beta)}}{\partial x \partial y} \right) \delta M_{xy}^{(\beta)} + \left( \frac{\partial^2 M_x^{(\beta)}}{\partial x^2} + \frac{\partial^2 M_y^{(\beta)}}{\partial y^2} + 2 \frac{\partial^2 M_{xy}^{(\beta)}}{\partial x \partial y} + \bar{q}^{(\beta)} \right) \delta w^{(\beta)} \Big) dx dy \\ & + \int_{\Gamma_u^{(\beta)} \cup \Gamma_{u\sigma}^{(\beta)}} (w^{(\beta)} - \bar{w}^{(\beta)}) \delta V_n^{(\beta)} ds - \int_{\Gamma_\sigma^{(\beta)}} (V_n^{(\beta)} - \bar{V}_n^{(\beta)}) \delta w^{(\beta)} ds \\ & - \int_{\Gamma_u^{(\beta)}} \left( \frac{\partial w^{(\beta)}}{\partial n^{(\beta)}} + \bar{\psi}_n^{(\beta)} \right) \delta M_n^{(\beta)} ds + \int_{\Gamma_\sigma^{(\beta)} \cup \Gamma_{u\sigma}^{(\beta)}} (M_n^{(\beta)} - \bar{M}_n^{(\beta)}) \frac{\partial \delta w^{(\beta)}}{\partial n^{(\beta)}} ds \\ & \left. - \int_{\Gamma^{(\alpha, \beta)}} \left( \frac{\partial w^{(\beta)}}{\partial n^{(\beta)}} \delta M_n^{(\beta)} - w^{(\beta)} \delta V_n^{(\beta)} \right) ds, \right) \end{aligned} \quad (C.7)$$

where the integration by parts in two variables [304]

$$\begin{aligned} \iint_{\Omega^{(\beta)}} w^{(\beta)} \delta \left( \frac{\partial^2 M_x^{(\beta)}}{\partial x^2} + \frac{\partial^2 M_y^{(\beta)}}{\partial y^2} + 2 \frac{\partial^2 M_{xy}^{(\beta)}}{\partial x \partial y} \right) dx dy &= \int_{\Gamma^{(\beta)}} \left( w^{(\beta)} \delta V_n^{(\beta)} - \frac{\partial w^{(\beta)}}{\partial n^{(\beta)}} \delta M_n^{(\beta)} \right) ds \\ &+ \iint_{\Omega^{(\beta)}} \left( \frac{\partial^2 w^{(\beta)}}{\partial x^2} \delta M_x^{(\beta)} + \frac{\partial^2 w^{(\beta)}}{\partial y^2} \delta M_y^{(\beta)} + 2 \frac{\partial^2 w^{(\beta)}}{\partial x \partial y} \delta M_{xy}^{(\beta)} \right) dx dy \end{aligned} \quad (\text{C.8})$$

is used.

The variation of the additional energy term of the interface  $\Gamma^{(\alpha, \beta)}$  (Equation (C.4)) results in

$$\delta H_{pc}^{(\alpha, \beta)} = \int_{\Gamma^{(\alpha, \beta)}} \left( M_n^{(\beta)} \frac{\partial \delta w^{(\alpha)}}{\partial n^{(\alpha)}} + \frac{\partial w^{(\alpha)}}{\partial n^{(\alpha)}} \delta M_n^{(\beta)} + w^{(\alpha)} \delta V_n^{(\beta)} + V_n^{(\beta)} \delta w^{(\alpha)} \right) ds. \quad (\text{C.9})$$

The dynamic problem of thin plates can be described either by modifying the external normal load  $\bar{q}^{(l)} \mapsto \bar{q}^{(l)} - \rho h \ddot{w}^{(l)}$  (d'Alembert's principle) or by introducing the kinetic energy density of a thin plate  $T = \frac{\rho h}{2} \dot{w}^{(l)2}$  (rotatory inertia is neglected) and defining the functional

$$L = \int_{t_0}^{t_1} \left( \iint_{\Omega} T dx dy - \Pi \right) dt \quad (\text{C.10})$$

through integration over time between fixed limits ( $t_0, t_1$ ) at which  $\delta w^{(l)} = 0$  and setting the first variation  $\delta L = 0$  [303]. The variation of the kinetic energy  $\delta T$  is given by Equation (B.26) if the rotatory inertia terms are neglected.

Combining Equations (C.5), (C.7), (C.9) and (B.26) (without rotatory inertia terms) leads to the final result

$$\begin{aligned} \delta L = 0 = \int_{t_0}^{t_1} & \left( \sum_l \iint_{\Omega^{(l)}} \left( \left( \frac{\partial \bar{U}_b^{(l)}}{\partial \kappa_x^{(l)}} - M_x^{(l)} \right) \delta \kappa_x^{(l)} + \left( \frac{\partial \bar{U}_b^{(l)}}{\partial \kappa_y^{(l)}} - M_y^{(l)} \right) \delta \kappa_y^{(l)} \right. \right. \\ & + \left( \frac{\partial \bar{U}_b^{(l)}}{\partial \kappa_{xy}^{(l)}} - 2 M_{xy}^{(l)} \right) \delta \kappa_{xy}^{(l)} - \left( \kappa_x^{(l)} + \frac{\partial^2 w^{(l)}}{\partial x^2} \right) \delta M_x^{(l)} - \left( \kappa_y^{(l)} + \frac{\partial^2 w^{(l)}}{\partial y^2} \right) \delta M_y^{(l)} \\ & - 2 \left( \kappa_{xy}^{(l)} + \frac{\partial^2 w^{(l)}}{\partial x \partial y} \right) \delta M_{xy}^{(l)} - \left( \frac{\partial^2 M_x^{(l)}}{\partial x^2} + \frac{\partial^2 M_y^{(l)}}{\partial y^2} + 2 \frac{\partial^2 M_{xy}^{(l)}}{\partial x \partial y} + \bar{q}^{(l)} \right. \\ & \left. \left. - \rho h \ddot{w}^{(l)} \right) \delta w^{(l)} \right) dx dy - \int_{\Gamma_u^{(l)} \cup \Gamma_{u\sigma}^{(l)}} (w^{(l)} - \bar{w}^{(l)}) \delta V_n^{(l)} ds + \int_{\Gamma_{\sigma}^{(l)}} (V_n^{(l)} - \bar{V}_n^{(l)}) \delta w^{(l)} ds \right. \\ & + \int_{\Gamma_u^{(l)}} \left( \frac{\partial w^{(l)}}{\partial n^{(l)}} + \bar{\psi}_n^{(l)} \right) \delta M_n^{(l)} ds - \int_{\Gamma_{\sigma}^{(l)} \cup \Gamma_{u\sigma}^{(l)}} (M_n^{(l)} - \bar{M}_n^{(l)}) \frac{\partial \delta w^{(l)}}{\partial n^{(l)}} ds \\ & + \int_{\Gamma^{(\alpha, \beta)}} \left( (M_n^{(\beta)} - M_n^{(\alpha)}) \frac{\partial \delta w^{(\alpha)}}{\partial n^{(\alpha)}} + (V_n^{(\alpha)} + V_n^{(\beta)}) \delta w^{(\alpha)} \right. \\ & \left. \left. + \left( \frac{\partial w^{(\alpha)}}{\partial n^{(\alpha)}} + \frac{\partial w^{(\beta)}}{\partial n^{(\beta)}} \right) \delta M_n^{(\beta)} + (w^{(\alpha)} - w^{(\beta)}) \delta V_n^{(\beta)} \right) ds \right) dt. \end{aligned} \quad (\text{C.11})$$



## D Regularity conditions for integer eigenvalues in an infinite wedge domain

The relation between the Bessel function of the first and second kind in Equation (6.16) is only valid for non-integer orders. The series representation of the Bessel function of the second kind for integer orders  $n$  [284]

$$Y_n(z) = -\frac{1}{\pi} \sum_{k=0}^{n-1} \left( \frac{(n-k-1)! z^{2k-n}}{k! 2^{2k-n}} \right) + \frac{2}{\pi} \ln\left(\frac{z}{2}\right) J_n(z) - \frac{1}{\pi} \sum_{k=0}^{\infty} \left( (\psi_0(k+1) + \psi_0(n+k+1)) \frac{(-1)^k z^{2k+n}}{k! (n+k)! 2^{2k+n}} \right), \quad n \in \mathbb{N}_0, \quad (\text{D.1})$$

where  $\psi_0(\bullet)$  is the digamma function, can be applied to define the required relations between the constants  $A_{i\lambda}$  and  $B_{i\lambda}$  ( $i = \{1, 2, 3\}$ ) for  $\lambda \in \mathbb{N}_0$ .

Using Equations (6.14), (6.18) and (D.1) in the regularity condition for the out-of-plane displacement (Equation (6.11)) results in

$$\begin{aligned} \lim_{r \rightarrow 0} w(r, \varphi) &= \lim_{r \rightarrow 0} -\frac{1}{\pi} \sum_{k=0}^{\lambda-1} \left( \frac{(\lambda-k-1)!}{k! 2^{2k-\lambda}} (k_{f1}^{2k-\lambda} B_{1\lambda} + k_{f2}^{2k-\lambda} B_{2\lambda}) r^{2k-\lambda} \right) \\ &+ \frac{2}{\pi} \sum_{k=0}^{\infty} \left( \frac{(-1)^k}{k! 2^{2k+\lambda} \Gamma(k+\lambda+1)} (k_{f1}^{2k+\lambda} B_{1\lambda} + k_{f2}^{2k+\lambda} B_{2\lambda}) r^{2k+\lambda} \ln(r) \right) = \text{finite}, \end{aligned} \quad (\text{D.2})$$

where  $\ln\left(\frac{k_{f1} r}{2}\right) = \ln\left(\frac{k_{f1}}{2}\right) + \ln(r)$  and  $\ln\left(\frac{k_{f2} r}{2}\right) = \ln\left(\frac{k_{f2}}{2}\right) + \ln(r)$  are used and the multiplication with  $\cos(\lambda_k^s \varphi)$  or  $\sin(\lambda_k^a \varphi)$  is omitted. The following cases have to be distinguished to further simplify Equation (D.2):

**Case I:**  $\lambda = 0$

If  $\lambda_k^a = 0$ , the functions  $w_1$  and  $w_2$  and the out-of-plane displacement  $w(r, \varphi)$  are identical to zero in the whole domain and no restriction on  $B_{1\lambda}$  and  $B_{2\lambda}$  are required. For  $\lambda_k^s = 0$ , it follows from Equation (D.2) and

$$\lim_{z \rightarrow 0} \ln(z) z^\nu = 0 \quad \text{for } \nu > 0 \quad (\text{D.3})$$

that the condition  $B_{10} + B_{20} = 0$  has to be fulfilled.

**Case II:**  $\lambda = \{1, 2\}$

In this case, only the coefficients of  $r^{2k-\lambda}$  with  $k = 0$  have to be equal to zero, since all other terms are bounded in the limit. This leads to the relation

$$k_{f1}^{-\lambda} B_{1\lambda} + k_{f2}^{-\lambda} B_{2\lambda} = 0, \quad (\text{D.4})$$

which is identical to Equation (6.19).

**Case III:**  $\lambda = \{3, 4, \dots\}$

For these values of  $\lambda$  more than one linearly independent function has to be satisfied to fulfill Equation (D.2) (coefficients of  $r^{2k-\lambda}$  with  $k = \{0, 1, \dots\}$  have to be zero), which leads to the trivial solution  $B_{1\lambda} = B_{2\lambda} = 0$ .

Considering the two regularity conditions for the rotations (Equations (6.12) and (6.13)), the following cases are distinguished:

**Case I:**  $\lambda = 0$

If  $\lambda_k^a = 0$ , the rotation  $\psi_r(r, \varphi)$  is identical to zero in the whole domain, while the rotation  $\psi_\varphi(r, \varphi)$  in the vicinity of the corner is given by

$$\lim_{r \rightarrow 0} \psi_\varphi(r, \varphi) = \lim_{r \rightarrow 0} k_s B_{30} Y_1(k_s r) = \text{finite}, \quad (\text{D.5})$$

which leads to  $B_{30} = 0$ . For  $\lambda_k^s = 0$ , the rotation  $\psi_\varphi(r, \varphi)$  is identical to zero and the regularity condition for the rotation  $\psi_r(r, \varphi)$  simplifies to

$$\lim_{r \rightarrow 0} -(\mu_1 - 1) k_{f1} B_{10} Y_1(k_{f1} r) - (\mu_2 - 1) k_{f2} B_{20} Y_1(k_{f2} r) = \text{finite}. \quad (\text{D.6})$$

Using the series representation of the Bessel function of the second kind in Equation (D.6) leads to the condition  $(\mu_1 - 1) B_{10} + (\mu_2 - 1) B_{20} = 0$  (coefficient of  $r^{-1}$  has to be equal to zero). Combining this condition with the relation derived for the out-of-plane displacement leads to the trivial result  $B_{10} = B_{20} = 0$ , since more than one linear independent equation has to be fulfilled.

**Case II:**  $\lambda = \{1, 2, \dots\}$

In this case, the two regularity conditions for the rotations (Equations (6.12) and (6.13)) can be simplified to

$$\begin{aligned} \lim_{r \rightarrow 0} \psi_r(r, \varphi) &= \lim_{r \rightarrow 0} \frac{(\mu_1 - 1) k_{f1} B_{1\lambda}}{2} (Y_{\lambda-1}(k_{f1} r) - Y_{\lambda+1}(k_{f1} r)) \\ &+ \frac{(\mu_2 - 1) k_{f2} B_{2\lambda}}{2} (Y_{\lambda-1}(k_{f2} r) - Y_{\lambda+1}(k_{f2} r)) - \frac{\lambda B_{3\lambda}}{r} Y_\lambda(k_s r) = \text{finite}, \end{aligned} \quad (\text{D.7})$$

$$\begin{aligned} \lim_{r \rightarrow 0} \psi_\varphi(r, \varphi) &= \lim_{r \rightarrow 0} \frac{(\mu_1 - 1) \lambda B_{1\lambda}}{r} Y_\lambda(k_{f1} r) + \frac{(\mu_2 - 1) \lambda B_{2\lambda}}{r} Y_\lambda(k_{f2} r) \\ &- \frac{k_s B_{3\lambda}}{2} (Y_{\lambda-1}(k_s r) - Y_{\lambda+1}(k_s r)) = \text{finite}. \end{aligned} \quad (\text{D.8})$$

Inserting Equations (D.1) and (6.18) into the simplified forms and using Equations (6.14) and (D.3) results in the trivial solution  $B_{1\lambda} = B_{2\lambda} = B_{3\lambda} = 0$ .

All cases therefore conclude that  $B_{1\lambda} = B_{2\lambda} = B_{3\lambda} = 0$  for  $\lambda \in \mathbb{N}_0$  and  $A_{i\lambda}$  ( $i = \{1, 2, 3\}$ ) can be chosen arbitrary.

## **E Additional results for the validation examples**

In this appendix all contour plots, absolute error plots compared to the reference solution, convergence curves of the WBM with respect to the total number of degrees of freedom and the convergence curves of the WBM compared to the FEM with respect to the calculation time, which are not shown in Section 6.4, are presented. For a detailed discussion of the results for the single domain problems (clamped, free, cantilever and simply-supported plate), the reader is referred to Section 6.4.1 and for the results of the multi domain clamped plate to Section 6.4.2.

**Single domain clamped plate**

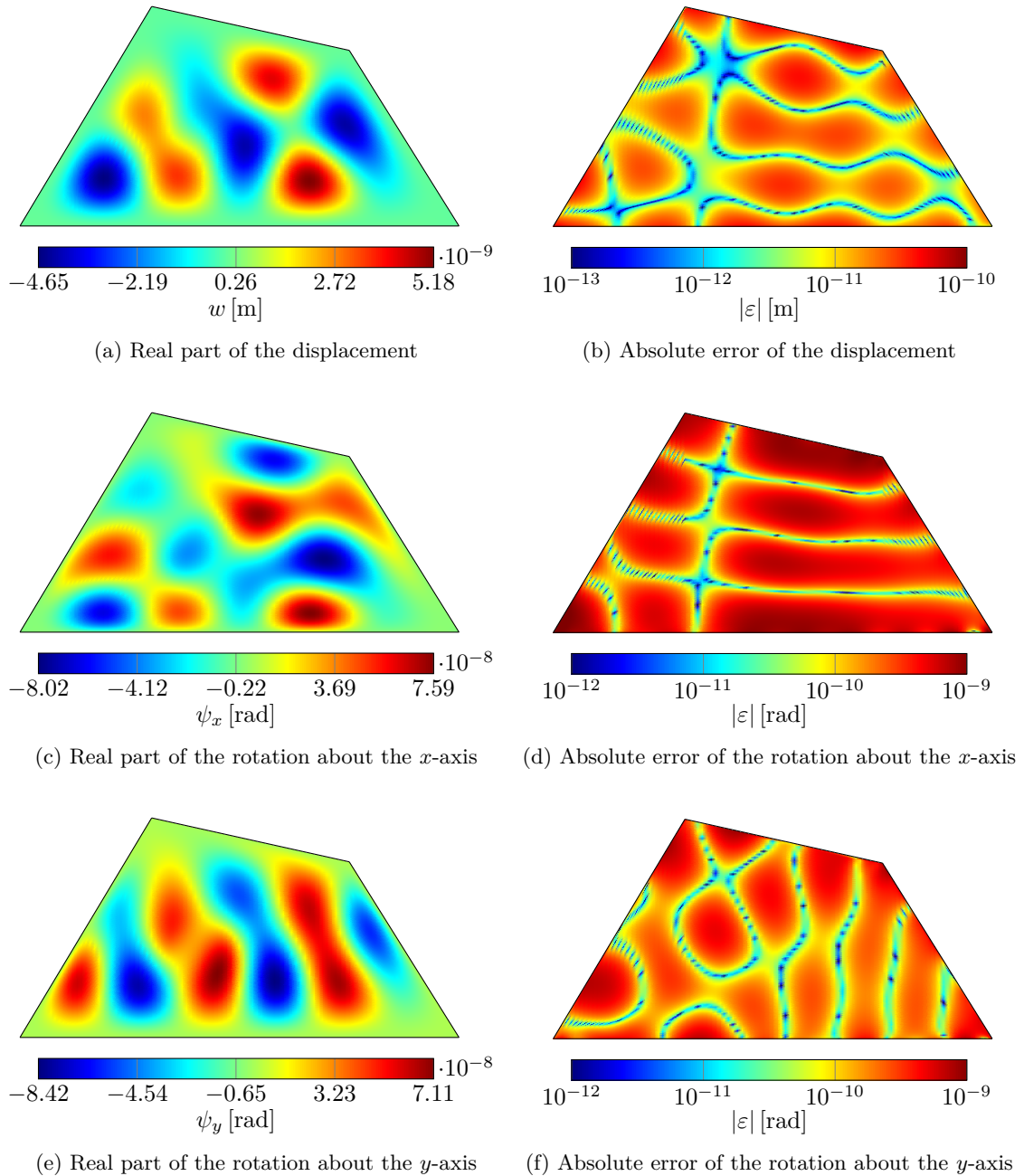


Figure E.1: Out-of-plane displacement and rotations about the  $x$ - and  $y$ -axis of a clamped plate ( $h = 0.005$  m) excited by an alternating circular load at 850 Hz calculated with the original WBM using only the function set 1 and a truncation factor  $T = 2$

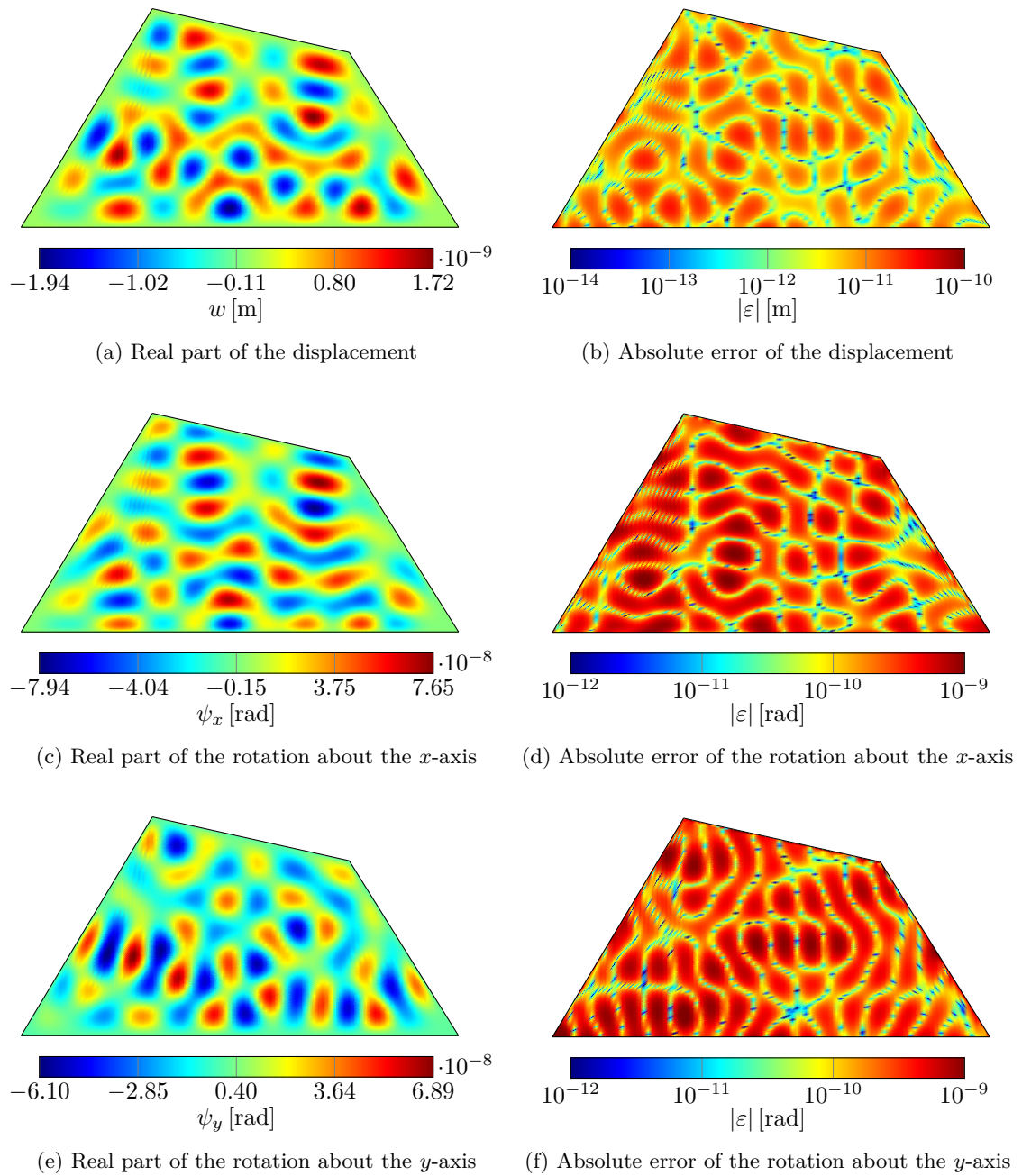


Figure E.2: Out-of-plane displacement and rotations about the  $x$ - and  $y$ -axis of a clamped plate ( $h = 0.005$  m) excited by an alternating circular load at 4195 Hz calculated with the original WBM using only the function set 1 and a truncation factor  $T = 2$

E Additional results for the validation examples

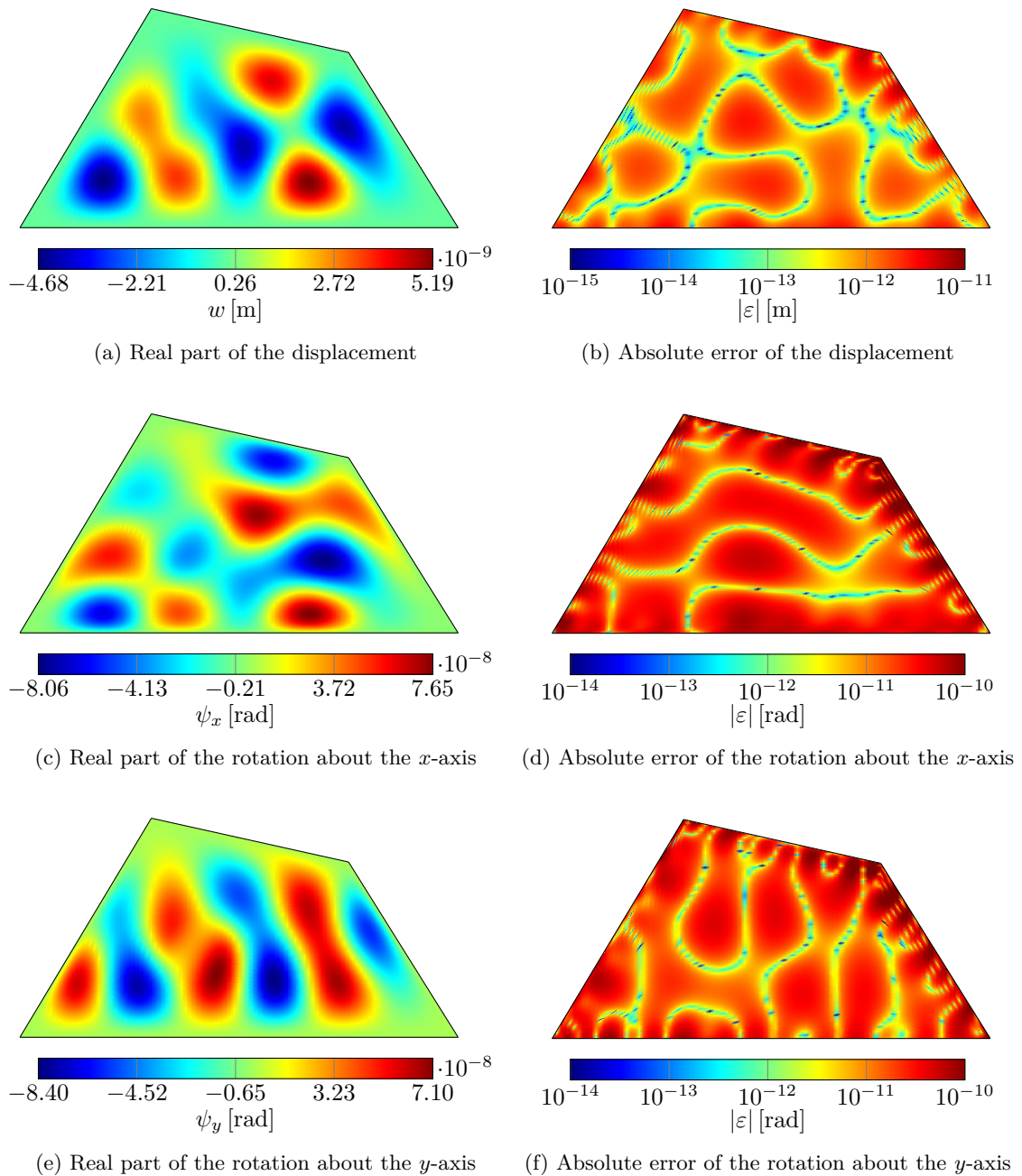


Figure E.3: Out-of-plane displacement and rotations about the  $x$ - and  $y$ -axis of a clamped plate ( $h = 0.005$  m) excited by an alternating circular load at 850 Hz calculated with the modified WBM using only the function set 1 and a truncation factor  $T = 2$

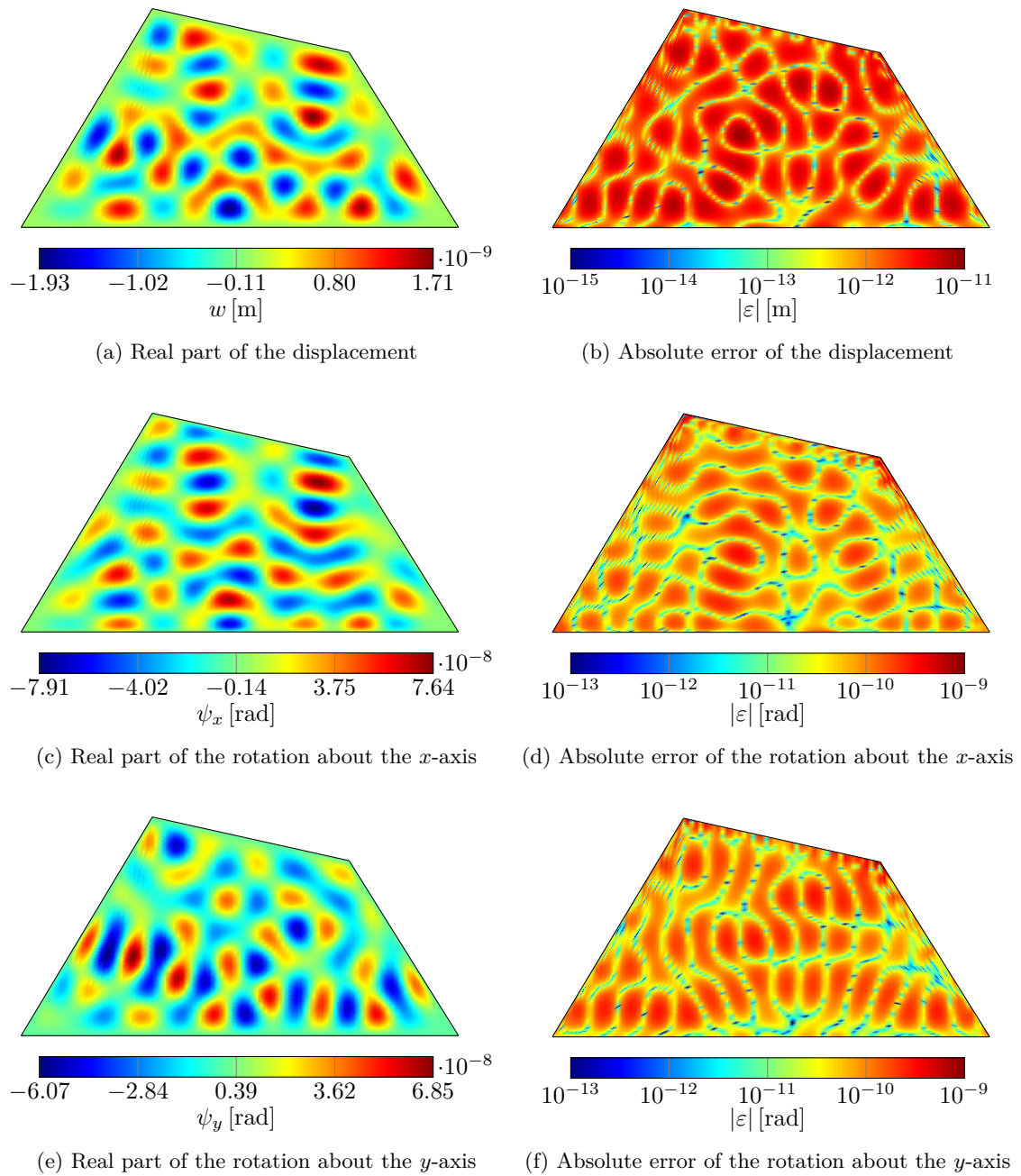


Figure E.4: Out-of-plane displacement and rotations about the  $x$ - and  $y$ -axis of a clamped plate ( $h = 0.005$  m) excited by an alternating circular load at 4195 Hz calculated with the modified WBM using only the function set 1 and a truncation factor  $T = 2$

E Additional results for the validation examples

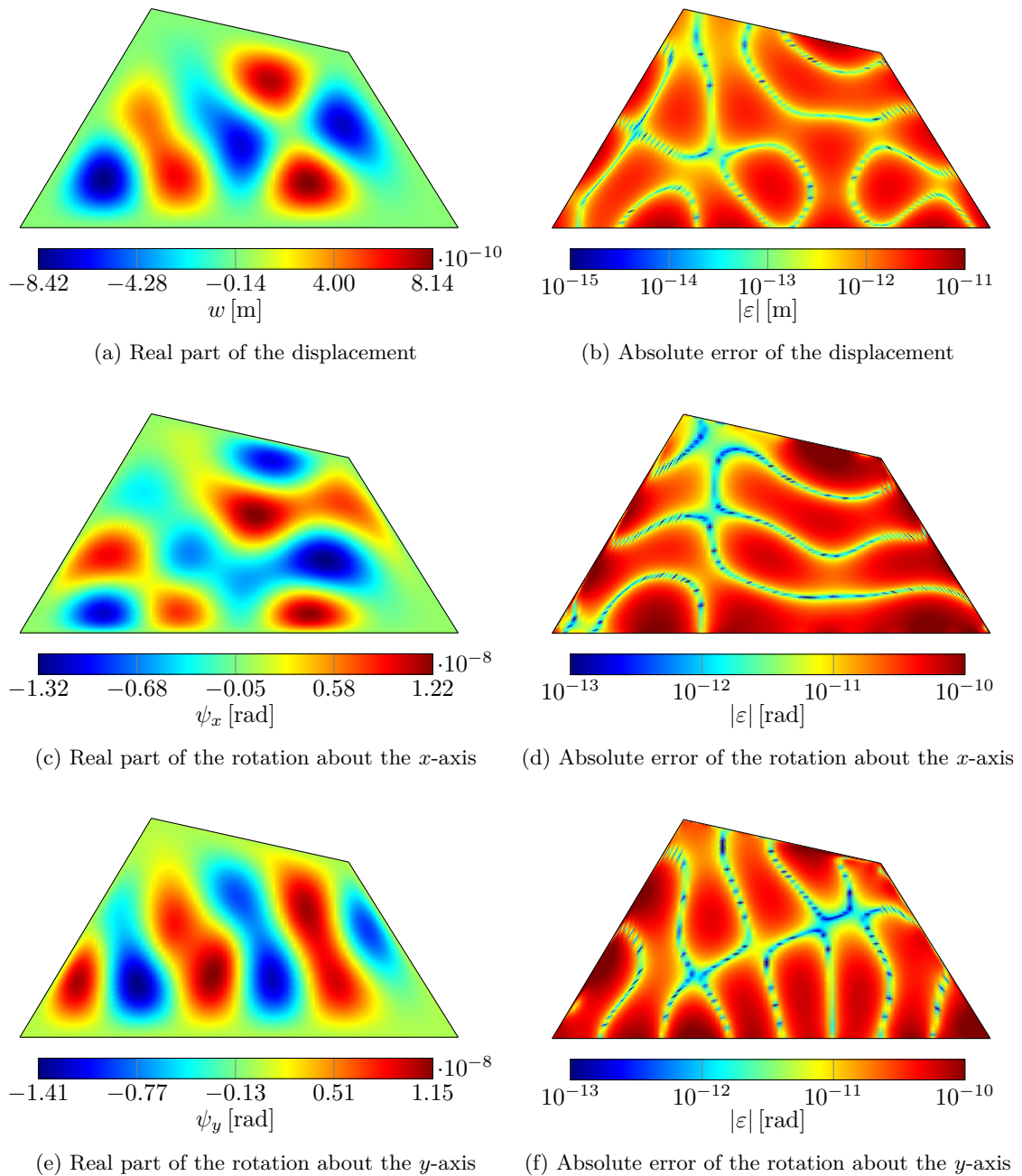


Figure E.5: Out-of-plane displacement and rotations about the  $x$ - and  $y$ -axis of a clamped plate ( $h = 0.01$  m) excited by an alternating circular load at 1650 Hz calculated with the original WBM using only the function set 1 and a truncation factor  $T = 2$

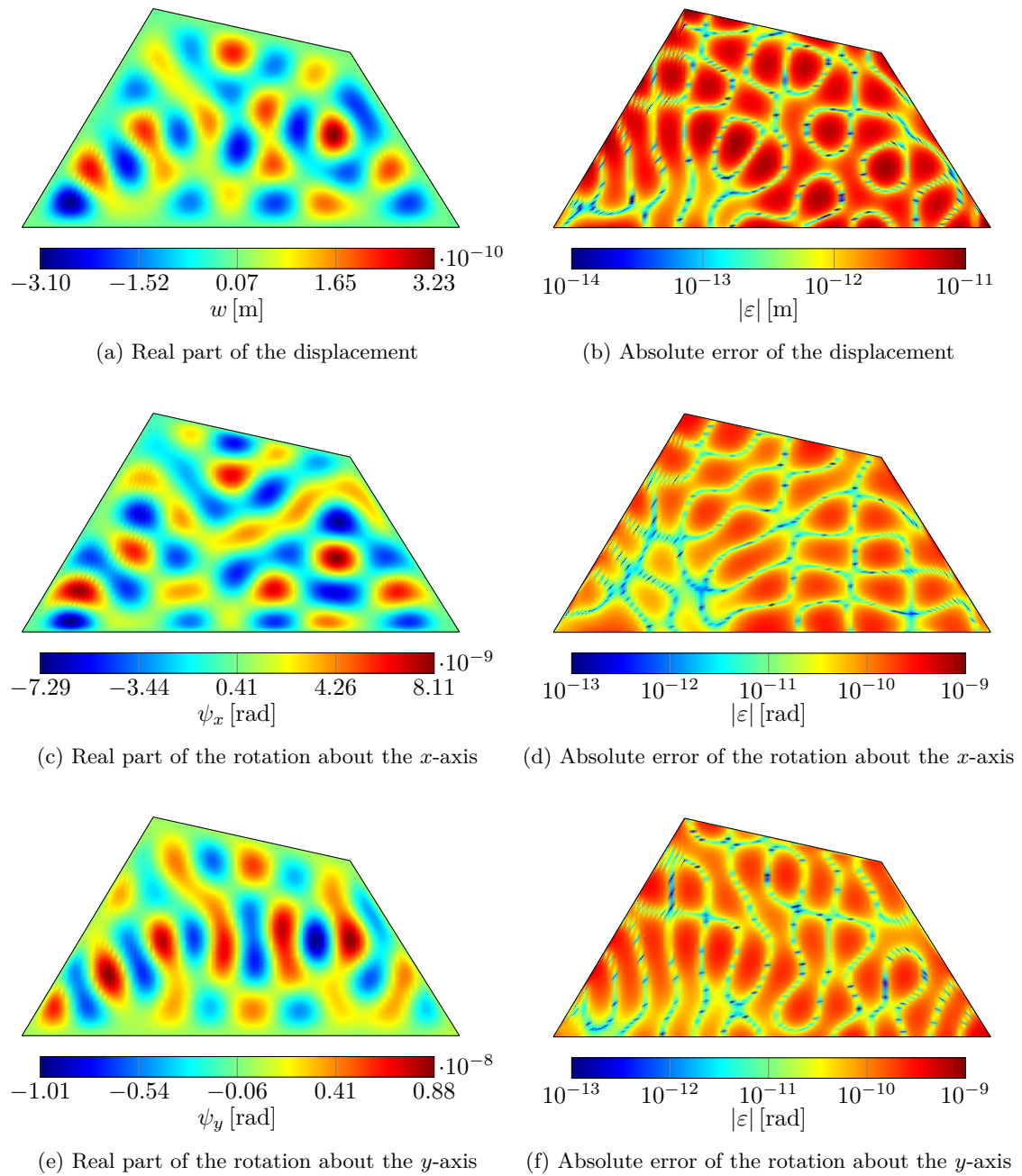


Figure E.6: Out-of-plane displacement and rotations about the  $x$ - and  $y$ -axis of a clamped plate ( $h = 0.01$  m) excited by an alternating circular load at 5080 Hz calculated with the original WBM using only the function set 1 and a truncation factor  $T = 2$

E Additional results for the validation examples

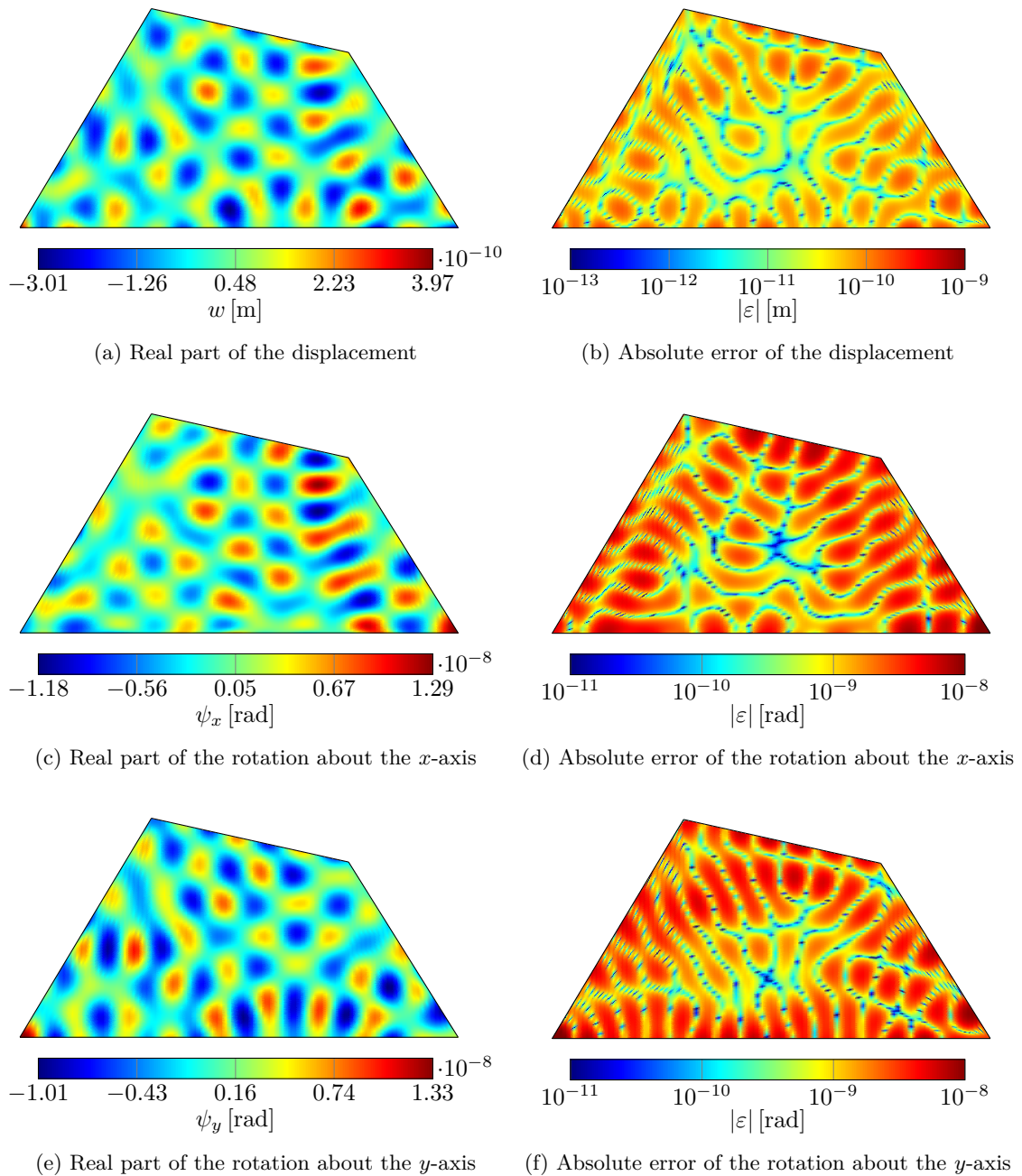


Figure E.7: Out-of-plane displacement and rotations about the  $x$ - and  $y$ -axis of a clamped plate ( $h = 0.01$  m) excited by an alternating circular load at 8000 Hz calculated with the original WBM using only the function set 1 and a truncation factor  $T = 2$

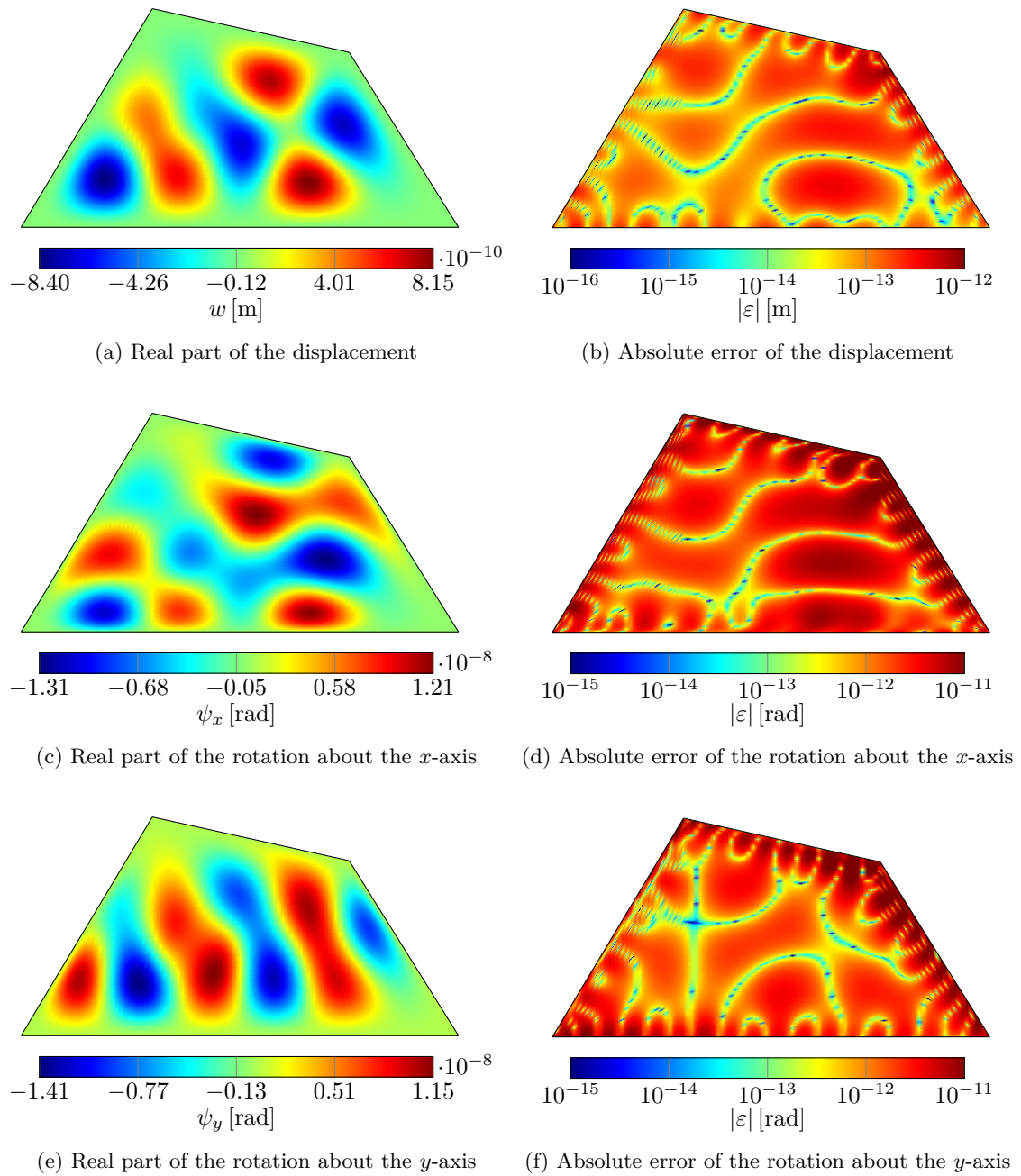


Figure E.8: Out-of-plane displacement and rotations about the  $x$ - and  $y$ -axis of a clamped plate ( $h = 0.01$  m) excited by an alternating circular load at 1650 Hz calculated with the modified WBM using only the function set 1 and a truncation factor  $T = 2$

E Additional results for the validation examples

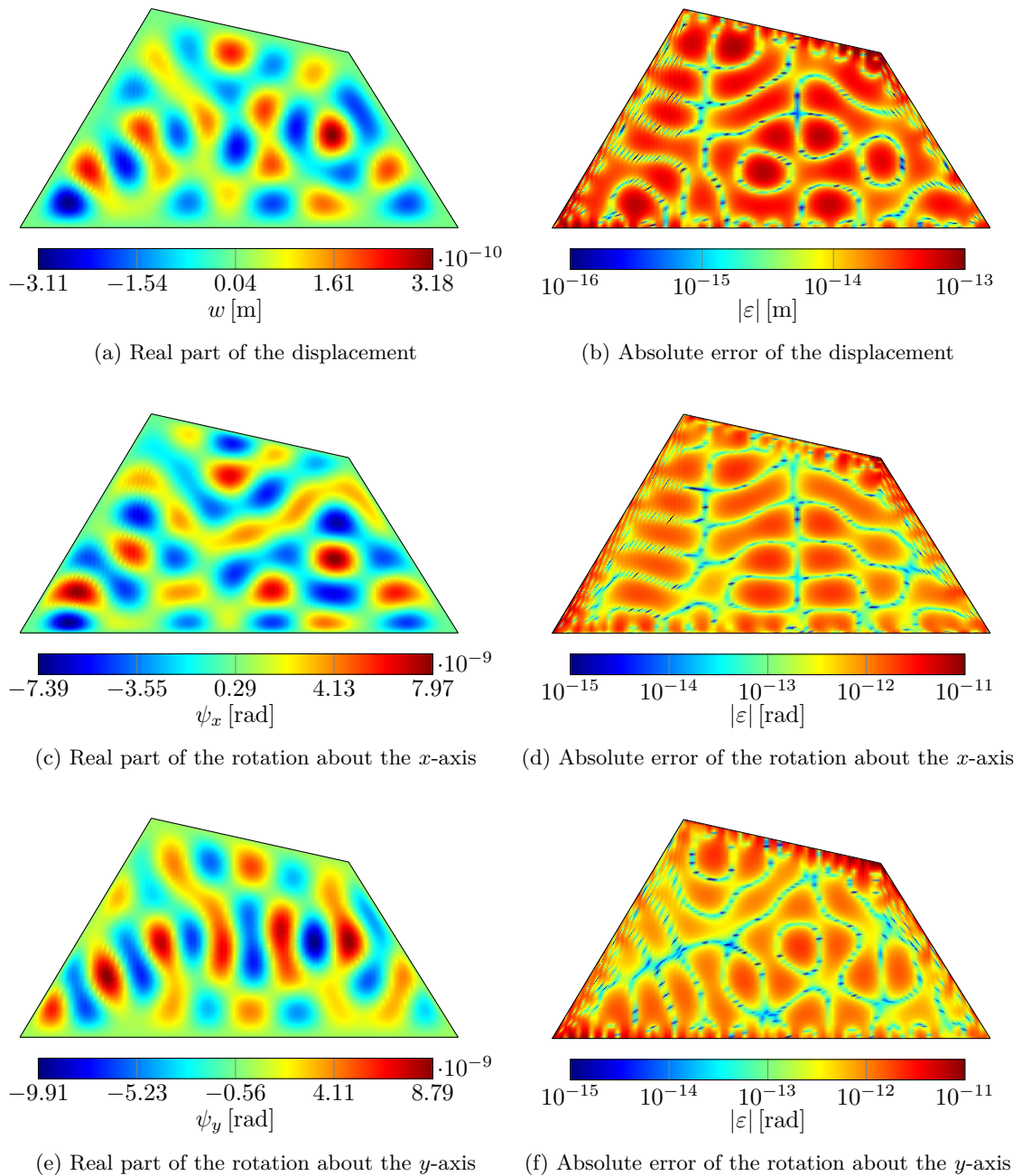


Figure E.9: Out-of-plane displacement and rotations about the  $x$ - and  $y$ -axis of a clamped plate ( $h = 0.01$  m) excited by an alternating circular load at 5080 Hz calculated with the modified WBM using only the function set 1 and a truncation factor  $T = 2$

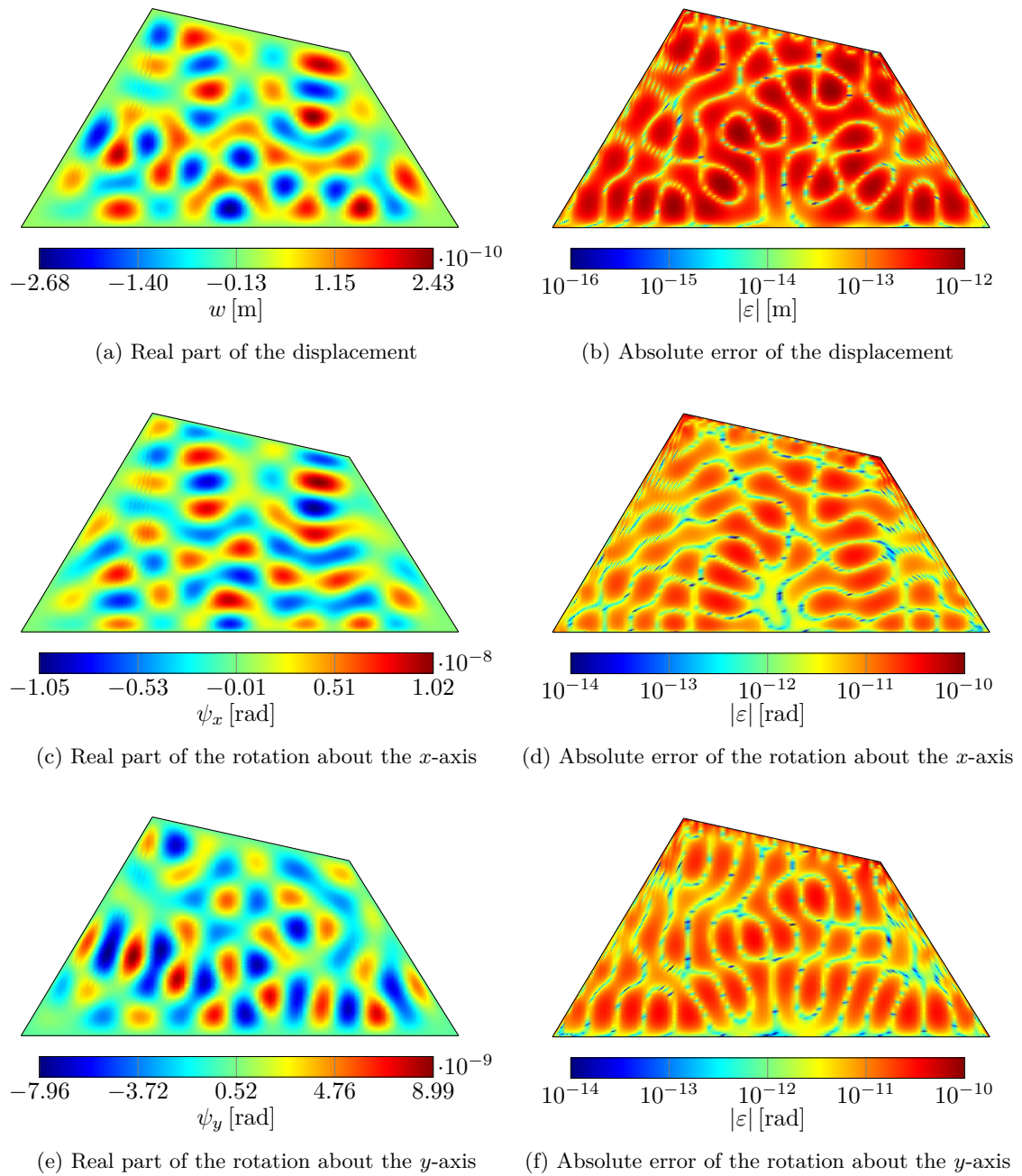


Figure E.10: Out-of-plane displacement and rotations about the  $x$ - and  $y$ -axis of a clamped plate ( $h = 0.01$  m) excited by an alternating circular load at 8000 Hz calculated with the modified WBM using only the function set 1 and a truncation factor  $T = 2$

E Additional results for the validation examples

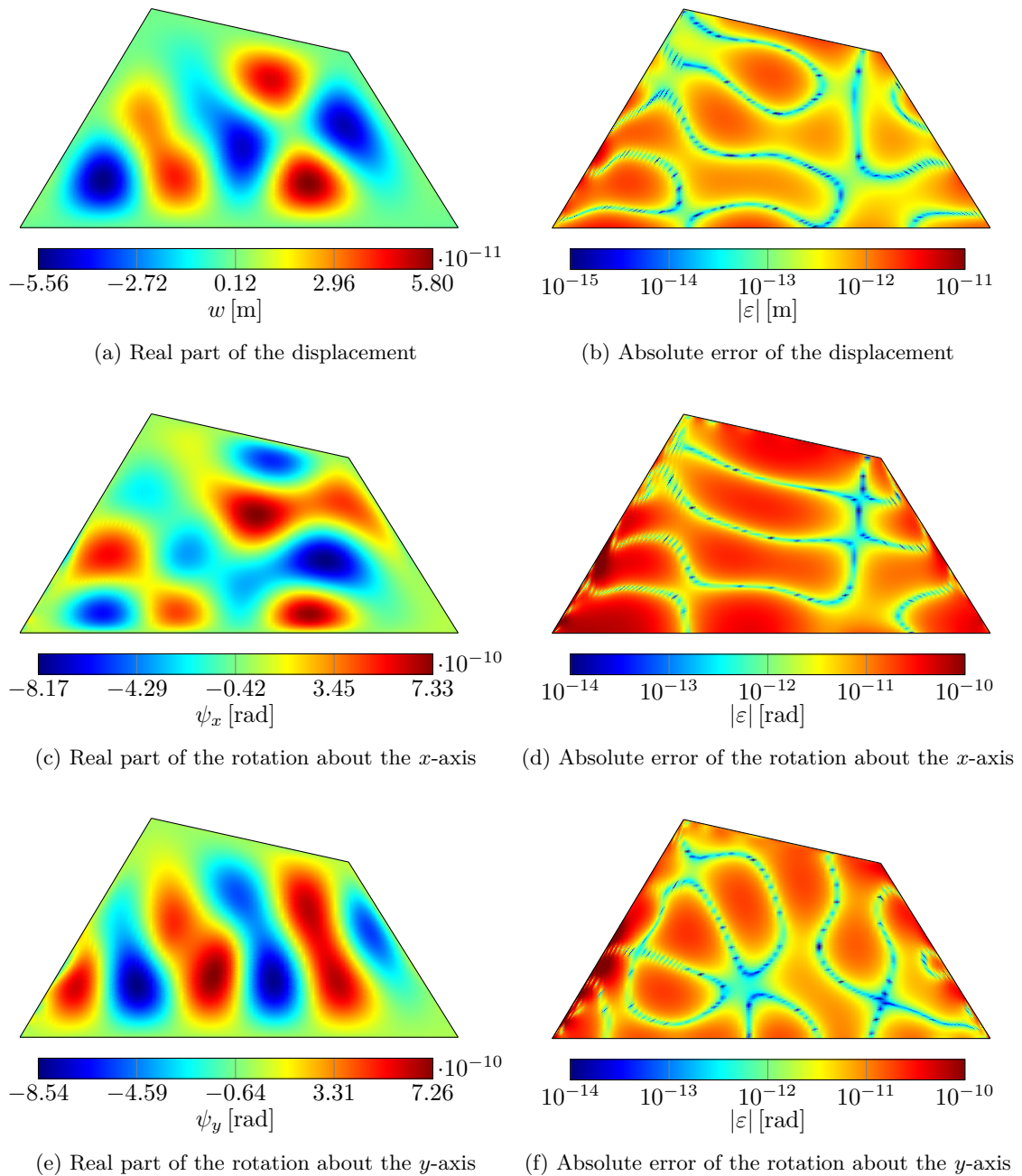


Figure E.11: Out-of-plane displacement and rotations about the  $x$ - and  $y$ -axis of a clamped plate ( $h = 0.025$  m) excited by an alternating circular load at 3850 Hz calculated with the original WBM using only the function set 1 and a truncation factor  $T = 2$

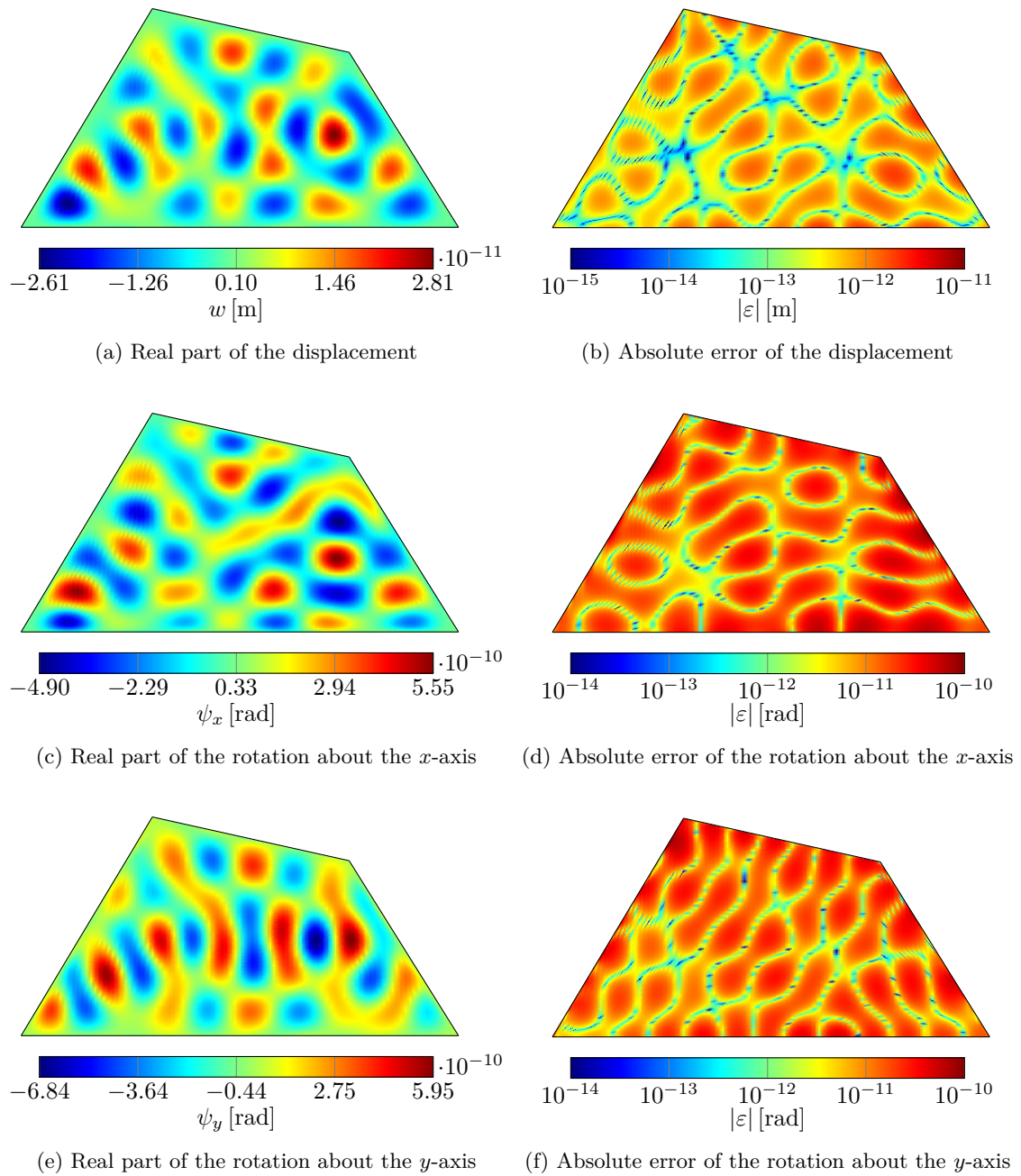


Figure E.12: Out-of-plane displacement and rotations about the  $x$ - and  $y$ -axis of a clamped plate ( $h = 0.025$  m) excited by an alternating circular load at 10700 Hz calculated with the original WBM using only the function set 1 and a truncation factor  $T = 2$

E Additional results for the validation examples

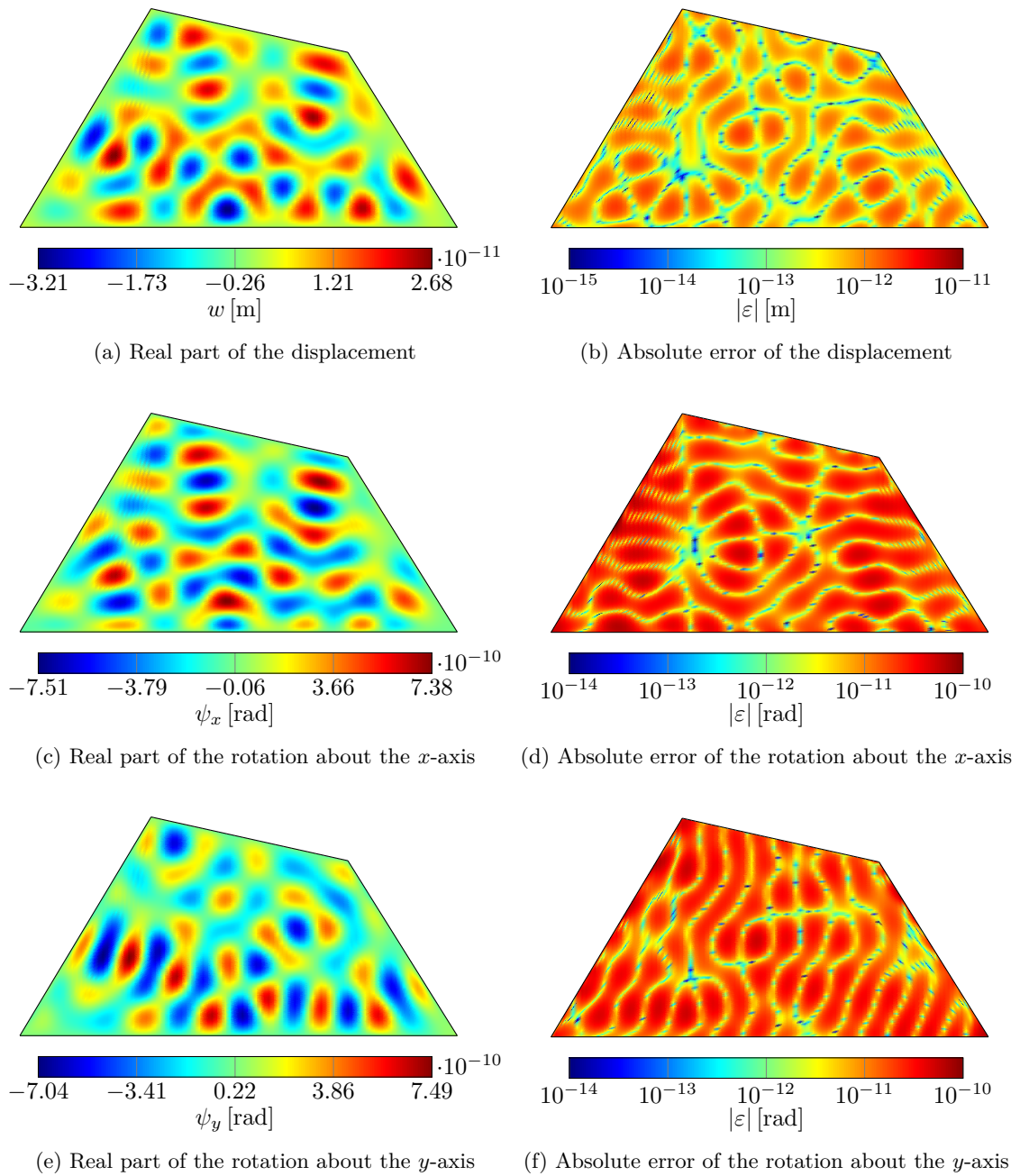


Figure E.13: Out-of-plane displacement and rotations about the  $x$ - and  $y$ -axis of a clamped plate ( $h = 0.025$  m) excited by an alternating circular load at 15870 Hz calculated with the original WBM using only the function set 1 and a truncation factor  $T = 2$

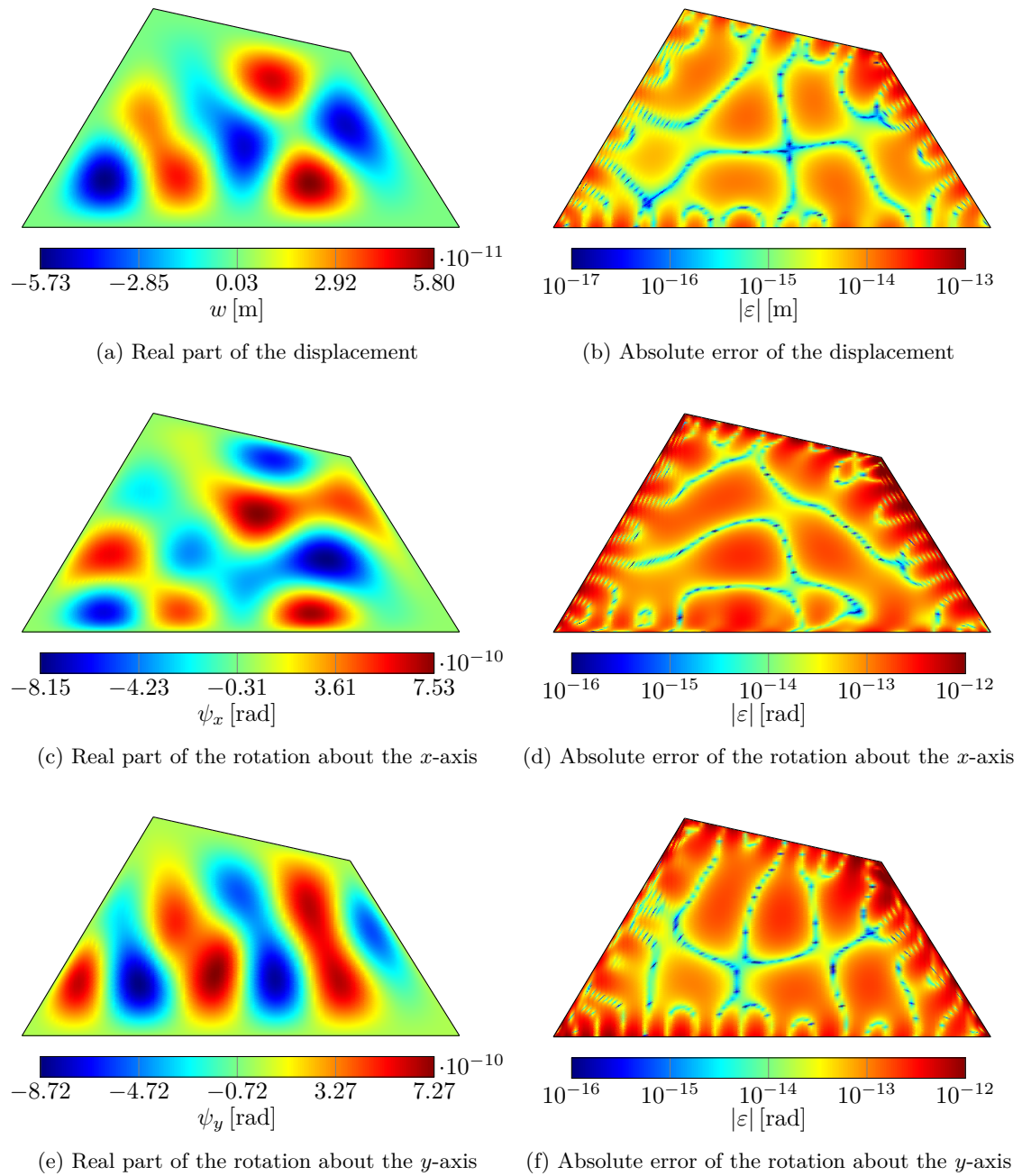


Figure E.14: Out-of-plane displacement and rotations about the  $x$ - and  $y$ -axis of a clamped plate ( $h = 0.025$  m) excited by an alternating circular load at 3850 Hz calculated with the modified WBM using only the function set 1 and a truncation factor  $T = 2$

E Additional results for the validation examples

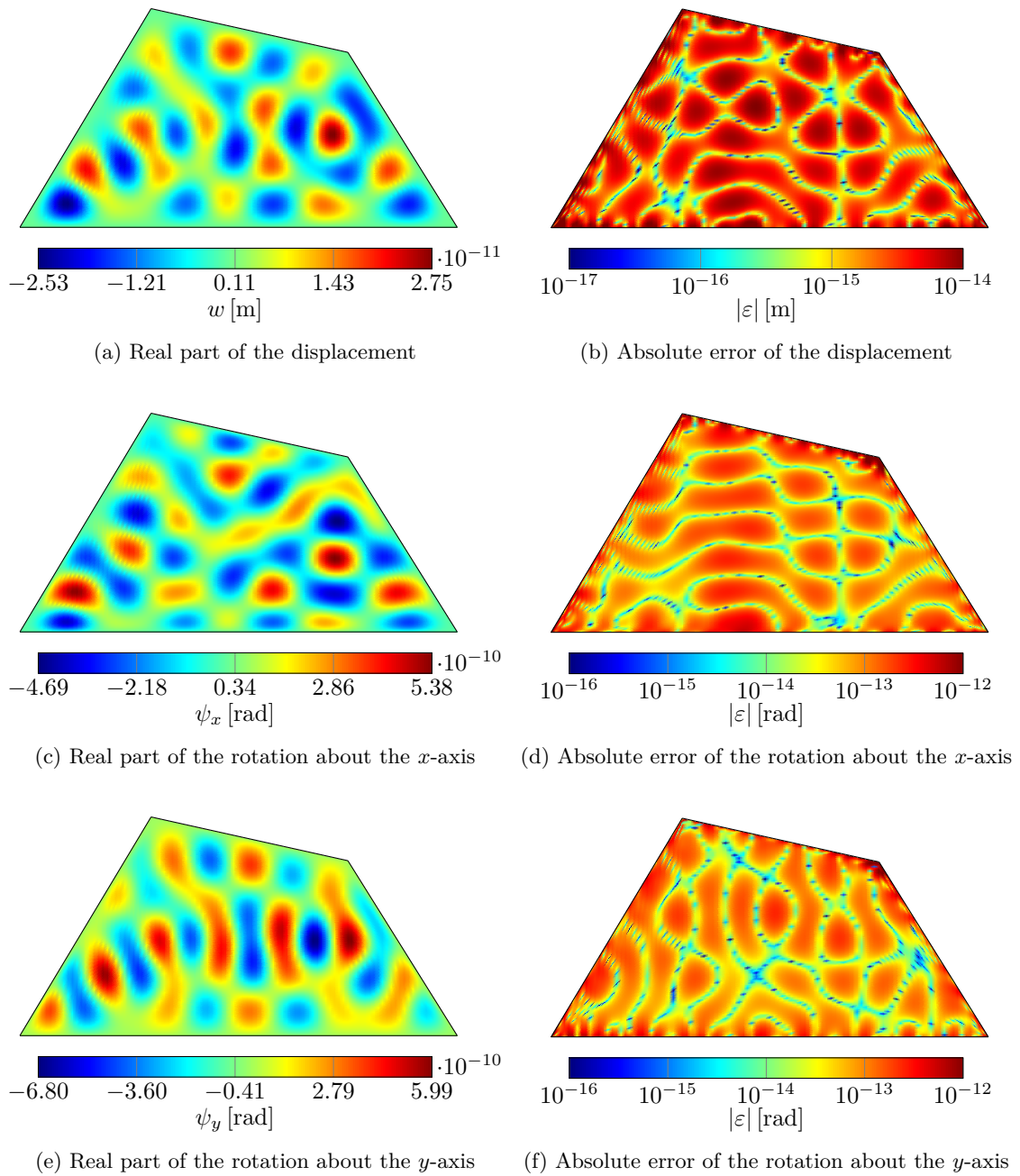


Figure E.15: Out-of-plane displacement and rotations about the  $x$ - and  $y$ -axis of a clamped plate ( $h = 0.025$  m) excited by an alternating circular load at 10700 Hz calculated with the modified WBM using only the function set 1 and a truncation factor  $T = 2$

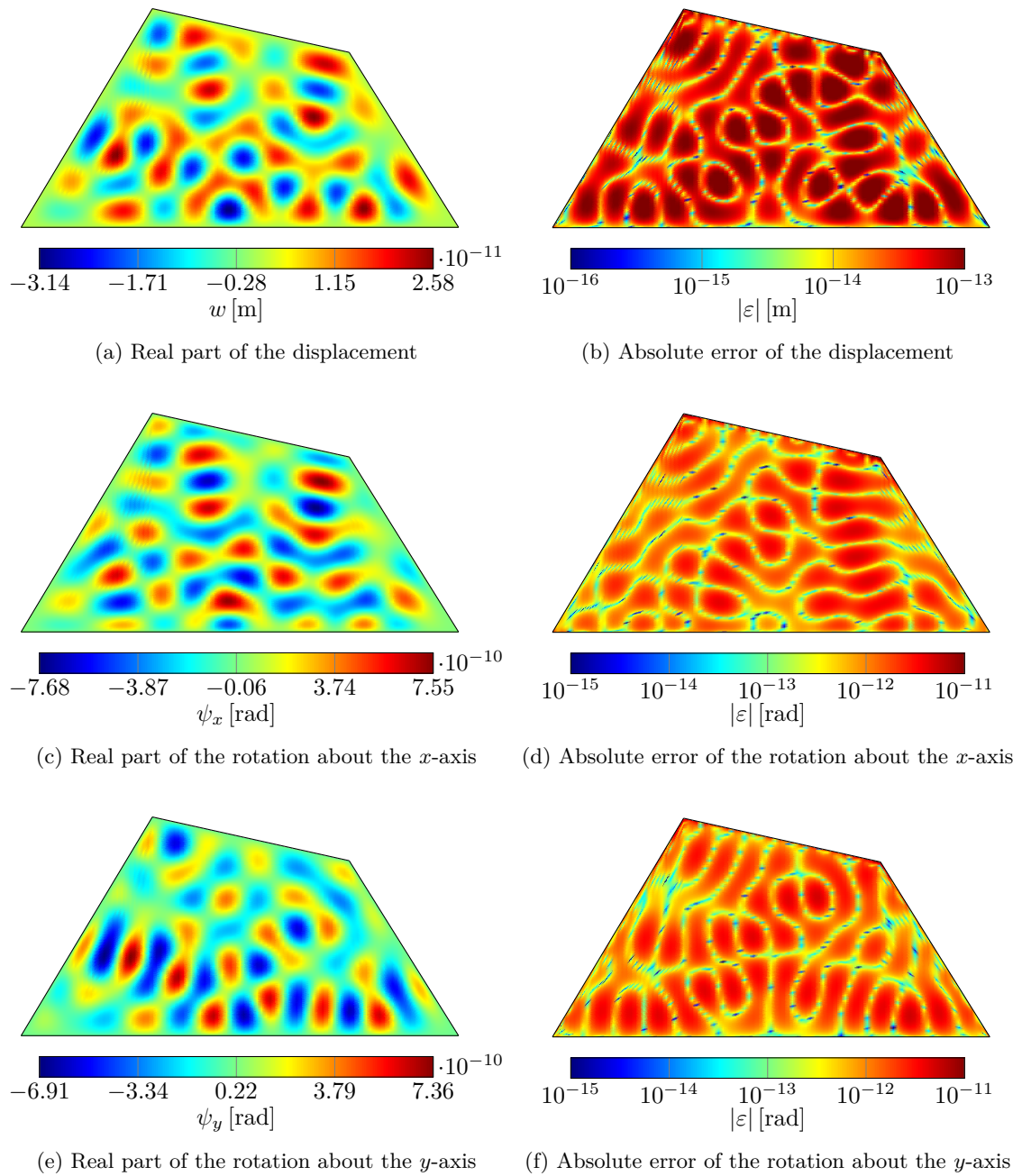


Figure E.16: Out-of-plane displacement and rotations about the  $x$ - and  $y$ -axis of a clamped plate ( $h = 0.025$  m) excited by an alternating circular load at 15870 Hz calculated with the modified WBM using only the function set 1 and a truncation factor  $T = 2$

E Additional results for the validation examples

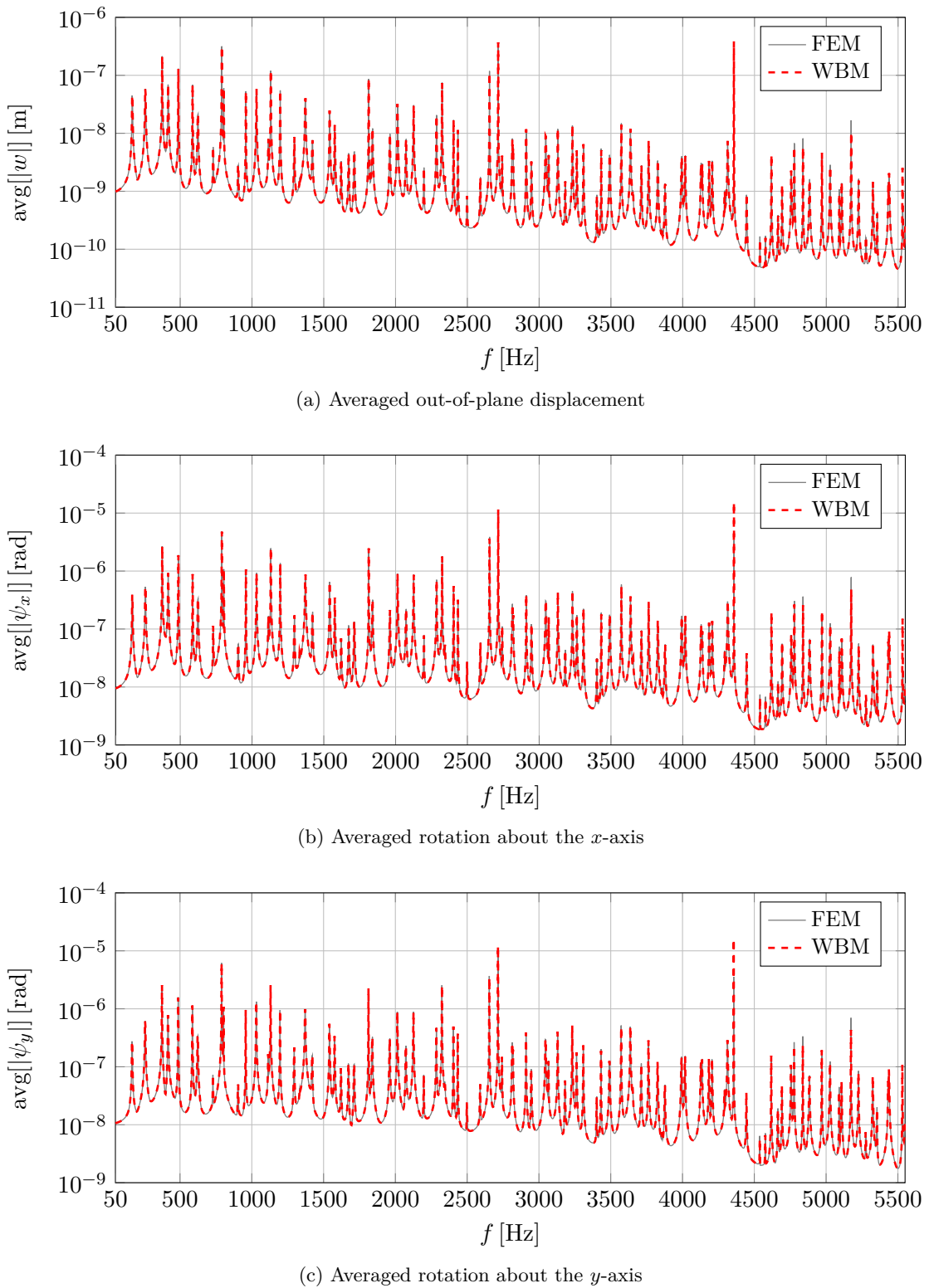
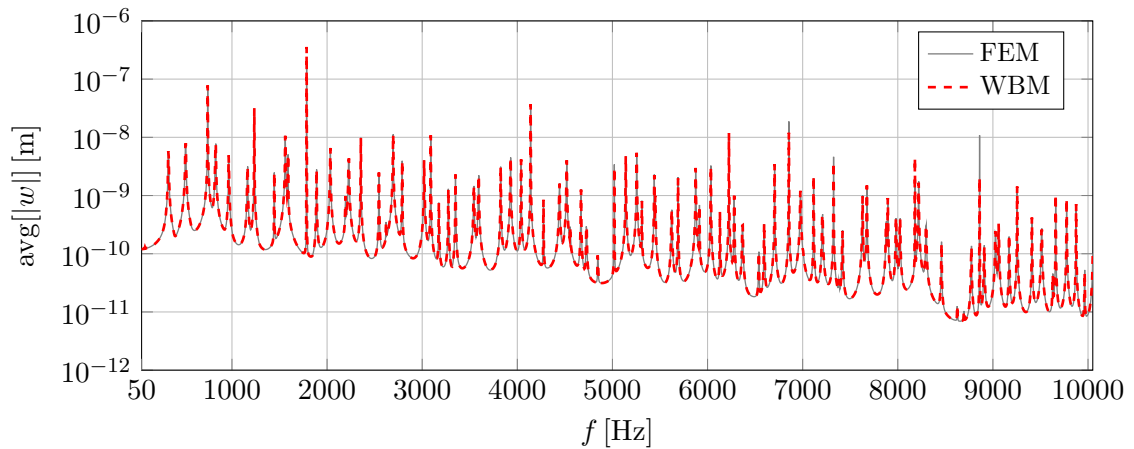
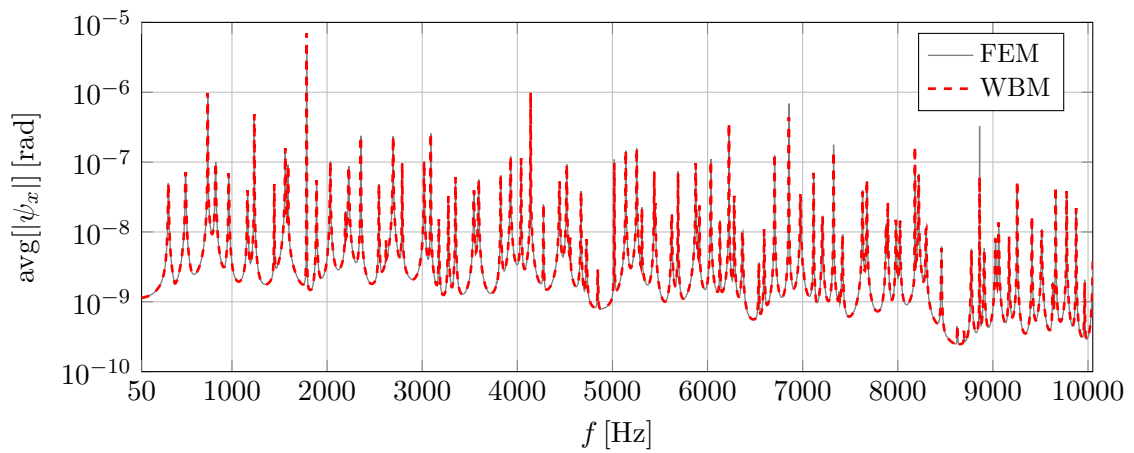


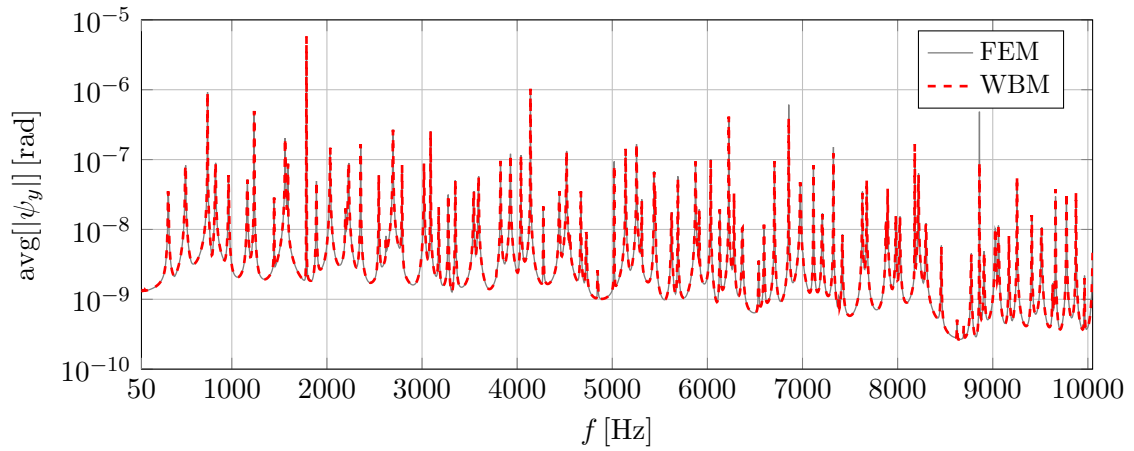
Figure E.17: Frequency response functions of a clamped plate ( $h = 0.005$  m) excited by an alternating circular load calculated with the FEM (reference mesh) and the modified WBM (function set 1 and set 2,  $T = 2$ )



(a) Averaged out-of-plane displacement



(b) Averaged rotation about the  $x$ -axis



(c) Averaged rotation about the  $y$ -axis

Figure E.18: Frequency response functions of a clamped plate ( $h = 0.01 \text{ m}$ ) excited by an alternating circular load calculated with the FEM (reference mesh) and the modified WBM (function set 1 and set 2,  $T = 2$ )

## E Additional results for the validation examples

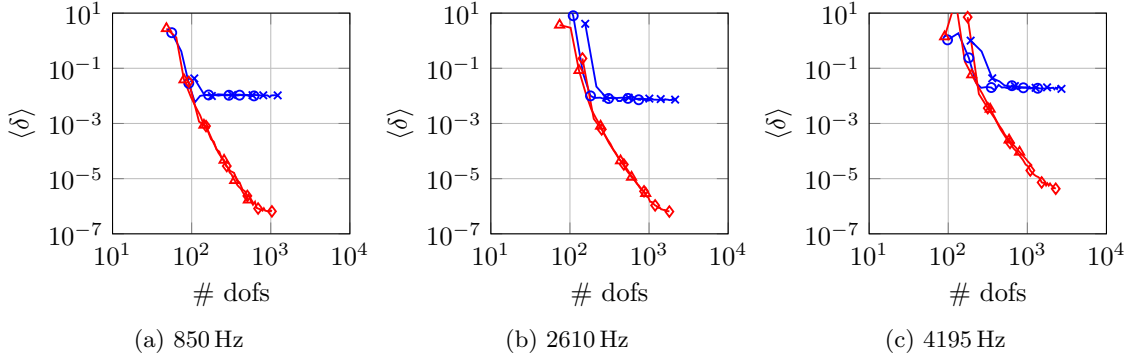


Figure E.19: Convergence curves of the out-of-plane displacement (clamped plate with  $h = 0.005$  m) for the original WBM (set1 (—○—), set1a2 (—\*—)) and the modified WBM (set1 (—▲—), set1a2 (—◆—))

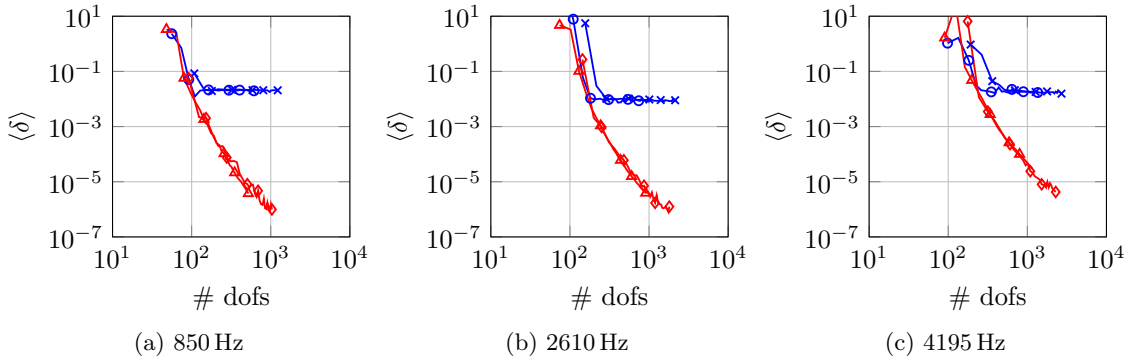


Figure E.20: Convergence curves of the rotation about the  $x$ -axis (clamped plate with  $h = 0.005$  m) for the original WBM (set1 (—○—), set1a2 (—\*—)) and the modified WBM (set1 (—▲—), set1a2 (—◆—))

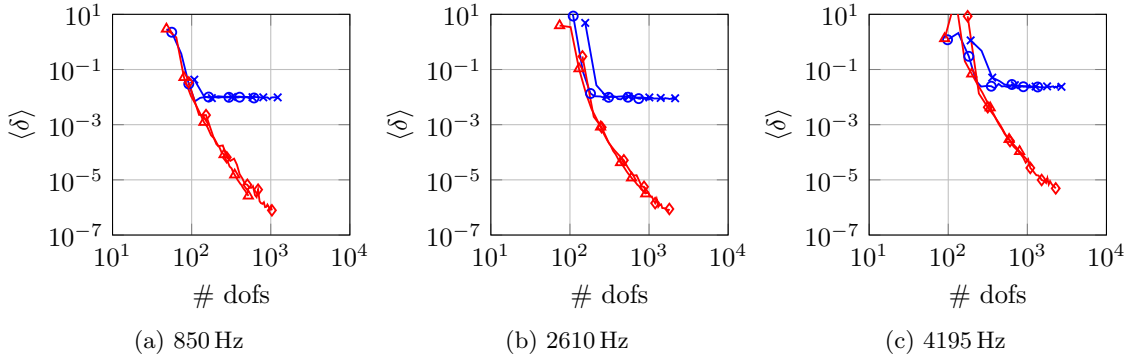


Figure E.21: Convergence curves of the rotation about the  $y$ -axis (clamped plate with  $h = 0.005$  m) for the original WBM (set1 (—○—), set1a2 (—\*—)) and the modified WBM (set1 (—▲—), set1a2 (—◆—))

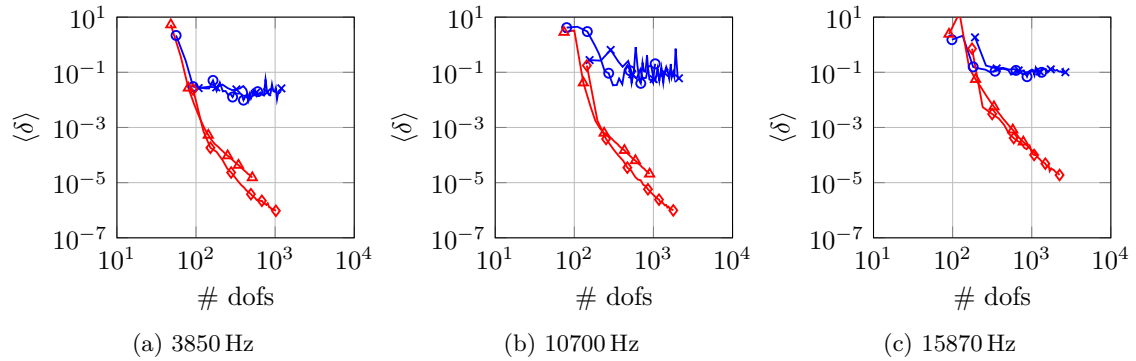


Figure E.22: Convergence curves of the out-of-plane displacement (clamped plate with  $h = 0.025$  m) for the original WBM (set1 (—○—), set1a2 (—\*—)) and the modified WBM (set1 (—▲—), set1a2 (—◆—))

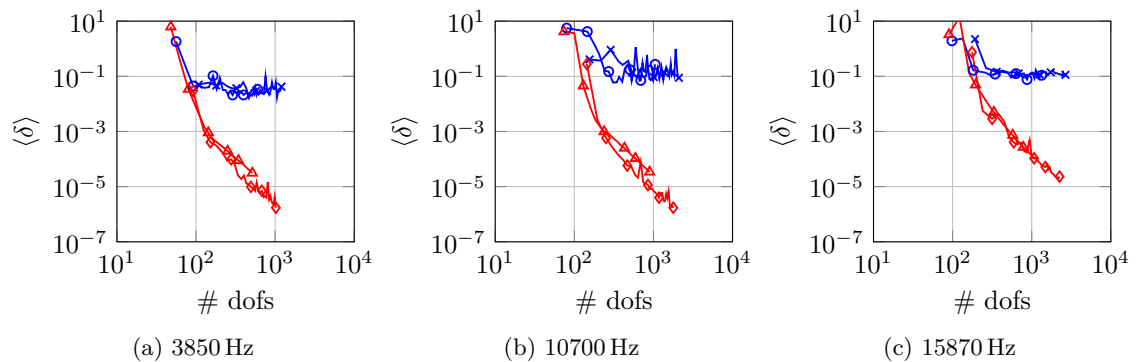


Figure E.23: Convergence curves of the rotation about the  $x$ -axis (clamped plate with  $h = 0.025$  m) for the original WBM (set1 (—○—), set1a2 (—\*—)) and the modified WBM (set1 (—▲—), set1a2 (—◆—))

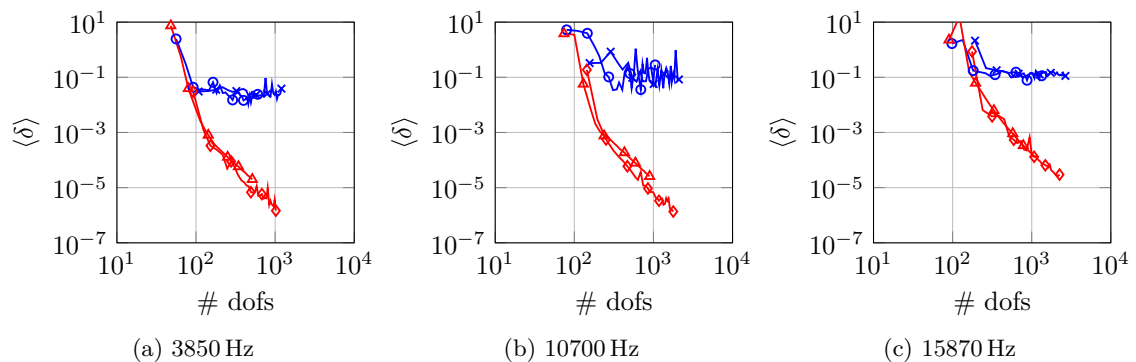


Figure E.24: Convergence curves of the rotation about the  $y$ -axis (clamped plate with  $h = 0.025$  m) for the original WBM (set1 (—○—), set1a2 (—\*—)) and the modified WBM (set1 (—▲—), set1a2 (—◆—))

**Single domain free plate**

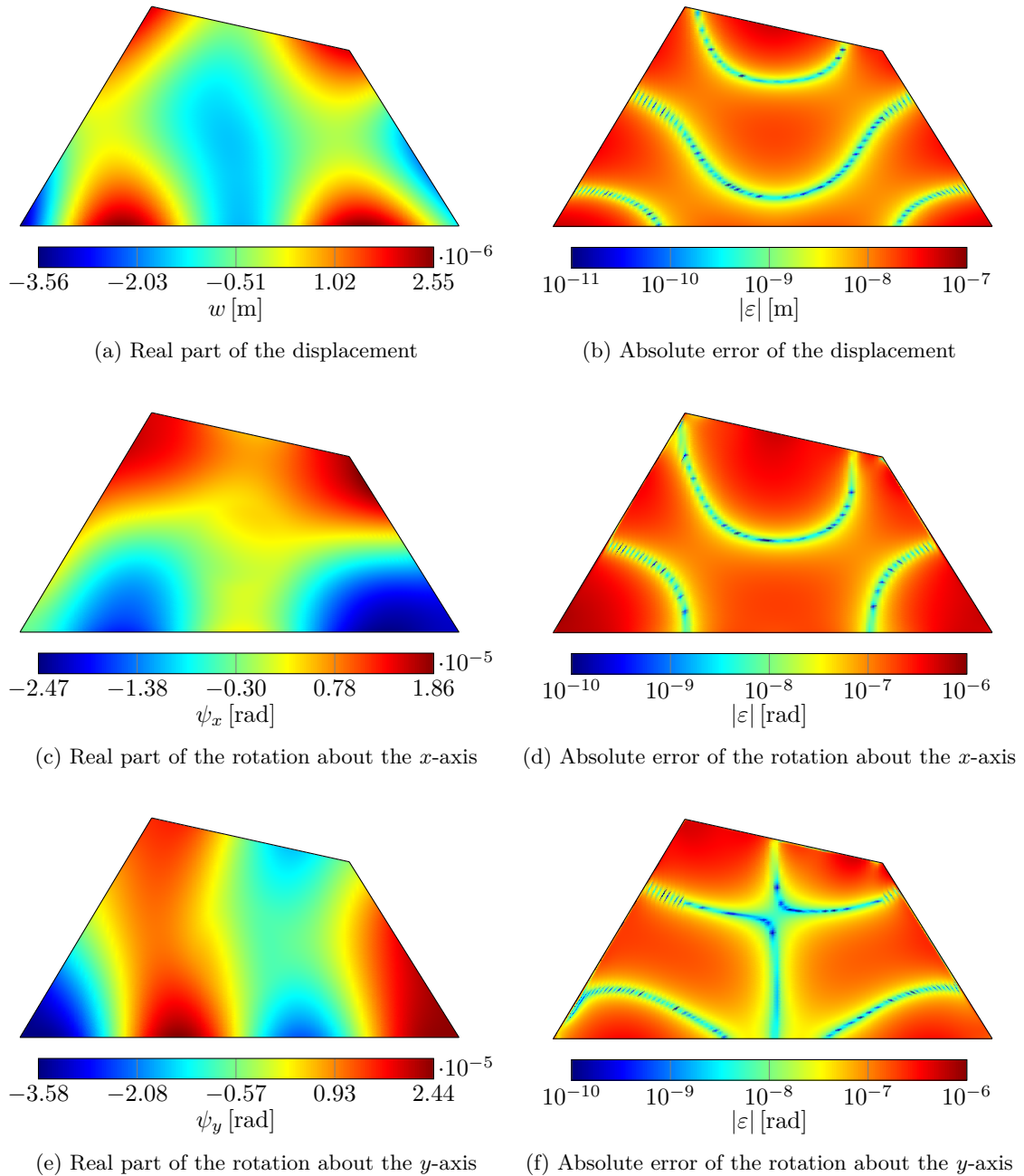


Figure E.25: Out-of-plane displacement and rotations about the  $x$ - and  $y$ -axis of a free plate ( $h = 0.005 \text{ m}$ ) excited by a constant ring load at 220 Hz calculated with the original WBM using only the function set 1 and a truncation factor  $T = 2$

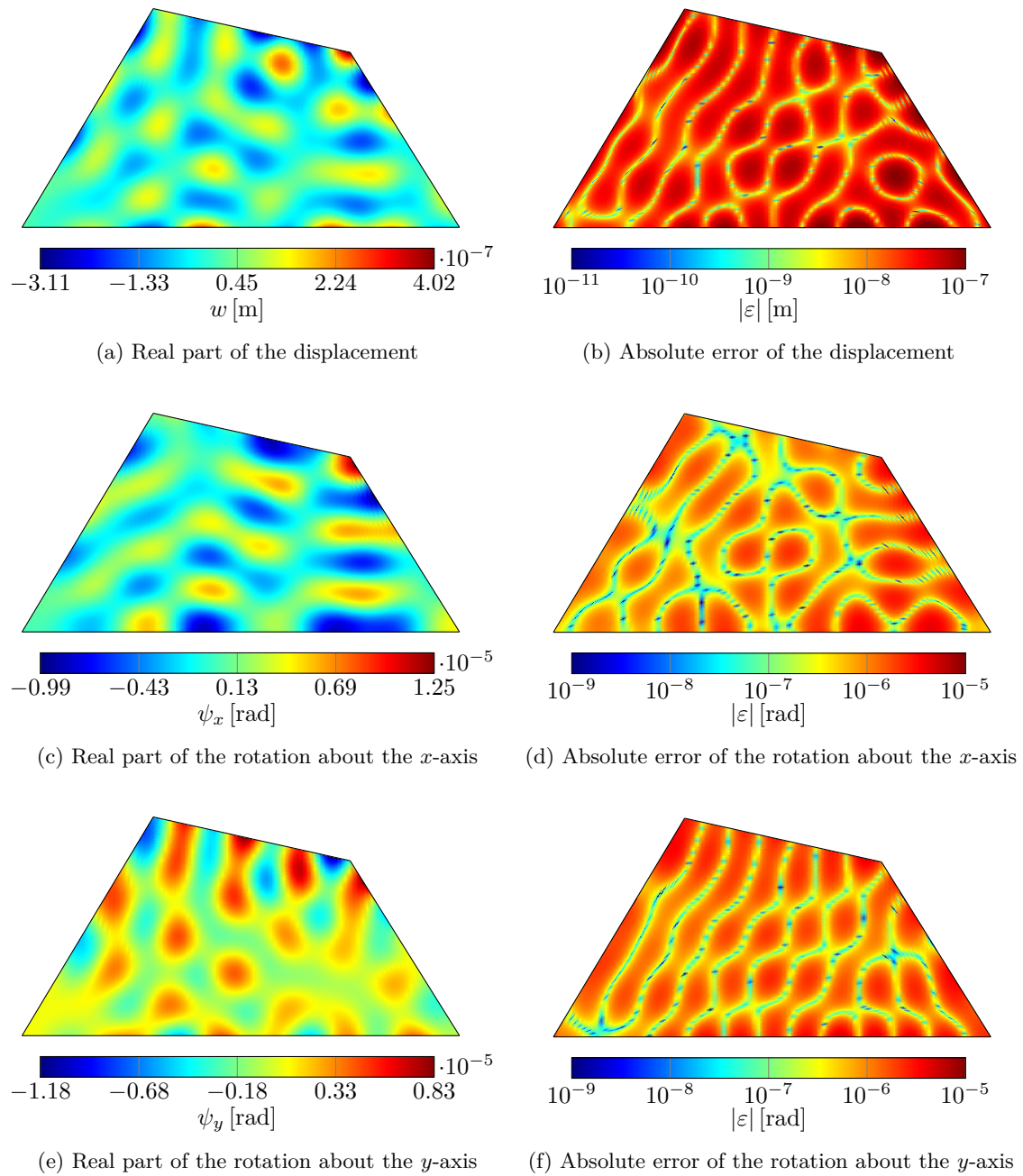


Figure E.26: Out-of-plane displacement and rotations about the  $x$ - and  $y$ -axis of a free plate ( $h = 0.005$  m) excited by a constant ring load at 2550 Hz calculated with the original WBM using only the function set 1 and a truncation factor  $T = 2$

E Additional results for the validation examples

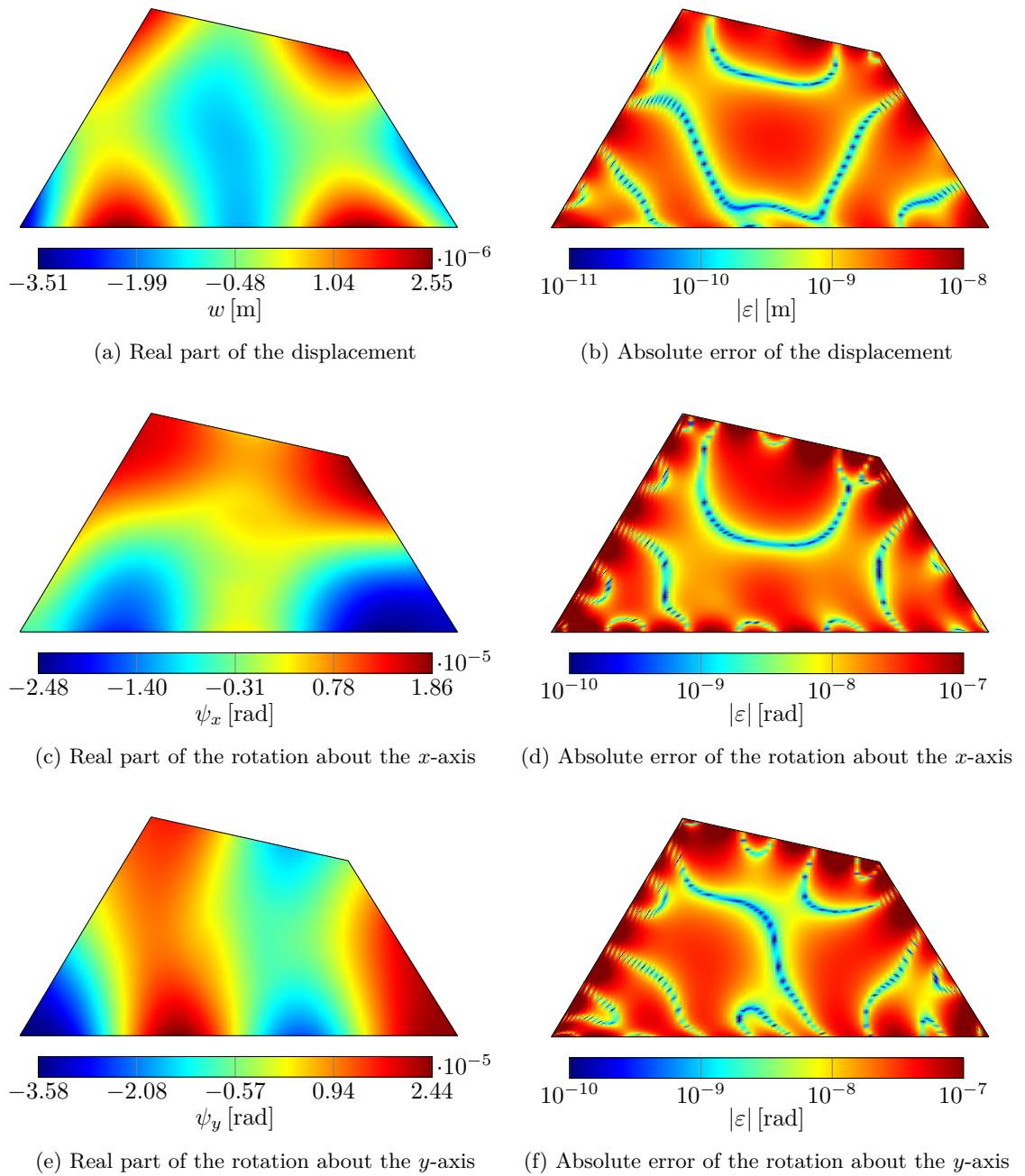


Figure E.27: Out-of-plane displacement and rotations about the  $x$ - and  $y$ -axis of a free plate ( $h = 0.005$  m) excited by a constant ring load at 220 Hz calculated with the modified WBM using only the function set 1 and a truncation factor  $T = 2$

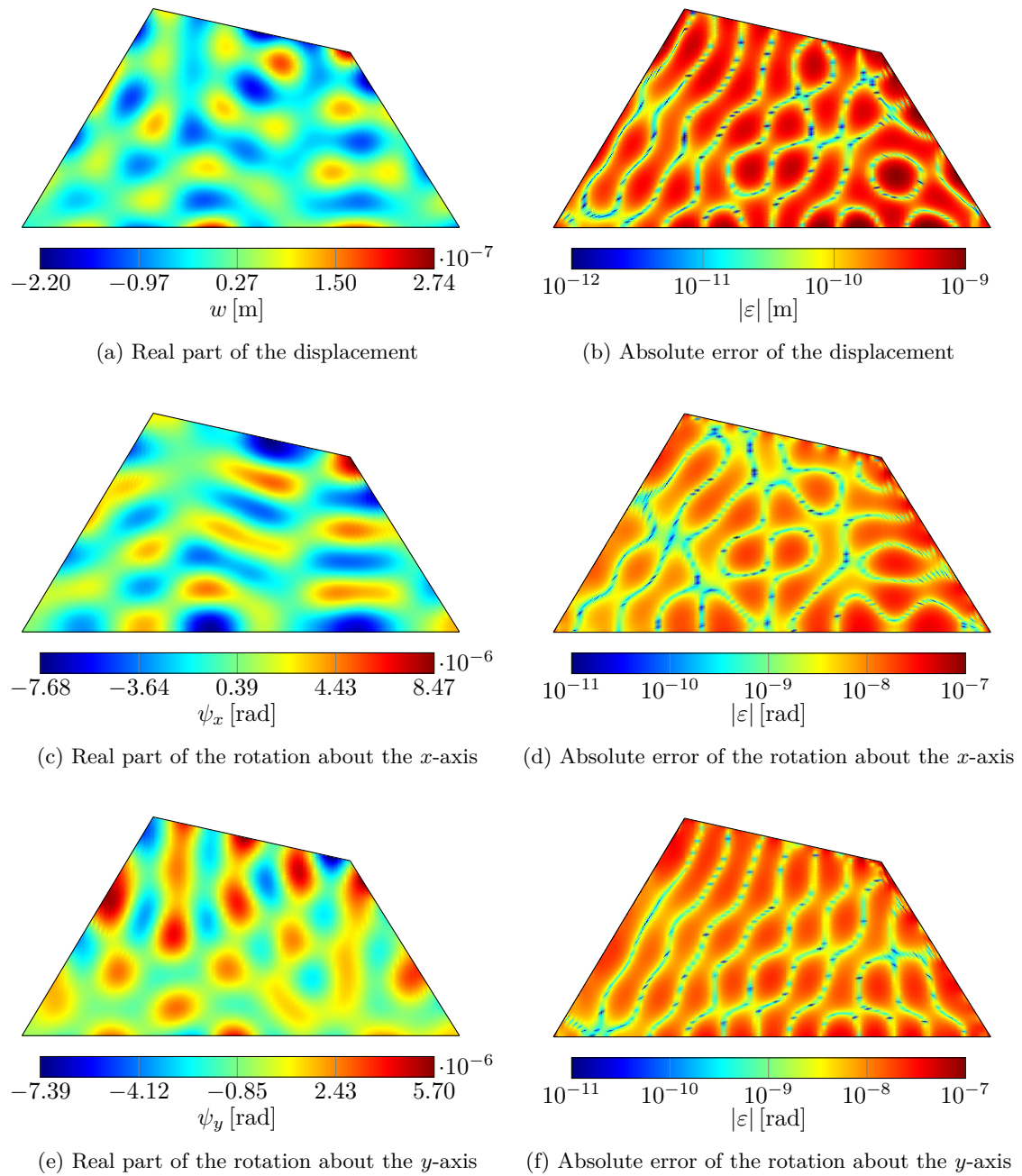


Figure E.28: Out-of-plane displacement and rotations about the  $x$ - and  $y$ -axis of a free plate ( $h = 0.005$  m) excited by a constant ring load at 2550 Hz calculated with the modified WBM using only the function set 1 and a truncation factor  $T = 2$

E Additional results for the validation examples

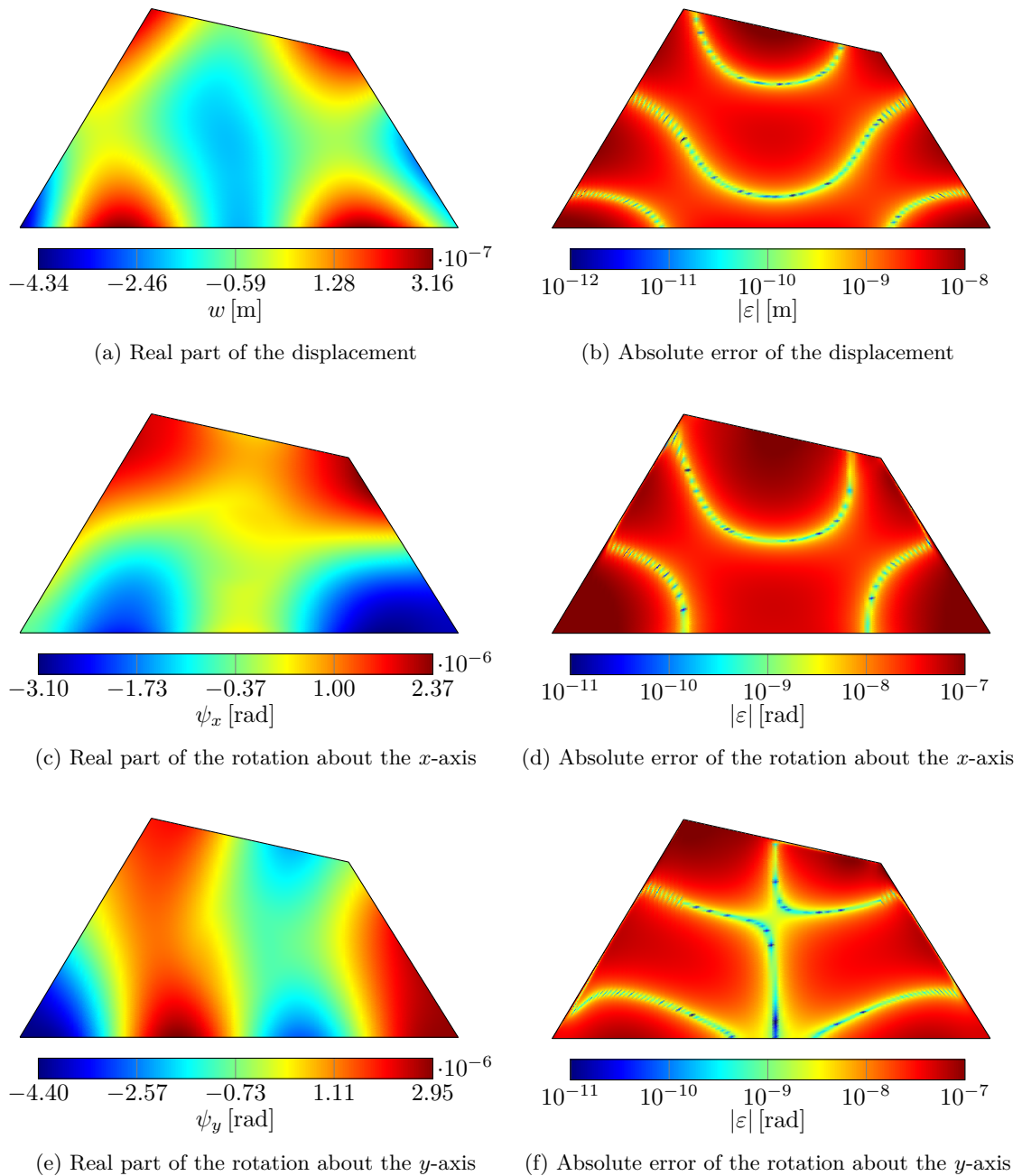


Figure E.29: Out-of-plane displacement and rotations about the  $x$ - and  $y$ -axis of a free plate ( $h = 0.01$  m) excited by a constant ring load at 440 Hz calculated with the original WBM using only the function set 1 and a truncation factor  $T = 2$

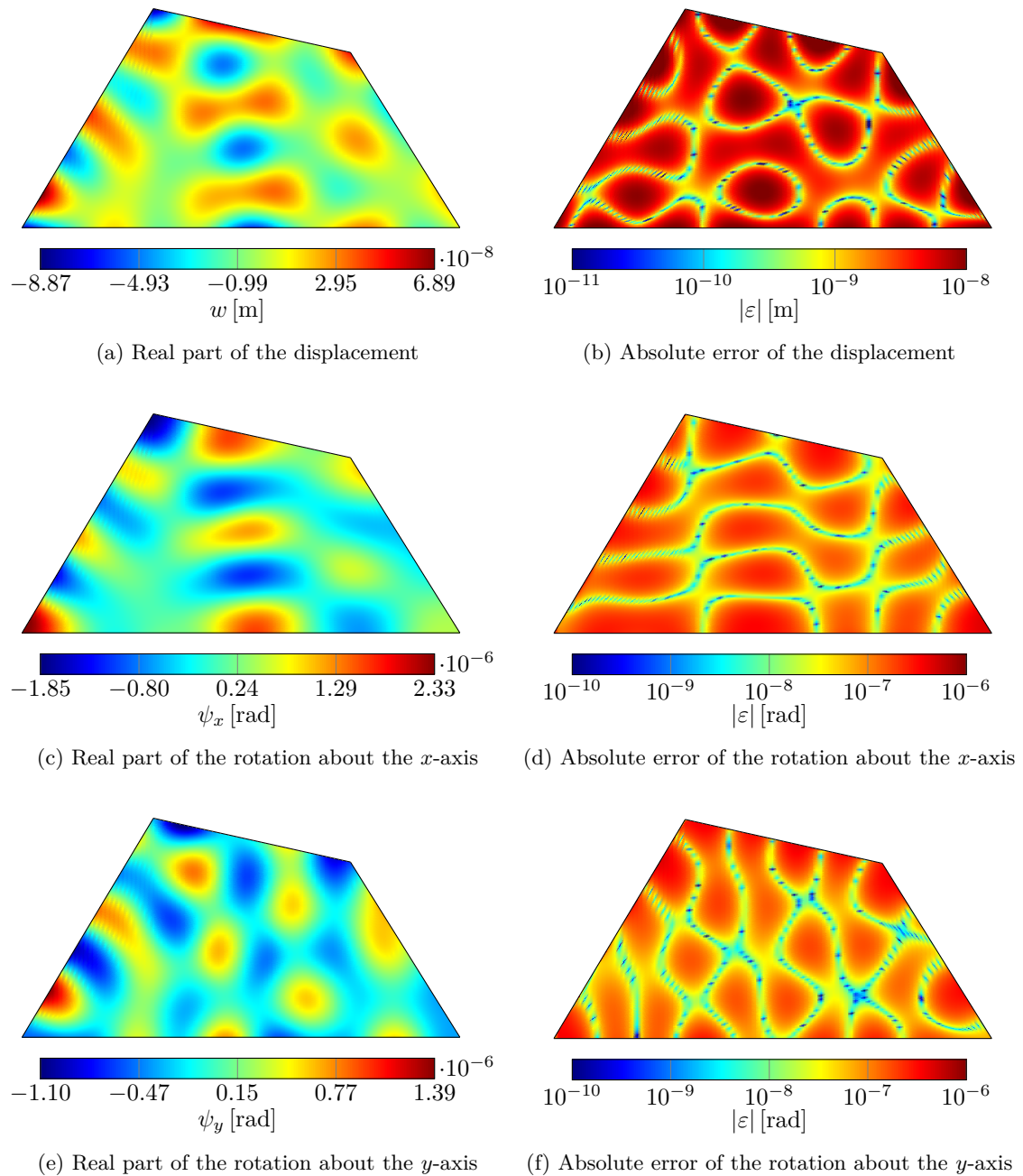


Figure E.30: Out-of-plane displacement and rotations about the  $x$ - and  $y$ -axis of a free plate ( $h = 0.01$  m) excited by a constant ring load at 2580 Hz calculated with the original WBM using only the function set 1 and a truncation factor  $T = 2$

E Additional results for the validation examples

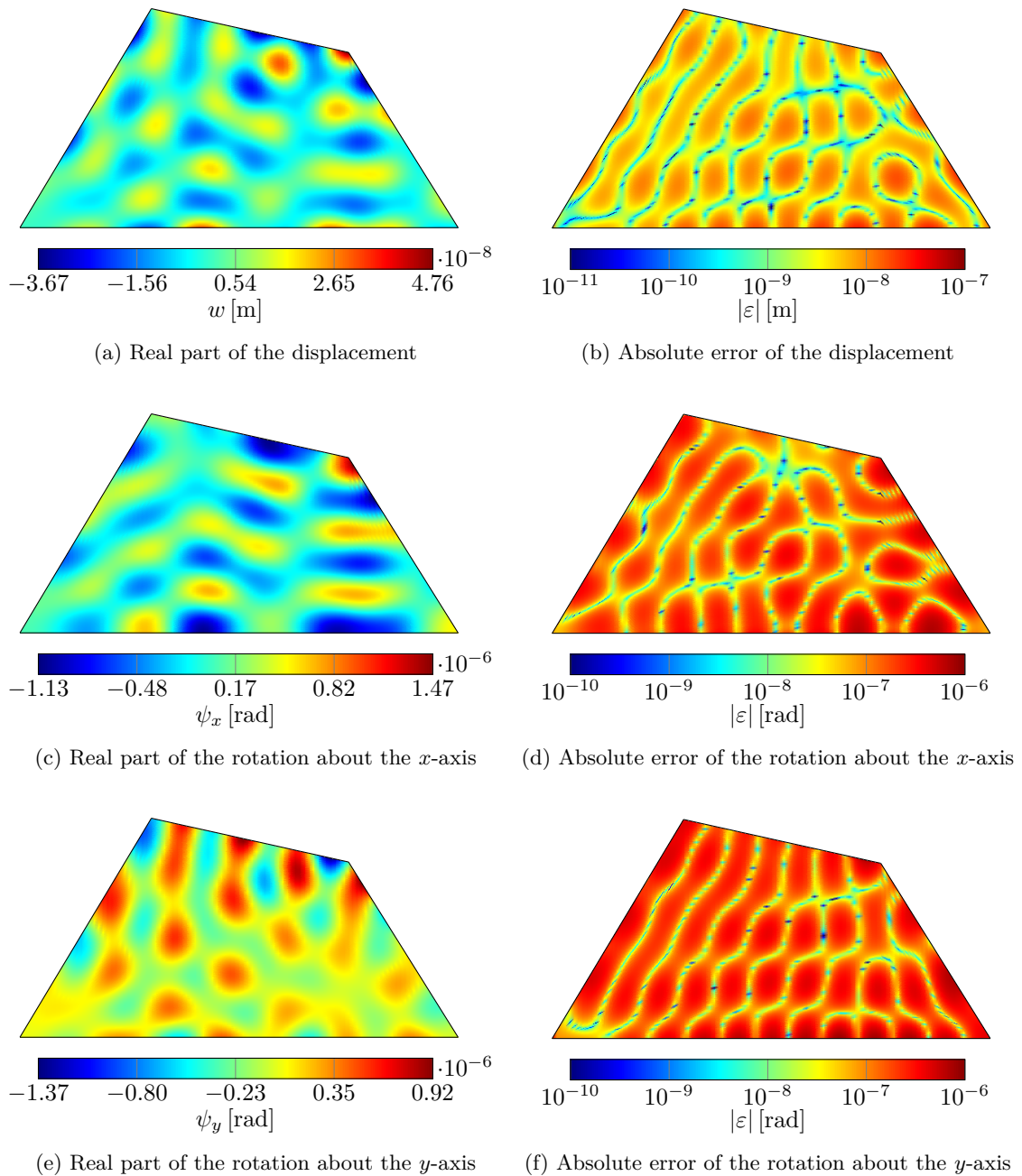


Figure E.31: Out-of-plane displacement and rotations about the  $x$ - and  $y$ -axis of a free plate ( $h = 0.01$  m) excited by a constant ring load at 4970 Hz calculated with the original WBM using only the function set 1 and a truncation factor  $T = 2$

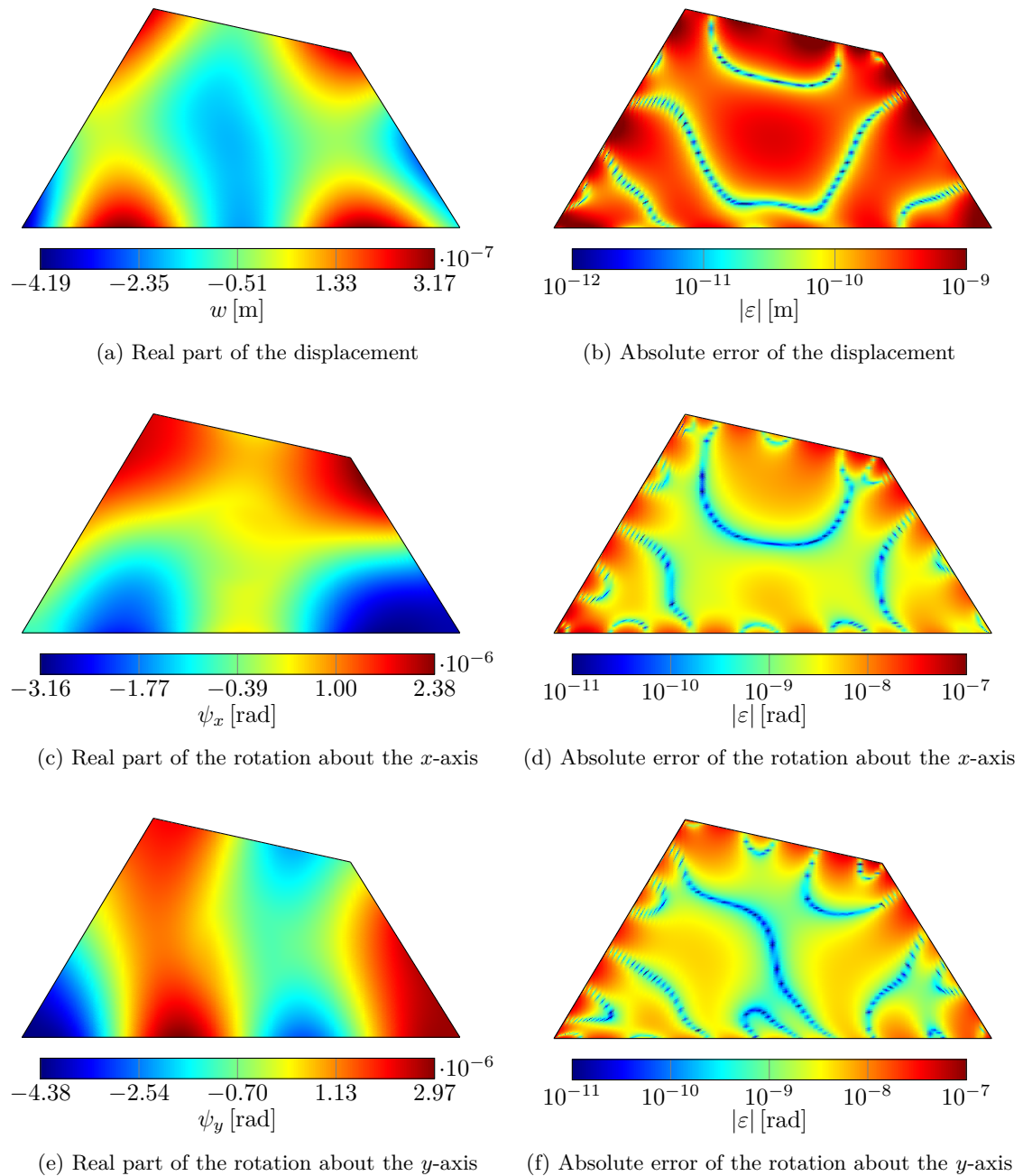


Figure E.32: Out-of-plane displacement and rotations about the  $x$ - and  $y$ -axis of a free plate ( $h = 0.01$  m) excited by a constant ring load at 440 Hz calculated with the modified WBM using only the function set 1 and a truncation factor  $T = 2$

E Additional results for the validation examples

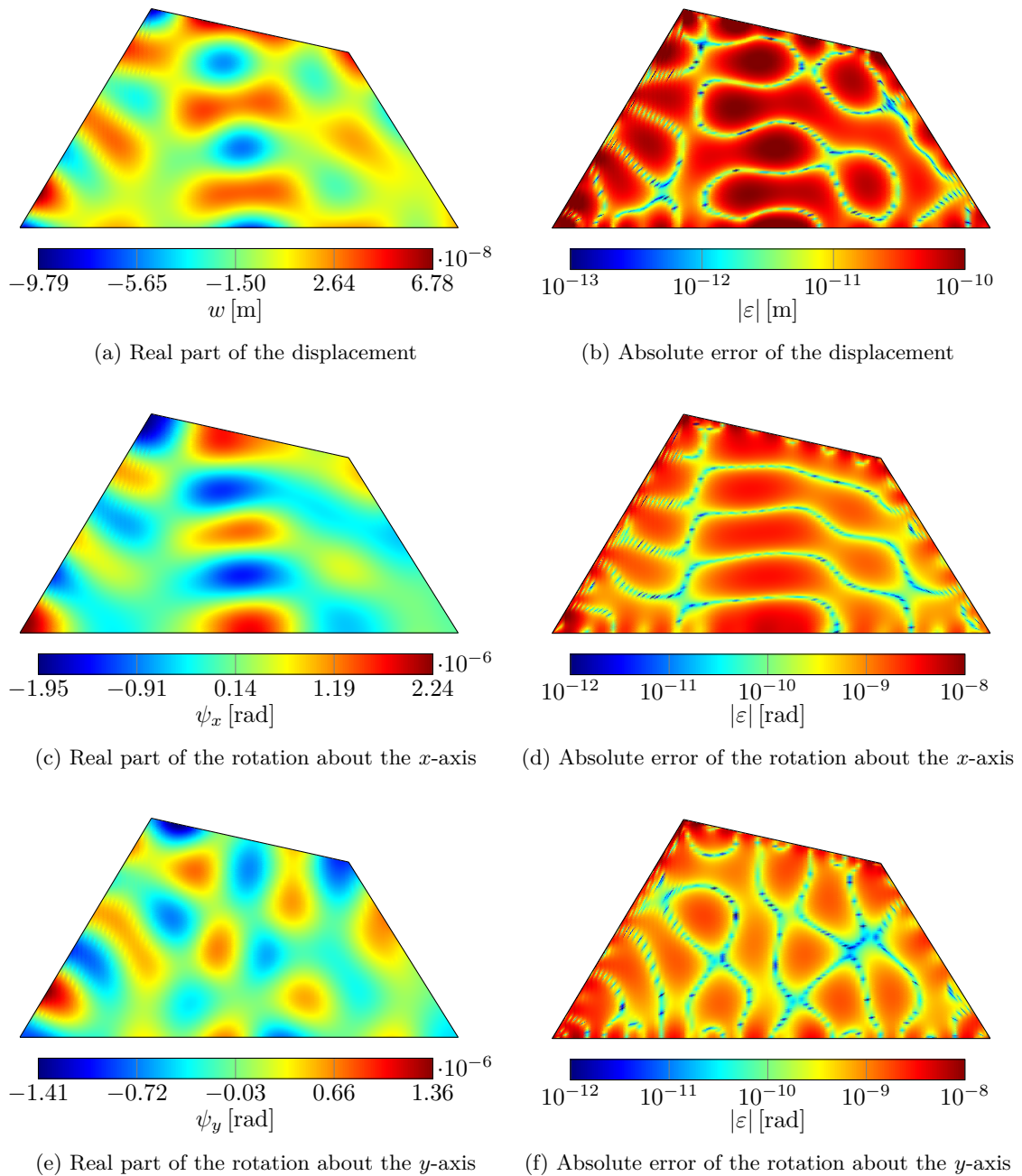


Figure E.33: Out-of-plane displacement and rotations about the  $x$ - and  $y$ -axis of a free plate ( $h = 0.01$  m) excited by a constant ring load at 2580 Hz calculated with the modified WBM using only the function set 1 and a truncation factor  $T = 2$

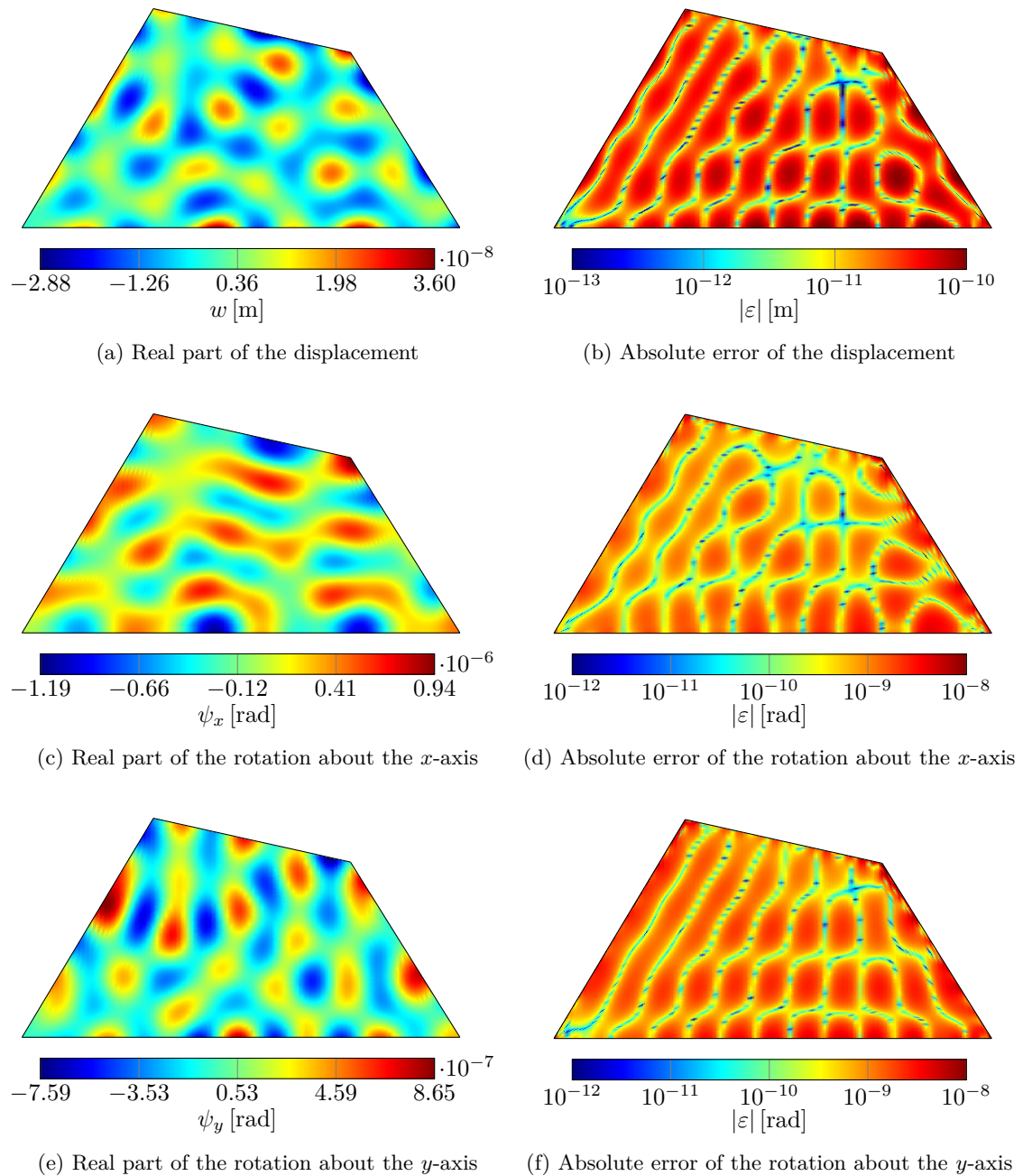


Figure E.34: Out-of-plane displacement and rotations about the  $x$ - and  $y$ -axis of a free plate ( $h = 0.01$  m) excited by a constant ring load at 4970 Hz calculated with the modified WBM using only the function set 1 and a truncation factor  $T = 2$

E Additional results for the validation examples

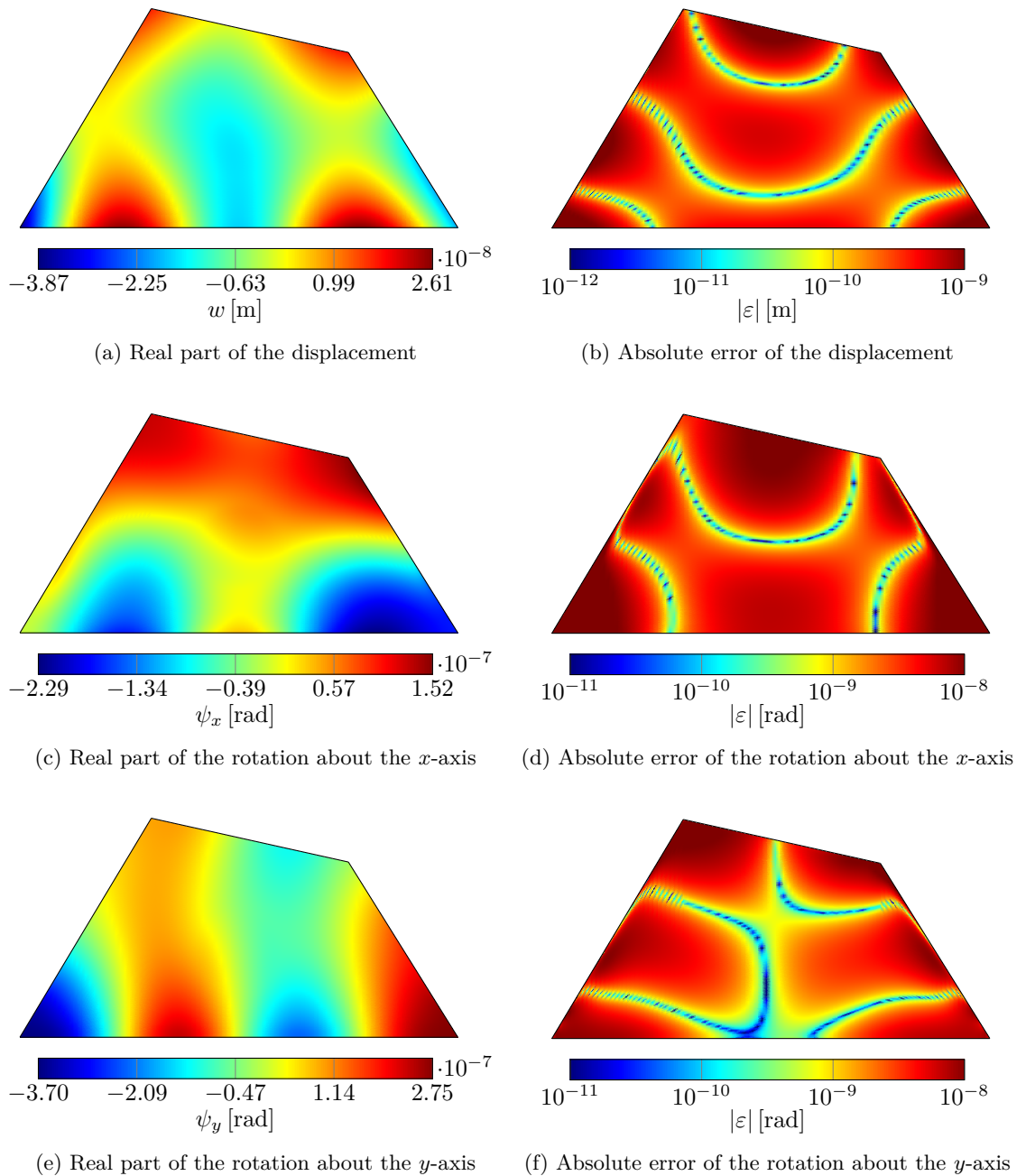


Figure E.35: Out-of-plane displacement and rotations about the  $x$ - and  $y$ -axis of a free plate ( $h = 0.025$  m) excited by a constant ring load at 1050 Hz calculated with the original WBM using only the function set 1 and a truncation factor  $T = 2$

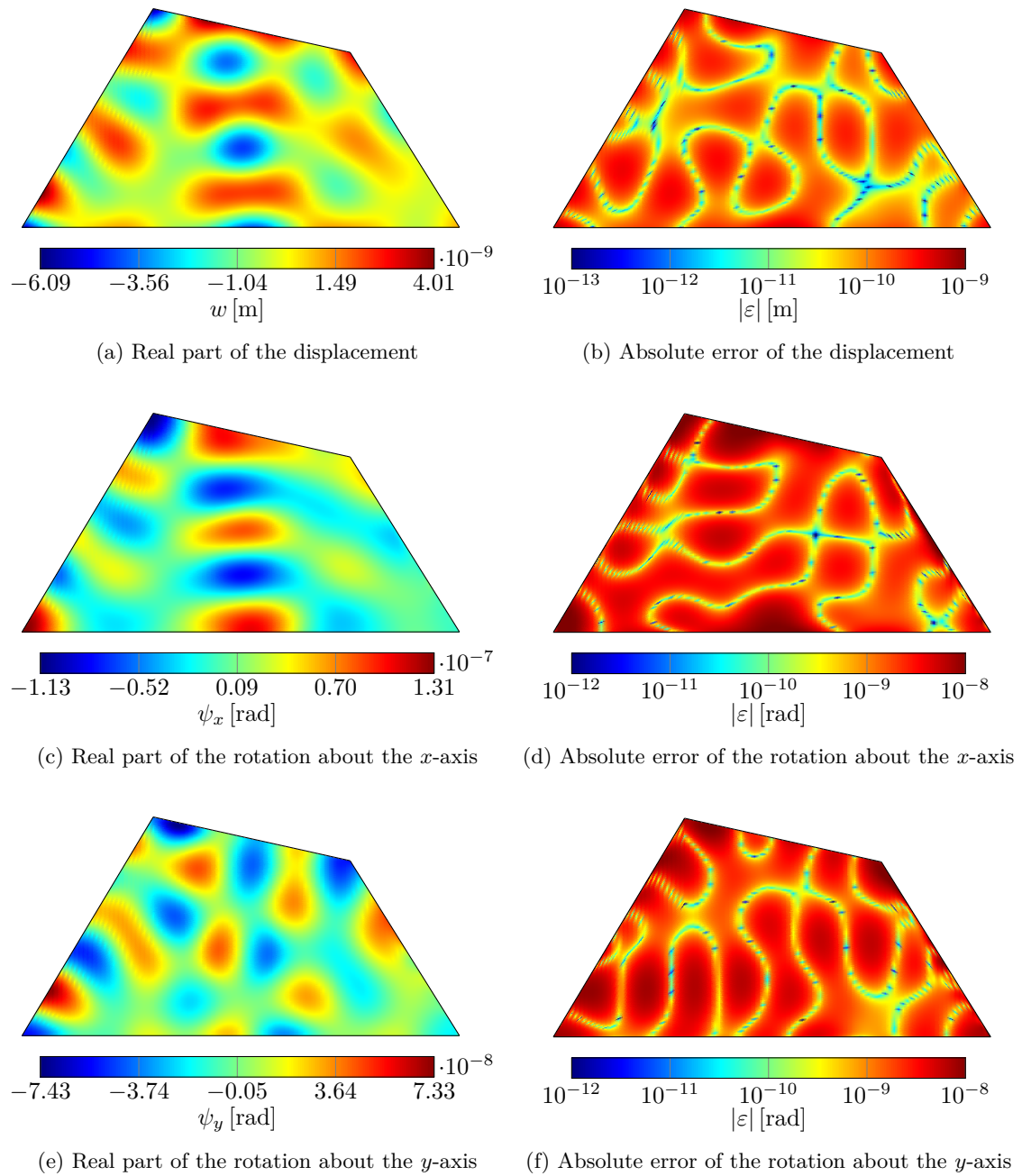


Figure E.36: Out-of-plane displacement and rotations about the  $x$ - and  $y$ -axis of a free plate ( $h = 0.025$  m) excited by a constant ring load at 5900 Hz calculated with the original WBM using only the function set 1 and a truncation factor  $T = 2$

E Additional results for the validation examples

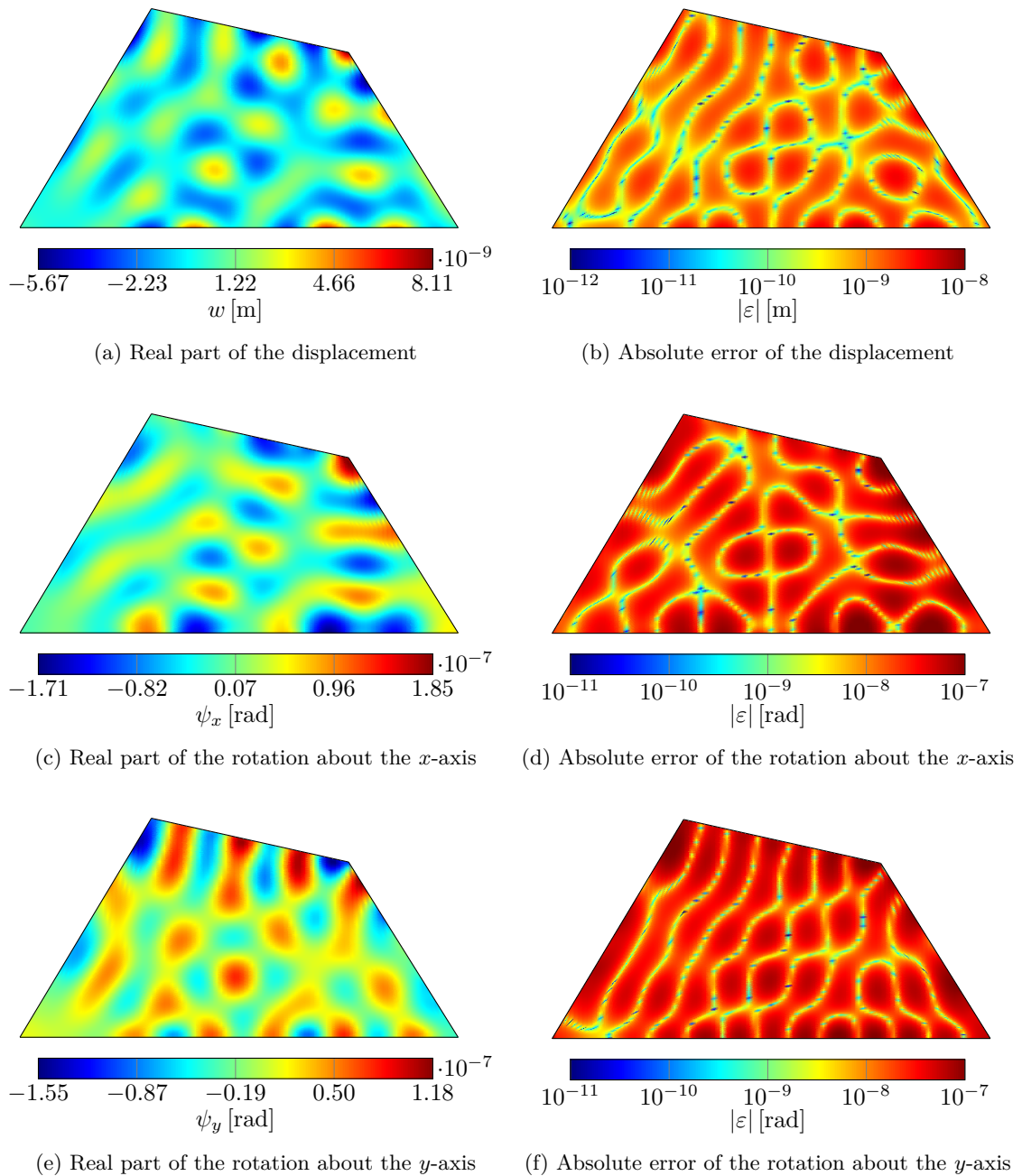


Figure E.37: Out-of-plane displacement and rotations about the  $x$ - and  $y$ -axis of a free plate ( $h = 0.025$  m) excited by a constant ring load at 10700 Hz calculated with the original WBM using only the function set 1 and a truncation factor  $T = 2$

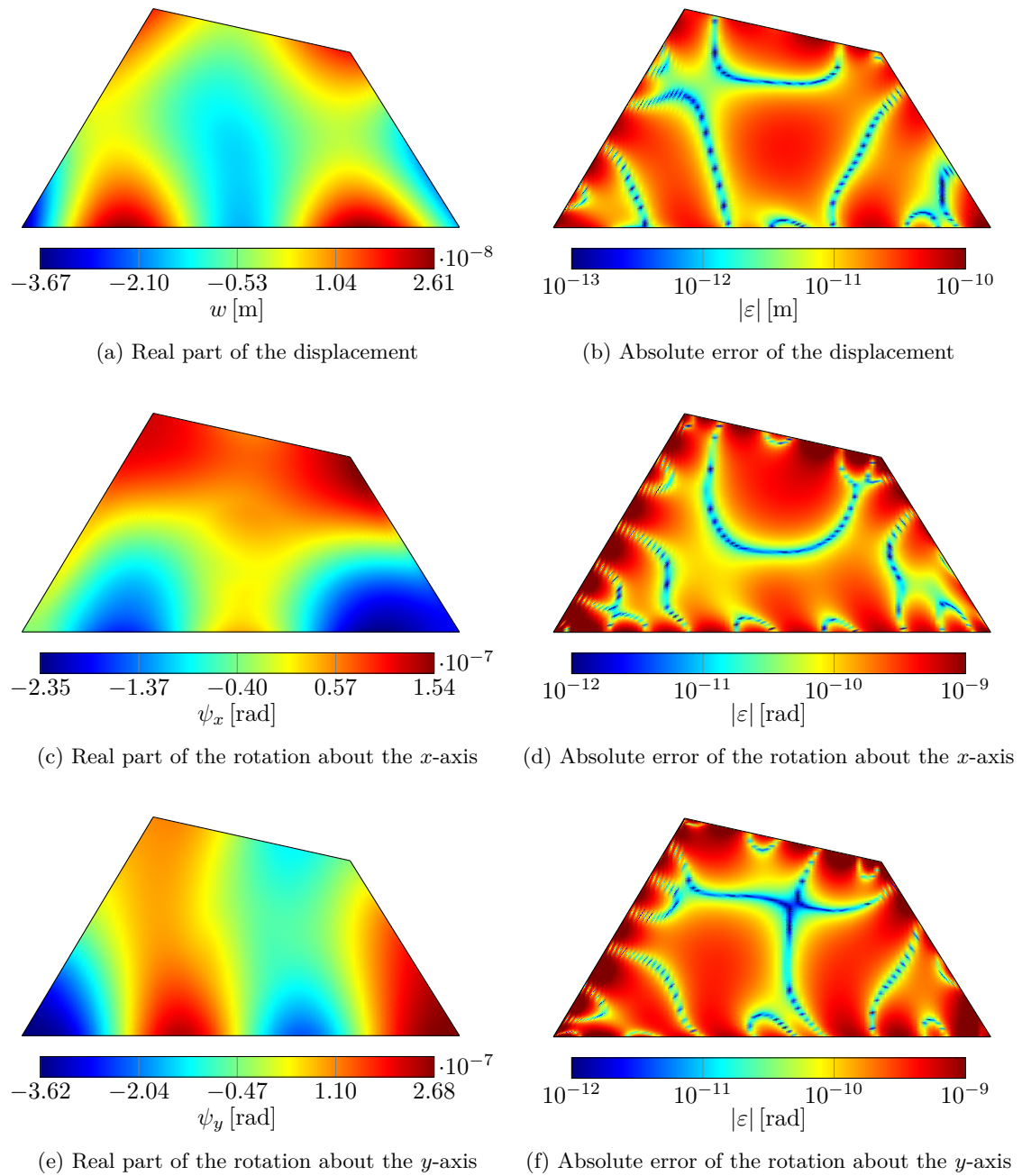


Figure E.38: Out-of-plane displacement and rotations about the  $x$ - and  $y$ -axis of a free plate ( $h = 0.025$  m) excited by a constant ring load at 1050 Hz calculated with the modified WBM using only the function set 1 and a truncation factor  $T = 2$

E Additional results for the validation examples

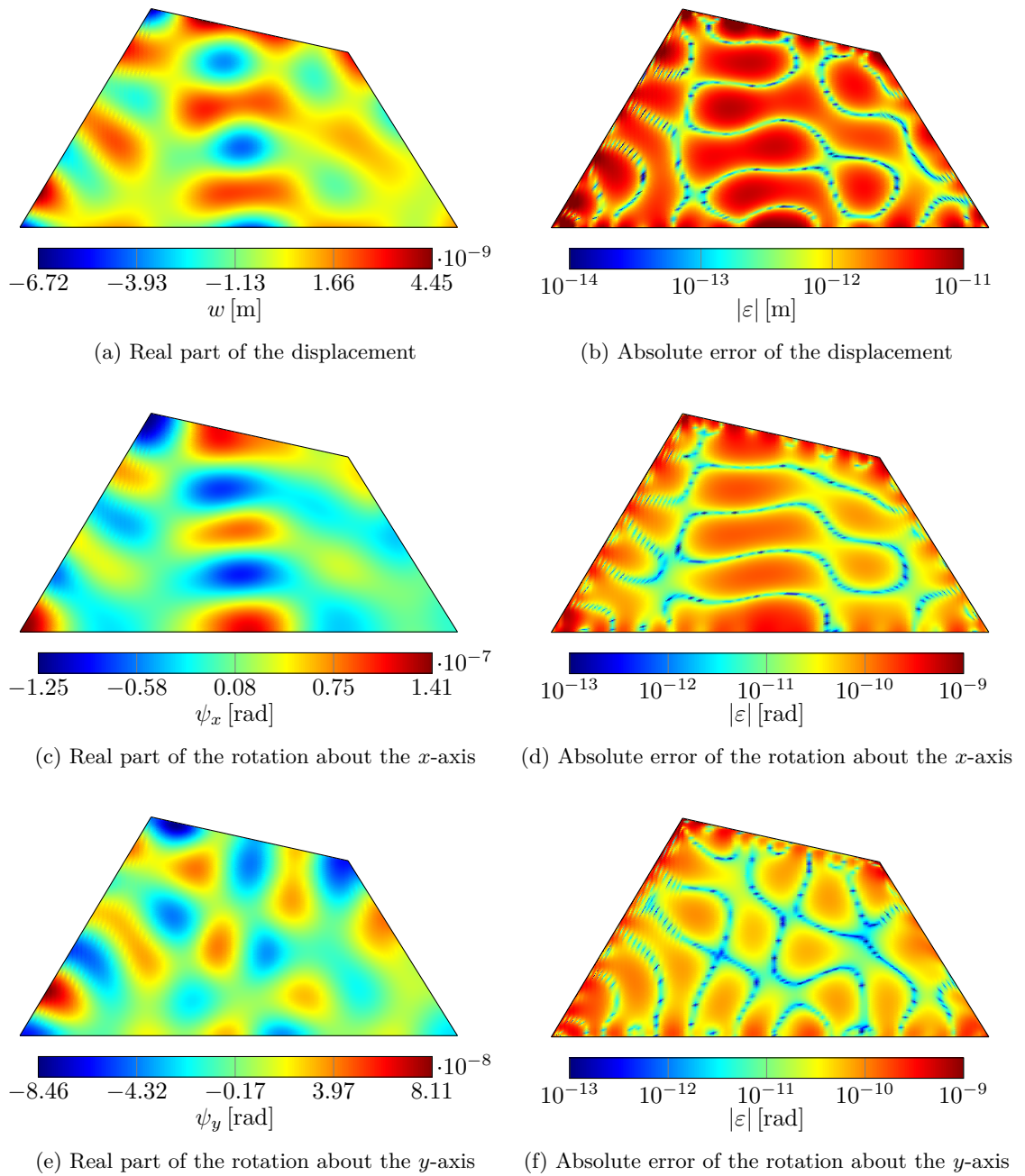


Figure E.39: Out-of-plane displacement and rotations about the  $x$ - and  $y$ -axis of a free plate ( $h = 0.025$  m) excited by a constant ring load at 5900 Hz calculated with the modified WBM using only the function set 1 and a truncation factor  $T = 2$

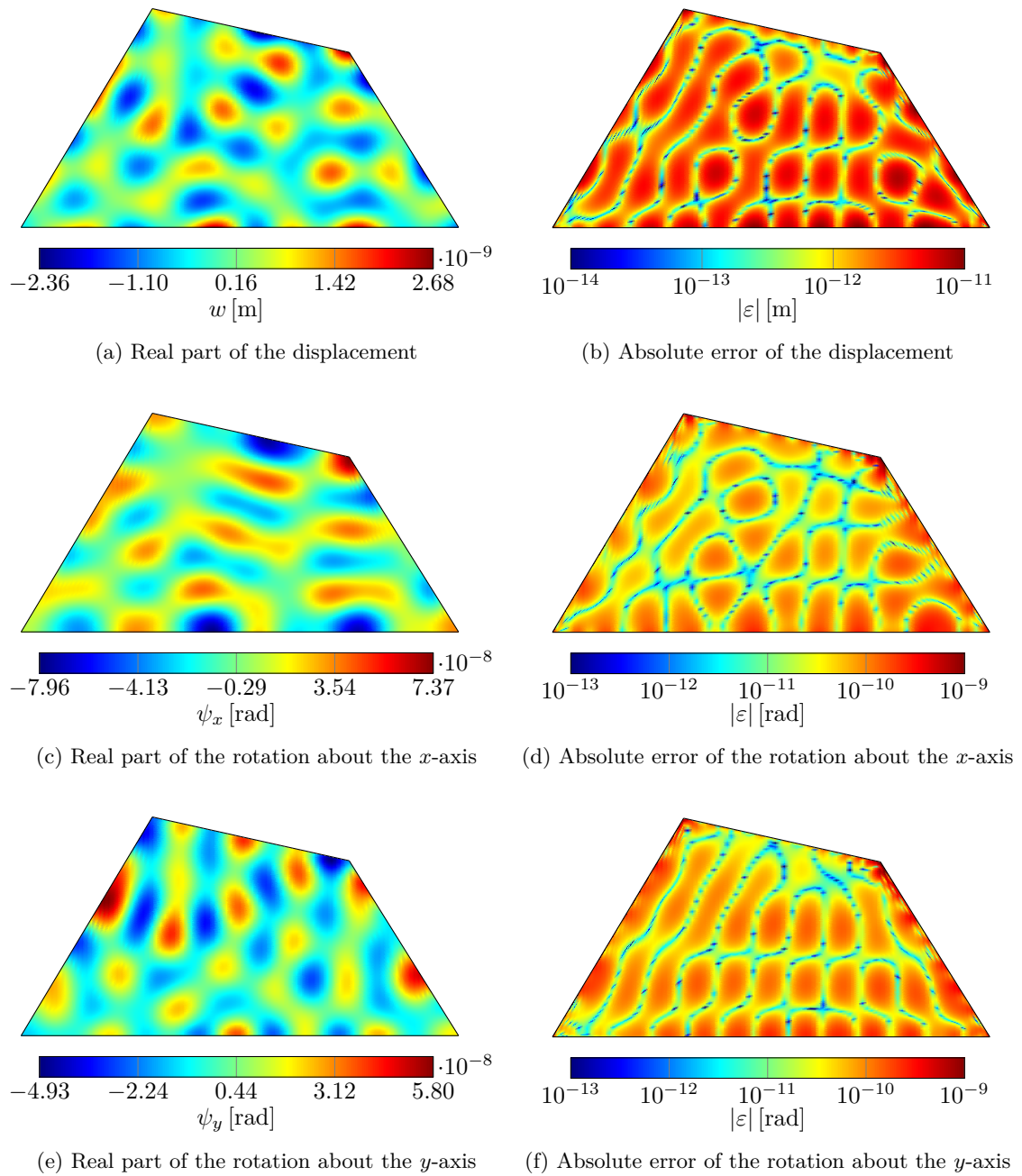


Figure E.40: Out-of-plane displacement and rotations about the  $x$ - and  $y$ -axis of a free plate ( $h = 0.025$  m) excited by a constant ring load at 10700 Hz calculated with the modified WBM using only the function set 1 and a truncation factor  $T = 2$

E Additional results for the validation examples

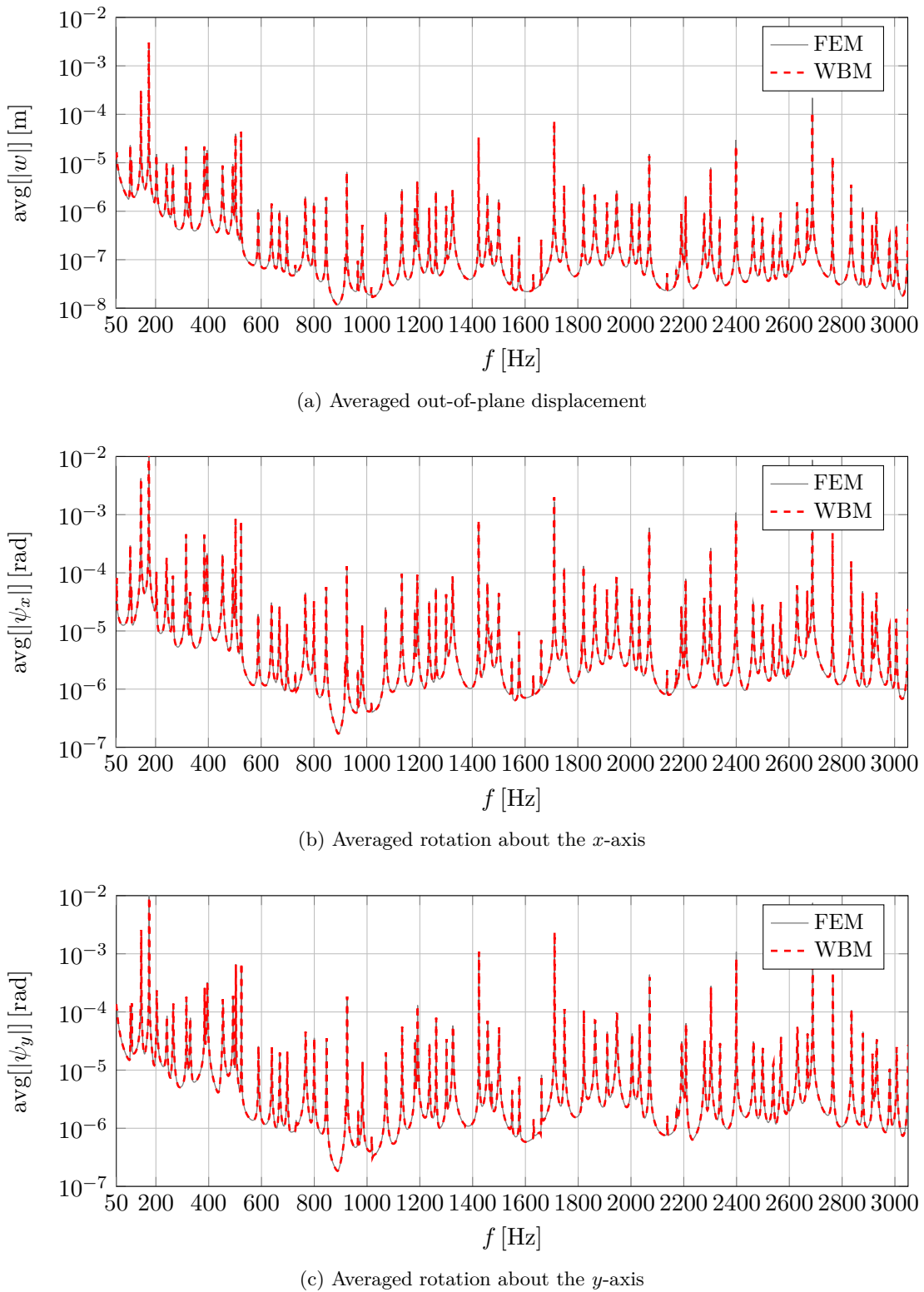
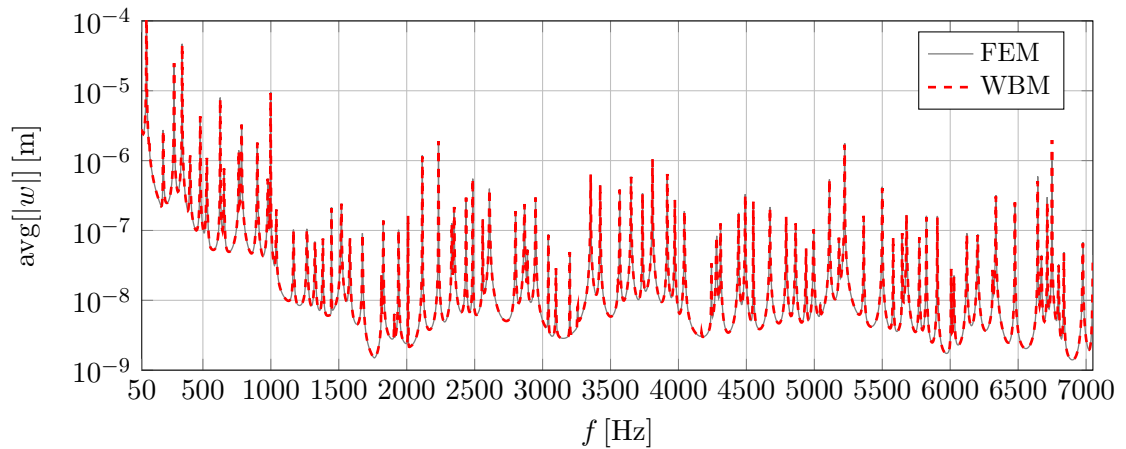
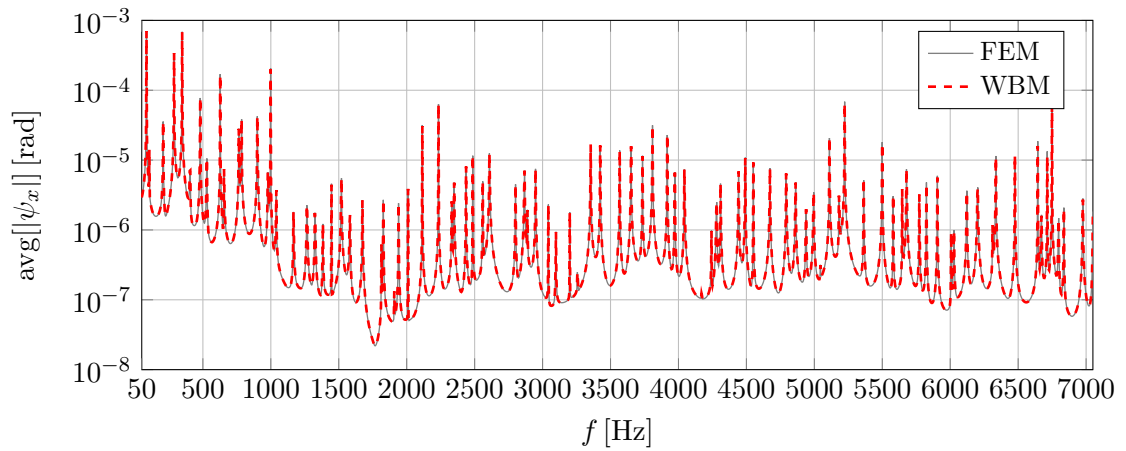


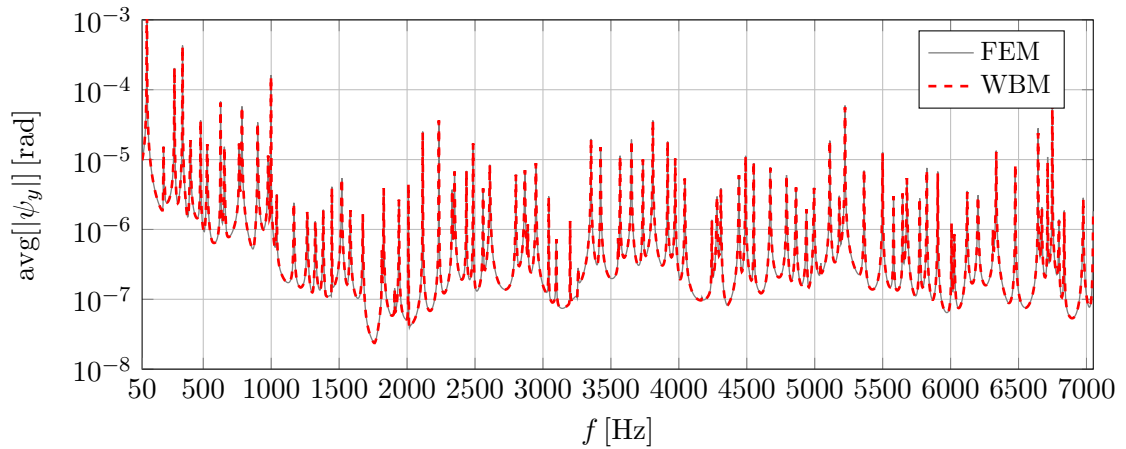
Figure E.41: Frequency response functions of a free plate ( $h = 0.005$  m) excited by a constant ring load calculated with the FEM (reference mesh) and the modified WBM (function set 1 and set 2,  $T = 2$ )



(a) Averaged out-of-plane displacement



(b) Averaged rotation about the  $x$ -axis



(c) Averaged rotation about the  $y$ -axis

Figure E.42: Frequency response functions of a free plate ( $h = 0.01$  m) excited by a constant ring load calculated with the FEM (reference mesh) and the modified WBM (function set 1 and set 2,  $T = 2$ )

## E Additional results for the validation examples

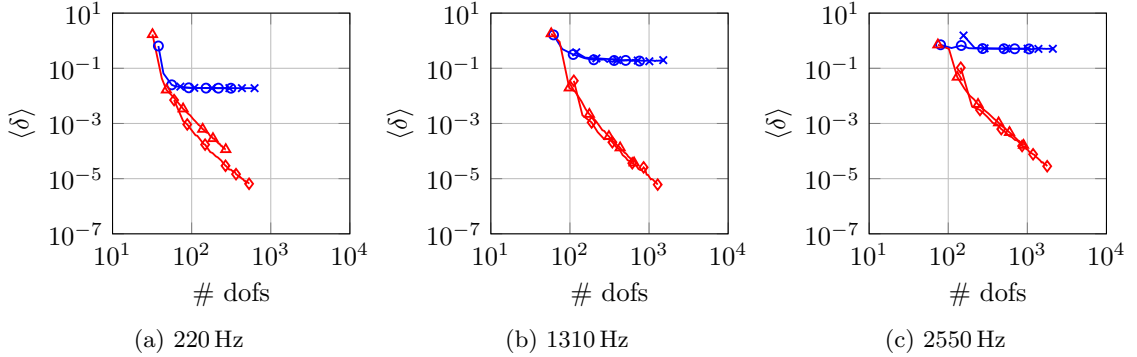


Figure E.43: Convergence curves of the out-of-plane displacement (free plate with  $h = 0.005$  m) for the original WBM ( $set1$  (—○—),  $set1a2$  (—\*—)) and the modified WBM ( $set1$  (—▲—),  $set1a2$  (—◆—))

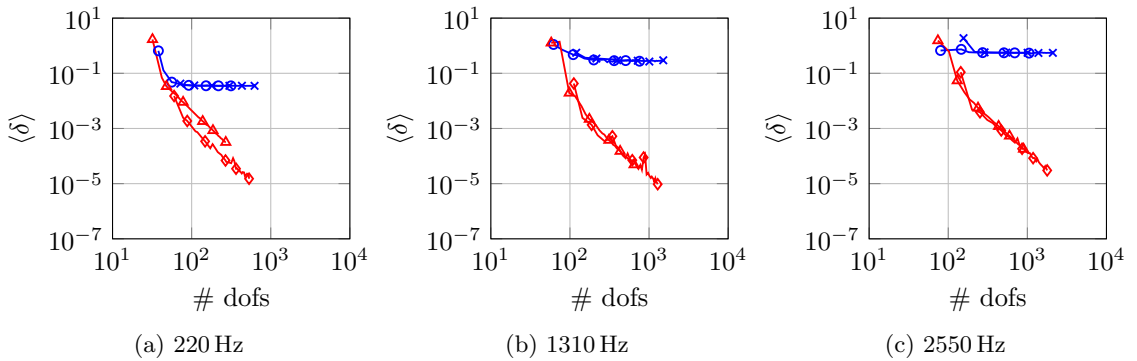


Figure E.44: Convergence curves of the rotation about the  $x$ -axis (free plate with  $h = 0.005$  m) for the original WBM ( $set1$  (—○—),  $set1a2$  (—\*—)) and the modified WBM ( $set1$  (—▲—),  $set1a2$  (—◆—))

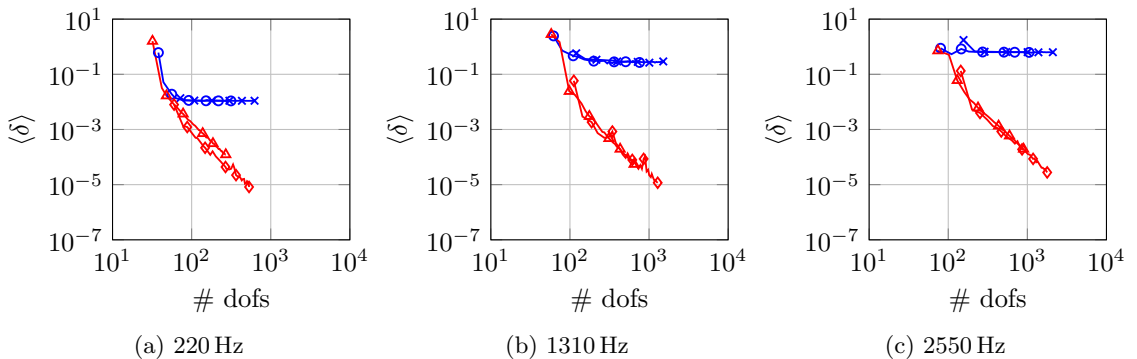


Figure E.45: Convergence curves of the rotation about the  $y$ -axis (free plate with  $h = 0.005$  m) for the original WBM ( $set1$  (—○—),  $set1a2$  (—\*—)) and the modified WBM ( $set1$  (—▲—),  $set1a2$  (—◆—))

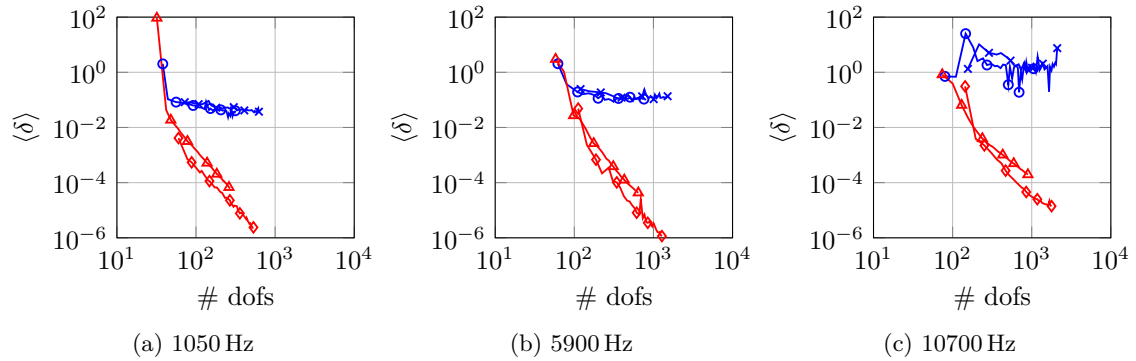


Figure E.46: Convergence curves of the out-of-plane displacement (free plate with  $h = 0.025$  m) for the original WBM (*set1* (—○—), *set1a2* (—\*—)) and the modified WBM (*set1* (—▲—), *set1a2* (—◆—))

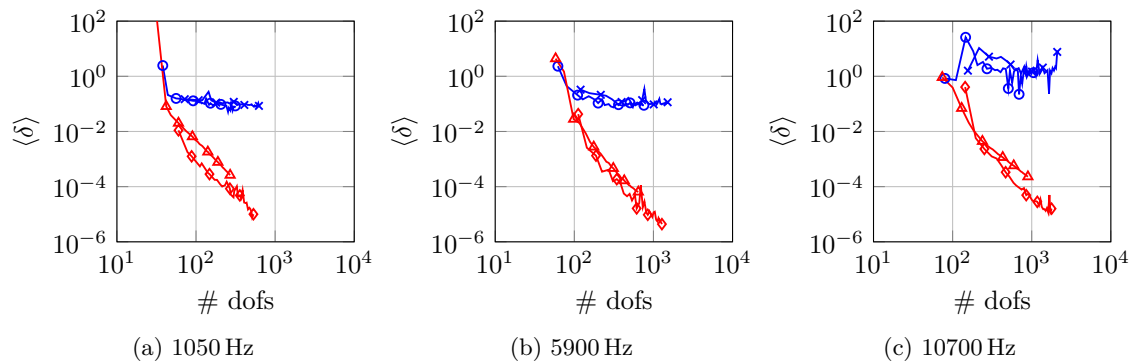


Figure E.47: Convergence curves of the rotation about the  $x$ -axis (free plate with  $h = 0.025$  m) for the original WBM (*set1* (—○—), *set1a2* (—\*—)) and the modified WBM (*set1* (—▲—), *set1a2* (—◆—))

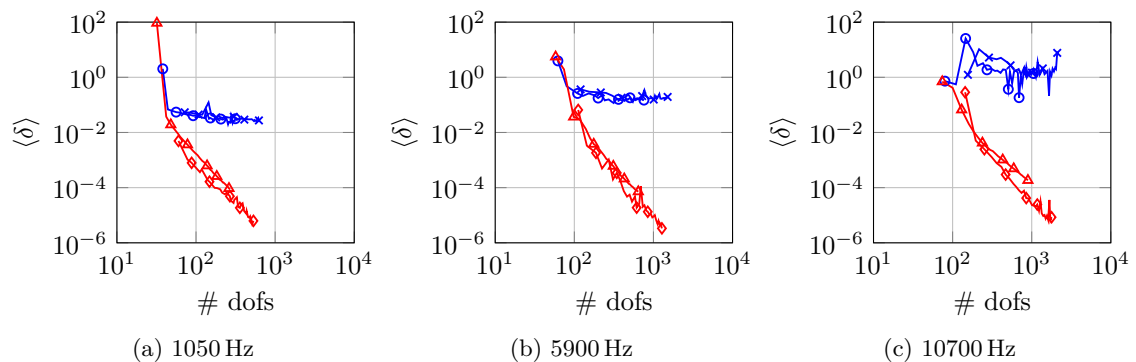


Figure E.48: Convergence curves of the rotation about the  $y$ -axis (free plate with  $h = 0.025$  m) for the original WBM (*set1* (—○—), *set1a2* (—\*—)) and the modified WBM (*set1* (—▲—), *set1a2* (—◆—))

**Single domain cantilever plate**

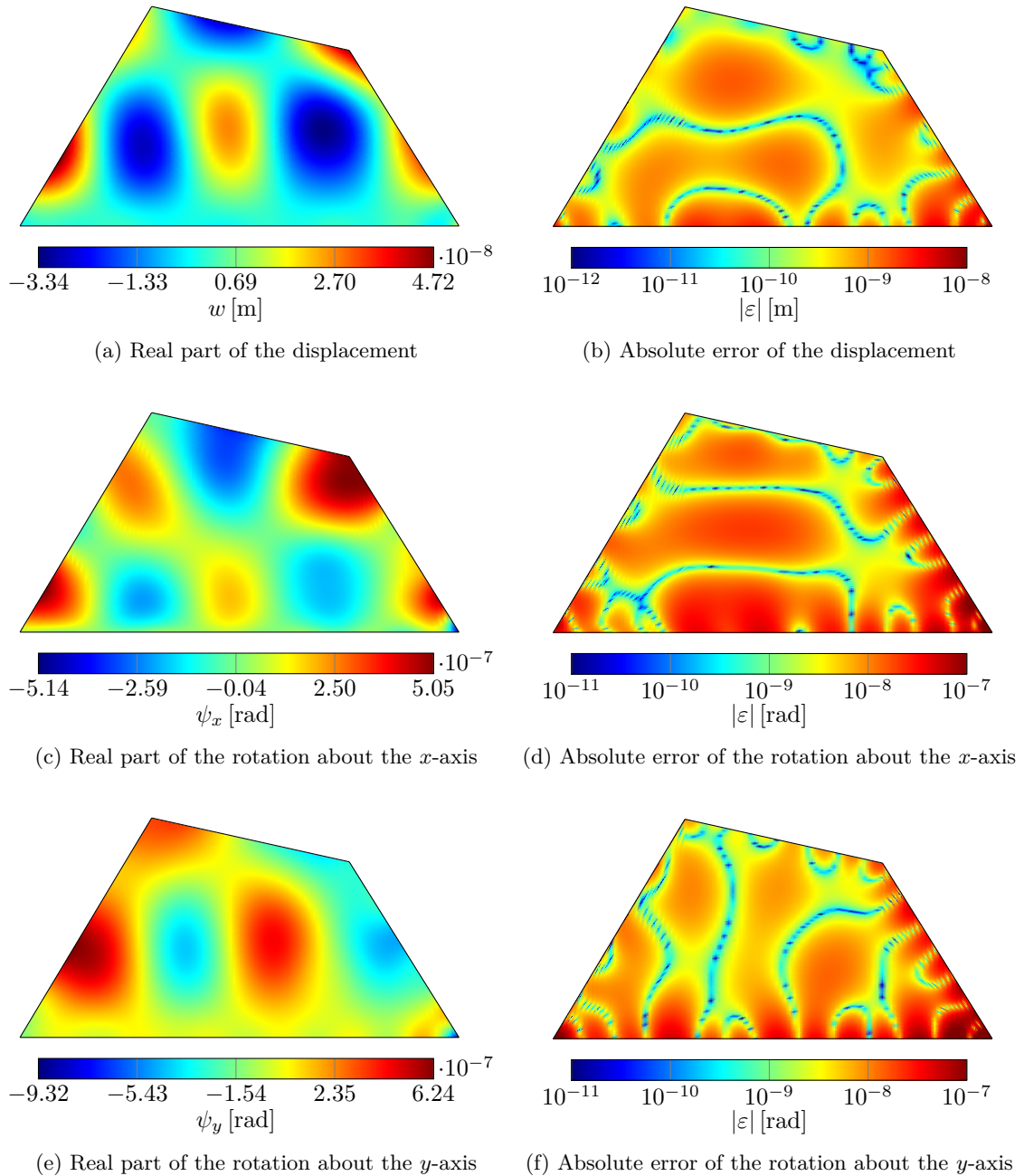


Figure E.49: Out-of-plane displacement and rotations about the  $x$ - and  $y$ -axis of a cantilever plate ( $h = 0.005$  m) excited by a constant circular load at 420 Hz calculated with the modified WBM using only the function set 1 and a truncation factor  $T = 2$

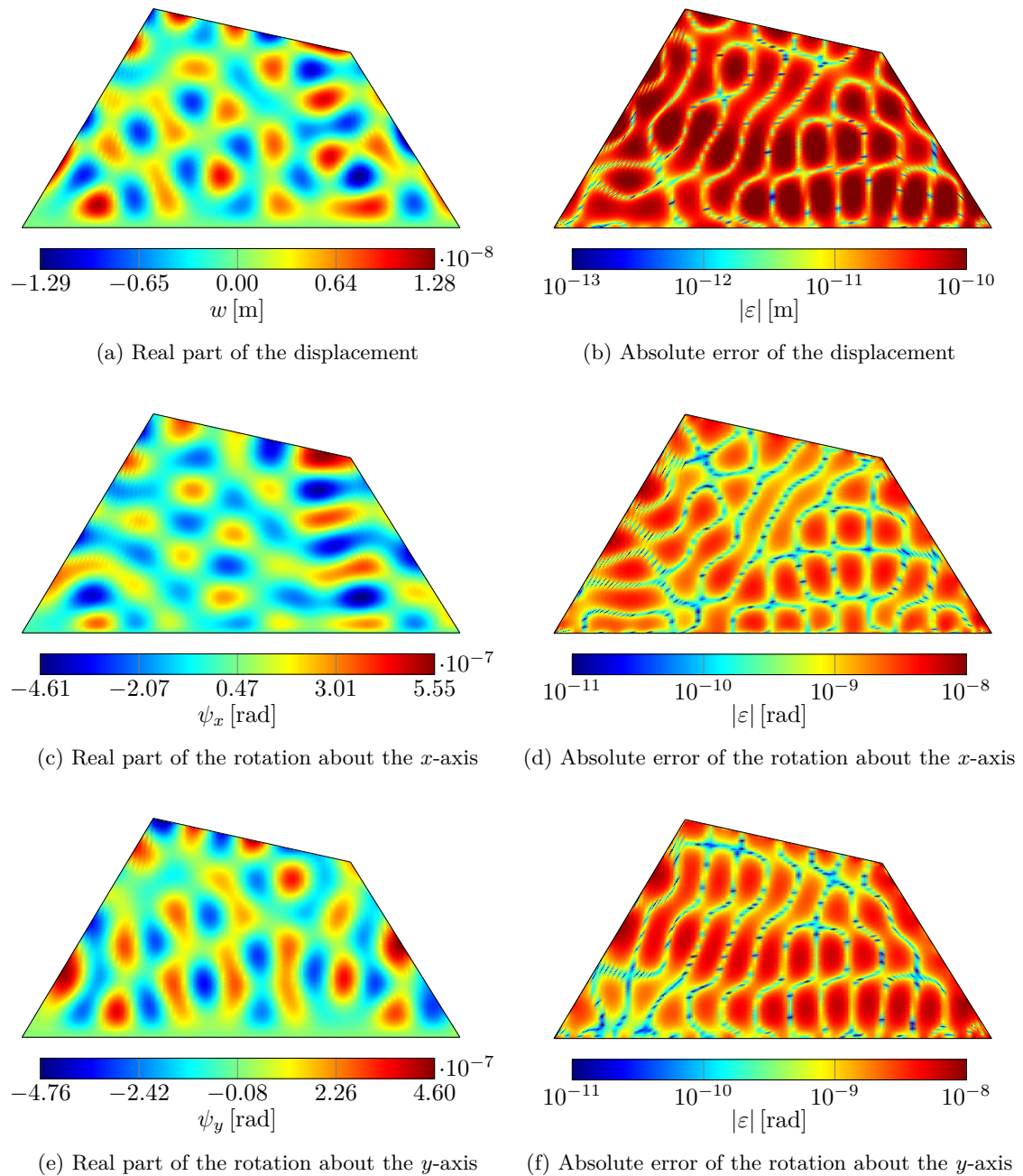


Figure E.50: Out-of-plane displacement and rotations about the  $x$ - and  $y$ -axis of a cantilever plate ( $h = 0.005$  m) excited by a constant circular load at 3170 Hz calculated with the modified WBM using only the function set 1 and a truncation factor  $T = 2$

E Additional results for the validation examples

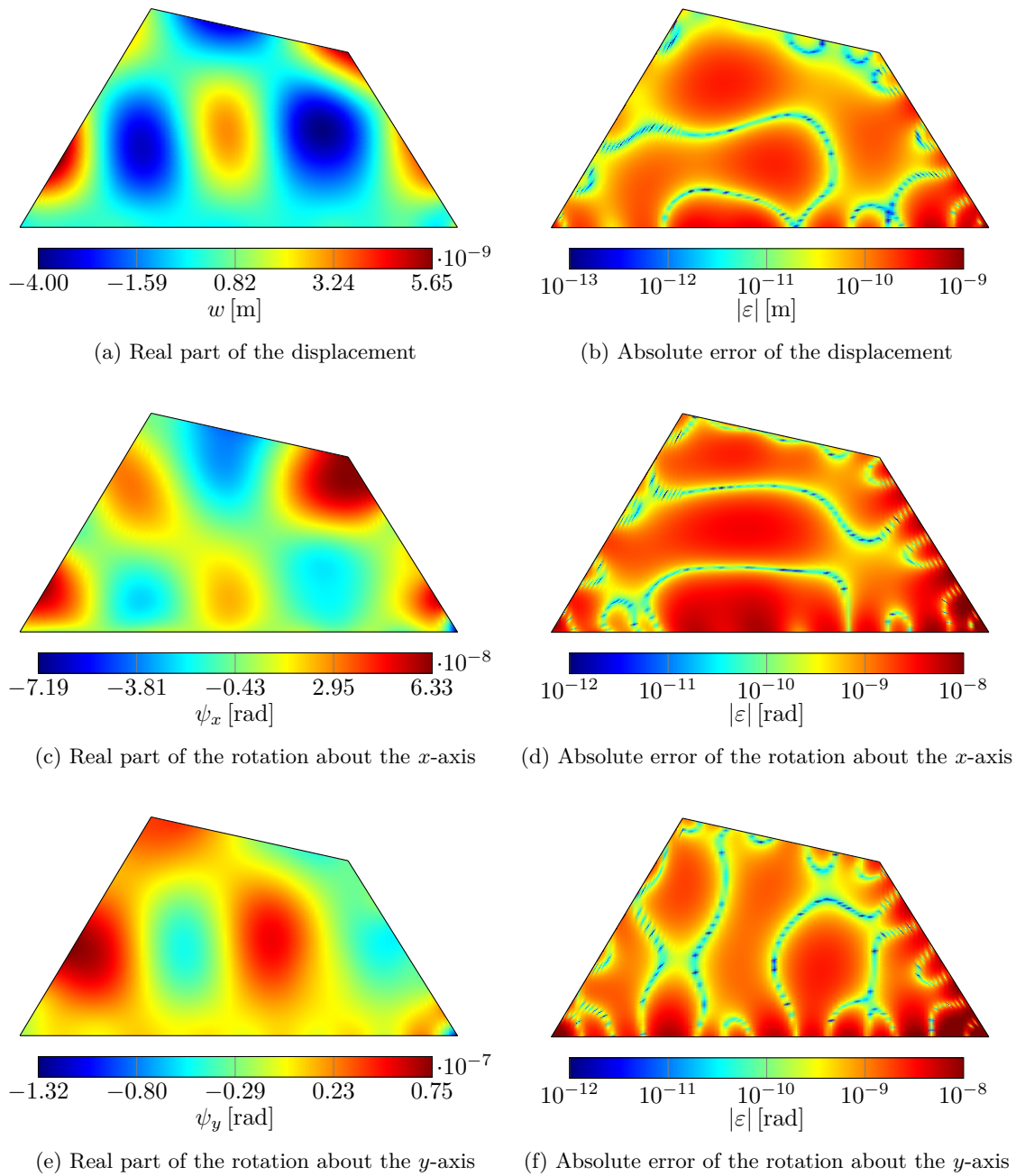


Figure E.51: Out-of-plane displacement and rotations about the  $x$ - and  $y$ -axis of a cantilever plate ( $h = 0.01$  m) excited by a constant circular load at 840 Hz calculated with the modified WBM using only the function set 1 and a truncation factor  $T = 2$

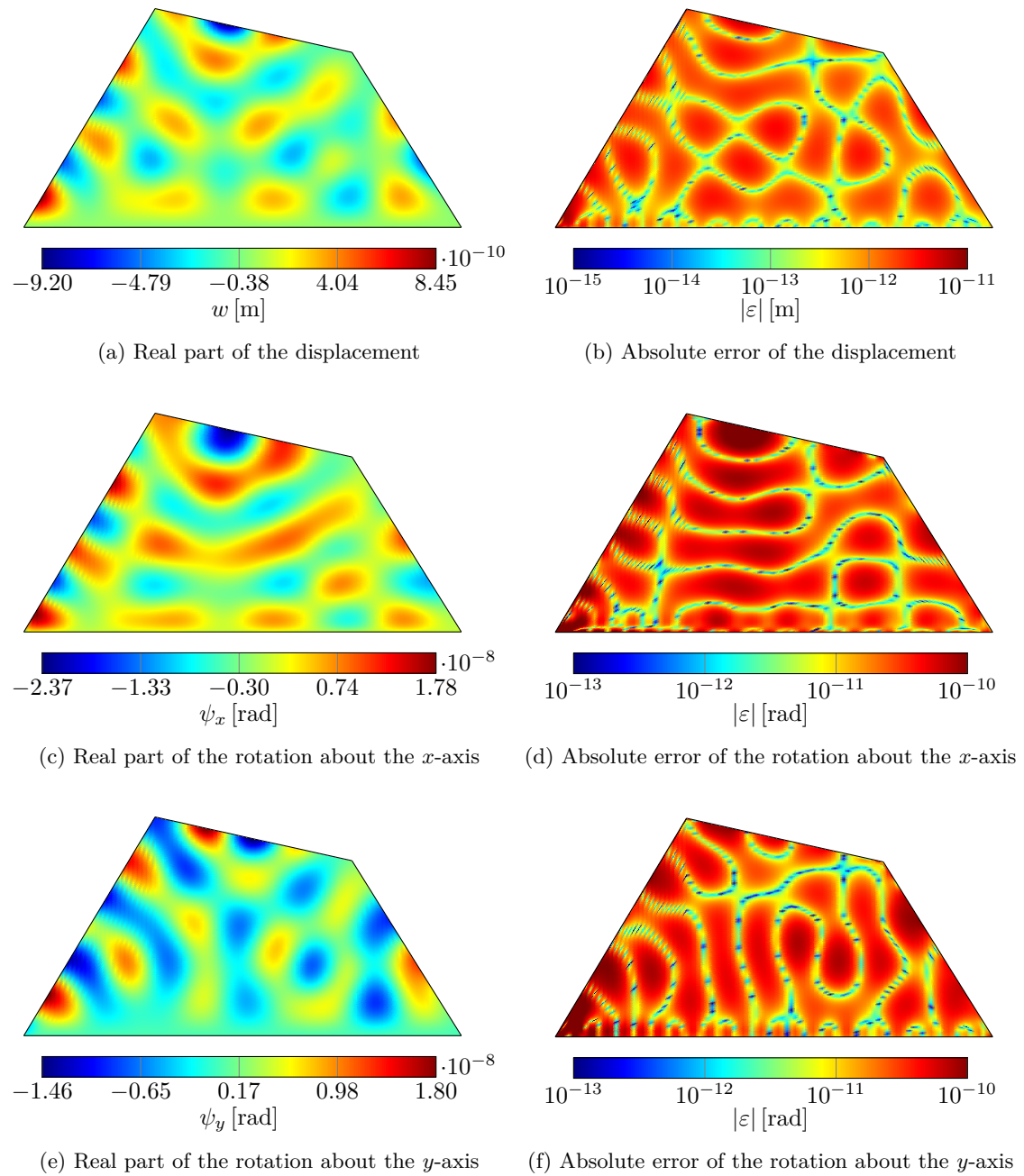


Figure E.52: Out-of-plane displacement and rotations about the  $x$ - and  $y$ -axis of a cantilever plate ( $h = 0.01$  m) excited by a constant circular load at 3500 Hz calculated with the modified WBM using only the function set 1 and a truncation factor  $T = 2$

E Additional results for the validation examples

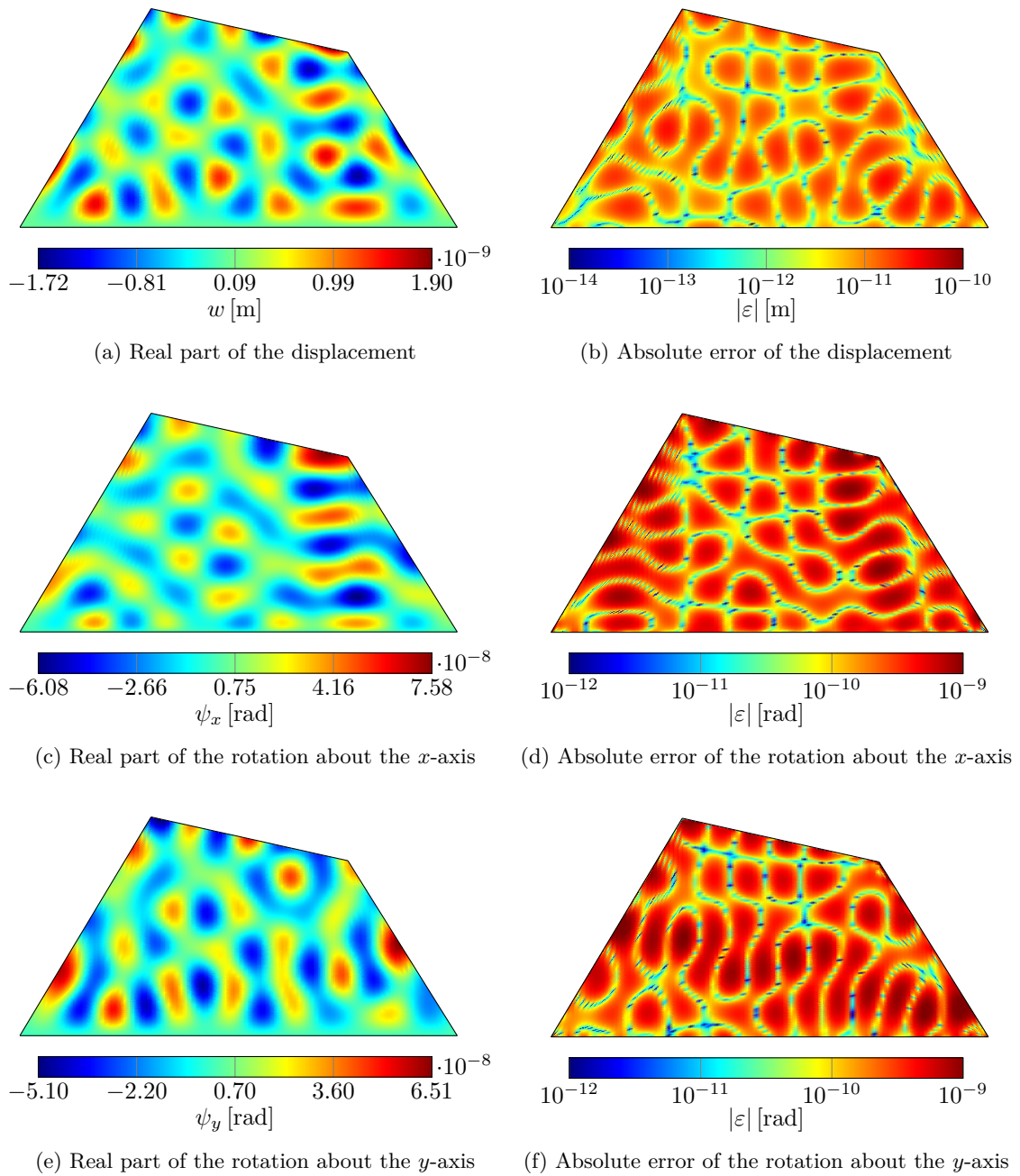


Figure E.53: Out-of-plane displacement and rotations about the  $x$ - and  $y$ -axis of a cantilever plate ( $h = 0.01$  m) excited by a constant circular load at 6120 Hz calculated with the modified WBM using only the function set 1 and a truncation factor  $T = 2$

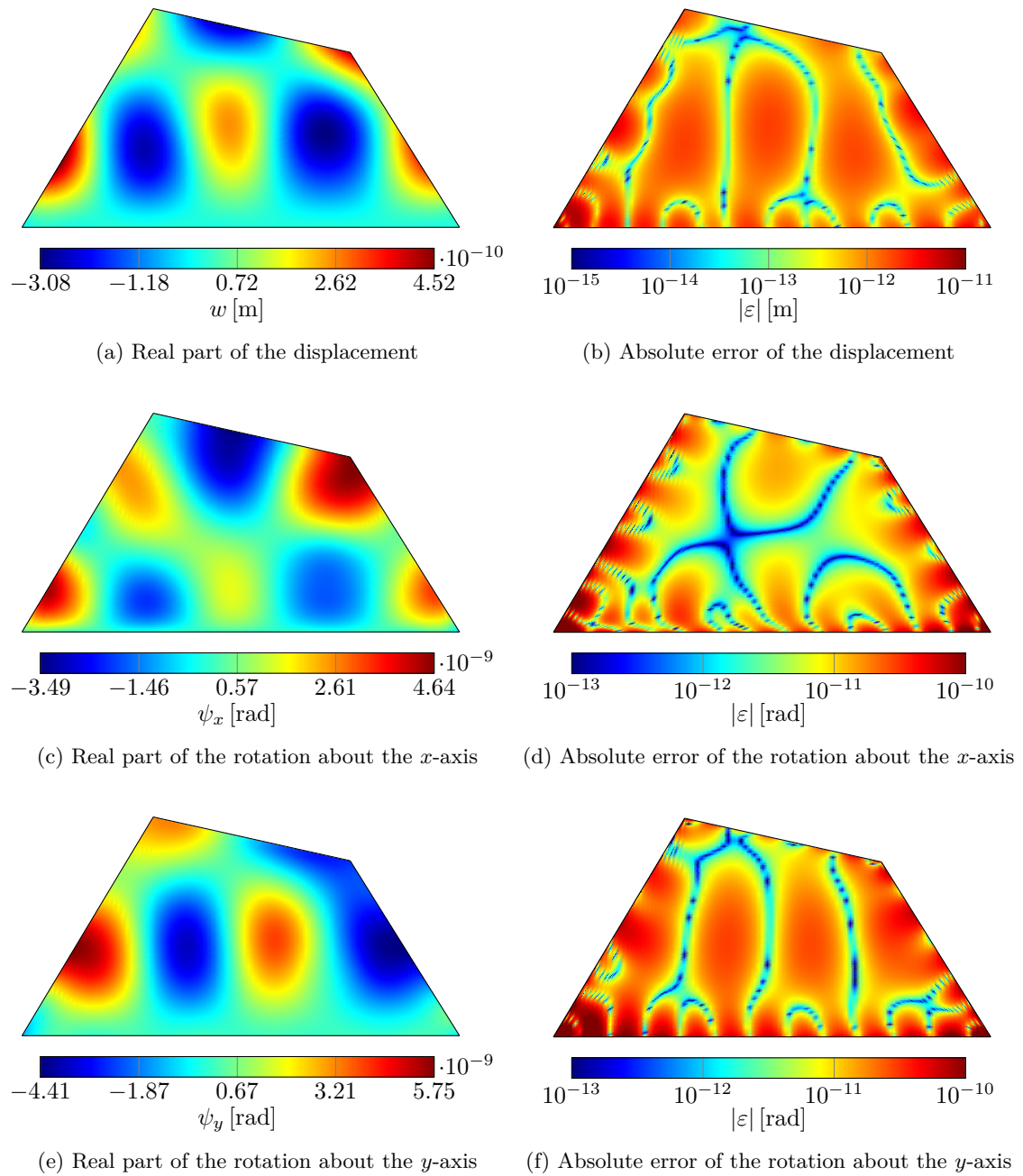


Figure E.54: Out-of-plane displacement and rotations about the  $x$ - and  $y$ -axis of a cantilever plate ( $h = 0.025$  m) excited by a constant circular load at 2000 Hz calculated with the modified WBM using only the function set 1 and a truncation factor  $T = 2$

E Additional results for the validation examples

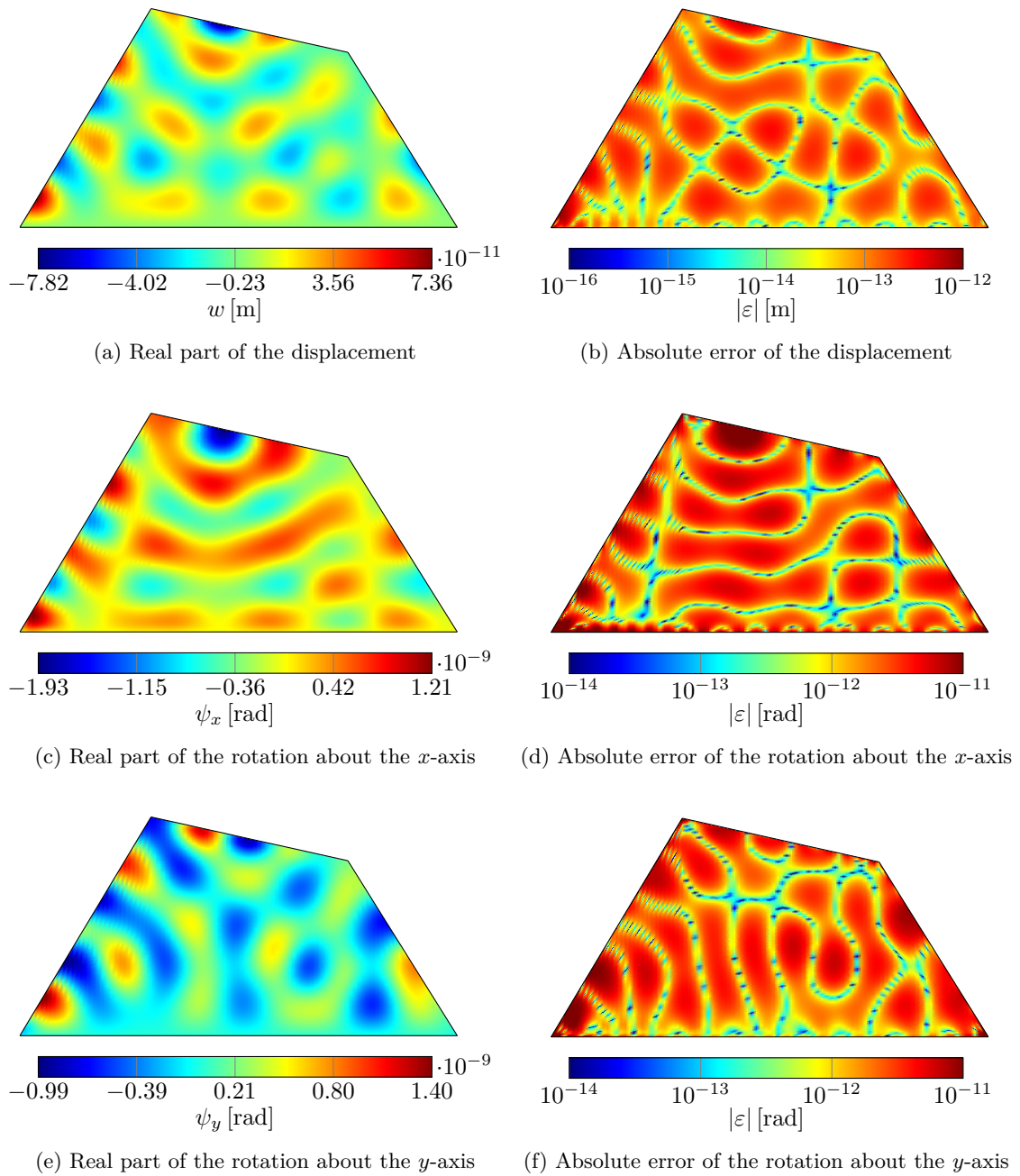


Figure E.55: Out-of-plane displacement and rotations about the  $x$ - and  $y$ -axis of a cantilever plate ( $h = 0.025$  m) excited by a constant circular load at 7750 Hz calculated with the modified WBM using only the function set 1 and a truncation factor  $T = 2$

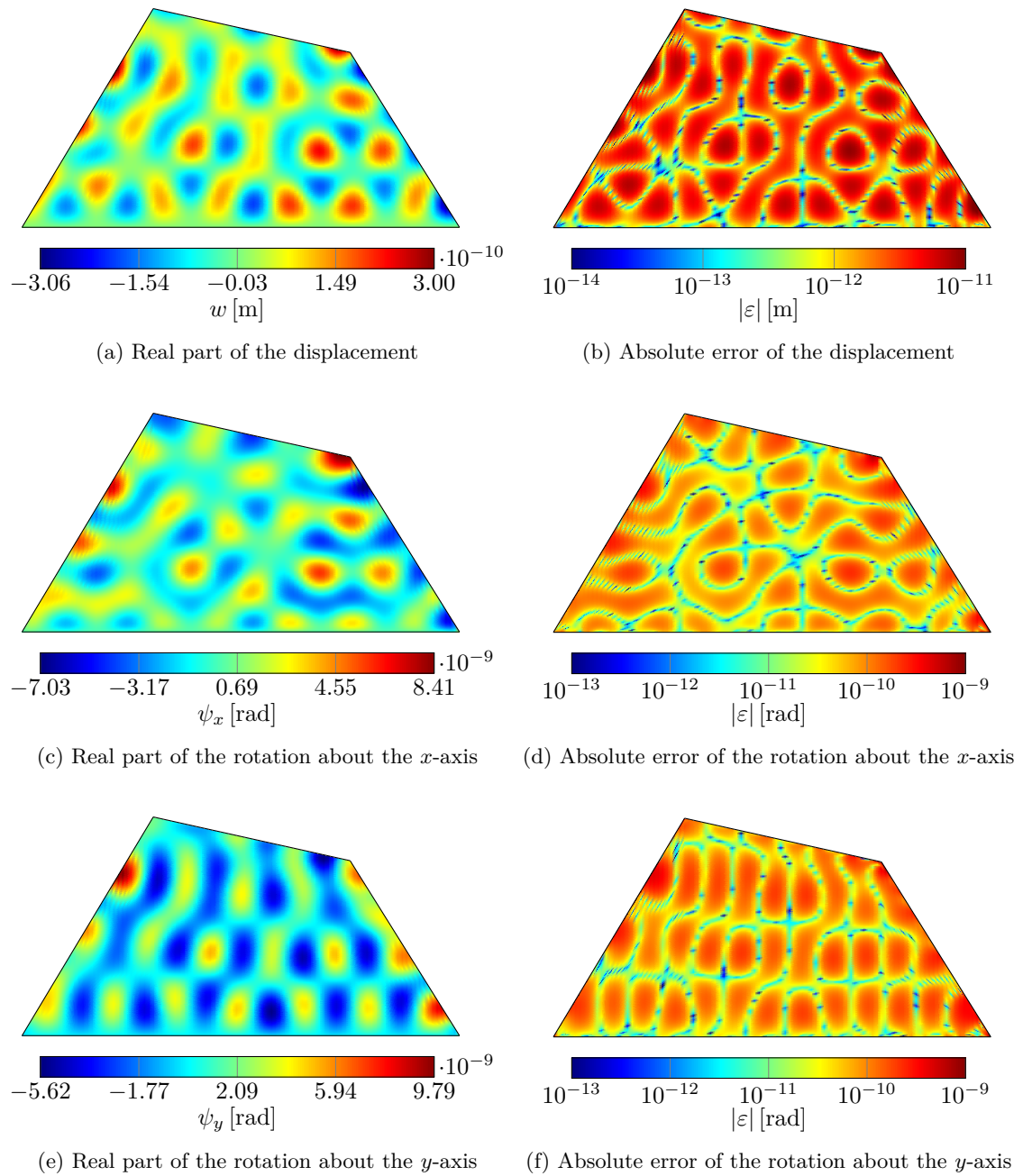


Figure E.56: Out-of-plane displacement and rotations about the  $x$ - and  $y$ -axis of a cantilever plate ( $h = 0.025$  m) excited by a constant circular load at 12770 Hz calculated with the modified WBM using only the function set 1 and a truncation factor  $T = 2$

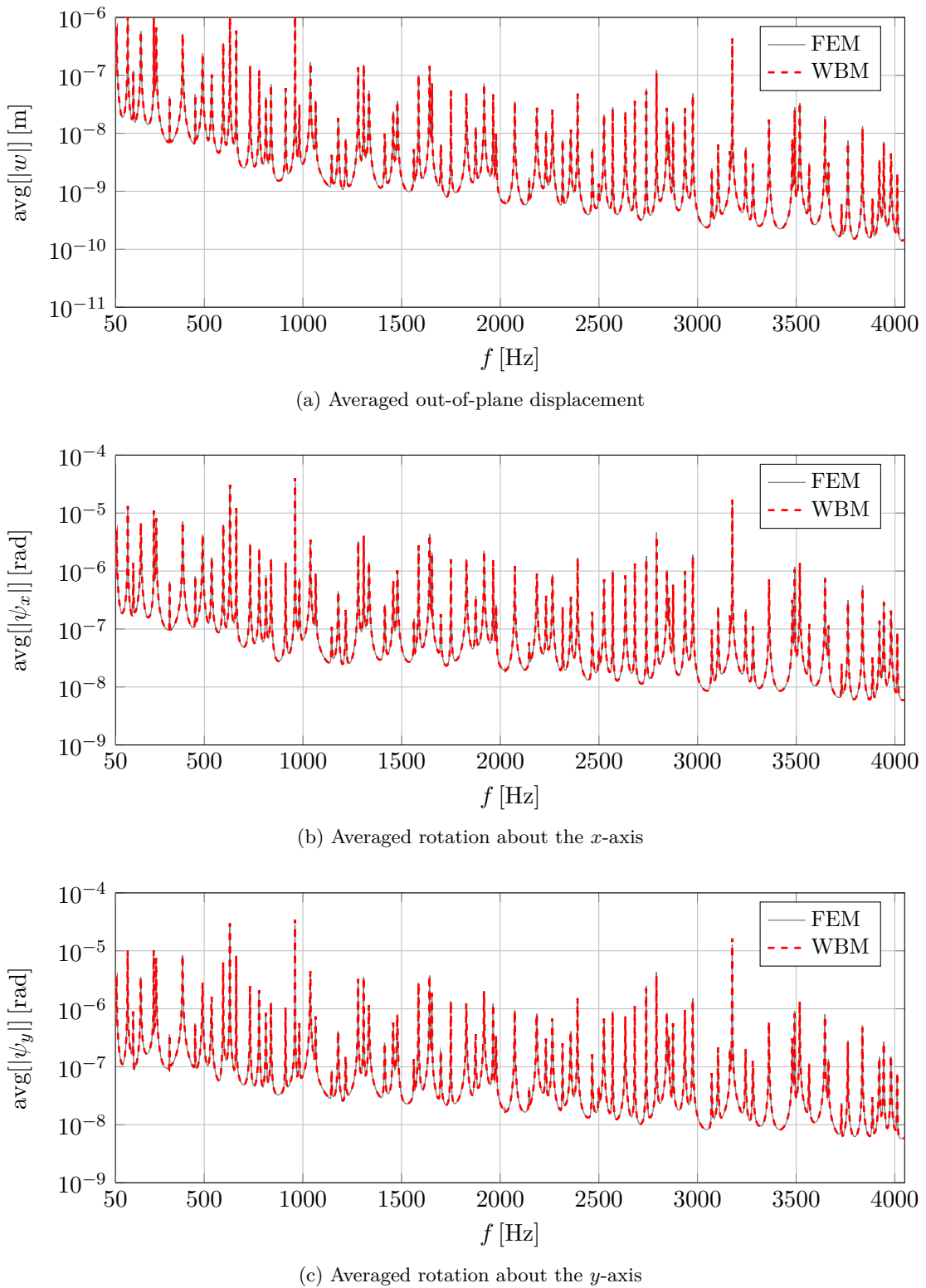
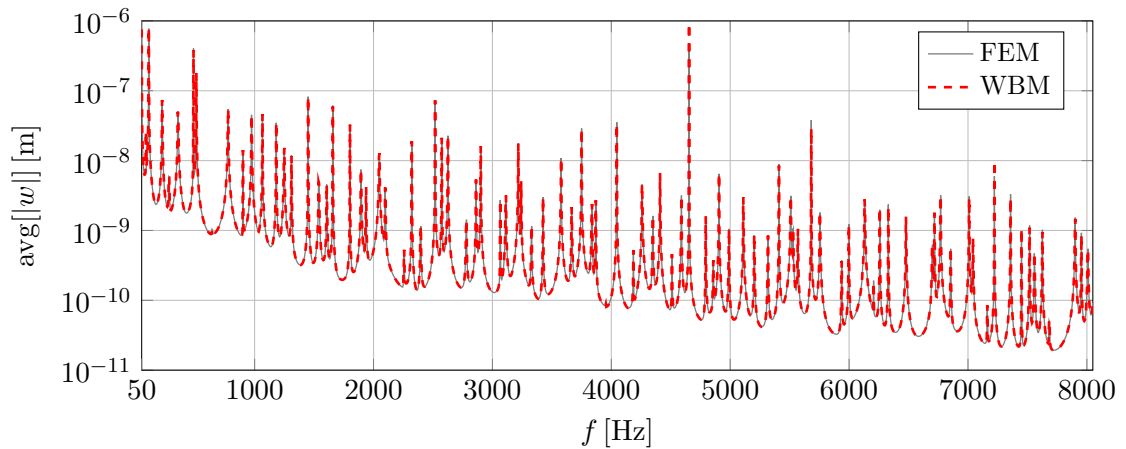
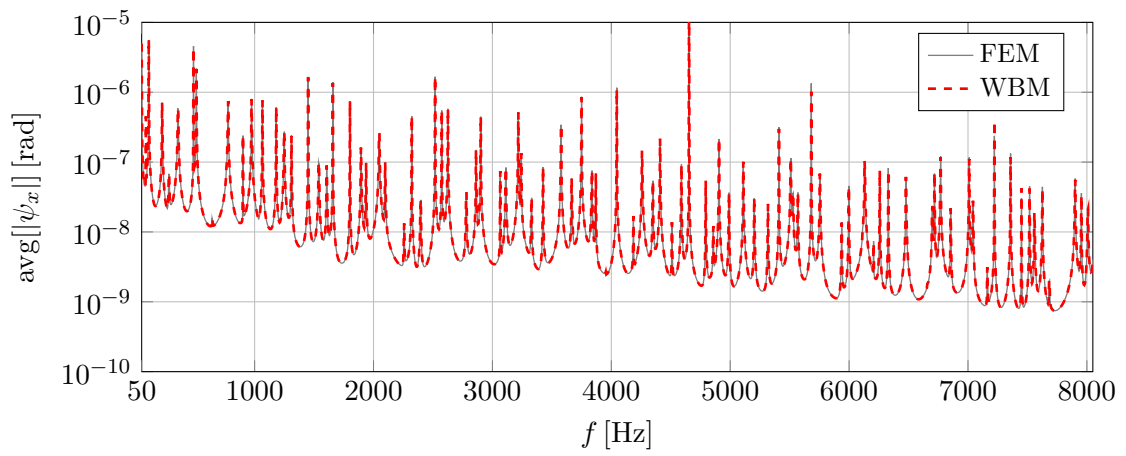


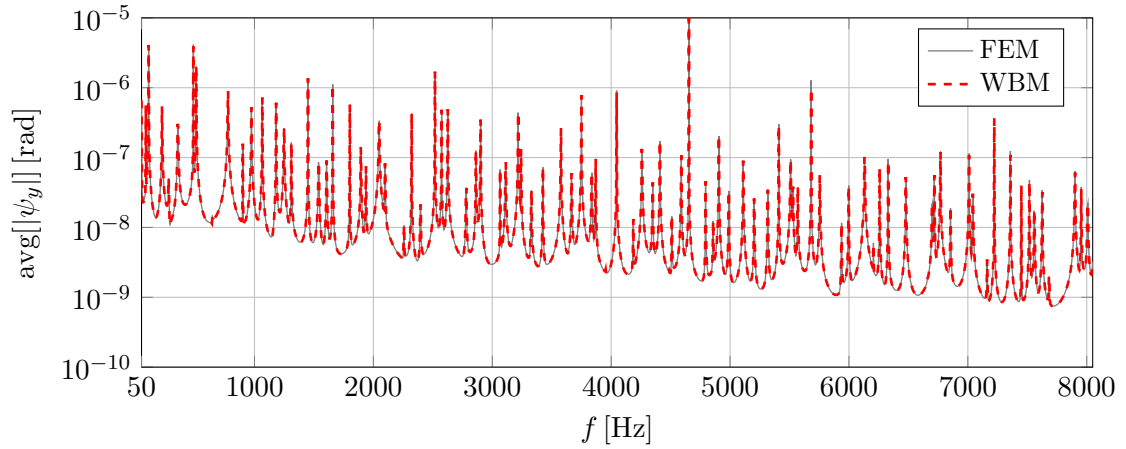
Figure E.57: Frequency response functions of a cantilever plate ( $h = 0.005$  m) excited by a constant circular load calculated with the FEM (reference mesh) and the modified WBM (function set 1 and set 2,  $T = 2$ )



(a) Averaged out-of-plane displacement



(b) Averaged rotation about the  $x$ -axis



(c) Averaged rotation about the  $y$ -axis

Figure E.58: Frequency response functions of a cantilever plate ( $h = 0.01$  m) excited by a constant circular load calculated with the FEM (reference mesh) and the modified WBM (function set 1 and set 2,  $T = 2$ )

## E Additional results for the validation examples

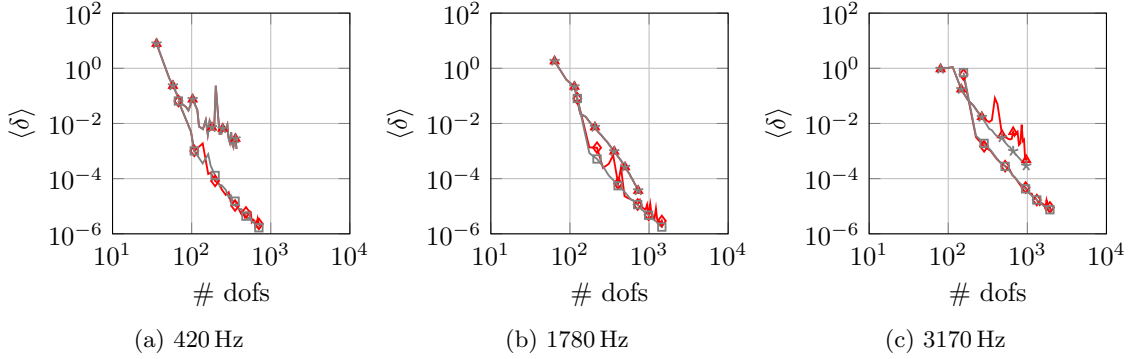


Figure E.59: Convergence curves of the out-of-plane displacement (cantilever plate with  $h = 0.005$  m) for the modified WBM solved with the LU (set1 (—▲—), set1a2 (—◆—)) and the SVD (set1 (—\*—), set1a2 (—□—))

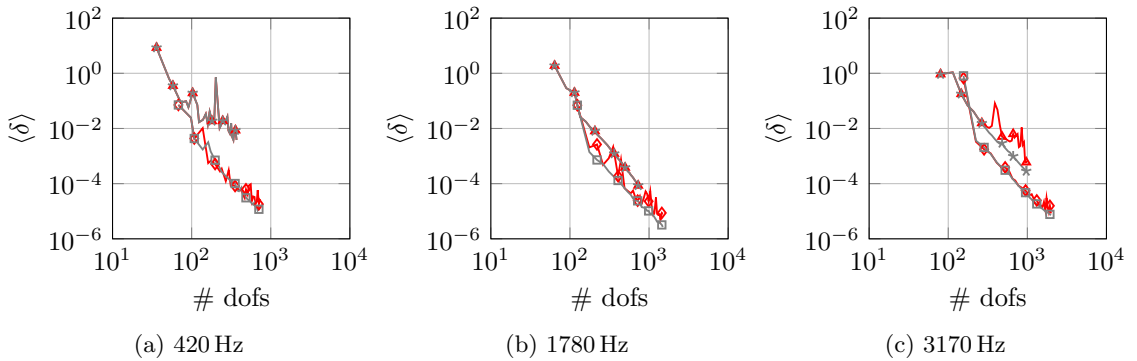


Figure E.60: Convergence curves of the rotation about the  $x$ -axis (cantilever plate with  $h = 0.005$  m) for the modified WBM solved with the LU (set1 (—▲—), set1a2 (—◆—)) and the SVD (set1 (—\*—), set1a2 (—□—))

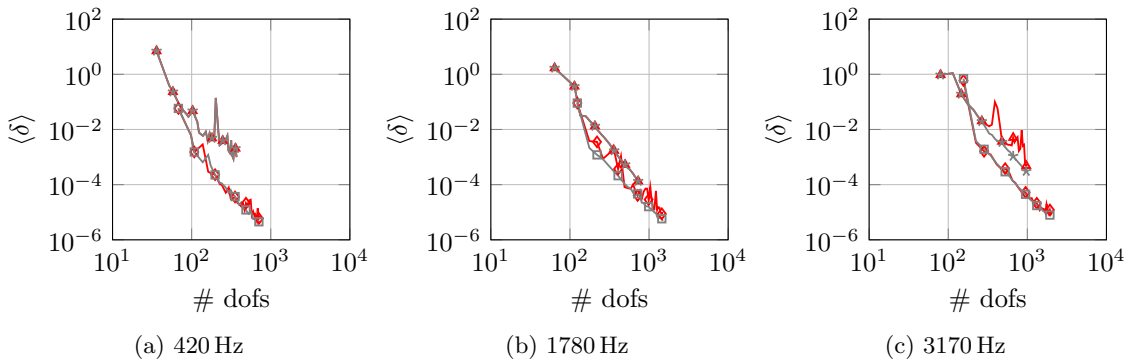


Figure E.61: Convergence curves of the rotation about the  $y$ -axis (cantilever plate with  $h = 0.005$  m) for the modified WBM solved with the LU (set1 (—▲—), set1a2 (—◆—)) and the SVD (set1 (—\*—), set1a2 (—□—))

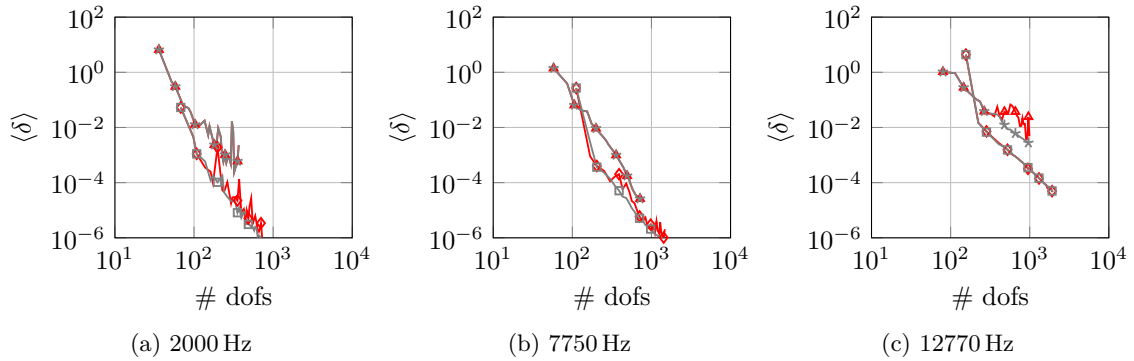


Figure E.62: Convergence curves of the out-of-plane displacement (cantilever plate with  $h = 0.025$  m) for the modified WBM solved with the LU (set1 (—▲—), set1a2 (—◆—)) and the SVD (set1 (—\*—), set1a2 (—□—))

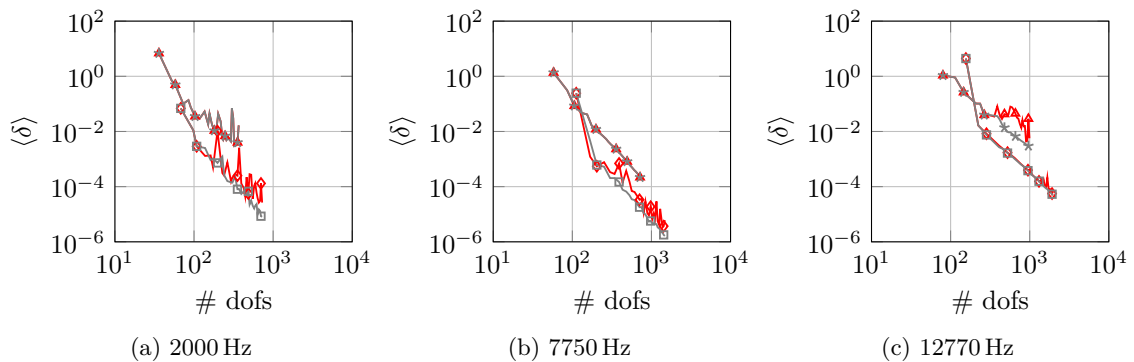


Figure E.63: Convergence curves of the rotation about the  $x$ -axis (cantilever plate with  $h = 0.025$  m) for the modified WBM solved with the LU (set1 (—▲—), set1a2 (—◆—)) and the SVD (set1 (—\*—), set1a2 (—□—))

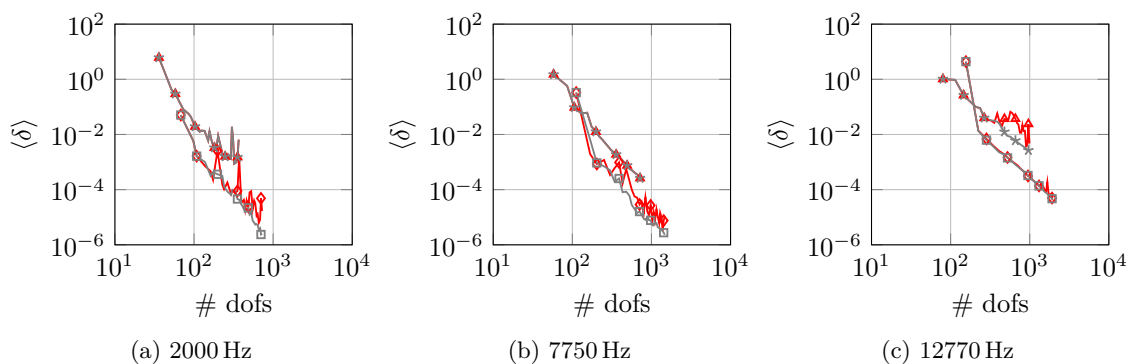


Figure E.64: Convergence curves of the rotation about the  $y$ -axis (cantilever plate with  $h = 0.025$  m) for the modified WBM solved with the LU (set1 (—▲—), set1a2 (—◆—)) and the SVD (set1 (—\*—), set1a2 (—□—))

**Single domain simply-supported plate**

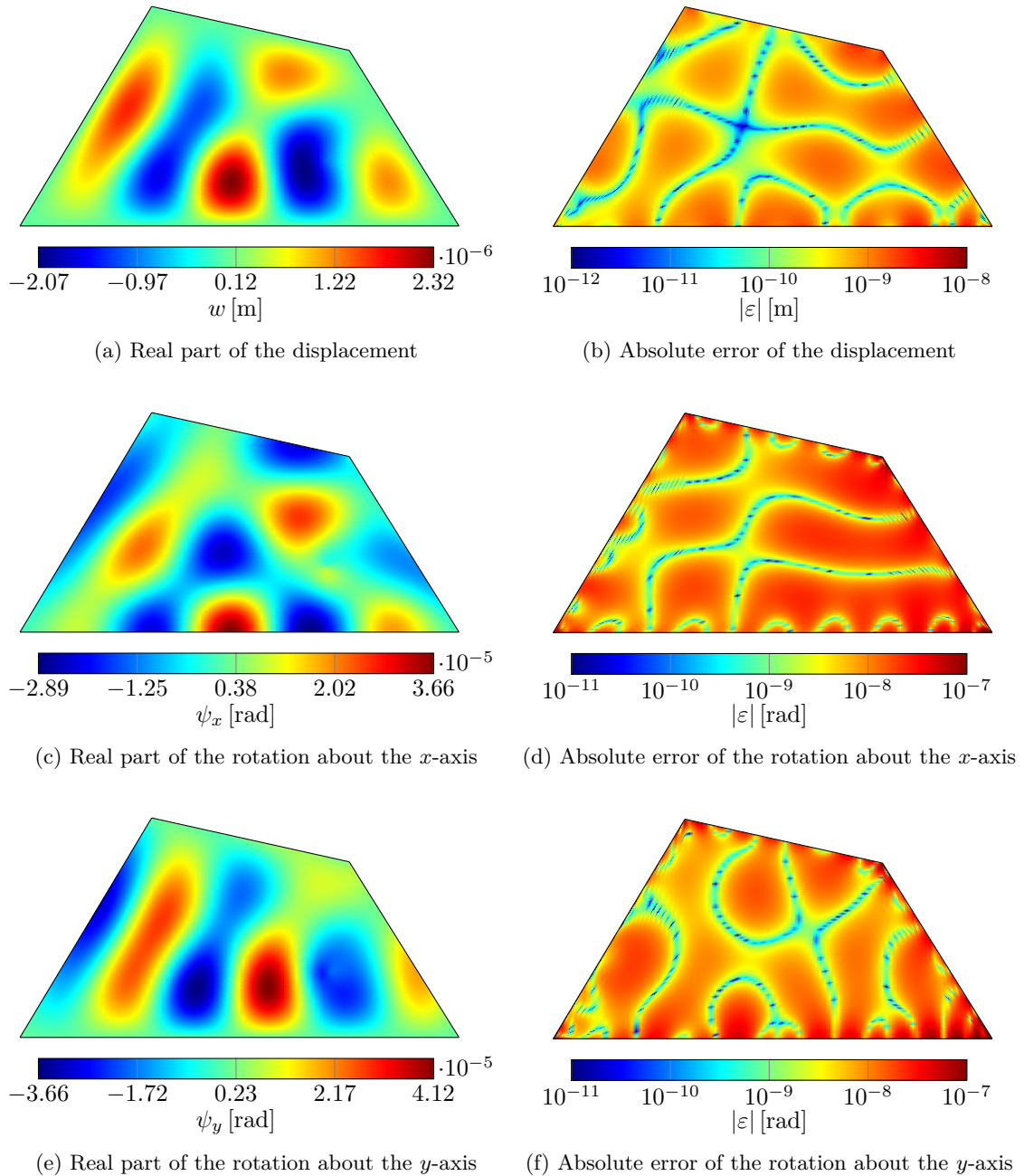
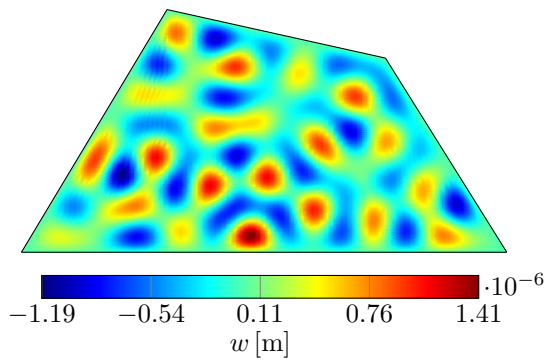
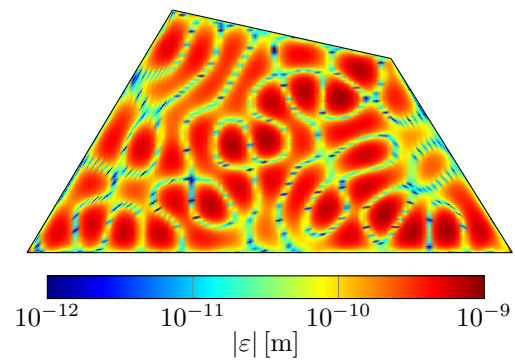


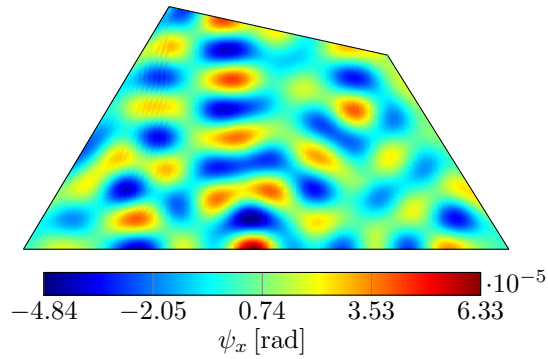
Figure E.65: Out-of-plane displacement and rotations about the  $x$ - and  $y$ -axis of a hard simply-supported plate ( $h = 0.005$  m) excited by a point load at 670 Hz calculated with the modified WBM using the function set 1, corner functions and a truncation factor  $T = 2$



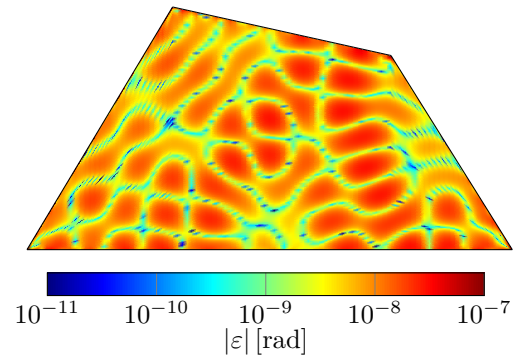
(a) Real part of the displacement



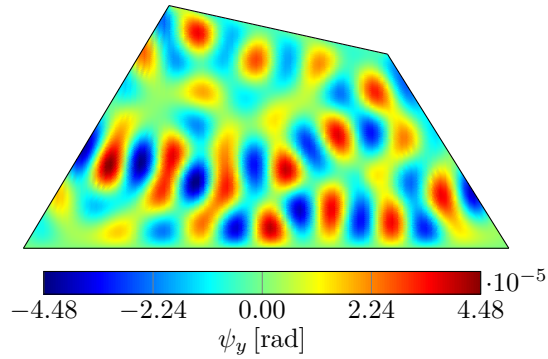
(b) Absolute error of the displacement



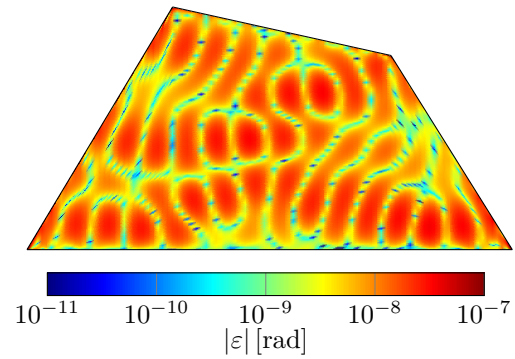
(c) Real part of the rotation about the  $x$ -axis



(d) Absolute error of the rotation about the  $x$ -axis



(e) Real part of the rotation about the  $y$ -axis



(f) Absolute error of the rotation about the  $y$ -axis

Figure E.66: Out-of-plane displacement and rotations about the  $x$ - and  $y$ -axis of a hard simply-supported plate ( $h = 0.005$  m) excited by a point load at 3800 Hz calculated with the modified WBM using the function set 1, corner functions and a truncation factor  $T = 2$

E Additional results for the validation examples

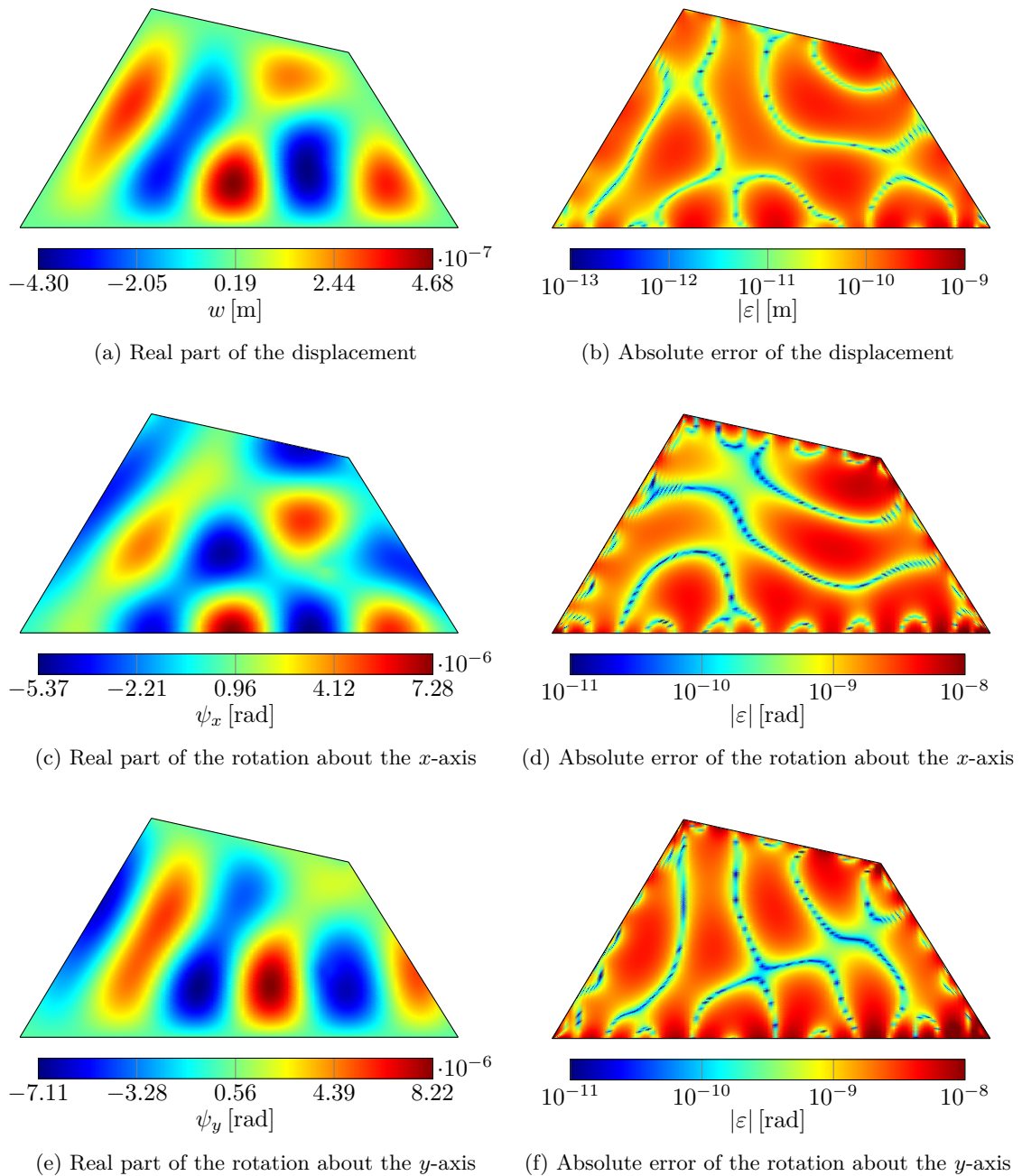


Figure E.67: Out-of-plane displacement and rotations about the  $x$ - and  $y$ -axis of a hard simply-supported plate ( $h = 0.01$  m) excited by a point load at 1300 Hz calculated with the modified WBM using the function set 1, corner functions and a truncation factor  $T = 2$

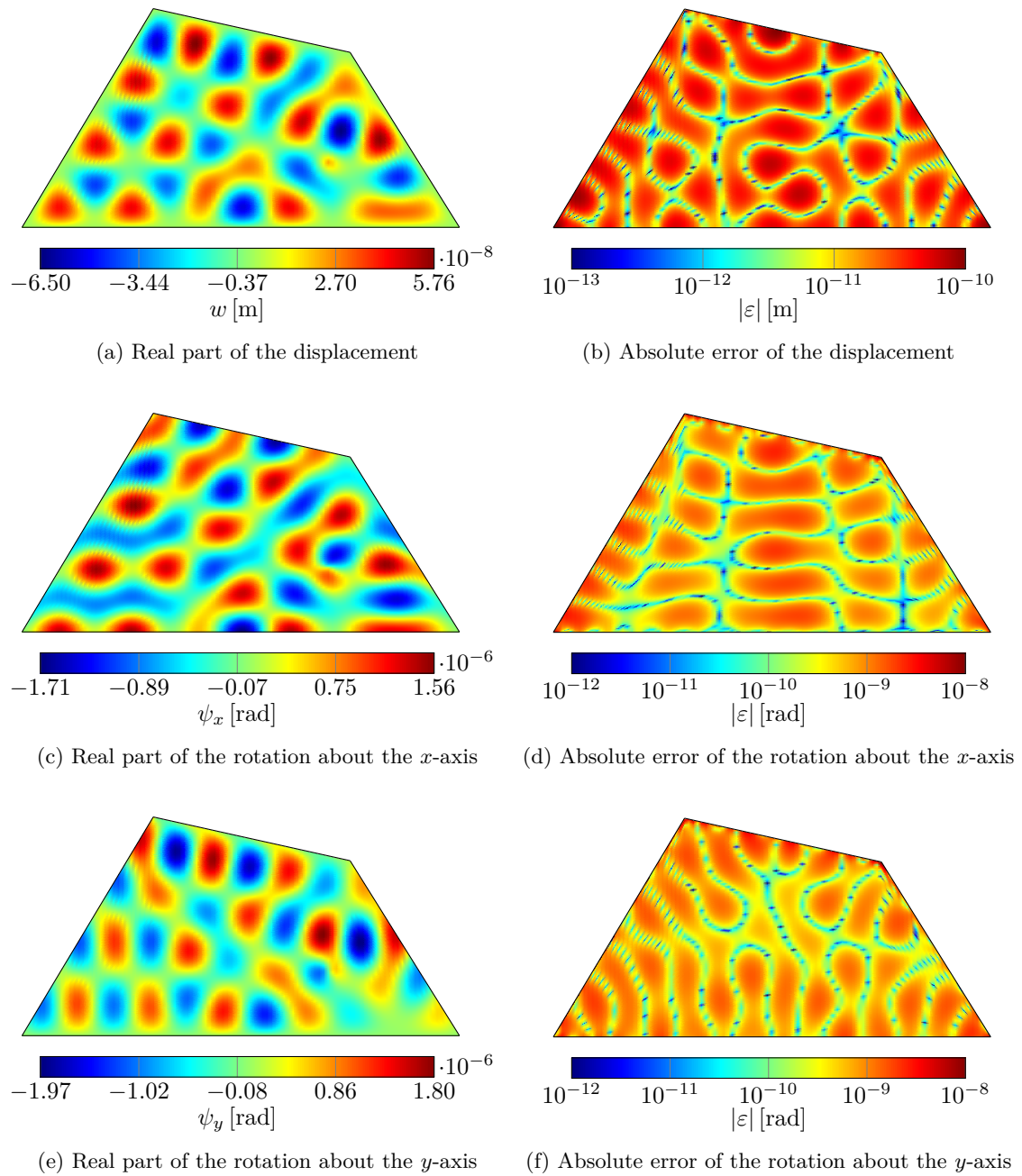


Figure E.68: Out-of-plane displacement and rotations about the  $x$ - and  $y$ -axis of a hard simply-supported plate ( $h = 0.01$  m) excited by a point load at 4600 Hz calculated with the modified WBM using the function set 1, corner functions and a truncation factor  $T = 2$

E Additional results for the validation examples

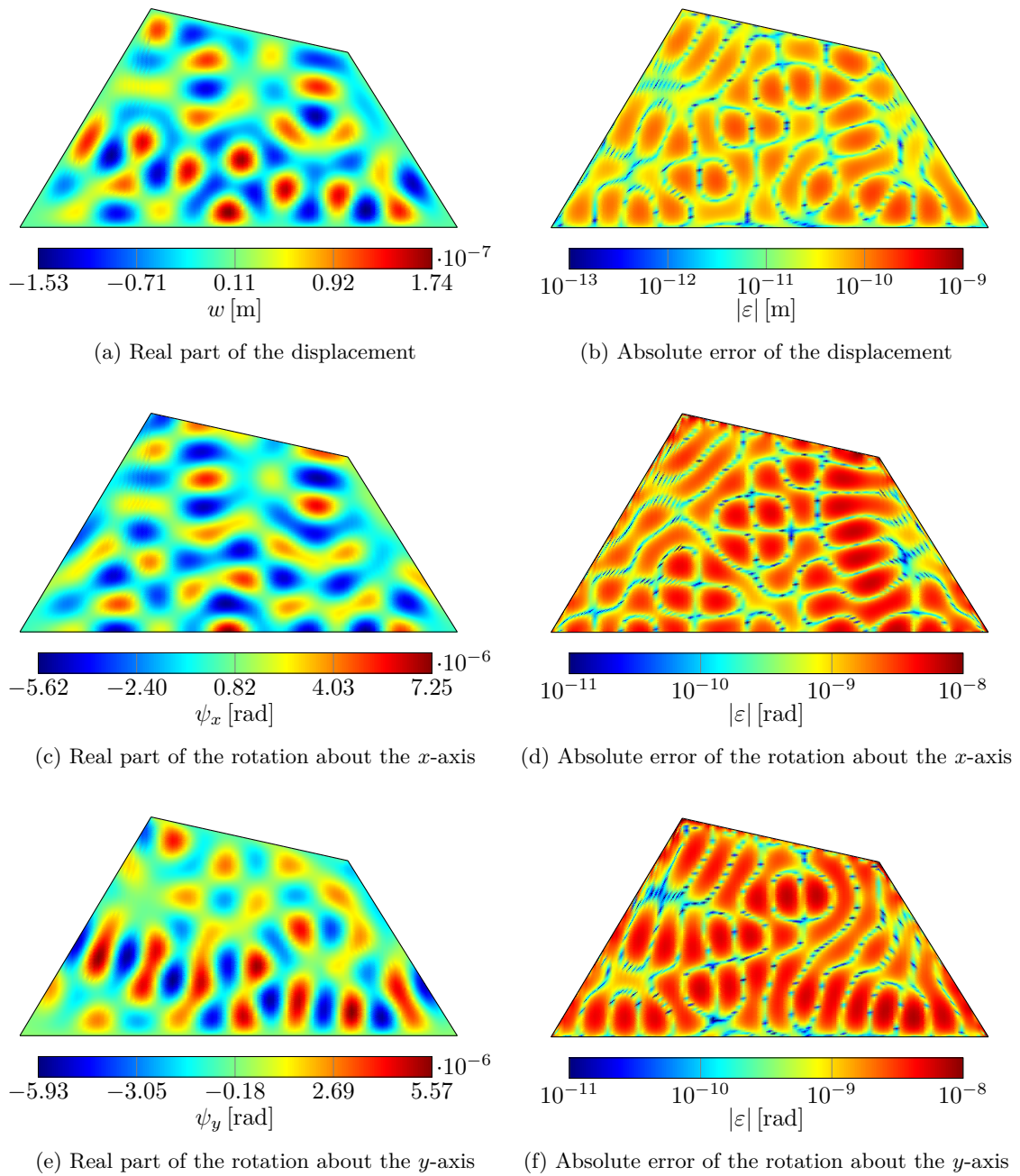


Figure E.69: Out-of-plane displacement and rotations about the  $x$ - and  $y$ -axis of a hard simply-supported plate ( $h = 0.01$  m) excited by a point load at 7310 Hz calculated with the modified WBM using the function set 1, corner functions and a truncation factor  $T = 2$

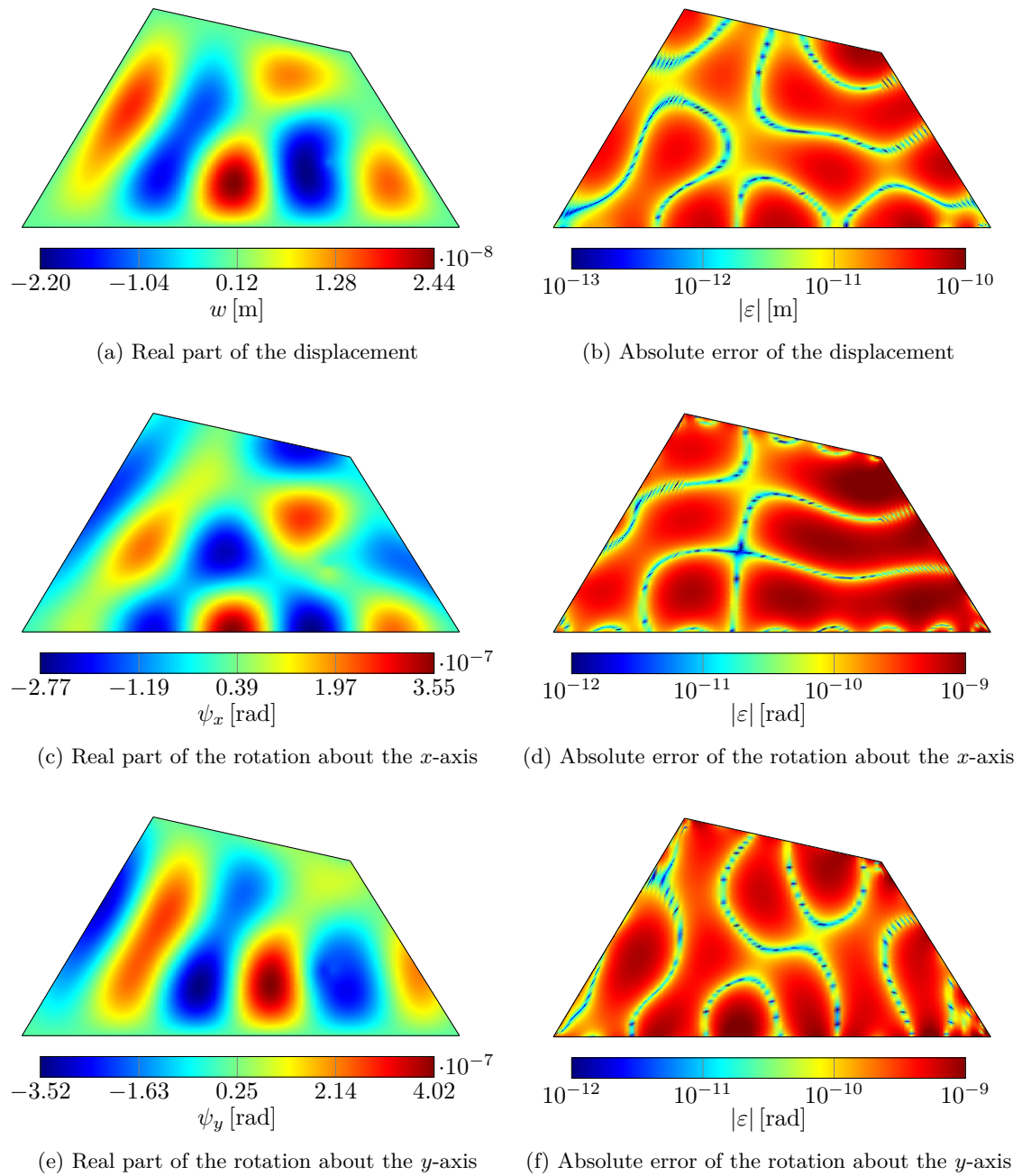


Figure E.70: Out-of-plane displacement and rotations about the  $x$ - and  $y$ -axis of a hard simply-supported plate ( $h = 0.025$  m) excited by a point load at 3150 Hz calculated with the modified WBM using the function set 1, corner functions and a truncation factor  $T = 2$

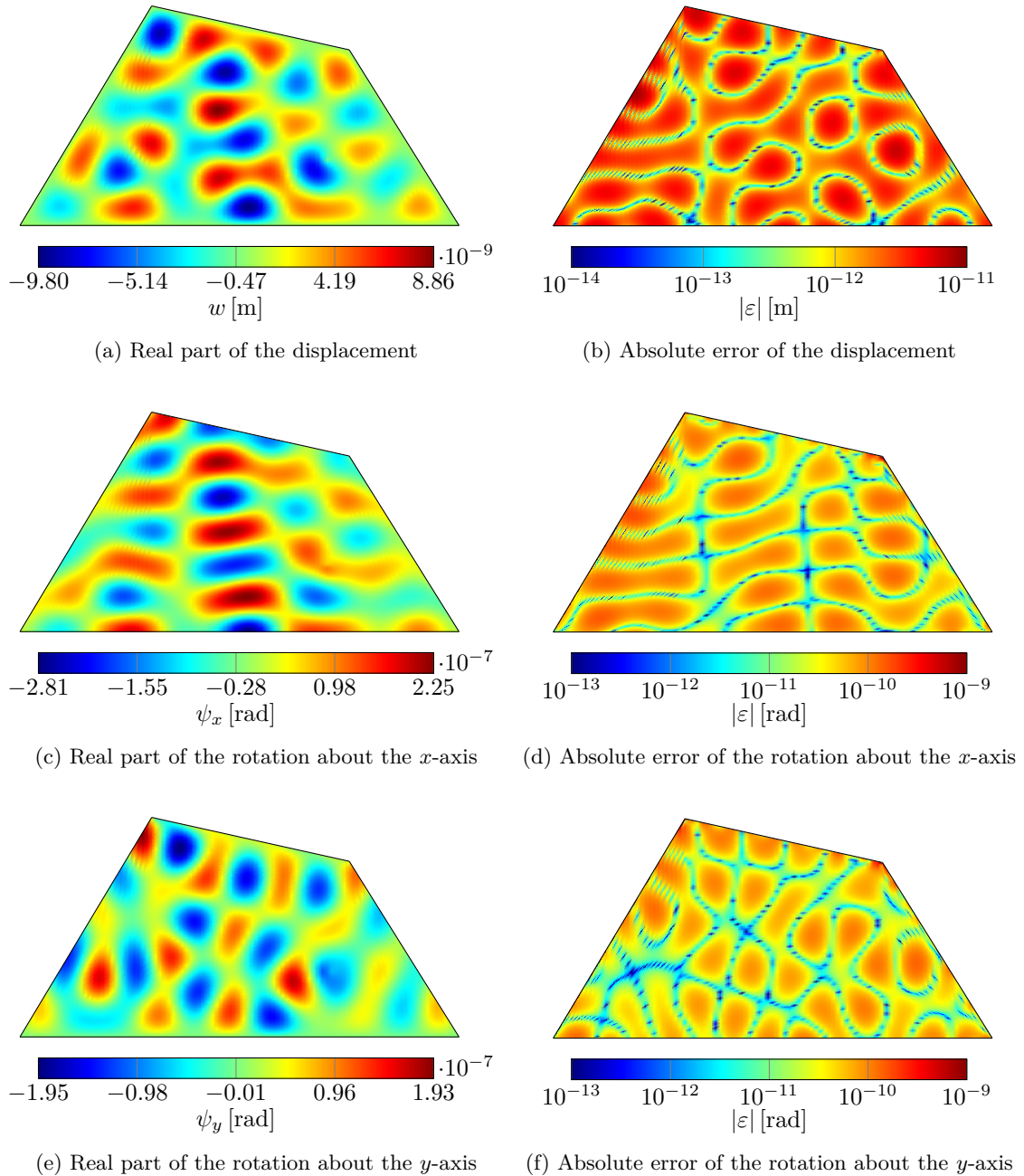


Figure E.71: Out-of-plane displacement and rotations about the  $x$ - and  $y$ -axis of a hard simply-supported plate ( $h = 0.025$  m) excited by a point load at 9800 Hz calculated with the modified WBM using the function set 1, corner functions and a truncation factor  $T = 2$

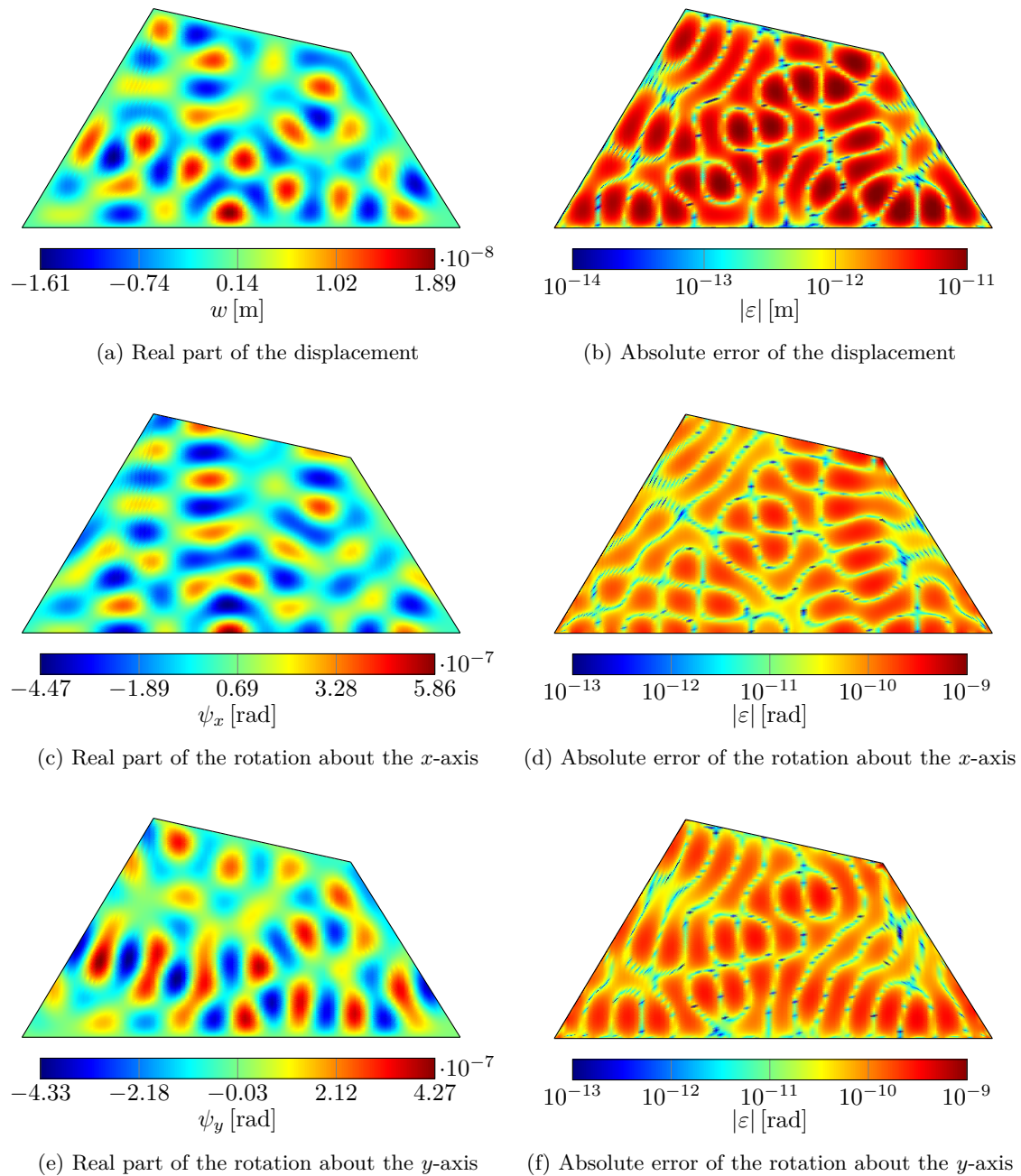


Figure E.72: Out-of-plane displacement and rotations about the  $x$ - and  $y$ -axis of a hard simply-supported plate ( $h = 0.025 \text{ m}$ ) excited by a point load at 15060 Hz calculated with the modified WBM using the function set 1, corner functions and a truncation factor  $T = 2$

E Additional results for the validation examples

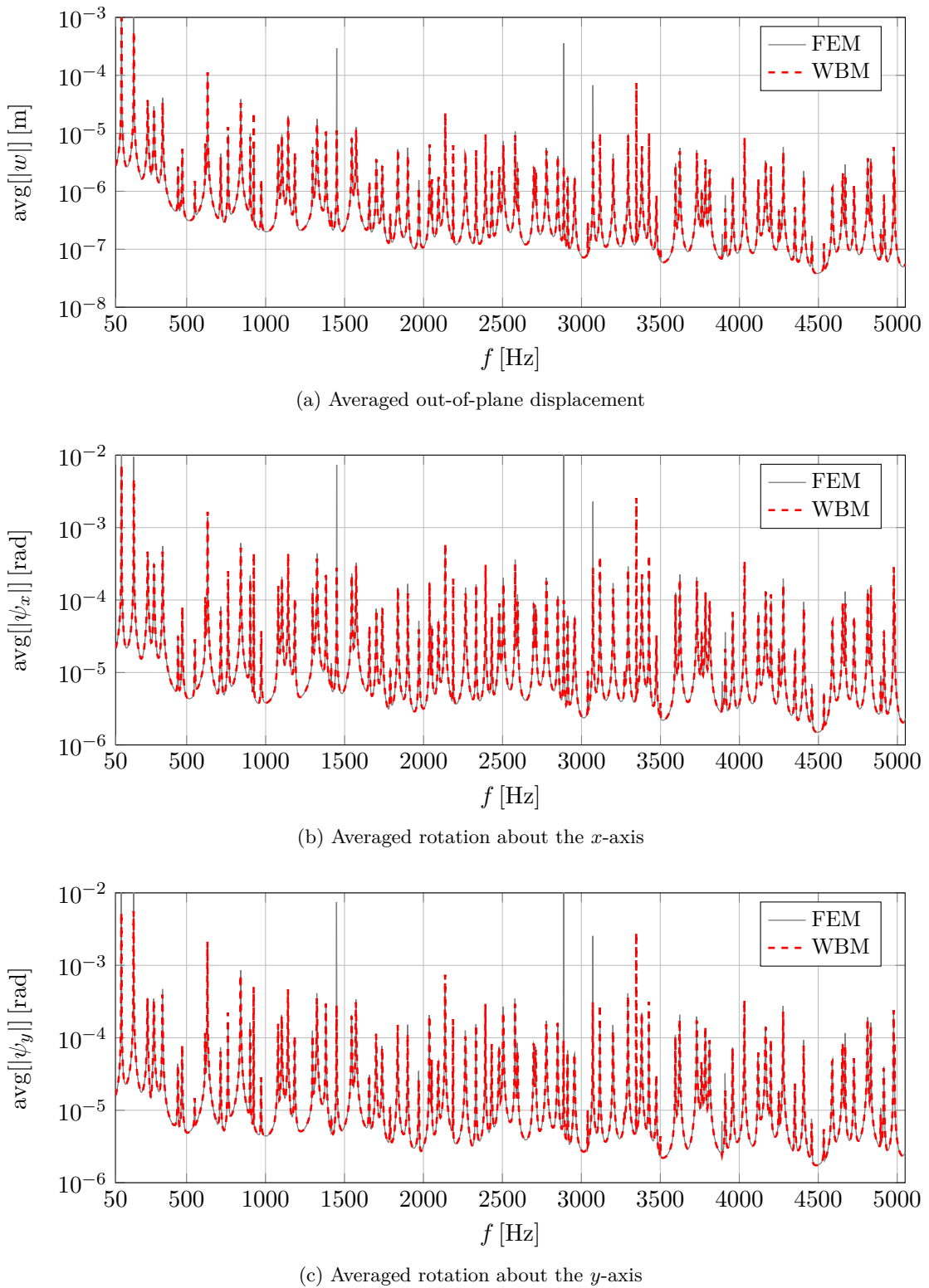
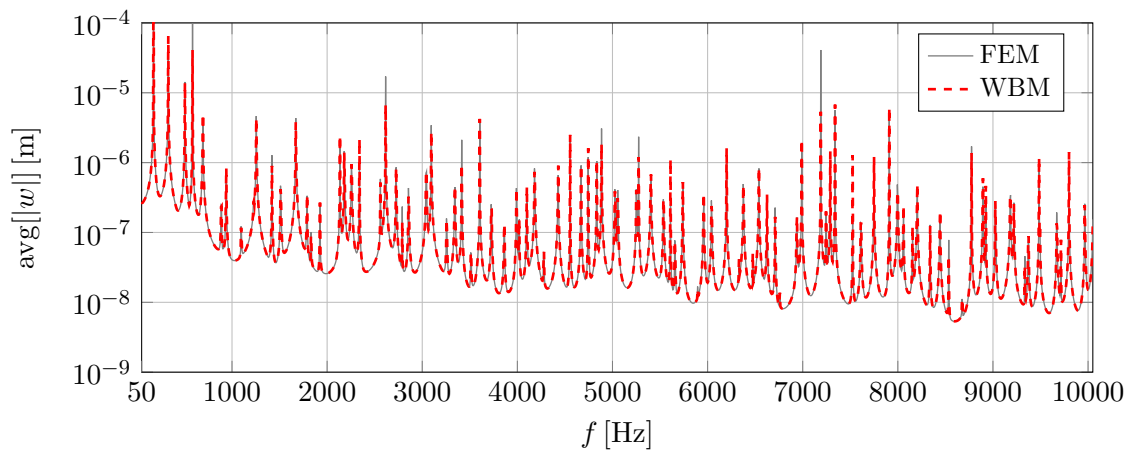
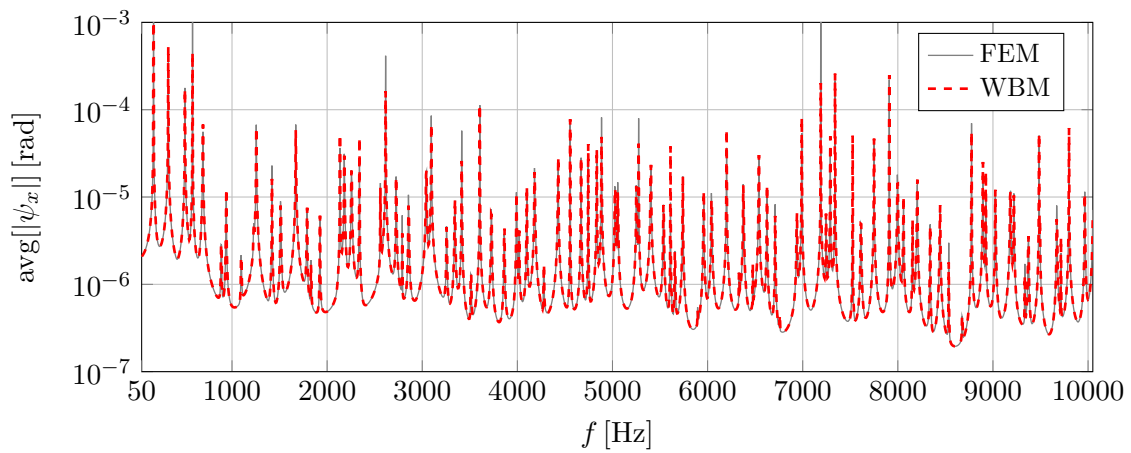


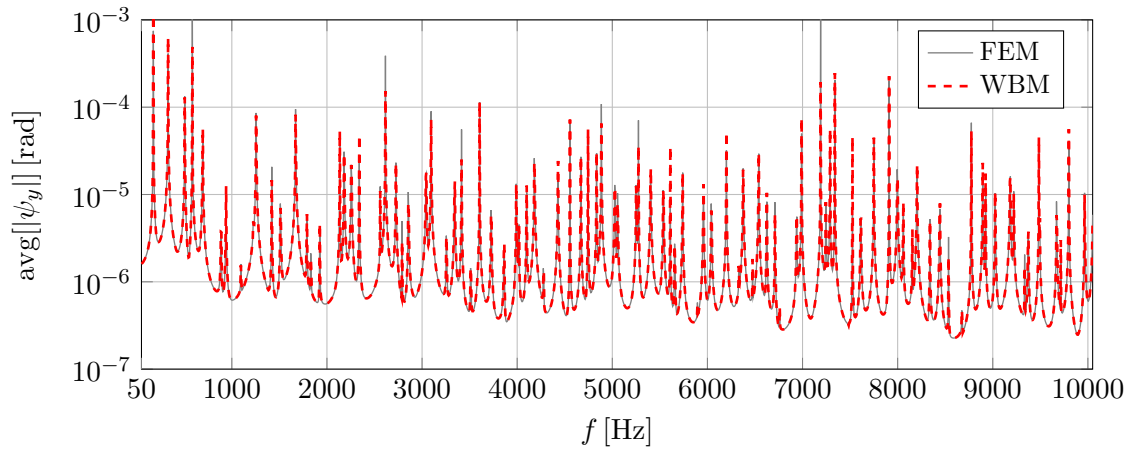
Figure E.73: Frequency response functions of a hard simply-supported plate ( $h = 0.005$  m) excited by a point load calculated with the FEM (reference mesh) and the modified WBM (function set 1 and set 2, corner functions,  $T = 2$ )



(a) Averaged out-of-plane displacement



(b) Averaged rotation about the  $x$ -axis



(c) Averaged rotation about the  $y$ -axis

Figure E.74: Frequency response functions of a hard simply-supported plate ( $h = 0.01$  m) excited by a point load calculated with the FEM (reference mesh) and the modified WBM (function set 1 and set 2, corner functions,  $T = 2$ )

## E Additional results for the validation examples

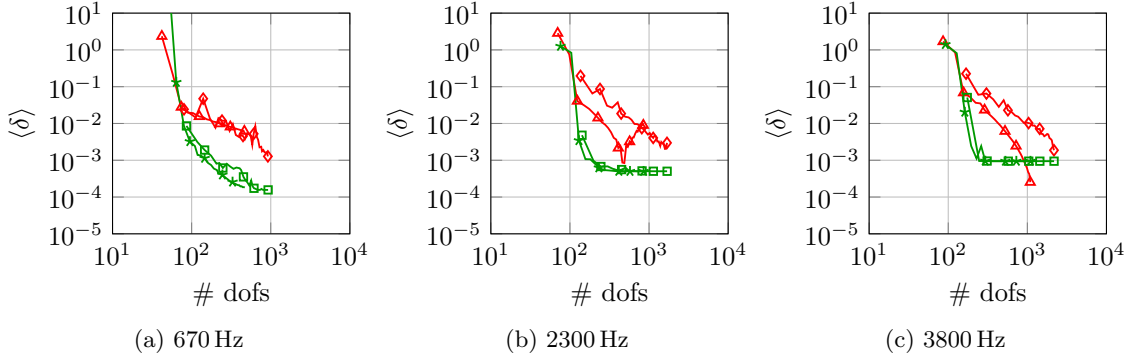


Figure E.75: Convergence curves of the out-of-plane displacement (hard SS plate with  $h = 0.005$  m) for the modified WBM (*set1* (—▲—), *set1a2* (—◆—), *set1CF* (—★—), *set1a2CF* (—■—))

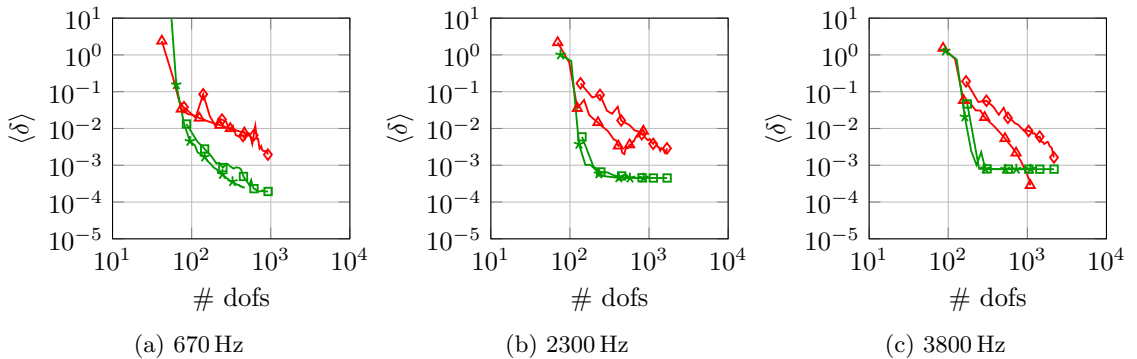


Figure E.76: Convergence curves of the rotation about the  $x$ -axis (hard SS plate with  $h = 0.005$  m) for the modified WBM (*set1* (—▲—), *set1a2* (—◆—), *set1CF* (—★—), *set1a2CF* (—■—))

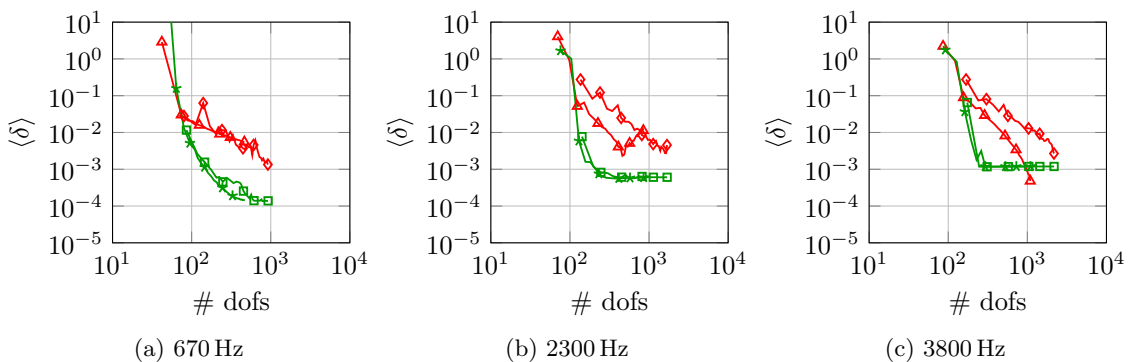


Figure E.77: Convergence curves of the rotation about the  $y$ -axis (hard SS plate with  $h = 0.005$  m) for the modified WBM (*set1* (—▲—), *set1a2* (—◆—), *set1CF* (—★—), *set1a2CF* (—■—))

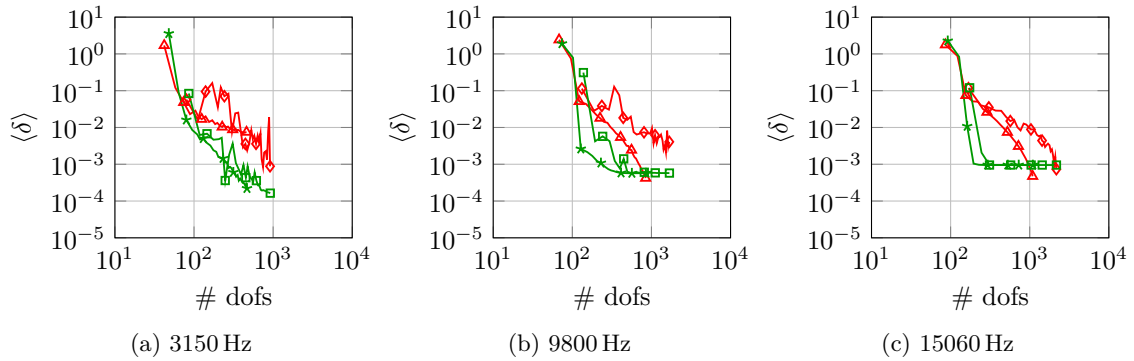


Figure E.78: Convergence curves of the out-of-plane displacement (hard SS plate with  $h = 0.025$  m) for the modified WBM (set1 (red triangle), set1a2 (red diamond), set1CF (green asterisk), set1a2CF (green square))

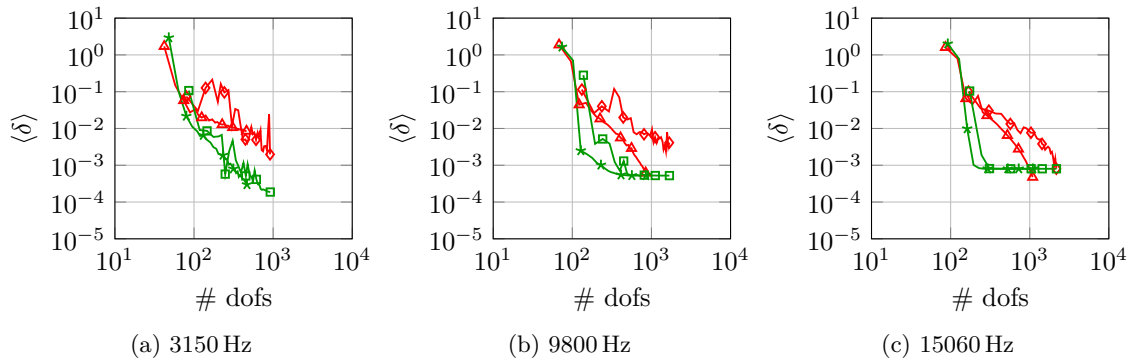


Figure E.79: Convergence curves of the rotation about the  $x$ -axis (hard SS plate with  $h = 0.025$  m) for the modified WBM (set1 (red triangle), set1a2 (red diamond), set1CF (green asterisk), set1a2CF (green square))

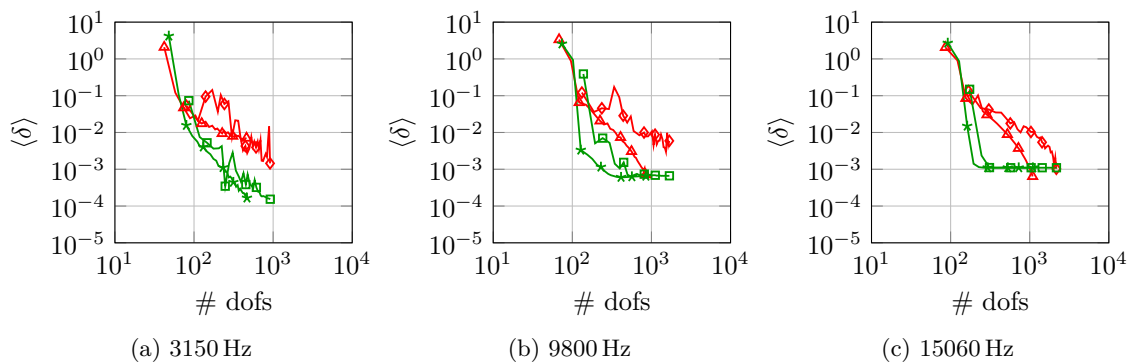


Figure E.80: Convergence curves of the rotation about the  $y$ -axis (hard SS plate with  $h = 0.025$  m) for the modified WBM (set1 (red triangle), set1a2 (red diamond), set1CF (green asterisk), set1a2CF (green square))

**Multi domain clamped plate**

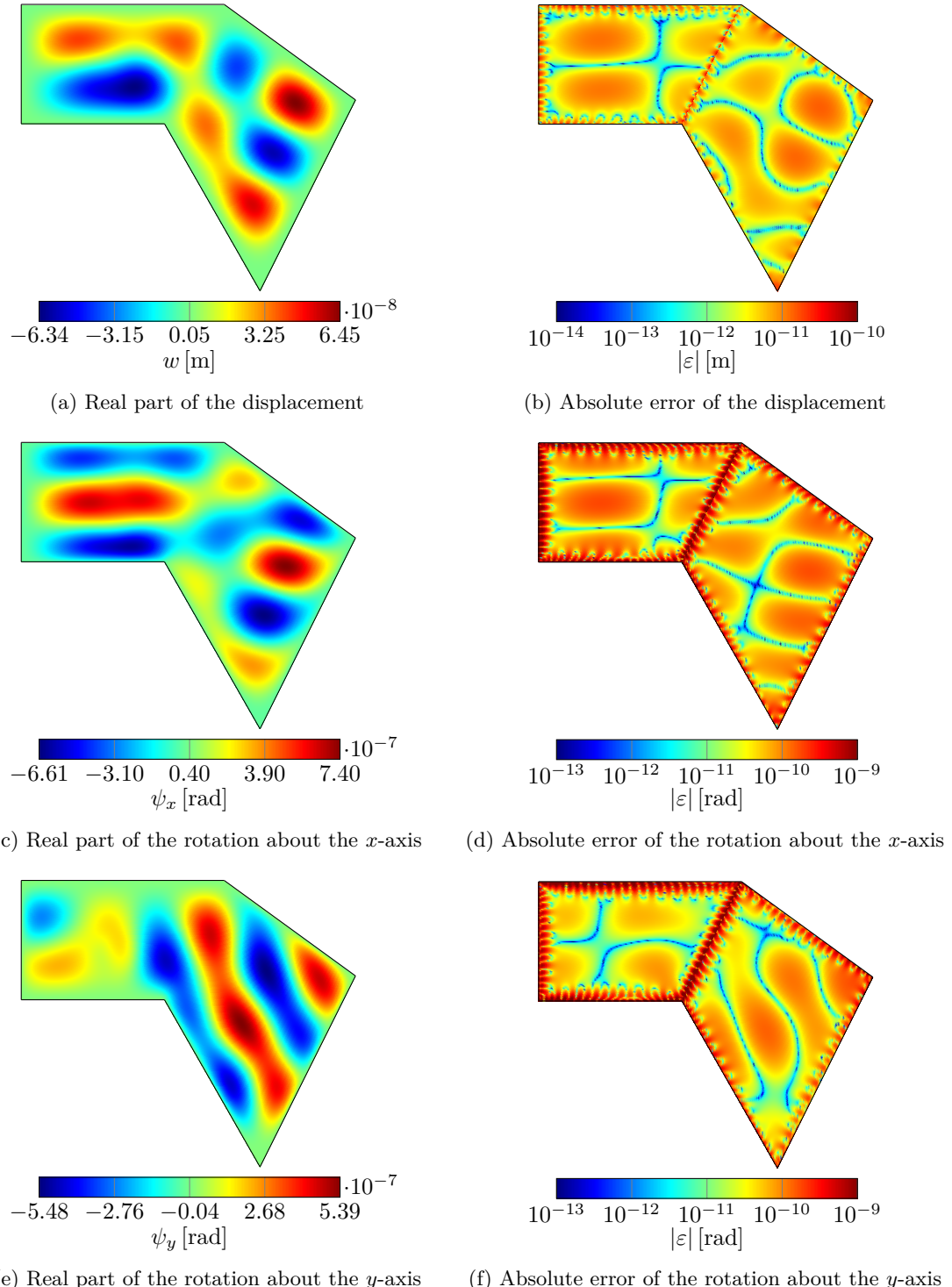
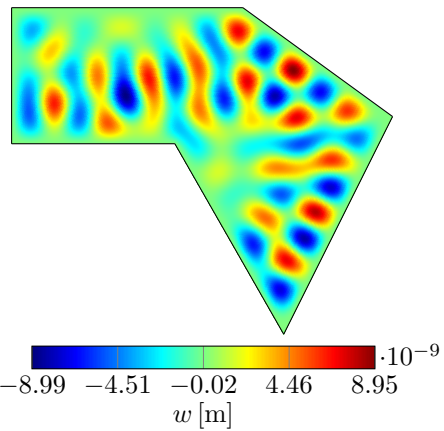
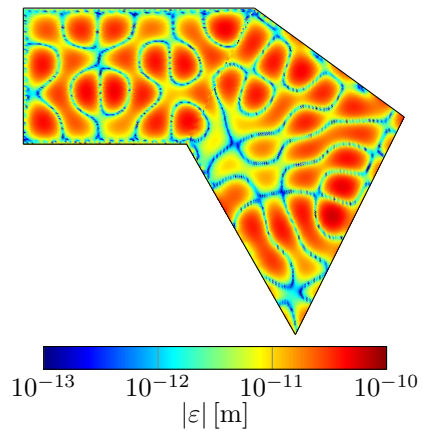


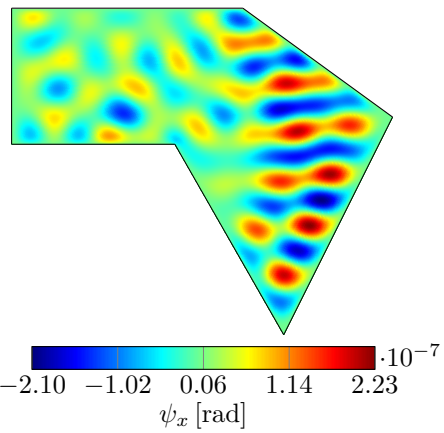
Figure E.81: Out-of-plane displacement and rotations about the  $x$ - and  $y$ -axis of a multi domain clamped plate ( $h = 0.005$  m) excited by a constant circular load at 350 Hz calculated with the modified WBM using both function sets, corner functions and a truncation factor  $T = 4$



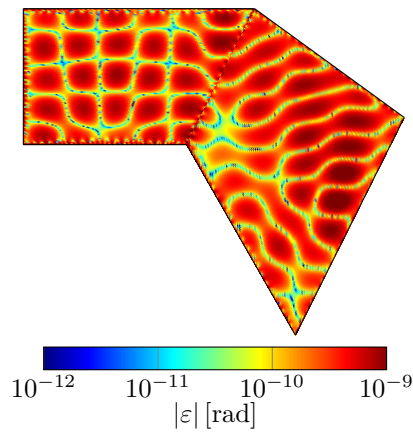
(a) Real part of the displacement



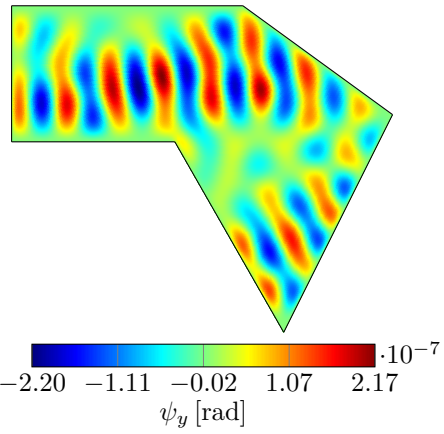
(b) Absolute error of the displacement



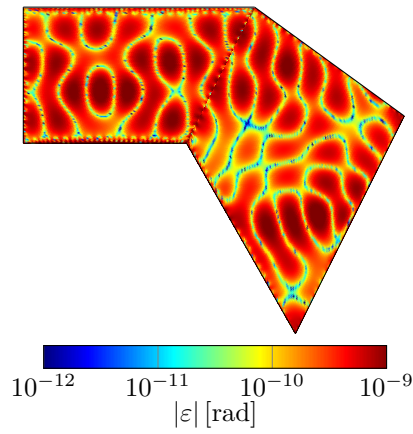
(c) Real part of the rotation about the  $x$ -axis



(d) Absolute error of the rotation about the  $x$ -axis



(e) Real part of the rotation about the  $y$ -axis



(f) Absolute error of the rotation about the  $y$ -axis

Figure E.82: Out-of-plane displacement and rotations about the  $x$ - and  $y$ -axis of a multi domain clamped plate ( $h = 0.005$  m) excited by a constant circular load at 1650 Hz calculated with the modified WBM using both function sets, corner functions and a truncation factor  $T = 4$

E Additional results for the validation examples

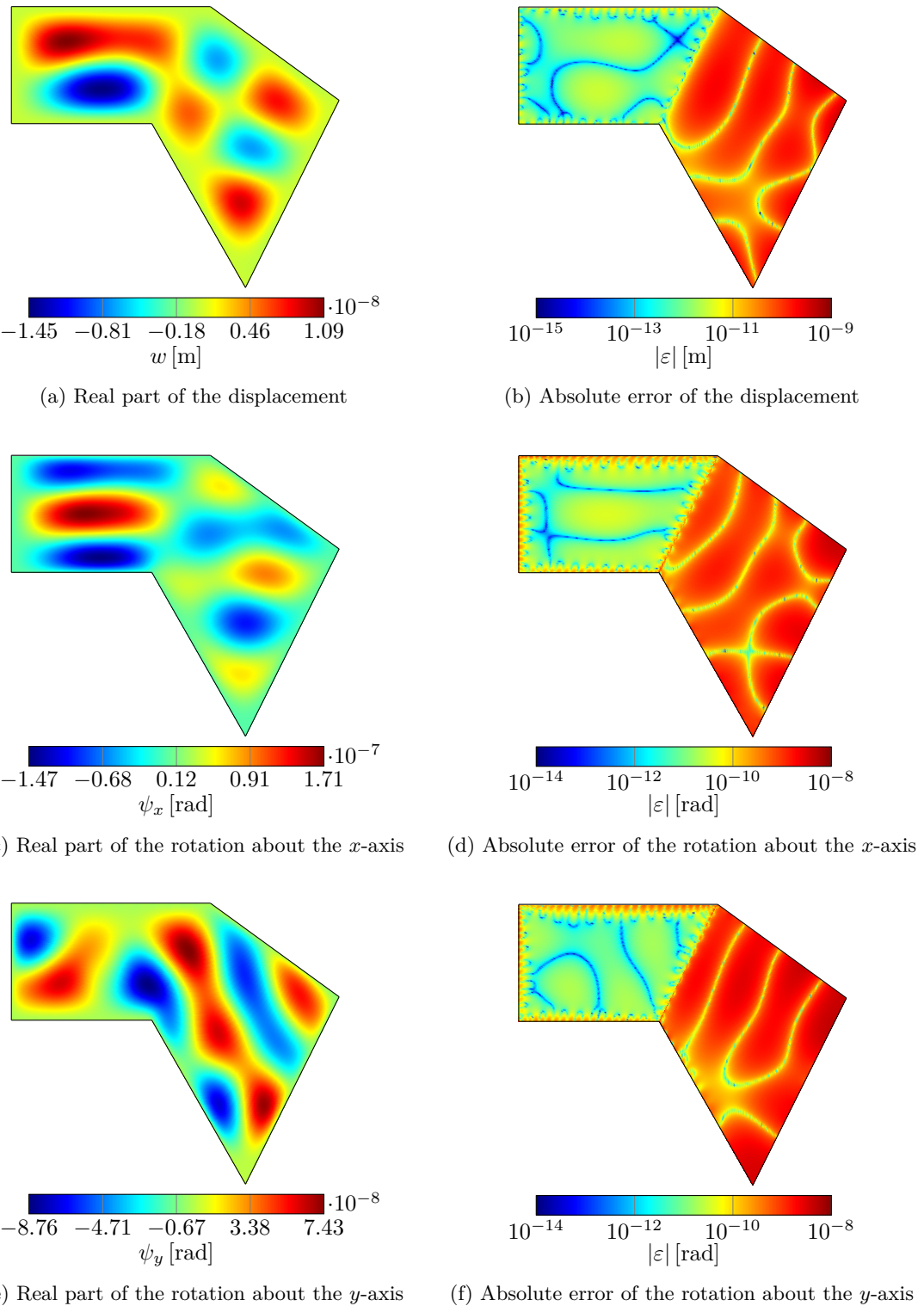
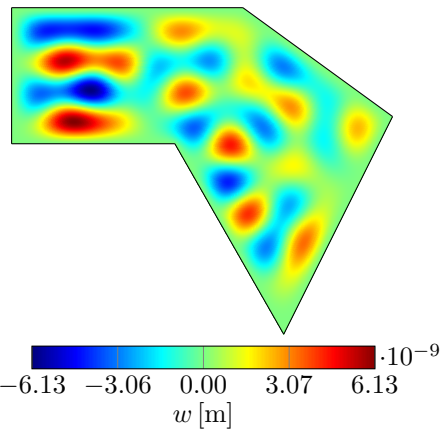
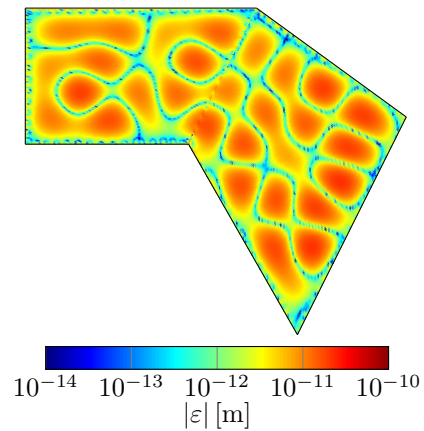


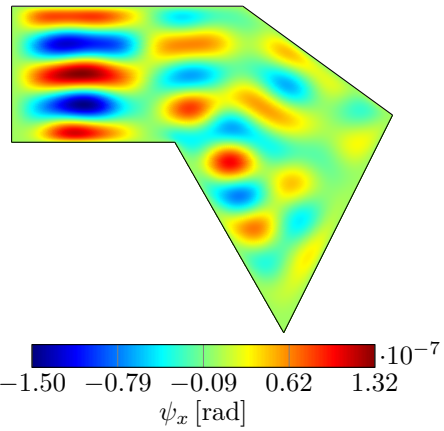
Figure E.83: Out-of-plane displacement and rotations about the  $x$ - and  $y$ -axis of a multi domain clamped plate ( $h = 0.01$  m) excited by a constant circular load at 680 Hz calculated with the modified WBM using both function sets, corner functions and a truncation factor  $T = 4$



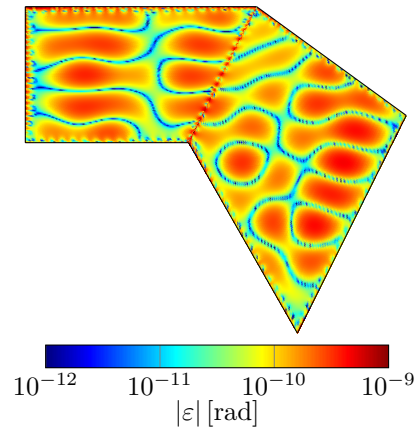
(a) Real part of the displacement



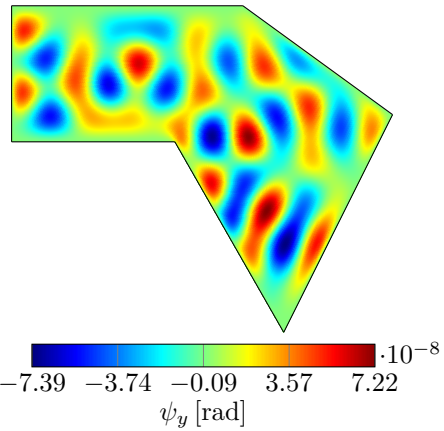
(b) Absolute error of the displacement



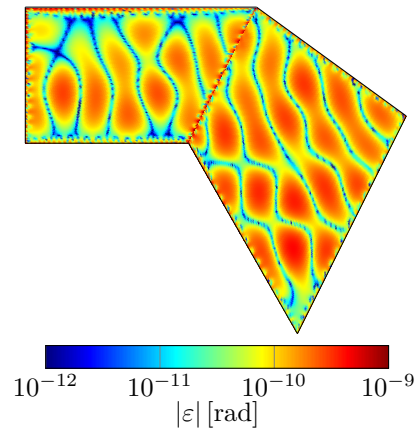
(c) Real part of the rotation about the  $x$ -axis



(d) Absolute error of the rotation about the  $x$ -axis



(e) Real part of the rotation about the  $y$ -axis



(f) Absolute error of the rotation about the  $y$ -axis

Figure E.84: Out-of-plane displacement and rotations about the  $x$ - and  $y$ -axis of a multi domain clamped plate ( $h = 0.01$  m) excited by a constant circular load at 2060 Hz calculated with the modified WBM using both function sets, corner functions and a truncation factor  $T = 4$

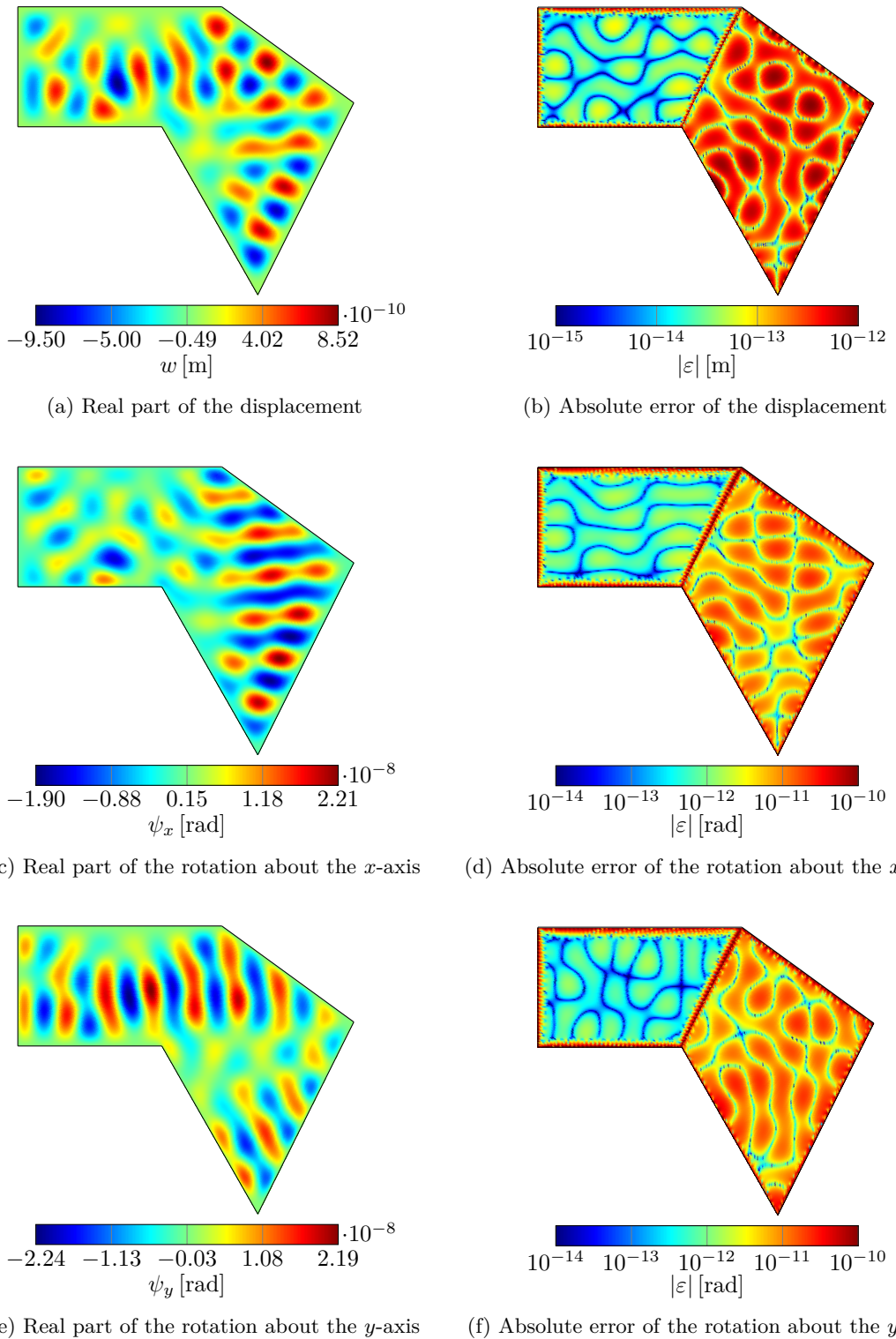
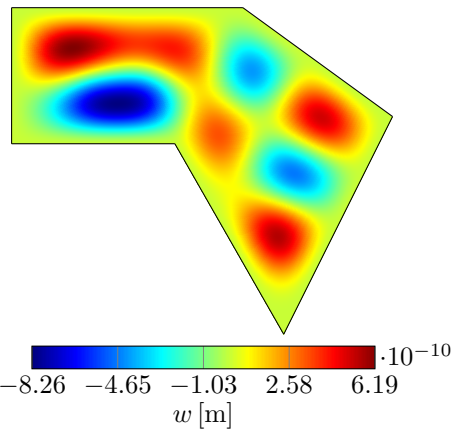
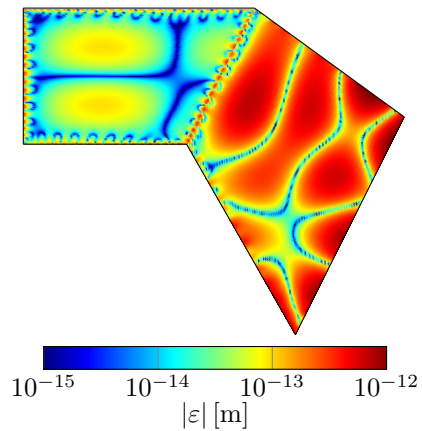


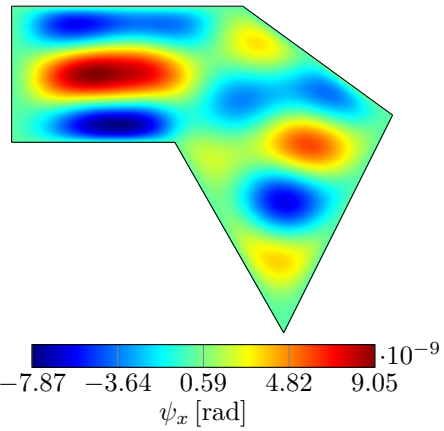
Figure E.85: Out-of-plane displacement and rotations about the  $x$ - and  $y$ -axis of a multi domain clamped plate ( $h = 0.01$  m) excited by a constant circular load at 3240 Hz calculated with the modified WBM using both function sets, corner functions and a truncation factor  $T = 4$



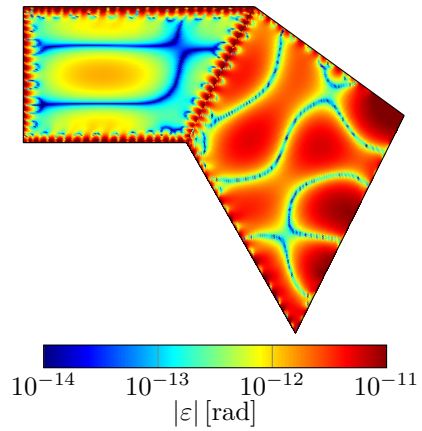
(a) Real part of the displacement



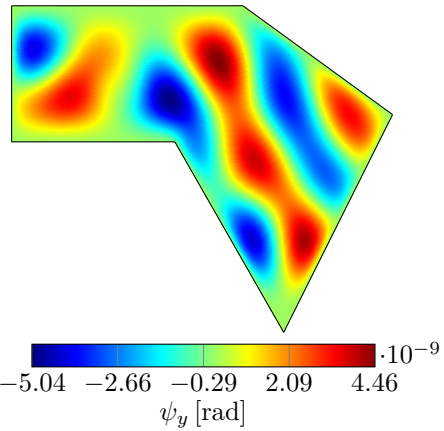
(b) Absolute error of the displacement



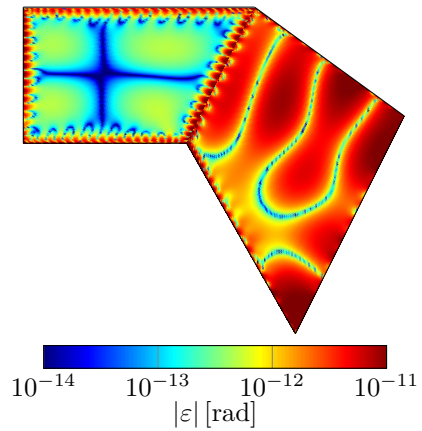
(c) Real part of the rotation about the  $x$ -axis



(d) Absolute error of the rotation about the  $x$ -axis



(e) Real part of the rotation about the  $y$ -axis



(f) Absolute error of the rotation about the  $y$ -axis

Figure E.86: Out-of-plane displacement and rotations about the  $x$ - and  $y$ -axis of a multi domain clamped plate ( $h = 0.025$  m) excited by a constant circular load at 1650 Hz calculated with the modified WBM using both function sets, corner functions and a truncation factor  $T = 4$

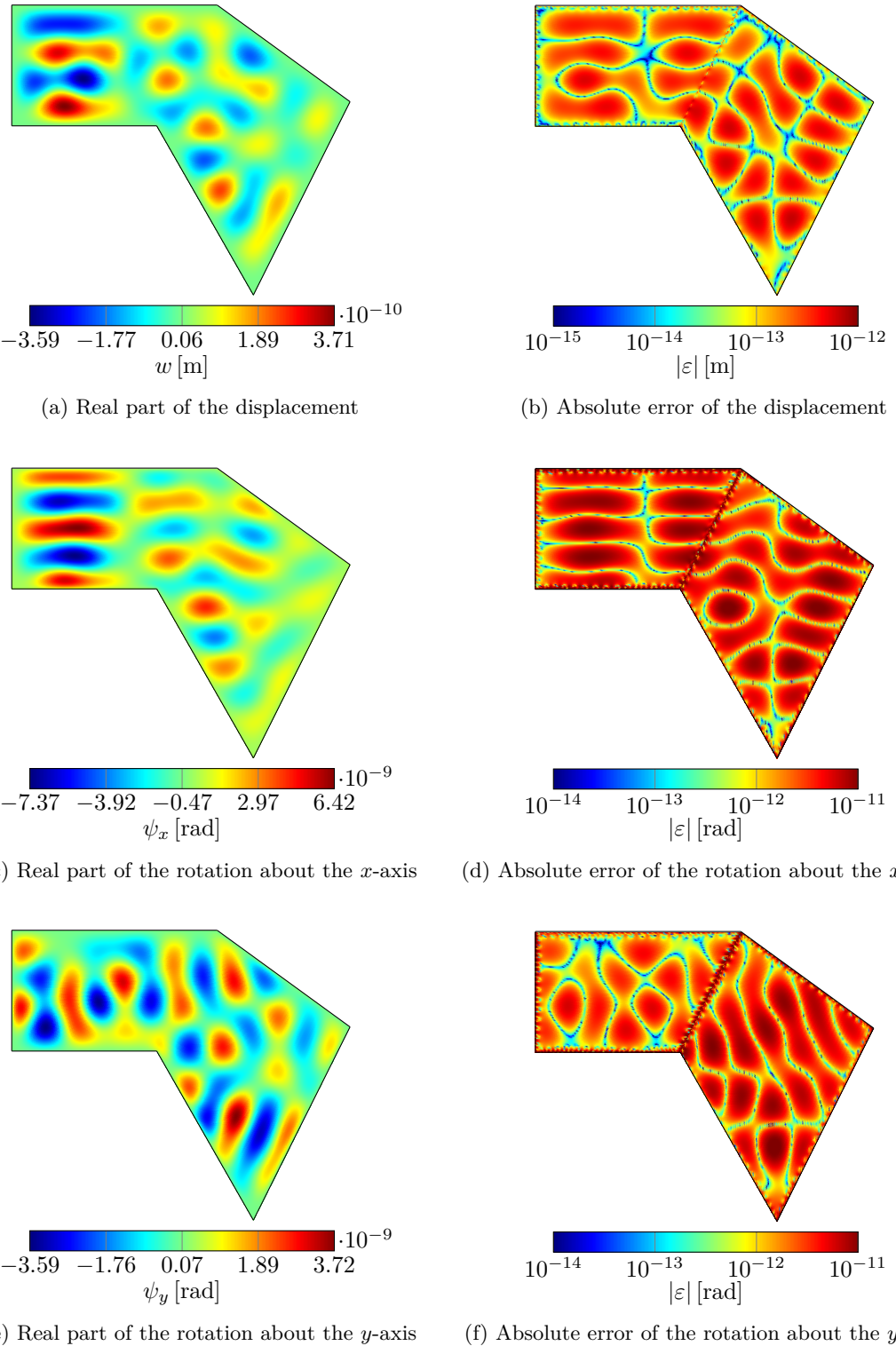
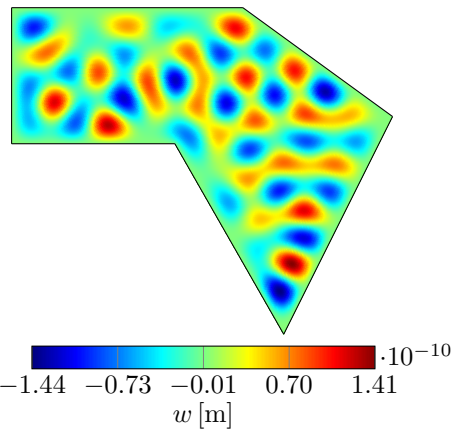
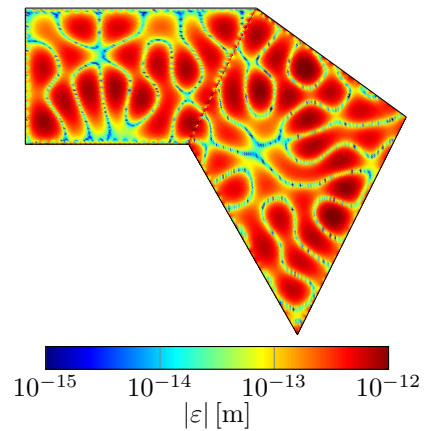


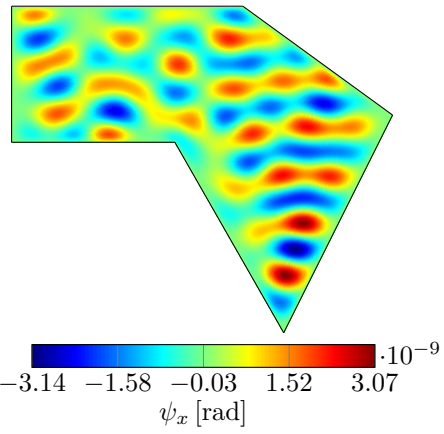
Figure E.87: Out-of-plane displacement and rotations about the  $x$ - and  $y$ -axis of a multi domain clamped plate ( $h = 0.025$  m) excited by a constant circular load at 4740 Hz calculated with the modified WBM using both function sets, corner functions and a truncation factor  $T = 4$



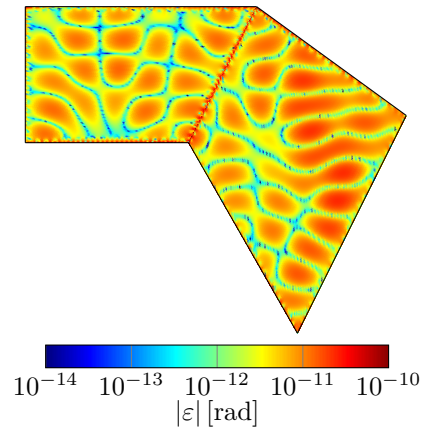
(a) Real part of the displacement



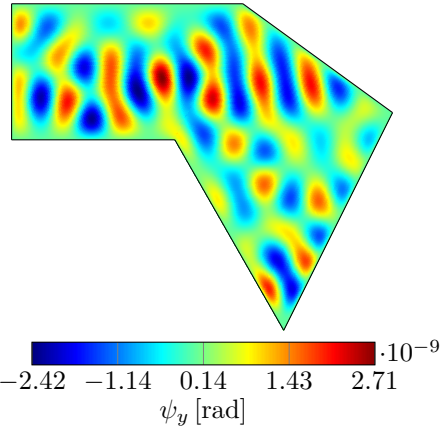
(b) Absolute error of the displacement



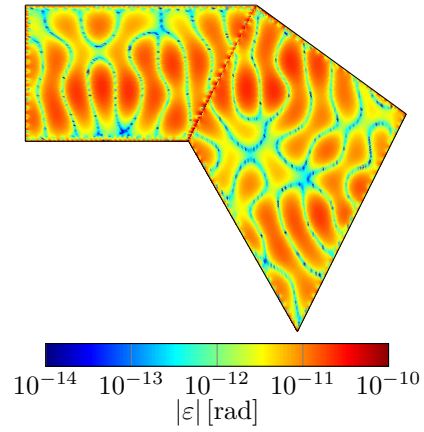
(c) Real part of the rotation about the  $x$ -axis



(d) Absolute error of the rotation about the  $x$ -axis



(e) Real part of the rotation about the  $y$ -axis



(f) Absolute error of the rotation about the  $y$ -axis

Figure E.88: Out-of-plane displacement and rotations about the  $x$ - and  $y$ -axis of a multi domain clamped plate ( $h = 0.025$  m) excited by a constant circular load at 7200 Hz calculated with the modified WBM using both function sets, corner functions and a truncation factor  $T = 4$

E Additional results for the validation examples

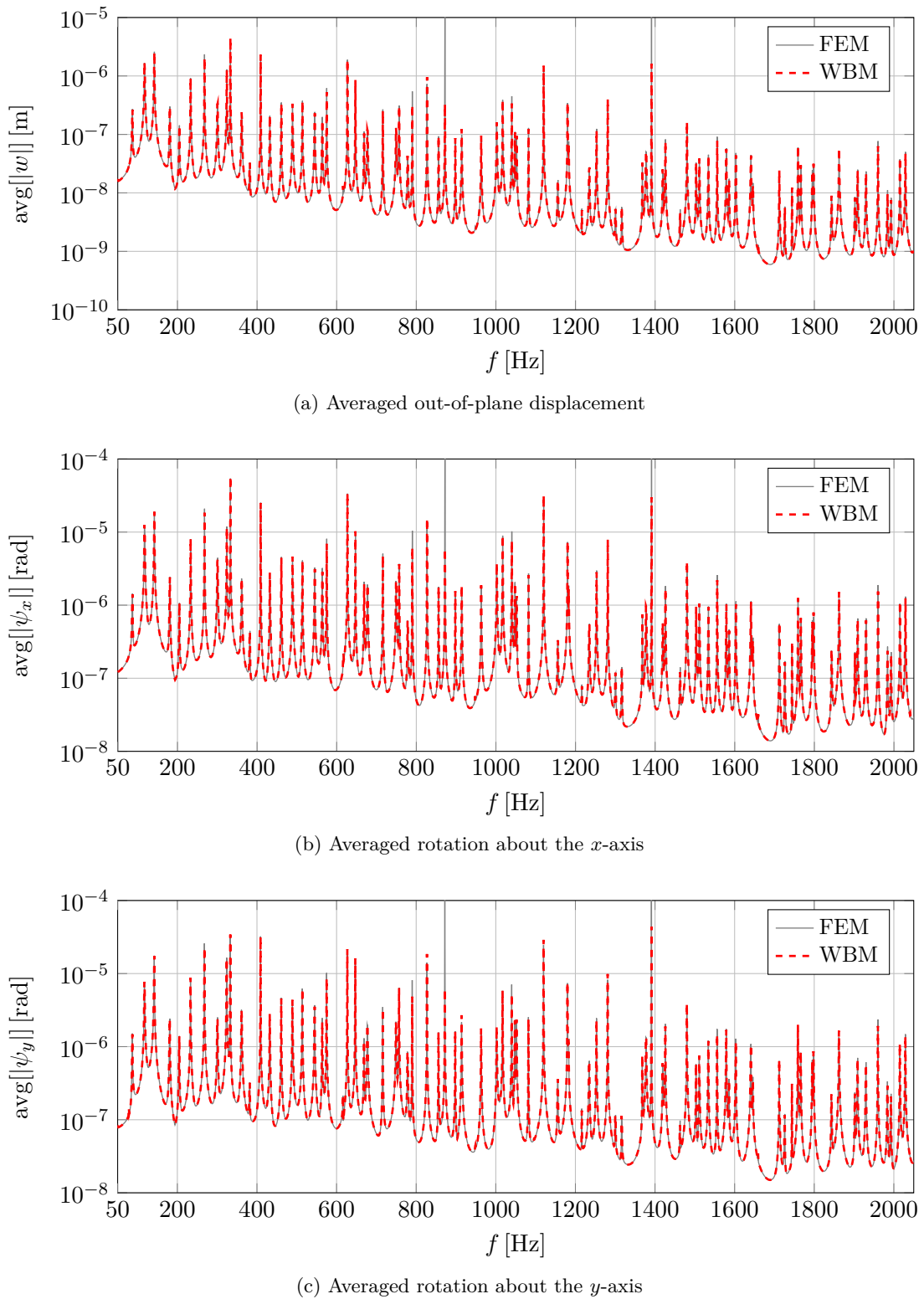
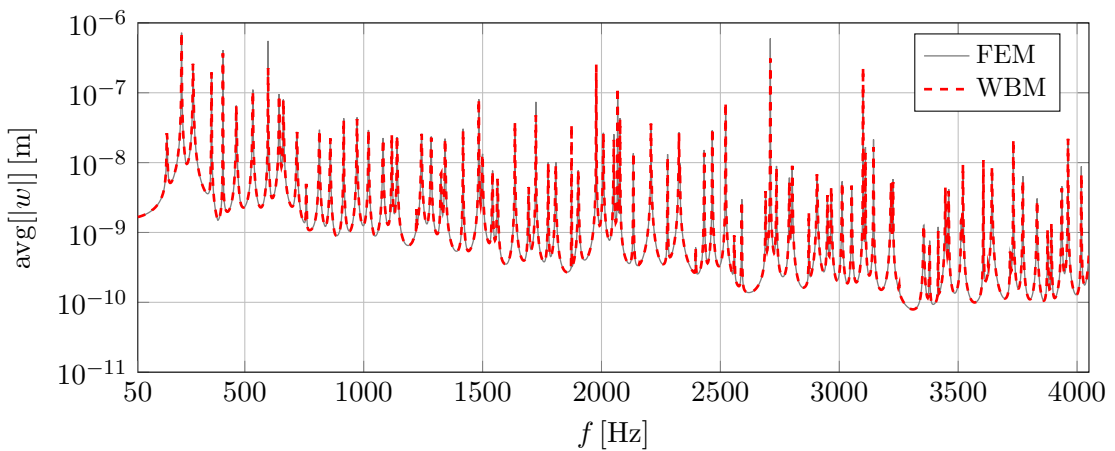
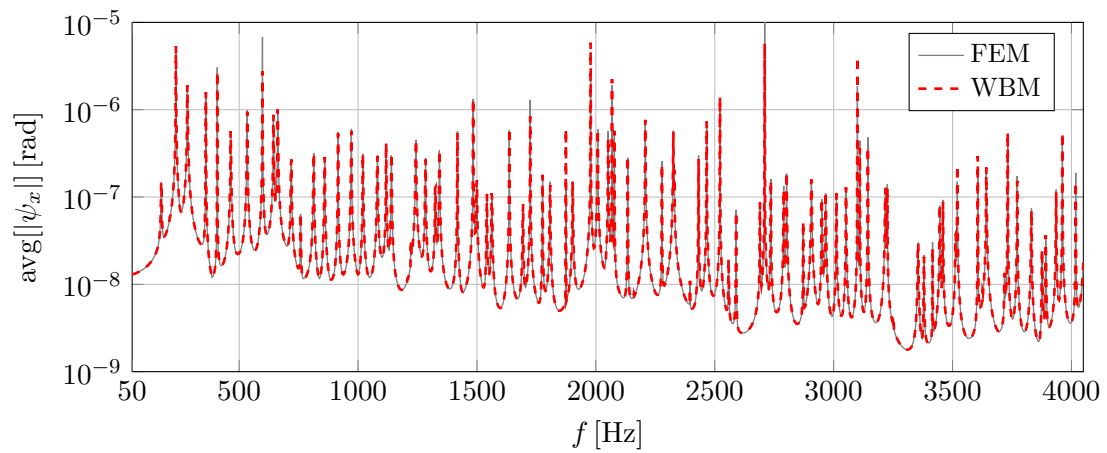


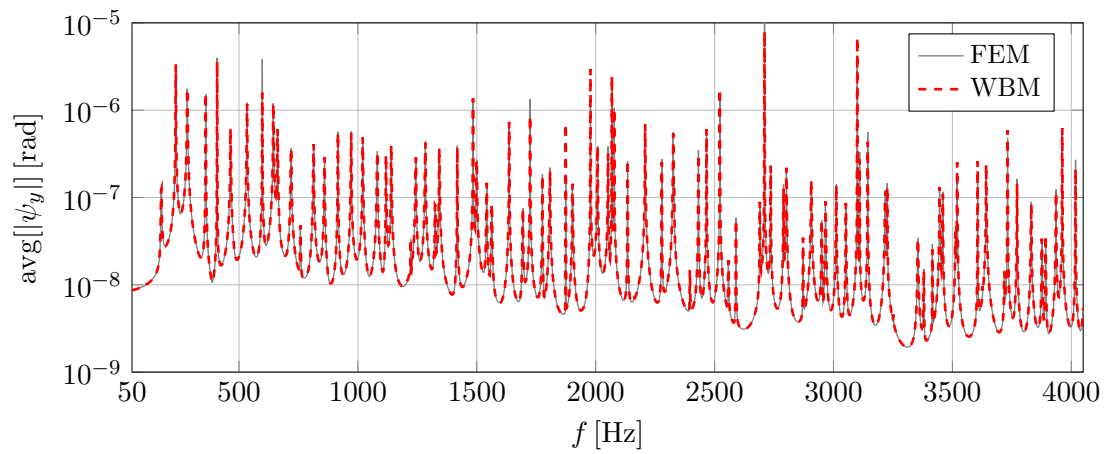
Figure E.89: Frequency response functions of a multi domain clamped plate ( $h = 0.005$  m) excited by a constant circular load calculated with the FEM (reference mesh) and the modified WBM (function set 1 and set 2, corner functions,  $T = 4$ )



(a) Averaged out-of-plane displacement



(b) Averaged rotation about the  $x$ -axis



(c) Averaged rotation about the  $y$ -axis

Figure E.90: Frequency response functions of a multi domain clamped plate ( $h = 0.01$  m) excited by a constant circular load calculated with the FEM (reference mesh) and the modified WBM (function set 1 and set 2, corner functions,  $T = 4$ )

## E Additional results for the validation examples

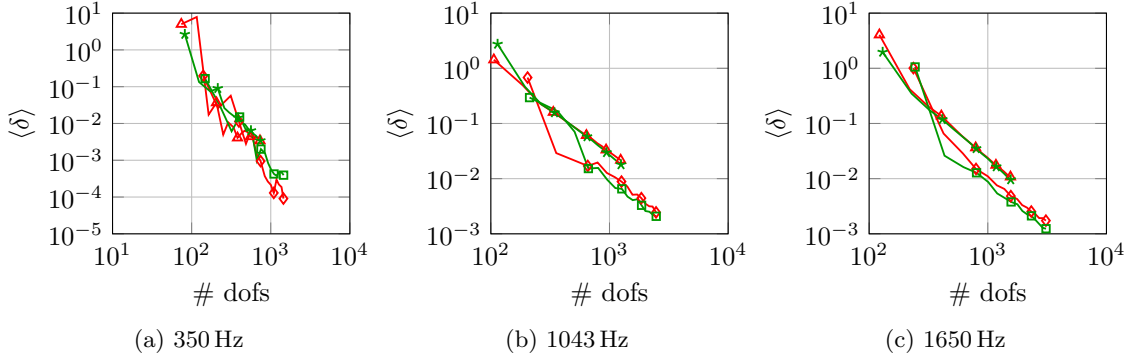


Figure E.91: Convergence curves of the out-of-plane displacement (multi domain clamped plate with  $h = 0.005$  m) for the modified WBM (set1 (—▲—), set1a2 (—◆—), set1CF (—★—), set1a2CF (—■—))

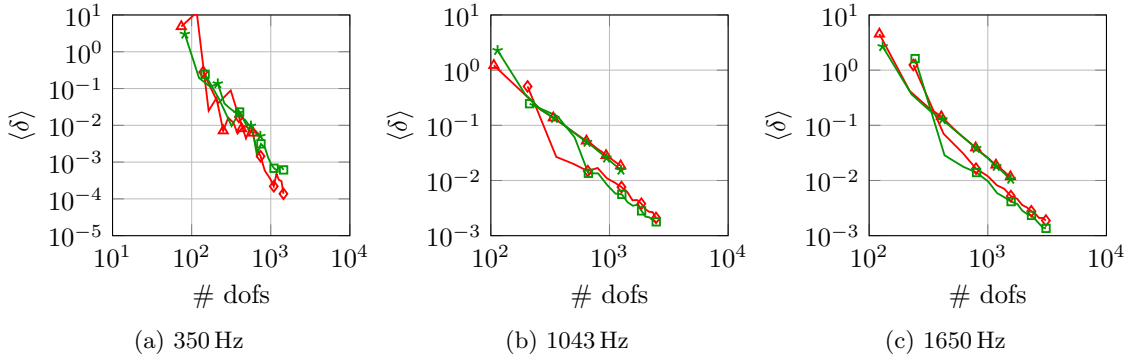


Figure E.92: Convergence curves of the rotation about the  $x$ -axis (multi domain clamped plate with  $h = 0.005$  m) for the modified WBM (set1 (—▲—), set1a2 (—◆—), set1CF (—★—), set1a2CF (—■—))

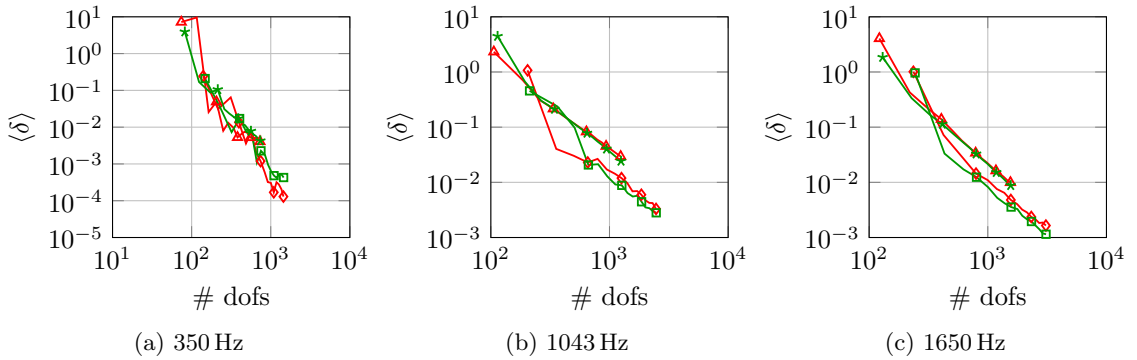


Figure E.93: Convergence curves of the rotation about the  $y$ -axis (multi domain clamped plate with  $h = 0.005$  m) for the modified WBM (set1 (—▲—), set1a2 (—◆—), set1CF (—★—), set1a2CF (—■—))

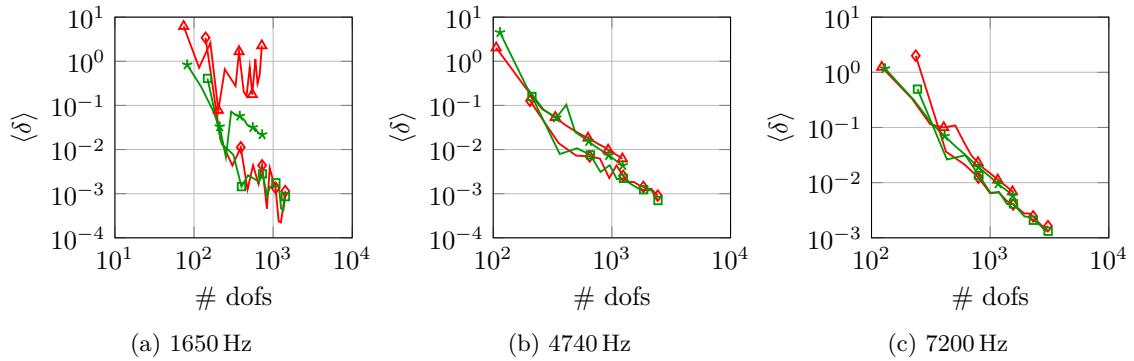


Figure E.94: Convergence curves of the out-of-plane displacement (multi domain clamped plate with  $h = 0.025$  m) for the modified WBM (*set1* (—▲—), *set1a2* (—◆—), *set1CF* (—★—), *set1a2CF* (—■—))

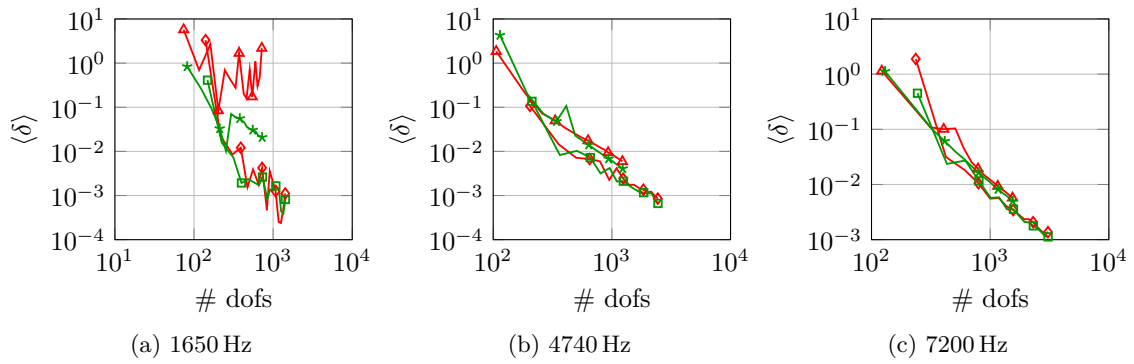


Figure E.95: Convergence curves of the rotation about the  $x$ -axis (multi domain clamped plate with  $h = 0.025$  m) for the modified WBM (*set1* (—▲—), *set1a2* (—◆—), *set1CF* (—★—), *set1a2CF* (—■—))

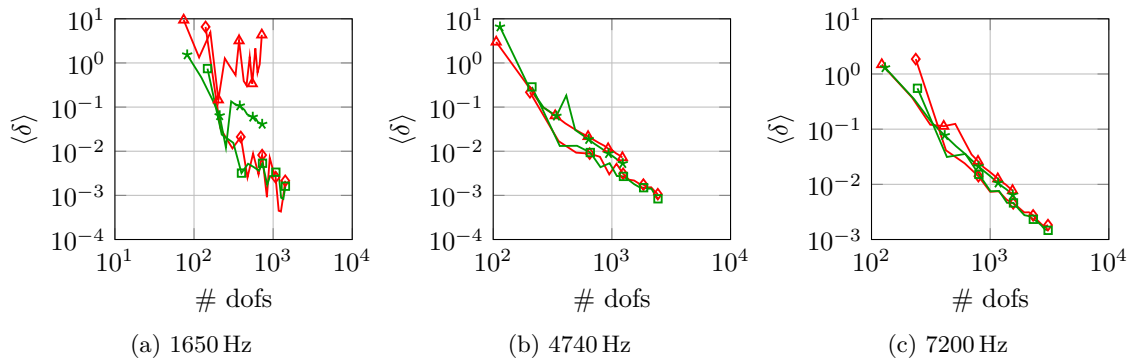


Figure E.96: Convergence curves of the rotation about the  $y$ -axis (multi domain clamped plate with  $h = 0.025$  m) for the modified WBM (*set1* (—▲—), *set1a2* (—◆—), *set1CF* (—★—), *set1a2CF* (—■—))



# Bibliography

- [1] S. C. Wheelwright, K. B. Clark, *Revolutionizing Product Development: Quantum Leaps in Speed, Efficiency, and Quality*, The Free Press, New York, 1992.
- [2] E. Abele, A. Reiner, H. Birkhofer, *Environmentally-Friendly Product Development: Methods and Tools*, Springer-Verlag, London, 2005.
- [3] EU, Decision No 1386/2013/EU of the European Parliament and of the Council of 20 November 2013 on a General Union Environment Action Programme to 2020 'Living well, within the limits of our planet', Official Journal of the European Union L 354/171.
- [4] K. Genuit, The sound quality of vehicle interior noise: a challenge for the NVH-engineers, *International Journal of Vehicle Noise and Vibration* 1 (1-2) (2004) 158–168.
- [5] L. Cremer, M. Heckl, B. A. T. Petersson, *Structure-Born Sound*, Springer-Verlag, Berlin, 2005.
- [6] M. C. Becker, P. Salvatore, F. Zirpoli, The impact of virtual simulation tools on problem-solving and new product development organization, *Research Policy* 34 (9) (2005) 1305–1321.
- [7] W. Choi, J. Woodhouse, R. S. Langley, Sound radiation from a vibrating plate with uncertainty, *Journal of Sound and Vibration* 333 (17) (2014) 3966–3980.
- [8] J. Cuenca, Wave models for the flexural vibratoins of thin plates - Model of the vibrations of polygonal plates by the image source method - Vibration damping using the acoustic black hole effect, Ph.D. thesis, Universit é du Maine (2009).
- [9] J. N. Reddy, *Theory and Analysis of Elastic Plates and Shells*, CRC Press, Boca Raton, 2007.
- [10] B. Kirchhoff, Über das Gleichgewicht und die Bewegung einer elastischen Scheibe, *Journal für die reine und angewandte Mathematik* 40 (1850) 51–88.
- [11] R. D. Mindlin, Influence of Rotatory Inertia and Shear on Flexural Motions of Isotropic, Elastic Plates, *Journal of Applied Mechanics* 18 (1951) 31–38.
- [12] S. A. Hambric, S. H. Sung, D. J. Nefske, *Engineering vibroacoustic analysis: Methods and applications*, John Wiley & Sons, Chichester, 2016.
- [13] K. Vergote, Dynamic Analysis of Structural Components in the Mid Frequency Range Using the Wave Based Method - Non-Determinism and Inhomogeneities, Ph.D. thesis, Katholieke Universiteit Leuven (2012).

## Bibliography

- [14] E. Deckers, O. Atak, L. Coox, R. D'Amico, H. Devriendt, S. Jonckheere, K. Koo, B. Pluymers, D. Vandepitte, W. Desmet, The wave based method: An overview of 15 years of research, *Wave Motion* 51 (4) (2014) 550–565.
- [15] E. Trefftz, Ein Gegenstueck zum ritzschen Verfahren, in: In Proceedings of the 2nd International Congress of Applied Mechanics, Orell Fussli Verlag, Zurich, 1926, pp. 131 – 137.
- [16] C. Vanmaele, D. Vandepitte, W. Desmet, An efficient wave based prediction technique for plate bending vibrations, *Computer Methods in Applied Mechanics and Engineering* 196 (33-34) (2007) 3178–3189.
- [17] C. Vanmaele, Development of a Wave Based Prediction Technique for the Efficient Analysis of Low- and Mid-Frequency Structural Vibrations, Ph.D. thesis, Katholieke Universiteit Leuven (2007).
- [18] C. Vanmaele, D. Vandepitte, W. Desmet, An efficient wave based prediction technique for dynamic plate bending problems with corner stress singularities, *Computer Methods in Applied Mechanics and Engineering* 198 (30-32) (2009) 2227–2245.
- [19] S. Jonckheere, D. Vandepitte, W. Desmet, A Wave Based approach for the dynamic bending analysis of Kirchhoff plates under distributed deterministic and random excitation, *Computers and Structures* 156 (2015) 42–57.
- [20] S. Jonckheere, Wave Based and Hybrid Methodologies for Vibro-Acoustic Simulation with Complex Damping Treatments, Ph.D. thesis, Katholieke Universiteit Leuven (2015).
- [21] W. Desmet, A Wave Based Prediction Technique for Coupled Vibro-Acoustic Analysis, Ph.D. thesis, Katholieke Universiteit Leuven (1998).
- [22] S. S. Rao, *Vibration of Continuous Systems*, John Wiley & Sons, New Jersey, 2007.
- [23] Y.-Y. Yu, *Vibrations of Elastic Plates*, Springer-Verlag, New York, 1996.
- [24] M. A. Slawinski, *Waves and Rays in Elastic Continua*, World Scientific Publishing, Singapore, 2010.
- [25] P. Hagedorn, A. DasGupta, *Vibrations and Waves in Continuous Mechanical Systems*, John Wiley & Sons, Chichester, 2007.
- [26] Y.-Q. Long, S. Cen, Z.-F. Long, *Advanced Finite Element Method in Structural Engineering*, Springer-Verlag, Berlin, 2009.
- [27] J. N. Reddy, A Simple Higher-Order Theory for Laminated Composite Plates, *Journal of Applied Mechanics* 51 (4) (1984) 745–752.
- [28] Y.-H. Park, S.-Y. Hong, Vibrational power flow models for transversely vibrating finite Mindlin plate, *Journal of Sound and Vibration* 317 (3-5) (2008) 800–840.
- [29] I. Babuška, J. Pitkäranta, The Plate Paradox for Hard and Soft Simple Support, *SIAM Journal on Mathematical Analysis* 21 (3) (1990) 551–576.
- [30] Y.-C. Long, Subregion generalized variational principles for elastic thick plates, *Applied Mathematics and Mechanics* 4 (2) (1983) 175–184.

- [31] I. Harari, I. Sokolov, S. Krylov, Consistent loading for thin plates, *Journal of Mechanics of Materials and Structures* 6 (5) (2011) 765–790.
- [32] Y.-Q. Long, Sub-region generalized variational principles in elastic thin plates, Springer-Verlag, Dordrecht, 1987, Ch. Progress in Applied Mechanics, pp. 121–134.
- [33] K. M. Liew, Y. Xiang, S. Kitipornchai, Research on Thick Plate Vibration: A Literature Survey, *Journal of Sound and Vibration* 180 (1) (1995) 163–176.
- [34] Y. M. Ghugal, R. P. Shimpi, A Review of Refined Shear Deformation Theories of Isotropic and Anisotropic Laminated Plates, *Journal of Reinforced Plastics and Composites* 21 (9) (2002) 775–813.
- [35] C. M. Wang, J. N. Reddy, K. H. Lee, *Shear Deformable Beams and Plates: Relationships with Classical Solutions*, Elsevier Science Ltd, Oxford, 2000.
- [36] F. Essenburg, On the Significance of the Inclusion of the Effect of Transverse Normal Strain in Problems Involving Beams With Surface Constraints, *Journal of Applied Mechanics* 42 (1) (1975) 127–132.
- [37] F. B. Hildebrand, E. Reissner, G. B. Thomas, Notes on the Foundation of the Theory of Small Displacements of Orthotropic Shells, Tech. Rep. 1833, National Advisory Committee for Aeronautics (1949).
- [38] K. S. Pister, R. A. Westmann, Bending of Plates on an Elastic Foundation, *Journal of Applied Mechanics* 29 (2) (1962) 369–374.
- [39] J. M. Whitney, C. T. Sun, A Higher Order Theory for Extensional Motion of Laminated Composites, *Journal of Sound and Vibration* 30 (1) (1973) 85–97.
- [40] R. B. Nelson, D. R. Lorch, A Refined Theory for Laminated Orthotropic Plates, *Journal of Applied Mechanics* 41 (1) (1974) 177–183.
- [41] K. H. Lo, R. M. Christensen, E. M. Wu, A High-Order Theory of Plate Deformation Part 1: Homogeneous Plates, *Journal of Applied Mechanics* 44 (4) (1977) 663–668.
- [42] T. Kant, Numerical Analysis of Thick Plates, *Computer Methods in Applied Mechanics and Engineering* 31 (1) (1982) 1–18.
- [43] G. Jemielita, On Kinematical Assumptions of Refined Theories of Plates: A Survey, *Journal of Applied Mechanics* 57 (4) (1990) 1088–1091.
- [44] J. N. Reddy, *Mechanics of Laminated Composite Plates and Shells: Theory and Analysis*, CRC Press, Boca Raton, 2004.
- [45] K. M. Liew, C. M. Wang, Y. Xiang, S. Kitipornchai, *Vibration of Mindlin Plates: Programming the P-Version Ritz Method*, Elsevier Science Ltd, Oxford, 1998.
- [46] K. Chandrashekara, *Theory of Plates*, Universities Press (India) Limited, Hyderabad, 2001.
- [47] E. Ventsel, T. Krauthammer, *Thin Plates and Shells: Theory, Analysis, and Application*, Marcel Dekker, New York, 2001.
- [48] R. Szilard, *Theories and Applications of Plate Analysis: Classical, Numerical and Engineering Methods*, John Wiley & Sons, New Jersey, 2004.

## Bibliography

- [49] H. Altenbach, W. Becker, *Modern Trends in Composite Laminates Mechanics*, Springer-Verlag, Wien, 2003.
- [50] R. D. Mindlin, *An Introduction to the Mathematical Theory of Vibrations of Elastic Plates*, World Scientific Publishing, Singapore, 2006.
- [51] L. R. F. Rose, C. H. Wang, Mindlin plate theory for damage detection: Source solutions, *The Journal of the Acoustical Society of America* 116 (1) (2004) 154–171.
- [52] M. S. Qato, *Vibration of Laminated Shells and Plates*, Elsevier Science Ltd, Oxford, 2004.
- [53] S. Srinivas, C. V. Joga Rao, A. K. Rao, An Exact Analysis for Vibration of Simply-Supported Homogeneous and Laminated Thick Rectangular Plates, *Journal of Sound and Vibration* 12 (2) (1970) 187–199.
- [54] R. D. Mindlin, Waves and Vibrations in Isotropic, Elastic Plates, in: *Proceedings of the 1st Symposium on Naval Structural Mechanics*, Oxford, UK, 1960, pp. 199–232.
- [55] L. Rayleigh, On the free vibrations of an infinite plate of homogeneous isotropic elastic matter, *Proceedings of the London Mathematical Society S1-20* (1) (1888) 225–237.
- [56] H. Lamb, On the flexure of an elastic plate, *Proceedings of the London Mathematical Society S1-21* (1) (1889) 70–91.
- [57] R. D. Mindlin, A. Schacknow, H. Deresiewicz, Flexural Vibrations of Rectangular Plates, *Journal of Applied Mechanics* 23 (1956) 430–436.
- [58] W. H. Wittrick, Analytical Three-Dimensional Elasticity Solutions to Some Plate Problems, and Some Observations on Mindlin's Plate Theory, *International Journal of Solids and Structures* 23 (4) (1987) 441–464.
- [59] R. C. Batra, S. Aimmanee, Missing frequencies in previous exact solutions of free vibrations of simply supported rectangular plate, *Journal of Sound and Vibration* 265 (4) (2003) 887–896.
- [60] S. Aimmanee, R. C. Batra, Analytical solution for vibration of an incompressible isotropic linear elastic rectangular plate, and frequencies missed in previous solutions, *Journal of Sound and Vibration* 302 (3) (2007) 613–620.
- [61] M. Malik, C. W. Bert, Three-Dimensional Elasticity Solutions for Free Vibrations of Rectangular Plates by the Differential Quadrature Method, *International Journal of Solids and Structures* 35 (3-4) (1998) 299–318.
- [62] K. M. Liew, T. M. Teo, Three-Dimensional Vibration Analysis of Rectangular Plates Based on Differential Quadrature Method, *Journal of Sound and Vibration* 220 (4) (1999) 577–599.
- [63] K. M. Liew, K. C. Hung, M. K. Lim, A Continuum Three-Dimensional Vibration Analysis of Thick Rectangular Plates, *International Journal of Solids and Structures* 30 (24) (1993) 3357–3379.

- [64] S. H. Hashemi, M. Arsanjani, Exact characteristic equations for some of classical boundary conditions of vibrating moderately thick rectangular plates, *International Journal of Solids and Structures* 42 (3-4) (2005) 819–853.
- [65] K. M. Liew, Y. Xiang, S. Kitipornchai, Transverse Vibration of Thick Rectangular Plates - I. Comprehensive Sets of Boundary Conditions, *Computers & Structures* 49 (1) (1993) 1–29.
- [66] K. M. Liew, K. C. Hung, M. K. Lim, Vibration of Mindlin Plates Using Boundary Characteristic Orthogonal Polynomials, *Journal of Sound and Vibration* 182 (1) (1995) 77–90.
- [67] A. W. Leissa, The Free Vibration of Rectangular Plates, *Journal of Sound and Vibration* 31 (3) (1973) 257–293.
- [68] K. M. Liew, B. Yang, Three-dimensional elasticity solutions for free vibrations of circular plates: a polynomials-Ritz analysis, *Computer Methods in Applied Mechanics and Engineering* 175 (1-2) (1999) 189–201.
- [69] D. Zhou, F. T. K. Au, Y. K. Cheung, S. H. Lo, Three-dimensional vibration analysis of circular and annular plates via the Chebyshev-Ritz method, *International Journal of Solids and Structures* 40 (12) (2003) 3089–3105.
- [70] T. Irie, G. Yamada, S. Aomura, Natural Frequencies of Mindlin Circular Plates, *Journal of Applied Mechanics* 47 (3) (1980) 652–655.
- [71] A. W. Leissa, Vibration of plates, *Tech. Rep. NASA SP-160*, National Aeronautics and Space Administration (1969).
- [72] K. M. Liew, T. Y. Ng, B. P. Wang, Vibration of annular sector plates from three-dimensional analysis, *The Journal of the Acoustical Society of America* 110 (1) (2001) 233–242.
- [73] D. Zhou, S. H. Lo, Y. K. Cheung, 3-D vibration analysis of annular sector plates using the Chebyshev-Ritz method, *Journal of Sound and Vibration* 320 (1-2) (2009) 421–437.
- [74] C. S. Huang, O. G. McGee, Exact Analytical Solutions for Free Vibrations of Thick Sectorial Plates with Simply Supported Radial Edges, *International Journal of Solids and Structures* 31 (11) (1994) 1609–1631.
- [75] C. S. Huang, A. W. Leissa, O. G. McGee, Exact Analytical Solutions for the Vibrations of Sectorial Plates With Simply-Supported Radial Edges, *Journal of Applied Mechanics* 60 (2) (1993) 478–483.
- [76] X. Wang, Y. Wang, Free vibration analyses of thin sector plates by the new version of differential quadrature method, *Computer Methods in Applied Mechanics and Engineering* 193 (36-38) (2004) 3957–3971.
- [77] O. G. McGee, A. W. Leissa, J. W. Kim, Y. S. Kim, Vibration of Plates with Constrained V-Notches or Cracks, *Journal of Engineering Mechanics* 129 (7) (2003) 812–822.

## Bibliography

- [78] O. G. McGee, J. W. Kim, Y. S. Kim, Influence of boundary stress singularities on the vibration of clamped and simply-supported sectorial plates with arbitrary radial edge conditions, *Journal of Sound and Vibration* 329 (26) (2010) 5563–5583.
- [79] F.-L. Liu, K. M. Liew, Free vibration analysis of Mindlin sector plates: numerical solutions by differential quadrature method, *Computer Methods in Applied Mechanics and Engineering* 177 (1-2) (1999) 77–92.
- [80] C. S. Huang, M. J. Chang, A. W. Leissa, Vibrations of Mindlin Sectorial Plates Using the Ritz Method Considering Stress Singularities, *Journal of Vibration and Control* 12 (6) (2006) 635–657.
- [81] A. Ambroziak, *Shell Structures: Theory and Application*, Vol. 3, CRC Press, Leiden, 2013, Ch. 85, pp. 369–372.
- [82] P. Bouillard, F. Ihlenburg, Error estimation and adaptivity for the finite element method in acoustics: 2D and 3D applications, *Computer Methods in Applied Mechanics and Engineering* 176 (1-4) (1999) 147–163.
- [83] F. Ihlenburg, I. Babuška, Finite element solution of the Helmholtz equation with high wave number Part I: The h-version of the FEM, *Computers & Mathematics with Applications* 30 (9) (1995) 9–37.
- [84] F. Ihlenburg, I. Babuška, Finite element solution of the Helmholtz equation with high wave number Part II: The h-p version of the FEM, *SIAM Journal on Numerical Analysis* 34 (1) (1997) 315–358.
- [85] M. Dauge, Z. Yosibash, Boundary layer realization in thin elastic three-dimensional domains and two-dimensional Hierarchic plate models, *International Journal of Solids and Structures* 37 (17) (2000) 2443–2471.
- [86] D. W. Zietlow, D. C. Griffin, T. R. Moore, The limitations on applying classical thin plate theory to thin annular plates clamped on the inner boundary, *AIP Advances* 2 (4) (2012) 042103–1–8.
- [87] M. L. Williams, Surface Stress Singularities Resulting from Various Boundary Conditions in Angular Plates under Bending, in: *Proceedings of the First U.S. National Congress of Applied Mechanics*, 1952, pp. 325–329.
- [88] K. S. Numayr, R. H. Haddad, M. A. Haddad, Free vibration of composite plates using the finite difference method, *Thin-Walled Structures* 42 (3) (2004) 399–414.
- [89] S. Vlachoutsis, Shear correction factors for plates and shells, *International Journal for Numerical Methods in Engineering* 33 (7) (1992) 1537–1552.
- [90] A. H.-D. Cheng, D. T. Cheng, Heritage and early history of the boundary element method, *Engineering Analysis with Boundary Elements* 29 (3) (2005) 268–302.
- [91] O. C. Zienkiewicz, R. L. Taylor, J. Z. Zhu, *The Finite Element Method: Its Basis and Fundamentals*, Butterworth-Heinemann, Oxford, 2013.
- [92] K.-J. Bathe, *Finite Element Procedures*, Klaus-Jürgen Bathe, Watertown, 2014.
- [93] C. A. Brebbia, J. C. F. Telles, L. C. Wrobel, *Boundary Element Techniques: Theory and Applications in Engineering*, Springer -Verlag, Berlin, 1984.

- [94] J. T. Katsikadelis, The Boundary Element Method for Plate Analysis, Elsevier Inc., Oxford, 2014.
- [95] W. Desmet, Mid-frequency vibro-acoustic modelling: challenges and potential solutions, in: Proceedings of the International Conference on Noise and Vibration Engineering ISMA2002, Leuven, Belgium, 2002, pp. 835–862.
- [96] B. van Hal, Automation and Performance Optimization of the Wave Based Method for Interior Structural-Acoustic Problems, Ph.D. thesis, Katholieke Universiteit Leuven (2004).
- [97] A. Deraemaeker, I. Babuška, P. Bouillard, Dispersion and pollution of the FEM solution for the Helmholtz equation in one, two and three dimensions, International Journal for Numerical Methods in Engineering 46 (4) (1999) 471–499.
- [98] F. Ihlenburg, I. Babuška, Dispersion analysis and error estimation of Galerkin finite element methods for the Helmholtz equation, International Journal for Numerical Methods in Engineering 38 (22) (1995) 3745–3774.
- [99] B. Pluymers, Wave Based Modelling Methods for Steady-State Vibro-Acoustics, Ph.D. thesis, Katholieke Universiteit Leuven (2006).
- [100] L. L. Thompson, P. M. Pinsky, Complex wavenumber Fourier analysis of the p-version finite element method, Computational Mechanics 13 (4) (1994) 255–275, <http://dx.doi.org/10.1007/BF00350228>.
- [101] B. Van Genechten, D. Vandepitte, W. Desmet, A direct hybrid finite element - Wave based modelling technique for efficient coupled vibro-acoustic analysis, Computer Methods in Applied Mechanics and Engineering 200 (5-8) (2011) 742–764.
- [102] I. Babuška, B. A. Szabo, I. N. Katz, The p-Version of the Finite Element Method, SIAM Journal on Numerical Analysis 18 (3) (1981) 515–545.
- [103] A. Côté, F. Charron, On the selection of p-version shape functions for plate vibration problems, Computers & Structures 79 (1) (2001) 119–130.
- [104] B. Guo, I. Babuška, The h-p version of the finite element method, Computational Mechanics 1 (1) (1986) 21–41.
- [105] M. Hocine, B. B. Bel Abbes, H. Abdelhamid, hp-finite element for free vibration analysis of the orthotropic triangular and rectangular plates, Mathematical and Computer Modelling of Dynamical Systems 13 (6).
- [106] M. S. Lenzi, S. Lefteriu, H. Beriot, W. Desmet, A fast frequency sweep approach using Padé approximations for solving Helmholtz finite element models, Journal of Sound and Vibration 332 (8) (2013) 1897–1917.
- [107] P. Avery, C. Farhat, G. Reese, Fast frequency sweep computations using a multi-point Padé-based reconstruction method and an efficient iterative solver, International Journal for Numerical Methods in Engineering 69 (13).
- [108] B. F. Smith, P. E. Bjørstad, W. D. Gropp, Domain decomposition: parallel multilevel methods for elliptic partial differential equations, Cambridge University Press, New York, 1996.

## Bibliography

- [109] A. Toselli, O. Widlund, *Domain Decomposition Methods - Algorithms and Theory*, Springer-Verlag, Berlin, 2005.
- [110] V. Dolean, P. Jolivet, F. Ntaf, *An Introduction to Domain Decomposition Methods: Algorithms, Theory, and Parallel Implementation*, The Society for Industrial and Applied Mathematics, Philadelphia, 2015.
- [111] I. Harari, T. J. R. Hughes, Finite element methods for the Helmholtz equation in an exterior domain: Model problems, *Computer Methods in Applied Mechanics and Engineering* 87 (1) (1991) 59–96.
- [112] L. L. Thompson, P. M. Pinsky, A Galerkin least-squares finite element method for the two-dimensional Helmholtz equation, *International Journal for Numerical Methods in Engineering* 38 (3) (1995) 371–397.
- [113] I. Harari, S. Haham, Improved finite element methods for elastic waves, *Computer Methods in Applied Mechanics and Engineering* 166 (1-2) (1998) 143–164.
- [114] L. P. Franca, E. G. Dutra Do Carmo, The Galerkin gradient least-squares method, *Computer Methods in Applied Mechanics and Engineering* 74 (1) (1989) 41–54.
- [115] K. Grosh, P. M. Pinsky, Design of Galerkin Generalized Least Squares methods for Timoshenko beams, *Computer Methods in Applied Mechanics and Engineering* 132 (1-2) (1996) 1–16.
- [116] K. Grosh, P. M. Pinsky, Galerkin generalized least squares finite element methods for time-harmonic structural acoustics, *Computer Methods in Applied Mechanics and Engineering* 154 (3-4) (1998) 299–318.
- [117] J. M. Melenk, I. Babuška, The partition of unity finite element method: Basic theory and applications, *Computer Methods in Applied Mechanics and Engineering* 139 (1-4) (1996) 289–314.
- [118] N. Hu, H. H. Wang, B. Yan, H. Fukunaga, D. R. Mahapatra, S. Gopalakrishnan, The partition of unity finite element method for elastic wave propagation in Reissner-Mindlin plates, *International Journal for Numerical Methods in Engineering* 70 (12) (2007) 1451–1479.
- [119] C. Farhat, I. Harari, L. P. Franca, The discontinuous enrichment method, *Computer Methods in Applied Mechanics and Engineering* 190 (48) (2001) 6455–6479.
- [120] P. Massimi, R. Tezaur, C. Farhat, A discontinuous enrichment method for the efficient solution of plate vibration problems in the medium-frequency regime, *International Journal for Numerical Methods in Engineering* 84 (2) (2010) 127–148.
- [121] M. N. Guddati, B. Yue, Modified integration rules for reducing dispersion error in finite element methods, *Computer Methods in Applied Mechanics and Engineering* 193 (3-5) (2004) 275–287.
- [122] A. V. Idesman, M. Schmidt, J. R. Foley, Accurate finite element modeling of linear elastodynamics problems with the reduced dispersion error, *Computational Mechanics* 47 (5) (2011) 555–572.

- [123] R. H. Lyon, R. G. DeJong, *Theory and Application of Statistical Energy Analysis*, Butterworth-Heinemann, Newtown, 1995.
- [124] A. J. Keane, W. G. Price, *Statistical Energy Analysis: An Overview, with Applications in Structural Dynamics*, Cambridge University Press, New York, 1997.
- [125] F. J. Fahy, *Statistical Energy Analysis: A Critical Overview*, *Philosophical Transactions of the Royal Society of London A: Mathematical, Physical and Engineering Sciences* 346 (1681) (1994) 431–447.
- [126] T. Lafont, N. Totaro, A. Le Bot, *Review of statistical energy analysis hypotheses in vibroacoustics*, *Proceedings of the Royal Society A: Mathematical, Physical and Engineering Science* 470 (2162) (2014) 1–20.
- [127] C. B. Burroughs, R. W. Fischer, F. R. Kern, *An introduction to statistical energy analysis*, *The Journal of the Acoustical Society of America* 101 (4) (1997) 1779–1789.
- [128] S. Finnveden, *A quantitative criterion validating coupling power proportionality in statistical energy analysis*, *Journal of Sound and Vibration* 330 (1) (2011) 87–109.
- [129] R. S. Langley, *A wave intensity technique for the analysis of high frequency vibrations*, *Journal of Sound and Vibration* 159 (3) (1992) 483–502.
- [130] R. S. Langley, A. N. Bercin, *Wave Intensity Analysis of High Frequency Vibrations*, *Philosophical Transactions: Physical Sciences and Engineering* 346 (1681) (1994) 489–499.
- [131] L. Maxit, J.-L. Guyader, *Extension of SEA model to subsystems with non-uniform modal energy distribution*, *Journal of Sound and Vibration* 265 (2) (2003) 337–358.
- [132] B. R. Mace, P. J. Shorter, *Energy Flow Models from Finite Element Analysis*, *Journal of Sound and Vibration* 233 (3) (2000) 369–389.
- [133] B. R. Mace, *Statistical energy analysis, energy distribution models and system modes*, *Journal of Sound and Vibration* 264 (2) (2003) 391–409.
- [134] A. Sestieri, A. Carcaterra, *Vibroacoustic: The challenges of a mission impossible?*, *Mechanical Systems and Signal Processing* 34 (1-2) (2013) 1–18.
- [135] E. Kita, N. Kamiya, *Trefftz method: an overview*, *Advances in Engineering Software* 24 (1-3) (1995) 3–12.
- [136] A. P. Zieliński, I. Herrera, *Trefftz method: Fitting boundary conditions*, *International Journal for Numerical Methods in Engineering* 24 (5) (1987) 871–891.
- [137] B. Pluymers, B. van Hal, D. Vandepitte, W. Desmet, *Trefftz-Based Methods for Time-Harmonic Acoustics*, *Archives of Computational Methods in Engineering* 14 (4) (2007) 343–381.
- [138] Y. K. Cheung, W. G. Jin, O. C. Zienkiewicz, *Solution of Helmholtz equation by Trefftz method*, *International Journal for Numerical Methods in Engineering* 32 (1) (1991) 63–78.

## Bibliography

- [139] J. R. Chang, R. F. Liu, W. Yeih, S. R. Kuo, Applications of the direct Trefftz boundary element method to the free-vibration problem of a membrane, *The Journal of the Acoustical Society of America* 112 (2) (2002) 518–527.
- [140] W. G. Jin, Y. K. Cheung, O. C. Zienkiewicz, Application of the Trefftz method in plane elasticity problems, *International Journal for Numerical Methods in Engineering* 30 (6) (1990) 1147–1161.
- [141] W. G. Jin, Y. K. Cheung, O. C. Zienkiewicz, Trefftz method for Kirchhoff plate bending problems, *International Journal for Numerical Methods in Engineering* 36 (5) (1993) 765–781.
- [142] W. G. Jin, Y. K. Cheung, Trefftz method applied to a moderately thick plate, *International Journal for Numerical Methods in Engineering* 44 (7) (1999) 1011–1024.
- [143] R. Hiptmair, A. Moiola, I. Perugia, *A Survey of Trefftz Methods for the Helmholtz Equation*, Springer International Publishing, Cham, 2016, pp. 237–279.
- [144] M. Ochmann, The Source Simulation Technique for Acoustic Radiation Problems, *Acta Acustica united with Acustica* 81 (6) (1995) 512–527.
- [145] G. Fairweather, A. Karageorghis, The method of fundamental solutions for elliptic boundary value problems, *Advances in Computational Mathematics* 9 (1) (1998) 69–95.
- [146] G. Fairweather, A. Karageorghis, P. A. Martin, The method of fundamental solutions for scattering and radiation problems, *Engineering Analysis with Boundary Elements* 27 (7) (2003) 759–769.
- [147] M. E. Johnson, S. J. Elliott, K.-H. Baek, J. Garcia-Bonito, An equivalent source technique for calculating the sound field inside an enclosure containing scattering objects, *The Journal of the Acoustical Society of America* 104 (3) (1998) 1221–1231.
- [148] L. Koopmann, G. H. Song, J. B. Fahline, A method for computing acoustic fields based on the principle of wave superposition, *The Journal of the Acoustical Society of America* 86 (6) (1989) 2433–2438.
- [149] J. Y. Zhang, F. Z. Wang, Boundary Knot Method: An Overview and Some Novel Approaches, *Computer Modeling in Engineering & Sciences* 88 (2) (2012) 141–152.
- [150] W. Chen, Symmetric boundary knot method, *Engineering Analysis with Boundary Elements* 26 (6) (2002) 489–494.
- [151] S. Lee, Review: The Use of Equivalent Source Method in Computational Acoustics, *Journal of Computational Acoustics*, 25 (1) (2017) 1–19.
- [152] Y. Leviatan, E. Erez, M. J. Beran, A source-model technique for analysis of flexural wave scattering in a heterogeneous thin plate, *The Quarterly Journal of Mechanics and Applied Mathematics* 45 (3) (1992) 499–514.
- [153] D. Young, C. Tsai, Y. Lin, C. Chen, The Method of Fundamental Solutions for Eigenfrequencies of Plate Vibrations, *CMC-Computers Materials & Continua* 4 (1).

- [154] C. J. S. Alves, P. R. S. Antunes, The method of fundamental solutions applied to the calculation of eigensolutions for 2D plates, *International Journal for Numerical Methods in Engineering* 77 (2) (2009) 177–194.
- [155] C. S. Wu, D. L. Young, C. M. Fan, Frequency response analyses in vibroacoustics using the method of fundamental solutions, *Computational Mechanics* 47 (5) (2011) 519–533.
- [156] J. Shi, W. Chen, C. Wang, Free Vibration Analysis of Arbitrary Shaped Plates by Boundary Knot Method, *Acta Mechanica Solida Sinica* 22 (4) (2009) 328–336.
- [157] Q.-H. Qin, Trefftz Finite Element Method and Its Applications, *Applied Mechanics Reviews* 58 (5) (2005) 316–337.
- [158] J. A. Teixeira de Freitas, Hybrid-Trefftz displacement and stress elements for elastodynamic analysis in the frequency domain, *Computer Assisted Methods in Engineering and Sciences* 4 (3) (1997) 345–368.
- [159] J. Jirousek, A T-element approach to forced vibration analysis and its application to thin plates, *Tech. Rep. LSC Internal Report 97/03*, Swiss Federal Institute of Technology, Lausanne (1997).
- [160] Q.-H. Qin, Transient plate bending analysis by hybrid Trefftz element approach, *Communications in Numerical Methods in Engineering* 12 (10) (1996) 609–616.
- [161] C. Farhat, I. Harari, U. Hetmaniuk, A discontinuous Galerkin method with Lagrange multipliers for the solution of Helmholtz problems in the mid-frequency regime, *Computer Methods in Applied Mechanics and Engineering* 192 (11-12) (2003) 1389–1419.
- [162] C. Farhat, R. Tezaur, P. Weidemann-Goiran, Higher-order extensions of a discontinuous Galerkin method for mid-frequency Helmholtz problems, *International Journal for Numerical Methods in Engineering* 61 (11) (2004) 1938–1956.
- [163] R. Tezaur, C. Farhat, Three-dimensional discontinuous Galerkin elements with plane waves and Lagrange multipliers for the solution of mid-frequency Helmholtz problems, *International Journal for Numerical Methods in Engineering* 66 (5) (2006) 796–815.
- [164] A. Karageorghis, Efficient Trefftz collocation algorithms for elliptic problems in circular domains, *Numerical Algorithms* 64 (3) (2013) 427–453.
- [165] P. Monk, D.-Q. Wang, A least-squares method for the Helmholtz equation, *Computer Methods in Applied Mechanics and Engineering* 175 (1-2) (1999) 121–136.
- [166] O. Cessenat, B. Despres, Application of an Ultra Weak Variational Formulation of Elliptic PDEs to the Two-Dimensional Helmholtz Problem, *SIAM Journal on Numerical Analysis* 35 (1) (1998) 255–299.
- [167] T. Luostari, T. Huttunen, P. Monk, Improvements for the ultra weak variational formulation, *International Journal for Numerical Methods in Engineering* 94 (6) (2013) 598–624.

## Bibliography

- [168] T. Huttunen, P. Monk, F. Collino, J. P. Kaipio, The Ultra-Weak Variational Formulation for Elastic Wave Problems, *SIAM Journal on Scientific Computing* 25 (5) (2004) 1717–1742.
- [169] T. Luostari, T. Huttunen, P. Monk, The ultra weak variational formulation of thin clamped plate problems, *Journal of Computational Physics* 260 (2014) 85–106.
- [170] P. Ladevèze, L. Arnaud, P. Rouch, C. Blanzé, The variational theory of complex rays for the calculation of medium-frequency vibrations, *Engineering Computations* 18 (1-2) (2001) 193–214.
- [171] P. Rouch, P. Ladevèze, The variational theory of complex rays: a predictive tool for medium-frequency vibrations, *Computer Methods in Applied Mechanics and Engineering* 192 (28-30) (2003) 3301–3315.
- [172] B. Bergen, Wave Based Modelling Techniques for Unbounded Acoustic Problems, Ph.D. thesis, Katholieke Universiteit Leuven (2011).
- [173] I. Herrera, Boundary Methods: an Algebraic Theory, Pitman Advanced Publishing Program, London, 1984.
- [174] B. Van Genechten, B. Bergen, D. Vandepitte, W. Desmet, A Trefftz-based numerical modelling framework for Helmholtz problems with complex multiple-scatterer configurations, *Journal of Computational Physics* 229 (18) (2010) 6623–6643.
- [175] B. Van Genechten, K. Vergote, D. Vandepitte, W. Desmet, A multi-level wave based numerical modelling framework for the steady-state dynamic analysis of bounded Helmholtz problems with multiple inclusions, *Computer Methods in Applied Mechanics and Engineering* 199 (29-32) (2010) 1881–1905.
- [176] E. Deckers, B. Drofmans, B. Van Genechten, B. Bergen, D. Vandepitte, W. Desmet, Spline-based boundaries: A first step towards generic geometric domain descriptions for efficient mid-frequency acoustic analysis using the Wave Based Method, *Journal of Computational and Applied Mathematics* 235 (8) (2011) 2679–2693.
- [177] J. M. Varah, A Practical Examination of Some Numerical Methods for Linear Discrete Ill-Posed Problems, *SIAM Review* 21 (1) (1979) 100–111.
- [178] J. M. Varah, Pitfalls in the Numerical Solution of Linear Ill-Posed Problems, *SIAM Journal on Scientific and Statistical Computing* 4 (2) (1983) 164–176.
- [179] B. Pluymers, W. Desmet, D. Vandepitte, P. Sas, Wave based modelling methods for steady-state interior acoustics: an overview, in: Proceedings of the International Conference on Noise and Vibration Engineering ISMA2006, Leuven, Belgium, 2006, pp. 2303–2357.
- [180] W. Desmet, B. Pluymers, C. Vanmaele, D. Vandepitte, A review of the wave based prediction technique for efficient interior acoustic analysis, in: Proceedings of the Forum Acousticum 2005, Budapest, Hungary, 2005, pp. 151–160.
- [181] K. Vergote, C. Vanmaele, D. Vandepitte, W. Desmet, On the use of an efficient wave based method for steady-state structural dynamic analysis, in: Proceedings of the 5th International Workshop on Trefftz Methods (Trefftz.08), Leuven, Belgium, 2008, pp. 433–459.

- [182] E. Deckers, S. Jonckheere, D. Vandepitte, W. Desmet, Modelling Techniques for Vibro-Acoustic Dynamics of Poroelastic Materials, *Archives of Computational Methods in Engineering* 22 (2) (2015) 183–236.
- [183] B. van Hal, A. Hepberger, H.-H. Priebsch, W. Desmet, P. Sas, High performance implementation and conceptual development of the wave based method for steady-state dynamic analysis of acoustic problems, in: *Proceedings of the International Conference on Noise and Vibration Engineering ISMA2002*, Leuven, Belgium, 2002, pp. 817–826.
- [184] B. Pluymers, W. Desmet, B. Van Hal, D. Vandepitte, P. Sas, An object-oriented implementation scheme for an efficient wave based prediction technique for steady-state vibro-acoustic problems, in: *Proceedings of the Ninth International Congress on Sound and Vibration*, Orlando, USA, 2002, pp. 1–8.
- [185] A. Hepberger, H.-H. Priebsch, W. Desmet, B. van Hal, B. Pluymers, P. Sas, Application of the Wave Based Method for the Steady-State Acoustic Response Prediction of a Car Cavity in the Mid-frequency Range, in: *Proceedings of the International Conference on Noise and Vibration Engineering ISMA2002*, Leuven, Belgium, 2002, pp. 877–884.
- [186] B. Van Genechten, O. Atak, B. Bergen, E. Deckers, S. Jonckheere, J. S. Lee, A. Maresca, K. Vergote, B. Pluymers, D. Vandepitte, W. Desmet, An efficient Wave Based Method for solving Helmholtz problems in three-dimensional bounded domains, *Engineering Analysis with Boundary Elements* 36 (1) (2012) 63–75.
- [187] A. Hepberger, F. Diwoky, K. Jalics, H.-H. Priebsch, Application of Wave Based Technique for a cavity considering forced excitation at boundaries and effects of absorption materials, in: *Proceedings of the International Conference on Noise and Vibration Engineering ISMA2004*, Leuven, Belgium, 2004, pp. 1643–1657.
- [188] A. Hepberger, B. Pluymers, K. Jalics, H.-H. Priebsch, W. Desmet, Validation of a Wave Based Technique for the analysis of a multi-domain 3D acoustic cavity with interior damping and loudspeaker excitation, in: *Proceedings of the 33th International Congress on Noise Control Engineering Inter-Noise 2004*, Prague, Czech Republic, 2004, pp. 1–8.
- [189] E. Deckers, D. Vandepitte, W. Desmet, A Wave Based Method for the axisymmetric dynamic analysis of acoustic and poroelastic problems, *Computer Methods in Applied Mechanics and Engineering* 257 (2013) 1–16.
- [190] J. Rejlek, B. Pluymers, F. Diwoky, A. Hepberger, H.-H. Priebsch, W. Desmet, Validation of the wave based technique for the analysis of 2D steady-state acoustic radiation problems, in: *Proceedings of the International Conference on Engineering Dynamics ICED2007*, Carvoeiro, Portugal, 2007, pp. 1–8.
- [191] B. Bergen, B. Van Genechten, D. Vandepitte, W. Desmet, An Efficient Trefftz-Based Method for Three-Dimensional Helmholtz Problems in Unbounded Domains, *Computer Modeling in Engineering and Sciences* 61 (2) (2010) 155–175.

## Bibliography

- [192] J. Rejlek, Wave Based Technique for the Numerical Mid-Frequency Modelling of Coupled, Unbounded Vibro-Acoustic Problems, Ph.D. thesis, University of Technology Graz (2012).
- [193] F. Diwoky, A. Hepberger, T. Mócsai, H. Pramberger, H.-H. Priebsch, Application of the Wave Based Method to 3D radiation problems, in: Proceedings of the 5th International Workshop on Trefftz Methods (Trefftz.08), Leuven, Belgium, 2008, pp. 1–15.
- [194] T. Mócsai, A. Hepberger, F. Diwoky, H.-H. Priebsch, Engine radiation simulation up to 3kHz using the Wave Based Technique, in: Proceedings of the 16th International Congress on Sound and Vibration ICSV 2009, Kraków, Poland, 2009, pp. 1–8.
- [195] T. Mócsai, A. Hepberger, F. Diwoky, H.-H. Priebsch, Investigations on potential improvements of the Wave Based Technique for the application to radiation problems under anechoic conditions, in: Proceedings of the International Conference on Noise and Vibration Engineering ISMA2008, Leuven, Belgium, 2008, pp. 1547–1562.
- [196] B. Bergen, B. Pluymers, B. Van Genechten, D. Vandepitte, W. Desmet, A Trefftz based method for solving Helmholtz problems in semi-infinite domains, *Engineering Analysis with Boundary Elements* 36 (1) (2012) 30–38.
- [197] J. Rejlek, B. Pluymers, A. Hepberger, H.-H. Priebsch, W. Desmet, Application of the Wave Based Technique for steady-state semi-infinite sound radiation analysis, *Computer Assisted Mechanics and Engineering Sciences* 15 (3/4) (2008) 337–351.
- [198] C. Vanmaele, K. Vergote, D. Vandepitte, W. Desmet, Simulation of in-plane vibrations of 2D structural solids with singularities using an efficient wave based prediction technique, *Computer Assisted Methods in Engineering and Science* 19 (2) (2012) 135–171.
- [199] B. van Hal, W. Desmet, D. Vandepitte, P. Sas, An efficient prediction technique for the steady-state dynamic analysis of flat plates, in: Proceedings of the 29th International Congress on Noise Control Engineering Inter-Noise 2000, Nice, France, 2000, pp. 1–5.
- [200] B. van Hal, W. Desmet, D. Vandepitte, Steady-state response analysis of a flat convex plate by the wave based prediction technique, in: Proceedings of the 5th National Congress on Theoretical and Applied Mechanics, Louvain-la-Neuve, Belgium, 2000, pp. 87–90.
- [201] B. van Hal, W. Desmet, D. Vandepitte, P. Sas, Application of the efficient wave based prediction technique for the steady-state dynamic analysis of flat plates, in: Proceedings of the International Conference on Noise and Vibration Engineering ISMA25, Leuven, Belgium, 2000, pp. 607–614.
- [202] H. Devriendt, D. Vandepitte, W. Desmet, Vibro-acoustic simulation of damped orthotropic plates with the wave based method, in: Proceedings of the International Conference on Noise and Vibration Engineering ISMA2014 including USD2014, Leuven, Belgium, 2014, pp. 2261–2276.
- [203] X. Xia, Z. Xu, Z. Zhang, Y. He, Bending vibration prediction of orthotropic plate with wave-based method, *Journal of Vibroengineering* 19 (3) (2017) 1546–1556.

- [204] C. Vanmaele, W. Desmet, D. Vandepitte, On the use of the wave based method for the steady-state dynamic analysis of three-dimensional plate assemblies, in: Proceedings of the International Conference on Noise and Vibration Engineering ISMA2004, Leuven, Belgium, 2004, pp. 1643–1657.
- [205] K. Vergote, C. Vanmaele, D. Vandepitte, W. Desmet, An efficient wave based approach for the time-harmonic vibration analysis of 3D plate assemblies, *Journal of Sound and Vibration* 332 (8) (2013) 1930–1946.
- [206] W. Desmet, P. Sas, D. Vandepitte, A Wave Based Prediction Technique for Vibro-Acoustic Systems with Cylindrical Shell Components, in: Proceedings of the Fifth International Congress on Sound and Vibration, Adelaide, Australia, 1997, pp. 1–11.
- [207] M. Chen, J. Wei, K. Xie, N. Deng, G. Hou, Wave based method for free vibration analysis of ring stiffened cylindrical shell with intermediate large frame ribs, *Shock and Vibration* 20 (3) (2013) 459–479.
- [208] J. Wei, M. Chen, G. Hou, K. Xie, N. Deng, Wave Based Method for Free Vibration Analysis of Cylindrical Shells With Nonuniform Stiffener Distribution, *Journal of Vibration and Acoustics* 135 (6) (2013) 1–13.
- [209] M. Chen, K. Xie, K. Xu, P. Yu, Wave Based Method for Free and Forced Vibration Analysis of Cylindrical Shells With Discontinuity in Thickness, *Journal of Vibration and Acoustics* 137 (5) (2015) 1–14.
- [210] K. Xie, M. Chen, L. Zhang, D. Xie, Wave based method for vibration analysis of elastically coupled annular plate and cylindrical shell structures, *Applied Acoustics* 123 (2017) 107–122.
- [211] K. Xie, M. Chen, L. Zhang, D. Xie, Free and forced vibration analysis of non-uniformly supported cylindrical shells through wave based method, *International Journal of Mechanical Sciences* 128-129 (2017) 512–526.
- [212] W. Desmet, P. Sas, D. Vandepitte, An indirect Trefftz method for the steady-state dynamic analysis of coupled vibro-acoustic systems, *Computer Assisted Methods in Engineering and Science* 8 (2/3) (2001) 271–288.
- [213] W. Desmet, B. van Hal, P. Sas, D. Vandepitte, A computationally efficient prediction technique for the steady-state dynamic analysis of coupled vibro-acoustic systems, *Advances in Engineering Software* 33 (7-10) (2002) 527–540.
- [214] B. Pluymers, W. Desmet, D. Vandepitte, P. Sas, Application of the wave based prediction technique for the analysis of the coupled vibro-acoustic behaviour of a 3D cavity, in: Proceedings of the International Conference on Noise and Vibration Engineering ISMA2002, Leuven, Belgium, 2002, pp. 891–900.
- [215] B. Pluymers, W. Desmet, D. Vandepitte, P. Sas, Application of an efficient wave-based prediction technique for the analysis of vibro-acoustic radiation problems, *Journal of Computational and Applied Mathematics* 168 (1) (2004) 353–364.
- [216] B. Pluymers, W. Desmet, D. Vandepitte, P. Sas, On the use of a wave based prediction technique for steady-state structural-acoustic radiation analysis, *Computer Modeling in Engineering and Sciences* 7 (2) (2005) 173–183.

## Bibliography

- [217] J. Rejlek, H.-H. Priebsch, Wave based technique for the analysis of fully coupled structural-acoustic unbounded problems, in: Proceedings of the International Conference on Noise and Vibration Engineering ISMA2010 including USD2010, Leuven, Belgium, 2010, pp. 2407–2424.
- [218] R. Lanoye, G. Vermeir, W. Lauriks, F. Sgard, W. Desmet, Application of the wave based technique for the sound field prediction above a patchwork of acoustic absorbing materials, in: Proceedings of the Forum Acousticum 2005, Budapest, Hungary, 2005, pp. 1–6.
- [219] R. Lanoye, G. Vermeir, W. Lauriks, F. Sgard, W. Desmet, Prediction of the sound field above a patchwork of absorbing materials, *The Journal of the Acoustical Society of America* 123 (2) (2008) 793–802.
- [220] E. Deckers, A Wave Based Approach for Steady-State Biot Models of Poroelastic Materials, Ph.D. thesis, Katholieke Universiteit Leuven (2012).
- [221] E. Deckers, N.-E. Hörlin, D. Vandepitte, W. Desmet, A Wave Based Method for the efficient solution of the 2D poroelastic Biot equations, *Computer Methods in Applied Mechanics and Engineering* 201-204 (2012) 245–262.
- [222] E. Deckers, B. Van Genechten, D. Vandepitte, W. Desmet, Efficient treatment of stress singularities in poroelastic wave based models using special purpose enrichment functions, *Computers and Structures* 89 (11-12) (2011) 1117–1130.
- [223] J. Jegorovs, On the convergence of the WBM solution in certain nonconvex domains, in: Proceedings of the International Conference on Noise and Vibration Engineering ISMA2006, Leuven, Belgium, 2006, pp. 2201–2209.
- [224] C. Vanmaele, D. Vandepitte, W. Desmet, Application of the Wave Based Prediction Technique for structural problems with stress singularities, in: Proceedings of the International Conference on Noise and Vibration Engineering ISMA2006, Leuven, Belgium, 2006, pp. 2405–2424.
- [225] E. Deckers, B. Bergen, B. Van Genechten, D. Vandepitte, W. Desmet, An efficient Wave Based Method for 2D acoustic problems containing corner singularities, *Computer Methods in Applied Mechanics and Engineering* 241-244 (2012) 286–301.
- [226] E. Deckers, D. Vandepitte, W. Desmet, An efficient wave based method for 2D dynamic poroelastic problems with corner stress singularities, in: Proceedings of the International Conference on Noise and Vibration Engineering ISMA2010 including USD2010, Leuven, Belgium, 2010, pp. 2267–2284.
- [227] J. S. Lee, E. Deckers, S. Jonckheere, W. Desmet, Y. Y. Kim, A direct hybrid finite element-wave based modelling technique for efficient analysis of poroelastic materials in steady-state acoustic problems, *Computer Methods in Applied Mechanics and Engineering* 304 (2016) 55–80.
- [228] B. Van Genechten, B. Bergen, B. Pluymers, D. Vandepitte, W. Desmet, A novel modelling approach for sound propagation analysis in a multiple scatterer environment, in: Proceedings of Acoustics08, 2008, pp. 5223–5228.

- [229] O. Atak, Wave Based Modeling Methods for Acoustic Inclusion and Multiple Scattering Problems in the Mid-Frequency Range, Ph.D. thesis, Katholieke Universiteit Leuven (2014).
- [230] B. Van Genechten, Trefftz-Based Mid-Frequency Analysis of Geometrically Complex Vibro-Acoustic Systems - Hybrid Methodologies and Multi-Level Modelling, Ph.D. thesis, Katholieke Universiteit Leuven (2010).
- [231] E. Deckers, S. Jonckheere, W. Desmet, A Multi-Level Wave Based Method to predict the dynamic response of 2D poroelastic materials containing inclusions, in: Proceedings of the 10th European Congress and Exposition on Noise Control Engineering EuroNoise2015, Maastricht, Netherlands, 2015, pp. 1155–1160.
- [232] L. Chen, L. Li, Wave-based prediction analysis for dynamic-response problem in non-convex domain, *Journal of Vibroengineering* 17 (4) (2015) 1671–1683.
- [233] B. van Hal, W. Desmet, D. Vandepitte, P. Sas, A coupled finite element-wave based approach for the steady-state dynamic analysis of acoustic systems, *Journal of Computational Acoustics* 11 (2) (2003) 285–303.
- [234] B. van Hal, W. Desmet, D. Vandepitte, P. Sas, Hybrid Finite Element - Wave Based Method for Acoustic Problems, *Computer Assisted Methods in Engineering and Science* 10 (4) (2003) 479–494.
- [235] P. Silar, A. Hepberger, B. Pluymers, W. Desmet, T. Bartosch, H. Pramberger, Investigation of a coupled finite element-wave based technique for 2D steady-state acoustic analysis comparing a direct and an indirect approach, in: Proceedings of the Thirteenth International Congress on Sound and Vibration ICSV13, Vienna, Austria, 2006, pp. 1–8.
- [236] B. van Hal, W. Desmet, D. Vandepitte, Hybrid finite element - wave-based method for steady-state interior structural-acoustic problems, *Computers and Structures* 83 (2) (2005) 167–180.
- [237] B. Pluymers, C. Vanmaele, W. Desmet, D. Vandepitte, Application of a hybrid finite element - Trefftz approach for acoustic analysis, *Computer Assisted Mechanics and Engineering Sciences* 13 (3) (2006) 427–444.
- [238] B. Pluymers, B. Van Genechten, P. Silar, A. Hepberger, W. Desmet, Validation of a direct/indirect hybrid finite element-wave based method for 3D steady-state acoustic analysis, in: Proceedings of the International Conference on Engineering Dynamics ICED2007, Carvoeiro, Portugal, 2007, pp. 1–8.
- [239] B. Van Genechten, D. Vandepitte, W. Desmet, A hybrid wave based vibro-acoustic modelling technique for the prediction of interior noise in an aircraft fuselage, in: Proceedings of the 25th Congress of International Council of the Aeronautical Sciences ICAS2006, Hamburg, Germany, 2006, pp. 1–10.
- [240] S. Jonckheere, M. Vivolo, B. Pluymers, D. Vandepitte, W. Desmet, Vibro-Acoustic Characterisation of Lightweight Structures: A Numerical-Experimental Approach, in: Proceedings of the 7th International Styrian Nose, Vibration & Harshness Congress ISNVH2012, Graz, Austria, 2012, pp. 1–15.

## Bibliography

- [241] B. Van Genechten, B. Pluymers, C. Vanmaele, D. Vandepitte, W. Desmet, On the coupling of Wave Based models with modally reduced Finite Element models for structural-acoustic analysis, in: Proceedings of the International Conference on Noise and Vibration Engineering ISMA2006, Leuven, Belgium, 2006, pp. 2383–2403.
- [242] B. Van Genechten, D. Vandepitte, W. Desmet, On the coupling of Wave Based models with modally reduced Finite Element models for 3D interior acoustic analysis, in: Proceedings of the International Conference on Noise and Vibration Engineering ISMA2008, Leuven, Belgium, 2008, pp. 1631–1651.
- [243] B. Van Genechten, B. Pluymers, D. Vandepitte, W. Desmet, A Hybrid Wave Based - Modally Reduced Finite Element Method for the Efficient Analysis of Low- and Mid-Frequency Car Cavity Acoustics, *SAE International Journal of Passenger Cars - Mechanical Systems* 2 (1) (2009) 1494–1504.
- [244] A. Maressa, S. Jonckheere, B. Van Genechten, B. Pluymers, W. Desmet, Hybrid Finite Element-Wave Based techniques for interior vibro-acoustics. Application to a large-sized vehicle model, in: Proceedings of the International Conference on Noise and Vibration Engineering ISMA2012 including USD2012, Leuven, Belgium, 2012, pp. 3937–3950.
- [245] B. Bergen, E. Deckers, B. Van Genechten, D. Vandepitte, W. Desmet, An explicit Wave based model as alternative to the DtN map for solving unbounded Helmholtz problems with the finite element method, *Engineering Analysis with Boundary Elements* 55 (2015) 58–66.
- [246] C. Vanmaele, W. Desmet, D. Vandepitte, A direct hybrid finite element - wave based prediction technique for the steady state dynamic analysis of two dimensional solids, in: Proceedings of the 12th International Congress on Sound and Vibration ICSV12, Lisbon, Portugal, 2005, pp. 1–8.
- [247] J. S. Lee, E. Deckers, S. Jonckheere, W. Desmet, A direct hybrid wave based - finite element modeling of poroelastic materials, in: Proceedings of the Symposium on the Acoustics of Poro-Elastic Materials SAPEM2011, Ferrara, Italy, 2011.
- [248] S. Jonckheere, E. Deckers, B. Van Genechten, D. Vandepitte, W. Desmet, A direct hybrid Finite Element - Wave Based Method for the steady-state analysis of acoustic cavities with poro-elastic damping layers using the coupled Helmholtz-Biot equations, *Computer Methods in Applied Mechanics and Engineering* 263 (2013) 144–157.
- [249] O. Atak, B. Bergen, D. Huybrechs, B. Pluymers, W. Desmet, Coupling of Boundary Element and Wave Based Methods for the efficient solution of complex multiple scattering problems, *Journal of Computational Physics* 258 (2014) 165–184.
- [250] O. Atak, D. Huybrechs, B. Pluymers, W. Desmet, Coupling of Boundary Element and Wave Based Methods for the efficient solution of bounded acoustic problems with inclusions, in: Proceedings of the International Conference on Noise and Vibration Engineering ISMA2014 including USD2014, Leuven, Belgium, 2014, pp. 4247–4257.

- [251] O. Atak, S. Jonckheere, E. Deckers, D. Huybrechs, B. Pluymers, W. Desmet, A hybrid Boundary Element-Wave Based Method for an efficient solution of bounded acoustic problems with inclusions, *Computer Methods in Applied Mechanics and Engineering* 283 (2015) 1260–1277.
- [252] K. Vergote, B. Van Genechten, D. Vandepitte, W. Desmet, On the analysis of vibro-acoustic systems in the mid-frequency range using a hybrid deterministic-statistical approach, *Computers and Structures* 89 (11-12) (2011) 868–877.
- [253] R. S. Langley, J. A. Cordioli, Hybrid deterministic-statistical analysis of vibro-acoustic systems with domain couplings on statistical components, *Journal of Sound and Vibration* 321 (3-5) (2009) 893–912.
- [254] A. Dijckmans, G. Vermeir, Development of a hybrid wave based-transfer matrix model for sound transmission analysis, *The Journal of the Acoustical Society of America* 133 (4) (2013) 2157–2168.
- [255] A. Dijckmans, G. Vermeir, Hybrid wave based - transfer matrix modeling of sound insulation problems, in: *Proceedings of the International Conference on Noise and Vibration Engineering ISMA2014 including USD2014*, Leuven, Belgium, 2014, pp. 2277–2292.
- [256] S. Jonckheere, D. Vandepitte, W. Desmet, A Wave Based Transfer Matrix Method for accurate simulation of acoustic problems with multilayered damping treatment, in: *Proceedings of the 10th European Congress and Exposition on Noise Control Engineering EuroNoise2015*, Maastricht, Netherlands, 2015, pp. 1149–1154.
- [257] B. van Hal, W. Desmet, B. Pluymers, P. Sas, D. Vandepitte, Improving the Wave Based Method for the Steady-State Dynamic Analysis of Acoustic Systems, in: *Proceedings of the 9th International Congress on Sound and Vibration ICSV 9*, Orlando, USA, 2002, pp. 1–8.
- [258] J. Jegorovs, J. Mohring, Wave Based Method in a complex domain: accuracy improvement, in: *Proceedings of the International Conference on Noise and Vibration Engineering ISMA2008*, Leuven, Belgium, 2008, pp. 1533–1545.
- [259] J. Rejlek, F. Diwoky, A. Hepberger, B. Pluymers, Wave Based Technique: enrichment of the set of basis functions, in: *Proceedings of the International Conference on Noise and Vibration Engineering ISMA2008*, Leuven, Belgium, 2008, pp. 1533–1545.
- [260] T. Mócsai, F. Diwoky, H.-H. Priebsch, The application of the Wave Based Technique for 3D free-field radiation calculation using a residual error controlled adaptive strategy, in: *Proceedings of the International Conference on Noise and Vibration Engineering ISMA2010 including USD2010*, Leuven, Belgium, 2010, pp. 2393–2405.
- [261] T. Mócsai, F. Diwoky, A. Hepberger, H.-H. Priebsch, F. Augusztinovicz, Application and analysis of an adaptive wave-based technique based on a boundary error indicator for the sound radiation simulation of a combustion engine model, *Computer Assisted Methods in Engineering and Science* 22 (1) (2015) 3–30.

## Bibliography

- [262] K. Vergote, B. Van Genechten, B. Pluymers, D. Vandepitte, W. Desmet, A Wave Based Prediction Technique for the Dynamic Response Analysis of Plates with Random Point Mass Distributions, in: Proceedings of the 9th International Conference on Computational Structures Technology CST2008, Athens, Greece, 2008, pp. 1–14.
- [263] B. Xia, H. Yin, D. Yu, Nondeterministic wave-based methods for low- and mid-frequency response analysis of acoustic field with limited information, *Mechanical Systems and Signal Processing* 84 (A) (2017) 169–183.
- [264] J. Jegorovs, Wave based method: new applicability areas, *Tech. Rep.* 178, Fraunhofer-Institut für Techno- und Wirtschaftsmathematik (2009).
- [265] J. Jegorovs, On hidden potentials of the wave based method, in: Proceedings of the International Conference on Noise and Vibration Engineering ISMA2010 including USD2010, Leuven, Belgium, 2010, pp. 2361–2370.
- [266] J. Jegorovs, On the extension of the wave based method, in: Proceedings of the International Conference Days on Diffraction 2010, St. Petersburg, Russia, 2010, pp. 85–92.
- [267] A. Dijckmans, G. Vermeir, W. Lauriks, Sound transmission through finite light-weight multilayered structures with thin air layers, *The Journal of the Acoustical Society of America* 128 (6) (2010) 3513–3524.
- [268] E. Deckers, C. Claeys, O. Atak, J.-P. Groby, O. Dazel, W. Desmet, A wave based method to predict the absorption, reflection and transmission coefficient of two-dimensional rigid frame porous structures with periodic inclusions, *Journal of Computational Physics* 312 (2016) 115–138.
- [269] X.-S. He, Q.-B. Huang, W.-C. Peng, Wave based method for mid-frequency analysis of coupled vibro-acoustic problem, *International Journal of Mechanics and Materials in Design* 4 (1) (2008) 21–29.
- [270] K. Koo, B. Pluymers, W. Desmet, S. Wang, Acoustic Design Sensitivity Analysis of 3D vibro-acoustic problems using the Wave Based Method, in: Proceedings of the International Conference on Noise and Vibration Engineering ISMA2010 including USD2010, Leuven, Belgium, 2010, pp. 2371–2380.
- [271] K. Koo, B. Pluymers, W. Desmet, S. Wang, Vibro-acoustic design sensitivity analysis using the wave-based method, *Journal of Sound and Vibration* 330 (17) (2011) 4340–4351.
- [272] S. Goo, S. Wang, J. Kook, K. Koo, J. Hyun, Topology optimization of bounded acoustic problems using the hybrid finite element-wave based method, *Computer Methods in Applied Mechanics and Engineering* 313 (2017) 834–856.
- [273] O. Atak, D. Huybrechs, B. Pluymers, W. Desmet, The design of Helmholtz resonator based acoustic lenses by using the symmetric Multi-Level Wave Based Method and genetic algorithms, *Journal of Sound and Vibration* 333 (15) (2014) 3367–3381.

- [274] K. Vergote, D. Vandepitte, W. Desmet, Application of the Wave Based Method for the calculation of structural intensity and power flow in plates, in: Proceedings of the International Conference on Noise and Vibration Engineering ISMA2008, Leuven, Belgium, 2008, pp. 1653–1665.
- [275] R. D'Amico, K. Vergote, R. Langley, W. Desmet, On the use of the Lorentzian function for the evaluation of the frequency averaged input power into plates, in: Proceedings of the International Conference on Noise and Vibration Engineering ISMA2012 including USD2012, Leuven, Belgium, 2012, pp. 1747–1760.
- [276] K. Vergote, J. S. Lee, C. C. Claeys, D. Vandepitte, W. Desmet, On the potential of the wave based method for the efficient optimisation of local vibration control treatments for structural components, in: Proceedings of the International Conference on Noise and Vibration Engineering ISMA2012 including USD2012, Leuven, Belgium, 2012, pp. 1985–2002.
- [277] S. Jonckheere, D. Vandepitte, W. Desmet, Accuracy of vibro-acoustic simulations with approximative multilayer damping models, in: Proceedings of the International Conference on Noise and Vibration Engineering ISMA2014 including USD2014, Leuven, Belgium, 2014, pp. 4233–4248.
- [278] L. Debnath, D. Bhatta, Integral Transforms and Their Applications, CRC Press, Boca Raton, 2014.
- [279] D. Mitrinović, J. D. Kečkić, The Cauchy Method of Residues, D. Reidel Publishing Company, Dordrecht, 1984.
- [280] J. S. Rao, Dynamics of Plates, Narosa Publishing House, New Delhi, 1999.
- [281] G. N. Watson, A Treatise on the Theory of Bessel Functions, Cambridge University Press, London, 1944.
- [282] P. J. T. Filippi, Vibrations and Acoustic Radiation of Thin Structures: Physical Basis, Theoretical Analysis and Numerical Methods, Wiley, Hoboken, 2010.
- [283] W. Magnus, F. Oberhettinger, R. P. Soni, Formulas and Theorems for the Special Functions of Mathematical Physics, Springer Verlag, Berlin, 1966.
- [284] M. Abramowitz, I. A. Stegun, Handbook of Mathematical Functions: with Formulas, Graphs, and Mathematical Tables, Dover Publications, New York, 1972.
- [285] G. Martinček, Dynamics of Pavement Structures, Taylor & Francis, London, 1994.
- [286] Q.-G. Lin, Infinite integrals involving Bessel functions by an improved approach of contour integration and the residue theorem, *The Ramanujan Journal* 35 (3) (2014) 443–466.
- [287] B. G. Korenev, Bessel Functions and their Applications, Taylor & Francis, London, 2002.
- [288] M. Klanner, K. Ellermann, Solutions of vibration problems for thin infinite plates subjected to harmonic loads, *Journal of Theoretical and Applied Mechanics* 55 (3) (2017) 949–961.

## Bibliography

- [289] G. B. Sinclair, Stress singularities in classical elasticity – I: Removal, interpretation, and analysis, *Applied Mechanics Reviews* 57 (4) (2004) 251–298.
- [290] C. S. Huang, Stress singularities at angular corners in first-order shear deformation plate theory, *International Journal of Mechanical Science* 45 (1) (2003) 1–20.
- [291] G. B. Sinclair, Stress singularities in classical elasticity – II: Asymptotic identification, *Applied Mechanics Reviews* 57 (5) (2004) 385–439.
- [292] R. D. Mindlin, H. Deresiewicz, Thickness-Shear and Flexural Vibrations of a Circular Disk, *Journal of Applied Physics* 25 (10) (1954) 1329–1332.
- [293] W. S. Burton, G. B. Sinclair, On the Singularities in Reissner’s Theory for the Bending of Elastic Plates, *Journal of Applied Mechanics* 53 (1) (1986) 220–222.
- [294] D. H. Y. Yen, M. Zhou, On the Corner Singularities in Reissner’s Theory for the Bending of Elastic Plates, *Journal of Applied Mechanics* 56 (3) (1989) 726–729.
- [295] A. Rössle, A.-M. Sändig, Corner Singularities and Regularity Results for the Reissner/Mindlin Plate Model, *Journal of Elasticity* 103 (2) (2011) 113–135.
- [296] J. Felger, W. Becker, A complex potential method for the asymptotic solution of wedge problems using first-order shear deformation plate theory, *European Journal of Mechanics - A/Solids* 61 (2017) 383–392.
- [297] W. Yao, Z. Zhang, X. Hu, Jordan form asymptotic solutions near the tip of a V-shaped notch in Reissner plate, *International Journal of Solids and Structures* 75-76 (2015) 225–234.
- [298] C. S. Huang, Corner singularities in bi-material Mindlin plates, *Composite Structures* 56 (3) (2002) 315–327.
- [299] A. Jeffrey, *Advanced Engineering Mathematics*, Harcourt/Academic Press, San Diego, 2002.
- [300] G. H. Golub, C. F. Van Loan, *Matrix Computations*, The Johns Hopkins University Press, Baltimore, 2013.
- [301] Multiprecision Computing Toolbox for MATLAB 4.4.7.12739, Advanpix LLC., Yokohama, Japan.
- [302] O. A. Bauchau, *Flexible Multibody Dynamics*, Springer-Verlag, Dordrecht, 2011.
- [303] J. S. Rao, *History of Rotating Machinery Dynamics*, Springer-Verlag, Dordrecht, 2011.
- [304] S. S. Holland, *Applied Analysis by the Hilbert Space Method*, Marcel Dekker, New York, 1990.

# Curriculum Vitae

## Personal data

Michael Klanner

° September 9, 1988 in Wels, Austria

[michael.klanner@tugraz.at](mailto:michael.klanner@tugraz.at)

## Education

### 2013-2018

Ph.D student at the Doctorial School of Mechanical Engineering (University of Technology Graz, Graz, Austria).

Title: *"Wave Based Method for Structural Vibrations of Thick Plates"*.

### 2011-2013

MSc in Mechanical Engineering and Business Economics, option Computational Engineering and Mechatronics, University of Technology Graz (Austria)

Title: *"Erweiterung eines Modells zur Simulation der strukturdynamischen Anregung von elektrischen Maschinen"*.

### 2008-2011

BSc in Mechanical Engineering and Business Economics, University of Technology Graz (Austria)

Title: *"Eignung der Trochoidenverzahnung für hochübersetzende Getriebe"*.

## Work

### 2013-2018

University assistant

Faculty Mechanical Engineering and Economic Sciences, Institute of Mechanics  
University of Technology Graz, Graz, Austria



## List of Publications

- [1] M. Klanner, M. Mair, F. Diwoky, O. Biro, K. Ellermann, Coupling node reduction of a synchronous machine using multipoint-constraints, in: 8th International Styrian Noise, Vibration & Harshness Congress: The European Automotive Noise Conference, no. 2014-01-2067, Graz, Austria, 2014.
- [2] M. Klanner, K. Ellermann, Wave Based Method for the steady-state vibrations of thick plates, *Journal of Sound and Vibration* 345 (2015) 146–161.
- [3] M. Klanner, K. Ellermann, Application of the Wave Based Method to steady-state vibrations of thick plates, in: Proceedings of ICoEV 2015 International Conference on Engineering Vibration, Ljubljana, Slovenia, 2015, pp. 163–172.
- [4] M. Klanner, K. Ellermann, Improvement of the Wave Based Method for thick plate vibrations, *International Journal of Acoustics and Vibration* (2016) accepted for publication.
- [5] M. Klanner, K. Ellermann, Wave Based Method for the vibrations of moderately thick plates including corner stress singularities, in: Proceedings of ISMA2016 International Conference on Noise and Vibration Engineering, Leuven, Belgium, 2016, pp. 1975–1989.
- [6] M. Klanner, K. Ellermann, Solutions of vibration problems for thin infinite plates subjected to harmonic loads, *Journal of Theoretical and Applied Mechanics* 55 (3) (2017) 949–961.
- [7] A. Acri, E. Nijman, M. Klanner, R. Corradi, G. Offner, On the influence of cyclic variability on surface noise contribution analysis of internal combustion engines, *Applied Acoustics* 132 (2018) 97–108.



